

Computer Science, Technology and Applications

# Scientific Computing



Caj Erling  
Editor

## Studies and Applications

NOVA

In: Scientific Computing  
Editor: Caj Erling

ISBN: 978-1-53612-564-1  
© 2017 Nova Science Publishers, Inc.

*Chapter 3*

# EFFICIENT NUMERICAL TOOLS FOR SOLVING THE NONLINEAR SCHRÖDINGER EQUATION

*Vladimir Lončar, Ivana Vasić and Antun Balazž\**

Scientific Computing Laboratory,  
Center for the Study of Complex Systems,  
Institute of Physics Belgrade, University of Belgrade,  
Belgrade, Serbia

## Abstract

The nonlinear Schrödinger equation or Gross-Pitaevskii equation plays an important role in several areas of physical sciences. It is used in various forms to describe prominent physical phenomena, such as propagation of light in a nonlinear medium and the dynamics of weakly interacting Bose-Einstein condensates studied in experiments with ultracold quantum gases. Large-scale numerical simulations for realistically large physical systems based on this equation have provided valuable insights into the properties of many interesting phenomena. Furthermore, numerical solutions of this equation are now routinely used for interpretation of experimental data and are indispensable for day-to-day operation of many laboratories, as well as for the design of new experimental setups.

In this chapter we review an efficient numerical algorithm for solving this nonlinear partial differential equation in three spatial coordinates

---

\*Corresponding Author Email: antun.balaz@ipb.ac.rs.



and either real or imaginary time, based on the Crank-Nicolson split-step semi-implicit method. Integration over imaginary time provides a direct access to stationary solutions of the full time-dependent problem. General spatially anisotropic solutions in three spatial variables are considered, as well as dimensionally-reduced problems such as radially or spherically symmetric cases.

Stability and efficiency of the presented method is ensured in the following way. The discretization error in both time and spatial step is of the second order. Moreover, integration over the time variable is split into two steps that are dealt with in a different, but optimized way. In the first step, only local part of the equation is taken into account and integration is performed exactly with respect to it. In this way the nonlinear term is considered in a straightforward, but optimized way that allows for a treatment of strong nonlinearities. In the second step, spatial derivatives are considered separately. Semi-implicit nature of the algorithm also contributes to its stability.

This method is numerically implemented using the standard C programming language. Further computational optimization is achieved by employing the state-of-the-art parallelization techniques for different computing platforms: OpenMP (for shared memory multiprocessing), OpenMP/MPI (for distributed memory systems, where each compute node uses OpenMP to maximize performance), CUDA (for single GPGPUs), CUDA/MPI (for distributed memory systems, where each compute node has GPGPU installed), as well as their hybrid combinations. The scalability of the algorithm with the number of processors and compute nodes is discussed.

As applications and extensions of the above developed algorithms, we present three relevant examples from the field of ultracold atoms. The first application illustrates how the non-equilibrium dynamics of multicomponent Bose-Einstein condensates can be numerically studied, including the excitation dynamics of a condensate with a coupling of the effective spin and angular momentum in the second application. The third application demonstrates how formation of vortices can be studied in a condensate featuring contact, as well as long-range dipole-dipole interaction.

**PACS:** 02.60.Lj, 02.60.Jh, 02.60.Cb, 03.75.-b

**Keywords:** Bose-Einstein condensate, Gross-Pitaevskii equation, Dipole-dipole interaction, OpenMP, MPI, CUDA, Crank-Nicolson method

## 1. Introduction

One of the important breakthroughs in physics of the twentieth century was the development of quantum mechanics. The key ingredient of this theory is the Schrödinger equation: a linear equation that governs the time evolution of a quantum system. In one of its common representations, Schrödinger equation is a partial differential equation.

Full quantum description of an interacting many-body system easily becomes computationally demanding due to exponentially increasing underlying vector space with the system size. For this reason, approximate descriptions that capture main physical phenomena are highly sought-after. The nonlinear Schrödinger (NLS) equation represents an effective, mean-field description of a quantum system. It is of great relevance in the field of cold atoms, in particular for a description and understanding of a weakly interacting bosonic systems at low temperatures in the regime of Bose-Einstein condensation [1]. In this context, the equation is widely known as Gross-Pitaevskii equation [2, 3] and it has provided valuable theoretical understanding of experimental results. Another field of research where the NLS equation plays a prominent role is the field of nonlinear optics that was initiated by the discovery of lasers in 1960 [4]. As analytical solutions of the NLS equation are limited to just a few special cases, the NLS equation was investigated numerically starting in the seventies using several different numerical methods [5]. The development of present-day computer architectures promotes numerical simulations and enables studies of more complex physical problems for experimentally relevant system sizes.

In this chapter we first introduce the NLS equation and derive an algorithm for obtaining its solutions based on a split-step method. In the next step we present an optimized implementation of this algorithm that heavily exploits parallelization techniques available on present-day state-of-the-art computer architectures. In the last sections of this chapter we illustrate applications of the described method for three examples that are currently in a research focus of cold-atom community.

## 2. Algorithm and Computational Implementation

### 2.1. Introduction

The time–dependent nonlinear Schrödinger equation in a dimensionless form is given by

$$i \frac{\partial \psi(\mathbf{r}, t)}{\partial t} = \left( -\frac{1}{2} \Delta + V(\mathbf{r}) + g |\psi(\mathbf{r}, t)|^2 \right) \psi(\mathbf{r}, t), \quad (1)$$

where  $\Delta$  is the three-dimensional Laplace operator  $\Delta \equiv \frac{\partial^2}{\partial x^2} + \frac{\partial^2}{\partial y^2} + \frac{\partial^2}{\partial z^2}$ . The usual Schrödinger equation describing the time–evolution of a single–particle wave function  $\psi(\mathbf{r}, t)$  is recovered by eliminating the nonlinear term by setting  $g = 0$ . The wave function depends on four variables: three spatial coordinates  $\mathbf{r} = (x, y, z)$  and time  $t$ . The real–valued function  $V(\mathbf{r})$  corresponds to an external potential, and before mentioned Laplacian stems from the kinetic energy. Initial conditions are appropriately set by fixing  $\psi(\mathbf{r}, t = 0) = \psi_{\text{initial}}(\mathbf{r})$  and then the time evolution for  $t > 0$  is studied. The equation (1) conserves the normalization of the function  $\psi(\mathbf{r}, t)$

$$\int d\mathbf{r} |\psi(\mathbf{r}, t)|^2 = 1, \quad (2)$$

which in physical terms corresponds to the conservation of the particle number, as well as the total energy of the system,

$$E = \int d\mathbf{r} \psi^*(\mathbf{r}, t) \left( -\frac{1}{2} \Delta + V(\mathbf{r}) + \frac{g}{2} |\psi(\mathbf{r}, t)|^2 \right) \psi(\mathbf{r}, t). \quad (3)$$

In the context of cold atoms, the complex–valued function  $\psi(\mathbf{r}, t)$  stands for a condensate wave function – an effective single particle wave function macroscopically occupied by bosonic particles. The constant  $g$  is set by weak atomic interactions that we approximate by contact interactions: repulsive interactions yield  $g > 0$ , while attractive interactions are described by  $g < 0$ . The phase of a system described by the nonlinear Schrödinger equation is called a Bose–Einstein condensate (BEC). Macroscopic occupation of a single particle state (a finite condensate fraction) is a consequence of bosonic statistics (Bose–Einstein statistics) that becomes of key importance at very low temperatures. The phenomenon of Bose–Einstein condensation was predicted in early days of quantum mechanics in 1924 when the Bose–Einstein statistics was derived for the

first time. After several decades of experimental efforts, first experimental realization of a BEC with nanokelvin-cold atoms was reported in 1995 [6, 7, 8]. This success marked the onset of intense research activity in the field of cold atoms where the description based on the nonlinear Schrödinger equation played an important role [9, 10, 11, 12, 1, 13, 14]. Formally, the equation (1) can be derived by using the time–dependent variational principle. The time–dependent spatial density distribution of a condensate is given by

$$n(\mathbf{r}, t) = |\psi(\mathbf{r}, t)|^2. \quad (4)$$

Equation (1) governs the time evolution of a weakly interacting BEC. Another relevant question concerns finding a stationary solution  $\psi(\mathbf{r})$  that minimizes the energy

$$E_0 = \int d\mathbf{r} \psi^*(\mathbf{r}) \left( -\frac{1}{2}\Delta + V(\mathbf{r}) + \frac{g}{2}|\psi(\mathbf{r})|^2 \right) \psi(\mathbf{r}), \quad (5)$$

for a given potential  $V(\mathbf{r})$  and interaction constant  $g$ . For a moment we are considering a stationary problem, so  $\psi$  is a function of three spatial variables only. To address this question we will use a variant of a well established gradient descent method [15]. To this end, we introduce a label  $n = 0, 1, \dots$ , where  $\psi(\mathbf{r})_0$  is our initial guess for the stationary solution. In the next step, the function  $\psi$  is incrementally changed as

$$\psi(\mathbf{r})_{n+1} - \psi(\mathbf{r})_n = -\epsilon \frac{\delta E_0(\psi)}{\delta \psi^*}, \quad (6)$$

where  $\epsilon$  is an optimally chosen update step. The reasoning behind equation (6) is a general idea of the gradient descent method: we move through the space of functions  $\psi(\mathbf{r})$  along the direction in which the energy functional exhibits the fastest decay. For a stationary solution  $\psi_0(\mathbf{r})$  it holds true  $\frac{\delta E_0(\psi)}{\delta \psi^*} = 0$  and it corresponds to an extremum (minimum) of  $E_0$ . The last equation can be rewritten as

$$\frac{\partial \psi(\mathbf{r}, \tau)}{\partial \tau} = - \left( -\frac{1}{2}\Delta + V(\mathbf{r}) + g|\psi(\mathbf{r}, \tau)|^2 \right) \psi(\mathbf{r}, \tau). \quad (7)$$

where  $\tau = n\epsilon$  is a label that keeps track of propagation through the space of functions  $\psi(\mathbf{r})$ . We notice that equation (7) can be derived from equation (1) by a formal replacement  $t \rightarrow i\tau$ . For this reason, the variable  $\tau$  is named imaginary

time. In contrast to the energy conservation (3), imaginary time propagation by its construction ensures that with a right choice of initial function, we will reach a minimum of the energy functional (5) at long enough  $\tau$ . Moreover, imaginary time propagation as given in (7) does not preserve normalization (2), so this condition should be provided additionally, either by introducing an appropriate Lagrange multiplier or by re-normalizing  $\psi(\mathbf{r}, \tau)$  in each propagation step (6). Finally, we note that the solution  $\psi_0(\mathbf{r})$  which minimizes  $E_0$  evolves in time according to the nonlinear equation (1) as

$$\psi(\mathbf{r}, t) = e^{-i\mu t} \psi_0(\mathbf{r}), \quad (8)$$

where  $\mu$  is a chemical potential

$$\mu = \int d\mathbf{r} \psi_0^*(\mathbf{r}) \left( -\frac{1}{2}\Delta + V(\mathbf{r}) + g|\psi_0(\mathbf{r})|^2 \right) \psi_0(\mathbf{r}). \quad (9)$$

More recent experimental progress in the field of cold atoms has enabled study of more complex and fascinating physical systems whose theoretical understanding necessitates generalizations and extensions of the basic NLS equation (1). One of the topics that has attracted lot of attention recently is realization of a BEC of atoms with strong magnetic dipole moment [16, 17, 18]. To describe the system, we define  $z$ -axis as the polarization axis of the dipole moments. In this case the dipole-dipole interaction is proportional to [19]

$$V_{\text{dd}}(\mathbf{R}) = \frac{1 - 3 \cos^2 \theta}{|\mathbf{R}|^3}, \quad (10)$$

where vector  $\mathbf{R} = \mathbf{r} - \mathbf{r}'$  stands for the relative position of the two dipoles, and  $\theta$  is the angle between the vector  $\mathbf{R}$  and the  $z$ -axis. The dipolar NLS equation is given by

$$i \frac{\partial \psi(\mathbf{r}, t)}{\partial t} = \left( -\frac{1}{2}\Delta + V(\mathbf{r}) + g|\psi(\mathbf{r}, t)|^2 + g_{\text{dd}} \int d\mathbf{r}' V_{\text{dd}}^{3D}(\mathbf{r} - \mathbf{r}') |\psi(\mathbf{r}', t)|^2 \right) \psi(\mathbf{r}, t). \quad (11)$$

The coefficient  $g_{\text{dd}}$  sets the strength of the dipolar interaction. Other generalizations of the NLS equation (1) will be discussed in sections 3 (two-component BEC) and 4 (BEC with the coupling of spin and angular momentum).

In order to further illustrate wide applicability of the NLS equation, here we present its form used in nonlinear fiber optics. Starting with Maxwell's equations and using several justified approximations, it can be shown that the

propagation of the pulse field envelope  $A(x, y, t, z)$  along the  $z$  direction is governed by the NLS equation of the form [20, 4]

$$i \frac{\partial A(x, y, t, z)}{\partial z} = \left[ -\frac{1}{2} \left( \frac{\partial^2}{\partial x^2} + \frac{\partial^2}{\partial y^2} + \beta \frac{\partial^2}{\partial t^2} \right) + \gamma |A(x, y, t, z)|^2 \right] A(x, y, t, z), \quad (12)$$

where the coefficient  $\beta$  describes dispersive effects and the coefficient  $\gamma$  describes nonlinear effects. In the following, we mainly consider equations (1) and (11), but we note that all the discussed algorithms and their numerical implementations can be used to simulate equation (12) as well.

## 2.2. Algorithm

As the NLS equation (1) has been widely used and solved numerically, various types of numerical methods have been applied to this purpose [5]. A recent review paper [21] provides extensive comparison of the properties of different numerical methods used to solve the NLS equation. Broadly speaking, numerical methods for solving equation (1) are either finite difference approximations, pseudo spectral methods or finite element methods. Depending on the applied time–discretization scheme, a finite difference method can be explicit, implicit, semi–implicit or split–step approximation. Here we follow derivations from reference [22, 23] and present a simple and efficient numerical method to integrate the NLS equation (1). From the numerical point of view, real–time propagation according to equation (1) and imaginary–time propagation (7) can be implemented in a very similar manner.

In order to integrate equations (1) and (7) in time, we perform time discretization  $t \equiv t_0 + n\varepsilon$ ,  $n = 0, 1, 2, \dots$ ,  $\psi(\mathbf{r}, t) \rightarrow \psi(\mathbf{r})_n$ . It turns out that optimal ways to deal with spatially local and non–local terms of these equations are different, hence we further split integration over time into two consecutive pieces. This approximation formally corresponds to a replacement of equation (1) by a set of two equations

$$i \frac{\partial \psi(\mathbf{r}, t)}{\partial t} = (V(\mathbf{r}) + g|\psi(\mathbf{r}, t)|^2) \psi(\mathbf{r}, t) \quad (13)$$

$$i \frac{\partial \psi(\mathbf{r}, t)}{\partial t} = -\frac{1}{2} \Delta \psi(\mathbf{r}, t), \quad (14)$$

assuming that the result of integration of equation (13) is the initial condition for solving equation (14). The split–step approximation given by (13) and (14) is valid only for short-enough time interval  $\varepsilon$  and introduces a numerical error of the order  $O(\varepsilon^2)$ .

For practical reasons in a general three-dimensional situation, we further split equation (14) into three parts treating spatial derivatives over the three spatial coordinates separately. Thus, in this way we obtain a set of four consecutive equations

$$i \frac{\partial \psi(\mathbf{r}, t)}{\partial t} = H_i \psi(\mathbf{r}, t) \quad (15)$$

where  $i \in \{1, 2, 3, 4\}$  and we introduced

$$H_1 = V(\mathbf{r}) + g|\psi(\mathbf{r}, t)|^2, \quad (16)$$

$$H_2 = -\frac{1}{2} \frac{\partial^2}{\partial x^2}, \quad H_3 = -\frac{1}{2} \frac{\partial^2}{\partial y^2}, \quad H_4 = -\frac{1}{2} \frac{\partial^2}{\partial z^2}. \quad (17)$$

Accordingly, between configurations  $n$  and  $n + 1$ , we introduce three intermediate states labeled by  $n + \frac{1}{4}$ ,  $n + \frac{2}{4}$ ,  $n + \frac{3}{4}$  such that

$$\psi(\mathbf{r})_{n+\frac{1}{4}} = \exp[-i\varepsilon (V(\mathbf{r}) + g|\psi(\mathbf{r})_n|^2)] \psi(\mathbf{r})_n, \quad (18)$$

and

$$\psi(\mathbf{r})_{n+\frac{2}{4}} - \psi(\mathbf{r})_{n+\frac{1}{4}} = \frac{i\varepsilon}{4} \frac{\partial^2}{\partial x^2} \left[ \psi(\mathbf{r})_{n+\frac{2}{4}} + \psi(\mathbf{r})_{n+\frac{1}{4}} \right], \quad (19)$$

$$\psi(\mathbf{r})_{n+\frac{3}{4}} - \psi(\mathbf{r})_{n+\frac{2}{4}} = \frac{i\varepsilon}{4} \frac{\partial^2}{\partial y^2} \left[ \psi(\mathbf{r})_{n+\frac{3}{4}} + \psi(\mathbf{r})_{n+\frac{2}{4}} \right], \quad (20)$$

$$\psi(\mathbf{r})_{n+1} - \psi(\mathbf{r})_{n+\frac{3}{4}} = \frac{i\varepsilon}{4} \frac{\partial^2}{\partial z^2} \left[ \psi(\mathbf{r})_{n+1} + \psi(\mathbf{r})_{n+\frac{3}{4}} \right]. \quad (21)$$

The result (18) gives an exact, analytical solution of equation (13). In this way the nonlinear term has been properly taken into account providing a stability of the employed numerical scheme for arbitrary strong nonlinearity coefficient  $g$ . In the equations (19, 20, 21), we have used the semi-implicit Crank–Nicolson method [24], which is second-order accurate in the time step  $\varepsilon$  and unconditionally stable method. The accuracy of the approximation is  $O(\varepsilon^2)$ .

To reduce the obtained differential equations to the algebraic form, we additionally perform space discretizations with the discretization steps  $h_x$ ,  $h_y$ , and  $h_z$ . To this end, we introduce integer indices  $i, j, k$ , which take values  $0 \leq i \leq N_x$ ,  $0 \leq j \leq N_y$ ,  $0 \leq k \leq N_z$ , such that  $\psi(x_i, y_j, z_k)_n \equiv \psi_{i,j,k,n}$ , where  $x_i \equiv (-\frac{N_x}{2} + i) h_x$ , and similarly for  $y$  and  $z$ . We also approximate second-order spatial derivatives in the standard way via the central difference

formula:

$$\frac{\partial^2 \psi(\mathbf{r})_n}{\partial x^2} \rightarrow \frac{1}{h_x^2} (\psi_{i+1,j,k,n} - 2\psi_{i,j,k,n} + \psi_{i-1,j,k,n}), \quad (22)$$

with the error of the order of  $h_x^2$ . We consider large enough grids such that we can use boundary conditions  $\psi(0, j, k)_n \approx 0$ ,  $\psi(N_x, j, k)_n \approx 0$  and similarly in the other two spatial directions. As a result of using approximation (22) in equation (19), we obtain a tridiagonal system of equations

$$-A\psi_{i+1,j,k,n+\frac{2}{4}} + B\psi_{i,j,k,n+\frac{2}{4}} - A\psi_{i-1,j,k,n+\frac{2}{4}} = \delta_i, \quad (23)$$

for each  $j$  and  $k$ , where  $A = \frac{i\varepsilon}{4h_x^2}$ ,  $B = 1 + \frac{i\varepsilon}{2h_x^2}$  and

$$\delta_i = A\psi_{i+1,j,k,n+\frac{1}{4}} + B^*\psi_{i,j,k,n+\frac{1}{4}} + A\psi_{i-1,j,k,n+\frac{1}{4}}.$$

A solution of this tridiagonal system of equations can be cast in the form

$$\psi_{i+1,j,k,n+\frac{2}{4}} = \alpha_i\psi_{i,j,k,n+\frac{2}{4}} + \beta_i, \quad (24)$$

and from this ansatz we find the recursive relations for the solution:

$$\alpha_{i-1} = \frac{A}{B - A\alpha_i}, \quad \beta_{i-1} = \frac{\delta_i + A\beta_i}{B - A\alpha_i}. \quad (25)$$

From the boundary condition  $\psi_{N_x,j,k,n+\frac{2}{4}} = \psi_{N_x,j,k,n+\frac{1}{4}} = 0$ , we derive initial values for  $\alpha$  and  $\beta$ ,  $\alpha_{N_x-1} = \beta_{N_x-1} = 0$ , which we use to solve the recursive equations (25). With another boundary condition  $\psi_{0,j,k,n+\frac{2}{4}} = 0$ , we finally solve equation (24). Similar procedure is afterwards followed in  $y$  and  $z$  direction. Due to the tridiagonal form of the above system of equations, the complexity of the overall algorithm is proportional to the number of discretization points, i.e.,  $O(N_x N_y N_z)$ .

Once the ground-state solution  $\psi_0(\mathbf{r})$  is calculated using the imaginary-time version of the above algorithm, the corresponding value of the ground-state energy  $E_0$  of the system can be calculated by numerically integrating expression (5). The described algorithm is implemented using the Fortran programming language [22] and the C programming language [23]. Further computational optimization is achieved by employing the state-of-the-art parallelization techniques for different computing platforms: OpenMP (for shared memory multiprocessing) [25] and hybrid OpenMP/MPI (for distributed memory systems, where each compute node uses OpenMP to maximize performance) [26].



In order to solve the dipolar NLS equation (11) numerically, we need to deal with the integral on the right-hand side of this equation efficiently. To this end, we exploit the fact that the Fourier transform of a convolution integral is given by a product of Fourier transforms of its components

$$I_{\text{dd}}(\mathbf{r}, t) = \int d\mathbf{r}' V_{\text{dd}}(\mathbf{r} - \mathbf{r}') n(\mathbf{r}', t) = \int \frac{d\mathbf{k}}{(2\pi)^3} e^{-i\mathbf{k}\mathbf{r}} \tilde{V}_{\text{dd}}(\mathbf{k}) \tilde{n}(\mathbf{k}, t), \quad (26)$$

where we define the direct and the inverse Fourier transformation as:

$$\tilde{A}(\mathbf{k}) = \int d\mathbf{r} A(\mathbf{r}) e^{i\mathbf{k}\mathbf{r}}, \quad A(\mathbf{r}) = \frac{1}{(2\pi)^3} \int d\mathbf{k} \tilde{A}(\mathbf{k}) e^{-i\mathbf{k}\mathbf{r}}. \quad (27)$$

The Fourier transform of the geometric factor (10) stemming from the dipolar interaction can be obtained analytically and is given by

$$\tilde{V}_{\text{dd}}(\mathbf{k}) = \frac{4\pi}{3} \left( \frac{3k_z^2}{\mathbf{k}^2} - 1 \right). \quad (28)$$

The Fourier transform of  $n(\mathbf{r}', t)$  and the inverse Fourier transform from equation (26) are calculated numerically using optimized libraries such as FFTW [27]. Finally, the obtained numerical value  $I_{\text{dd}}(\mathbf{r}, t)$  of the integral (26) is used in the first part of the split-step approach (18) as:

$$\psi(\mathbf{r})_{n+\frac{1}{4}} = \exp \left[ -i\varepsilon \left( V(\mathbf{r}) + g|\psi(\mathbf{r})_n|^2 + g_{\text{dd}} I_{\text{dd}}(\mathbf{r}, n) \right) \right] \psi(\mathbf{r})_n. \quad (29)$$

Numerical codes implementing the described algorithm for solving the time-dependent dipolar NLS equation are written in the Fortran and in the C programming languages [28]. CUDA parallel version of the algorithm is developed for single GPGPUs [29], as well as a hybrid CUDA/MPI version for distributed memory systems, where each compute node has GPGPU installed [30].

### 2.3. Parallelization of the Algorithm

Let us note that the tridiagonal systems of equations (23) can be solved separately for different values of  $j$  and  $k$ . This feature is essential and can be directly exploited to parallelize numerical implementation of the above described algorithm. In fact, this has been done for practically all available modern computer architectures and platforms, and we briefly outline all implementations.

Initial algorithm for solving the NLS equation with the contact interaction term using Crank-Nicolson method was published in reference [22], which also

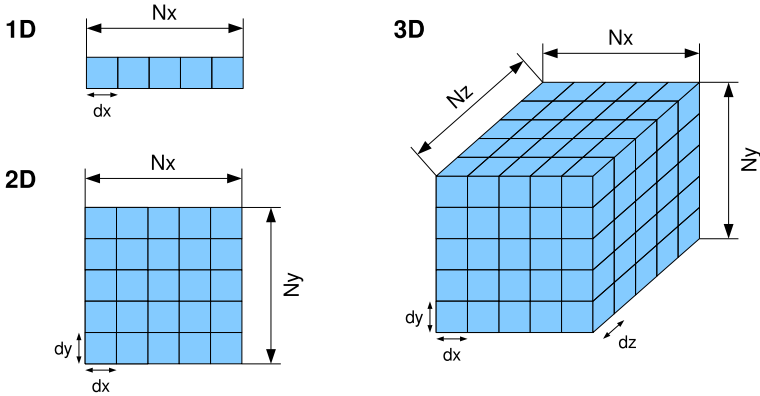


Figure 1. Example of 1D, 2D and 3D meshes with  $N_x$ ,  $N_y$  and  $N_z$  discretization points in  $x$ ,  $y$  and  $z$  direction, respectively, and the corresponding spacings  $dx$ ,  $dy$  and  $dz$ .

includes a serial implementation in Fortran. This was followed by the implementation written in C [23], which includes serial and parallel implementation for shared memory systems consisting of one or more multi-core CPUs using OpenMP approach. Fortran OpenMP implementation was also provided [25], as well as a full parallel MPI version for distributed memory systems, i.e., computer clusters with multi-core CPU nodes [26]. An extension of the algorithm to include the dipolar interaction term was published in reference [28], where the authors provided two serial implementations, in C and Fortran. This was followed by an implementation written in Nvidia CUDA for hardware accelerators in the form of GPUs [29], and later by a comprehensive suite of programs that includes OpenMP, MPI, CUDA, as well as their hybrid combinations [30].

To introduce the parallelization strategy, we start with the description of the discretization scheme used by the algorithm. Let  $N_x$ ,  $N_y$  and  $N_z$  be the number of points in each direction, corresponding to the  $x$ ,  $y$  and  $z$  directions in one, two or three dimensions (1D, 2D and 3D, respectively). In other words, the number of points in 1D is defined by  $N_x$ , in 2D by  $N_x$  and  $N_y$ , and in 3D by  $N_x$ ,  $N_y$  and  $N_z$ . Discretization points in each direction are equidistant, with their spacing defined in dimensionless units by variables  $dx$ ,  $dy$  and  $dz$ , illustrated in Figure 1.

The mesh determines how the space is discretized, but the actual values of

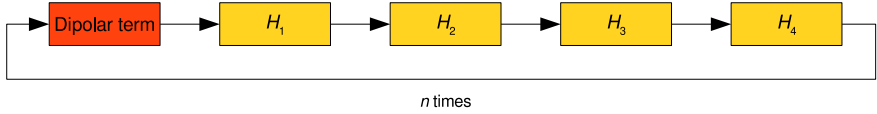


Figure 2. Main loop of the real-time propagation algorithm in 3D.

the wave function, which is also discretized by the mesh, need to be stored in a separate array. For convenience, we refer to this array as `psi` variable. This variable is defined as a vector of size  $N_x$  in 1D, as  $N_x \times N_y$  matrix in 2D and as  $N_x \times N_y \times N_z$  tensor in 3D. In real-time propagation, the wave function values are complex, while in imaginary-time propagation they are purely real, which determines the type of `psi` variable.

Time is discretized according to  $t_n = t_0 + n\varepsilon$ , with the time step  $\varepsilon$  stored in a variable `dt`. Taking into account the time step and the total amount of physical time we wish to simulate, we determine the number of iterations required. The main part of the algorithm is a loop where each iteration corresponds to one time step of the propagation. Inside the loop, we update the wave function by propagating it in time with respect to different parts of the Hamiltonian, according to the split-step scheme described in section 2.2 This is illustrated in Figure 2.

In each step of the main loop, wave function values are computed along the discretization mesh in several smaller steps. First such substep is the calculation of the dipolar interaction term (for programs where it is taken into account, otherwise it is omitted). We have two further substeps in 1D, pertaining to propagation w.r.t.  $H_1$  and  $H_2$ . In 2D and 3D we follow a similar procedure and add further substeps for  $H_3$  and  $H_4$ . Each substep produces intermediate values of the wave function that are used in the next substep. The order of the substeps dealing with parts of the Hamiltonian with spatial derivatives ( $H_2$ ,  $H_3$  and  $H_4$ ) can be arbitrary, a feature useful in hybrid and distributed memory algorithms. Propagation of the wave function w.r.t.  $H_1$  relies on the availability of the dipolar interaction term value, which is computed in the first substep, before we start with the update of the wave function.

When necessary, the dipolar interaction term is computed using the discrete Fourier transform (DFT). DFT of a sequence is commonly implemented by relying on the *Fast Fourier transform* (FFT) algorithm via an external library. From equation (26) it follows that we first need a DFT of a sequence consisting

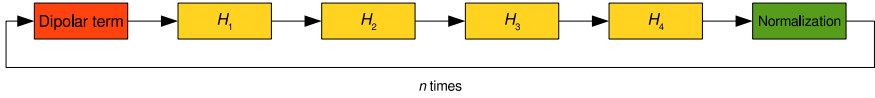


Figure 3. Main loop of the imaginary-time propagation algorithm in 3D, which introduces an additional step of normalization.

of absolute squares of wave function values. The resulting complex-valued sequence is then multiplied by the Fourier transform of the dipolar potential. This transform is a known function (28), precomputed for a chosen spatial mesh and stored in an array. Next, by performing the inverse DFT we get the dipolar interaction term stored in the resulting array, which we then use to propagate the wave function w.r.t.  $H_1$ . In 2D and 3D, we need multidimensional DFT, which can be computed by the composition of a sequence of 1D DFTs along each direction.

The substep in which the wave function is propagated w.r.t. the Hamiltonian part without spatial derivatives ( $H_1$ ) proceeds by employing further nested loops over mesh points. Part of the  $H_1$  is the trap potential  $V(\mathbf{r})$ , which, like Fourier transform of the dipolar potential, can be computed only once during the initialization, and then reused. We assume that the trap potential is static, but in case of a time-varying trap potential, the algorithm can be modified to update the trap potential before this substep, i.e., at the beginning of each iteration. The remaining substep, or substeps in 2D and 3D, propagates the wave function by relying on the Crank-Nicolson scheme. We need to perform a backward sweep of the mesh in each direction to determine the corresponding Crank-Nicolson coefficients  $\alpha$ ,  $\beta$  and  $\delta$  for each direction, followed by a forward sweep to determine the solution for the entire space range. The algorithm for imaginary-time propagation is similar to the one discussed above, with the addition of the normalization step at the end of each iteration of the main loop, as illustrated in Figure 3. To normalize the wave function, we first need to compute its norm and then to divide the wave function values with that norm.

We see that the algorithm is computationally very demanding, as it requires multiple passes over the entire mesh in each iteration of the main loop. In 2D and 3D, the total number of discretized points sharply increases, making this problem even greater. As we have identified above, several variables can be moved out of the main loop and computed only once, however the remaining calculations are still very demanding, hence the need for parallelization.

The described substeps cannot be executed concurrently, as the intermediate values they produce are used in subsequent substeps. Instead, parallelization of the algorithm can only be achieved by focusing on the mesh loops inside substeps. This is an obvious choice for shared memory systems, as all data stored in the memory is local and accessible to all participating processes, removing the need for data transfers between processes. The loops themselves can easily be parallelized if they do not contain recursive relations. This is true for the substeps dealing with the computation of the dipolar term and propagation w.r.t.  $H_1$ . Substep involving  $H_2$  cannot be easily parallelized in 1D, as it has recursive relations in both backward and forward sweeps. In general, recursive relations can be parallelized using the *scan* algorithm [31] (also known as the generalization of *prefix sum* algorithm [32]), however the implementation complexity of such an algorithm made us discard this approach. In 2D and 3D, we can exploit the fact that the recursive relations appear only in the innermost loops of the substeps involving  $H_2$ ,  $H_3$  and  $H_4$ . Thus, we can achieve parallelization by dividing the work among the processes at the level of the outermost loop.

In addition to the above outlined parallelization that can be naturally implemented on a single computer using OpenMP approach, one can also utilize modern GPUs to parallelize the algorithm on a single node, and even combine CPU and GPU into a hybrid algorithm. We first discuss CUDA-based parallelization, introduced in reference [29]. The significant differences in architecture of the GPU and its accompanying execution model on one side, and CPU architecture with its conventional execution model on the other side, do not result in significant changes to the main algorithm for the case of Nvidia CUDA implementation. From the algorithm's point of view, both CPU and GPU are shared memory systems with multiple processing units, even though they are vastly different, and therefore can be used in a similar manner. Main loop of the algorithm remains unchanged, as well as each substep. However, one has to replace the FFTW library used by C/OpenMP programs with the cuFFT library, which is available in CUDA. cuFFT provides two interfaces: the native one and the FFTW one [33]. FFTW interface is intended to be used as a drop-in replacement for FFTW, allowing programs written primarily with FFTW in mind to use CUDA GPUs with minimal modifications to the source code. While this interface could be used as a temporary solution during the development of CUDA programs, the goal of using CUDA for all computation relating to the propagation of the wave function could only be reached with the native cuFFT

interface. This interface is modeled after FFTW but differs from it in the way plans are created and executed. In cuFFT, precision and data type of the transform is determined by the functions initiating execution of plans, which results in a slightly different sequence of function calls and in improved performance.

In order to use CPU and GPU at the same time for hybrid algorithms, the work has to be divided efficiently between them. If we put aside the obvious hardware architecture difference between CPU and GPU, we can consider the computer with GPU as being similar to the distributed memory system consisting of two computing nodes with different characteristics. Both CPU and GPU have their own memory, and are connected through a fast interconnect, in this case the PCI-Express. This means that we need an approach similar to the one distributed memory algorithms use to achieve the desired parallelization. The most important difference here is that all data is available in main (CPU) memory, and only portions of it need to be transferred to GPU memory, as opposed to the true distributed memory systems, where no single part of the system has all the data. Therefore, the general approach to perform this type of hybrid computation is to:

1. designate a portion of data to be processed by GPU,
2. copy that data to GPU while simultaneously using CPU for computation over the remaining data,
3. transfer the data back from GPU, overwriting old data, and
4. synchronize CPU and GPU.

This flow is illustrated in Figure 4.

Note that data can be offloaded from CPU to GPU in various ways [34, 35] and, in general, any data distribution scheme which targets distributed memory systems may be used. However, we settled on a simple approach using 1D decomposition, also known as *slab decomposition*. When using slab decomposition, data is distributed along one dimension, usually the slowest-changing one, and the remaining dimension (in 2D programs) or dimensions (in 3D programs) of data remain local. This means that we can perform computation on the local data efficiently, and no data exchanges are necessary. Depending on a data access pattern, in our programs we rely on decompositions either along the  $x$  direction (discretized with the  $N_x$  spatial points), or along the  $y$  direction (discretized with the  $N_y$  spatial points). In 3D programs, there is no need

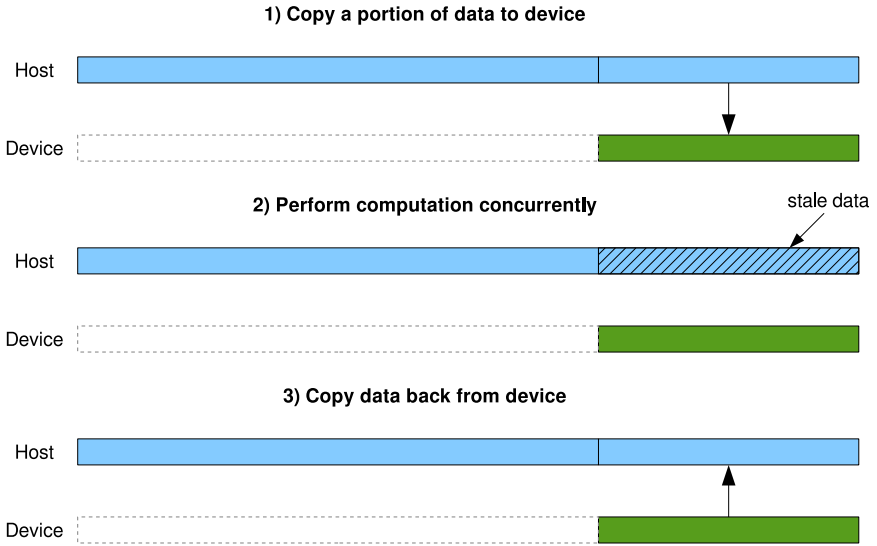


Figure 4. Flow of data between host and device.

to decompose the data along the  $z$  direction. In case we need data from the distributed dimension to become local in order to perform some computation (e.g., to update the wave function values when data are decomposed along the  $x$  direction), we have to reassemble data in host memory and decompose again along the appropriate dimension. Figure 5 illustrates this concept.

With the decomposition scheme in place, we can consider how to divide the computation of the wave function propagation in time between CPU and GPU. Once the data have been distributed between CPU and GPU, on the CPU side only the exit condition of the outer loop needs to be adjusted, so that the CPU processes a smaller number of elements (e.g., by replacing  $N_x$  with  $\text{cpu}N_x$ ). Similar changes are required on the GPU side as well, however we also need to ensure that GPU has valid data to work with, and that data are reassembled in host memory after the computation on GPU is done.

Therefore, in the hybrid implementation we initially distribute the data along the slowest-changing dimension. This allows CPU and GPU to simultaneously perform computation of wave function propagation w.r.t.  $H_1$  and  $H_3$  parts of the Hamiltonian (and  $H_4$  when working in 3D). The propagation of the wave function w.r.t.  $H_2$ , corresponding to the  $x$  direction, can be done locally

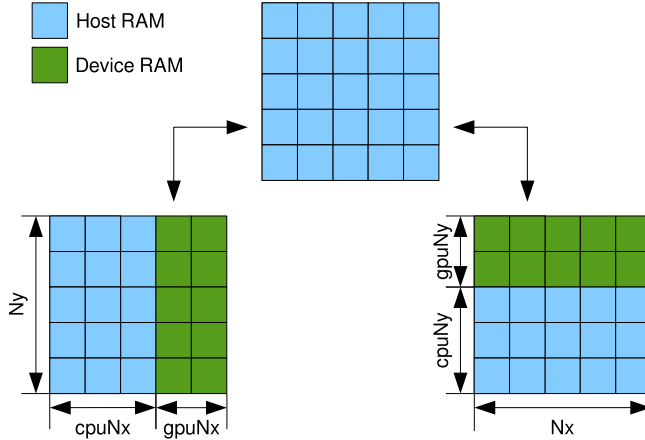


Figure 5. Two offload patterns used. If offloaded along  $x$  direction, the  $y$  direction remains local. If we need to access whole  $x$  direction data, we need to decompose along  $y$  direction.

only if we decompose the data along the  $y$  direction beforehand. Note that we do not have to transfer data from GPU back to host memory at the end of each function, due to the fact that time propagation w.r.t.  $H_2$ ,  $H_3$  and  $H_4$  parts of the Hamiltonian can be done in arbitrary order in each step. Without this, the time propagation workflow of 3D programs would have to involve the following steps, according to Figure 2:

1. calculate the dipolar term,
2. transfer the data decomposed along  $x$  direction to GPU,
3. propagate the wave function w.r.t.  $H_1$
4. reassemble the data in host memory,
5. transfer the data decomposed along  $y$  direction to GPU,
6. propagate the wave function w.r.t.  $H_2$ ,
7. reassemble the data in host memory,
8. transfer the data decomposed along  $x$  direction to GPU,



9. propagate the wave function w.r.t.  $H_3$ ,
10. propagate the wave function w.r.t.  $H_4$ ,
11. reassemble the data in host memory.

Rearranging the order of time-propagation substeps allows us to remove one transfer of data to GPU and its subsequent reassembly in host memory:

1. calculate the dipolar term,
2. transfer the data decomposed along  $x$  direction to GPU,
3. propagate the wave function w.r.t.  $H_1$ ,
4. propagate the wave function w.r.t.  $H_3$ ,
5. propagate the wave function w.r.t.  $H_4$ ,
6. reassemble the data in host memory,
7. transfer the data decomposed along  $y$  direction to GPU,
8. propagate the wave function w.r.t.  $H_2$ ,
9. reassemble the data in host memory.

Therefore, we use the above, optimized sequence in all 3D programs, and similarly in 2D.

To complete the hybrid algorithm, we also need to distribute computation of the dipolar term between CPU and GPU, where complexity arises in performing DFT on distributed data. Currently available FFT libraries target either CPU or GPU for their computation, but unfortunately not both at the same time. There are numerous attempts to develop specialized FFT libraries which would enable this [36, 37, 38], however a full-featured library with support for R2C transforms with advanced data layout is still not available. The approach we used is to rely on existing libraries for actual transforms, but perform data distributions manually. The libraries we use, FFTW on CPU and cuFFT on GPU, support advanced data layouts as well as working on a subset of the whole data, allowing for an efficient implementation.

To perform the Fourier transform simultaneously on CPU host and GPU device, we have to split the single multidimensional transform into a series of

1D transforms along each dimension of the input data, which can be computed on CPU and GPU independently. This approach is known as the *row-column* algorithm [39], and is often used in FFT libraries. The essence of this algorithm can best be summarized in an example of a 2D FFT. Given a matrix  $N_x \times N_y$ , we compute the DFT in the following way:

1. Transfer portion of the input array, decomposed along the  $x$  direction, to device memory. We transfer last  $g_{\text{gpu}}N_x \times N_y$  consecutive array elements to GPU. This can be done as a single memory copy operation due to the flat allocation that was used. The choice whether to offload data to GPU memory from the beginning or the end of the input array is arbitrary.
2. Perform DFT along the  $y$  direction on both CPU and GPU concurrently. CPU will perform  $c_{\text{cpu}}N_x$  such transformations, while the GPU will perform  $g_{\text{gpu}}N_x$  1D DFTs. Each of these transforms will take a subset of the input array, which are  $N_y/2 + 1$  elements apart. Note that CPU will not do anything with the last  $g_{\text{gpu}}N_x \times N_y$  elements.
3. Copy the array with the transform back from GPU to CPU, writing over the stale data with the relevant portion transformed on GPU. After this step, we have the complete array transformed along the  $y$  direction residing in host memory.
4. Transfer portion of the input array, decomposed along the  $y$  direction, to GPU memory. Similarly to step 1, we transfer last  $N_x \times g_{\text{gpu}}N_y$  elements to GPU.
5. Perform DFT along the  $x$  direction on both CPU and GPU. This time, CPU will perform  $c_{\text{cpu}}N_y/2 + 1$  such transformations, while GPU will perform remaining  $g_{\text{gpu}}N_y/2$  transformations. The halving of the number of transformations is due to use of R2C transformations. In each transform, elements are  $N_y/2 + 1$  places apart, while the first element of each transform is adjacent to the previous one.
6. Copy the array with the transform back from GPU to CPU. With this step completed, we have the full FFT of the input array residing in host memory. This step may be omitted if the computation that follows does not require the FFT of input data to be fully assembled in host memory. This is the case in our algorithm, as we use the resulting transformed array

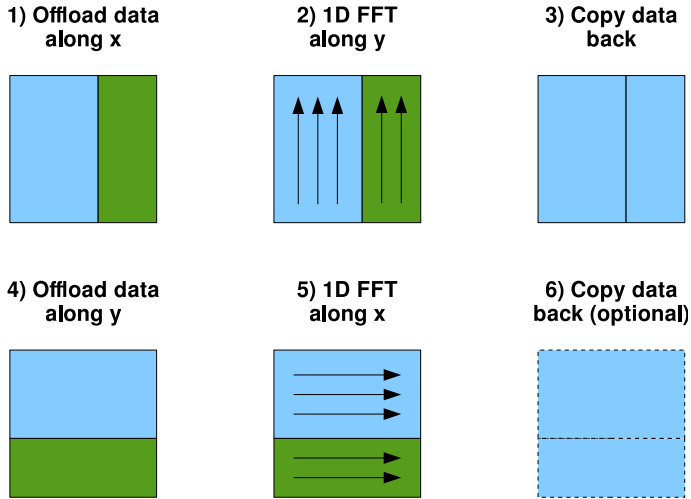


Figure 6. Hybrid algorithm for concurrent FFT on host and device.

only for subsequent computation on GPU. Since the memory transfer is expensive, omitting this step leads to significant performance improvement.

The inverse Fourier transform can be done in an analogous way. In 3D, the general principle remains the same, however, we do not separate the DFT into three 1D transforms, but to one 2D and one 1D transform. We do this due to better performance of 2D transforms, which in both libraries used is found to be better than two 1D transforms. Figure 6 illustrates the DFT algorithm described above.

And finally let us mention that several distributed memory implementations, targeting computer clusters, were developed as well:

1. pure CPU version, which is built on top of the shared memory algorithm (OpenMP/MPI),
2. pure GPU version, which is built on top of the CUDA implementation of the shared memory algorithm (CUDA/MPI),
3. hybrid version, which is based on the algorithm described in Chapter (Hybrid/MPI).

Two of the three implementations, the OpenMP/MPI and CUDA/MPI implementations, have been published in reference [30] and are available for download [40, 41]. The Hybrid/MPI implementation is also publicly available [41]. The main challenges in the development of distributed memory and hybrid algorithms were devising an efficient data distribution scheme that facilitates fast data shuffling between computing resources. In the MPI implementations this was done via a transpose operation realized in two ways, one relying on FFTW and the other relying on MPI vector types and collective communications. Further details can be found in reference [42].

## **2.4. Performance of Parallel Algorithms: Measurement Results and Modeling**

In previous section we presented various parallel implementations of programs solving the dipolar and contact interaction GP equation without providing details of their measured performance. This section is dedicated to filling that gap. We tested various scaling scenarios, strong and weak, from a single computing node to the cluster. All testing was done at the PARADOX supercomputing facility located at the Scientific Computing Laboratory, Center for the Study of Complex Systems of the Institute of Physics Belgrade.

Performance of hybrid implementations is highly dependent on the amount of work offloaded to GPU(s), so the key to maximizing performance of these versions is proper selection of parameters which control this feature. We used evolutionary computation techniques to find the optimal solutions, as described here. In the remaining subsections we give an overview of the tests and the methodology they relied on, present the performance results and their modeling, and finally discuss how to select the optimal algorithm for a given hardware platform.

### **2.4.1. Optimization of Input Parameters for Hybrid Implementations**

Hybrid implementations, running on a single computer or a cluster with multiple computing nodes, can potentially offer the best performance of all algorithms presented in this thesis, by utilizing all allocated computing resources. For this to happen, work must be divided between CPU and GPU in such a way as to maximize their throughput and minimize their idle time. A question that naturally arises is how to achieve this for any possible mesh size for a given CPU/GPU combination. Unfortunately, there is no single best way to divide the

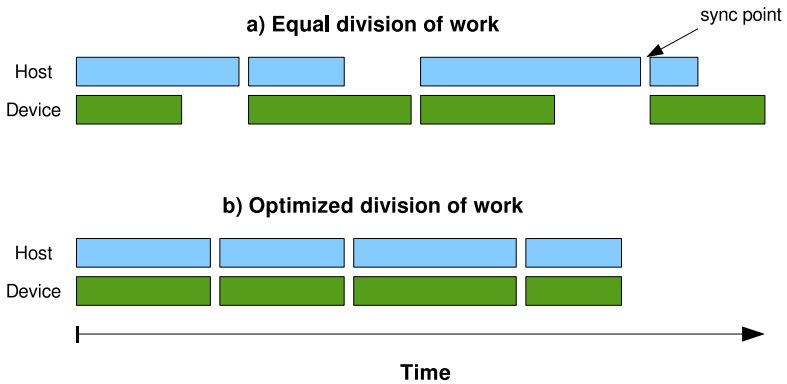


Figure 7. Execution timeline in a hybrid system: (a) with equal data distribution, leading to unbalanced computation time; (b) with optimized data distribution and ideal computation load.

work, since processing powers of CPUs and GPUs vary significantly. For example, in a computer where a powerful new GPU is paired with an older type of CPU, more work should be offloaded to the GPU, and vice versa for computers with a powerful CPU and low-performing GPU. Even if the installed CPU and GPU offer similar performance in terms of floating point operations per second (as is the case for the PARADOX cluster), the differing architectures mean that certain portions of the algorithm are better suited to CPU or GPU. If we were to divide the work naively, e.g., equally, this would lead to unbalanced computation, as illustrated in Figure 7(a), which in turn increases the computation time.

To get over this problem, the described hybrid implementations have an option to manually specify each parameter that controls the work being done on a GPU. Ideally, this flexibility would allow us to overlap computation on CPU and GPU as much as possible, thus minimizing the execution and idle time of each resource. The execution timeline for the ideal case looks like the illustration in Figure 7(b).

The aforementioned parameters include the total amount of data transferred to GPU, the number of chunks, kernel grid size parameters and a special parameter controlling whether some functions will even be offloaded to GPU or not, which is useful in situations where the CPU is much more powerful than the

GPU. In 3D programs, this amounts to 33 integer-valued parameters for which we would like to find the optimal values for the desired mesh size on a given computing system (with given hardware characteristics). Furthermore, there are constraints that the parameters must satisfy. For example, the total amount of data transferred to GPU must be divisible by the number of chunks, and the size of a block that kernel launches must fit within the limits imposed by the underlying GPU.

To evaluate any combination of parameters, the programs have to be executed, and their execution time measured. The search space of 33 parameters is clearly too large to be exhaustively traversed in a reasonable amount of time. Fortunately, we can reduce the number of parameters we have to search through at any single time by grouping them based on the synchronization point. After the CPU and GPU synchronize, data have to be divided again, so the only relevant parameters in the region between two synchronization points are the ones controlling the division of work and the ones controlling the kernels which are executed in that region. During a single iteration, CPU and GPU have to synchronize four times:

1. after the FFT on local dimensions,
2. after the inverse FFT on the non-local dimension,
3. before the function performing propagation w.r.t.  $H_2$ , and
4. after that function (which represents the end of a single iteration).

This gives us four distinct parameter sets to optimize:  $PS_1$  with 6 parameters,  $PS_2$  also with 6 parameters,  $PS_3$  with 15 parameters and  $PS_4$  with 5 parameters. We can consider each parameter set independently.

We investigated several approaches to optimization of parameter sets: naive brute-force search, iterative optimization via gradient descent, and metaheuristic via genetic algorithm. Our goal was not to find the best possible optimization algorithm for our problem, but rather to implement a reasonably good one. By this we mean the algorithm which is not difficult to implement, which will give us a set of parameters that are close to the optimal ones, and will not take a long time to finish. Our focus was on 3D variants of both single node and MPI versions of hybrid programs. The concepts presented here apply equally to 2D variants and there is no important difference between the single node and

the MPI version, so we will not make this distinction in the remainder of this section. We will now describe how the three approaches were implemented.

A brute-force search (BFS), or exhaustive search, considers every possible combination of parameter values in order to find the optimal one. Even with parameters divided into smaller sets, the exhaustive search takes too long, and is only feasible if we narrow down the ranges of all parameters involved. Unfortunately, this is only possible when we have a deep understanding of the performance of the CPU and GPU models used, when we can provide a reasonable guess for the optimal solution. An alternative is to consider only certain values along the range of a single parameter, rather than every value in the range. This approach is feasible and we were able to find reasonably good parameter values using it. The downside is that this way we may miss the optimal values of parameters, as they often lie between the selected test points. For instance, on one PARADOX computing node and a mesh size  $256 \times 256 \times 256$ , with the work divided between CPU and GPU along the outermost,  $x$  dimension, if we test only for the values of offloaded data to GPU that are multiples of 32 (i.e.,  $32 \times 256 \times 256$ ,  $64 \times 256 \times 256$ , etc.), we will miss the optimal value which lies around  $140 \times 256 \times 256$  (assuming all other parameters are fixed). Even though BFS is often not feasible, it is useful as the baseline for the evaluation of other methods we implemented.

With the BFS implemented as a baseline, we switched our focus to the implementation of an iterative optimization algorithm. A well-known and widely used algorithm is *gradient descent* (GD) [15]. It is an iterative procedure in which every iteration aims to get closer to the minimum of the given function  $F(\mathbf{x})$ , where  $\mathbf{x}$  represents a vector of function parameters. If the function  $F(\mathbf{x})$  is defined and differentiable around some point  $\mathbf{a}$ , then  $F(\mathbf{x})$  decreases fastest in the direction of the negative gradient of  $F$  at  $\mathbf{a}$ . GD exploits this fact and defines  $\mathbf{b}$  as

$$\mathbf{b} = \mathbf{a} - \gamma \nabla F(\mathbf{a}), \quad (30)$$

so that  $F(\mathbf{b}) \leq F(\mathbf{a})$ , for  $\gamma$  small enough. This observation is used as a building block for the algorithm. We start from an initial guess  $\mathbf{x}_0$  for a location of the minimum of  $F$  and construct a sequence  $\mathbf{x}_n (n \geq 1)$  such that:

$$\mathbf{x}_n = \mathbf{x}_{n-1} - \gamma \nabla F(\mathbf{x}_{n-1}). \quad (31)$$

This sequence will eventually converge to the local minimum, if one exists. GD is most applicable to functions for which the gradient can be computed analytically, however it can also be used when the derivative can only be obtained

numerically. To apply it here, the execution time of our programs will be the function  $F$  that we minimize, and its arguments are the  $n = 33$  parameters that control the GPU. The execution time is measured as the average time of a single iteration of the main time-propagation loop, sampled over a given number of iterations. As explained earlier, we can divide the problem into four separate minimization problems, with four sets of parameters of dimensionality  $m_i$  ( $i = 1, 2, 3, 4$ ), in the same way as in BFS. To numerically compute the  $k$ -th partial derivative of one of the minimization functions at a set of candidate parameters  $a_1, a_2, \dots, a_m$ , we use first order approximation:

$$\frac{\partial F}{\partial x_k}(a_1, \dots, a_m) \approx \frac{F(a_1, \dots, a_k + h_k, \dots, a_m) - F(a_1, \dots, a_k, \dots, a_m)}{h_k}, \quad (32)$$

where  $h_k$  is the increment of a given parameter. Since the parameters are integer-valued, we have to carefully choose the value of  $h_k$ , to be as small as possible, while still satisfying all the constraints that the corresponding parameter may have w.r.t. other parameters. We note that in order to evaluate the full gradient of  $F$  at  $(a_1, \dots, a_m)$  we need to execute our programs  $m + 1$  times.

We stress that execution times of our programs are not always the same due to the hardware, software and OS scheduling issues, making the minimization functions noisy. This noise affects the calculation of the gradient and could point the algorithm in the wrong direction. We can detect this by checking if the value of minimization function has increased in subsequent GD iteration, and discard this move if necessary. While useful, resorting to this tactic means that in case the GD gets stuck in a local minimum, it will not be able to get out and thus will never reach the global minimum. A naive way to check if this is the case would be to start over from a different initial point, and see if the GD algorithm converges to the same minimum. There are more sophisticated approaches to addressing this issue, which we discuss later.

In general, it is not possible to completely eliminate noise, due to inherent problems of accurately measuring time on a computer. However, we can try to minimize it by increasing the precision of execution time measurement of our programs. This can be achieved by averaging execution times over larger number of iterations of the main time-propagation loop. Unfortunately, this also means that the total execution time of the GD algorithm will significantly increase.

Another issue in our implementation of GD arises when we have to select the next values of our parameters based on the output values of previous GD



iteration. These output values are real-valued, meaning that we need to convert them to integers somehow. Simply rounding them up or down to the nearest integer will not be enough, especially for small value of  $\gamma$ . For example, if we set the initial value of some parameter to 10, and after one GD iteration the proposed value of that parameter is 10.2, rounding it down will reset the value back to 10, effectively discarding the whole GD iteration. To avoid getting stuck in this way, our implementation selects the next possible value in the direction of change. In the example above it would mean selecting 11 as the new value. This change makes it impossible for the algorithm to converge, but it will usually stay close the minimum where all proposed solutions are of similar quality.

With the GD algorithm implemented as described above, we are able to get a set of optimized parameters from a random set of initial values. However, such optimized parameters are often suboptimal, and do not have the best performance. This is due to the fact that in most cases the GD will converge to the nearest local minimum, and there is no guarantee that that local minimum is also the global one. Using our previous example from BFS, a mesh of  $256 \times 256 \times 256$ , with GD we obtain that local minima exist for all power of two values, i.e., parameters suggest offloading  $2^n \times 256 \times 256$  to the GPU. If we randomly select a small initial value, GD will get stuck in the nearest local minimum, which in this example will be far from the global one, thus producing a very bad solution. We can attempt to avoid getting stuck in a local minimum by adapting the parameter  $\gamma$ , also known as *learning rate* in machine learning literature. Keeping the learning rate high for a first few iterations would allow the algorithm to find the general location of the minimum, after which we could gradually lower the learning rate until convergence is achieved, in a process called *annealing* [43]. In practice this did not completely solve the problem, as we found that the optimal learning rate to start with varies with the initial set of parameters and the mesh size, and thus has to be manually selected. This complicates attempts to automate the process of finding the optimal parameters for a range of mesh sizes, which we needed as part of the tests of both hybrid implementations. A method to remove the manual tuning of the learning rate exists [44], but we find it to be too complex to implement for our programs, because it would require significant changes to the way the parameters are selected.

From the discussion above, we conclude that the GD is not the best-suited method for the optimization in our case, mostly because our minimization function is noisy and the numerical computation of the gradient is costly. Derivative-free optimization methods would be better suited to the problem, e.g., stochastic

approximation algorithms like simultaneous perturbation (SPSA) [45, 46], or metaheuristics like genetic algorithms. We decided to use a genetic algorithm approach, as it is simple to understand and implement, as well as easy to adjust to get the desired behavior.

Genetic algorithm (GA) is an optimization method based on natural selection that mimics the process found in biological evolution [47]. GA works by creating a population of individual solutions, which it then evaluates and modifies, creating a new population, and iterating this process. Unlike the classical algorithms like GD, which iterate a single candidate solution towards the optimal one, the GA iterates a population of solutions in which the best individuals approach the optimal solution. The initial population is usually created at random, giving the GA different points in the search space to start from. The individual solutions are evaluated using a user-supplied fitness function, giving each individual a score based on how well they perform the given task. Individuals with the highest score are then selected to “reproduce” and create new offspring, after which they may be mutated randomly. The offspring form a new population, and the process can be repeated again. The GA continues until a suitable solution is found, or after a certain number of generations has passed.

To implement a GA, we first have to decide how to represent an individual. Individuals are created based on their blueprint, called *chromosome* in GA terminology. The most often used representation is bit-string [48], where all properties of an individual (its *genes*) are serialized to an array of bits, and then concatenated. More advanced representations exist, e.g., for encoding real values, permutations and general data structures [49, 50], however since our individuals are sets of integer parameters, we did not develop any special representation and instead we used ordinary arrays of integers as a chromosome. Therefore, each gene in a chromosome is a single GPU parameter of our programs. Individuals need to be evaluated using a fitness function. In our case, this means executing the programs with the parameters extracted from the individual’s chromosome, and reporting the execution time as fitness score, with lower execution time being better.

Next step is the implementation of the three GA operators: selection, reproduction (*crossover* in GA terminology) and mutation. Each operator can be implemented in different ways. Most common type of the selection operator is *roulette wheel* selection. This is a type of fitness-proportionate selection, with the idea to give each individual a slice of the circular roulette wheel based on their fitness. The wheel is then spun, and when the roulette ball stops, the in-

dividual in whose region the ball stopped is selected. In this way, the fittest individuals have the greatest chance of being selected for reproduction, while the ones with very low score quickly die out. We also tested an alternative type of selection, the *tournament* selection. In this type of selection, we randomly select several individuals, and host a tournament for them. The individual with the best fitness score wins, and is selected for reproduction. By changing the size of the tournament we can control the selection pressure, e.g., by using small tournament size in the first few iterations we can prevent premature convergence and increase it in later generations when we have explored the search space enough. In our tests, the tournament selection gave slightly better results for smaller populations, by keeping the population diverse in early generations. For larger population size, both selection rules performed equally. Alongside the main selection algorithm, we also used *elitist* selection, where first few individuals are copied to the next generation without changing their chromosome. This prevented the loss of the best individuals in the next generation, but has to be used carefully as it may lead to premature convergence to a suboptimal solution.

To produce the next generation, selected individuals should combine their chromosomes and produce offspring. This is the task of the crossover operator. Crossover exchanges parts of the chromosomes, mimicking the biological recombination from nature. In its most basic form, crossover works by randomly selecting a point and exchanging segments before and after the point to create two new offspring from two parents. This type of crossover is called *single-point crossover*, and is illustrated in Figure 8(a). Other popular crossover techniques are *two-point crossover* and *uniform crossover*, illustrated in Figures 8(b) and 8(c). Two-point crossover is similar to the single-point crossover, just with two points instead of one. On the other hand, in the uniform crossover each gene of the offspring is selected randomly, either from the first parent or from the second one, with some fixed probability, typically 0.5. Using the uniform crossover leads to a wider exploration of the search space [51], but this may not always result in better performance of the operator [52]. We tested single- and two-point crossover and found that there is little difference in terms of performance between them. Since some of our parameters have constraints, it is important to select only the crossover points which lead to an allowed recombination of genes. Unfortunately, this made the implementation of uniform crossover impossible, and we did not pursue it further.

The final step in producing the next generation is to apply the mutation operator on the new population. The mutation operator randomly changes genes

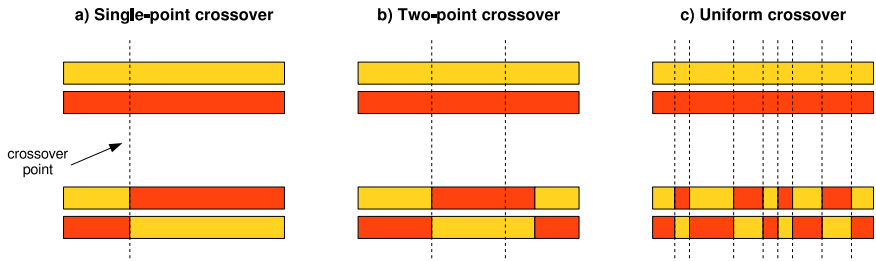


Figure 8. Three different crossover techniques in GA: a) single-point crossover, b) two-point crossover and c) uniform crossover.

to new values, which is equivalent of performing a random walk through the search space. Changing every gene would not be desired, so mutation operates with a very small probability, meaning most of the genes will be left unchanged. When chromosomes are implemented as bits, the mutation would be equivalent to flipping a random bit. However, we could not implement mutation this way, as random changes to the chromosome would often result in non-functioning individuals, e.g., parameter constraints would not be satisfied. Special care must be taken to ensure that the mutation produces a healthy individual, similarly to the crossover operator. The importance of mutation operator and its relation to the crossover is often debated [53, 54], with its role being defined as “to maintain diversity within the population and inhibit premature convergence” [55], as the crossover operator does not introduce new information to the population. In our tests, the mutation plays a crucial role if the population size is small, e.g., less than 20 individuals, in accordance with references [56, 57]. If the population size is large, e.g., over 200 individuals, the positive effects of mutation on the population fitness are not that evident.

GA is typically iterated for a fixed number of generations, as is the case in our implementation. Alternatively, we could have implemented some exit clause in the main loop of the GA which would stop the evolution after the best individuals have not been improved for some number of generations. After each run of the GA, there is usually several highly fit individuals in the population. Since randomness is an integral part of any GA, different runs of the algorithm produce slightly different results. Therefore, our GA does not converge to a single solution, but produces candidate solutions that have very similar parameter values and overall fitness. Among the candidate solutions, there may be

small differences in the amount of data offloaded to GPU or the kernel parameters, with the execution times negligibly different. The number of generations required to produce a good solution also varies due to the randomness in the initial population and the population size. In our tests, it has a value between 10 and 50.

The implementation described above provides only the basis for a successful application of GA to the problem at hand. As can be seen, there are several important parameters of GA to tune in order to get optimal results. These include the population size, the number of generations, mutation rate, and the selection parameters (e.g., elite selection rate, the tournament size). We did not perform thorough testing of the performance of the GA that would allow us to obtain the best values for these parameters, as we were more focused on the quality of the candidate solutions GA creates. However, we observed that our GA finds good solutions faster if the initial population size is between 100 and 200, with the number of generations between 10 and 20, depending on the set of parameters we wish to optimize.

To get a perspective of how the three optimization methods perform, we tested them by comparing their final solutions, as well as by recording the number of program executions needed to get to the optimal set of parameters. For this test, we used 3D real-time propagation hybrid program on a single computing node. All three methods were allowed to execute the program up to 1000 times. The mesh sizes used range from  $80 \times 80 \times 80$  to  $600 \times 600 \times 600$ , all of which could potentially be offloaded to GPU. We tested parameter set  $PS_3$  (with 15 parameters), which controls the execution of FFT and the kernels in the subsequent functions that perform propagation w.r.t.  $H_1$ ,  $H_3$ , and  $H_4$ . The BFS algorithm was used as the baseline. Note that the range of parameters and a small number of allowed executions implies that the BFS algorithm takes the values of parameters with large stride, potentially missing the optimal solution. GD method is used as described, with the learning rate  $\gamma$  initially set to a higher value, which was gradually decreased. We performed the GD for 60 iterations, which amounts to 960 program executions. The GA was run on a population of 100 individuals, for 10 generations, amounting to the same the number of program executions as the BFS. We have used mutation rate of 5%, and the tournament selection, with the tournament size equal to 10% of the population size. Elitism was also included, with the top 2% of the population copied over. All algorithms were tested five times, to minimize the effects of random initialization of both GD and GA methods. The results are shown in Table 1.

**Table 1. A comparison of three optimization methods. Reported times are given in milliseconds, for a single iteration of the main time-propagation loop, averaged over 50 iterations. The last column contains the minimal execution times obtained by manual tuning. The reported time for each algorithm represents the minimal achieved value in five test runs**

Mesh size	BFS	GD	GA	Best
$80 \times 80 \times 80$	7	6	6	6
$128 \times 128 \times 128$	18	27	16	16
$240 \times 240 \times 240$	154	272	135	126
$256 \times 256 \times 256$	181	199	169	156
$360 \times 360 \times 360$	343	387	312	298
$480 \times 480 \times 480$	981	1049	868	829
$512 \times 512 \times 512$	1452	1628	1312	1242
$600 \times 600 \times 600$	2591	2984	2227	2159

From the results we conclude that the GA was the most effective optimization method of the three approaches. As expected, GA found better solutions than BFS due to large strides BFS had to use. The randomness in the initial population has a big effect on the convergence of the GA method, sometimes enabling it to find the optimal solution after just three generations. Even if the fitness of the initial population is very bad, the GA still converges to very good solutions after 10 generations. On the other hand, GD performed very poorly, mainly because the noise in program execution times has often thrown it in the wrong direction. Also, GD would get stuck in the nearest local minimum, which often was not the global one. When the initial position of GD is near the global minimum it converged to toward the optimal solution, which was rarely the case. For mesh sizes larger than the tested ones (relevant for MPI-based implementations), corresponding to a larger range of parameters, GD would be even less effective. Both BFS and GD can be made more usable if the range of parameters can be narrowed, i.e., if we know the relative performance of the GPU in comparison to the CPU. However, the GD would still be somewhat inefficient, due to its higher susceptibility to noise.

Since the GA method is shown to be superior to the other two approaches, we use GA as our optimization method of choice in the next two sections.

### 2.4.2. Testing Methodology

All programs were tested on the PARADOX-IV cluster, which is a part of the PARADOX supercomputing facility. This cluster is comprised of computing nodes with two Intel Xeon E5-2670 Sandy Bridge CPUs (with a total of  $2 \times 8 = 16$  cores), with 32 GB of RAM and one Nvidia Tesla M2090 GPU with 6 GB of GPU RAM, each connected by InfiniBand QDR interconnect. We used Intel's compiler (version 2016) to compile the serial and OpenMP programs, and CUDA 7.5 for the GPU portions of the CUDA and hybrid programs. MPI-based implementations were compiled with Open MPI (version 1.10), which itself relied on underlying Intel and CUDA compilers. In the case of Hybrid/MPI programs, we performed tests using both FFTW and our own transpose routines. We found the minimal execution times to be about the same for both approaches, but the FFTW transpose would sometimes exhibit very bad performance due to the creation of suboptimal communication plan. For this reason, the execution times reported for Hybrid/MPI implementation are obtained using only our own transpose routines.

The base of all performance evaluations was the measured execution time of critical regions of the programs, i.e., the portions performing wave function propagation in imaginary or in real time. This measurement excluded the time spent in other parts of the programs, e.g., initialization of OpenMP/CUDA/MPI environment, memory allocation and deallocation, creation and destruction of FFTW plans, initialization of variables and I/O operations. Measuring average execution time of a single iteration of the main time-propagation loop allows us to predict the performance and total execution time of a given simulation, as the number of iterations is specific to the problem at hand and may vary significantly between different simulations. All measurements were collected using high precision timers based on `clock_gettime` POSIX function on the CPU side, and CUDA event API on the GPU side. The execution time of a single iteration of serial programs depends on the mesh size, controlled by variables  $N_x$ ,  $N_y$  and  $N_z$ . For parallel programs, we can measure speedup and scaling efficiency as a function of the varying number of processing elements (OpenMP threads or MPI processes).

We tested performance of 1D, 2D and 3D programs on a range of mesh sizes, for a varying number of OpenMP threads and MPI processes, as shown in Table 2. Mesh sizes were chosen from the corresponding range, and we did not focus solely on mesh sizes which maximize performance of the programs, to

obtain a more realistic assessment. We varied the number of OpenMP threads from 1 to 16, in increments of one thread. Similarly, we tested the MPI-based implementations by varying number of MPI processes, each bound to a different cluster node. In this way we tested MPI-based implementations on 2, 4, 8, 12, 16, 20, 24, 28 and 32 computing nodes. Note that varying the number of processing elements is not applicable to the single-GPU implementations of the programs, as they always use all available processing resources on a GPU. Only one of the two 1D and 2D programs were tested (corresponding to  $x$  direction in 1D and  $x$ - $y$  plane in 2D), because, performance-wise, there is no difference between them (e.g., `imag1dX-th` vs. `imag1dZ-th`).

The main performance indicator is the execution time, the wall-clock time of one iteration of the main loop, averaged over 5 executions of 1000 iterations, reported in milliseconds. Using the results obtained, we calculated the speedup of all programs compared to the published serial C implementation. We were also interested in examining the scaling efficiency, or *scalability*, of the OpenMP and MPI programs. We tested both *strong* scaling, when the mesh size stays the same but the number of processing elements varies, and *weak* scaling, when the amount of work each processing element performs stays the same while the number of processing elements increases. More formally, given the execution time of a single iteration of serial programs ( $T(1)$ ), and the corresponding execution time for parallel programs performed with  $N$  processing elements ( $T(N)$ ), we calculated speedup as  $S(N) = T(1)/T(N)$  and strong scaling efficiency as  $E(N) = S(N)/N$ . Weak scaling is computed as  $E_W(N) = T_W(1)/T_W(N)$ , where  $T_W(1)$  is the execution time of a program using single processing element performing the work assigned to it, while  $T_W(N)$  is the execution time of a program using  $N$  processing elements performing  $N$  times more work. We achieve this by increasing the mesh size.

### 2.4.3. Performance Test Results and Modeling of Single Node Programs

In this section we present the results obtained for single computing node OpenMP, CUDA and hybrid programs, and compare them to the previously published [23] serial implementation.



**Table 2. Performance testing matrix, showing the mesh sizes and numbers of processing elements (threads or processes) used to test the programs, as well as the baseline program used for comparison**

Program	Mesh size		Processing elements		Baseline
	Min	Max	Min	Max	
OpenMP programs					
imag1dX-th	1000	1000000	1	16	imag1d
real1dX-th	1000	1000000			real1d
imag2dXY-th	1000 × 1000	15000 × 15000	1	16	imag2dXY
real2dXY-th	1000 × 1000	13000 × 13000			real2dXY
imag3d-th	50 × 50 × 50	800 × 800 × 800	1	16	imag3d
real3d-th	50 × 50 × 50	800 × 800 × 800			real3d
CUDA programs					
imag2dXY-cuda	1000 × 1000	15000 × 15000	1	1	imag2dXY
real2dXY-cuda	1000 × 1000	13000 × 13000			real2dXY
imag3d-cuda	50 × 50 × 50	600 × 600 × 600	1	1	imag3d
real3d-cuda	50 × 50 × 50	540 × 540 × 540			real3d
Hybrid programs					
imag2dXY-hetero	1000 × 1000	15000 × 15000	16+1	16+1	imag2dXY-th
real2dXY-hetero	1000 × 1000	13000 × 13000			real2dXY-th
imag3d-hetero	50 × 50 × 50	600 × 600 × 600	16+1	16+1	imag3d-th
real3d-hetero	50 × 50 × 50	600 × 600 × 600			real3d-th
OpenMP/MPI programs					
imag3d-mpi	480 × 480 × 250	1920 × 1920 × 960	1 × 16	32 × 16	imag3d-th
real3d-mpi	480 × 480 × 250	1920 × 1920 × 960			real3d-th
CUDA/MPI programs					
imag3d-mpicuda	480 × 480 × 250	1920 × 1920 × 960	1	32	imag3d-cuda
real3d-mpicuda	480 × 480 × 250	1920 × 1920 × 960			real3d-cuda
Hybrid/MPI programs					
imag3d-mpihetero	480 × 480 × 250	1920 × 1920 × 960	1 × (16+1)	32 × (16+1)	imag3d-hetero
real3d-mpihetero	480 × 480 × 250	1920 × 1920 × 960			real3d-hetero

**Table 3. Wall-clock execution times of a single iteration of the main time-propagation loop of single-node OpenMP programs (in milliseconds) for different number of OpenMP threads  $N_{\text{th}}$  and speedup  $S(16)$  in strong scaling tests. The speedup is calculated w.r.t. the execution times of previously published serial versions of programs [23], given in the second column**

Program	Serial	$N_{\text{th}} = 1$	$N_{\text{th}} = 2$	$N_{\text{th}} = 4$	$N_{\text{th}} = 8$	$N_{\text{th}} = 16$	$S(16)$
imag1dX-th	9.1	7.1	4.7	3.4	2.9	2.8	2.5
real1dX-th	15.2	14.2	10.5	8.2	7.3	7.2	2.0
imag2dXY-th	13657	7314	4215	2159	1193	798	9.2
real2dXY-th	17281	11700	6417	3271	1730	1052	11.1
imag3d-th	16064	9353	5201	2734	1473	888	10.5
real3d-th	22611	17496	9434	4935	2602	1466	11.9

Strong scaling performance test results for the OpenMP-based implementation using methodology described in the previous section are given in Table 3 and Figure 9. They show the obtained execution times, speedups and strong scaling efficiencies for different number of OpenMP threads. Columns  $N_{\text{th}} = 1$ ,  $N_{\text{th}} = 4$ ,  $N_{\text{th}} = 8$  and  $N_{\text{th}} = 16$  in Table 3 correspond to the number of threads used, while the last column shows the obtained speedup  $S(16)$  with 16 OpenMP threads compared to one OpenMP thread. Strong scaling efficiency  $E(N_{\text{th}}) = S(N_{\text{th}})/N_{\text{th}}$  in Figure 9 is calculated as a fraction of the obtained speedup compared to a theoretical maximum. The mesh size used in 1D is  $10^5$ , in 2D  $10^4 \times 10^4$ , while in 3D the mesh size is  $480 \times 480 \times 480$ . Execution times and speedups of imag1dZ-th, real1dZ-th, imag2dXZ-th, and real2dXZ-th (not reported here) are similar to those of imag1dX-th, real1dX-th, imag2dXY-th, and real2dXY-th, respectively.

The change from C2C to R2C FFT routine has a big impact on the execution time of single-threaded ( $N_{\text{th}} = 1$ ) programs compared to the previous serial programs. As we can see from the table, these improvements alone yield a speedup of 1.3 to 1.9 in 2D and 3D programs, and somewhat smaller speedup for 1D programs, 1.1 to 1.3. The use of additional threads brings about further speedup (reported in the last column) of 2 to 2.5 for 1D programs, and 9 to 12 for 2D and 3D programs. In Figure 9 we see that the efficiency rapidly decreases for 1D programs, even though speedup increases with the number of threads used.

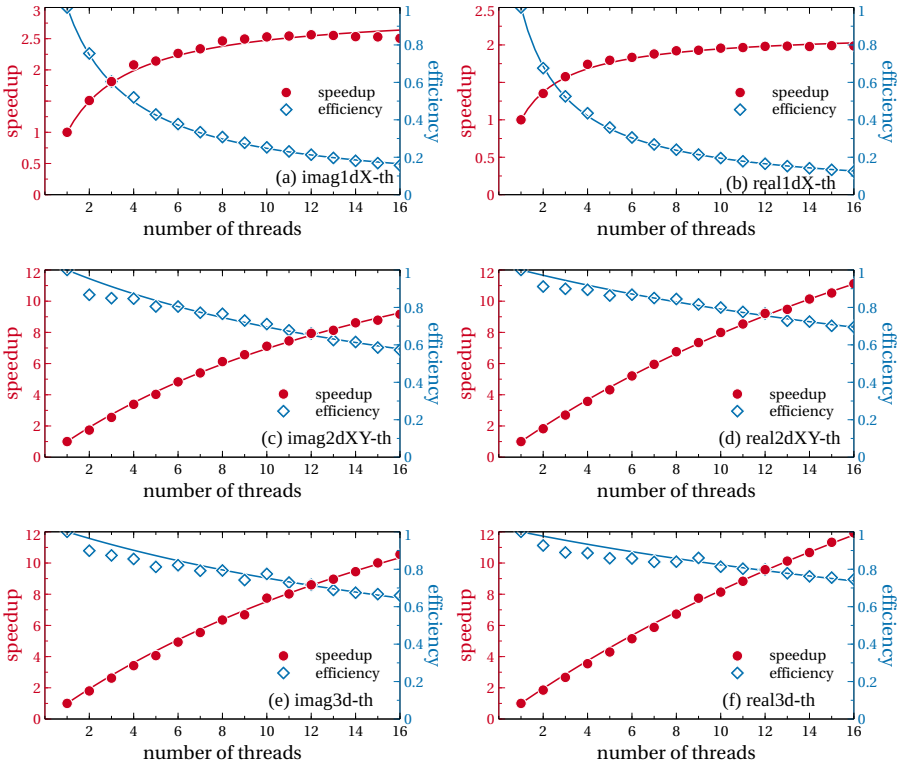


Figure 9. Speedup in the execution time and strong scaling efficiency of OpenMP programs compared to single-threaded runs for: (a) `imag1dX-th`, (b) `real1dX-th`, (c) `imag2dXY-th`, (d) `real2dXY-th`, (e) `imag3d-th`, (f) `real3d-th`. Solid lines represent fits to measured data, where fit model functions are given in the text and obtained fit parameters are listed in Table 4. Note that the model parameter  $p$  is fitted only to the speedup data, and then used to plot the efficiency model curve.

This is expected, as parts of the algorithm dealing with the recursive relations for calculation of the CN coefficients are inherently serial. In 1D, already with  $N_{\text{th}} = 4$  threads we almost achieve the maximal speedup, while still keeping the efficiency around 50%. We also see that, as expected, speedup and efficiency of multidimensional programs behave quite well as we increase the numbers of threads. In particular, we note that the efficiency always remains above 60%,

making the use of all available CPU cores worthwhile.

From Figure 9 we observe that the speedup of 1D programs saturate quickly due to inherent serial nature of the portion of the algorithm, while in 2D and 3D the speedup behaves almost linearly. Despite their obvious differences, all curves in Figure 9 can be successfully modeled based on Amdahl's law [58]. Namely, the measured execution time  $T(N_{\text{th}})$  of one iteration of the main loop can be expressed as

$$T(N_{\text{th}}) = T(1) \left( s + \frac{p}{N_{\text{th}}} \right), \quad (33)$$

where  $N_{\text{th}}$  is the number of threads used,  $T(1)$  is the execution time of a single-threaded run,  $s$  is the serial fraction of the loop code, and  $p$  is the corresponding parallel fraction. By definition,  $s + p = 1$ , and therefore the speedup can be modeled by

$$S(N_{\text{th}}) = \frac{T(1)}{T(N_{\text{th}})} = \frac{1}{1 - p + p/N_{\text{th}}}, \quad (34)$$

where the parallel fraction of the main loop code  $p$  is the only fit parameter. Table 4 gives the obtained model fit parameter values for the data from Figure 9. As we can see, the fits match the obtained measurement data very well. Note that the efficiency can be expressed in terms of the speedup model

$$E(N_{\text{th}}) = \frac{S(N_{\text{th}})}{N_{\text{th}}} = \frac{1}{N_{\text{th}}} \frac{1}{1 - p + p/N_{\text{th}}}, \quad (35)$$

and is not fitted independently. Figure 9 shows that this model with the parameter  $p$  fitted on the speedup data matches very well with the efficiency data points.

From the obtained values of the parallel fraction of the algorithm, we see that 2D and 3D programs are almost ideally parallelizable, with  $p$  over 95%. In 1D case, however, the parallel fraction is around 66% for imaginary-time propagation and around 54% for real-time propagation, due to the fact that calculation of CN coefficients in the function `calclux` cannot be parallelized. Note that the parallel fraction of imaginary-time 1D program is higher than that of the real-time 1D program due to the larger amount of arithmetic operations required to process complex-valued data in the real-time version of the serial function `calclux`.

OpenMP programs were also tested for weak scalability. We were mostly interested in 3D variants of the programs, which we tested by fixing the amount

**Table 4. Values of obtained strong scaling model fit parameter  $p$  and the estimated fit errors for OpenMP-parallelized programs**

Program	$p$	$\Delta p$
imag1dX-th	0.662	0.004
real1dX-th	0.541	0.003
imag2dXY-th	0.9514	0.0007
real2dXY-th	0.9706	0.0004
imag3d-th	0.9635	0.0008
real3d-th	0.9762	0.0006

of work to 6,912,000 spatial points of the mesh, which corresponds to a mesh size of  $240 \times 240 \times 120$ . By increasing the number of OpenMP threads, we also increase the mesh size to be the multiple of 6,912,000. This means that the mesh has to be increased in such a way that, when divided among the threads, each thread gets 6,912,000 spatial points to process. The mesh sizes that satisfy this requirement cannot always be obtained by multiplying all three array dimensions with the same number, so we have to work with mesh sizes in which the size of each dimension may be different. For such mesh sizes, we tested all possible combinations, however no significant difference has been observed. Table 5 contains mesh sizes we used for testing for  $N_{\text{th}} = 1, 2, 4, 8, 12, 16$  threads, along with the execution times (in milliseconds) and the weak scaling efficiency. The testing was also done for  $N_{\text{th}} = 6$  and 10 threads, but the corresponding mesh sizes are omitted from the table for brevity. However, Figure 10 presents complete data collected in this test, for all  $N_{\text{th}}$  values, averaged over mesh sizes used. The figure shows that the real-time 3D programs have better weak scaling efficiency, which is about 75% at 16 threads, while imaginary-time programs demonstrate smaller, but still significant efficiency of about 60%.

To model weak scaling efficiency, we compare execution times of a single iteration of the main loop  $T_W(N_{\text{th}})$ , performed with  $N_{\text{th}}$  threads, where for each value of  $N_{\text{th}}$  the total amount of work is  $N_{\text{th}}$  times the work being performed in a single-threaded run, i.e., the amount of work per thread is constant. The weak scaling efficiency is defined as

$$E_W(N_{\text{th}}) = \frac{T_W(1)}{T_W(N_{\text{th}})}, \quad (36)$$

where  $T_W(1) = T(1)$  is the execution time of a single-threaded run for a given

**Table 5. Weak scaling efficiency of OpenMP-parallelized 3D programs.**  
**Wall-clock execution times  $T_W$  are given in milliseconds, efficiencies  $E_W$**   
**in percents**

Mesh size	imag3d-th		real3d-th	
	$T_W$	$E_W$	$T_W$	$E_W$
$N_{th} = 1$				
$120 \times 240 \times 240$	699	98.2	1259	99.5
$240 \times 120 \times 240$	711	96.5	1271	100
$240 \times 240 \times 120$	686	100	1275	98.2
$N_{th} = 2$				
$240 \times 240 \times 240$	718	95.5	1254	99.9
$N_{th} = 4$				
$240 \times 240 \times 480$	755	90.9	1312	95.5
$240 \times 480 \times 240$	778	88.2	1301	96.3
$480 \times 240 \times 240$	754	91	1310	95.6
$N_{th} = 8$				
$240 \times 480 \times 480$	875	78.4	1405	89.9
$480 \times 240 \times 480$	847	81	1393	89.1
$480 \times 480 \times 240$	886	77.5	1431	87.7
$N_{th} = 12$				
$360 \times 480 \times 480$	1010	67.9	1532	81.7
$480 \times 360 \times 480$	981	69.9	1514	82.7
$480 \times 480 \times 360$	1004	68.4	1581	79.2
$N_{th} = 16$				
$480 \times 480 \times 480$	1155	59.4	1680	74.5

workload (in our case, 6,912,000 spatial points). The expected execution time of a workload assigned to a simulation with  $N_{th}$  threads, executed in a single-threaded run, is  $N_{th}T(1)$ . In weak scaling tests, this workload is executed with  $N_{th}$  threads and therefore the expected execution time can be modeled by

$$T_W(N_{th}) = N_{th}T(1) \left( 1 - p + \frac{p}{N_{th}} \right). \quad (37)$$

According to this argument, we model the weak scaling efficiency by a single-parameter function

$$E_W(N_{th}) = \frac{1}{p + (1 - p)N_{th}}. \quad (38)$$

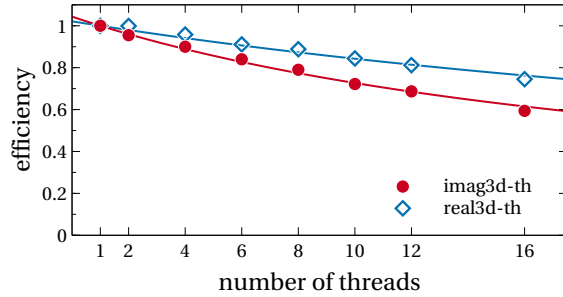


Figure 10. Weak scaling efficiency of OpenMP-parallelized 3D programs, averaged over all mesh sizes tested for each value of  $N_{th}$ . Solid lines represent fits to measured data, where fit model functions are given in the text.

We fitted this model to data presented in Figure 10 and the obtained fit parameters are given in Table 6. As we can see from the figure, the above model is an excellent fit to experimental data, and both 3D OpenMP-parallelized programs have high (above 95%) parallel fraction of the code, in agreement with the results of strong scaling tests (Table 4).

**Table 6. Values of obtained weak scaling model fit parameter  $p$  and the estimated fit errors for OpenMP-parallelized programs**

Program	$p$	$\Delta p$
imag3d-th	0.958	0.002
real3d-th	0.9792	0.0009

Overall, we conclude that imaginary-time OpenMP-parallelized programs show smaller speedup and efficiency across all tests, except in 1D. This can be attributed to the additional step of wave function normalization in each iteration of the imaginary-time propagation, as well as the fact that real-time programs work with complex-valued data that require more arithmetic operations for the same mesh size. Since much of the computation inside loops requires simple arithmetic, the throughput of the CPU is often not fully exploited in imaginary-time programs, thus the pressure of memory bandwidth makes these programs less efficient. The real-time programs are also affected by this, however to a somewhat lesser extent.

Next, we consider the CUDA implementation of the shared memory algorithm. GPU functions as a single processing element, therefore we cannot test CUDA implementation by varying both the mesh size and the number of processing elements. However, just varying the mesh size gives us valuable insight into the behavior of this implementation, due to the difference in programming models and the libraries used. Tables 7 and 8 show the execution times (in milliseconds) for a number of mesh sizes tested, as well as the average speedup  $\langle S \rangle$  compared to the serial programs [23]. Figure 11 shows the speedup obtained for all mesh sizes tested, and horizontal lines represent average speedups obtained for each program. Note that the dispersion of data is due to the use of `FFTW_ESTIMATE` flag in library calls to `FFTW` in the serial programs. Use of this flag results in a choice of suboptimal FFT algorithm for some mesh sizes. The vertical lines in Figure 11 denote the change in `POTMEM` parameter. The speedups left of the first vertical line are obtained with `POTMEM=2` and thus demonstrate the best speedup. Second group of results, between the two vertical lines, is obtained with `POTMEM=1`, and we note that the speedup decreases slightly, while the results right of the second vertical line are obtained with `POTMEM=2`, and show the smallest speedup due to the use of mapped memory. The 2D programs in  $x$ - $z$  plane exhibited very similar performance to those of  $x$ - $y$  plane, and therefore we did not include them in the figures.

**Table 7. Wall-clock execution times of a single iteration of the main time-propagation loop of single-node 2D CUDA programs (in milliseconds) for different mesh sizes, and average speedup w.r.t. to the execution times of serial 2D programs [23]**

Program	2000 <sup>2</sup>	4000 <sup>2</sup>	6000 <sup>2</sup>	8000 <sup>2</sup>	10000 <sup>2</sup>	12000 <sup>2</sup>	Avg. speedup
imag2dXY-cuda	24.1	104.3	235.2	386.1	657.1	1150.4	10
real2dXY-cuda	29.9	112.4	266.4	444.0	749.0	1528.3	14

For small mesh sizes, the GPU remains underutilized, resulting in a smaller speedup. For large mesh sizes, where the GPU memory usage approaches the limit, we also see declining speedup. This is due to the inevitable use of `POTMEM` parameter, which keeps some arrays in the host memory when they cannot fit in the memory of the GPU. Overall, the CUDA implementation shows execution times similar to the OpenMP implementation for imaginary-time propagation, and slightly lower for real-time propagation. We stress that these results strongly depend on the type of GPU used and that the obtained speedups



**Table 8. Wall-clock execution times of a single iteration of the main time-propagation loop of single-node 3D CUDA programs (in milliseconds) for different mesh sizes, and average speedup w.r.t. to the execution times of serial 3D programs [23]**

Program	$100^3$	$200^3$	$300^3$	$400^3$	$500^3$	Avg. speedup
imag3d-cuda	10.6	79.3	298.8	674.5	1260.2	7.1
real3d-cuda	10.9	84.1	302.5	682.4	1467.4	13.5

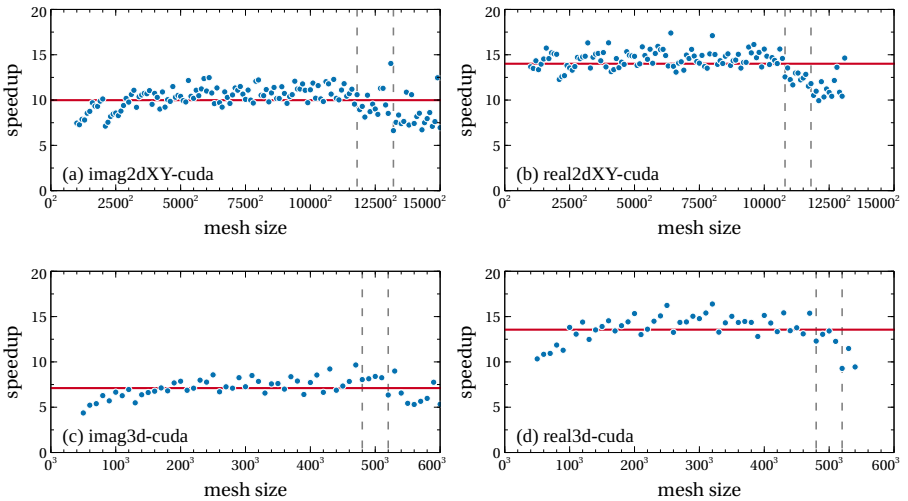


Figure 11. Speedup in the execution time of CUDA programs compared to the serial programs for all tested mesh sizes: (a) *imag2dXY-cuda*, (b) *real2dXY-cuda*, (c) *imag3d-cuda*, (d) *real3d-cuda*. Horizontal lines represent  $\langle S \rangle$ , while dashed vertical lines represent different values of POTMEM parameter (see text).

may be even better for newer-generation GPUs (e.g., *Kepler*-, *Maxwell*-, *Pascal*- and *Volta*-based GPUs).

Hybrid OpenMP/CUDA implementation was tested on a range of mesh sizes, similarly to the OpenMP- and CUDA-based implementations. Since OpenMP implementation showed that all cores should be used for 2D and 3D programs, we kept the number of OpenMP threads fixed at 16 in our hybrid algorithm. The parameters governing the amount of data offloaded to GPU were optimized using our GA method from section 2.4.1 An illustrative subset of the

results for 3D programs is shown in Table 9, which gives execution times for a single iteration of the main loop, for different mesh sizes. A comparison of execution times of hybrid and pure OpenMP programs with  $N_{\text{th}} = 16$  threads is given in Figure 12(a), while Figure 12(b) compares the performance of hybrid and pure CUDA programs, for all tested mesh sizes.

**Table 9. Wall-clock execution times of a single iteration of the main time-propagation loop of single-node 3D hybrid programs (in milliseconds) for different mesh sizes. Offload parameters are optimized using the GA optimization method**

	$80^3$	$200^3$	$320^3$	$440^3$	$560^3$	$680^3$	$800^3$
imag3d-hetero	6.3	67.1	271.4	678.9	1493.3	2750.9	4461.6
real3d-hetero	8.0	94.7	374.1	922.8	1985.2	4020.2	6676.6

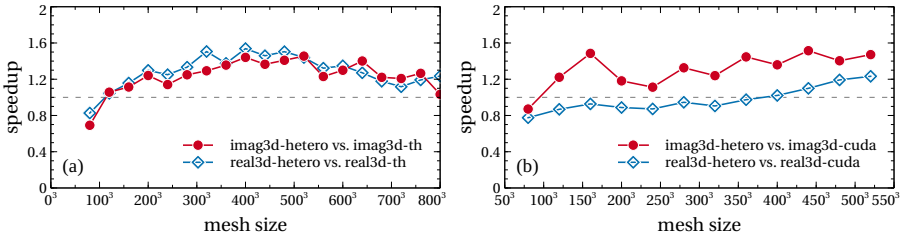


Figure 12. Speedup in the execution time of 3D hybrid programs compared to: (a) OpenMP programs with  $N_{\text{th}} = 16$  threads, (b) CUDA programs. Dashed horizontal lines correspond to a speedup value  $S = 1$ .

From Figure 12 we see that the hybrid implementation outperforms the OpenMP one for all mesh sizes except for the smallest one. The same applies to the comparison of imaginary-time hybrid and CUDA programs, while real-time hybrid program outperforms the corresponding CUDA program only for mesh sizes larger than  $400 \times 400 \times 400$ . Although one would expect that the speedup of the optimized hybrid algorithm is always equal to or larger than one, we see that this is not the case for all mesh sizes in Figure 12. This is due to the fact that the hybrid FFT algorithm is always employed in hybrid programs, meaning

that even if no or all data are offloaded to GPU, the splitting of FFT will still take place. Therefore, in these limiting cases we do not obtain pure OpenMP or CUDA algorithms that would yield maximal performance. Splitting the computation of FFT along one direction in `calcpsidd2` function disables some of the potential optimizations that libraries like FFTW and cuFFT exploit, and introduces data copies between host and device which cannot be fully offset using CUDA streams. The hybrid algorithm can compensate for this if the amount of offloaded data to GPU is sufficiently large, which is not the case for the smallest mesh size.

**Table 10. Optimal fraction of total data offloaded to GPU for different mesh sizes in hybrid 3D programs, obtained using the GA optimization method**

Mesh size	GPU portion of data [%]							
	imag3d-hetero				real3d-hetero			
	PS <sub>1</sub>	PS <sub>2</sub>	PS <sub>3</sub>	PS <sub>4</sub>	PS <sub>1</sub>	PS <sub>2</sub>	PS <sub>3</sub>	PS <sub>4</sub>
80 × 80 × 80	20	3	60	33	23	3	40	10
120 × 120 × 120	12	10	25	28	23	10	25	27
160 × 160 × 160	15	7	31	24	44	19	34	23
200 × 200 × 200	38	27	37	28	44	26	46	26
240 × 240 × 240	38	28	40	30	38	28	47	25
280 × 280 × 280	40	31	30	33	46	22	37	25
320 × 320 × 320	33	38	29	36	45	28	69	44
360 × 360 × 360	41	33	27	36	49	33	43	31
400 × 400 × 400	38	25	30	38	46	24	47	21
440 × 440 × 440	31	35	29	39	45	35	43	32
480 × 480 × 480	16	19	22	41	45	33	62	35
520 × 520 × 520	40	31	28	46	45	25	40	37
560 × 560 × 560	38	41	30	43	36	24	35	32
600 × 600 × 600	37	27	30	43	29	29	29	28
640 × 640 × 640	36	40	30	43	24	22	24	23
680 × 680 × 680	26	38	28	38	20	16	20	20
720 × 720 × 720	23	26	25	32	17	13	17	17
760 × 760 × 760	21	22	25	27	14	14	14	13
800 × 800 × 800	19	23	23	21	11	8	12	12

Given that pure CUDA programs performing imaginary-time propagation demonstrated smaller speedup than the corresponding OpenMP programs (Figure 11 vs. Figure 9), it is expected that CUDA portion of the hybrid imaginary-time propagation programs would yield smaller improvement, which is evident when we compare hybrid implementation with the OpenMP one in Figure 12(a), except for the largest mesh sizes. We can reach the same conclusion if we consider that, in real-time propagation, CUDA implementation shows the highest speedup of all single-node programs, and therefore the corresponding hybrid programs show better speedup than imaginary-time propagation programs parallelized with OpenMP. On the other hand, when compared with the CUDA implementation in Figure 12(b), the situation is reversed, and we see much better performance of the hybrid imaginary-time propagation programs, while the hybrid real-time propagation programs achieve speedup larger than one only for mesh sizes larger than  $400 \times 400 \times 400$ . This result can be attributed to the fact that in real-time propagation the amount of data copied between host and device is larger, given that some of the copied arrays are complex-valued.

Also, we can observe that the speedup in Figure 12(a) declines with mesh size. This is due to the memory saturation of the GPU device, as only a small portion of the data can be offloaded when the mesh is large. The amount of data offloaded to GPU for all tested mesh sizes is given in Table 10, where we can see that the total amount of data processed by the GPU declines with increasing mesh size. As a result, the computation is unbalanced, given that the host has to work with a much larger portion of the data. This is reflected in the optimization step, where our GA quickly converges to the highest possible mesh size that can be offloaded to the device, implying that a greater amount of device memory would be required to get a balanced computation.

To make an optimal choice of programs to be used on a single node for a particular hardware platform, one has to perform detailed tests using the methodology presented in section 2.4.2. The results presented in this section apply to hardware comparable to the one available at PARADOX supercomputing facility, but one can expect similar behavior for all modern types of CPU and GPU.

#### **2.4.4. Performance Test Results and Modeling of MPI Programs**

Following on from the previous section, here we present the results obtained for MPI-parallelized programs, executed on a computer cluster consisting of varying number of computing nodes, and compare them with the corresponding

single-node programs.

MPI programs are highly dependent on the configuration of the cluster, mainly on the speed of interconnect, but also on the distribution of processes and threads, NUMA configuration, MPI configuration, etc. Getting the best performance out of the programs requires some experimentation with several different configurations. The results presented are obtained without extensive tuning of the cluster or MPI runtime, with the aim to show the base performance.

Strong scaling of MPI-based implementations is tested in a similar way to the single-node testing, by varying number of cluster nodes  $N_p$  from 2 to 32. On each node, a single MPI process is launched, which then uses the node's resources, either by further spawning 16 OpenMP threads in case of OpenMP/MPI and Hybrid/MPI implementations, or by invoking the CUDA kernels utilizing the node's GPU in case of CUDA/MPI implementation. In this test, the baseline used for comparison was the equivalent single-node implementation, i.e., OpenMP/MPI programs are compared with OpenMP programs executing with  $N_{th} = 16$  threads, CUDA/MPI programs are compared to the single-node pure CUDA programs, and Hybrid/MPI programs is compared to the single-node hybrid programs.

Mesh size we use in this test is  $480 \times 480 \times 250$ . Since the values of  $N_x$  and  $N_y$  parameters must be divisible by the number of processes  $N_p$ , this mesh cannot be distributed over 28 processes. In this case we use slightly modified mesh, taking into account the multiple of 28 that is closest to 480, yielding a mesh size of  $476 \times 476 \times 250$ . Data is never distributed along  $z$  direction, so no such requirement exists for  $N_z$ . The resulting mesh has slightly fewer spatial points, and thus less work per process, potentially allowing for a better performance, but in our tests the smaller mesh did not have a significant impact on the measured execution time.

Note that strong scaling tests, where the mesh size is fixed, inevitably lead to saturation and decrease in measured speedup and efficiency values. Whatever the chosen mesh size, increase in the number of cluster nodes used will eventually yield insufficient amount of work per MPI process, such that communication will start to dominate over computation. Therefore, in our strong scaling tests we can expect that execution times initially decrease with increasing values of  $N_p$ , but eventually performance of MPI-based programs will decline. This issue is addressed by considering weak scaling tests.

**Table 11. Wall-clock execution times of a single iteration of the main time-propagation loop of OpenMP/MPI, CUDA/MPI and Hybrid/MPI programs (in milliseconds) for different number of MPI processes  $N_p$  and speedup  $S(32)$  in strong scaling tests. The speedup is calculated w.r.t. the baseline execution times of the corresponding single-node programs (OpenMP, CUDA and hybrid, respectively), given in the second column.**

Program	Baseline	$N_p = 4$	$N_p = 8$	$N_p = 16$	$N_p = 24$	$N_p = 32$	$S(32)$
imag3d-mpi	1124	541	262	134	89	64	17.5
real3d-mpi	2140	700	358	207	155	98	21.8
imag3d-mpicuda	579	438	210	103	71	59	9.8
real3d-mpicuda	800	609	291	142	95	79	10.1
imag3d-mpihetero	489	299	162	99	84	81	6.0
real3d-mpihetero	613	407	255	154	135	101	6.0

The illustrative portion of obtained execution times of a single iteration of the main loop for the three MPI-parallelized implementations are shown in Table 11, together with the execution times of the corresponding baseline single-node program. Columns  $N_p = 4$ ,  $N_p = 8$ ,  $N_p = 16$  and  $N_p = 32$  correspond to the number of cluster nodes used, while the last column shows the obtained speedup  $S(32)$  with  $N_p = 32$  nodes compared to baseline single-node programs.

The maximal speedup of OpenMP/MPI implementation ranges from 17 for imaginary-time propagation to 22 for real-time propagation programs for  $N_p = 32$ . The complete measurement results for speedup and efficiency are depicted in Figure 13(a) and 13(b), where we see that the speedup grows linearly with the number of nodes used, while the efficiency remains mostly constant in the range between 40% and 60%, thus making the use of OpenMP/MPI programs highly advantageous for simulations with large mesh size. In general, we can expect even better efficiency for larger mesh sizes.

Similar behavior is observed for CUDA/MPI implementation. The obtained speedup with  $N_p = 32$  nodes ranges from 9 to 10, with the slightly lower efficiency, between 30% and 40%, as shown in Figure 13(c) and 13(d). Even though the efficiency is lower for this implementation, the speedup still grows linearly and the execution times are lower than for the OpenMP/MPI implementation. This makes CUDA/MPI programs ideal choice for use on GPU-enabled computer clusters. Additional benefit of using CUDA/MPI programs is their low CPU usage (using only one CPU core per cluster node), allowing for the possibility that the same cluster nodes are used for other CPU-intensive simulations in a time-sharing fashion.

As we see in Figure 13(e) and 13(f), the linear growth of speedup is also present for the Hybrid/MPI implementation, however, as the amount of work per-process shrinks, the efficiency drastically drops down to 20% with  $N_p = 32$  nodes. For the mesh size used in this test, we observe that the Hybrid/MPI implementation performs very well on  $N_p < 16$  processes, providing the lowest execution times, but with  $N_p \geq 16$  processes its execution times become larger than for the CUDA/MPI implementation (especially for real-time propagation programs), and eventually even for the OpenMP/MPI implementation, as illustrated in Figure 14. This is again due to the insufficient amount of work each computing node performs after data are distributed among the MPI processes, which can be seen from the amount of data offloaded to GPU for all tested values of  $N_p$  in Table 12. Similar saturation in performance will eventually happen

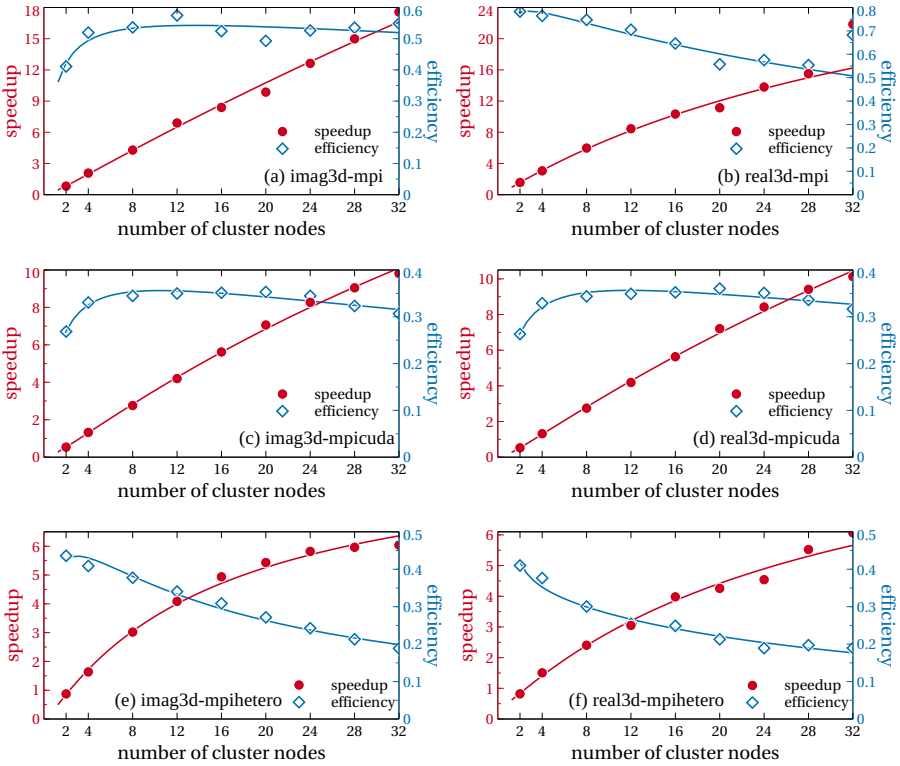


Figure 13. Speedup in the execution time and strong scaling efficiency of MPI-based programs compared to single-node runs: (a) *imag3d-mpi*, (b) *real3d-mpi*, (c) *imag3d-mpicuda*, (d) *real3d-mpicuda*, (e) *imag3d-mpihetero*, (f) *real3d-mpihetero*. Solid lines represent fits to measured data, where fit model functions are given in the text and obtained fit parameters are listed in Table 13. Note that the model parameters are fitted only to the speedup data, and then used to plot the efficiency model curve.

for the OpenMP/MPI and CUDA/MPI implementations for larger values of  $N_p$ .

We thus conclude that Hybrid/MPI implementation has the best performance of the three MPI-based implementations if the amount of work per process remains high enough to justify the use of hybrid algorithm. Otherwise, either of the other two MPI-based implementations should be considered first. The energy efficiency of this and other MPI-based implementations was not



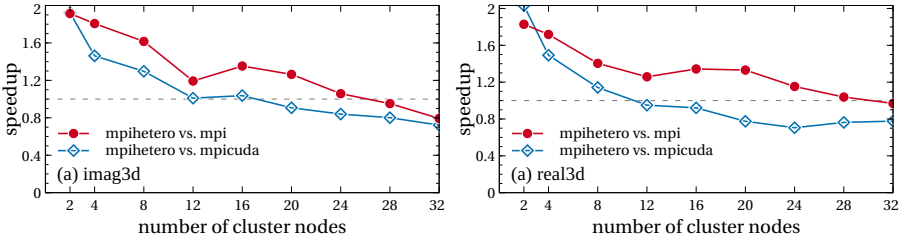


Figure 14. Speedup in the execution time of Hybrid/MPI programs in strong scaling tests compared to the other two MPI-based programs: (a) OpenMP/MPI, (b) CUDA/MPI.

explored due to the difficulty in making precise measurements. If the energy consumption is not an issue, Hybrid/MPI implementation will yield the best performance, providing the cluster has powerful GPUs installed and the mesh size used is large enough.

**Table 12. Optimal fraction of total data offloaded to GPU per process for different values of  $N_p$  in Hybrid/MPI programs, obtained using the GA optimization method in strong scaling tests**

$N_p$	GPU portion of data [%]							
	imag3d-mpihetero				real3d-mpihetero			
	PS <sub>1</sub>	PS <sub>2</sub>	PS <sub>3</sub>	PS <sub>4</sub>	PS <sub>1</sub>	PS <sub>2</sub>	PS <sub>3</sub>	PS <sub>4</sub>
1	30	17.5	34.4	36.7	45.2	32.5	55	35
2	25	10	17.5	16.7	20.8	11.5	23.8	16
4	10	5.2	9.2	9.4	10	5.2	15	6.7
8	5	2.9	5.8	6.7	6.3	2.1	6.7	5
12	3.3	1.7	4.2	4.2	4	1.3	5	3.3
16	2.9	1.3	2.9	2.1	3.1	0.4	2.9	2.1
20	1.7	0.6	2.5	1	2.5	0.4	2.5	1.7
24	1.7	1.3	2.1	1.7	2.1	1.3	2.5	0.8
28	1.7	0.4	2.1	1.3	1.7	0.4	1.7	1.3
32	0.8	0.4	1.7	0.8	1.5	0.4	2.1	0.8

We now model the speedup and strong scaling efficiency of MPI-based programs. In general, the execution time of a program can be expressed as

$$T(N_p) = \alpha + \beta L + \gamma \frac{M}{N_p} + \beta V \frac{M}{N_p^2}, \tag{39}$$

where  $\alpha$  represents the average time to perform serial portion of the code,  $L$  is the communication latency associated with one MPI message,  $\beta$  is the frequency of MPI messaging,  $\gamma$  is the average time to process one spatial point,  $V$  is related to data transfer speed (throughput), and  $M$  is the mesh size ( $N_x \times N_y \times N_z$ ). The communication overhead of one all-to-all message passing instance is equal to  $L + VM/N_p^2$ , where each of  $N_p$  processes communicates its  $M/N_p$  part of the mesh evenly to all other processes, leading to a message size of  $M/N_p^2$ . Taking into account that in the strong scaling tests the mesh size is fixed, the above model can be simplified to

$$T(N_p) = T(1) \left( a + \frac{b}{N_p} + \frac{c}{N_p^2} \right), \tag{40}$$

while the speedup can be modeled by

$$S(N_p) = \frac{T(1)}{T(N_p)} = \frac{1}{a + b/N_p + c/N_p^2}. \tag{41}$$

**Table 13. Values of obtained strong scaling model fit parameters  $a, b$  and  $c$ , as well as the estimated fit errors for MPI-parallelized programs**

Program	$a$	$\Delta a$	$b$	$\Delta b$	$c$	$\Delta c$
imag3d-mpi	0.008	0.006	1.6	0.2	1.4	0.4
real3d-mpi	0.026	0.006	1.1	0.1	0.2	0.3
imag3d-mpicuda	0.025	0.008	2.3	0.2	2.8	0.6
real3d-mpicuda	0.020	0.008	2.3	0.2	2.8	0.6
imag3d-mpihetero	0.104	0.009	1.7	0.2	0.9	0.5
real3d-mpihetero	0.09	0.02	2.7	0.3	-1.0	0.6

This model is fitted to the obtained strong scaling measurement data and the results are presented in Table 13, while the corresponding model curves are

shown as solid lines in Figure 13. As we see, the proposed model agrees very well with the experimental data. The only exception is the speedup and efficiency of real-time OpenMP/MPI program (real3d-mpi) on  $N_p = 32$  processes, where FFTW library creates an optimal transform plan that works very well with the given mesh size. However, changing the mesh size even slightly gives the performance comparable to the model prediction. We note that the value of the model parameter  $c$  is negative for real-time Hybrid/MPI program (real3d-mpihetero), which should not be the case since its parameter is related to data transfer speed. However, due to uncertainty of the optimization choice by the GA method and the fact that the fraction of total data offloaded to GPU gradually decreases (Table 12), leading from real hybrid algorithm to almost pure OpenMP/MPI one with hybrid FFT, it is not surprising that the obtained value differs from expected. Taking into account relatively large fit error  $\Delta c/c = 60\%$  for this parameter, we can still use expression (41) to model performance of Hybrid/MPI programs.

Next, we test weak scaling of MPI-based implementations. The same number of cluster nodes (and thus MPI processes) was used as in previous tests, while the starting mesh, which corresponds to a unit workload, had a size of  $480 \times 480 \times 480$ , amounting to 110,595,000 spatial points. This number of spatial points was kept constant per process, similarly to the weak test of OpenMP programs. There is an exception to this scheme, the case when programs are executed on  $N_p = 28$  nodes, as the scaled number of spatial points cannot be evenly distributed among 28 processes. In this case we compare the weak scalability by scaling up a starting mesh of  $476 \times 476 \times 476$ , which has 107,850,176 spatial points, just slightly less than for other values of  $N_p$ . The base of comparison was the execution time of a single iteration of the main loop with the corresponding MPI-based program running as a single process ( $N_p = 1$ ). While we used this configuration as the baseline, we do not recommend running MPI-based programs with  $N_p = 1$  processes, because no special handling of such case has been implemented. This means that MPI-parallelized programs are always transposing the data, which is unnecessary with  $N_p = 1$  as all data is local to the single process. Instead, we recommend using single-node variants of the programs outside cluster environment.

**Table 14. Weak scaling of MPI-based programs. Wall-clock execution times  $T_W$  are given in milliseconds, efficiencies  $E_W$  in percents**

Mesh size	imag3d-mpi		real3d-mpi		imag3d-mpicuda		real3d-mpicuda		imag3d-mpihetero		real3d-mpihetero	
	$T_W$	$E_W$	$T_W$	$E_W$	$T_W$	$E_W$	$T_W$	$E_W$	$T_W$	$E_W$	$T_W$	$E_W$
$N_p = 1$												
480 × 480 × 480	1758	100	2956	100	4338	100	6346	100	1971	100	2877	100
$N_p = 2$												
480 × 480 × 960	3858	45.6	4910	60.2	3785	114.6	5430	116.9	2044	96.4	2878	100
480 × 960 × 480	3704	47.5	5035	58.7	3825	113.4	5573	113.9	1997	98.7	2928	98.3
960 × 480 × 480	3758	46.8	5506	53.7	3871	112.1	5609	113.1	2019	97.6	2980	96.5
$N_p = 4$												
480 × 960 × 960	4267	41.2	6033	49.2	2995	144.8	4278	148.3	2149	91.7	3009	95.6
960 × 480 × 960	3877	45.4	5223	56.6	3042	142.6	4318	146.9	2218	88.9	3274	87.9
960 × 960 × 480	4000	44	5063	58.4	3078	140.9	4424	143.4	2148	91.8	3106	92.6
$N_p = 8$												
960 × 960 × 960	4327	40.6	6285	47	2952	146.9	4167	152.3	2369	83.2	3338	86.2
$N_p = 12$												
1440 × 960 × 960	4400	40	6729	43.9	2902	149.5	4254	149.2	2335	84.4	3504	82.1
960 × 1440 × 960	4268	41.2	6263	47.2	2953	146.9	4167	152.3	2412	81.7	3440	83.6
960 × 960 × 1440	4234	40.2	6299	46.9	2865	151.4	4153	152.8	2413	81.7	3351	85.9
$N_p = 16$												
1920 × 960 × 960	4356	40.4	6419	46	3001	144.5	4278	148.3	2392	82.4	3434	83.8
960 × 1920 × 960	4266	41.2	6376	46.4	2970	146.1	4170	152.2	2552	77.2	3525	81.6
960 × 960 × 1920	4234	40.2	6508	45.4	2888	150.2	4148	153	2639	74.7	3606	79.8
$N_p = 24$												
1440 × 1920 × 960	4677	40	6895	42.9	2924	148.4	4266	148.8	2552	77.3	3770	76.3
1440 × 960 × 1920	4796	38.3	7076	41.8	2984	145.4	4235	149.8	2611	75.5	3699	77.8
1920 × 1440 × 960	4470	40.6	6439	45.9	3007	144.2	4286	148.1	2546	77.4	3504	82.1
1920 × 960 × 1440	4450	40.8	6425	46	2984	145.3	4251	149.3	2551	77.3	3550	81.1
960 × 1440 × 1920	4364	41.1	6846	43.2	2879	150.7	4105	154.6	2682	73.5	3725	77.2
960 × 1920 × 1440	4346	41	6806	43.4	2878	150.7	4133	153.5	2501	78.8	3562	80.8
$N_p = 32$												
1920 × 1920 × 960	4452	39.5	6704	44.1	3183	136.3	4518	140.5	2585	76.3	3715	77.5
1920 × 960 × 1920	4520	38.9	6802	43.4	3163	137.2	4480	141.7	2632	74.9	3769	76.3
960 × 1920 × 1920	4301	40.9	6663	44.4	3014	143.9	4351	145.9	2776	71	3933	73.0

Table 14 lists mesh sizes used and execution times obtained for  $N_p = 1, 2, 4, 8, 12, 16$  and 32 cluster nodes. We also tested weak scaling on  $N_p = 20, 24$  and 28, but have excluded them from the table for brevity. A complete comparison is shown in Figure 15. The ordering of mesh dimensions had a slightly greater impact than with single-node OpenMP programs, varying up to 10% for the OpenMP/MPI programs, and less for the other two MPI-based implementations. This means that for meshes of the same size, thus implying equal work, execution times were mostly lower for those with larger values of  $N_x$  (e.g., the execution time for a  $960 \times 480 \times 960$  mesh is lower than for a  $480 \times 960 \times 960$  one). However, no distinct pattern emerges that would give us a clue as to which order is the most favorable. Upon inspection, we find that the difference in execution times is due to the different FFT plans employed by the FFTW and cuFFT libraries. The communication time remains mostly the same, as is expected since the amount of data exchanged is the same.

The results of weak scaling tests warrant further discussion as the execution times and plotted efficiencies appear misleading. On one hand, OpenMP/MPI programs show poor scaling results, achieving only 40% efficiency, while on the other hand the CUDA/MPI show efficiency well above 100%, a seemingly impossible result. The lower efficiency of the OpenMP/MPI programs is due to the very good performance of the baseline run. Here, the FFTW creates a very good FFT and transpose plans, which exploit the fact that all data are local, and thus have very good execution time. With  $N_p = 2$  nodes the execution time increases significantly, and efficiency drops to about 45-55%. However, adding more work and nodes has much smaller impact on efficiency, which only drops to 40-45% with  $N_p = 32$  nodes. If we use  $N_p = 2$  as the baseline, we see that the efficiency remains above 80%, a very good result.

In contrast to the OpenMP/MPI version, CUDA/MPI version performs very badly when executed on one node. Due to message sizes, MPI implementation used (Open MPI) relies on asynchronous copies through host memory [59] to perform the required communication. This results in bad performance due to a lack of overlap when copying data, as there is only one process involved. With  $N_p = 2$  processes the situation improves, as multiple streams are used, much like how we employ streams to overlap computation and data transfers in implementation of the hybrid algorithm. Between  $N_p = 4$  and 16 processes we get the best performance, and further increasing the number of processes only slightly reduces efficiency due to the size and amount of messages passed. If we compare the weak scaling efficiency with the best result as the baseline

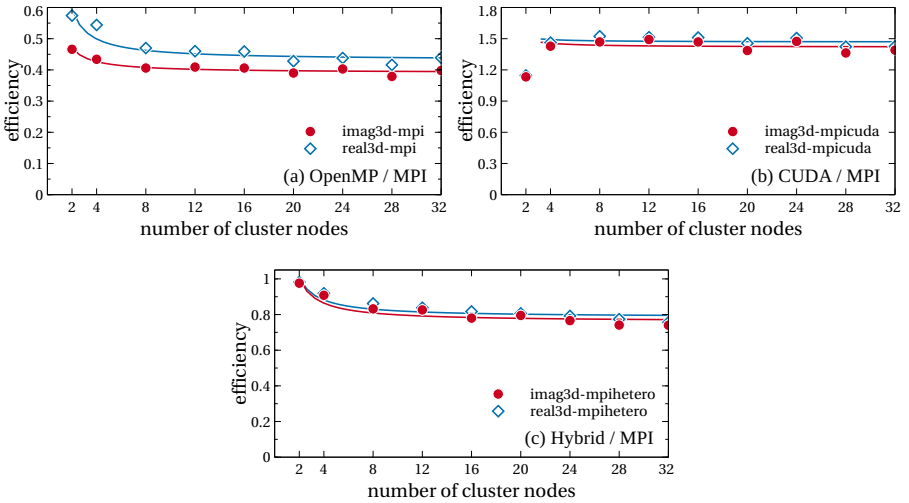


Figure 15. Weak scaling efficiency of three MPI-based implementations, averaged over all mesh sizes tested for each value of  $N_p$ . Solid lines represent fits to measured data, where fit model functions are given in the text.

(obtained with  $N_p = 16$  processes), we see that the efficiency is lower than for the OpenMP/MPI version, due to the different transpose routine used and divided multidimensional FFT that has to be employed. However, we stress that, in terms of absolute execution times, CUDA/MPI is faster than OpenMP/MPI version for  $N_p \geq 4$ .

The Hybrid/MPI version behaves as expected and demonstrates weak scaling efficiency of about 70-75% with  $N_p = 32$  nodes. Since data are transposed only in host memory, this version does not suffer the penalty of memory copies like the CUDA/MPI version, and therefore achieves much better efficiency with small number of cluster nodes. In terms of absolute execution times, Hybrid/MPI version is the fastest of all three implementations for  $N_p \geq 2$  and is therefore the algorithm of choice for distributed memory systems. Of course, it assumes previous optimization of offloading parameters using the GA method, which itself is time-consuming and has to be taken into consideration when making the choice. Table 15 provides data on the optimal fraction of total data offloaded to GPU in our weak scaling tests. As the number of processes increases, one expects that the amount of data offloaded to GPU remains constant, which is the case, as we see from the table. The only exceptions are when the

**Table 15. Optimal fraction of total data offloaded to GPU in weak scaling tests for different mesh sizes in Hybrid/MPI programs, obtained using the GA optimization method**

Mesh size	imag3d-mpihetero				real3d-mpihetero			
	PS <sub>1</sub>	PS <sub>2</sub>	PS <sub>3</sub>	PS <sub>4</sub>	PS <sub>1</sub>	PS <sub>2</sub>	PS <sub>3</sub>	PS <sub>4</sub>
$N_p = 1$								
480 × 480 × 480	35	20	31	44	46	30	40	35
$N_p = 2$								
480 × 480 × 960	46	33	33	47	38	29	37	38
480 × 960 × 480	50	67	17	47	45	60	19	40
960 × 480 × 480	50	15	70	34	43	15	67	35
$N_p = 4$								
480 × 960 × 960	40	65	18	47	40	63	17	37
960 × 480 × 960	50	10	67	42	40	12	75	33
960 × 960 × 480	33	29	33	40	45	22	33	40
$N_p = 8$								
960 × 960 × 960	53	25	33	47	40	27	40	28
$N_p = 12$								
1440 × 960 × 960	37	20	53	45	42	18	60	63
960 × 1440 × 960	40	38	27	47	45	35	27	35
960 × 960 × 1440	50	25	38	45	45	25	40	40
$N_p = 16$								
1920 × 960 × 960	47	13	67	27	42	13	80	30
960 × 1920 × 960	47	47	35	37	47	53	20	25
960 × 960 × 1920	50	20	33	33	47	20	40	27
$N_p = 24$								
1440 × 1920 × 960	47	40	30	53	47	33	25	63
1440 × 960 × 1920	50	17	60	45	47	13	60	70
1920 × 1440 × 960	40	20	50	40	45	20	53	27
1920 × 960 × 1440	53	13	60	45	45	10	80	25
960 × 1440 × 1920	50	30	27	47	45	30	27	27
960 × 1920 × 1440	40	50	18	45	45	50	20	30
$N_p = 32$								
1920 × 1920 × 960	47	27	33	30	47	17	40	27
1920 × 960 × 1920	50	13	60	40	47	10	80	40
960 × 1920 × 1920	47	47	40	33	47	40	23	27

value of  $N_Y$  is greater than  $N_X$  where we see a larger fraction of data offloaded to GPU in  $PS_2$  and  $PS_4$ , and when the value of  $N_Y$  is smaller than  $N_X$  where we see a smaller fraction of data offloaded to GPU in  $PS_2$  and  $PS_4$ .

To model the obtained weak scaling results, we start from equation (39) for the execution time of a single iteration of the main loop. In weak scaling tests, the mesh size is increased proportionally to the number of MPI processes  $N_p$ , and therefore the execution time is given by

$$T_W(N_p) = \alpha + \beta L + \gamma \frac{MN_p}{N_p} + \beta V \frac{MN_p}{N_p^2} = \alpha + \beta L + \gamma M + \beta V \frac{M}{N_p}. \quad (42)$$

The weak scaling efficiency

$$E_W(N_p) = \frac{T_W(1)}{T_W(N_p)}, \quad (43)$$

can thus be modeled by

$$E_W(N_p) = \frac{1}{a + b/N_p}. \quad (44)$$

We fitted this model to data presented in Figure 15 and the obtained fit parameters are given in Table 16. Note that the model is fitted to CUDA/MPI scaling data only for  $N_p \geq 4$ . The agreement between the model and measurement data is very good, although we note that the parameter  $b$  has negative values, contrary to its expected relation to the communication cost. Therefore, we conclude that the above expression can be successfully used for modeling of the performance of all three MPI-based implementations.

To summarize, in all test results of MPI-based programs, we note an expected declining of the scaling efficiency. This is due to the introduction of distributed transposes of data, creating overhead that negatively impacts scaling efficiency. It is most evident in both strong and weak scaling tests of the CUDA/MPI version, as the transpose algorithm is inferior to the one provided by FFTW, used in OpenMP/MPI implementation. In our tests, all three MPI versions of programs failed to achieve actual speedup ( $S(N_p) > 1$ ) on less than  $N_p = 4$  nodes, due to the introduction of these transpose routines. We therefore recommend using MPI versions only on  $N_p = 4$  or more cluster nodes.



**Table 16. Values of obtained weak scaling model fit parameters  $a$  and  $b$ , as well as the estimated fit errors for MPI-parallelized programs**

Program	$a$	$\Delta a$	$b$	$\Delta b$
imag3d-mpi	2.56	0.06	-0.9	0.3
real3d-mpi	2.32	0.05	-1.3	0.2
imag3d-mpicuda	0.70	0.02	-0.1	0.2
real3d-mpicuda	0.68	0.02	-0.1	0.2
imag3d-mpihetero	1.32	0.03	-0.6	0.2
real3d-mpihetero	1.27	0.03	-0.6	0.2

#### 2.4.5. Selecting the Optimal Algorithm

In previous sections we presented results of detailed performance tests and associated models for all developed programs. Here we provide general guidelines for obtaining the best performance from each implementation.

We note that the extensive testing performed shows that the best performance can be achieved by evenly distributing the workload among the MPI processes and OpenMP threads, and by using mesh sizes which are optimal for FFT. In particular, the single-node OpenMP programs have the best performance if the number of spatial points in all directions, controlled by parameters  $N_x$ ,  $N_y$  and  $N_z$ , is divisible by the number of OpenMP threads used. Similarly, the OpenMP/MPI implementation achieves the best performance if  $N_x$  and  $N_y$  are divisible by a product of the number of MPI processes and the number of OpenMP threads used.

On the other hand, CUDA implementation works best if all the data for a given mesh size can fit into the GPU memory. In the case of a small mesh size, CUDA programs may not be able to saturate all Streaming Multiprocessors (SM) of a given GPU, and in this case the OpenMP programs may be considered first. For CUDA/MPI programs, the best performance is achieved if  $N_x$  and  $N_y$  are divisible by a product of the number of MPI processes and the number of SMs in the GPU used. Note that CUDA-based implementations write output files (e.g., density profiles) by transferring data from GPU memory to host memory, where a single thread writes to a file. Therefore, these implementations may not be suitable for simulations that require the output to be written frequently, after a small number of time propagation steps.

Best performance of hybrid implementations can be obtained by following

the same guidelines. Furthermore, we recommend using these programs with the optimization methods described in section 2.4.1 to optimally divide the work between host and device. If manual tuning of offload parameters is required, we recommend that the guidelines above are followed for both CPU and GPU portions of the mesh. In the case of large disparity in the performance of host or device, hybrid versions will not provide the lowest execution times, and in such cases the pure CPU or GPU implementations with or without MPI could be better suited.

In addition to the guidelines for mesh sizes presented above, all programs benefit from the mesh size which is also optimal for FFT. The best FFT performance on CPU with FFTW library is obtained if  $N_x$ ,  $N_y$  and  $N_z$  can be expressed as  $2^a 3^b 5^c 7^d 11^e 13^f$ , where  $e$  and  $f$  are either 0 or 1, and the other exponents are non-negative integer numbers [60]. Similarly, for cuFFT the best performance is achieved for transform sizes of the form  $2^a 3^b 5^c 7^d$ . In hybrid implementations, the same applies to the host and device portions of  $N_x$  and  $N_y$ , i.e.,  $\text{cpu}N_x$ ,  $\text{cpu}N_y$ ,  $\text{gpu}N_x$  and  $\text{gpu}N_y$ .

## 2.5. Applications

The applicability and accuracy of the NLS equation for the description of BEC properties has been established in early studies addressing time-of-flight expansion and collective modes of the condensate [61, 1]. More recently, numerical algorithms [22, 23, 25, 26] for solving the NLS equation (1), have been used to investigate: nonlinear frequency shifts of the collective mode induced by a harmonic modulation of interaction [62]; onset and features of Faraday waves in BEC [63, 64, 65]; phase-separation dynamics of two-component BECs [66]; geometric resonances in a BEC with two- and three-body interactions [67]; non-equilibrium dynamics of a stirred BEC [68, 69, 70]; localization of a two-component BEC in a random potential [71]; vortex lattice melting in the presence of impurities [72]; classification of fractional vortices in a spinor BEC [73]; BEC dynamics in a dimple trap [74, 75, 76]; dynamics of localized impurity in BEC [77]; analysis of localized states in a multi-component BEC [78]; BEC dynamics induced by a sudden change of an optical lattice geometry [79]; BEC dynamics in a gravito-optical surface trap [80]; emergence of a Bose glass phase in a BEC in the presence of disorder [81]; vortex dynamics [82]; vortex generation in a stirred BEC [83]; dynamics of a self-bound droplet in the presence of an attractive two-body and a very small repulsive three-body interaction

[84, 85]. The dynamics of light bullets in a cubic–quintic nonlinear medium based on an extension of equation (12) has been published in reference [86]. As an illustration, in section 3 we present results of the study addressing the phase–separation dynamics of two–component BECs [66].

Furthermore, the codes [22, 23] have been extended to incorporate effects of the spin–orbit coupling which are currently intensely explored in the systems of cold atoms. In particular, the following subjects have been investigated: phase separation in a spin–orbit coupled BEC [87]; soliton dynamics in spin–orbit coupled BEC [88, 89, 90, 91]; dynamics of a BEC with spin–angular momentum coupling [92]. In section 4 we present recently obtained results about dipole mode and breathing mode excitations of a BEC in the presence of the coupling of pseudo spin and angular momentum [66].

The algorithms [28, 29, 30] for solving the dipolar NLS equation (11) have been applied to the study of: vortex dynamics in a dipolar BEC [93, 94, 95, 96]; phase separation in a binary dipolar BEC [97]; dynamics of a dipolar BEC droplet [98]; stability and dynamics of a dipolar Bose–Fermi mixture [99, 100]; solitons in a dipolar BEC [101, 102, 103, 104, 105, 106, 107]; self–trapping of a dipolar BEC in a double–well [108]. As a final illustration, in section 5 we present a study of vortex formation in a dipolar BEC.

### 3. Phase Separation Dynamics of a Two–Component BEC

Systems of multi–component BECs involve an additional degree of freedom and enrich the physics that can be explored within cold atom setups. These systems are either realized as mixtures of different bosonic atoms or different hyperfine states of the same atomic species. In this section we extend the previously described numerical algorithm and apply it for a study of a two–component system, described by two condensate wave functions  $\psi_1(x, t)$  and  $\psi_2(x, t)$  in a quasi one–dimensional geometry. The ground state configuration can be obtained as a minimum of the following energy functional

$$E_0 = \int dx \left[ (\psi_1^*(x) \psi_2^*(x)) H_0 \begin{pmatrix} \psi_1(x) \\ \psi_2(x) \end{pmatrix} + \frac{g_{11}}{2} |\psi_1(x)|^4 + \frac{g_{22}}{2} |\psi_2(x)|^4 + g_{12} |\psi_1(x)|^2 |\psi_2(x)|^2 \right], \quad (45)$$

where  $H_0$  corresponds to the non-interacting Hamiltonian

$$H_0 = \left( -\frac{1}{2} \frac{\partial^2}{\partial x^2} + V(x) \right) \mathcal{I}_2, \quad (46)$$

with  $\mathcal{I}_2$  being a  $2 \times 2$  identity matrix. As the total number of atoms of each species is conserved, the normalization condition is implemented as  $\int dx |\psi_1(x)|^2 = \int dx |\psi_2(x)|^2 = 1$ . The expression (45) encompasses three interaction constants:  $g_{11}$  for atoms of the first species,  $g_{22}$  for atoms of the second species and  $g_{12}$  interaction constant between the atoms of the two species. We assume that all these interactions are repulsive, i.e.,  $g_{11} \geq 0$ ,  $g_{22} \geq 0$ ,  $g_{12} \geq 0$ . For  $g_{12} = 0$ , the two species do not "feel" each other and energy defined in (45) consists of two copies of single-component energy (5). In this case density distributions of the two species  $|\psi_1(x)|^2$  and  $|\psi_2(x)|^2$  may fully overlap in space. As intra-component repulsion  $g_{12}$  gets stronger, two-component mixtures may exhibit phase separation [13]. Simply, as it is energetically costly for the two species to overlap, they spatially separate instead. In the homogeneous case  $V(x) = 0$ , the necessary condition for the onset of phase separation is given by [109]

$$g_{11}g_{22} < g_{12}^2. \quad (47)$$

Often the two-component condensate is not prepared as the ground state of (45), but using a dynamical protocol [110, 111, 112] that we describe in the following. The dynamics of a two-component condensate in the mean-field regime is governed by two coupled Gross-Pitaevskii equations [113]:

$$i \frac{\partial \psi_1(x, t)}{\partial t} = \left[ -\frac{1}{2} \frac{\partial^2}{x^2} + \frac{1}{2} \lambda^2 x^2 + g_{11} |\psi_1(x, t)|^2 + g_{12} |\psi_2(x, t)|^2 \right] \psi_1(x, t), \quad (48)$$

$$i \frac{\partial \psi_2(x, t)}{\partial t} = \left[ -\frac{1}{2} \frac{\partial^2}{x^2} + \frac{1}{2} \lambda^2 x^2 + g_{12} |\psi_1(x, t)|^2 + g_{22} |\psi_2(x, t)|^2 \right] \psi_2(x, t). \quad (49)$$

Wave functions of the condensates  $\psi_1(x, t)$  and  $\psi_2(x, t)$  are normalized to unity and  $\lambda$  is the strength of the harmonic trap  $V(x) = \lambda^2 x^2 / 2$ . The non-equilibrium dynamics of a two-component BEC captured by the coupled NLS equations (48) and (49) has attracted lot of theoretical interest [114, 115, 116, 117, 118].

Initially, a single-component condensate is produced. We model this situation as a two-component BEC with  $g_{11} = g_{22} = g_{12}$  and prepare initial state as the ground state of (45) for  $g_{11} = g_{22} = g_{12}$ . At  $t = 0$  a pulse is applied and half

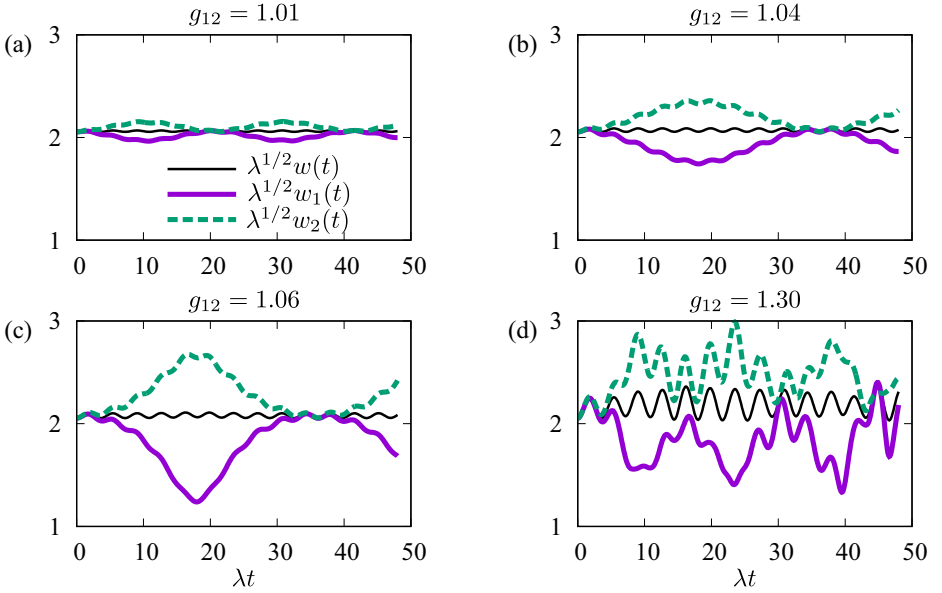


Figure 16. Time evolution of condensate widths for several values of  $g_{12}$ : (a)  $g_{12} = 1.01$ , (b)  $g_{12} = 1.04$ , (c)  $g_{12} = 1.06$ , (d)  $g_{12} = 1.3$ . Other parameters:  $\lambda = 10^{-3}$ ,  $g_{11} = 1$ ,  $g_{22} = 1.01$ .

the atoms are transferred into another hyperfine state. An important assumption of our analysis is that the process is completely spatially symmetric, i.e. the two BECs overlap perfectly at the initial moment. Due to the transfer, values of  $g_{22}$  and  $g_{12}$  are suddenly changed and dynamics of the two components is started. We monitor the time dependence of the widths of the two components,

$$w_{1,2}^2(t) = \int_{-\infty}^{\infty} dx x^2 |\psi_{1,2}(x, t)|^2, \quad (50)$$

as well as the total width  $w(t) = \sqrt{(w_1(t)^2 + w_2(t)^2)/2}$ . Typical results obtained for different final values of  $g_{12}$  and  $\lambda = 10^{-3}$ ,  $g_{11} = 1$ ,  $g_{22} = 1.01$  are presented in Figure 16. We observe fast oscillations in the total width with a frequency unaffected by a change in  $g_{12}$ . These oscillations correspond to the so-called breathing mode. In a quasi one-dimensional geometry it turns out that their period is  $2\pi/(\sqrt{3}\lambda)$ . On top of this, we notice slow oscillations in the width of each of the two component for  $g_{12} = 1.01$  as shown in Figure 16(a).

These out-of-phase oscillations correspond to the "spin" mode, and their frequency decreases with increase in  $g_{12}$ . In particular, the oscillation period of the spin mode is about 20 for  $g_{12} = 1.01$  (see Figure 16(a)) and about 30 for  $g_{12} = 1.04$  (see Figure 16(b)). Above a certain threshold value of  $g_{12}$ , oscillation amplitudes sharply increase and the width dynamics becomes aperiodic and irregular (see Figure 16(c) for  $g_{12} = 1.06$ ). Irregularity of the width dynamics is even more apparent for  $g_{12} = 1.3$  as shown in Figure 16(d).

In Figure 17 we show the dynamics of the "spin density"  $|\psi_1(x, t)|^2 - |\psi_2(x, t)|^2$  for the same parameters as in Figure 16. The plots Figure 17(a) and (b) show regular oscillations. By comparing plots Figure 17(b) and (c) we note a sharp change in the color scales that matches the sharp increase in the oscillation amplitude observed earlier. Finally, in Figure 17(d) we observe a clear onset of pattern dynamics. By applying a suitable linear stability analysis, it was shown that the onset of aperiodic motion is marked by emergence of an unstable mode around a referent stationary state [66]. This behavior is known as modulation instability and by investigating a range of values  $\lambda \in (10^{-5}, 10^{-1})$ , we found that in a realistic experimental situation, stronger trapping potential strength  $\lambda$  shifts the instability condition (47) toward higher values of  $g_{12}$ .

#### 4. Excitations of a BEC with Spin-Angular Momentum Coupling

Experimental realization of an effective spin-orbit coupling in ultracold atom systems [119, 120, 121, 122, 123, 124, 125] has allowed for new quantum phases to be explored. Bosonic systems with spin-orbit coupling are interesting as they have no direct analogues in condensed matter systems and provide a new research playground [126, 127]. In recent references [128, 129, 130, 131] the following Hamiltonian for a two-component bosonic system has been introduced:

$$H_{\text{SOC}} = \left( -\frac{1}{2}\Delta + \frac{r^2}{2} \right) \mathcal{I}_2 + \frac{\Omega^2 r^2}{2} \begin{pmatrix} 1 & e^{-2i\phi} \\ e^{2i\phi} & 1 \end{pmatrix}, \quad (51)$$

where  $\mathcal{I}_2$  is a  $2 \times 2$  identity matrix and the effective spin  $1/2$  comes from the two bosonic components involved. The system is assumed to be effectively two-dimensional (tightly trapped in the longitudinal direction). The value of  $\Omega$  is set by the intensity of two co-propagating Laguerre-Gauss laser beams

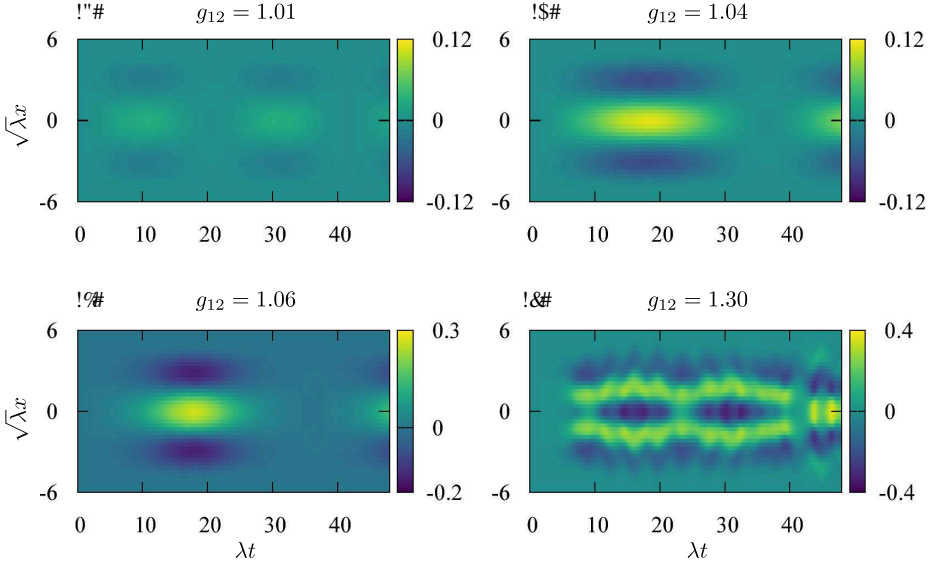


Figure 17. Spin dynamics illustrated via the density difference given by  $\lambda^{-1/2} (|\psi_1(x, t)|^2 - |\psi_2(x, t)|^2)$ , induced by a quench of  $g_{12}$  and  $g_{22}$ . Parameters: (a)  $g_{12} = 1.01$ , (b)  $g_{12} = 1.04$ , (c)  $g_{12} = 1.06$ , (d)  $g_{12} = 1.3$  and  $\lambda = 10^{-3}$ ,  $g_{11} = 1$ ,  $g_{22} = 1.01$ .

that carry a unit of angular momentum in the opposite rotational directions. The last,  $\phi$ -dependent term, where  $\phi$  is the polar angle, provides the coupling between the spin and angular momentum, as can be explicated by using a proper unitary transformation [129]. In this section we extend the algorithms presented in subsection 2.2 and use them to investigate excitations of a BEC with spin-angular momentum coupling as defined in equation (51).

The total energy per particle of the condensed state with the order parameter  $(\psi_1(\mathbf{r}) \psi_2(\mathbf{r}))^T$  is given by

$$E_0 = \int d\mathbf{r} \left[ (\psi_1^* \ \psi_2^*) H_{\text{SOC}} \begin{pmatrix} \psi_1 \\ \psi_2 \end{pmatrix} + \frac{g}{2} |\psi_1|^4 + \frac{g}{2} |\psi_2|^4 + g |\psi_1|^2 |\psi_2|^2 \right], \quad (52)$$

where we assume spin-symmetric interactions  $g_{11} = g_{22} = g_{12} = g$ . Due to off-diagonal terms in (51), which allow for the conversion of one atomic state into the other, only the total number of atoms is conserved and the normalization condition is given by  $\int d\mathbf{r} (|\psi_1(\mathbf{r})|^2 + |\psi_2(\mathbf{r})|^2) = 1$ .

To implement the spin–angular momentum coupling in the propagation routine, we split the step of imaginary–time propagation into four pieces. As usual, in the first step we take into account harmonic potential and nonlinear terms, according to equation (13). The second step comprises the spin–angular momentum coupling, and in the last two steps we perform integrations of the type (14) with respect to the two spatial variables  $x$  and  $y$ . Explicitly, the off–diagonal terms from (51) are treated separately starting from

$$-\frac{\partial\psi_1(\mathbf{r},\tau)}{\partial\tau} = e^{-2i\phi} c(r)\psi_2(\mathbf{r},\tau), \quad (53)$$

$$-\frac{\partial\psi_2(\mathbf{r},\tau)}{\partial\tau} = e^{2i\phi} c(r)\psi_1(\mathbf{r},\tau), \quad (54)$$

where  $c(r) = \frac{1}{2}\Omega^2 r^2$ . By differentiating the two last equations we obtain two independent equations

$$\frac{\partial^2\psi_1(\mathbf{r},\tau)}{\partial\tau^2} = c(r)^2\psi_1(\mathbf{r},\tau), \quad \frac{\partial^2\psi_2(\mathbf{r},\tau)}{\partial\tau^2} = c(r)^2\psi_2(\mathbf{r},\tau) \quad (55)$$

that are solved by

$$\begin{aligned} \psi_1(\mathbf{r},\tau) &= A_1(\mathbf{r}) e^{-c(r)\tau} + B_1(\mathbf{r}) e^{c(r)\tau}, \\ \psi_2(\mathbf{r},\tau) &= A_2(\mathbf{r}) e^{-c(r)\tau} + B_2(\mathbf{r}) e^{c(r)\tau}. \end{aligned} \quad (56)$$

From the initial conditions for the second part of the  $n$ –th integration step at  $\tau' = (n + \frac{1}{4})\varepsilon$  we obtain a set of algebraic equations for the coefficients

$$\begin{aligned} A_1(\mathbf{r}) + B_1(\mathbf{r}) &= \psi_1(\mathbf{r},\tau'), \\ -c(r)A_1(\mathbf{r}) + c(r)B_1(\mathbf{r}) &= -e^{-2i\phi} c(r)\psi_2(\mathbf{r},\tau'), \\ A_2(\mathbf{r}) + B_2(\mathbf{r}) &= \psi_2(\mathbf{r},\tau'), \\ -c(r)A_2(\mathbf{r}) + c(r)B_2(\mathbf{r}) &= -e^{2i\phi} c(r)\psi_1(\mathbf{r},\tau'), \end{aligned}$$

that finally leads to

$$\begin{aligned} A_1(\mathbf{r}) &= \frac{1}{2} \left[ \psi_1(\mathbf{r},\tau') + e^{-2i\phi} \psi_2(\mathbf{r},\tau') \right], \\ B_1(\mathbf{r}) &= \frac{1}{2} \left[ \psi_1(\mathbf{r},\tau') - e^{-2i\phi} \psi_2(\mathbf{r},\tau') \right], \\ A_2(\mathbf{r}) &= \frac{1}{2} \left[ \psi_2(\mathbf{r},\tau') + e^{2i\phi} \psi_1(\mathbf{r},\tau') \right], \\ B_2(\mathbf{r}) &= \frac{1}{2} \left[ \psi_2(\mathbf{r},\tau') - e^{2i\phi} \psi_1(\mathbf{r},\tau') \right]. \end{aligned} \quad (57)$$



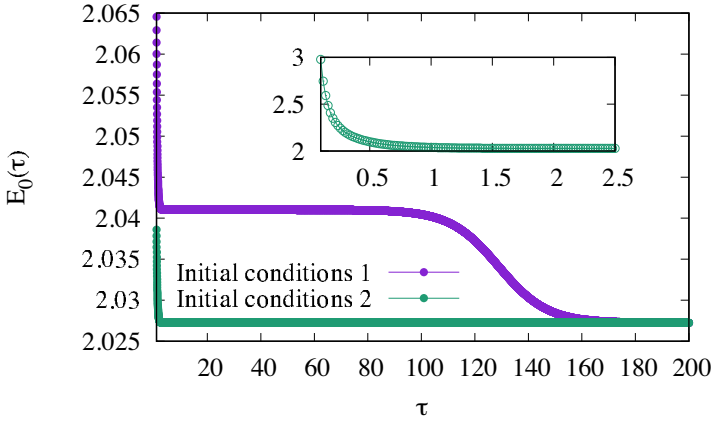


Figure 18. The energy of the ground state  $E_0(\tau)$  defined in equation (52) vs. imaginary time  $\tau$  obtained for different initial conditions. In the first case, we start from a random initial state and observe slow convergence toward the global minimum. In the second case, initial conditions have proper dependence on the polar angle  $\phi$ , as given in equation (58) and the convergence toward the ground state is exponentially fast as shown in the inset. Parameters:  $\Omega = 3.2$  and  $g = 1$ .

In our numerical implementation we make direct use of equations (56) and (57).

Before turning to numerical simulations, we first briefly present an important analytical result available for  $g = 0$ . General symmetry considerations imply that the ground state configurations of (52) for  $g = 0$  can be expressed in a form

$$\phi_m(r, \phi) = \frac{e^{im\phi}}{\sqrt{2\pi}} \begin{pmatrix} f_m(r)e^{-i\phi} \\ g_m(r)e^{i\phi} \end{pmatrix}, \quad (58)$$

where  $m$  is an integer. In particular for  $\Omega < \Omega_c$ , with  $\Omega_c = 3.35$  there are two degenerate ground states  $m = \pm 1$  and for  $\Omega > \Omega_c$  the ground state configuration corresponds to  $m = 0$ . The  $m = \pm 1$  states are denoted as half-vortices, and  $m = 0$  state is named vortex-antivortex pair. In order to explore ground state configurations for a finite value of interaction constant  $g$ , we perform minimization of energy functional (52) using imaginary time propagation. How quickly we reach the ground state strongly depends on the choice of initial configuration as shown in Figure 18. Starting with random initial values, we find

that propagation routine may first reach a metastable configuration (local minimum of  $E_0$ ) and eventually, only after very long propagation time, it selects the right minimum. With a better choice of initial configuration, motivated by exact results (58), the right minimum is found with substantially less iterations. Considerations of this kind are relevant whenever there are several configurations that are nearly degenerate – i.e., have close values of the corresponding energies (52) and represent local minima of the functional (52).

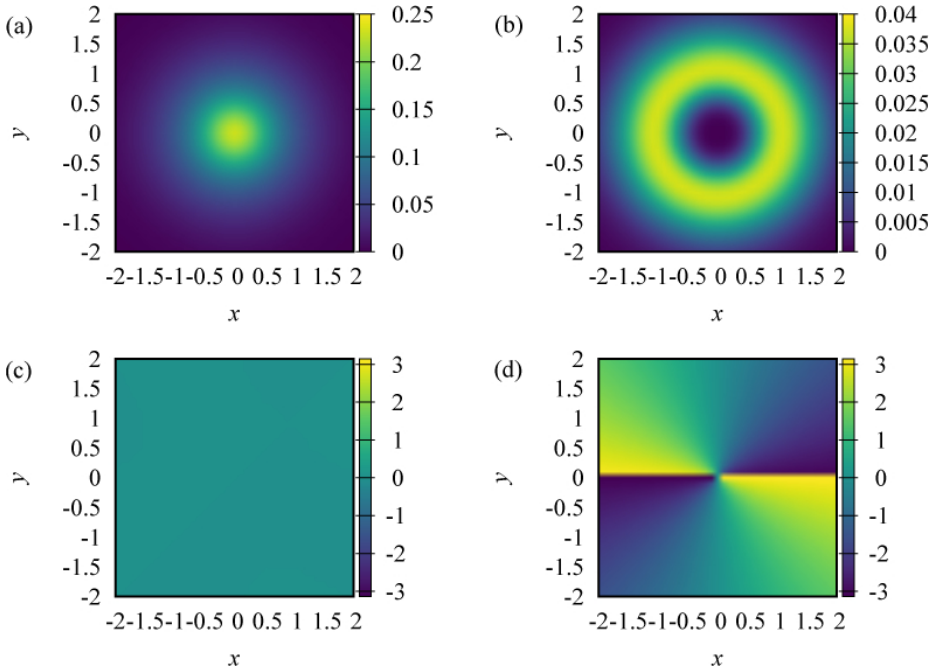


Figure 19. The  $m = 1$  ground state obtained for  $\Omega = 3.2$ ,  $g = 1$ . We plot: (a) the density distribution of the first component  $|\psi_1(\mathbf{r})|^2$ , (b) the density distribution of the second component  $|\psi_2(\mathbf{r})|^2$ , (c) the argument of  $\psi_1(\mathbf{r})$  and (d) the argument of  $\psi_2(\mathbf{r})$ .

Two examples of the ground state configurations are given in Figs. 19 and 20. We find that at finite values of  $g$ , ground states can also be distinguished according to their dependence on polar angle  $\phi$ , as given in equation (58). In Figure 19 we present the ground state solution for  $\Omega = 3.2$  and  $g = 1$ . This is a half-skyrmion configuration characterized by  $m = 1$ . We note that the

first component is confined around the trap center and its phase dependence is trivial. In contrast, the second bosonic species exhibits double phase winding, see Figure 19(d). In Figure 20 we present the ground state solution for  $\Omega = 3.5$  and  $g = 1$ . The densities of the two components overlap in space, Figure 20(a) and (b), and exhibit phase winding in opposite directions, Figure 20 (c) and (d). This is an example of  $m = 0$  state called a vortex–antivortex pair.

In general, quantum phases can be distinguished according to their low-lying spectra. In cold atom experiments routinely accessible with great precision are breathing mode and dipole mode excitations. To probe these modes, initially the system is prepared in its ground state and then a sudden quench of the potential  $V(\mathbf{r})$  is performed. We now theoretically address these excitations for the half-skyrmion and vortex–antivortex state.

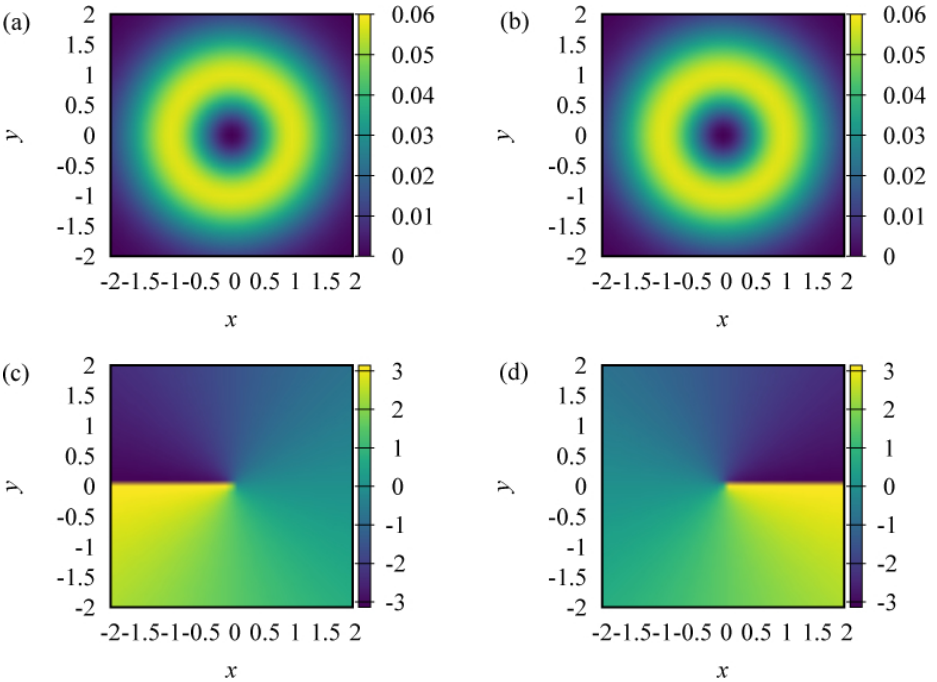


Figure 20. The  $m = 0$  ground state obtained for  $\Omega = 3.5$ ,  $g = 1$ . We plot: (a) the density distribution of the first component  $|\psi_1(\mathbf{r})|^2$ , (b) the density distribution of the second component  $|\psi_2(\mathbf{r})|^2$ , (c) the argument of  $\psi_1(\mathbf{r})$  and (d) the argument of  $\psi_2(\mathbf{r})$ .

The dynamics of a BEC with spin–angular momentum coupling is governed by two coupled time–dependent Gross-Pitaevskii equations for  $\psi_1(\mathbf{r}, t)$  and  $\psi_2(\mathbf{r}, t)$ :

$$i \frac{\partial \psi_1}{\partial t} = \left[ -\frac{1}{2} \left( \frac{\partial^2}{\partial x^2} + \frac{\partial^2}{\partial y^2} \right) + V(r) + \frac{r^2 \Omega^2}{2} + g (|\psi_1|^2 + |\psi_2|^2) \right] \psi_1 + \frac{r^2 \Omega^2}{2} e^{-2i\phi} \psi_2, \quad (59)$$

$$i \frac{\partial \psi_2}{\partial t} = \left[ -\frac{1}{2} \left( \frac{\partial^2}{\partial x^2} + \frac{\partial^2}{\partial y^2} \right) + V(r) + \frac{r^2 \Omega^2}{2} + g (|\psi_2|^2 + |\psi_1|^2) \right] \psi_2 + \frac{r^2 \Omega^2}{2} e^{2i\phi} \psi_1. \quad (60)$$

The trapping potential is assumed to be harmonic, initially set to  $V(r) = r^2/2$ . To induce a breathing mode, we perturb the trap strength

$$V_{\text{pert}} = (1 + \eta) \frac{r^2}{2}, \quad (61)$$

and calculate the time evolution of the width of the probability distribution,

$$\langle r^2(t) \rangle = \int_0^{2\pi} d\phi \int_0^\infty dr r^3 [|\psi_1(\mathbf{r}, t)|^2 + |\psi_2(\mathbf{r}, t)|^2]. \quad (62)$$

By inspecting the corresponding Fourier transform, we identify the lowest excited frequency as the breathing mode  $\omega_B$ .

In a typical harmonically trapped two–dimensional system, without the spin–orbit coupling  $\Omega = 0$ , the Gross–Pitaevskii description predicts that the breathing mode frequency is  $\omega_B = 2$  (in the units of the harmonic trap frequency), independent of interaction constant  $g$  [132]. Analytical arguments and numerical results (not presented here) show that this general conclusion holds true for the vortex–antivortex state. On the other hand, the breathing mode frequency of a half–skyrmion state depends on both the coupling  $\Omega$  and on the interaction strength  $g$ . Illustrative results for  $\langle r^2(t) \rangle$  are presented in Figure 21(a) for  $\Omega = 3.2$ ,  $\eta = 0.1$  and several values of  $g$ . From the related Fourier transforms shown in Figure 21(b), we find that the breathing mode frequency increases for several percent with  $g$ .

To excite a dipole mode, we consider a shift of the trap bottom in  $x$  direction,

$$V_{\text{pert}} = \frac{r^2}{2} - \delta x \frac{r}{2} \left( e^{i\phi} + e^{-i\phi} \right), \quad (63)$$

and monitor the motion of the center of mass of the system in that direction,

$$\langle x(t) \rangle = \int_0^{2\pi} d\phi \frac{e^{i\phi} + e^{-i\phi}}{2} \int_0^\infty dr r^2 [|\psi_1(\mathbf{r}, t)|^2 + |\psi_2(\mathbf{r}, t)|^2], \quad (64)$$

as well as  $\langle y(t) \rangle$ .

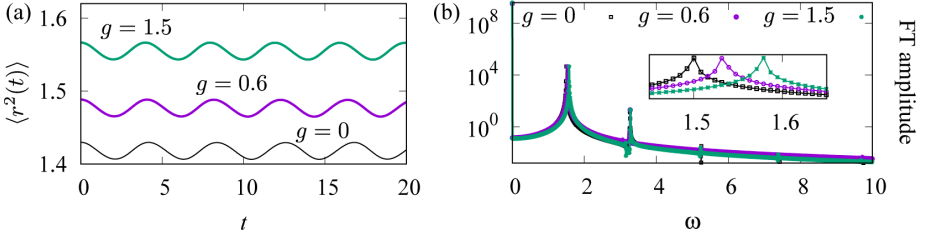


Figure 21. Breathing mode oscillations in half-skyrmion phase: (a)  $\langle r^2(t) \rangle$  versus  $t$  and (b) corresponding Fourier transform. From the inset we observe increase of the breathing mode frequency with  $g$ . Motion is induced by changing harmonic trap potential as  $\frac{r^2}{2} \rightarrow 1.01 \frac{r^2}{2}$ ,  $\Omega = 3.2$ .

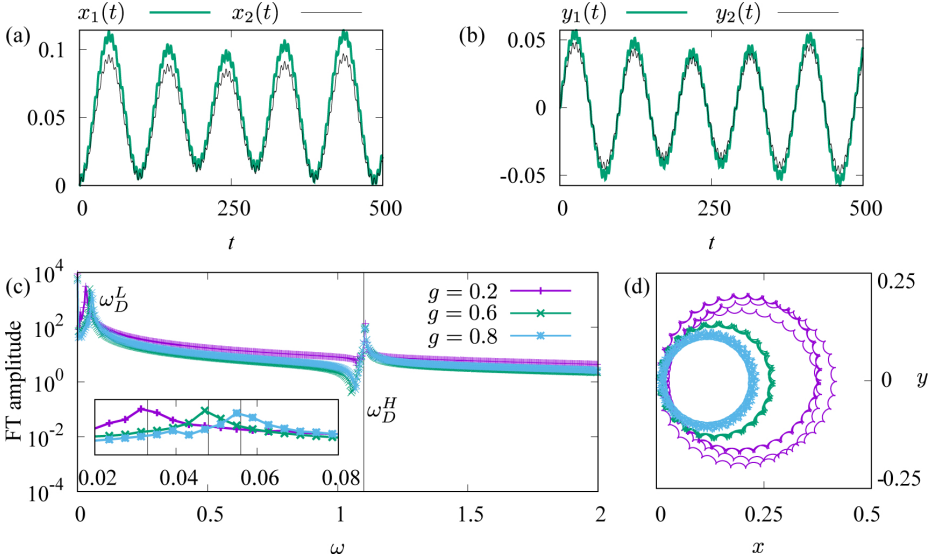


Figure 22. Dipole mode oscillations of half-skyrmion state in interacting case for  $\Omega = 3.2$ . Motion is induced by shifting the harmonic trap bottom for  $\delta x = 0.01$ . In (a) and (b)  $g = 1$ . In (c) motion of the center of mass,  $y(t)$  versus  $x(t)$ , is plotted. The trajectory radius gets smaller with increasing  $g$ . In (d) vertical lines give results for  $\omega_D^L$  (in the inset) and  $\omega_D^H$  (in the main panel) obtained using the Bogoliubov method, and dots represent Fourier transform of  $x(t)$ .

In the conventional harmonically trapped system ( $\Omega = 0$ ), this perturbation excites the Kohn mode – an oscillation with the trap frequency along  $x$

axis unaffected by interactions. Illustrative results for a half-skyrmion state are presented in Figure 22 for  $\Omega = 3.2$  and they obviously exhibit more complex behavior in comparison to the results for  $\Omega = 0$ . We observe that oscillatory motion in  $x$  direction is coupled to the motion along  $y$  direction. Moreover, we find that there are two frequencies involved. We label them as  $\omega_D^L$  (low) and  $\omega_D^H$  (high). In Figure 22(a) and 22(b) we see that two bosonic components oscillate in-phase in both directions. The frequency  $\omega_D^L$  exhibits a strong increase with  $g$ , as is depicted in Figure 22(c). As the frequency  $\omega_D^L$  gets larger, the induced oscillation amplitude gets weaker, Figure 22(d). For the considered case, the frequency  $\omega_D^H$  is found to be almost independent of  $g$ , see Figure 22(c). Results based on the complementary Bogoliubov approach, match quite well to the numerical data obtained from direct numerical simulations of equations (59)–(60), see Figure 22(c).

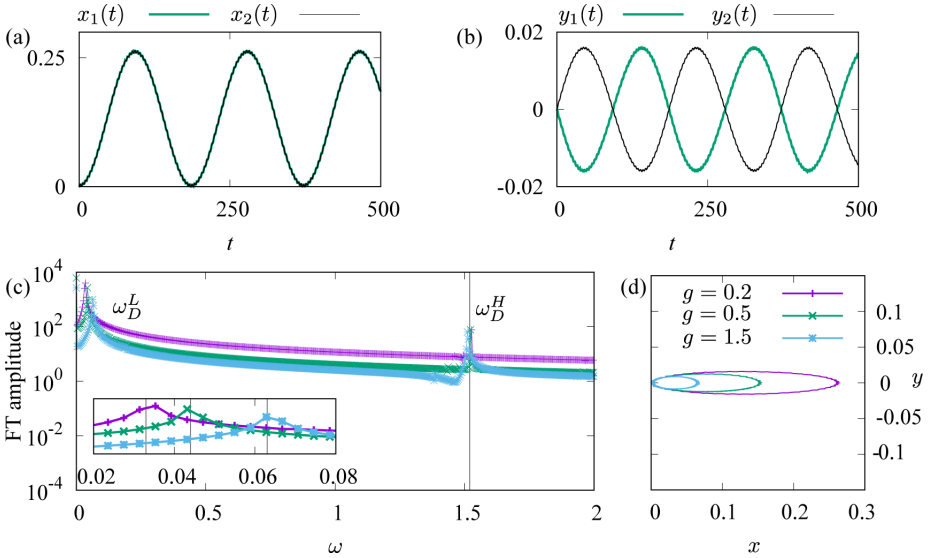


Figure 23. Dipole mode oscillations of the  $m = 0$  solution in interacting case for  $\Omega = 3.5$ . Motion is induced by shifting harmonic trap bottom for  $\delta x = 0.01$ . In (a) and (b)  $g = 0.2$ . In (c) trajectory of the center of mass of a single bosonic component,  $y_1(t)$  versus  $x_1(t)$ , is plotted. In (d) vertical lines give results for  $\omega_D^L$  (in the inset) and  $\omega_D^H$  (in the main panel) obtained using Bogoliubov method and dots represent Fourier transform of  $x(t)$ .

In the vortex–antivortex state, the two bosonic components exhibit an out-of-phase oscillation in  $y$  direction, see Figure 23(b), and consequently the center of mass only oscillates in  $x$  direction with the frequency  $\omega_D^L$  that exhibits an increase with  $g$ , see Figure 23(c). The trajectory of the center of mass of each of the components is given by an ellipse, which is strongly elongated in  $x$  direction, see Figure 23(d).

## 5. Study of Critical Velocity for Vortex Formation

As we have already seen, the programs presented in this chapter can be used to model and study a variety of systems. In this section we demonstrate the versatility of developed programs on a simulation of vortex formation in a BEC. We use the MPI-based programs to simulate the effects of a moving obstacle in an oblate atomic BEC. The obstacle, a repulsive Gaussian laser beam, moves through the condensate and sheds quantum vortices, elementary excitation of a superfluid [14, 13]. The vortices appear only when the obstacle is moving above some critical speed, consistent with the Landau’s criterion of superfluidity. At low obstacle velocities above a critical value, vortex dipoles emerge, and as the speed is increased further, individual vortices and rotating vortex pairs are also formed.

In the first subsection we document how our programs can be used to simulate the experiment reported in reference [133], and compare experimental and numerical results. The experiment measured critical velocity for the emergence of vortex dipoles and rotating vortex pairs in a BEC of sodium atoms ( $^{23}\text{Na}$ ), which do not exhibit the dipolar interaction. Therefore, in this section we also demonstrate how our programs can be modified to switch off the dipolar interaction term when solving NLS equation. The agreement of the results obtained numerically and experimental observations provides an external check of the correctness of our algorithms and their implementations.

In the second subsection we investigate the formation of vortices in a dipolar BEC of dysprosium atoms ( $^{164}\text{Dy}$ ). Our simulations follow the same methodology as the experiment with sodium atoms, only with atomic species exhibiting strong dipolar interaction. We study effects of the dipolar interaction on the critical velocity for the emergence of vortices, as well as the interplay between contact and dipolar interaction. The visualization extensions presented in reference [42] have proven to be indispensable during these simulations, as they allow much easier study of the results and control of the simulation.

### 5.1. Formation of Vortices in a BEC

BEC is a superfluid quantum liquid and one of its hallmarks are quantized vortices, which appear as elementary excitations of the system. Quantization of vortices is connected to excitation spectrum and, according to Landau's criterion, leads to the existence of a minimal velocity an obstacle moving through the superfluid has to have in order to generate such elementary excitations. This critical velocity  $v_c$  can be experimentally measured and, in principle, depends on the experimental protocol used.

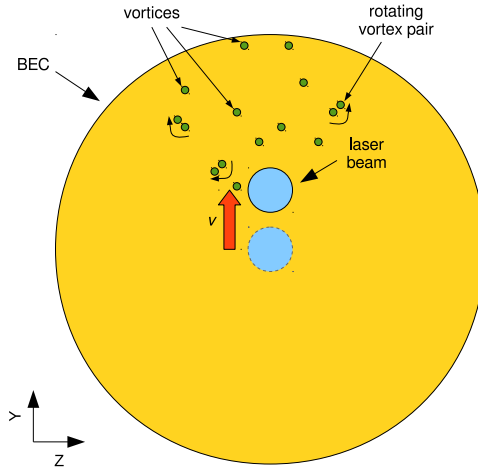


Figure 24. Illustration of the experimental setup used in reference [133] to study vortex formation in a BEC of sodium atoms. A repulsive Gaussian laser beam is initially at the center of the condensate and moves along  $y$  direction with a constant velocity  $v$  until it reaches its final position. The beam is then switched off during a period of 0.5 s. For sufficiently large velocity vortices and vortex pairs are generated.

Reference [133] reports the study of vortex formation in an oblate BEC of  $N_{\text{at}} = 3.2 \times 10^6$  sodium atoms. The trapping potential frequencies used are  $(\omega_x, \omega_y, \omega_z) = 2\pi \times (9, 9, 400)$  Hz, and the  $s$ -wave scattering length determining the strength of contact interaction was  $a_s = 51.9 a_0$ , where  $a_0 = 0.0529$  nm is the Bohr radius. The moving obstacle is realized by a repulsive Gaussian laser



beam corresponding to an additional potential of the form

$$V_B(\mathbf{r}; t) = V_0 \exp \left\{ -2 \frac{[y - y_0(t)]^2 + z^2}{\sigma^2} \right\}, \quad (65)$$

where  $V_0$  represents the strength of the beam,  $\sigma$  is the  $1/e^2$  beam waist, while  $y_0(t) = vt$  determines the center of the beam position  $(0, y_0(t), 0)$ . In our simulations, as in the experiment, the initial position of the beam is at the condensate center and then it moves with the velocity  $v$  along  $y$  direction for  $24 \mu\text{m}$ . Afterwards, the beam is switched off linearly during  $0.5 \text{ s}$ . Illustration of the experimental setup is given in Figure 24. Using imaginary-time propagation, we calculate the ground state of the system with the trapping potential  $V(\mathbf{r}) + V_B(\mathbf{r}; t)$ , where  $V(\mathbf{r})$  corresponds to the harmonic part, with the frequencies given above. The experiment measured critical velocity for the emergence of vortex dipoles, pairs of vortices of the opposite sign. We numerically addressed this setup and calculated this critical velocity for the values of the parameters  $\sigma = 1.3l$  and  $V_0 = 250 \hbar\tilde{\omega}$ , where  $l = 6.988 \mu\text{m}$  is the harmonic oscillator length for the referent frequency  $\tilde{\omega} = \omega_x$ .

Before running simulations with the parameters described above, we had to implement the time-dependent potential  $V(\mathbf{r}) + V_B(\mathbf{r}; t)$ . Initialization of  $V(\mathbf{r})$  remains the same, i.e., it is initialized before the main loop and stored in an array, while calculation of  $V_B(\mathbf{r}; t)$  is implemented in a separate function that is called in each iteration within the main loop. Two distinct phases of  $V_B(\mathbf{r}; t)$  exist: one relating to the movement of the beam, and the other relating to the beam shutdown during  $0.5 \text{ s}$ . Each phase is implemented as a separate function, and the active phase is determined by the current time, i.e., iteration number.

Figure 25 shows several snapshots of a typical dynamical evolution of the system. Imaginary-time propagation yields ground state of the system, which is shown in Figure 25(a), where we plot integrated 2D density profile in  $y$ - $z$  plane. To model local inhomogeneities always present in the experiment, we add uniformly distributed random noise to the wave function of the order of 10%. Such modified ground state represents initial state of the system, and the beam starts to move along  $y$  direction at time  $t = 0$  with the speed  $v = 1.26 \text{ mm/s}$ . Figures 25(b) and 25(c) show 2D density profile of the system at times  $t = 52.17 \text{ ms}$  and  $t = 358.1 \text{ ms}$ , respectively. In Figure 25(b) the beam already reached its final position and its switch-off started. We can observe that several vortices (vortex dipoles) are generated and that the used speed exceeds the critical velocity. Generated vortices are stable and can be seen after extended

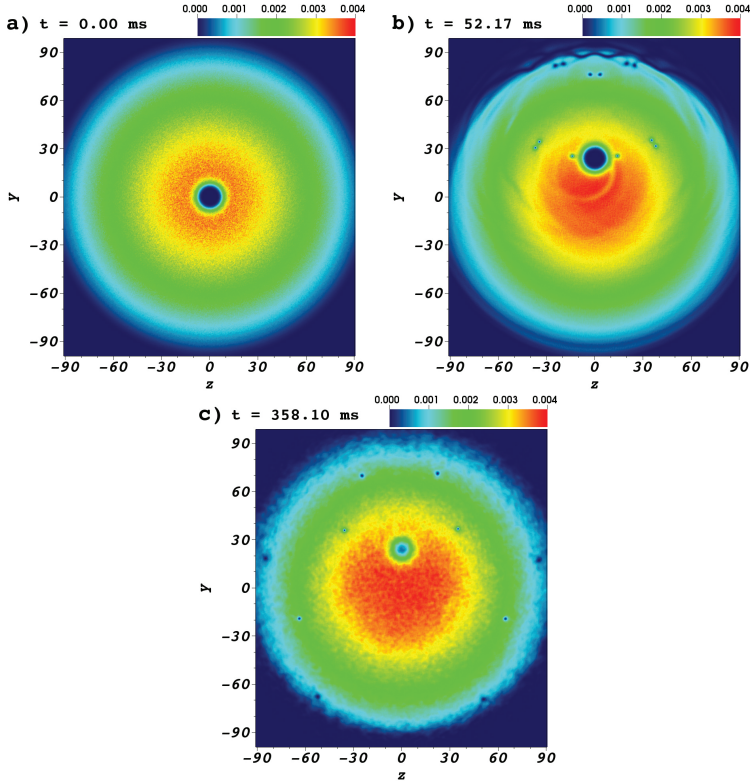


Figure 25. Time evolution of 2D density profile of BEC of sodium atoms with an obstacle moving at speed  $v = 1.26 \text{ mm/s} > v_c$ , when several vortices are generated. Each panel shows integrated 2D density profile in  $y$ - $z$  plane at different time  $t$ . All lengths are expressed in units of  $\mu\text{m}$ , and particle density is given in units  $N_{\text{at}}/l^2$ .

period of time, Figure 25(c). To confirm that we indeed have vortices and not just localized density minima, we plot the  $x = 0$  slice of the phase of the wave function in Figure 26. We observe characteristic braiding and jumps of the phase in the vicinity of density minima, which is a well-known hallmark of a vortex.

When the obstacle is moving with an under-critical velocity, no vortices are generated, as in Figure 27. The velocity  $v = 0.87 \text{ mm/s}$  is just slightly lower than the the critical one, and we can see precursors of vortices at the beam edge in Figures 27(a) and 27(b). At higher velocities, vortices emerge, as we have

seen in Figure 25. At even higher velocities, Figure 28, rotating vortex pairs are generated, in addition to individual vortices.

The obtained results are in good agreement with experimental findings of reference [133] and show that the programs developed within this thesis can be successfully used to model BEC systems with contact interaction, even for the most complex setup, when vortices are generated due to a moving obstacle.

## 5.2. Effects of Dipolar Interactions on Vortex Formation in a BEC

To further test our programs, we model vortex formation in a BEC of dysprosium atoms ( $^{164}\text{Dy}$ ), which exhibit strong magnetic dipole moment. In par-

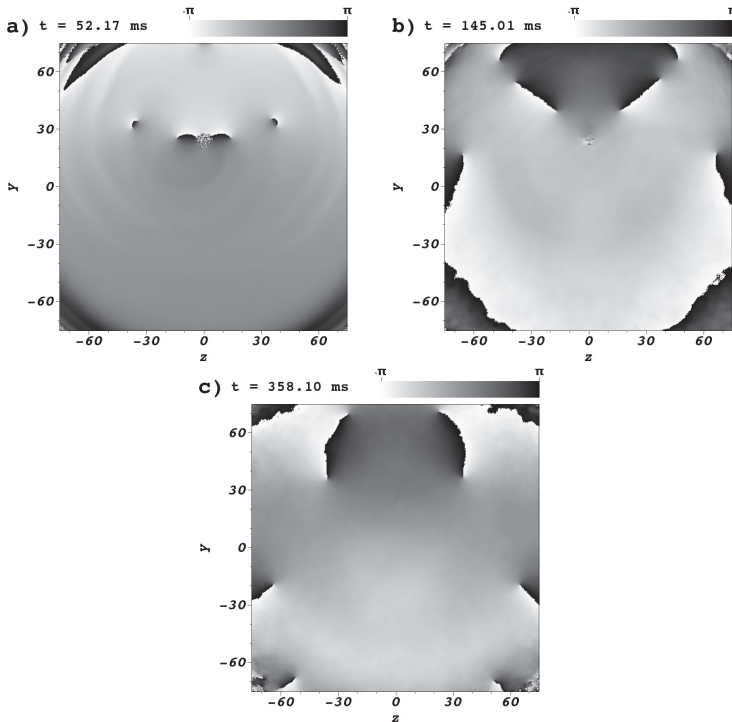


Figure 26. Time evolution of the wave function phase of BEC of sodium atoms with an obstacle moving at speed  $v = 1.26 \text{ mm/s} > v_c$ , when several vortices are generated. Each panel shows  $x = 0$  slice of the phase of the wave function in  $y$ - $z$  plane at different time  $t$ . All lengths are expressed in units of  $\mu\text{m}$ .

ticular, we study effects of the dipolar interaction strength for varying  $s$ -wave scattering lengths on the critical velocity for the emergence of vortices, which was not investigated experimentally. Dysprosium atoms have the largest magnetic dipole moment ( $m = 10\mu_B$ ) available in ultracold atom experiments, corresponding the characteristic dipole-dipole interaction length  $a_{dd} = 132 a_0$ . External magnetic field can be used to align all atomic dipoles in the same direction, as well as to tune their strength up to a maximal value given above. The same applies to the  $s$ -wave scattering length, which determines the contact

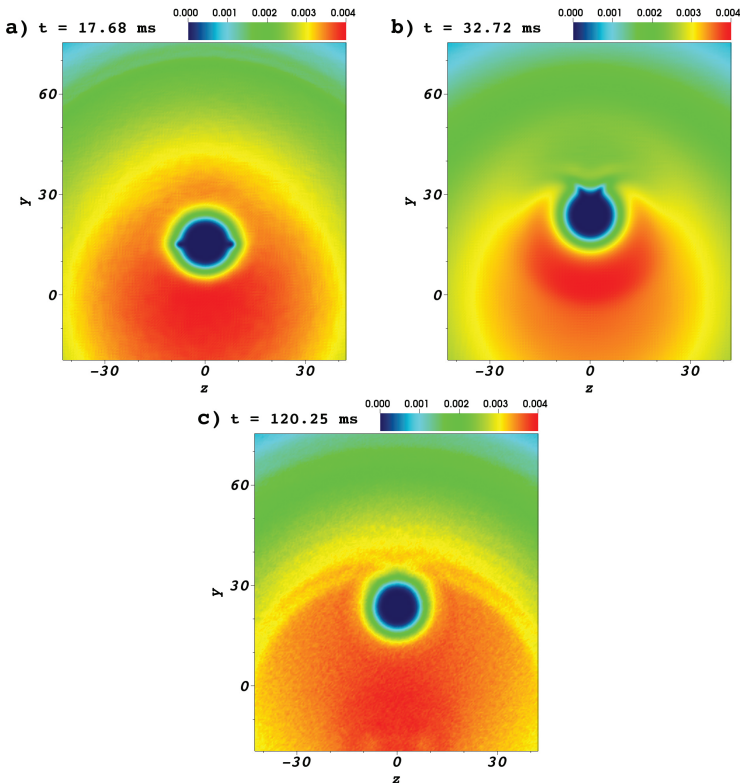


Figure 27. Time evolution of 2D density profile of BEC of sodium atoms with an obstacle moving at speed  $v = 0.87 \text{ mm/s} \lesssim v_c$ , when no vortices are generated. Each panel shows integrated 2D density profile in  $y$ - $z$  plane at different time  $t$ . All lengths are expressed in units of  $\mu\text{m}$ , and particle density is given in units  $N_{\text{at}}/l^2$ .

interaction strength and which can also be tuned using the Feshbach resonance technique. Following reference [134], we take the same range of possible values for  $a_s$  as for  $a_{\text{dd}}$ , i.e., up to a maximal value of  $132 a_0$ . With this we show how the developed programs can be used to model and theoretically address new physical phenomena, before they are studied experimentally. Such approach is essential for the design of many upcoming experiments, since otherwise it would be extremely difficult to predict what would be the relevant range of physical quantities to be measured, thus making it very challenging to perform

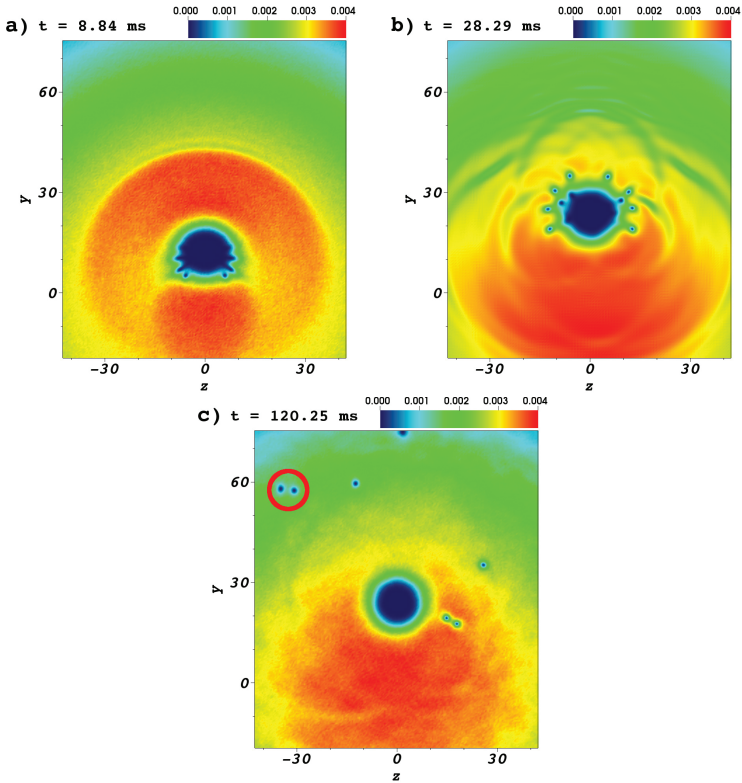


Figure 28. Time evolution of 2D density profile of BEC of sodium atoms with an obstacle moving at speed  $v = 1.4$  mm/s  $\gg v_c$ , when rotating vortex pairs are also generated. Each panel shows integrated 2D density profile in  $y$ - $z$  plane at different time  $t$ . A rotating vortex pair is highlighted in panel (c). All lengths are expressed in units of  $\mu\text{m}$ , and particle density is given in units  $N_{\text{at}}/l^2$ .

the experiments. Having the results of detailed numerical simulations for the particular system enables experiments to target appropriate range of all relevant quantities, and to focus on discovering new phenomena.

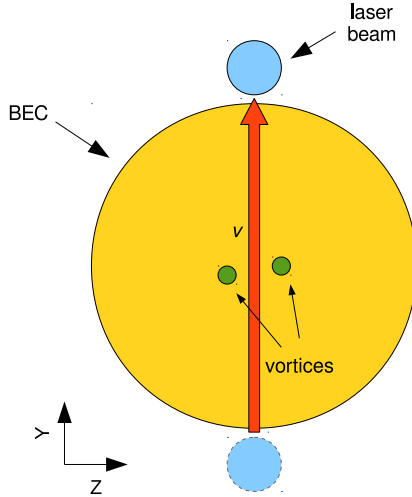


Figure 29. Illustration of the setup we use to study vortex formation in a dipolar BEC of dysprosium atoms. A repulsive Gaussian laser beam is initially outside of the condensate and moves along  $y$  direction with a constant velocity  $v$  until it reaches its final position on the other side. For sufficiently large velocity vortices are generated.

The experiment follows the same methodology as in previous section and uses the same parameters where applicable. Namely, the trap frequencies remain the same, i.e.,  $(\omega_x, \omega_y, \omega_z) = 2\pi \times (9, 9, 400)$  Hz, as well as strength of the beam  $V_0 = 250 \hbar\tilde{\omega}$ . Due to the strong dipolar interactions affecting the stability of the BEC, we had to use a much smaller number of atoms,  $N_{\text{at}} = 8 \times 10^4$ . This resulted in a much smaller BEC, so we had to reduce the  $1/e^2$  beam waist to  $\sigma = l$ , where  $l = 2.617 \mu\text{m}$  is harmonic oscillator length corresponding to dysprosium atoms. Also, we positioned the beam outside of the condensate, and move it all the way to the other side, as illustrated in Figure 29. The potential  $V_B(\mathbf{r}; t)$  has the same form (65) as in previous section, just the center of the beam is now given by  $y_0(t) = y_{00} + vt$ , where  $y_{00} = -15$  in units of  $l$ .

Modifications to the programs presented in the previous section can be

reused for this numerical experiment and we only need to re-enable previously disabled calculation of the dipolar term in the main time propagation loop. As before, the ground state of the system is obtained using imaginary-time program, which then serves as the initial state of the real-time propagation program, with uniformly distributed random noise of 10% added. To calculate critical velocity  $v_c$  for the emergence of vortices, we search for the minimal speed of the laser beam for which two vortices appear, as illustrated in Figure 29.

Figure 30 shows several 2D density profiles of a typical dynamical evolu-

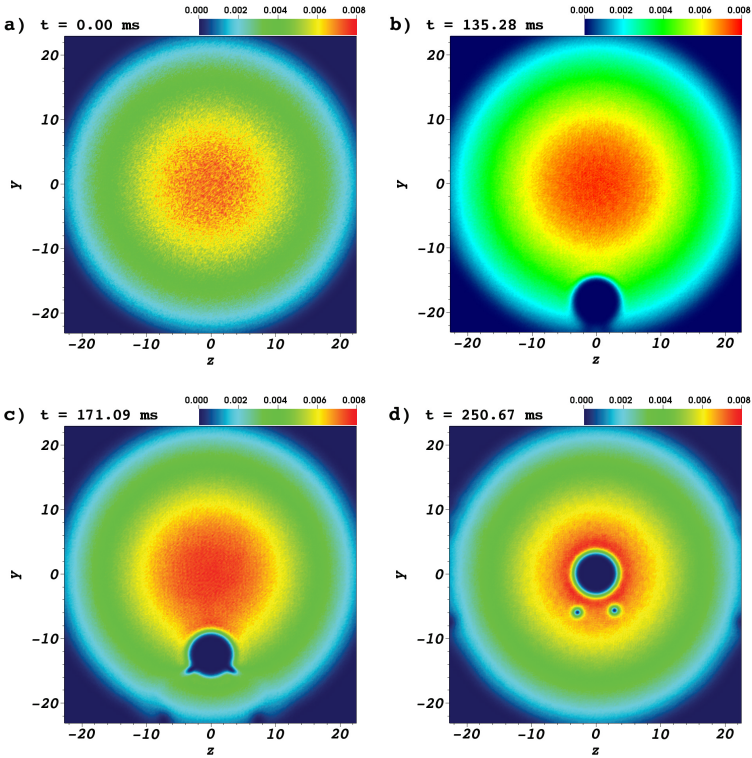


Figure 30. Time evolution of 2D density profile of BEC of dysprosium atoms for  $a_s = 66a_0$  and  $a_{dd} = 44a_0$ , with an obstacle moving at speed  $v = v_c = 0.16$  mm/s, when two individual vortices are generated. Each panel shows integrated 2D density profile in  $y$ - $z$  plane at different time  $t$ . All lengths are expressed in units of  $\mu\text{m}$ , and particle density is given in units  $N_{\text{at}}/l^2$ .

tion of the system for velocity  $v = v_c = 0.16$  mm/s. The ground state, obtained through imaginary-time propagation is shown in Figure 30(a). The beam, initially outside of the condensate, moves along the  $y$  direction, as seen in Figures 30(b) through 30(f). In Figure 30(c) the precursors of the vortices form on the edges of the beam, which then separate from the beam if  $v \geq v_c$ , a situation seen in Figure 30(d). In Figures 30(e) and 30(f) we see that the generated vortices are stable, and survive for long propagation times.

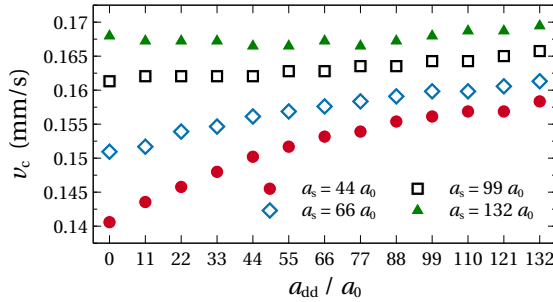


Figure 31. Critical velocity  $v_c$  for the emergence of vortices generated by a moving obstacle as a function of the characteristic dipolar interaction length  $a_{dd}$  (in units of  $a_0$ ) for varying values of the  $s$ -wave scattering length  $a_s$ .

Figure 31 shows results of our numerical study of the dipolar interaction effects on the critical velocity. We see that for large values of the  $s$ -wave scattering length, i.e., for the contact interaction comparable or larger than the dipole interaction, effects of decreasing  $a_{dd}$  are very small and probably could not be experimentally measured. On the other hand, when contact interaction is tuned down so that the dipole interaction starts to dominate the behavior of the system, critical velocity depends much stronger on  $a_{dd}$  and could be easily measured in future experiments.

The above study represents an example on how our programs can be used to verify and compare results of current experiments, as well as to theoretically investigate new phenomena and plan future experiments.

## Conclusion

In this chapter we have reviewed an efficient numerical algorithm for solving the nonlinear Schrödinger equation. The stability and efficiency of the used finite



difference approach is ensured through properly chosen discretization schemes: the split-step Crank-Nicolson method for the time derivatives and central difference formula for the spatial derivatives. In a computational implementation, the presented numerical algorithm is well suited for various parallelization techniques. We have exploited several parallelization approaches available on present-day computer architectures: OpenMP (for shared memory multiprocessing), OpenMP/MPI (for distributed memory systems, where each compute node uses OpenMP to maximize performance), CUDA (for single GPGPUs), CUDA/MPI (for distributed memory systems, where each compute node has GPGPU installed), as well as their hybrid combinations. For efficient hybrid implementations it is essential to divide the work in a way that is suited to the performances of the available computer architecture. To this purpose additional input parameters are introduced and it is shown that their optimal values can be set using a variant of a genetic algorithm. Both strong and weak scalability of the algorithm are explicitly demonstrated by detailed measurements and subsequent analysis. The scalability is proved to be of high importance as parallel versions of the algorithm allow for efficient studies of realistically large system sizes, which are needed in order to make a direct connection to actual physical experiments. As illustrative examples, three applications of the presented algorithms to the topics of current interest in the field of cold atomic BECs were presented. In section 3 a study of phase separation dynamics of a two-component BEC is performed. In section 4 we addressed excitations of a BEC with the coupling of spin and angular momentum and finally in section 5 we investigated vortex formation dynamics in a stirred BEC in the presence of dipolar interactions.

## Acknowledgments

The authors acknowledge valuable discussions with Sadhan K. Adhikari. This work was supported by the Ministry of Education, Science, and Technological Development of the Republic of Serbia under project ON171017. Numerical simulations were performed on the PARADOX supercomputing facility at the Scientific Computing Laboratory of the Institute of Physics Belgrade.

## References

- [1] Dalfovo, F., Giorgini, S., Pitaevskii, L. P., and Stringari, S. Theory of

- Bose-Einstein condensation in trapped gases. *Rev. Mod. Phys.* 71 (1999), 463–512.
- [2] Gross, E. P. Structure of a quantized vortex in boson systems. *Il Nuovo Cimento* 20 (1961), 454–477.
- [3] Pitaevskii, L. P. Vortex Lines in an Imperfect Bose Gas. *Sov. Phys. JETP* 13 (1961), 451.
- [4] Agrawal, G. P. Nonlinear fiber optics: its history and recent progress. *J. Opt. Soc. Am. B* 28 (2011), A1.
- [5] Taha, T. R., and Ablowitz, M. I. Analytical and Numerical Aspects of Certain Nonlinear Evolution Equations. II. Numerical, Nonlinear Schrödinger Equation. *J. Comput. Phys.* 55 (1984), 203–230.
- [6] Anderson, M. H., Ensher, J. R., Matthews, M. R., Wieman, C. E., and Cornell, E. A. Observation of Bose-Einstein Condensation in a Dilute Atomic Vapor. *Science* 269 (1995), 198–201.
- [7] Davis, K. B., Mewes, M.-O., Andrews, M. R., van Druten, N. J., Durfee, D. S., Kurn, D. M., and Ketterle, W. Bose-Einstein condensation in a gas of sodium atoms. *Phys. Rev. Lett.* 75 (1995), 3969–3973.
- [8] Bradley, C. C., Sackett, C. A., Tollett, J. J., and Hulet, R. G. Evidence of Bose-Einstein Condensation in an Atomic Gas with Attractive Interactions. *Phys. Rev. Lett.* 75 (1995), 1687–1690.
- [9] Edwards, M., and Burnett, K. Numerical solution of the nonlinear Schrödinger equation for small samples of trapped neutral atoms. *Phys. Rev. A* 51 (1995), 1382–1386.
- [10] Ruprecht, P. A., Holland, M. J., Burnett, K., and Edwards, M. Time-dependent solution of the nonlinear Schrödinger equation for Bose-condensed trapped neutral atoms. *Phys. Rev. A* 51 (1995), 4704–4711.
- [11] Dalfovo, F., and Stringari, S. Bosons in anisotropic traps: Ground state and vortices. *Phys. Rev. A* 53 (1996), 2477–2485.
- [12] Holland, M., and Cooper, J. Expansion of a Bose-Einstein condensate in a harmonic potential. *Phys. Rev. A* 53 (1996), R1954–R1957.

- 
- [13] Pethick, C. J., and Smith, H. *Bose-Einstein Condensation in Dilute Gases*. Cambridge University Press, 2008.
- [14] Pitaevskii, L. P., and Stringari, S. *Bose-Einstein Condensation*. Oxford University Press, 2003.
- [15] Snyman, J. *Practical Mathematical Optimization*. Springer, 2005.
- [16] Koch, T., Lahaye, T., Metz, J., Fröhlich, B., Griesmaier, A., and Pfau, T. Stabilization of a purely dipolar quantum gas against collapse. *Nat. Phys.* 4 (2008), 218–222.
- [17] Lu, M., Burdick, N. Q., Youn, S. H., and Lev, B. L. Strongly Dipolar Bose-Einstein Condensate of Dysprosium. *Phys. Rev. Lett.* 107 (2011), 190401.
- [18] Aikawa, K., Frisch, A., Mark, M., Baier, S., Rietzler, A., Grimm, R., and Ferlaino, F. Bose-Einstein Condensation of Erbium. *Phys. Rev. Lett.* 108 (2012), 210401.
- [19] Góral, K., and Santos, L. Ground state and elementary excitations of single and binary Bose-Einstein condensates of trapped dipolar gases. *Phys. Rev. A* 66 (2002), 023613.
- [20] Agrawal, G. P. *Nonlinear Fiber Optics*. Academic Press, 2012.
- [21] Antoine, X., Bao, W., and Besse, C. Computational methods for the dynamics of the nonlinear Schrödinger/Gross-Pitaevskii equations. *Comput. Phys. Commun.* 184 (2013), 2621–2633.
- [22] Muruganandam, P., and Adhikari, S. Fortran programs for the time-dependent Gross-Pitaevskii equation in a fully anisotropic trap. *Comput. Phys. Commun.* 180 (2009), 1888–1912.
- [23] Vudragović, D., Vidanović, I., Balaž, A., Muruganandam, P., and Adhikari, S. K. C programs for solving the time-dependent Gross-Pitaevskii equation in a fully anisotropic trap. *Comput. Phys. Commun.* 183 (2012), 2021–2025.
- [24] Press, W. H., Teukolsky, S. A., Vetterling, W. T., and Flannery, B. P. *Numerical Recipes 3rd Edition: The Art of Scientific Computing*, 3 ed. Cambridge University Press, New York, NY, USA, 2007.

- [25] Young-S., L. E., Vudragović, D., Muruganandam, P., Adhikari, S. K., and Balaž, A. OpenMP Fortran and C programs for solving the time-dependent Gross-Pitaevskii equation in an anisotropic trap. *Comput. Phys. Commun.* 204 (2016), 209–213.
- [26] Satarić, B., Slavnić, V., Belić, A., Balaž, A., Muruganandam, P., and Adhikari, S. K. Hybrid OpenMP/MPI programs for solving the time-dependent Gross-Pitaevskii equation in a fully anisotropic trap. *Comput. Phys. Commun.* 200 (2016), 411–417.
- [27] Frigo, M., and Johnson, S. G. The design and implementation of FFTW3. *Proc. IEEE* 93 (2005), 216–231.
- [28] Kumar, R. K., Young-S., L. E., Vudragović, D., Balaž, A., Muruganandam, P., and Adhikari, S. Fortran and C programs for the time-dependent dipolar Gross-Pitaevskii equation in an anisotropic trap. *Comput. Phys. Commun.* 195 (2015), 117–128.
- [29] Lončar, V., Balaž, A., Bogojević, A., Škrbić, S., Muruganandam, P., and Adhikari, S. K. CUDA programs for solving the time-dependent dipolar Gross-Pitaevskii equation in an anisotropic trap. *Comput. Phys. Commun.* 200 (2016), 406–410.
- [30] Lončar, V., Young-S., L. E., Škrbić, S., Muruganandam, P., Adhikari, S. K., and Balaž, A. OpenMP, OpenMP/MPI, and CUDA/MPI C programs for solving the time-dependent dipolar Gross-Pitaevskii equation. *Comput. Phys. Commun.* 209 (2016), 190–196.
- [31] Blelloch, G. Scans as primitive parallel operations. *IEEE Trans. Comput.* 38 (1989), 1526–1538.
- [32] Blelloch, G. E. *Prefix sums and their applications*. Tech. rep., School of Computer Science, Carnegie Mellon University, 1990.
- [33] NVIDIA Corporation. *cuFFT Library User's Guide*, 7.5 ed., 2017.
- [34] Lee, J., Samadi, M., Park, Y., and Mahlke, S. Transparent cpu-gpu collaboration for data-parallel kernels on heterogeneous systems. In *Proceedings of the 22Nd International Conference on Parallel Architectures and Compilation Techniques* (Piscataway, NJ, USA, 2013), PACT '13, IEEE Press, pp. 245–256.

- [35] Papadrakakis, M., Stavroulakis, G., and Karatarakis, A. A new era in scientific computing: Domain decomposition methods in hybrid CPU–GPU architectures. *Comput. Meth. Appl. Mech. Eng.* 200 (2011), 1490–1508.
- [36] Li, Y., Diamond, J. R., Wang, X., Lin, H., Yang, Y., and Han, Z. Large-scale fast fourier transform on a heterogeneous multi-core system. *Int. J. High Perform. Comput. Appl.* 26 (2012), 148–158.
- [37] Ogata, Y., Endo, T., Maruyama, N., and Matsuoka, S. An efficient, model-based CPU-GPU heterogeneous FFT library. In *2008 IEEE International Symposium on Parallel and Distributed Processing* (2008), IEEE.
- [38] Chen, S., and Li, X. A hybrid GPU/CPU FFT library for large FFT problems. In *2013 IEEE 32nd International Performance Computing and Communications Conference (IPCCC)* (2013), IEEE.
- [39] Chu, E., and George, A. *Inside the FFT Black Box*. CRC Press, 1999.
- [40] Lončar, V., Young-S., L. E., Škrbić, S., Muruganandam, P., Adhikari, S. K., and Balaž, A. *DBEC-OMP-CUDA-MPI package*. <https://data.mendeley.com/datasets/j3z9z379m8/2>, 2016.
- [41] Lončar, V., Young-S., L. E., Škrbić, S., Muruganandam, P., Adhikari, S. K., and Balaž, A. *Repository of DBEC-GP family of programs*. <https://git.ipb.ac.rs/vloncar/DBEC-GP>, 2016. Accessed: 2017-04-10.
- [42] Lončar, V. Hybrid parallel algorithms for solving nonlinear Schrödinger equation. *PhD Thesis, University of Novi Sad* (2017).
- [43] Darken, C., Chang, J., and Moody, J. Learning rate schedules for faster stochastic gradient search. In *Neural Networks for Signal Processing II Proceedings of the 1992 IEEE Workshop* (1992), IEEE.
- [44] Schaul, T., Zhang, S., and LeCun, Y. No more pesky learning rates. In *Proceedings of the 30th International Conference on Machine Learning* (Atlanta, Georgia, USA, 2013), S. Dasgupta and D. McAllester, Eds., vol. 28 of *Proceedings of Machine Learning Research*, PMLR, pp. 343–351.

- [45] Spall, J. C. Implementation of the simultaneous perturbation algorithm for stochastic optimization. *IEEE Trans. Aerosp. Electron. Syst.* 34 (1998), 817–823.
- [46] Spall, J. C. Stochastic optimization and the simultaneous perturbation method. In *Proceedings of the 31st conference on Winter simulation Simulation—a bridge to the future - WSC 1999* (1999), ACM Press.
- [47] Holland, J. H. *Adaptation in Natural and Artificial Systems*. MIT University Press Group Ltd, 1992.
- [48] Mitchell, M. *An Introduction to Genetic Algorithms*. MIT Press, 1998.
- [49] Gen, M., and Cheng, R. *Genetic Algorithms and Engineering Optimization*. John Wiley & Sons Inc, 1999.
- [50] Kumar, A. Encoding schemes in genetic algorithm. *Int. J. Adv. Res. IT Eng.* 2 (2013), 1–7.
- [51] Eshelman, L. J., Caruana, R. A., and Schaffer, J. D. Biases in the crossover landscape. In *Proceedings of the Third International Conference on Genetic Algorithms* (San Francisco, CA, USA, 1989), Morgan Kaufmann Publishers Inc., pp. 10–19.
- [52] Spears, V. M., and Jong, K. A. D. On the virtues of parameterized uniform crossover. In *Proceedings of the Fourth International Conference on Genetic Algorithms* (1991), pp. 230–236.
- [53] Richter, J. N. *On mutation and crossover in the theory of evolutionary algorithms*. PhD thesis, Montana State University, 2010.
- [54] White, D. R., and Poulding, S. A rigorous evaluation of crossover and mutation in genetic programming. In *Lecture Notes in Computer Science*, vol. 5481. Springer Berlin Heidelberg, 2009, pp. 220–231.
- [55] da Silva, A. P. A., and Falcao, D. M. Fundamentals of genetic algorithms. In *Modern Heuristic Optimization Techniques: Theory and Applications to Power Systems*, K. Y. Lee and M. A. El-Sharkawi, Eds. John Wiley & Sons Inc, 2008, ch. 2, pp. 25–42.

- [56] Luke, S., and Spector, L. A comparison of crossover and mutation in genetic programming. In *Genetic Programming 1997: Proceedings of the Second Annual Conference* (1997), J. R. e. a. Koza, Ed., Morgan Kaufmann, pp. 240–248.
- [57] Luke, S., and Spector, L. A revised comparison of crossover and mutation in genetic programming. In *Genetic Programming 1998: Proceedings of the Third Annual Conference* (1998), J. R. e. a. Koza, Ed., Morgan Kaufmann, pp. 208–213.
- [58] Amdahl, G. M. Validity of the single processor approach to achieving large scale computing capabilities. In *Proceedings of the April 18-20, 1967, Spring Joint Computer Conference - AFIPS '67 (Spring)* (1967), ACM Press.
- [59] Open MPI project. *Faq: Running cuda-aware open mpi*. <https://www.open-mpi.org/faq/?category=runcuda>, 2016. Accessed: 2017-04-10.
- [60] Frigo, M., and Johnson, S. G. *FFTW 3 documentation*, version 3.3.6. [http://www.fftw.org/fftw3\\_doc/](http://www.fftw.org/fftw3_doc/), 2017. Accessed: 2017-04-10.
- [61] Edwards, M., Ruprecht, P. A., Burnett, K., Dodd, R. J., and Clark, C. W. Collective Excitations of Atomic Bose-Einstein Condensates. *Phys. Rev. Lett.* 77 (1996), 1671–1674.
- [62] Vidanović, I., Balaž, A., Al-Jibbouri, H., and Pelster, A. Nonlinear Bose-Einstein-condensate dynamics induced by a harmonic modulation of the s-wave scattering length. *Phys. Rev. A* 84 (2011), 013618.
- [63] Balaž, A., and Nicolin, A. I. Faraday waves in binary nonmiscible Bose-Einstein condensates. *Phys. Rev. A* 85 (2012), 023613.
- [64] Balaž, A., Paun, R., Nicolin, A. I., Balasubramanian, S., and Ramaswamy, R. Faraday waves in collisionally inhomogeneous Bose-Einstein condensates. *Phys. Rev. A* 89 (2014), 023609.
- [65] Sudharsan, J. B., Radha, R., Carina Raportaru, M., Nicolin, A. I., and Balaž, A. Faraday and resonant waves in binary collisionally-inhomogeneous Bose-Einstein condensates. *J. Phys. B-At. Mol. Opt. Phys.* 49 (2016), 165303.

- 
- [66] Vidanović, I., van Druten, N. J., and Haque, M. Spin modulation instabilities and phase separation dynamics in trapped two-component Bose condensates. *New J. Phys.* 15 (2013), 035008.
- [67] Al-Jibbouri, H., Vidanović, I., Balaž, A., and Pelster, A. Geometric resonances in Bose-Einstein condensates with two- and three-body interactions. *J. Phys. B-At. Mol. Opt. Phys.* 46 (2013), 065303.
- [68] Sakhel, R. R., Sakhel, A. R., and Ghassib, H. B. Nonequilibrium Dynamics of a Bose-Einstein Condensate Excited by a Red Laser Inside a Power-Law Trap with Hard Walls. *J. Low Temp. Phys.* 173 (2013), 177–206.
- [69] Sakhel, R. R., Sakhel, A. R., and Ghassib, H. B. On the phase-correlation and phase-fluctuation dynamics of a strongly excited Bose gas. *Physica B* 478 (2015), 68–76.
- [70] Sakhel, R. R., Sakhel, A. R., Ghassib, H. B., and Balaz, A. Conditions for order and chaos in the dynamics of a trapped Bose-Einstein condensate in coordinate and energy space. *Eur. Phys. J. D* 70 (2016), 66.
- [71] Xi, K.-T., Li, J., and Shi, D.-N. Localization of a two-component Bose-Einstein condensate in a one-dimensional random potential. *Physica B* 459 (2015), 6–11.
- [72] Mithun, T., Porsezian, K., and Dey, B. Disorder-induced vortex lattice melting in a Bose-Einstein condensate. *Phys. Rev. A* 93 (2016), 013620.
- [73] Gautam, S., and Adhikari, S. K. Fractional-charge vortex in a spinor Bose-Einstein condensate. *Phys. Rev. A* 93 (2016), 013630.
- [74] Akram, J., and Pelster, A. Sculpting quasi-one-dimensional Bose-Einstein condensate to generate calibrated matter waves. *Phys. Rev. A* 93 (2016), 023606.
- [75] Akram, J., and Pelster, A. Statics and dynamics of quasi one-dimensional Bose-Einstein condensate in harmonic and dimple trap. *Laser Phys.* 26 (2016), 065501.
- [76] Sakhel, R. R., and Sakhel, A. R. Application of the Lagrangian variational method to a one-dimensional Bose gas in a dimple trap. *J. Phys. B-At. Mol. Opt. Phys.* 50 (2017), 105301.



- 
- [77] Akram, J., and Pelster, A. Numerical study of localized impurity in a Bose-Einstein condensate. *Phys. Rev. A* 93 (2016), 033610.
- [78] Manikandan, K., Muruganandam, P., Senthilvelan, M., and Lakshmanan, M. Manipulating localized matter waves in multicomponent Bose-Einstein condensates. *Phys. Rev E* 93 (2016), 032212.
- [79] Lai, C.-Y., and Chien, C.-C. Geometry-Induced Memory Effects in Isolated Quantum Systems: Cold-Atom Applications. *Phys. Rev. Applied* 5 (2016), 034001.
- [80] Akram, J., Girodias, B., and Pelster, A. Quasi one-dimensional Bose-Einstein condensate in a gravito-optical surface trap. *J. Phys. B-At. Mol. Opt. Phys.* 49 (2016), 075302.
- [81] Khellil, T., Balaž, A., and Pelster, A. Analytical and numerical study of dirty bosons in a quasi-one-dimensional harmonic trap. *New J. Phys.* 18 (2016), 063003.
- [82] Nakamura, K., Babajanov, D., Matrasulov, D., Kobayashi, M., and Muruganandam, P. Dynamics of trapped interacting vortices in Bose-Einstein condensates: a role of breathing degree of freedom. *J. Phys. A-Math. Theor.* 49 (2016), 315102.
- [83] Sakhel, R. R., and Sakhel, A. R. Elements of Vortex-Dipole Dynamics in a Nonuniform Bose-Einstein Condensate. *J. Low Temp. Phys.* 184 (2016), 1092–1113.
- [84] Adhikari, S. K. Statics and dynamics of a self-bound dipolar matter-wave droplet. *Laser Phys. Lett.* 14 (2017), 025501.
- [85] Adhikari, S. K. Statics and dynamics of a self-bound matter-wave quantum ball. *Phys. Rev. A* 95 (2017), 023606.
- [86] Adhikari, S. K. Elastic collision and molecule formation of spatiotemporal light bullets in a cubic-quintic nonlinear medium. *Phys. Rev E* 94 (2016), 032217.
- [87] Gautam, S., and Adhikari, S. K. Phase separation in a spin-orbit-coupled Bose-Einstein condensate. *Phys. Rev. A* 90 (2014), 043619.

- [88] Gautam, S., and Adhikari, S. K. Mobile vector soliton in a spin-orbit coupled spin-1 condensate. *Laser Phys. Lett.* 12 (2015), 045501.
- [89] Gautam, S., and Adhikari, S. K. Vector solitons in a spin-orbit-coupled spin-2 Bose-Einstein condensate. *Phys. Rev. A* 91 (2015), 063617.
- [90] Gautam, S., and Adhikari, S. K. Vortex-bright solitons in a spin-orbit-coupled spin-1 condensate. *Phys. Rev. A* 95 (2017), 013608.
- [91] Vinayagam, P. S., Radha, R., Bhuvaneswari, S., Ravisankar, R., and Muruganandam, P. Bright soliton dynamics in spin orbit-Rabi coupled Bose-Einstein condensates. *Commun. Nonlinear Sci. Numer. Simulat.* 50 (2017), 68–76.
- [92] Vasić, I., and Balaž, A. Excitation spectra of a Bose-Einstein condensate with an angular spin-orbit coupling. *Phys. Rev. A* 94 (2016), 033627.
- [93] Kishor Kumar, R., and Muruganandam, P. Vortex dynamics of rotating dipolar Bose-Einstein condensates. *J. Phys. B-At. Mol. Opt. Phys.* 45 (2012), 215301.
- [94] Kishor Kumar, R., and Muruganandam, P. Numerical studies on vortices in rotating dipolar Bose-Einstein condensates. In *J. Phys.: Conf. Ser.* (2014), vol. 497, p. 012036.
- [95] Kumar, R. K., and Muruganandam, P. Effect of optical lattice potentials on the vortices in rotating dipolar Bose-Einstein condensates. *Eur. Phys. J. D* 68 (2014), 289.
- [96] Kishor Kumar, R., Sriraman, T., Fabrelli, H., Muruganandam, P., and Gammal, A. Three-dimensional vortex structures in a rotating dipolar Bose-Einstein condensate. *J. Phys. B-At. Mol. Opt. Phys.* 49 (2016), 155301.
- [97] Young-S., L. E., and Adhikari, S. K. Mixing, demixing, and structure formation in a binary dipolar Bose-Einstein condensate. *Phys. Rev. A* 86 (2012), 063611.
- [98] Young-S., L. E., and Adhikari, S. K. Dipolar droplet bound in a trapped Bose-Einstein condensate. *Phys. Rev. A* 87 (2013), 013618.

- 
- [99] Adhikari, S. K. Stability of trapped degenerate dipolar Bose and Fermi gases. *J. Phys. B-At. Mol. Opt. Phys.* *46* (2013), 115301.
- [100] Adhikari, S. K. Stability and collapse of fermions in a binary dipolar boson-fermion  $^{164}\text{Dy}$ - $^{161}\text{Dy}$  mixture. *Phys. Rev. A* *88* (2013), 043603.
- [101] Kishor Kumar, R., Muruganandam, P., and Malomed, B. A. Vortical and fundamental solitons in dipolar Bose-Einstein condensates trapped in isotropic and anisotropic nonlinear potentials. *J. Phys. B-At. Mol. Opt. Phys.* *46* (2013), 175302.
- [102] Adhikari, S. K. Stable and mobile excited two-dimensional dipolar Bose-Einstein condensate solitons. *J. Phys. B-At. Mol. Opt. Phys.* *47* (2014), 225304.
- [103] Adhikari, S. K. Stable, mobile, dark-in-bright, dipolar Bose-Einstein-condensate solitons. *Phys. Rev. A* *89* (2014), 043615.
- [104] Adhikari, S. K. Demixing and symmetry breaking in binary dipolar Bose-Einstein-condensate solitons. *Phys. Rev. A* *89* (2014), 013630.
- [105] Adhikari, S. K. Bright dipolar Bose-Einstein-condensate soliton mobile in a direction perpendicular to polarization. *Phys. Rev. A* *90* (2014), 055601.
- [106] Adhikari, S. K. Two-dimensional bright and dark-in-bright dipolar Bose-Einstein condensate solitons on a one-dimensional optical lattice. *Laser Phys. Lett.* *13* (2016), 085501.
- [107] Adhikari, S. K. Stable and mobile two-dimensional dipolar ring-dark-in-bright Bose-Einstein condensate soliton. *Laser Phys. Lett.* *13* (2016), 035502.
- [108] Adhikari, S. K. Self-trapping of a dipolar Bose-Einstein condensate in a double well. *Phys. Rev. A* *89* (2014), 043609.
- [109] Ho, T.-L., and Shenoy, V. B. Binary Mixtures of Bose Condensates of Alkali Atoms. *Phys. Rev. Lett.* *77* (1996), 3276–3279.
- [110] Matthews, M. R., Hall, D. S., Jin, D. S., Ensher, J. R., Wieman, C. E., Cornell, E. A., Dalfovo, F., Minniti, C., and Stringari, S. Dynamical

- Response of a Bose-Einstein Condensate to a Discontinuous Change in Internal State. *Phys. Rev. Lett.* 81 (1998), 243–247.
- [111] Hall, D. S., Matthews, M. R., Ensher, J. R., Wieman, C. E., and Cornell, E. A. Dynamics of Component Separation in a Binary Mixture of Bose-Einstein Condensates. *Phys. Rev. Lett.* 81 (1998), 1539–1542.
- [112] Miesner, H.-J., Stamper-Kurn, D. M., Stenger, J., Inouye, S., Chikkatur, A. P., and Ketterle, W. Observation of Metastable States in Spinor Bose-Einstein Condensates. *Phys. Rev. Lett.* 82 (1999), 2228–2231.
- [113] Salasnich, L., Parola, A., and Reatto, L. Effective wave equations for the dynamics of cigar-shaped and disk-shaped Bose condensates. *Phys. Rev. A* 65 (2002), 043614.
- [114] Pu, H., and Bigelow, N. P. Collective Excitations, Metastability, and Nonlinear Response of a Trapped Two-Species Bose-Einstein Condensate. *Phys. Rev. Lett.* 80 (1998), 1134–1137.
- [115] Timmermans, E. Phase Separation of Bose-Einstein Condensates. *Phys. Rev. Lett.* 81 (1998), 5718–5721.
- [116] Kasamatsu, K., and Tsubota, M. Multiple Domain Formation Induced by Modulation Instability in Two-Component Bose-Einstein Condensates. *Phys. Rev. Lett.* 93 (2004), 100402.
- [117] Kasamatsu, K., and Tsubota, M. Modulation instability and solitary-wave formation in two-component Bose-Einstein condensates. *Phys. Rev. A* 74 (2006), 013617.
- [118] Navarro, R., Carretero-González, R., and Kevrekidis, P. G. Phase separation and dynamics of two-component Bose-Einstein condensates. *Phys. Rev. A* 80 (2009), 023613.
- [119] Lin, Y.-J., Jiménez-García, K., and Spielman, I. B. Spin-orbit-coupled Bose-Einstein condensates. *Nature (London)* 471 (2011), 83–86.
- [120] Beeler, M. C., Williams, R. A., Jiménez-García, K., Leblanc, L. J., Perry, A. R., and Spielman, I. B. The spin Hall effect in a quantum gas. *Nature (London)* 498 (2013), 201–204.

- 
- [121] Zhang, J.-Y., Ji, S.-C., Chen, Z., Zhang, L., Du, Z.-D., Yan, B., Pan, G.-S., Zhao, B., Deng, Y.-J., Zhai, H., Chen, S., and Pan, J.-W. Collective Dipole Oscillations of a Spin-Orbit Coupled Bose-Einstein Condensate. *Phys. Rev. Lett.* *109* (2012), 115301.
- [122] Khamehchi, M. A., Zhang, Y., Hamner, C., Busch, T., and Engels, P. Measurement of collective excitations in a spin-orbit-coupled Bose-Einstein condensate. *Phys. Rev. A* *90* (2014), 063624.
- [123] Cheuk, L. W., Sommer, A. T., Hadzibabic, Z., Yefsah, T., Bakr, W. S., and Zwierlein, M. W. Spin-injection spectroscopy of a spin-orbit coupled fermi gas. *Phys. Rev. Lett.* *109* (2012), 095302.
- [124] Li, J., Huang, W., Shteynas, B., Burchesky, S., Top, F. C., Su, E., Lee, J., Jamison, A. O., and Ketterle, W. Spin-Orbit Coupling and Spin Textures in Optical Superlattices. *Phys. Rev. Lett.* *117* (2016), 185301.
- [125] Li, J.-R., Lee, J., Huang, W., Burchesky, S., Shteynas, B., Top, F. Ç., Jamison, A. O., and Ketterle, W. A stripe phase with supersolid properties in spin-orbit-coupled Bose-Einstein condensates. *Nature (London)* *543* (2017), 91–94.
- [126] Galitski, V., and Spielman, I. B. Spin-orbit coupling in quantum gases. *Nature (London)* *494* (2013), 49–54.
- [127] Zhai, H. Degenerate quantum gases with spin-orbit coupling: a review. *Rep. Prog. Phys.* *78* (2015), 026001.
- [128] Hu, Y.-X., Miniatura, C., and Grémaud, B. Half-skyrmion and vortex-antivortex pairs in spinor condensates. *Phys. Rev. A* *92* (2015), 033615.
- [129] DeMarco, M., and Pu, H. Angular spin-orbit coupling in cold atoms. *Phys. Rev. A* *91* (2015), 033630.
- [130] Qu, C., Sun, K., and Zhang, C. Quantum phases of Bose-Einstein condensates with synthetic spin-orbital-angular-momentum coupling. *Phys. Rev. A* *91* (2015), 053630.
- [131] Sun, K., Qu, C., and Zhang, C. Spin-orbital-angular-momentum coupling in Bose-Einstein condensates. *Phys. Rev. A* *91* (2015), 063627.

- [132] Pitaevskii, L. P., and Rosch, A. Breathing modes and hidden symmetry of trapped atoms in two dimensions. *Phys. Rev. A* 55 (1997), R853–R856.
- [133] Kwon, W. J., Moon, G., Seo, S. W., and Shin, Y. Critical velocity for vortex shedding in a Bose-Einstein condensate. *Phys. Rev. A* 91 (2015), 053615.
- [134] Kadau, H., Schmitt, M., Wenzel, M., Wink, C., Maier, T., Ferrier-Barbut, I., and Pfau, T. Observing the Rosensweig instability of a quantum ferrofluid. *Nature (London)* 530 (2016), 194–197.



**Bosonic fractional quantum Hall states in driven optical lattices**Ana Hudomal,<sup>1</sup> Nicolas Regnault,<sup>2,3</sup> and Ivana Vasić<sup>1</sup><sup>1</sup>*Scientific Computing Laboratory, Center for the Study of Complex Systems, Institute of Physics Belgrade, University of Belgrade, Pregrevica 118, 11080 Belgrade, Serbia*<sup>2</sup>*Joseph Henry Laboratories and Department of Physics, Princeton University, Princeton, New Jersey 08544, USA*<sup>3</sup>*Laboratoire de Physique de l'École Normale Supérieure, ENS, Université PSL, CNRS, Sorbonne Université, Université Paris-Diderot, Sorbonne Paris Cité, 75005 Paris, France*

(Received 2 September 2019; published 27 November 2019)

Strong synthetic magnetic fields have been successfully implemented in periodically driven optical lattices. However, the interplay of the driving and interactions introduces detrimental heating, and for this reason it is still challenging to reach a fractional quantum Hall state in cold-atom setup. By performing a numerical study, we investigate stability of a bosonic Laughlin state in a small atomic sample exposed to driving. We identify an optimal regime of microscopic parameters, in particular interaction strength  $U$  and the driving frequency  $\omega$ , such that the stroboscopic dynamics supports the basic  $\nu = 1/2$  Laughlin state. Moreover, we explore slow ramping of a driving term and show that the considered protocol allows for the preparation of the Laughlin state on experimentally realistic time-scales.

DOI: [10.1103/PhysRevA.100.053624](https://doi.org/10.1103/PhysRevA.100.053624)**I. INTRODUCTION**

Cold atoms in optical lattices provide a highly tunable platform for quantum simulations of relevant many-body Hamiltonians [1,2]. Since early experiments with quantum gases, there has been a strong interest in the realization of fractional quantum Hall (FQH) states in these setups [3–17]. Despite numerous experimental achievements and a variety of theoretical proposals, FQH physics has still not been reached in cold-atom experiments.

A milestone in the field has been recently achieved by the realization of artificial gauge potentials [18–28]. In particular, the topological index of a resulting energy band of an optical lattice featuring a strong synthetic magnetic field has been directly probed [22]. At first glance, both key requirements for the emergence of FQH states—atomic interactions and strong synthetic magnetic fields—are now experimentally available. However, there are several specific details in the implementation of strong synthetic magnetic fields for cold atoms that make the realization of FQH states still challenging.

The most advanced recent realizations of artificial gauge potentials exploit periodically driven optical lattices [19–28]. Using Floquet theory, the stroboscopic dynamics of a noninteracting driven system can be related to an effective time-independent Hamiltonian [29–32]. This approach, Floquet engineering, enriches the set of quantum models that can be simulated in cold-atom experiments. However, general arguments and numerical studies [33–35] suggest that the interplay of interactions and driving in a thermodynamically large system introduces heating, leading to a featureless infinite-temperature state in the long-time limit.

Although this general result might sound discouraging, the heating process can be very slow in some driven systems for specific regime of microscopic parameters. There, the system can be described by a physically interesting

“prethermal” Floquet state on experimentally relevant time-scales [36–42]. Moreover, the onset of thermalization in a finite-size interacting system may exhibit unexpected features, not found in the thermodynamic limit [43,44]. Heating rates and resulting instabilities have been recently investigated both theoretically and experimentally for the driven Bose-Hubbard model in the weakly interacting regime [38,45–47]. Moreover, experimental studies of the driven Fermi-Hubbard model in a honeycomb lattice have established a timescale of the order of 100 tunneling times for the regime where the effective-model description applies [48,49].

In this paper, we consider small systems of several interacting bosonic atoms in a periodically driven optical lattice featuring synthetic magnetic flux. The focus of our study is on finding optimal microscopic parameters that would allow to prepare and probe the basic bosonic Laughlin state in this setup. To this end, we employ exact numerical simulations of the driven Bose-Hubbard model [50] for small system sizes.

From one point of view, it is expected that a small driven system exhibits low heating rates for a driving frequency set above a finite bandwidth of an effective model [33]. However, driving a system with such a high frequency may lead to undesirable effects, such as coupling of the lowest band to higher bands of the underlying optical lattice, thus making the initial description based on the lowest-band Hubbard model inapplicable. These effects have been addressed in a recent study [51] where an optimal intermediate frequency window for Floquet engineering has been established.

In our study, we go a step further in the search for the optimal regime that might allow for the bosonic Laughlin states under driving. In particular, for a realistic, intermediate value of a driving frequency, the interaction term complicates the effective model by introducing several higher-order terms. Their effect on the topological states has been addressed only recently [52,53] and it has been found that typically these



terms work against the topological state. For this reason, the stability of the Laughlin state at intermediate driving frequency requires a separate study, that we perform here. Moreover, we numerically investigate an experimentally relevant preparation protocol for the Laughlin state in a driven system [54]. For a reference, we note that a simpler but closely related question concerning the static (undriven systems) has gained lot of attention [6,7,15,55].

The paper is organized as follows: in Sec. II we introduce the model under study and briefly review key features of the particle-entanglement spectra that we will exploit in the identification of the Laughlin-like state. Then, in Sec. III A we investigate general heating effects of interacting bosons exposed to the driving. By extending this approach, in Sec. III B we construct the stroboscopic time-evolution operator and inspect its eigenstates in order to identify possible FQH states. Finally, in Sec. IV we address the possibility of accessing these states in an experiment through a slow ramp of the driving term.

## II. MODEL AND METHOD

In this section we first introduce the driven model and explain the basis of Floquet engineering. Then we summarize several key features of the particle-entanglement spectra that we use to characterize the bosonic Laughlin states.

### A. Driven model

Properties of bosonic atoms in a deep optical lattice can be realistically described within the framework of the Bose-Hubbard model [1]. We consider a basic driving scheme [50] that introduces a uniform, synthetic magnetic flux into a *square* optical lattice here spanned by the two vectors  $\mathbf{e}_x$  and  $\mathbf{e}_y$ . The corresponding Hamiltonian is given by the driven Bose-Hubbard model

$$\begin{aligned} \hat{H}(t) = & -J_x \sum_{m,n} (\hat{a}_{m+1,n}^\dagger \hat{a}_{m,n} + \text{H.c.}) \\ & -J_y \sum_{m,n} (e^{i\omega t} \hat{a}_{m,n+1}^\dagger \hat{a}_{m,n} + \text{H.c.}) \\ & + \frac{\kappa}{2} \sum_{m,n} \sin[\omega t - (m+n-1/2)\phi] \hat{n}_{m,n} \\ & + \frac{U}{2} \sum_{m,n} \hat{n}_{m,n} (\hat{n}_{m,n} - 1), \end{aligned} \quad (1)$$

where operators  $\hat{a}_{m,n}$  ( $\hat{a}_{m,n}^\dagger$ ) annihilate (create) a boson at lattice position  $(m, n)$ , and local density operators are  $\hat{n}_{m,n} = \hat{a}_{m,n}^\dagger \hat{a}_{m,n}$ .  $J_x$  and  $J_y$  are tunneling amplitudes and  $U$  is the on-site local repulsive interaction. We use the units where  $\hbar = 1$  and the lattice constant  $a = 1$ . The driving scheme is defined by the driving frequency  $\omega$ , the driving amplitude  $\kappa$  and by a phase  $\phi$ . In the following we set  $\phi = \pi/2$  and  $\kappa/\omega = 0.5$ . These values were recently used in an experimental realization of the Harper-Hofstadter model [22]. The derivation of this model is briefly reviewed in Appendix. We assume periodic boundary conditions implemented using the vectors  $\mathbf{R}_1 = 4\mathbf{e}_x$ ,  $\mathbf{R}_2 = -\mathbf{e}_x + \mathbf{e}_y$ , as presented in Fig. 1. This choice is compatible with the driving term and it allows us

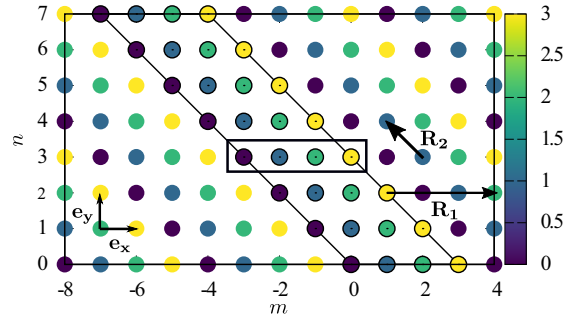


FIG. 1. Lattice geometry used throughout the paper. The parallelogram gives the exemplary lattice size  $(L_x, L_y) = (4, 8)$ . The color scale is defined by  $\text{mod}(m+n, 4)$ , in accordance with the driving term from Eq. (1). The vectors  $\mathbf{R}_1 = 4\mathbf{e}_x$ ,  $\mathbf{R}_2 = -\mathbf{e}_x + \mathbf{e}_y$  are used to implement periodic boundary conditions. The small rectangle gives the magnetic unit cell for the effective model in Eq. (3).

to exploit translational symmetry by working in the fixed quasimomentum basis.

Formally, by using the Floquet theory [29,30,56], it can be shown that the full time-evolution operator corresponding to this model is given by

$$\hat{U}(t, t_0) = e^{-i\hat{K}(t)} e^{-i(t-t_0)\hat{\mathcal{H}}_{\text{eff}}} e^{i\hat{K}(t_0)}, \quad (2)$$

where  $\hat{K}(t)$  is a periodic “kick” operator  $\hat{K}(t) = \hat{K}(t + 2\pi/\omega)$  and  $\hat{\mathcal{H}}_{\text{eff}}$  is a time-independent effective Hamiltonian. The full-time evolution operator is periodic as well and consequently the (quasi)eigenenergies of  $\hat{\mathcal{H}}_{\text{eff}}$  are defined up to modulo  $\omega$ . The last equation gives formal mapping of a periodically driven system to an effective model that captures the stroboscopic time evolution of the model.

In the noninteracting regime,  $U = 0$ , there are several well controlled approximations to obtain the effective Hamiltonian. These techniques are the essence of Floquet engineering, an approach where the driving scheme is implemented in such a way to yield a sought-after effective model. However, according to general analytical arguments and numerical insights, the corresponding effective model of a driven interacting many-body system in the thermodynamic limit exhibits nonphysical features [33,34]. In particular, the system thermalizes and in the long-time limit its steady state is a featureless, infinite-temperature state, independent of the initial state.

Here we consider small samples of several bosonic atoms. Due to a finite spectrum bandwidth, we expect the high-frequency expansion to be relevant for a finite range of the driving frequency. Within these assumptions, the leading-order (in  $1/\omega$ ) effective Hamiltonian is

$$\begin{aligned} \hat{H}_{\text{eff}} = & -J_x \sum_{m,n} (\hat{a}_{m+1,n}^\dagger \hat{a}_{m,n} + \text{H.c.}) \\ & -J'_y \sum_{m,n} (e^{i(m+n)\phi} \hat{a}_{m,n+1}^\dagger \hat{a}_{m,n} + \text{H.c.}) \\ & + \frac{U}{2} \sum_{m,n} \hat{n}_{m,n} (\hat{n}_{m,n} - 1). \end{aligned} \quad (3)$$

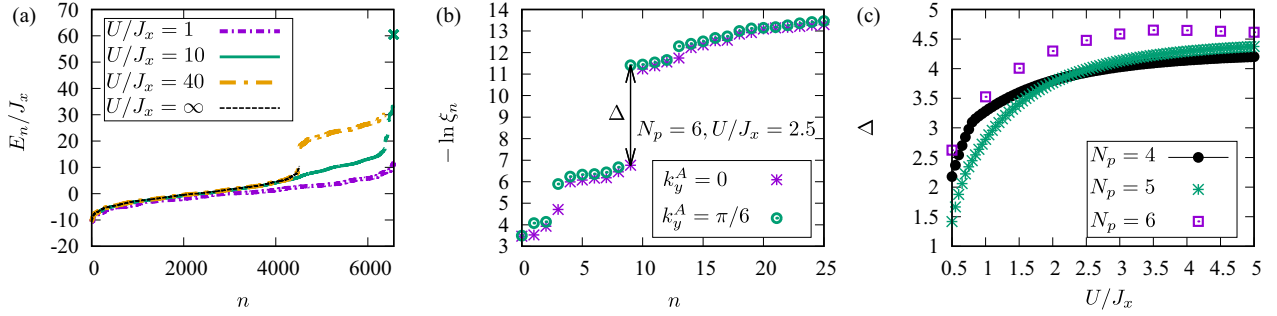


FIG. 2. (a) The energy spectrum  $E_n$  of the model from Eq. (3) in the  $k_x = 0, k_y = 0$  sector for  $N_p = 4$  and different values of interaction  $U/J_x = 1, 10, 40$  and  $U/J_x = \infty$  (hard-core bosons). The top part of the spectrum is at  $\approx (U/J_x)N_p(N_p - 1)/2$ . (Not shown for  $U/J_x = 40$ .) For a high ratio  $U/J_x$  the spectrum splits into bands. The lowest band corresponds to hard-core bosons. (b) The low-lying part of the particle-entanglement spectrum  $-\ln \xi_n$  of the ground-state incoherent superposition, Eq. (6), in the region A momentum sectors  $k_y^A = 0$  and  $k_y^A = \pi/6$ , and for  $N_p = 6, U/J_x = 2.5$ . (c) The particle-entanglement gap  $\Delta$  of the incoherent superposition Eq. (6) as a function of interaction strength  $U$  for  $N_p = 4, 5, 6$ .

The Hamiltonian (3) features complex hopping phases  $e^{i(m+n)\phi}$  that result in a uniform synthetic magnetic flux  $\phi$  per lattice plaquette. Due to the driving, the renormalized hopping amplitude along the  $y$  direction turns into

$$J'_y \equiv \frac{\kappa}{2\omega} \sin(\phi/2) J_y. \quad (4)$$

For the values  $\phi = 2\pi\alpha$ , where the flux density  $\alpha$  is set to  $\alpha = 1/4$ , and  $\kappa/\omega = 0.5$ , the tunneling amplitude along  $y$  direction in the effective model is  $J'_y \approx J_y \times 0.1768$ .

In a certain regime of microscopic parameters, the ground state of the model defined in Eq. (3) is given by the lattice version of the Laughlin state [7,9,57–59]. The Laughlin state is stabilized for the filling factor  $\nu = N_p/N_\phi = 1/2$ , where  $N_\phi = \alpha L_x \times L_y$  is the total number of fluxes ( $N_\phi$  being an integer) and  $N_p$  is the number of bosons, and for a strong-enough repulsion  $U$ . Another important requirement for the Laughlin state is to avoid the strong hopping anisotropy and to keep  $J_x \approx J'_y$ , so we set  $J_x = 0.2J_y$ . We consider system sizes  $N_p = 4, 5, 6$  and the respective lattices sizes  $(L_x, L_y) = (4, 8), (4, 10),$  and  $(4, 12)$ , see Fig. 1, where we expect the ground state to correspond to the  $\nu = 1/2$  Laughlin state. The Hilbert space sizes for  $k_x = k_y = 0$  are  $\dim \mathcal{H} = 6564, 108\,604,$  and  $1\,913\,364$  respectively. For this choice of microscopic parameters, the model ground state of Eq. (3) is approximately twofold degenerate. The two ground-states are found in the sectors  $k_x = 0, k_y = 0$  and  $k_x = 0, k_y = \pi$ . We denote them by  $|\psi_{\text{LGH}}^{0,0}\rangle$  and  $|\psi_{\text{LGH}}^{0,\pi}\rangle$ .

As we are mainly interested in the driven regime, not only the ground state, but the full spectrum of the model from Eq. (3) plays a role. A rough argument is that the system does not absorb energy provided that the driving frequency  $\omega$  is set above the bandwidth of the effective model. Several spectra of the model from Eq. (3) for  $k_x = 0, k_y = 0$  are presented in Fig. 2(a). It can be seen that the ground-state energy is weakly affected by the value of  $U \geq J_x$ , while the top part of the spectrum with few states is found at  $UN_p(N_p - 1)/2$ . For higher values of  $U$  the spectrum splits into bands where the lowest band corresponds to the hard-core bosons and higher bands include double and higher occupancies.

## B. Particle-entanglement spectra

There are several ways to characterize the ground states of the model from Eq. (3) as the Laughlin states. Usually, the starting point in this direction is the identification of the twofold degeneracy expected in the implemented torus geometry for  $\nu = 1/2$ . Another relevant quantity is the overlap of the numerically obtained state with the Laughlin analytical wave function in the torus geometry [9,59]. More direct evidence can be obtained through the calculation of the relevant topological index (Chern number) or the quantized Hall conductance. An additional convincing approach, that we pursue here, is based on the analysis of the entanglement spectra of the relevant states.

In the following we will use the particle-entanglement spectrum (PES) [59,60] to distinguish possible topologically nontrivial states. In order to obtain this type of entanglement spectrum, we partition  $N_p$  particles into two sets of  $N_A$  and  $N_B = N_p - N_A$  particles. For a given mixed state  $\rho$ , we construct a reduced density matrix  $\rho_A = \text{tr}_B \rho$  by performing a partial trace over  $N_B$  particles. The resulting PES is given by  $-\ln \xi_n$ , where  $\xi_n$  are eigenvalues of  $\rho_A$ . The related particle-entanglement entropy is given by [61,62]

$$S_A = -\text{tr}(\rho_A \ln \rho_A). \quad (5)$$

By partitioning particles, we keep the geometry of the system unchanged. For this reason, we will inspect the PES for the different momentum sectors  $k_y^A$  of the remaining  $N_A$  particles. An example of a PES is presented in Fig. 2(b). As proposed in Refs. [59,60], we have considered the incoherent superposition of the almost twofold degenerate ground state of Eq. (3) as the density matrix

$$\rho_{\text{GS}} = \frac{1}{2} (|\psi_{\text{LGH}}^{0,0}\rangle\langle\psi_{\text{LGH}}^{0,0}| + |\psi_{\text{LGH}}^{0,\pi}\rangle\langle\psi_{\text{LGH}}^{0,\pi}|). \quad (6)$$

For simplicity, we only present the PES for the two momenta  $k_y^A = 0$  and  $k_y^A = \pi/6$ . We observe a clear particle-entanglement gap  $\Delta$ . In addition, the counting of low-lying modes below this gap (ten modes for  $k_y^A = 0$  and nine modes for  $k_y^A = \pi/6$ , at  $N_A = 3, N_p = 6$ ) corresponds to the Laughlin state [59,60]. In this way the PES encodes topological features of the state  $\rho$  in the form of well defined number of excitations per momentum sector  $k_y^A$  [59,60]. This type of

TABLE I. Counting of modes  $\mathcal{N}_L(k_y^A)$  in the PES of the Laughlin state for several system sizes and particle partitions. The last column lists the  $\mathcal{N}_L(k_y^A)$  values for each momentum sector  $k_y^A = 2\pi i/L_y$ ,  $i = 0, \dots, L_y - 1$ .

$N_p$	$(L_x, L_y)$	$N_A$	PES: $\mathcal{N}_L(k_y^A)$
4	(4, 8)	2	3, 2, 3, 2, 3, 2, 3, 2
5	(4, 10)	2	4, 3, 4, 3, 4, 3, 4, 3
6	(4, 12)	3	10, 9, 9, 10, 9, 9, 10, 9, 9, 10, 9, 9

analysis is useful as it can identify topological features even without model states, as done for the case of fractional Chern insulators [63,64].

In the following we will consider specific particle partitions  $N_A = 2$ ,  $N_p = 4$ ;  $N_A = 2$ ,  $N_p = 5$ ; and  $N_A = 3$ ,  $N_p = 6$ . For these cases the counting of excitations  $\mathcal{N}_L(k_y^A)$  per momentum sector  $k_y^A$  is well established and given in Table I. In Fig. 2(c) we show the particle-entanglement gap of the mixtures, Eq. (6), obtained at different values of  $U$ . Numerical results for the obtained PES indicate that a reasonably large gap is found starting at  $U \sim 0.5J_x$  and the characteristic features of the Laughlin state persist with a further increase in  $U$ . We note that at lower values of the flux density,  $\alpha < 1/4$ , the Laughlin state can be found at even lower values of the repulsion  $U$  [9,59].

By analyzing the effective model from Eq. (1), we have obtained a guidance for the regime of microscopic parameters and for the geometry of the small system that can give rise to Laughlin states. In the next sections our aim is to go beyond the effective model from Eq. (3) and to identify topological states supported by the full driven dynamics as captured by the model given in Eq. (1).

### III. DRIVEN DYNAMICS

In this section we discuss the full driven dynamics as captured by the model given in Eq. (1).

#### A. Heating

First we address the onset of heating following the standard procedure discussed in Refs. [42,65]. The initial state of the system is prepared using the ground state of the effective model

$$|\psi(t=0)\rangle = e^{-i\hat{K}(t=0)}|\psi_{\text{LGH}}^{0,0}\rangle \quad (7)$$

and we monitor the stroboscopic time-evolution  $t = NT$ ,  $T \equiv 2\pi/\omega$  governed by the full driven model defined in Eq. (1). In our numerical simulations, we approximate the micromotion operator  $\hat{K}(t=0)$  using the leading-order high-frequency expansion; see Eq. (A12). The quantity of interest is the expectation value of the effective Hamiltonian (3):

$$\langle \hat{H}_{\text{eff}}(t=NT) \rangle_K = \langle \psi(t) | e^{-i\hat{K}(t=0)} \hat{H}_{\text{eff}} e^{i\hat{K}(t=0)} | \psi(t) \rangle. \quad (8)$$

We expect this quantity to reasonably correspond to the ground-state energy of the effective model  $E_0$  in the regime of very high frequency. On the other hand, for a “low” driving frequency we expect the system to quickly reach the

infinite-temperature  $\beta \rightarrow 0$  regime defined by

$$\lim_{\beta \rightarrow 0} \langle \hat{H}_{\text{eff}} \rangle = \frac{1}{\dim \mathcal{H}} \text{tr}(\hat{H}_{\text{eff}}). \quad (9)$$

For this reason we monitor the normalized total energy

$$Q(t=NT) = \frac{\langle \hat{H}_{\text{eff}}(t=NT) \rangle_K - E_0}{\lim_{\beta \rightarrow 0} \langle \hat{H}_{\text{eff}} \rangle - E_0} \quad (10)$$

and we present it in Fig. 3(a), for  $U/J_x = 10$ . In agreement with the known results [65], we find that the thermalization is quick for both a “high” driving frequency  $\omega/J_x \geq 20$  and for a “low” driving frequency  $\omega/J_x \leq 10$ . For the intermediate values of  $\omega$ , the heating process is slow [65] and the total energy exhibits a slow exponential growth captured by  $Q(t=NT) \approx 1 - b \exp(-ct)$ ,  $t \gg 1$ . An example of this behavior is given for  $\omega/J_x = 15$  in Fig. 3(a). The heating process can also be monitored through the particle-entanglement entropy  $S_A$  as a function of time. In Fig. 3(b) for  $N_p = 5$  and low driving frequency we find that this quantity quickly saturates to its maximal value. Indeed, for a thermal state at infinite temperature,  $S_A$  is given by

$$S_A^{\text{max}} \approx \ln \left( \frac{L_x L_y + N^A - 1}{N^A} \right), \quad (11)$$

marked by the horizontal, dot-dashed line in Fig. 3(b). Except for the highest frequency considered ( $\omega/J_x = 50$ ), we find that, in the process of heating, the particle-entanglement gap of the initial state quickly closes (not shown in the plots).

Here we briefly discuss finite-size effects by comparing numerical results for the normalized total energy for  $N_p = 4$ ,  $N_p = 5$ , and  $N_p = 6$ . In line with the known results [33,34,38], the “high-frequency” regime with low heating rates moves toward higher  $\omega$  as the system size increases. However, we find that the estimates obtained in this section ( $\omega/J_x \geq 20$  for the high- and  $\omega/J_x \leq 10$  for the low-frequency regime, for  $U/J_x = 10$ ) apply to all the three sizes  $N_p = 4, 5, 6$ , at least for the time-scales that we consider. A comprehensive study of the leading finite-size effects in driven systems can be found in Refs. [33,42,65].

#### B. The stroboscopic time-evolution operator

In order to better understand the limitations of the effective model, here we time evolve all relevant basis states for a single driving period  $T = 2\pi/\omega$  and construct the stroboscopic time-evolution operator

$$\hat{U}_F \equiv \hat{U}(t_0 + T, t_0 = 0) \quad (12)$$

such that  $\hat{U}(NT + t_0) = \hat{U}_F^N$ . In the next step, for a system size  $N_p = 4$ ,  $(L_x, L_y) = (4, 8)$  we fully diagonalize this operator and inspect its eigenstates  $|n\rangle$ . Following the described procedure, we obtain the long-time limit

$$\lim_{N \rightarrow \infty} \langle \hat{H}_{\text{eff}}(NT) \rangle_K = \sum_n | \langle n | \psi(t=0) \rangle |^2 \langle n | \hat{H}_{\text{eff}} | n \rangle_K, \quad (13)$$

where we define

$$\langle n | \hat{H}_{\text{eff}} | n \rangle_K = \langle n | e^{-i\hat{K}(t=0)} \hat{H}_{\text{eff}} e^{i\hat{K}(t=0)} | n \rangle. \quad (14)$$

Results for  $Q(t=NT)$  from Eq. (10) obtained in this way are summarized in Fig. 3(c), where we make a comparison

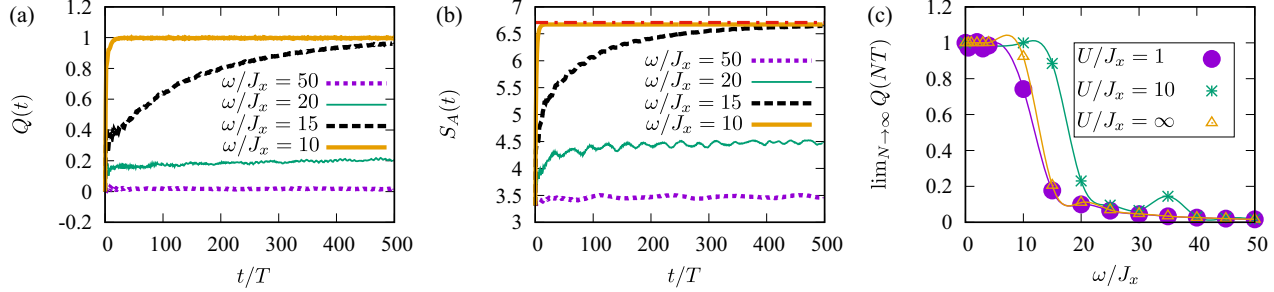


FIG. 3. (a) The normalized total energy  $Q(t = NT)$  from Eq. (10), and the (b) particle-entanglement entropy  $S_A(t = NT)$ , Eq. (5), during the time evolution governed by Eq. (1) for several driving frequencies  $\omega/J_x = 50, 20, 15, 10$ . Parameters:  $N_p = 5, U/J_x = 10$ . Note that the asymptotic value of  $S_A$  for  $\omega/J_x = 10$  and  $\omega/J_x = 15$  matches the one given in Eq. (11), as presented by the horizontal, dot-dashed line. (c) The long-time limit  $\lim_{N \rightarrow \infty} Q(NT)$  for  $N_p = 4$  and the on-site interactions  $U/J_x = 1, 10$  and  $U/J_x = \infty$  (hard-core bosons). The lines are only guides to the eye.

between the long-time energies for the case of hard-core bosons ( $U \rightarrow \infty$ ) and soft-core bosons (finite values of  $U$ ). The obtained results indicate that heating rates of hard-core bosons are closer to the case of  $U/J_x = 1$  in comparison to  $U/J_x = 10$ , which is expected from the bandwidths shown in Fig. 2(a). Overall we observe that the “high-frequency regime” is wider for lower ratios  $U/J_x$ .

In Fig. 4, we make a comparison between the exact driven model captured by  $\hat{U}_F$  and  $\hat{H}_{\text{eff}}$ . In Figs. 4(a) and 4(b) we inspect the distribution of expectation values  $\langle n | \hat{H}_{\text{eff}} | n \rangle_K$ . By comparing these values to the eigenenergies of the effective model, Eq. (3), we get an insight into the pertinence of the effective description [33,34]. In particular, for an interacting system in the thermodynamic limit, the distribution is flat and the effective description is useless. We state again that we consider only small atomic samples. For this reason, it is expected that for high values of  $\omega$  the full stroboscopic description nicely matches to the effective model values. Such an example is given in Fig. 4(a) for  $U/J_x = 1$  and  $\omega/J_x = 20$ . As the value of  $\omega$  gets lower the distribution becomes flatter, as can be seen in Fig. 4(b) for  $U/J_x = 10$  by comparing results for  $\omega/J_x = 50$  and  $\omega/J_x = 10$ .

The intermediate regime of frequencies, e.g.,  $\omega/J_x = 20$  for  $U/J_x = 10$ , is of the main experimental relevance [51]. We now investigate whether the driven stroboscopic dynamics supports some Laughlin-like states, by calculating the PES of

the mixture

$$\rho_F = \frac{1}{2}(|n_0(0, 0)\rangle\langle n_0(0, 0)| + |n_0(0, \pi)\rangle\langle n_0(0, \pi)|), \quad (15)$$

where  $|n_0(k_x, k_y)\rangle$  is the state from the  $k_x, k_y$  sector with the lowest expectation value  $\langle n | \hat{H}_{\text{eff}} | n \rangle_K$ . The results are presented in Fig. 4(c). We find that the states with a well defined gap and the Laughlin-like PES can be found down to  $\omega/J_x \geq 10$  for  $U/J_x = 1$ , and down to  $\omega/J_x \geq 20$  for  $U/J_x = 10$ . Having established existence of these states for small samples of  $N_p = 4$  particles, in the next section we discuss dynamical protocol which can be exploited to prepare these states.

IV. SLOW RAMP

The question about an optimal adiabatic protocol that can be used to prepare the Laughlin state in a cold-atom setup has gained lot of attention [6,7,15,55]. The situation becomes even more complex once the full driving process is taken into account. A general wisdom is that, by starting from a topologically trivial state, the topological index of a thermodynamically large system cannot be changed adiabatically. We consider a small atomic sample and follow the proposal of Ref. [15]. Our main contribution is that we extend this protocol to the case of the driven, interacting Bose-Hubbard model.

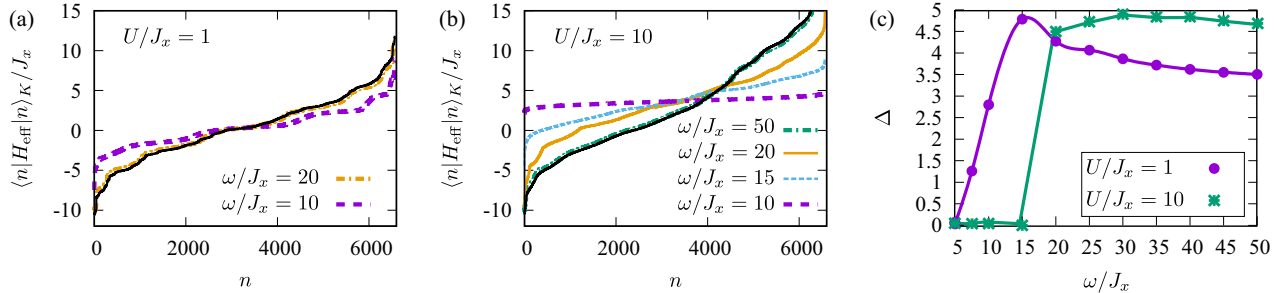


FIG. 4. Properties of the eigenstates  $|n\rangle$  of the stroboscopic time-evolution operator  $\hat{U}_F$ , Eq. (12), in the  $k_x = 0, k_y = 0$  sector for  $N_p = 4$ . Expectation values  $\langle n | \hat{H}_{\text{eff}} | n \rangle_K$  defined in Eq. 14 for (a)  $U/J_x = 1, \omega/J_x = 10, 20$  and (b)  $U/J_x = 10, \omega/J_x = 10, 15, 20, 50$ . The black solid lines mark eigenenergies of  $\hat{H}_{\text{eff}}$ , Eq. (3). Note that in (b) we do not include few states from the top of the spectrum of  $\hat{H}_{\text{eff}}$ , Eq. (3), for clarity. (c) The particle-entanglement gap  $\Delta$  of the incoherent superposition  $\rho_F$ , Eq. (15), for  $U/J_x = 1$  and  $U/J_x = 10, N_p = 4$ . The lines are only guides to the eye.



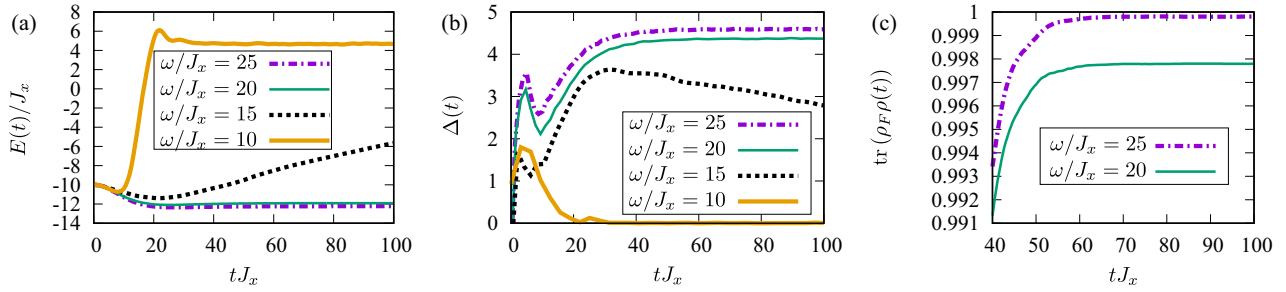


FIG. 5. (a) The expectation value  $E(t)$  defined in Eq. (19) and (b) the particle-entanglement gap  $\Delta(t)$  of  $\rho(t)$ , Eq. (18), during the time evolution governed by Eq. (17) for several driving frequencies  $\omega/J_x = 25, 20, 15, 10$ . Parameters:  $N_p = 5$ ,  $U/J_x = 10$ ,  $\eta/J_x = 0.05$ . (c) The overlap  $\text{tr}[\rho(t)\rho_F]$  of the time evolved state with the target eigenstates of  $\hat{U}_F$  for  $\omega/J_x = 25, 20$ . Parameters:  $N_p = 4$ ,  $U/J_x = 10$ ,  $\eta/J_x = 0.05$ .

### A. Model

Following results of Ref. [15], we consider a slow ramp of the tunneling amplitude along  $y$  direction,  $J_y(t)$ , as well as a slow ramp of the driving amplitude  $\kappa(t)$ . Namely, we start from a series of decoupled wires along the  $x$  direction and start coupling them. More precisely, initial states are selected as the ground states of  $\hat{H}_{\text{ini}}$ :

$$\begin{aligned} \hat{H}_{\text{ini}} = & -J_x \sum_{m,n} (\hat{a}_{m+1,n}^\dagger \hat{a}_{m,n} + \text{H.c.}) \\ & + \frac{U}{2} \sum_{m,n} \hat{n}_{m,n} (\hat{n}_{m,n} - 1). \end{aligned} \quad (16)$$

For the filling factors that we consider, the ground states of the  $\hat{H}_{\text{ini}}$  are simple noninteracting states with the ground state energy  $E_{0,\text{ini}} = -2J_x N_p$ . Out of the several degenerate ground states, we select those where atoms occupy every second wire. There are two such states and we label them as  $|\psi_+\rangle$  (even wires occupied) and  $|\psi_-\rangle$  (odd wires occupied). These states have finite projections only onto the sectors  $k_x = 0$ ,  $k_y = 0$  and  $k_x = 0$ ,  $k_y = \pi$  of the driven model from Eq. (1). Therefore we may expect the two initial states  $|\psi_\pm(t=0)\rangle$  to be transformed into the two Laughlin states during the ramp.

Having prepared the initial state, we slowly restore the tunneling amplitude along the  $y$  direction,  $J_y(t)$ , and slowly ramp up the driving amplitude  $\kappa(t)$ . The time-evolution is governed by

$$\begin{aligned} \hat{H}_{\text{sr}}(t) = & -J_x \sum_{m,n} (\hat{a}_{m+1,n}^\dagger \hat{a}_{m,n} + \text{H.c.}) \\ & - J_y(t) \sum_{m,n} (e^{i\omega t} \hat{a}_{m,n+1}^\dagger \hat{a}_{m,n} + \text{H.c.}) \\ & + \frac{\kappa(t)}{2} \sum_{m,n} \sin[\omega t - (m+n-1/2)\phi] \hat{n}_{m,n} \\ & + \frac{U}{2} \sum_{m,n} \hat{n}_{m,n} (\hat{n}_{m,n} - 1), \end{aligned} \quad (17)$$

where  $J_y(t) = J_y \tanh(\eta t)$ ,  $\kappa(t) = \kappa \tanh(\eta t)$ ,  $\eta$  being the ramping rate. In the long-time limit, we recover the original Hamiltonian from Eq. (1). During the ensuing time evolution we construct the mixture

$$\rho(t) = \frac{1}{2} (|\psi_+(t)\rangle\langle\psi_+(t)| + |\psi_-(t)\rangle\langle\psi_-(t)|). \quad (18)$$

We monitor stroboscopically the energy expectation value

$$E(t) = \text{tr}(\rho(t)\hat{H}_{\text{eff}}) \quad (19)$$

and the PES of  $\rho(t)$ .

### B. Results

In Fig. 5(a) we present the energy expectation value from Eq. (19) for  $U/J_x = 10$  and several driving frequencies  $\omega/J_x = 25, 20, 15, 10$ . Our numerical results indicate that ramps with the rates up to  $\eta/J_x \sim 0.1$  work reasonably well. Slower ramps give better results, but are less practical [15]. By construction, the initial state is a noninteracting state with particles delocalized along the  $x$  direction and therefore the initial energy is  $E(t=0) = -2N_p J_x$ . During the ramp with the rate  $\eta/J_x = 0.05$ , for the regime of high driving frequencies, down to approximately  $\omega/J_x = 20$ , we find that the energy initially decreases and reaches an almost constant value at around  $tJ_x \sim 20$ . On the other hand, for  $\omega/J_x = 15$ , the system slowly heats up during the ramping process, and for  $\omega/J_x = 10$  the system quickly reaches the infinite-temperature state.

One of our main results is summarized in Fig. 5(b), where we plot the particle-entanglement gap of  $\rho(t)$ , from Eq. (18), as a function of time. In the high-frequency regime  $\omega/J_x \geq 20$ , starting around  $tJ_x \sim 20$  we find a persistent particle-entanglement gap, marking the onset of a topologically nontrivial state. It is even more interesting that, even for  $\omega/J_x \sim 15$ , the state seems to exhibit a finite gap on intermediate time-scales. This is not the case for  $\omega/J_x \leq 10$ , where the gap quickly vanishes. In Fig. 5(c), we present the value of the overlap  $\text{tr}[\rho(t)\rho_F]$ , of the time-evolved mixed state with the relevant state from Eq. (15) for  $N_p = 4$ . Clearly, the slow ramp of the type given in Eq. (17) allows for the preparation of the relevant eigenstates of  $\hat{U}_F$  with high fidelity (better than 1%).

In Figs. 6(a) and 6(b) we show the time evolution of the PES in the two momentum sectors  $k_y^A = 0$  and  $k_y^A = \pi/6$  for  $N_p = 6$ ,  $U/J_x = 5$ , and  $\eta/J_x = 0.05$ . The PES of the initial state is easy to understand. As the  $L_y/2$  wires are occupied by single atoms, the reduced density matrix is proportional to the identity matrix with the proportionality factor yielding  $-\ln \xi_n = \ln(2 \binom{L_y/2}{N_A}) \approx 3.69$ . During the ramp we find that additional modes in PES are gaining weight and moving down in the spectrum. Finally, the state  $\rho(t)$  reached around  $t \approx 50T$  exhibits a well defined gap and the correct counting of the low-lying modes: there are ten low-lying modes for  $k_y^A = 0$

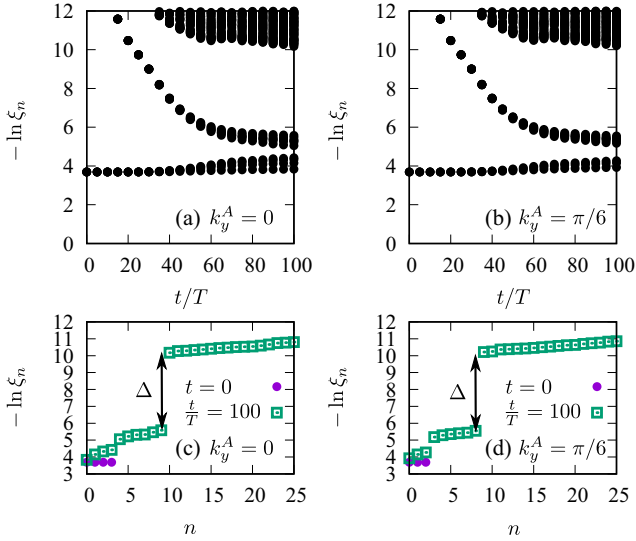


FIG. 6. The low-lying part of the particle-entanglement spectra  $-\ln \xi_n$  of  $\rho(t)$ , Eq. (18), during the time evolution governed by Eq. (17) in the (a)  $k_y^A = 0$  and (b)  $k_y^A = \pi/6$  momentum sectors. The low-lying part of the PES in the sectors (c)  $k_y^A = 0$  and (d)  $k_y^A = \pi/6$ , at two instances of time  $t = 0$  and  $t/T = 100$ . Parameters:  $N_p = 6$ ,  $U/J_x = 5$ ,  $\omega/J_x = 15$ ,  $\eta/J_x = 0.05$ .

and nine low-lying modes for  $k_y^A = \pi/6$ ; see Figs. 6(c) and 6(d) and also Table I.

In Fig. 7 we discuss a satisfactory range of ramping rates  $\eta$  for a given interaction strength  $U$  and a given driving frequency  $\omega$  that we fix at  $\omega/J_x = 15$ . The obtained numerical results suggest that at weaker interaction strengths  $U/J_x \leq 2$ , slower ramping rates are needed. One way to explain this behavior is by using the effective model and arguing that the gap protecting the Laughlin state is smaller at weaker  $U$ . On the other hand, for stronger interaction strengths  $U/J_x \geq 8$  the particle-entanglement gap closes at later stages as the heating process becomes dominant. Finally, in the intermediate range  $U/J_x \sim 5$ , faster ramps with  $\eta/J_x = 0.1$  lead to the sought-after state  $\rho(t)$  from Eq. (18), with persistent features in the PES up to  $t = 500T$ . These results indicate that, when optimizing the ramping protocol in an actual experiment, there will be a tradeoff between the unfavorable heating and a faster ramping into the desired state, as both of these processes are promoted by interactions.

## V. CONCLUSIONS

The technique of Floquet engineering has been successfully exploited for the implementation of synthetic magnetic fields in driven optical lattices. Following up on these achievements and on a long-standing pursuit for the FQH states in cold-atom setups, in this paper we have addressed possible realization of the bosonic Laughlin state in a small atomic sample in a periodically driven optical lattice. While a thermodynamically large interacting system generally heats up into an infinite-temperature state under driving, the heating process can be controlled to some extent in a few-particle system.

We have assumed a realistic driving protocol and finite on-site interactions, and we have identified the FQH state based

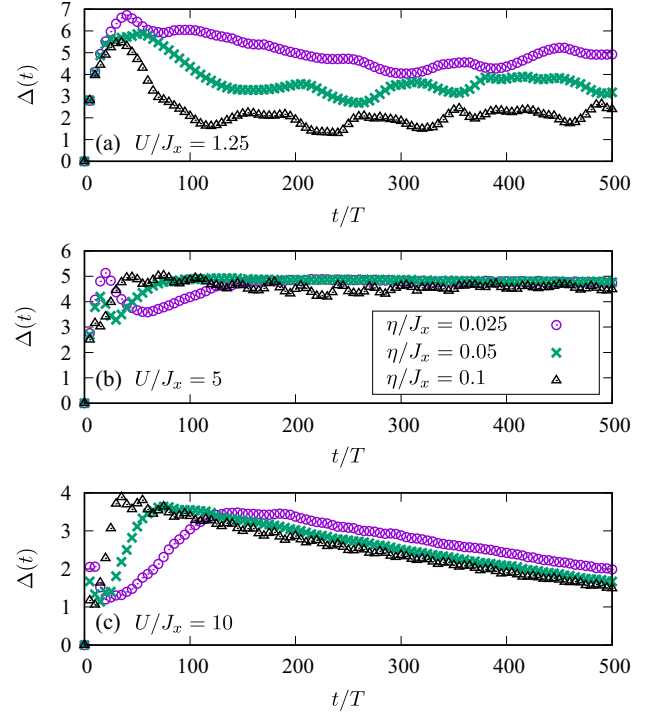


FIG. 7. The particle-entanglement gap  $\Delta(t)$  as a function of time during the time evolution governed by Eq. (17), for several interaction strengths (a)  $U/J_x = 1.25$  (b)  $U/J_x = 5$  and (c)  $U/J_x = 10$ , and several ramping rates  $\eta/J_x = 0.025, 0.05, 0.1$ . Other parameters:  $N_p = 5$ ,  $\omega/J_x = 15$ .

on analysis of its particle-entanglement spectra. Results of our numerical simulations show that the stroboscopic dynamics of  $N_p = 4, 5, 6$  particles supports the topological  $\nu = 1/2$  Laughlin state down to  $\omega/J_x = 20$  for  $U/J_x = 10$ , and down to  $\omega/J_x = 15$  for  $U/J_x = 1$ , for the driving amplitude  $\kappa/\omega = 0.5$ . These results are in reasonable agreement with the recent estimates of the optimal heating times [51] that take into account the contribution of the higher bands of the underlying optical lattice. In addition, we have investigated slow ramping of the driving term and found that it allows for the preparation of the Laughlin state on experimentally realistic time-scales of the order of  $20 \hbar/J_x$ , where  $\hbar/J_x$  is the tunneling time. Interestingly, we find that some topological features persist during an intermediate stage even in the regime where the system exhibits a slow transition into the infinite-temperature state (e.g.,  $\omega/J_x = 15$  for  $U/J_x = 10$ ).

In the future, we plan to address the preparation scheme for the relevant correlated states in a driven honeycomb lattice, which exhibits lower heating rates in comparison to a cubic lattice according to the recent experiments [48,49]. Another highly relevant question, that we have not tackled and that we postpone to future investigation, concerns suitable experimental probes of topological features. The recent progress in the field has led to the development of several detection protocols specially suited for the cold-atom systems [66–71]. For the type of systems considered in this paper, the most promising are results of the recent study [71] showing that fractional excitations can be probed even in small systems of several bosons.

### ACKNOWLEDGMENTS

This work was supported by the Ministry of Education, Science, and Technological Development of the Republic of Serbia under Project ON171017. N.R. was supported by the grants ANR TNSTRONG No. ANR-16-CE30-0025 and ANR TopO No. ANR-17-CE30-0013. Numerical simulations were performed on the PARADOX supercomputing facility at the Scientific Computing Laboratory of the Institute of Physics Belgrade. The authors would also like to acknowledge the contribution of the COST Action CA16221.

### APPENDIX: DRIVEN OPTICAL LATTICES

In this Appendix we review the derivation of the model given in Eq. (1). The system is described by

$$\hat{H}_{\text{lab}}(t) = \hat{H}_{BH} + \hat{H}_{\text{drive}}(t) + \omega \hat{V}, \quad (\text{A1})$$

where we start with the Bose-Hubbard model

$$\begin{aligned} \hat{H}_{BH} = & -J_x \sum_{m,n} (\hat{a}_{m+1,n}^\dagger \hat{a}_{m,n} + \text{H.c.}) \\ & - J_y \sum_{m,n} (\hat{a}_{m,n+1}^\dagger \hat{a}_{m,n} + \text{H.c.}) \\ & + \frac{U}{2} \sum_{m,n} \hat{n}_{m,n} (\hat{n}_{m,n} - 1), \end{aligned} \quad (\text{A2})$$

and we introduce an offset  $\omega \hat{V}$ :

$$\hat{V} = \sum_{m,n} n \hat{n}_{m,n}. \quad (\text{A3})$$

This shifted Bose-Hubbard model is exposed to a suitable resonant driving scheme:

$$\begin{aligned} \hat{H}_{\text{drive}}(t) = & \frac{\kappa}{2} \sum_{m,n} \sin\left(\omega t - \phi_{m,n} + \frac{\phi}{2}\right) \hat{n}_{m,n}, \\ \phi_{m,n} = & (m+n)\phi. \end{aligned} \quad (\text{A4})$$

We assume periodic boundary conditions compatible with the driving term (A4) in the laboratory frame. To this purpose we use vectors  $\mathbf{R}_1 = 4\mathbf{e}_x$  and  $\mathbf{R}_2 = -\mathbf{e}_x + \mathbf{e}_y$  as presented in Fig. 1. For simplicity, we work in the rotating frame

$$|\psi_{\text{rot}}(t)\rangle = e^{i\omega t \hat{V}} |\psi_{\text{lab}}(t)\rangle \quad (\text{A5})$$

and derive the Schrödinger equation

$$i \frac{d}{dt} |\psi_{\text{rot}}(t)\rangle = \hat{H}_{\text{rot}}(t) |\psi_{\text{rot}}(t)\rangle, \quad (\text{A6})$$

where

$$\hat{H}_{\text{rot}}(t) = (e^{i\omega t \hat{V}} \hat{H}_{\text{lab}}(t) e^{-i\omega t \hat{V}} - \omega \hat{V}). \quad (\text{A7})$$

Now we calculate  $\hat{H}_{\text{rot}}(t)$  explicitly. The only nontrivial action of this rotation on  $\hat{H}_{\text{lab}}$  comes from the nearest-neighbor hopping along  $y$  direction. Indeed, we have

$$e^{i\omega t \hat{V}} \hat{a}_{m,n}^\dagger \hat{a}_{m,n'} e^{-i\omega t \hat{V}} = e^{i\omega t (n-n')} \hat{a}_{m,n}^\dagger \hat{a}_{m,n'}. \quad (\text{A8})$$

In total we obtain

$$\begin{aligned} \hat{H}_{\text{rot}}(t) = & -J_x \sum_{m,n} (\hat{a}_{m+1,n}^\dagger \hat{a}_{m,n} + \text{H.c.}) + \frac{U}{2} \sum_{m,n} \hat{n}_{m,n} (\hat{n}_{m,n} - 1) \\ & + e^{i\omega t} \hat{H}_1 + e^{-i\omega t} \hat{H}_{-1} + e^{-i\omega t (L_y-1)} \hat{H}_{L_y-1} \\ & + e^{i\omega t (L_y-1)} \hat{H}_{-L_y+1}, \end{aligned} \quad (\text{A9})$$

with

$$\begin{aligned} \hat{H}_1 = & -J_y \sum_{m,n}^{\text{OBC}} \left( \hat{a}_{m,n+1}^\dagger \hat{a}_{m,n} - \frac{i}{4} \kappa e^{i(-\phi_{m,n} + \frac{\phi}{2})} \hat{n}_{m,n} \right), \\ \hat{H}_{-1} = & \hat{H}_1^\dagger, \\ \hat{H}_{-L_y+1} = & -J_y \sum_m \hat{a}_{m,0}^\dagger \hat{a}_{m-L_y,L_y-1}, \quad \hat{H}_{L_y-1} = \hat{H}_{-L_y+1}^\dagger. \end{aligned} \quad (\text{A10})$$

In the terms  $\hat{H}_{-L_y+1}$  and  $\hat{H}_{L_y-1}$  we take into account periodic boundary conditions along the direction parallel to  $\mathbf{R}_2$  as imposed in the laboratory frame. In order to limit the complexity of the numerical calculation, we keep translational invariance and impose the periodic boundary conditions in both directions in the rotating frame. This implies that we will neglect ‘‘phasors’’  $e^{-i\omega t (L_y-1)}$  and  $e^{i\omega t (L_y-1)}$ . Under these assumptions, we can recast Eq. (A9) into the time-dependent Hamiltonian given in Eq. (1). In practice, this would require engineering additional non-trivial terms in the laboratory frame.

The leading order of the kick operator is given by



$$\hat{K}(t=0) \approx -\frac{\kappa}{2\omega} \sum_{m,n} \cos(\phi_{m,n} - \phi/2) \hat{n}_{m,n}. \quad (\text{A12})$$

- 
- [1] I. Bloch, J. Dalibard, and W. Zwerger, *Rev. Mod. Phys.* **80**, 885 (2008).
- [2] W. Hofstetter and T. Qin, *J. Phys. B: At. Mol. Opt. Phys.* **51**, 082001 (2018).
- [3] N. K. Wilkin and J. M. F. Gunn, *Phys. Rev. Lett.* **84**, 6 (2000).
- [4] N. R. Cooper, N. K. Wilkin, and J. M. F. Gunn, *Phys. Rev. Lett.* **87**, 120405 (2001).
- [5] B. Paredes, P. Fedichev, J. I. Cirac, and P. Zoller, *Phys. Rev. Lett.* **87**, 010402 (2001).
- [6] M. Popp, B. Paredes, and J. I. Cirac, *Phys. Rev. A* **70**, 053612 (2004).
- [7] A. S. Sørensen, E. Demler, and M. D. Lukin, *Phys. Rev. Lett.* **94**, 086803 (2005).
- [8] E. H. Rezayi, N. Read, and N. R. Cooper, *Phys. Rev. Lett.* **95**, 160404 (2005).
- [9] M. Hafezi, A. S. Sørensen, E. Demler, and M. D. Lukin, *Phys. Rev. A* **76**, 023613 (2007).
- [10] B. Juliá-Díaz, D. Dagnino, K. J. Günter, T. Graß, N. Barberán, M. Lewenstein, and J. Dalibard, *Phys. Rev. A* **84**, 053605 (2011).
- [11] B. Juliá-Díaz, T. Graß, N. Barberán, and M. Lewenstein, *New J. Phys.* **14**, 055003 (2012).
- [12] T. Graß, B. Juliá-Díaz, and M. Lewenstein, *Phys. Rev. A* **89**, 013623 (2014).
- [13] A. Petrescu, M. Piraud, G. Roux, I. P. McCulloch, and K. Le Hur, *Phys. Rev. B* **96**, 014524 (2017).

- [14] M. Calvanese Strinati, E. Cornfeld, D. Rossini, S. Barbarino, M. Dalmonte, R. Fazio, E. Sela, and L. Mazza, *Phys. Rev. X* **7**, 021033 (2017).
- [15] Y.-C. He, F. Grusdt, A. Kaufman, M. Greiner, and A. Vishwanath, *Phys. Rev. B* **96**, 201103(R) (2017).
- [16] P. Rosson, M. Lubasch, M. Kiffner, and D. Jaksch, *Phys. Rev. A* **99**, 033603 (2019).
- [17] M. Calvanese Strinati, S. Sahoo, K. Shtengel, and E. Sela, *Phys. Rev. B* **99**, 245101 (2019).
- [18] Y.-J. Lin, R. L. Compton, K. Jiménez-García, J. V. Porto, and I. B. Spielman, *Nature (London)* **462**, 628 (2009).
- [19] H. Miyake, G. A. Siviloglou, C. J. Kennedy, W. C. Burton, and W. Ketterle, *Phys. Rev. Lett.* **111**, 185302 (2013).
- [20] M. Aidelsburger, M. Atala, M. Lohse, J. T. Barreiro, B. Paredes, and I. Bloch, *Phys. Rev. Lett.* **111**, 185301 (2013).
- [21] G. Jotzu, M. Messer, R. Desbuquois, M. Lebrat, T. Uehlinger, D. Greif, and T. Esslinger, *Nature (London)* **515**, 237 (2014).
- [22] M. Aidelsburger, M. Lohse, C. Schweizer, M. Atala, J. T. Barreiro, S. Nascimbène, N. R. Cooper, I. Bloch, and N. Goldman, *Nat. Phys.* **11**, 162 (2015).
- [23] C. J. Kennedy, W. C. Burton, W. C. Chung, and W. Ketterle, *Nat. Phys.* **11**, 859 (2015).
- [24] N. Fläschner, B. S. Rem, M. Tarnowski, D. Vogel, D.-S. Lühmann, K. Sengstock, and C. Weitenberg, *Science* **352**, 1091 (2016).
- [25] M. E. Tai, A. Lukin, M. Rispoli, R. Schittko, T. Menke, Dan Borgnia, P. M. Preiss, F. Grusdt, A. M. Kaufman, and M. Greiner, *Nature (London)* **546**, 519 (2017).
- [26] J. Dalibard, F. Gerbier, G. Juzeliūnas, and P. Öhberg, *Rev. Mod. Phys.* **83**, 1523 (2011).
- [27] A. Eckardt, *Rev. Mod. Phys.* **89**, 011004 (2017).
- [28] N. R. Cooper, J. Dalibard, and I. B. Spielman, *Rev. Mod. Phys.* **91**, 015005 (2019).
- [29] N. Goldman and J. Dalibard, *Phys. Rev. X* **4**, 031027 (2014).
- [30] N. Goldman, J. Dalibard, M. Aidelsburger, and N. R. Cooper, *Phys. Rev. A* **91**, 033632 (2015).
- [31] A. Eckardt and E. Anisimovas, *New J. Phys.* **17**, 093039 (2015).
- [32] K. Plekhanov, G. Roux, and K. Le Hur, *Phys. Rev. B* **95**, 045102 (2017).
- [33] L. D'Alessio and M. Rigol, *Phys. Rev. X* **4**, 041048 (2014).
- [34] A. Lazarides, A. Das, and R. Moessner, *Phys. Rev. E* **90**, 012110 (2014).
- [35] P. Ponte, A. Chandran, Z. Papić, and D. A. Abanin, *Ann. Phys. (NY)* **353**, 196 (2015).
- [36] D. A. Abanin, W. De Roeck, and F. Huveneers, *Phys. Rev. Lett.* **115**, 256803 (2015).
- [37] T. Mori, T. Kuwahara, and K. Saito, *Phys. Rev. Lett.* **116**, 120401 (2016).
- [38] M. Bukov, S. Gopalakrishnan, M. Knap, and E. Demler, *Phys. Rev. Lett.* **115**, 205301 (2015).
- [39] T. Kuwahara, T. Mori, and K. Saito, *Ann. Phys. (NY)* **367**, 96 (2016).
- [40] D. A. Abanin, W. De Roeck, W. W. Ho, and F. Huveneers, *Phys. Rev. B* **95**, 014112 (2017).
- [41] D. Abanin, W. De Roeck, W. W. Ho, and F. Huveneers, *Commun. Math. Phys.* **354**, 809 (2017).
- [42] F. Machado, G. D. Meyer, D. V. Else, C. Nayak, and N. Y. Yao, [arXiv:1708.01620](https://arxiv.org/abs/1708.01620).
- [43] A. Haldar, R. Moessner, and A. Das, *Phys. Rev. B* **97**, 245122 (2018).
- [44] K. Seetharam, P. Titum, M. Kolodrubetz, and G. Refael, *Phys. Rev. B* **97**, 014311 (2018).
- [45] S. Lellouch, M. Bukov, E. Demler, and N. Goldman, *Phys. Rev. X* **7**, 021015 (2017).
- [46] K. Wintersperger, M. Bukov, J. Näger, S. Lellouch, E. Demler, U. Schneider, I. Bloch, N. Goldman, and M. Aidelsburger, [arXiv:1808.07462](https://arxiv.org/abs/1808.07462).
- [47] T. Boulier, J. Maslek, M. Bukov, C. Bracamontes, E. Magnan, S. Lellouch, E. Demler, N. Goldman, and J. V. Porto, *Phys. Rev. X* **9**, 011047 (2019).
- [48] F. Görg, M. Messer, K. Sandholzer, G. Jotzu, R. Desbuquois, and T. Esslinger, *Nature (London)* **553**, 481 (2018).
- [49] M. Messer, K. Sandholzer, F. Görg, J. Minguzzi, R. Desbuquois, and T. Esslinger, *Phys. Rev. Lett.* **121**, 233603 (2018).
- [50] M. Bukov and A. Polkovnikov, *Phys. Rev. A* **90**, 043613 (2014).
- [51] G. Sun and A. Eckardt, [arXiv:1805.02443](https://arxiv.org/abs/1805.02443).
- [52] A. G. Grushin, A. Gómez-León, and T. Neupert, *Phys. Rev. Lett.* **112**, 156801 (2014).
- [53] M. Račiūnas, G. Žlabys, A. Eckardt, and E. Anisimovas, *Phys. Rev. A* **93**, 043618 (2016).
- [54] A. Dauphin, D.-T. Tran, M. Lewenstein, and N. Goldman, *2D Mater.* **4**, 024010 (2017).
- [55] J. Motruk and F. Pollmann, *Phys. Rev. B* **96**, 165107 (2017).
- [56] M. Grifoni and P. Hänggi, *Phys. Rep.* **304**, 229 (1998).
- [57] R. B. Laughlin, *Phys. Rev. Lett.* **50**, 1395 (1983).
- [58] F. D. M. Haldane and E. H. Rezayi, *Phys. Rev. B* **31**, 2529 (1985).
- [59] A. Sterdyniak, N. Regnault, and G. Möller, *Phys. Rev. B* **86**, 165314 (2012).
- [60] A. Sterdyniak, N. Regnault, and B. A. Bernevig, *Phys. Rev. Lett.* **106**, 100405 (2011).
- [61] O. S. Zozulya, M. Haque, and K. Schoutens, *Phys. Rev. A* **78**, 042326 (2008).
- [62] M. Haque, O. S. Zozulya, and K. Schoutens, *J. Phys. A: Math. Theor.* **42**, 504012 (2009).
- [63] N. Regnault and B. A. Bernevig, *Phys. Rev. X* **1**, 021014 (2011).
- [64] B. A. Bernevig and N. Regnault, *Phys. Rev. B* **85**, 075128 (2012).
- [65] M. Bukov, M. Heyl, D. A. Huse, and A. Polkovnikov, *Phys. Rev. B* **93**, 155132 (2016).
- [66] H. M. Price and N. R. Cooper, *Phys. Rev. A* **85**, 033620 (2012).
- [67] A. Dauphin and N. Goldman, *Phys. Rev. Lett.* **111**, 135302 (2013).
- [68] D. T. Tran, A. Dauphin, A. G. Grushin, P. Zoller, and N. Goldman, *Sci. Adv.* **3**, e1701207 (2017).
- [69] A. Hudomal, I. Vasić, H. Buljan, W. Hofstetter, and A. Balaž, *Phys. Rev. A* **98**, 053625 (2018).
- [70] C. Repellin and N. Goldman, *Phys. Rev. Lett.* **122**, 166801 (2019).
- [71] M. Račiūnas, F. N. Ünal, E. Anisimovas, and A. Eckardt, *Phys. Rev. A* **98**, 063621 (2018).



## Quantum scars of bosons with correlated hopping

Ana Hudomal <sup>1✉</sup>, Ivana Vasić <sup>1</sup>, Nicolas Regnault<sup>2,3</sup> & Zlatko Papić<sup>4</sup>

Recent experiments on Rydberg atom arrays have found evidence of anomalously slow thermalization and persistent density oscillations, which have been interpreted as a many-body analog of the phenomenon of quantum scars. Periodic dynamics and atypical scarred eigenstates originate from a “hard” kinetic constraint: the neighboring Rydberg atoms cannot be simultaneously excited. Here we propose a realization of quantum many-body scars in a 1D bosonic lattice model with a “soft” constraint in the form of density-assisted hopping. We discuss the relation of this model to the standard Bose-Hubbard model and possible experimental realizations using ultracold atoms. We find that this model exhibits similar phenomenology to the Rydberg atom chain, including weakly entangled eigenstates at high energy densities and the presence of a large number of exact zero energy states, with distinct algebraic structure.

<sup>1</sup>Institute of Physics Belgrade, University of Belgrade, 11080 Belgrade, Serbia. <sup>2</sup>Joseph Henry Laboratories and Department of Physics, Princeton University, Princeton, NJ 08544, USA. <sup>3</sup>Laboratoire de Physique de l’Ecole Normale Supérieure, ENS, Université PSL, CNRS, Sorbonne Université, Université Paris-Diderot, Sorbonne Paris Cité, 75005 Paris, France. <sup>4</sup>School of Physics and Astronomy, University of Leeds, Leeds LS2 9JT, UK. ✉email: [ana.hudomal@ipb.ac.rs](mailto:ana.hudomal@ipb.ac.rs)

Semiclassical studies of chaotic stadium billiards have revealed the existence of remarkable non-chaotic eigenfunctions called “quantum scars”<sup>1</sup>. Scarred eigenfunctions display anomalous enhancement in regions of the billiard that are traversed by one of the periodic orbits in the classical limit when  $\hbar \rightarrow 0$ . It was shown that quantum scars lead to striking experimental signatures in a variety of systems, including microwave cavities<sup>2</sup>, quantum dots<sup>3</sup>, and semiconductor quantum wells<sup>4</sup>.

A recent experiment on a quantum simulator<sup>5</sup>, and subsequent theoretical work<sup>6,7</sup>, have shown that quantum many-body scars can occur in strongly interacting quantum systems. The experiment used a one-dimensional Rydberg atom platform in the regime of the Rydberg blockade<sup>5,8,9</sup>, where nearest-neighbor excitations of the atoms were energetically prohibited. The experiment observed persistent many-body revivals of local observables after a “global quench”<sup>10</sup> from a certain initial state. In contrast, when the experiment was repeated for other initial configurations, drawn from the same type of “infinite” temperature ensemble, the system displayed fast equilibration and no revivals. These observations pointed to a different kind of out-of-equilibrium behavior compared to previous studies of quantum thermalization in various experimental platforms<sup>11–15</sup>.

In both single-particle and many-body quantum scars, the dynamics from certain initial states leads to periodic revivals of the wave function. In the former case, this happens when the particle is prepared in a Gaussian wave packet initialized along a periodic orbit<sup>1</sup>, while in the latter case the revivals can be interpreted as a nearly-free precession of a large emergent  $su(2)$  spin degree of freedom<sup>16,17</sup>. Another similarity between single- and many-body quantum scars is the existence of non-ergodic eigenstates. In the single-particle case, such eigenstates are easily identified by their non-uniform probability density that sharply concentrates along classical periodic orbits. In the many-body case, non-ergodic eigenstates are broadly defined as those that violate eigenstate thermalization hypothesis (ETH)<sup>18,19</sup>. Scarred eigenstates violate the ETH in a number of ways: for example, they appear at evenly spaced energies throughout the spectrum<sup>6,20,21</sup>, they have anomalous expectation values of local observables compared to other eigenstates at the same energy density, and their entanglement entropy obeys a sub-volume law scaling<sup>20</sup>.

In recent works, the existence of atypical eigenstates has been taken as a more general definition of quantum many-body scarring. For example, highly excited eigenstates with low entanglement have previously been analytically constructed in the non-integrable AKLT model<sup>22,23</sup>. A few of such exact eigenstates are now also available for the Rydberg atom chain model<sup>24</sup>. The collection of models that feature atypical eigenstates is rapidly expanding, including perturbations of the Rydberg atom chain<sup>20,25,26</sup>, theories with confinement<sup>27–29</sup>, Fermi–Hubbard model beyond one dimension<sup>30,31</sup>, driven systems<sup>32</sup>, quantum spin systems<sup>33,34</sup>, fractional quantum Hall effect in a one-dimensional limit<sup>35</sup>, and models with fracton-like dynamics<sup>36–39</sup>. In a related development, it was proposed that atypical eigenstates of one Hamiltonian can be “embedded” into the spectrum of another, thermalizing Hamiltonian<sup>40</sup>, causing a violation of a “strong” version of the ETH<sup>41,42</sup>. This approach allows to engineer scarred eigenstates in models of topological phases in arbitrary dimensions<sup>43</sup>. From a dynamical point of view, it has been shown that models with scarred dynamics can be systematically constructed by embedding periodic on-site unitary dynamics into a many-body system<sup>44</sup>.

A feature shared by many scarred models is the presence of some form of a kinetic constraint. In the Rydberg atom chain, the constraint results from strong van der Waals forces, which

project out the neighboring Rydberg excitations<sup>45</sup>. Such Hilbert spaces occur, for example, in models describing anyon excitations in topological phases of matter<sup>46–50</sup> and in lattice gauge theories<sup>51–53</sup>, including the Rydberg atom system<sup>54,55</sup>. Recent works on periodically driven optical lattices have started to explore such physics<sup>56,57</sup>. On the other hand, kinetic constraints have been investigated as a possible pathway to many-body localization without disorder<sup>58</sup>. In classical systems, non-thermalizing behavior without disorder is well known in the context of structural glasses<sup>59–61</sup>. The mechanism of this type of behavior is the excluded volume interactions that impose kinetic constraints on the dynamics<sup>62,63</sup>. Similar type of physics has recently been explored in quantum systems where a “quasi many-body localized” behavior was proposed to occur in the absence of disorder<sup>64–74</sup>.

In this paper, we investigate the relation between kinetic constraints, slow dynamics and quantum many-body scars. In contrast to previous work, which focused on models of spins and fermions that are closely related in one dimension due to the Jordan–Wigner mapping, here we study one-dimensional models of bosons with density-assisted hoppings, which realize both “hard” and “soft” kinetic constraints, whilst being non-integrable. Depending on the form of the hopping term, we demonstrate that the models encompass a rich phenomenology, including regimes of fast thermalization, the existence of periodic revivals and many-body scars, as well as the Hilbert space fragmentation that has been found in recent studies of fractonic models<sup>36–39</sup>. Unlike the experimentally realized Rydberg atom system, we find evidence of many-body scars in a bosonic model without a hard kinetic constraint, i.e., with a fully connected Hilbert space. We identify initial states that give rise to periodic many-body revivals in the quantum dynamics, and we introduce a “cluster approximation” that captures the scarred eigenstates that are responsible for periodic revivals. We discuss possible experimental realizations of these models using ultracold atoms.

## Results

**Models and their Hilbert spaces.** A fundamental ingredient of kinetically constrained models is “correlated hopping”: a particle can hop depending on the state of its neighbors. In this paper we consider a system of  $N_p$  bosons on a one-dimensional lattice with  $L$  sites. We consider models where the total filling factor,  $\nu = N_p/L$ , is conserved, and we will mainly present results in the dense regime,  $\nu = 1$ . We have studied models with  $\nu < 1$  and  $\nu > 1$ , but we found them to be either too constrained or not constrained enough, and therefore less interesting. We emphasize that the bosons in our study are not hard-core, i.e., the occupancy of any lattice site can take any value from 0 to  $N_p$ .

We study three different models, defined by the Hamiltonians:

$$H_1 = -J \sum_{j=1}^L \left( b_j^\dagger b_{j+1} n_j + n_{j-1} b_j^\dagger b_{j-1} \right), \quad (1)$$

$$H_2 = -J \sum_{j=1}^L \left( n_j b_j^\dagger b_{j+1} + b_j^\dagger b_{j-1} n_{j-1} \right), \quad (2)$$

$$H_3 = -J \sum_{j=1}^L \left( n_{j+1} b_j^\dagger b_{j+1} n_j + n_{j-1} b_j^\dagger b_{j-1} n_j \right). \quad (3)$$

All three models contain a free-boson hopping term,  $b_j^\dagger b_{j+1}$ , which is dressed in various ways by density operators,  $n_j = b_j^\dagger b_j$ . We will show that the position of the density operator  $n_j$  completely changes the behavior of these models, ranging from fast thermalization to the breakup of the Hamiltonian into

disconnected, exactly solvable sectors. For example, note that  $H_1$  and  $H_2$  are related to each other via free-boson hopping,

$$H_2 = H_1 - J \sum_j (b_j^\dagger b_{j+1} + b_j^\dagger b_{j-1}), \quad (4)$$

which can be easily proven using bosonic commutation relations. We will see below that this innocuous free-boson hopping leads to surprisingly different dynamical properties of the two models.

The motivation behind introducing three different models in Eqs. (1)–(3) can be summarized as follows. Hamiltonian  $H_1$  describes a model where a particle cannot hop to the left if that site is not already occupied by at least one particle, and cannot hop to the right if it is the only particle left on its initial site. This introduces constraints to the system. Conversely, there are no such constraints in the case of  $H_2$ . Indeed, the hopping coefficients are only modified in intensity by the particle-number operator. Hamiltonian  $H_3$  introduces additional constraints compared to  $H_1$ . The number of unoccupied sites and their positions remain constant under the action of this Hamiltonian. This leads to different connectivity of the Hilbert space in each of the models, as we explain in the next Section.

We consider periodic boundary conditions ( $L + 1 \equiv 1$ ) and set  $\hbar = J = 1$ . With periodic boundary conditions, all three Hamiltonians  $H_1$ ,  $H_2$  and  $H_3$  have translation symmetry, thus their eigenstates can be labeled by momentum quantum number,  $k$ , quantized in units of  $2\pi/L$ . In addition,  $H_3$  has inversion symmetry. We denote by  $I = 0$  and  $I = 1$  the sectors that are even and odd under inversion, respectively.

Without restrictions on the boson occupancy, the Hilbert space of  $H_1$ ,  $H_2$  and  $H_3$  grows very rapidly. For  $L = N_p = 12$ , the Hilbert space size of the  $k = 0$  sector is 112720 (the largest one we will consider for  $H_1$  and  $H_2$ ). As previously mentioned (see also the next Section), the Hilbert space of  $H_3$  splits into many disconnected components, thus it is possible to consider only one connected component at a time and disregard the unoccupied sites whose positions do not change. This is more relevant when

looking at properties such as thermalization, than fixing the filling factor. However, the boundary conditions are in that case no longer periodic, and the system does not have translation symmetry. Considering only a system with the size  $L/2$ , filling factor  $\nu = 2$ , open boundary conditions and minimal number of particles per site equal to 1 is completely equivalent to considering the largest component of the full system which has the size  $L$ , filling factor  $\nu = 1$ , periodic boundary conditions and no restrictions on the occupancies. The Hilbert space size of the symmetric invariant sector of the largest connected component of  $L = N_p = 22$  is 176484 and this is the largest sector that we will consider for  $H_3$ .

**Graph structure of the models.** Since we will be interested in the dynamical properties, it is convenient to first build some intuition about the structure of the Hamiltonians of the three models in Eqs. (1)–(3). A Hamiltonian can be viewed as the adjacency matrix of a graph whose vertices are Fock states of bosons,  $|n_1, n_2, \dots, n_L\rangle$ . If the Hamiltonian induces a transition between two Fock states, the corresponding vertices of the graph are connected by a link. The graphs that show how the configuration space is connected have very different structure for the three Hamiltonians  $H_1$ ,  $H_2$ , and  $H_3$ , as can be observed in Fig. 1.

The entire graph of  $H_2$  is well connected and it has the same structure as the graph of the standard Bose-Hubbard model: the particle-number operators in  $H_2$  do not introduce any constraints, but only affect the magnitude of the hopping coefficients. In contrast, the  $H_1$  graph shows several clusters of configurations that are weakly connected to the rest of the graph. “Weakly connected” means that there is a small number of connections leading outside the cluster and that their respective hopping coefficients are smaller in magnitude than those of the surrounding connections within the cluster. A state that is initially located inside a cluster is therefore more likely to stay inside during an initial stage of the time evolution, which increases the probability of revivals and slows down the growth of

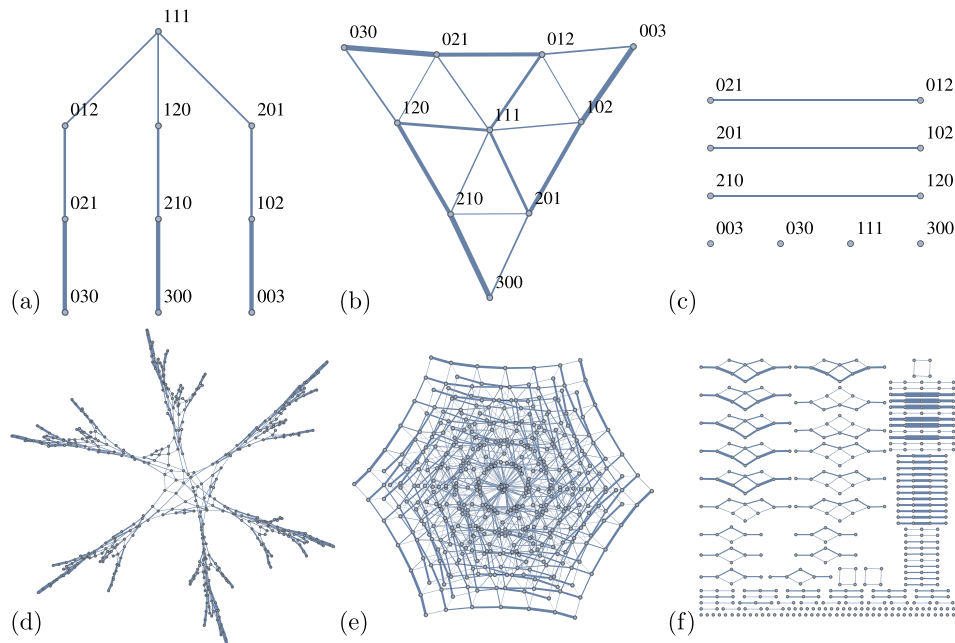


**Fig. 1 Connectivity of the Hilbert space.** Adjacency graph for **a**  $H_1$ , **b**  $H_2$ , **c**  $H_3$ , all for  $L = N_p = 3$ . **d-f** same as **a**, **b** and **c** but for  $L = N_p = 6$ . To avoid clutter, we do not label the vertices in **d-f**. All graphs are weighted, i.e., the line thickness is proportional to the magnitude of the corresponding hopping coefficient. Several different clusters of configurations are visible in the case of  $H_1$ . The clusters start to form already for  $L = 3$  (for example, the configurations 012-021-003 in **a**) and become more prominent for  $L = 6$  **d**. In the case of  $H_2$ , almost all configurations are well connected to the rest of the graph. The graphs for  $H_3$  show that the Hilbert space is highly reducible: its graph splits into many disconnected components.

entanglement entropy. We will provide a more quantitative description and examples that illustrate this in Section “Quantum scars in  $H_1$  and  $H_3$  models”. Finally, the graph of  $H_3$ , due to even stronger constraints, is actually disconnected, which is an example of Hilbert space fragmentation that was previously shown to cause non-ergodic behavior in fracton-like models<sup>37,38</sup>. This predicts that thermalization and dynamics in the three models will be very different, which we will confirm in the following Section. However, we note that the number of connections and the topology of the graph is not the only relevant factor for the dynamics. The magnitude of the hopping coefficients between different configurations is also important (Supplementary Note 1).

We note that the relation between  $H_1$  and  $H_3$  is reminiscent of the relation between the quantum East model<sup>75</sup> and the “PXP” model describing the atoms in the Rydberg blockade regime<sup>6,20,45</sup>. Like  $H_3$ , the PXP model is doubly constrained and inversion symmetric, while  $H_1$  and the quantum East model are asymmetric versions of those two models with only a single constraint. The graph of the quantum East model is similar to that of  $H_1$ , in that it contains bottlenecks which slow down the growth of entanglement entropy<sup>75</sup>.

**Dynamics and entanglement properties.** We now investigate the phenomenology of the models introduced in Eqs. (1)–(3). We use exact diagonalization to obtain the complete set of energy eigenvalues and eigenvectors, from which we evaluate the level statistics and the distribution of entanglement entropies for the three models. Furthermore, we probe dynamical properties of the models by studying a global quench, simulated via Krylov iteration.

The energy level statistics is a standard test for thermalization of models that cannot be solved exactly. A convenient way to

probe the level statistics is to examine the probability distribution  $P(r)$ <sup>76</sup> of ratios between consecutive energy gaps  $s_n = E_{n+1} - E_n$ ,

$$r = \frac{\min(s_n, s_{n+1})}{\max(s_n, s_{n+1})}. \quad (5)$$

The advantage of studying  $P(r)$ , instead of  $P(s_n)$ , is that there is no need to perform the spectrum unfolding procedure—see ref. 77. For standard random matrix theory ensembles, both  $P(r)$  and the mean  $\langle r \rangle$  are well known<sup>78</sup>. When computing the same quantities in a microscopic physical model, it is crucial to resolve all the symmetries of the model.

The probability distribution  $P(r)$  of the ratios of two consecutive energy gaps is shown in Fig. 2a–c for the three Hamiltonians  $H_1$ ,  $H_2$ , and  $H_3$  respectively, and two momentum or inversion sectors. In all three cases, the energy levels repel, i.e., the distribution tends to zero as  $r \rightarrow 0$ . For  $H_2$ , the distribution is particularly close to the Wigner–Dyson (non-integrable) line. For  $H_1$ , the distribution is also consistent with Wigner–Dyson when we restrict to the middle 1/3 of the spectrum (and after removing special states with  $E = 0$ ). We exclude the edges of the spectrum because they contain degeneracies which are not symmetry-related. However, such states do not appear to have a major effect on the level statistics distribution, which is still closer to the Wigner–Dyson than the Poisson distribution even if they are included. The level statistics of  $H_3$  within the largest connected component of the Hilbert space is shown in Fig. 2c and is also consistent with the Wigner–Dyson distribution without restricting the spectrum. However, we will demonstrate below that the dynamics in some smaller connected components of  $H_3$  can be exactly solved.

As a complementary diagnostic of thermalization, we next compute the entanglement entropy of all eigenstates. We divide the lattice into two sublattices, A and B, of lengths  $L_A$  and

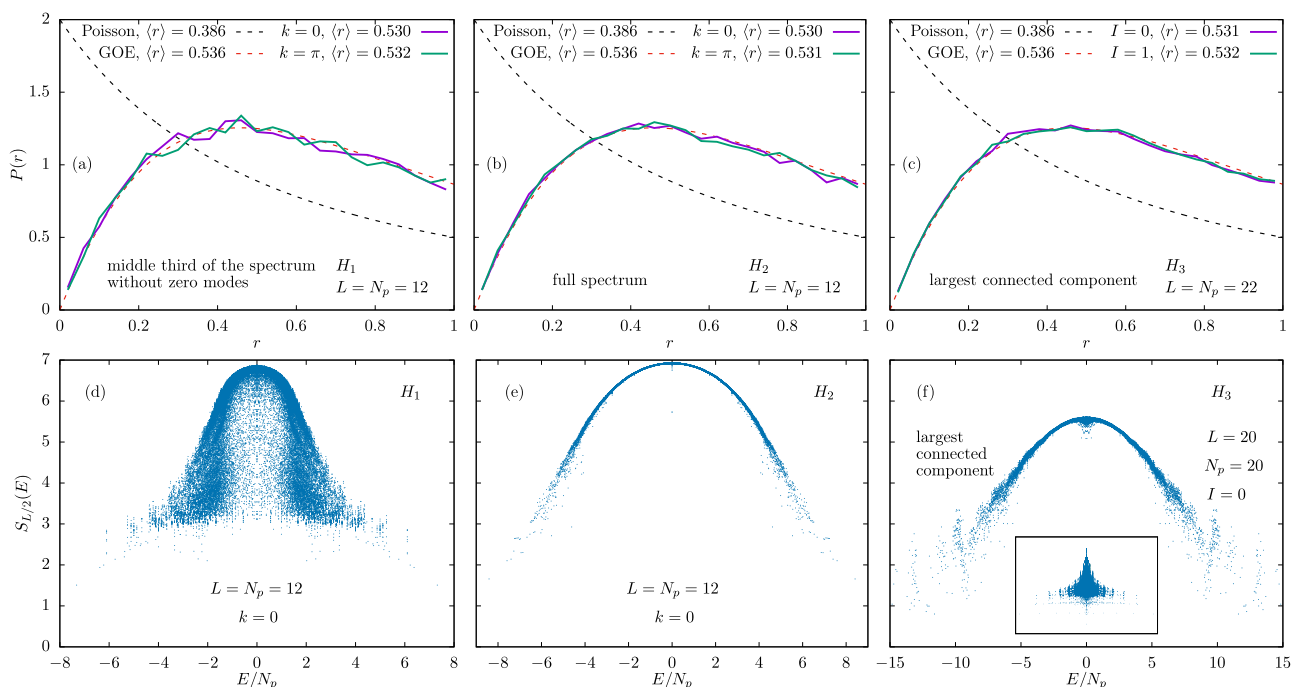


**Fig. 2 Level statistics and entanglement.** **a–c** Probability distribution of the ratios of two consecutive energy gaps. **a**  $H_1$  (middle third of the spectrum without  $E = 0$  states,  $L = N_p = 12$ ), **b**  $H_2$  (full spectrum,  $L = N_p = 12$ ) and **c**  $H_3$  (largest connected component of  $L = N_p = 22$ ). The black dashed line shows the Poisson distribution, which corresponds to the integrable case, while the red dashed line is the distribution of the Gaussian orthogonal ensemble, which corresponds to the thermalizing case. **d–f** Entanglement entropies  $S_{L/2}$  of all eigenstates plotted as a function of the eigenstate energy per particle,  $E/N_p$ . **d**  $H_1$  ( $L = N_p = 12$ ,  $L_A = 6$ ,  $k = 0$ ), **e**  $H_2$  (same) and **f**  $H_3$  in the largest connected component of  $L = N_p = 20$ ,  $L_A = 10$ ,  $I = 0$ . The inset shows all connected components for  $L = N_p = 12$ ,  $L_A = 6$ ,  $k = 0$ .



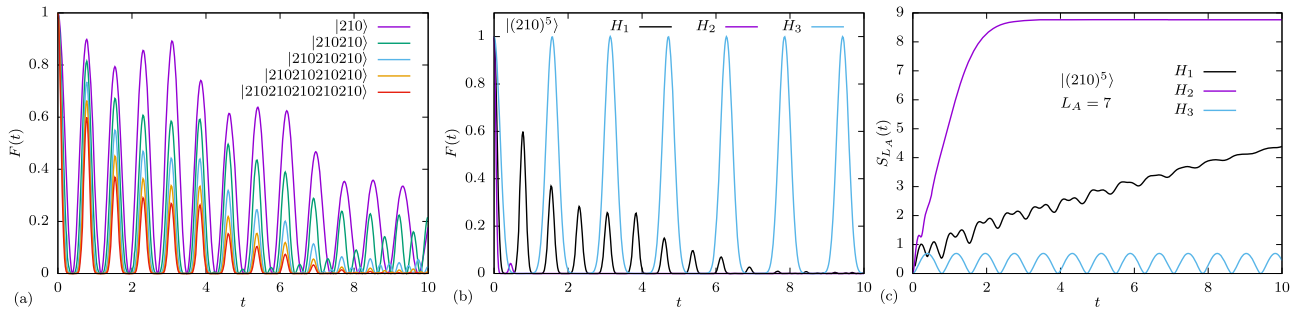


**Fig. 3 Dynamics of quantum fidelity and entanglement entropy for initial configurations in Eq. (9).** **a** Time evolution of fidelity  $F(t)$  in Eq. (8) for system sizes  $L = 3n$ . The evolution is governed by the Hamiltonian  $H_i$ , different colors represent different system sizes  $L$ . **b** Fidelity evolution  $F(t)$  for the Hamiltonians  $H_1$ ,  $H_2$  and  $H_3$  and system size  $L = 15$ . **c** Entanglement entropy evolution  $S_{L_A}(t)$  for the same cases as in **b**.

$L_B = L - L_A$ . For a given pure state  $|\psi\rangle$ , the entanglement entropy is defined as

$$S_A = -\text{tr}_A(\rho_A \ln \rho_A), \quad (6)$$

where  $\rho_A = \text{tr}_B|\psi\rangle\langle\psi|$  is the reduced density matrix of the subsystem A. The scatter plots, showing entanglement entropy of all eigenstates  $|E_n\rangle$  as a function of their energy  $E_n$  are displayed in Fig. 2d–f. Here we take into account the translation symmetry of the system and work in the momentum sector  $k = 0$  for  $H_1$  and  $H_2$ , and consider only the largest connected component and the inversion sector  $I = 0$  for  $H_3$ . The results for other sectors are qualitatively similar.

Entanglement entropy distribution in Fig. 2d, e reveals a striking difference between the Hamiltonians  $H_1$  and  $H_2$ , even though they only differ by a free-boson hopping term, Eq. (4). The model  $H_1$  is constrained, which leads to a large spread of the entropy distribution and many low-entropy eigenstates including in the bulk of the spectrum. From this perspective,  $H_1$  is reminiscent of PXP model<sup>20,25</sup>. By contrast,  $H_2$  has no such constraints and in this case the entanglement entropy is approximately a smooth function of the eigenstate energy. The Hamiltonian  $H_3$  is doubly constrained, and this is reflected in its entanglement distribution, which also shows a large spread and several disconnected bands, reminiscent of an integrable system like the XY model<sup>79</sup>.

**Global quenches.** The constraints in the models in Eqs. (1), (2), and (3) have significant effects on the dynamics governed by these Hamiltonians. We probe the dynamics by performing a global quench on the system. We assume the system is isolated and prepared in one of the Fock states,  $|\psi_0\rangle$ , at time  $t = 0$ . We restrict to  $|\psi_0\rangle$  being product states which are not necessarily translation-invariant, as such states are easier to prepare in experiment. However, our results remain qualitatively the same if we consider translation-invariant  $|\psi_0\rangle$ . After preparing the system in the state  $|\psi_0\rangle$ , which is not an eigenstate of the Hamiltonian, the system is let to evolve under unitary dynamics,

$$|\psi(t)\rangle = \exp\left(-\frac{i}{\hbar}Ht\right)|\psi_0\rangle. \quad (7)$$

where  $H$  is one of the Hamiltonians of interest. From the time-evolved state, we evaluate the quantum fidelity,

$$F(t) = |\langle\psi_0|\psi(t)\rangle|^2, \quad (8)$$

i.e., the probability for the wave function to return to the initial state. In a general many-body system, fidelity is expected to decay as  $F(t) \sim \exp(-L(Jt)^2)$ . It thus becomes exponentially suppressed in the system size for any fixed time  $t^*$ , i.e.,  $F(t^*) \sim \exp(-cL)$ , where  $c$  is a constant. In scarred models, such

as the Rydberg atom chain, fidelity at the first revival peak occurring at a time  $T$  still decays exponentially, but exponentially slower, i.e.,  $F(T) \sim \exp(-c'T)$ , with  $c' \ll c$ . In ref. 20, for a finite system with  $L \lesssim 32$  atoms, the fidelity at the first revival can be as high as  $\sim 70\%$ , and several additional peaks at times  $nT$  are also clearly visible.

We first consider the Hamiltonian  $H_1$ . Several configurations exhibit periodic revivals of the fidelity  $F(t)$ , which can in some cases be higher than 90%. Most of these configurations involve a very dense cluster of bosons such as  $|\dots 0N10\dots\rangle$ . In contrast, a completely uniform configuration  $|\dots 111\dots\rangle$  thermalizes very quickly. Here we focus on periodically-reviving configurations with density being as uniform as possible. One family of such reviving configurations involves  $n$  unit cells made of three lattice sites:

$$|210210\dots 210\rangle \equiv |(210)^n\rangle. \quad (9)$$

Time evolution of the fidelity for the initial state  $|(210)^n\rangle$  for different system sizes  $L = 3n$  is shown in Fig. 3a. The initial state is assumed to be the product state, e.g.,  $|\psi_0\rangle = |210\rangle$  for  $L = 3$ . The frequency of the revivals in Fig. 3 is approximately the same for all system sizes. We emphasize that similar results are obtained for a translation-symmetric initial state, e.g.,  $|\psi_0\rangle = \frac{1}{\sqrt{3}}(|210\rangle + |021\rangle + |102\rangle)$ . Both cases converge in the large system limit, and the differences are only significant for  $L = 3$  when the revival frequency of the initial state with transition symmetry differs from the frequencies of other system sizes.

In Fig. 3b we compare the fidelity for the initial state in Eq. (9) when it is evolved by all three Hamiltonians in Eqs. (1)–(3). The initial state is fixed to be  $|(210)^5\rangle$ . We observe that the dynamics with  $H_3$  has very prominent revivals; in fact as we will later show, these revivals are perfect and their period is approximately twice the revival period for  $H_1$ . In contrast, for  $H_2$  the fidelity quickly drops to zero without any subsequent revivals.

Finally, in Fig. 3c we plot the time evolution of entanglement entropy. As expected from the fast decay of the fidelity, the entropy for  $H_2$  rapidly saturates to its maximal value. Moreover, as expected from the perfect revivals in  $H_3$ , the entropy in that case oscillates around a constant value close to zero. For  $H_1$ , we observe a relatively slow growth of entropy, with oscillations superposed on top of that growth, again similar to PXP model<sup>6</sup>. For the initial state that is not translation-invariant, it is important how we cut the system, e.g.,  $|\dots 210|210\dots\rangle$  versus  $|\dots 2102|10\dots\rangle$ . In the first case, the entanglement entropy remains zero for  $H_3$  because no particle can hop from one subsystem to the other, while in the second case the entropy oscillates around a constant value, which is the case in Fig. 3c.

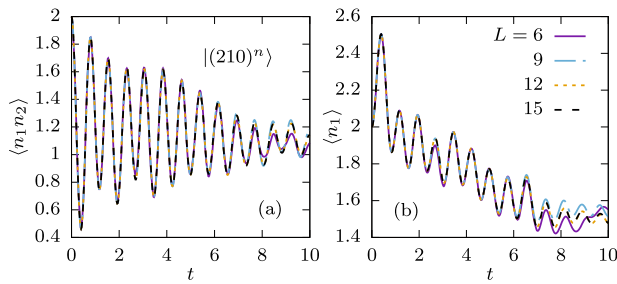


**Fig. 4 Evolution of local observables for the Hamiltonian  $H_1$ .** **a** Correlations between adjacent sites  $\langle n_1 n_2(t) \rangle$  for different system sizes and the initial state  $|(210)^n\rangle$ . **b** Density on one site  $\langle n_1(t) \rangle$ .

In Fig. 4 we show the  $H_1$  evolution of two local observables, density correlations between two adjacent sites  $\langle n_1 n_2(t) \rangle$  and density on the first site  $\langle n_1(t) \rangle$ , starting from the initial state  $|(210)^n\rangle$ . Unlike fidelity and entanglement entropy, these observables can be easily measured in experiment. Both observables robustly oscillate with approximately the same frequency as the fidelity. The heights of the first few revival peaks are approximately converged for the system sizes ranging from  $L = 6$  to  $L = 15$ , which suggests that revivals in such local observables can be observed in the thermodynamic limit. In the following Section, we will show that the oscillations observed in the dynamics from  $|(210)^n\rangle$  state in Eq. (9) and their frequency can be explained using a tractable model that involves only a small subset of all configurations in the Hilbert space, thus providing a realization of quantum scars in a correlated bosonic system. Our starting point will be the model  $H_3$ , whose graph explicitly separates into disconnected subsets which makes the toy model exact, hence we can analytically calculate the revival frequency. Based on these results, we then introduce an approximation scheme that describes the dynamics from the same initial state under the  $H_1$  Hamiltonian.

**Quantum scars in  $H_1$  and  $H_3$  models.** The quench dynamics of fidelity and entanglement entropy in Fig. 3 suggest that  $H_1$  and  $H_3$  models are candidate hosts for many-body scarred eigenstates that can be probed by initializing the system in product states  $|(210)^n\rangle$ . We now analyze the structure of these states using our approach called “cluster approximation” that is introduced in detail in Methods.

The dynamics of  $H_3$  within the sector containing the state  $|(210)^n\rangle$  can be solved exactly, as shown in Methods. The connected component of the state  $|(210)^n\rangle$  consists of all possible combinations of patterns 210 and 120. This means that triplets of sites evolve independently, and dynamically the system behaves as a collection of independent two level systems (spins-1/2). From this observation, it can be shown that revivals will be perfect with a period  $T_3 = \pi/2$ . The same period is obtained for initial product state  $|(210)^n\rangle$  and its translation-invariant version; if the initial state is both translation-invariant and inversion-symmetric, the period is doubled.

In contrast to the free dynamics in  $H_3$ , the  $H_1$  model exhibits decaying revivals and does not admit an exact description. In order to approximate the quench dynamics and scarred eigenstates in  $H_1$ , we project the Hamiltonian to smaller subspaces of the full Hilbert space. These subspaces contain clusters of states which are poorly connected to the rest of the Hilbert space and thereby cause dynamical bottlenecks. As explained in Methods, the clusters can be progressively expanded to yield an increasingly accurate description of the dynamics from a given initial state.

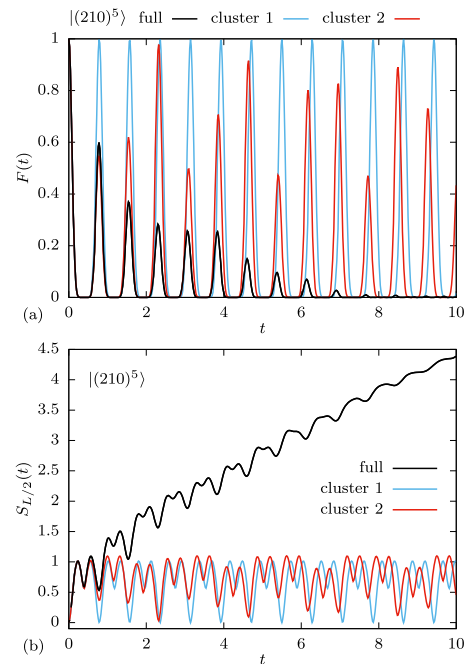


**Fig. 5 Comparison of the full dynamics against the minimal cluster (1) and extended cluster (2) approximation schemes.** We consider the system size  $L = 15$  with the initial state  $|(210)^5\rangle$ . **a** Time evolution of the fidelity. The frequency of revivals is approximately the same in both cases, but the results for the extended cluster show better agreement with the results for the full Hilbert space. **b** Time evolution of the entanglement entropy.

For our initial state  $|(210)^n\rangle$ , the minimal cluster is defined as one that contains all the states given by tensor products of 210, 120 and 300 patterns. Similar to the  $H_3$  case, within this approximation, triplets of sites again evolve independently, and the dimension of the reduced Hilbert space is  $\dim \mathcal{H}^c = 3^{L/3}$ . The time-evolved state within the cluster is given by

$$|\psi_n^c(t)\rangle = \cos^n(4t)| (210)^n \rangle + \dots, \tag{10}$$

where the dots denote other configurations. The fidelity is

$$F_n^c(t) = |\langle \psi_n^c(0) | \psi_n^c(t) \rangle|^2 = |\cos(4t)|^{2n}. \tag{11}$$

As in the case of  $H_3$ , this result is also valid for the translation-invariant initial state. We see that the period of revivals is  $T_1 = \pi/4$ , which is the same as for  $H_3$  with a translation and inversion symmetric initial state.

The result of the cluster approximation is compared against the exact result for system size  $L = 15$  in Fig. 5. The frequency of the fidelity revival, shown by the blue line in Fig. 5a, is accurately reproduced in this approximation, however the approximation does not capture the reduction in the magnitude of  $F(t)$ . Similarly, the dynamics of entanglement entropy, blue line in Fig. 5b, is only captured at very short times. In particular, we observe that the maximum entanglement within the cluster remains bounded even at long times  $t \sim 10$ , while the exact entropy continues to increase and reaches values that are several times larger.

To obtain a more accurate approximation, we can expand the minimal cluster with several neighboring configurations on the graph. We define the extended cluster as a set of all states which can be obtained using tensor products of the configurations 210, 120, 300, and 111. The enlarged cluster clearly contains the minimal cluster studied above, but it also includes additional configurations, resulting in a much better prediction for the first revival peak height, while still allowing for analytical treatment.

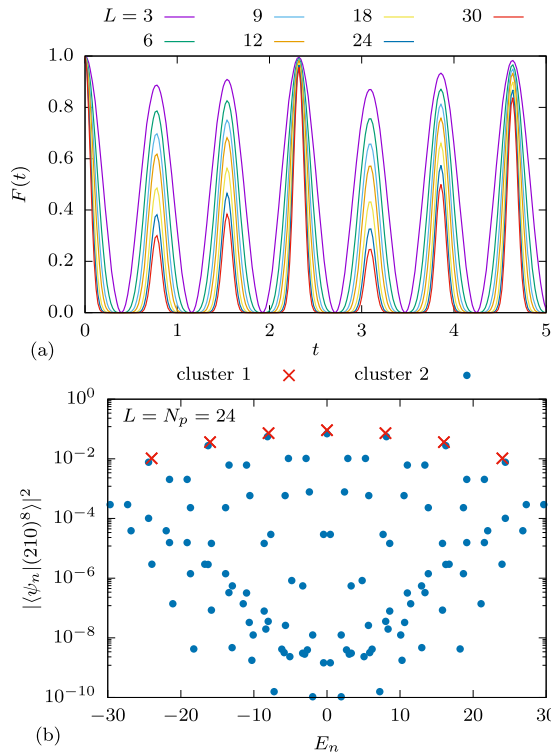


**Fig. 6 Cluster approximations.** **a** Fidelity  $F(t)$ , for the Hamiltonian  $H_1$  and initial states  $|(210)^n\rangle$ , in the extended cluster approximation for various system sizes. **b** Eigenstate overlap with the initial state  $|(210)^8\rangle$  plotted on a log scale, for both cluster approximations. In the case of degenerate eigenstates the sum of their overlaps is shown.

The dimension of the extended cluster grows as  $\dim \mathcal{H}^{\tilde{c}} = 4^{L/3}$ , and is thus exponentially larger than the minimal cluster approximation. Nevertheless, the extended cluster dimension is still exponentially smaller compared to the full Hilbert space, and within this approximation it is possible to numerically simulate the dynamics of larger systems,  $L \lesssim 30$ —see Fig. 6a. The revivals are no longer perfect, while their frequency is independent of the system size and closer to the frequency of revivals for the full Hilbert space compared to the minimal cluster approximation in Fig. 5. The overlap between the eigenstates of the Hamiltonian  $H_1$  reduced to both the minimal and extended cluster and the state  $|(210)^8\rangle$  is given in Fig. 6b. The eigenstates that correspond to the minimal cluster approximately survive in the extended cluster, where they form a band with the highest overlap.

For the initial product state  $(210)^n$ , it is possible to analytically obtain the fidelity within the improved approximation for arbitrary system size. Similar to the previous methods, it can be shown (see Supplementary Note 2)

$$F_{L=3n}^{\tilde{c}}(t) = 4^n |b^2 \cos(\alpha t) + d^2 \cos(\beta t)|^{2n}, \quad (12)$$

where  $\alpha = \sqrt{9 + \sqrt{57}} \approx 4.06815$ ,  $\beta = \sqrt{9 - \sqrt{57}} \approx 1.20423$ ,  $b \approx 0.694113$  and  $d \approx 0.134933$ . Eq. (12) is in excellent agreement with the numerical results in Fig. 6a. It was also found to be a very good approximation for the translation-invariant initial state when  $L \geq 9$  (data not shown).

Figure 7a shows that the logarithm of the fidelity per site,  $\log(F(T))/L$ , at the first peak, saturates at a finite value for large  $L$ . In the improved cluster approximation, the first peak height decays as  $e^{-0.04L}$  (Supplementary Note 2). For a completely random state, the fidelity would be  $F \sim 1/\dim_{\mathcal{H}}$ . In the case  $v = 1$  and large  $L$ , the Hilbert space dimension grows with the system

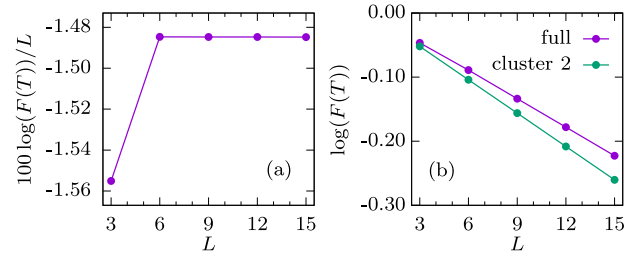


**Fig. 7 First peak height.** **a** Logarithm (base 10) of the first revival peak divided by the system size,  $\log(F(T))/L$ , seems to saturate at a finite value in the thermodynamic limit. **b** Comparison of the logarithm of the first revival peak height for the full dynamics and the improved cluster approximation. The approximation serves as a lower bound.

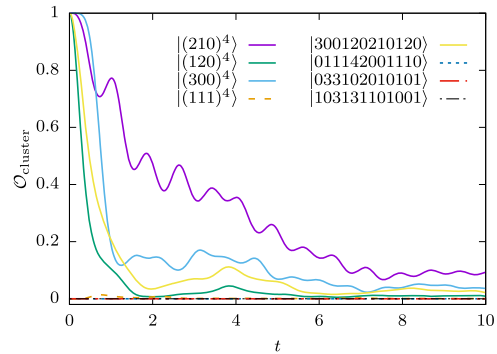


**Fig. 8 Evolution of the probability to remain inside the minimal cluster.**  $\mathcal{O}_{\text{cluster}}$  as defined in Eq. (14). Initial configurations are indicated in the legend. Solid lines: configurations initially inside the cluster (all except  $|(111)^4\rangle$  are randomly chosen). Dashed lines: configurations initially outside the cluster (all except  $|(111)^4\rangle$  are randomly chosen). Similar results are obtained for the extended cluster (not shown). System size  $L = 12$ .

size as

$$\dim_{\mathcal{H}} = \binom{2L-1}{L} \approx \binom{2L}{L} \approx \frac{4^L}{\sqrt{\pi L}}. \quad (13)$$

This back-of-the-envelope estimate suggests the fidelity of a random state is  $F \sim e^{-1.39L}$ , which decays considerably faster than the first peak height in Fig. 7. The improved cluster approximation correctly reproduces the short-time dynamics, including the first revival peak, and sets a lower bound for the first peak height – see Figs. 5 and 7b.

The evolution of the entanglement entropy for the extended cluster approximation is shown in Fig. 5b. Inside the cluster, entropy remains approximately constant with periodic oscillations that have the same frequency as the wave function revivals. Any further growth of the entanglement entropy can be attributed to the spreading of the wave function outside the cluster. To illustrate the “leakage” of the wave function outside the cluster, in Fig. 8 we compute the time evolution of the overlap with a cluster, i.e., the probability to remain inside a cluster at time  $t$ ,

$$\mathcal{O}_{\text{cluster}} = \sum_{a \in \text{Cluster}} |\langle a | \psi(t) \rangle|^2. \quad (14)$$

We consider several initial configurations that lie inside or outside the cluster. The configurations initially inside the cluster mostly stay there, and the configuration  $|(210)^4\rangle$  that has the highest revivals also has the highest overlap. Similarly, configurations initially outside the cluster continue to have negligible overlaps. The overlap starting from the configuration  $|(210)^4\rangle$

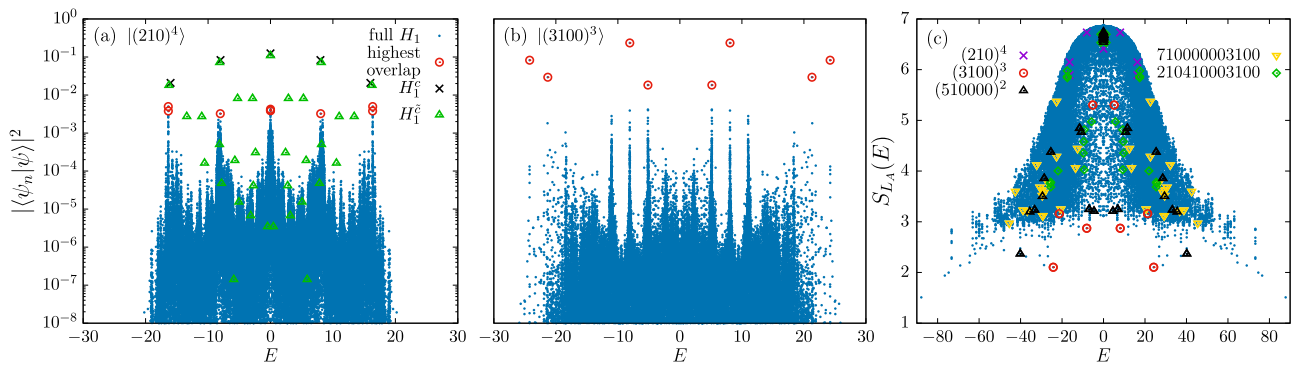


**Fig. 9 Non-ergodic eigenstates.** **a** Overlap of the configuration  $|(210)^4\rangle$  with all the eigenstates of  $H_1$ ,  $H_1^c$  and  $H_1^e$  versus the eigenstate energy for sector  $k = 0$  and system size  $L = N_p = 12$ . **b** Same for  $|(3100)^3\rangle$ . **c** Entanglement entropy, eigenstates which have the highest overlap with some product states are marked in different colors.

approximately predicts the revival peak heights for the full dynamics.

We now summarize the relation between  $H_3$  and  $H_1$  from the point of view of the cluster approximation. For the initial state  $|(210)^n\rangle$ , the two models yield similar dynamics, compare Eq. (23) and Eq. (12). The only difference is that the revival frequency is doubled in the latter case, which can be easily explained by the symmetry of the initial state and that of the Hamiltonian. Hamiltonian  $H_3$  is inversion-symmetric. If the initial state is also chosen to be inversion-symmetric, the frequency of the revivals doubles. The period is then  $T_3^{inv} = \pi/4$ , which is equal to the period of revivals  $T_1$  of  $H_1$  in the cluster approximation. This is also proven analytically in Methods, see Eq. (27). For comparison, the revival period for the full Hilbert space is approximately 0.77, which is slightly less than  $\pi/4 \approx 0.79$ . The Hamiltonian  $H_1$  is not inversion-symmetric, so the frequency does not double for an inversion-symmetric initial state, but the revivals are lower in that case. This shows that it is important for the symmetry of the initial state to match the symmetry of the Hamiltonian.

Finally, the eigenstates of  $H_1$ , projected to the subspace of the minimal cluster approximation, form several degenerate bands whose eigenenergies are equally spaced in integer multiples of 4. Interestingly, some of these eigenstates approximately survive in the full  $H_1$  model, and they are precisely the eigenstates that have the highest overlap with the configurations  $|(210)^n\rangle$ , see Fig. 9a. In small system sizes, such as  $L = 6$ , the surviving eigenstates are also the lowest entropy eigenstates in the middle of the spectrum, which is reminiscent of quantum scars in the PXP model<sup>20</sup>. In larger systems, e.g.,  $L = 12$ , the surviving eigenstates are slightly lower in entropy than their neighbors, but are far from being the lowest entropy eigenstates, as can be seen in Fig. 9. The lowest entropy eigenstates have high overlaps with other configurations, such as  $|(3100)^3\rangle$ , as shown in Fig. 9b, c. In the case of  $|(210)^n\rangle$ , the eigenstates surviving in the full system belong to every other band of eigenstates in the cluster approximation and the number of the surviving eigenstates is  $n + 1$ . For even system sizes this counting includes a zero-energy eigenstate. In Methods we discuss in more details the generalization of the cluster approximations to the states of the form  $|(N10\dots 0)^n\rangle$ , which were also found to have robust revivals and high overlaps with some low-entropy eigenstates.

## Discussion

In this paper, we have introduced three models of bosons with “soft” kinetic constraints, i.e., density-dependent hopping. We have demonstrated that some of these models exhibit similar phenomenology to other realizations of quantum many-body

scars, for example the Rydberg atom system<sup>5</sup>. We have studied quantum dynamics of these systems by performing global quenches from tensor-product initial states. We have shown that both the connectivity of the Hilbert space and the relative magnitude of the hopping coefficients have dramatic effects on the dynamics. For certain initial configurations, the constraints can lead to slow thermalization and revivals in the quantum fidelity. The revival frequency can be predicted by considering an exponentially reduced subset of the Hilbert space. For a family of initial configurations of the form  $|(210)^n\rangle$ , we have derived analytical expressions for the evolution of quantum fidelity within this approximation, which accurately capture the revival frequency obtained from exact numerical data. One notable difference between scarred dynamics in the present bosonic models and the PXP model is that the revivals exist in the absence of a hard kinetic constraint, i.e., in the fully connected Hilbert space. Our cluster approximation also explains the structure of some low-entropy eigenstates in the middle of the many-body spectrum. In addition, we have calculated the evolution of two local observables which are experimentally measurable, density correlations between two neighboring sites and density on a single site, and both of them show robust oscillations over a range of system sizes. We have also shown that the introduced models contain additional special properties, like the exponentially large zero-energy degeneracy which is related to the bipartite structure of the model.

We now comment on the possible experimental realizations of the models we studied. The implementation of a correlated hopping term  $(n_k b_i^\dagger b_j)$  in optical lattices has attracted lot of attention due to a possible onset of quantum phases related to high-Tc superconductivity<sup>80</sup>. An early theoretical proposal exploits asymmetric interactions between the two atomic states in the presence of a state-dependent optical lattice<sup>80</sup>. As a result, the obtained effective model corresponds to the inversion-symmetric form of  $H_1$ . In addition, the same term has been found to feature as a higher-order correction of the standard Bose-Hubbard model<sup>81–84</sup>. Although in this case the term typically represents a modification of the regular hopping term of the order of several percent, its contribution was directly measured<sup>85,86</sup>. More recently, the set of quantum models accessible in cold-atom experiments has been enriched through the technique of Floquet engineering<sup>87</sup>. As a notable example, a suitable driving scheme can renormalize or fully suppress the bare tunneling rate<sup>88</sup>. On top of that, by modulating local interactions an effective model with the density-dependent tunneling term has been engineered<sup>89</sup>. For the models considered in this paper the most promising is a more recent driving scheme exploiting a double modulation of a local potential and on-site interactions<sup>90</sup>. Related



sophisticated driving schemes have already enabled a realization of dynamical gauge fields<sup>56,57,91</sup> where both the amplitude and the phase of the effective tunneling are density-dependent. Although these experimental proposals explain how to realize some of the correlated hopping terms present in our models using ultracold atoms in optical lattices, finding a scheme that exactly realizes our models requires further study. We emphasize that other models which would exhibit non-ergodic dynamics and scarred eigenstates as a result of the same mechanism that was explained in this work could be built, for example a linear combination of  $H_1$  and  $H_2$ .

*Note added:* During the completion of this work, we became aware of ref.<sup>92</sup> which identified non-thermal eigenstates and slow dynamics in the quantum East model. Moreover, a recent study<sup>93</sup> proposed a Floquet scheme for a bosonic model with density-assisted hopping, finding signatures of quantum many-body scars.

### Methods

In order to more efficiently describe the dynamics of our models, we introduce a method—“cluster approximation”, that is based on Hilbert space truncation inspired by the bipartite graph structure of  $H_1$ . Before providing details about the cluster approximation for  $H_1$  and its generalizations, we present an exact solution for the perfect revivals in  $H_3$  model, which serves as a motivation for the more complicated case of  $H_1$ .

**Bipartite lattice and zero modes.** The graph of  $H_1$  is bipartite, i.e. all the basis configurations can be divided into two disjoint sets, and the action of the Hamiltonian connects configurations in one set only to the configurations in the other and vice-versa (the Hamiltonian is off-diagonal). One way to sort configurations into these two sets is by parity of the quantity

$$\Delta_a = \frac{|n_{\text{even}} - n_{\text{odd}} + C|}{2}, \quad (15)$$

where  $C = 0$  if  $L$  is even and  $C = 1$  if  $L$  is odd. We define  $n_{\text{even}}$  and  $n_{\text{odd}}$  as the total numbers of particles at even and odd sites, respectively,

$$n_{\text{even}} = \sum_{l=1}^{L_1} n_{2l}, \quad n_{\text{odd}} = \sum_{l=1}^{L_2} n_{2l-1}, \quad (16)$$

where  $L_1 = L_2 = L/2$  if  $L$  is even, and  $L_1 = (L - 1)/2$ ,  $L_2 = (L + 1)/2$  if  $L$  is odd. If only nearest-neighbor hoppings are allowed and if no two odd sites are coupled (if the system has open boundary conditions for any  $L$  or periodic boundary conditions for  $L$ -even), each hopping either increases  $n_{\text{even}}$  by one and decreases  $n_{\text{odd}}$  by one, or vice-versa. This means that each hopping can change  $\Delta_a$  only by  $\pm 1$ .

In special cases, like  $H_1$  at filling factor  $\nu = 1$ , it is also possible to define quantities like  $\Delta_a$  for odd system sizes and periodic boundary conditions. This is a consequence of the constraints imposed by  $H_1$ , i.e., the fact that a particle cannot hop to an empty site to its left (Supplementary Note 3). Note that  $H_2$  in the same geometry is not bipartite.

Another way to sort configurations into two sets is by parity of the distance from the configuration  $|111\dots 111\rangle$ , which we define as

$$d_a = \min_n \{ |111\dots 111|H_1^n|a\rangle \neq 0 \}. \quad (17)$$

In this case, the two sets are the configurations with even and with odd distances  $d_a$ . One hopping can change  $d_a$  only by  $\pm 1$  or 0. Changes by other values are not possible by definition if the Hamiltonian is Hermitian (all hoppings are reversible). Both  $d_a$  and  $\Delta_a$  have the same parity, thus  $d_a$  must always change after one hopping in even system sizes or in systems with open boundary conditions. As a consequence,  $d_a$  cannot change by 0 if  $\Delta_a$  can only change by  $\pm 1$ .

The graphs of bipartite systems do not contain any loops of odd dimension (triangles, pentagons, heptagons and so on). Moreover, the energy spectra of bipartite systems are symmetric around zero. Their Hamiltonians anticommute with the operator  $(-1)^{\Delta_a}$ . The presence of such an operator in a bipartite lattice leads to exact zero energy states in the spectrum<sup>94,95</sup>. It can be shown that the exponentially growing number of zero modes of  $H_1$  is related to the difference between the numbers of elements in the two sets of its bipartite graph (Supplementary Note 4). Additionally, the algebraic structure of zero energy eigenstates can be explained by the structure of the graph – such eigenstates can be constructed as superpositions of configurations from only one of the sets. Similar properties are found for  $H_2$  for even  $L$ , as its graph is also bipartite in that case. The properties of the zero-energy manifold are discussed in more detail in Supplementary Note 4.

**Perfect revivals in the  $H_3$  model.** We start with a warmup calculation for  $H_3$  acting on  $L = 3$  sites. The connected subspace of 210 contains only two

configurations, 120 and 210. The Hamiltonian reduced to this subspace is

$$H'_3 = - \begin{pmatrix} 0 & 2 \\ 2 & 0 \end{pmatrix}, \quad (18)$$

where the basis vectors are

$$\begin{pmatrix} 1 \\ 0 \end{pmatrix} = |210\rangle, \quad \begin{pmatrix} 0 \\ 1 \end{pmatrix} = |120\rangle. \quad (19)$$

The eigenvalues of  $H'_3$  are  $E_1 = -2$  and  $E_2 = 2$ . The initial state  $|\psi_1(t=0)\rangle = |210\rangle$  evolves as

$$|\psi_1(t)\rangle = \cos(2t)|210\rangle - i \sin(2t)|120\rangle, \quad (20)$$

and the state  $|\psi_2(t=0)\rangle = |120\rangle$  evolves as

$$|\psi_2(t)\rangle = -i \sin(2t)|210\rangle + \cos(2t)|120\rangle. \quad (21)$$

Previous results can be straightforwardly generalized to larger systems. Let the length of the system be  $L = 3n$  for simplicity. The connected component of the state  $|(210)^n\rangle$  consists only of combinations of patterns 210 and 120, which means that triplets of sites evolve independently. From Eq. (20), the initial state  $|\psi_n(t=0)\rangle = |(210)^n\rangle$  evolves as

$$|\psi_{L=3n}(t)\rangle = \cos^n(2t)|(210)^n\rangle + (-i)^n \sin^n(2t)|(120)^n\rangle + \dots \quad (22)$$

where “ $\dots$ ” denotes contributions of the basis configurations other than  $|(210)^n\rangle$  or  $|(120)^n\rangle$ . The fidelity is

$$F_{L=3n}(t) = |\langle \psi_n(0) | \psi_n(t) \rangle|^2 = |\cos 2t|^{2n}. \quad (23)$$

It follows that the revivals are perfect, with a period  $T_3 = \pi/2$ . This result is also valid for the translation-invariant initial state  $|(210)^n\rangle_T$ ,

$$|(210)^n\rangle_T \equiv \frac{1}{\sqrt{3}} (|(210)^n\rangle + |(021)^n\rangle + |(102)^n\rangle), \quad (24)$$

as the connected subspaces of 210, 021 and 102 do not overlap and therefore evolve independently.

However, an initial state that is both translation symmetric and inversion symmetric has different dynamics. The inverse of the configuration  $|(210)^n\rangle$  is the configuration  $|(012)^n\rangle$ , which is a translation of the state  $|(120)^n\rangle$  that belongs to the connected subspace of  $|(210)^n\rangle$ . The initial state

$$|\psi_n^{\text{inv}}(t=0)\rangle = \frac{1}{\sqrt{2}} |(210)^n\rangle_T + \frac{1}{\sqrt{2}} |(120)^n\rangle_T \quad (25)$$

evolves as

$$|\psi_n^{\text{inv}}(t)\rangle = (\cos^n 2t + (-i)^n \sin^n 2t) |\psi_n^{\text{inv}}(t=0)\rangle + \dots \quad (26)$$

and the fidelity is

$$F_n^{\text{inv}}(t) = |\langle \psi_n^{\text{inv}}(0) | \psi_n^{\text{inv}}(t) \rangle|^2 = |\cos^n 2t + (-i)^n \sin^n 2t|^2. \quad (27)$$

The frequency of the revivals is now doubled, so the period is  $T_3^{\text{inv}} = \pi/4$ .

**Cluster approximations for the  $H_1$  model.** Here we introduce a scheme for approximating the dynamics from initial states  $(210)^n$  in the  $H_1$  model. As can be observed in Fig. 3, the revival periods are approximately the same for different system sizes. We first focus on the non-trivial case  $L = 6$ . Figure 10 shows part of the graph that contains the initial state,  $|210210\rangle$ . Configurations labeled inside the ellipses denote representatives of an orbit of translation symmetry, i.e., the configurations are translation-invariant such as the one in Eq. (24).

The minimal subcluster of the graph is highlighted in blue color in Fig. 10. This cluster is indeed weakly connected to the rest of the configuration space, as it has only 3 connections that lead outside this cluster (dashed lines) and their hopping coefficients are slightly lower in magnitude than those inside the cluster, meaning that the probability is higher to stay inside the cluster than to leave. The hopping coefficients leading outside are not significantly smaller than the coefficients staying inside, but in combination with the relatively small number of connections this has significant effects on the dynamics. This effect is even more pronounced when the difference in magnitudes is further increased by squaring the particle-number operators (see Supplementary Note 1).

The minimal cluster from Fig. 10 contains all the states given by tensor products of 210, 120 and 300 configurations. The set of configurations belonging to this cluster could have been chosen differently, but this particular choice has at least two advantages. Firstly, inside this cluster, the evolution of the configuration  $|210210\rangle$  can be thought of as two subsystems 210 evolving separately. The evolution of all such configurations at different system sizes can be reduced to the evolution of  $L = 3$  subsystems 210, similar to the case of  $H_3$  in the connected subspace of  $(210)^n$ . Secondly, this definition allows easy generalization to different system sizes  $L = 3n$  with initial states  $(210)^n$ . We would like to emphasize that the cluster was not chosen arbitrarily. The calculations of the probability density distribution starting from the initial configuration  $|210210\rangle$  and evolving with  $H_1$

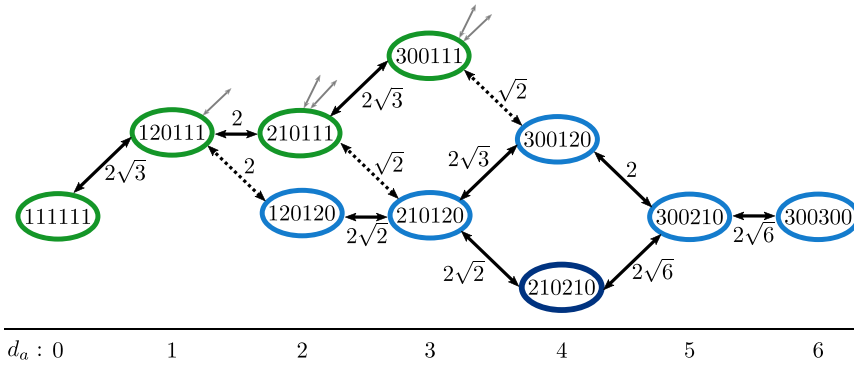


**Fig. 10 Minimal and extended clusters.** Hamiltonian  $H_1$  and system size  $L = N_p = 6$ . Configurations labeled inside the ellipses are representatives of an orbit of translation symmetry. The minimal cluster is defined by the blue configurations, while green configurations represent the additional components of the extended cluster. Gray arrows connect to configurations outside the extended cluster. The numbers below the graph show the distance  $d_a$  from the configuration 111111 evaluated using Eq. (17).

have shown that the probability density stays high in this region of the Hilbert space as long as the revivals in fidelity are visible. The configurations important for the dynamics were then identified by analyzing the structure of the graph around the initial configuration.

As an example, consider system size  $L = 3$ . The reduced Hilbert space of the cluster  $\mathcal{H}^c$  is spanned by the (non-translation-invariant) configurations

$$\begin{pmatrix} 1 \\ 0 \\ 0 \end{pmatrix} = |300\rangle, \begin{pmatrix} 0 \\ 1 \\ 0 \end{pmatrix} = |210\rangle, \begin{pmatrix} 0 \\ 0 \\ 1 \end{pmatrix} = |120\rangle. \quad (28)$$

The Hamiltonian reduced to this subspace is

$$H_1^c = - \begin{pmatrix} 0 & 2\sqrt{3} & 0 \\ 2\sqrt{3} & 0 & 2 \\ 0 & 2 & 0 \end{pmatrix}, \quad (29)$$

and its eigenvalues are  $E_1 = -4$ ,  $E_2 = 4$ ,  $E_3 = 0$ . The initial configuration  $|210\rangle$  evolves according to

$$|\psi_1^c(t)\rangle = -\frac{i}{2} \sin(4t) (\sqrt{3}|300\rangle + |120\rangle) + \cos(4t)|210\rangle. \quad (30)$$

By generalizing this result to larger systems, it is easy to prove Eqs. (10) and (11).

The minimal clusters can be expanded by adding several neighboring configurations. For similar reasons as in the case of minimal clusters, the extended clusters are defined as sets of all states which can be obtained using tensor products of the configurations 210, 120, 300 and 111. In the case of  $L = 6$ , the enlarged cluster can be observed in Fig. 10. It contains the minimal cluster studied previously, but it also includes additional configurations shown in green ellipses. Again, the approximation could be improved by including more configurations, but this particular choice is well suited for analytical treatment (Supplementary Note 2) and, as shown above, it gives a good prediction for the first revival peak height.

**Generalization to other clusters.** Building on the previous observation that some of the low-entropy eigenstates have large weight on  $|(3100)^3\rangle$  product state, we have investigated periodic revivals from such a larger class of initial states. We find that robust revivals are associated with initial product states of the form

$$\left| \left( (N-1)1 \underset{N-2}{0\dots 0} \right)^n \right\rangle, \quad (31)$$

where  $N$  is the length of the unit cell ( $L = Nn$ ). For example, some of these configurations are  $|(3100)^n\rangle$ ,  $|(41000)^n\rangle$  and  $|(510000)^n\rangle$ . Combinations of those patterns such as  $|310041000\rangle$  also exhibit similar properties, but we will restrict ourselves to the simpler former cases.

We can construct a generalization of the cluster approximation for configurations of the form in Eq. (31). As in the case of  $|(210)^n\rangle$ , the dynamics inside one unit cell explains the dynamics of the full system. The generalized clusters can be chosen in such a way that their Hilbert spaces are spanned by  $N$  configurations

$$|i\rangle = \left| \left( (N+1-i)(i-1) \underset{N-2}{0\dots 0} \right)^n \right\rangle, \quad (32)$$

where  $i$  takes values  $1, 2, \dots, N$ . If we consider only one unit cell ( $n = 1$ ), the graph that connects these configurations has a linear structure without any loops, i.e.,

each configuration  $|i\rangle$  is solely connected to the configurations  $|i \pm 1\rangle$ , except the two configurations at the edges,  $|1\rangle$  and  $|N\rangle$ , which are only connected to  $|2\rangle$  and  $|N-1\rangle$ , respectively.

The projection of the Hamiltonian  $H_1$  to this cluster, which we denote by  $H_1^c$ , has a very simple structure: it has the form of a tight-binding chain with the only nonzero matrix elements on the upper and lower diagonals:

$$H_{i,i+1}^c = H_{i+1,i}^c = (N-i)\sqrt{i(N+1-i)}. \quad (33)$$

The dynamics within a single unit cell under  $H_1^c$  corresponds to density fluctuations between the first and the second site. Following the same procedure as previously, we can now diagonalize  $H_1^c$  and compute the fidelity time series for the initial configuration  $|(N-1)10\dots 0\rangle$ . This result can be directly generalized to configurations of the form  $|(N-1)10\dots 0\rangle^n$ . The derivation is valid for both translation-invariant and non-translation-invariant initial configurations, as the cluster in Eq. (32) is disconnected from its translated copies. We stress that this disconnection, namely the absence of a hopping term between  $|1(N-1)0\dots 0\rangle$  and  $|0N0\dots 0\rangle$ , is a consequence of the constraints imposed by  $H_1$  and it would not hold for  $H_2$ . In this way, we have calculated the time evolution of the fidelity starting from the configurations  $|(3100)^n\rangle$  (for  $n = 1, 2, 3, 4$ ),  $|(41000)^n\rangle$  ( $n = 1, 2, 3$ ) and  $|(510000)^n\rangle$  ( $n = 1, 2$ ), and compared it with the exact numerical results for the full  $H_1$ . The cluster approximation captures both the revival frequency and the height of the first peak. Similar to the  $|(210)^n\rangle$  case, the approximation can be improved by adding further configurations to the clusters. Moreover, if we want to consider translation-invariant initial states, we can follow the same recipe for  $|(210)^n\rangle$  by summing translated patterns with the required phase factors given in terms of momenta in multiples of  $2\pi/N$ . We have checked that revivals appear in these momentum sectors, with roughly the same frequency.

We note that the configurations with larger units cells thermalize more quickly on shorter timescales, but slower at long times. Initially, the states starting from configurations with smaller  $N$  have lower entanglement entropies than those with larger  $N$ . The Hilbert spaces of large  $N$  unit cells are larger, so the entanglement entropy starting from these configurations rapidly grows to the maximal value for that unit cell. However, the only way for the wave function to spread through the entire Hilbert space is that a unit cell reaches a state close to  $111\dots 111$ , so that particles can hop to the other unit cells. This is less likely for large  $N$ , and therefore such configurations need long times to fully thermalize. As a result, smaller  $N$  entanglement entropies grow faster and after long enough time they overtake those for larger  $N$ . For example, in the case of  $L = 12$  and translation-invariant initial states,  $(210)^4$  overtakes  $(3100)^3$  and  $(510000)^2$  around  $t \sim 2$ , and  $(3100)^3$  overtakes  $(510000)^2$  around  $t \sim 80$  (Supplementary Fig. 3).

Finally, we note that non-thermal behavior reminiscent of the one studied here was previously observed in an unconstrained Bose-Hubbard model, for example in the context of ‘‘arrested expansion’’<sup>96,97</sup> and quenches from superfluid to Mott insulator phase<sup>98,99</sup>. In these cases, the main ingredient is the strong on-site interaction, which causes the energy spectrum to split into several bands. Due to the large energy differences between bands, the dynamics of an initial state from a particular band is at first limited only to the eigenstates that belong to the same band. Additionally, these energy bands are approximately equally spaced, which can lead to revivals in fidelity if several bands are populated. In contrast, our models do not feature on-site interaction, and the mechanism which slows down the spread of the wave function is correlated hopping, which suppresses connections between certain configurations and modifies the hopping amplitudes between others, thus creating bottlenecks that separate different clusters of states.

**Data availability**

The data that support the plots within this paper and other findings of this study are available at <https://doi.org/10.5518/810100>.

**Code availability**

Code is available upon reasonable request.

Received: 6 November 2019; Accepted: 5 May 2020;

Published online: 01 June 2020

**References**

- Heller, E. J. Bound-state eigenfunctions of classically chaotic Hamiltonian systems: Scars of periodic orbits. *Phys. Rev. Lett.* **53**, 1515–1518 (1984).
- Sridhar, S. Experimental observation of scarred eigenfunctions of chaotic microwave cavities. *Phys. Rev. Lett.* **67**, 785–788 (1991).
- Marcus, C. M., Rimberg, A. J., Westervelt, R. M., Hopkins, P. F. & Gossard, A. C. Conductance fluctuations and chaotic scattering in ballistic microstructures. *Phys. Rev. Lett.* **69**, 506–509 (1992).
- Wilkinson, P. B. et al. Observation of ‘scarred’ wavefunctions in a quantum well with chaotic electron dynamics. *Nature* **380**, 608–610 (1996).
- Bernier, H. et al. Probing many-body dynamics on a 51-atom quantum simulator. *Nature* **551**, 579–584 (2017).
- Turner, C. J., Michailidis, A. A., Abanin, D. A., Serbyn, M. & Papić, Z. Weak ergodicity breaking from quantum many-body scars. *Nat. Phys.* **14**, 745–749 (2018).
- Ho, W. W., Choi, S., Pichler, H. & Lukin, M. Periodic orbits, entanglement, and quantum many-body scars in constrained models: Matrix product state approach. *Phys. Rev. Lett.* **122**, 040603 (2019).
- Schauf, P. et al. Observation of spatially ordered structures in a two-dimensional Rydberg gas. *Nature* **491**, 87–91 (2012).
- Labuhn, H. et al. Tunable two-dimensional arrays of single Rydberg atoms for realizing quantum Ising models. *Nature* **534**, 667–670 (2016).
- Calabrese, P. & Cardy, J. Time dependence of correlation functions following a quantum quench. *Phys. Rev. Lett.* **96**, 136801 (2006).
- Kinoshita, T., Wenger, T. & Weiss, D. S. A quantum Newton’s cradle. *Nature* **440**, 900–903 (2006).
- Schreiber, M. et al. Observation of many-body localization of interacting fermions in a quasirandom optical lattice. *Science* **349**, 842–845 (2015).
- Smith, J. et al. Many-body localization in a quantum simulator with programmable random disorder. *Nat. Phys.* **12**, 907–911 (2016).
- Kucsko, G. et al. Critical thermalization of a disordered dipolar spin system in diamond. *Phys. Rev. Lett.* **121**, 023601 (2018).
- Kaufman, A. M. et al. Quantum thermalization through entanglement in an isolated many-body system. *Science* **353**, 794–800 (2016).
- Choi, S. et al. Emergent SU(2) dynamics and perfect quantum many-body scars. *Phys. Rev. Lett.* **122**, 220603 (2019).
- Bull, K., Desaulles, J.-Y. & Papić, Z. Quantum scars as embeddings of weakly broken Lie algebra representations. *Phys. Rev. B* **101**, 165139 (2020).
- Deutsch, J. M. Quantum statistical mechanics in a closed system. *Phys. Rev. A* **43**, 2046–2049 (1991).
- Srednicki, M. Chaos and quantum thermalization. *Phys. Rev. E* **50**, 888 (1994).
- Turner, C. J., Michailidis, A. A., Abanin, D. A., Serbyn, M. & Papić, Z. Quantum scarred eigenstates in a Rydberg atom chain: entanglement, breakdown of thermalization, and stability to perturbations. *Phys. Rev. B* **98**, 155134 (2018).
- Iadecola, T., Schechter, M. & Xu, S. Quantum many-body scars from magnon condensation. *Phys. Rev. B* **100**, 184312 (2019).
- Moudgalya, S., Rachel, S., Bernevig, B. A. & Regnault, N. Exact excited states of nonintegrable models. *Phys. Rev. B* **98**, 235155 (2018).
- Moudgalya, S., Regnault, N. & Bernevig, B. A. Entanglement of exact excited states of Affleck-Kennedy-Lieb-Tasaki models: exact results, many-body scars, and violation of the strong eigenstate thermalization hypothesis. *Phys. Rev. B* **98**, 235156 (2018).
- Lin, C.-J. & Motrunich, O. I. Exact quantum many-body scar states in the Rydberg-blockaded atom chain. *Phys. Rev. Lett.* **122**, 173401 (2019).
- Khemani, V., Laumann, C. R. & Chandran, A. Signatures of integrability in the dynamics of Rydberg-blockaded chains. *Phys. Rev. B* **99**, 161101 (2019).
- Michailidis, A. A., Turner, C. J., Papić, Z., Abanin, D. A. & Serbyn, M. Slow quantum thermalization and many-body revivals from mixed phase space. *Phys. Rev. X* **10**, 011055 (2020).
- Kormos, M., Collura, M., Takács, G. & Calabrese, P. Real-time confinement following a quantum quench to a non-integrable model. *Nat. Phys.* **13**, 246–249 (2016).
- James, A. J. A., Konik, R. M. & Robinson, N. J. Nonthermal states arising from confinement in one and two dimensions. *Phys. Rev. Lett.* **122**, 130603 (2019).
- Robinson, N. J., James, A. J. A. & Konik, R. M. Signatures of rare states and thermalization in a theory with confinement. *Phys. Rev. B* **99**, 195108 (2019).
- Vafek, O., Regnault, N. & Bernevig, B. A. Entanglement of exact excited eigenstates of the Hubbard model in arbitrary dimension. *SciPost Phys.* **3**, 043 (2017).
- Iadecola, T. & Žnidarič, M. Exact localized and ballistic eigenstates in disordered chaotic spin ladders and the Fermi-Hubbard model. *Phys. Rev. Lett.* **123**, 036403 (2019).
- Haldar, A., Sen, D., Moessner, R. & Das, A. Scars in strongly driven Floquet matter: resonance vs emergent conservation laws. Preprint at <http://arxiv.org/abs/1909.04064> (2019).
- Schechter, M. & Iadecola, T. Weak ergodicity breaking and quantum many-body scars in spin-1 XY magnets. *Phys. Rev. Lett.* **123**, 147201 (2019).
- Iadecola, T. & Schechter, M. Quantum many-body scar states with emergent kinetic constraints and finite-entanglement revivals. *Phys. Rev. B* **101**, 024306 (2020).
- Moudgalya, S., Bernevig, B. A. & Regnault, N. Quantum many-body scars in a Landau level on a thin torus. Preprint at <http://arxiv.org/abs/1906.05292> (2019).
- Pai, S. & Pretko, M. Dynamical scar states in driven fracton systems. *Phys. Rev. Lett.* **123**, 136401 (2019).
- Khemani, V. & Nandkishore, R. Local constraints can globally shatter Hilbert space: a new route to quantum information protection. Preprint at <http://arxiv.org/abs/1904.04815> (2019).
- Sala, P., Rakovszky, T., Verresen, R., Knap, M. & Pollmann, F. Ergodicity breaking arising from Hilbert space fragmentation in dipole-conserving Hamiltonians. *Phys. Rev. X* **10**, 011047 (2020).
- Khemani, V., Hermele, M. & Nandkishore, R. M. Localization from shattering: higher dimensions and physical realizations. Preprint at <http://arxiv.org/abs/1910.01137> (2019).
- Shiraishi, N. & Mori, T. Systematic construction of counterexamples to the eigenstate thermalization hypothesis. *Phys. Rev. Lett.* **119**, 030601 (2017).
- D’Alessio, L., Kafri, Y., Polkovnikov, A. & Rigol, M. From quantum chaos and eigenstate thermalization to statistical mechanics and thermodynamics. *Adv. Phys.* **65**, 239–362 (2016).
- Gogolin, C. & Eisert, J. Equilibration, thermalisation, and the emergence of statistical mechanics in closed quantum systems. *Rep. Prog. Phys.* **79**, 056001 (2016).
- Ok, S. et al. Topological many-body scar states in dimensions one, two, and three. *Phys. Rev. Res.* **1**, 033144 (2019).
- Bull, K., Martin, I. & Papić, Z. Systematic construction of scarred many-body dynamics in 1D lattice models. *Phys. Rev. Lett.* **123**, 030601 (2019).
- Lesanovsky, I. & Katsura, H. Interacting Fibonacci anyons in a Rydberg gas. *Phys. Rev. A* **86**, 041601 (2012).
- Feiguin, A. et al. Interacting anyons in topological quantum liquids: The golden chain. *Phys. Rev. Lett.* **98**, 160409 (2007).
- Trebst, S. et al. Collective states of interacting Fibonacci anyons. *Phys. Rev. Lett.* **101**, 050401 (2008).
- Chandran, A., Schulz, M. D. & Burnell, F. J. The eigenstate thermalization hypothesis in constrained Hilbert spaces: a case study in non-Abelian anyon chains. *Phys. Rev. B* **94**, 235122 (2016).
- Lan, Z. & Powell, S. Eigenstate thermalization hypothesis in quantum dimer models. *Phys. Rev. B* **96**, 115140 (2017).
- Chandran, A., Burnell, F. J. & Sondhi, S. L. Absence of Fibonacci anyons in Rydberg chains. *Phys. Rev. B* **101**, 075104 (2020).
- Lan, Z., van Horssen, M., Powell, S. & Garrahan, J. P. Quantum slow relaxation and metastability due to dynamical constraints. *Phys. Rev. Lett.* **121**, 040603 (2018).
- Smith, A., Knolle, J., Moessner, R. & Kovrizhin, D. L. Absence of ergodicity without quenched disorder: From quantum disentangled liquids to many-body localization. *Phys. Rev. Lett.* **119**, 176601 (2017).
- Brenes, M., Dalmonte, M., Heyl, M. & Scardicchio, A. Many-body localization dynamics from gauge invariance. *Phys. Rev. Lett.* **120**, 030601 (2018).
- Surace, F. M. et al. Lattice gauge theories and string dynamics in Rydberg atom quantum simulators. Preprint at <http://arxiv.org/abs/1902.09551> (2019).
- Magnifico, G. et al. Real time dynamics and confinement in the  $\mathbb{Z}_n$  Schwinger-Weyl lattice model for 1+1 QED. Preprint at <http://arxiv.org/abs/1909.04821> (2019).
- Görg, F. et al. Realization of density-dependent Peierls phases to engineer quantized gauge fields coupled to ultracold matter. *Nat. Phys.* **15**, 1161–1167 (2019).
- Schweizer, C. et al. Floquet approach to  $\mathbb{Z}_2$  lattice gauge theories with ultracold atoms in optical lattices. *Nat. Phys.* **15**, 1168–1173 (2019).
- Abanin, D. A., Altman, E., Bloch, I. & Serbyn, M. Colloquium: many-body localization, thermalization, and entanglement. *Rev. Mod. Phys.* **91**, 021001 (2019).
- Binder, K. & Young, A. P. Spin glasses: experimental facts, theoretical concepts, and open questions. *Rev. Mod. Phys.* **58**, 801–976 (1986).
- Berthier, L. & Biroli, G. Theoretical perspective on the glass transition and amorphous materials. *Rev. Mod. Phys.* **83**, 587–645 (2011).



61. Biroli, G. & Garrahan, J. P. Perspective: the glass transition. *J. Chem. Phys.* **138**, 12A301 (2013).
62. Fredrickson, G. H. & Andersen, H. C. Kinetic Ising model of the glass transition. *Phys. Rev. Lett.* **53**, 1244–1247 (1984).
63. Palmer, R. G., Stein, D. L., Abrahams, E. & Anderson, P. W. Models of hierarchically constrained dynamics for glassy relaxation. *Phys. Rev. Lett.* **53**, 958–961 (1984).
64. Carleo, G., Becca, F., Schiró, M. & Fabrizio, M. Localization and glassy dynamics of many-body quantum systems. *Sci. Rep.* **2**, 243 (2012).
65. De Roeck, W. & Huveneers, F. Asymptotic quantum many-body localization from thermal disorder. *Commun. Math. Phys.* **332**, 1017–1082 (2014).
66. Schiulaz, M. & Müller, J. Localization from superselection rules: many-body localization without quenched disorder *AIP Conf. Ser.* **1610**, 11 (2014).
67. Yao, N. Y., Laumann, C. R., Cirac, J. I., Lukin, M. D. & Moore, J. E. Quasi-many-body localization in translation-invariant systems. *Phys. Rev. Lett.* **117**, 240601 (2016).
68. Papić, Z., Stoudenmire, E. M. & Abanin, D. A. Many-body localization in disorder-free systems: the importance of finite-size constraints. *Ann. Phys.* **362**, 714–725 (2015).
69. van Horssen, M., Levi, E. & Garrahan, J. P. Dynamics of many-body localization in a translation-invariant quantum glass model. *Phys. Rev. B* **92**, 100305 (2015).
70. Veness, T., Essler, F. H. L. & Fisher, M. P. A. Quantum disentangled liquid in the half-filled Hubbard model. *Phys. Rev. B* **96**, 195153 (2017).
71. Smith, A., Knolle, J., Kovrizhin, D. L. & Moessner, R. Disorder-free localization. *Phys. Rev. Lett.* **118**, 266601 (2017).
72. Kim, I. H. & Haah, J. Localization from superselection rules in translationally invariant systems. *Phys. Rev. Lett.* **116**, 027202 (2016).
73. Yarloo, H., Langari, A. & Vaezi, A. Anyonic self-induced disorder in a stabilizer code: Quasi many-body localization in a translational invariant model. *Phys. Rev. B* **97**, 054304 (2018).
74. Michailidis, A. A. et al. Slow dynamics in translation-invariant quantum lattice models. *Phys. Rev. B* **97**, 104307 (2018).
75. van Horssen, M., Levi, E. & Garrahan, J. P. Dynamics of many-body localization in a translation-invariant quantum glass model. *Phys. Rev. B* **92**, 100305 (2015).
76. Oganesyan, V. & Huse, D. A. Localization of interacting fermions at high temperature. *Phys. Rev. B* **75**, 155111 (2007).
77. D'Alessio, L. & Rigol, M. Long-time behavior of isolated periodically driven interacting lattice systems. *Phys. Rev. X* **4**, 041048 (2014).
78. Mehta, M. L. *Random Matrices* Vol. 142 (Elsevier, 2004)
79. Alba, V., Fagotti, M. & Calabrese, P. Entanglement entropy of excited states. *J. Stat. Mech.* **2009**, P10020 (2009).
80. Eckholt, M. & Garcia-Ripoll, J. J. Correlated hopping of bosonic atoms induced by optical lattices. *New J. Phys.* **11**, 093028 (2009).
81. Mazzarella, G., Giampaolo, S. M. & Illuminati, F. Extended Bose Hubbard model of interacting bosonic atoms in optical lattices: From superfluidity to density waves. *Phys. Rev. A* **73**, 013625 (2006).
82. Bissbort, U., Deuretzbacher, F. & Hofstetter, W. Effective multibody-induced tunneling and interactions in the Bose-Hubbard model of the lowest dressed band of an optical lattice. *Phys. Rev. A* **86**, 023617 (2012).
83. Lühmann, D.-S., Jürgensen, O. & Sengstock, K. Multi-orbital and density-induced tunneling of bosons in optical lattices. *New J. Phys.* **14**, 033021 (2012).
84. Dutta, O. et al. Non-standard Hubbard models in optical lattices: a review. *Rep. Prog. Phys.* **78**, 066001 (2015).
85. Jürgensen, O., Meinert, F., Mark, M. J., Nägerl, H.-C. & Lühmann, D.-S. Observation of density-induced tunneling. *Phys. Rev. Lett.* **113**, 193003 (2014).
86. Baier, S. et al. Extended Bose-Hubbard models with ultracold magnetic atoms. *Science* **352**, 201–205 (2016).
87. Eckardt, A. Colloquium: Atomic quantum gases in periodically driven optical lattices. *Rev. Mod. Phys.* **89**, 011004 (2017).
88. Eckardt, A. et al. Exploring dynamic localization with a Bose-Einstein condensate. *Phys. Rev. A* **79**, 013611 (2009).
89. Meinert, F., Mark, M. J., Lauber, K., Daley, A. J. & Nägerl, H.-C. Floquet engineering of correlated tunneling in the Bose-Hubbard model with ultracold atoms. *Phys. Rev. Lett.* **116**, 205301 (2016).
90. Zhao, H., Knolle, J. & Mintert, F. Engineered nearest-neighbor interactions with doubly modulated optical lattices. *Phys. Rev. A* **100**, 053610 (2019).
91. Barbiero, L. et al. Coupling ultracold matter to dynamical gauge fields in optical lattices: From flux attachment to  $\mathbb{Z}_2$  lattice gauge theories. *Sci. Adv.* **5**, eaav7444 (2019).
92. Pancotti, N., Giudice, G., Cirac, J. I., Garrahan, J. P. & Bañuls, M. C. Quantum East model: localization, non-thermal eigenstates and slow dynamics. Preprint at <https://arxiv.org/abs/1910.06616> (2019).
93. Zhao, K., Vovrosh, J., Mintert, F. & Knolle, J. Quantum many-body scars in optical lattices. *Phys. Rev. Lett.* **124**, 160604 (2020).
94. Sutherland, B. et al. Localization of electronic wave functions due to local topology. *Phys. Rev. B* **34**, 5208–5211 (1986).
95. Inui, M., Trugman, S. A. & Abrahams, E. Unusual properties of midband states in systems with off-diagonal disorder. *Phys. Rev. B* **49**, 3190–3196 (1994).
96. Heidrich-Meisner, F. et al. Quantum distillation: dynamical generation of low-entropy states of strongly correlated fermions in an optical lattice. *Phys. Rev. A* **80**, 041603 (2009).
97. Ronzheimer, J. P. et al. Expansion dynamics of interacting bosons in homogeneous lattices in one and two dimensions. *Phys. Rev. Lett.* **110**, 205301 (2013).
98. Greiner, M., Mandel, O., Hänsch, T. W. & Bloch, I. Collapse and revival of the matter wave field of a Bose-Einstein condensate. *Nature* **419**, 51–54 (2002).
99. Kollath, C., Läuchli, A. M. & Altman, E. Quench dynamics and nonequilibrium phase diagram of the Bose-Hubbard model. *Phys. Rev. Lett.* **98**, 180601 (2007).
100. Hudomal, A., Vasić, I., Regnault, N. & Papić, Z. Supporting data for Quantum scars of bosons with correlated hopping. <https://doi.org/10.5518/810> (2020).

### Acknowledgements

The authors thank Thomas Iadecola for fruitful discussions. A.H. and I.V. acknowledge funding provided by the Institute of Physics Belgrade, through the grant by the Ministry of Education, Science, and Technological Development of the Republic of Serbia. N.R. was supported by the Department of Energy Grant No. DE-SC0016239, the National Science Foundation EAGER Grant No. DMR 1643312, Simons Investigator Grant No. 404513, ONR Grant No. N00014-14-1-0330, the Packard Foundation, the Schmidt Fund for Innovative Research, and a Guggenheim Fellowship from the John Simon Guggenheim Memorial Foundation. Z.P. acknowledges support by EPSRC grant EP/R020612/1 and the National Science Foundation under Grant No. NSF PHY-1748958. Part of the numerical simulations were performed on the PARADOX-IV supercomputing facility at the Scientific Computing Laboratory, National Center of Excellence for the Study of Complex Systems, Institute of Physics Belgrade. The authors would also like to acknowledge the contribution of the COST Action CA16221.

### Author contributions

A.H., I.V., N.R., and Z.P. contributed to developing the ideas, analyzing the results and writing the manuscript. A.H. performed the calculations and designed the figures.

### Competing interests

The authors declare no competing interests.

### Additional information

Supplementary information is available for this paper at <https://doi.org/10.1038/s42005-020-0364-9>.

Correspondence and requests for materials should be addressed to A.H.

Reprints and permission information is available at <http://www.nature.com/reprints>

Publisher's note Springer Nature remains neutral with regard to jurisdictional claims in published maps and institutional affiliations.



**Open Access** This article is licensed under a Creative Commons Attribution 4.0 International License, which permits use, sharing, adaptation, distribution and reproduction in any medium or format, as long as you give appropriate credit to the original author(s) and the source, provide a link to the Creative Commons license, and indicate if changes were made. The images or other third party material in this article are included in the article's Creative Commons license, unless indicated otherwise in a credit line to the material. If material is not included in the article's Creative Commons license and your intended use is not permitted by statutory regulation or exceeds the permitted use, you will need to obtain permission directly from the copyright holder. To view a copy of this license, visit <http://creativecommons.org/licenses/by/4.0/>.

© The Author(s) 2020

Collection

# Emergent Topics in Photonics: Science and Applications

## Submission status

Closed

This special issue aims to provide a contemporary and broad collection of nascent research topics related to both fundamental and technological aspects of photonic science. We kindly invite researchers to submit their contributions that concern original research in the fields of quantum and nonlinear optics, optical materials, ultracold systems, metamaterials, biophotonics, plasmonics, laser science and technology, optical communications, and ultrafast optical phenomena. — [show less](#)

## Editors



[Dr. Jelena Radovanovic \(Lead guest editor\),](#)



[Dr. Nikola Vukovic,](#)



[Dr. Aleksandar Demic,](#)



[Dr. Jelena Pajovic,](#)



[Dr. Radovan Dojcilovic,](#)



[Dr. Danka Stojanović &](#)



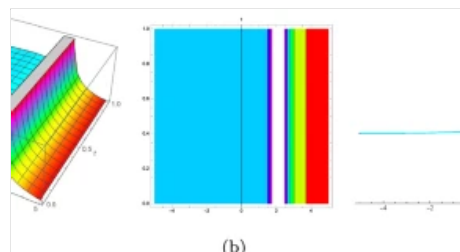
[Dr. Ivana Vasić](#)

## Articles (8 in this collection)

[On the nonlinear wave structures and stability analysis for the new generalized stochastic fractional potential-KdV model in dispersive medium](#)

Reem K. Alhefthi, Kalim U. Tariq ... Fozia Mehboob

OriginalPaper | Published: 12 February 2024





# Condensation versus long-range interaction: Competing quantum phases in bosonic optical lattice systems at near-resonant Rydberg dressing

Andreas Geißler,<sup>1,\*</sup> Ivana Vasić,<sup>1,2</sup> and Walter Hofstetter<sup>1</sup>

<sup>1</sup>*Institut für Theoretische Physik, Goethe-Universität, 60438 Frankfurt am Main, Germany*

<sup>2</sup>*Scientific Computing Laboratory, Center for the Study of Complex Systems, Institute of Physics Belgrade, University of Belgrade, Pregrevica 118, 11080 Belgrade, Serbia*

(Received 10 January 2017; published 15 June 2017)

Recent experiments have shown that (quasi)crystalline phases of Rydberg-dressed quantum many-body systems in optical lattices (OL) are within reach. Rydberg systems naturally possess strong long-range interactions due to the large polarizability of Rydberg atoms. Thus a wide range of quantum phases has been predicted, such as a devil's staircase of lattice-incommensurate density wave phases as well as the more exotic lattice supersolid order for bosonic systems, as considered in our work. Guided by results in the “frozen”-gas limit, we study the ground-state phase diagram at finite hopping amplitudes and in the vicinity of resonant Rydberg driving while fully including the long-range tail of the van der Waals interaction. Simulations within real-space bosonic dynamical mean-field theory yield an extension of the devil's staircase into the supersolid regime where the competition of condensation and interaction leads to a sequence of crystalline phases.

DOI: [10.1103/PhysRevA.95.063608](https://doi.org/10.1103/PhysRevA.95.063608)

## I. INTRODUCTION

Despite the high tunability of ultracold atomic systems as analog quantum emulators, strong long-range correlations still represent an important challenge in the field. While Feshbach resonances give access to tunable local interactions [1], recent experimental breakthroughs allow for the trapping, cooling, and control of ultracold polar molecules, as well as magnetic [2] and Rydberg atoms [3]. The significance of Rydberg excitations for creating strong nonlocal correlations has been pointed out [4–6].

Recent experiments have studied the statistical properties of dissipative Rydberg gases [7,8] and especially of superatoms [9–11], where the Rydberg blockade effect was analyzed. Using electromagnetically induced transparency, the occurrence of diffusive Förster energy transport has been shown [12]. Also, ultralong-range Rydberg molecule formation has already been observed [13], while crystallization of Rydberg atoms has been achieved up to a small number of excitations in the “frozen” limit [14,15]. There the system behaves like a spin- $\frac{1}{2}$  model with imbalanced interactions, as analyzed in numerous theoretical works [15–20], predicting a series of lattice incommensurate ordered phases (“devil's staircase”). The opposite limit of weak Rydberg dressing has extensively been investigated in theory [6,21–25], predicting the formation of (droplet) supersolids (SSs), while its experimental realization remains an open challenge [9,26–28].

## II. SYSTEM

In this work we focus on the far less understood intermediate regime of finite hopping at near-resonant and coherent excitation of the Rydberg state. Previous work in this regime so far has considered only either the nearest-neighbor (NN) limit for the interactions in a Gutzwiller mean-field simulation [29] or the low-dimensional case [30] with vanishing single-

particle hopping [31]. In the following we will introduce our approach for obtaining a ground-state phase diagram. The combination of a frozen-limit model and a real-space extension of bosonic dynamical mean-field theory (RB-DMFT) allows for an efficient quantitative analysis of the phase diagram for an arbitrary range of the interaction. We first introduce the two-species frozen-limit model, which we solve in the Hartree approximation. Then we outline the calculation of the phase diagram using RB-DMFT. Finally, we discuss the obtained quantum phases and the different types of long-range order observed.

Considering both ground  $|g\rangle$  and Rydberg excited  $|e\rangle$  states, our full grand-canonical Hamiltonian (in natural units  $\hbar = 1$ ) can be written in terms of bosonic annihilation operators  $\hat{b}_{\sigma,i}$  acting on site  $i$  of a square optical lattice (OL), where  $\hat{n}_i^\sigma = \hat{b}_{\sigma,i}^\dagger \hat{b}_{\sigma,i}$  and  $\sigma = g, e$ :

$$H = H_{2BH,\text{kin}} + \sum_i^N (H_{2BH,\text{loc},i} + H_{R,i} + H_{vdW,i}), \quad (1)$$

with the kinetic energy given by hopping of strength  $J$  and  $\eta J$  between all pairs of NN  $\langle i, j \rangle$  as  $H_{2BH,\text{kin}} = -J \sum_{\langle i, j \rangle} (\hat{b}_{g,i}^\dagger \hat{b}_{g,j} + \eta \hat{b}_{e,i}^\dagger \hat{b}_{e,j} + \text{H.c.})$  and local interaction terms for a two-species model included in

$$H_{2BH,\text{loc},i} = U \left[ \frac{\hat{n}_i^g}{2} (\hat{n}_i^g - 1) + \lambda \hat{n}_i^g \hat{n}_i^e + \tilde{\lambda} \frac{\hat{n}_i^e}{2} (\hat{n}_i^e - 1) \right] - \mu (\hat{n}_i^g + \hat{n}_i^e), \quad (2)$$

where  $U, \lambda U$ , and  $\tilde{\lambda} U$  are the strengths of the three Hubbard interaction terms and  $\mu$  is the chemical potential. The excited electronic (Rydberg) states of the atoms are populated via coherent driving, which leads to Rabi oscillations. This process is induced by the interaction with the laser light field [see, for example, Eq. (A.11) in Chap. V of [32]]. So, when using the

\*geissler@th.physik.uni-frankfurt.de

interaction picture, for a given atom we have

$$\begin{aligned} H_R^{(I)} &= -\hat{\mathbf{d}} \cdot \mathbf{E}_0 \cos(\omega_L t) \\ &= \frac{\Omega}{2} (e^{-i\omega_L t} + e^{i\omega_L t}) \hat{\sigma}^+(t) \\ &\quad + \frac{\Omega}{2}^* (e^{-i\omega_L t} + e^{i\omega_L t}) \hat{\sigma}^-(t). \end{aligned} \quad (3)$$

The time dependence of the (pseudospin-flip)  $\hat{\sigma}^\pm$  operators is given by the transition frequency  $\omega_0$ , while  $\omega_L$  is the frequency of the light field. If we thus insert  $\hat{\sigma}^\pm(t) = \hat{\sigma}_0^\pm e^{\pm i\omega_0 t}$  into (3) while also replacing  $\hat{\sigma}_0^\pm$  by appropriate products of bosonic creation and annihilation operators, we obtain the full expression in the interaction picture:

$$\begin{aligned} H_R^{(I)} &= \frac{\Omega}{2} (e^{-i\Delta t} + e^{i(\omega_L + \omega_0)t}) \hat{b}_e^\dagger \hat{b}_g \\ &\quad + \frac{\Omega}{2}^* (e^{-i(\omega_L + \omega_0)t} + e^{i\Delta t}) \hat{b}_g^\dagger \hat{b}_e. \end{aligned} \quad (4)$$

We can then assume that the Rabi frequency  $\Omega$ , as given by the dipole moment of the transition and the strength of the light field, is a real quantity. The detuning  $\Delta = \omega_L - \omega_0$  defines the slow time scale. Terms oscillating with fast frequencies can be discarded if  $\Delta \ll \omega_L + \omega_0$ , yielding the rotating-wave approximation [33]. The time-independent Hamiltonian in the rotating-wave approximation follows from the unitary transformation, defined by the time-dependent unitary transformation matrix  $U = U(t) = \hat{b}_g^\dagger \hat{b}_g + e^{i\Delta t} \hat{b}_e^\dagger \hat{b}_e$ :

$$H_R = U H_R^{(I)} U^{-1} + i \frac{dU}{dt} U^{-1} = \frac{\Omega}{2} (\hat{b}_g^\dagger \hat{b}_e + \hat{b}_e^\dagger \hat{b}_g) - \Delta \hat{n}^e. \quad (5)$$

This follows straight from  $[U, \frac{d}{dt}] = -(\frac{dU}{dt})$ , which simply has to be inserted into the Schrödinger equation, while the wave function transforms as  $\tilde{\psi} = U \psi$ . Thus the Rabi process for each lattice site in the rotating-wave approximation takes the following form:

$$H_{R,i} = \frac{\Omega}{2} (\hat{b}_{g,i}^\dagger \hat{b}_{e,i} + \hat{b}_{e,i}^\dagger \hat{b}_{g,i}) - \Delta \hat{n}_i^e. \quad (6)$$

In addition we also consider the nonlocal van der Waals (vdW) interaction between Rydberg states. At distances relevant in OLs, it is dominated by its long-range tail; thus for atoms at sites  $\mathbf{i}$  and  $\mathbf{j}$

$$H_{vdW,i} = \frac{V_{vdW}}{2} \sum_{j \neq i} \frac{\hat{n}_i^e \hat{n}_j^e}{|\mathbf{i} - \mathbf{j}|^6}, \quad (7)$$

where  $V_{vdW} = C_6/a^6$ , with the vdW coefficient  $C_6$  and the lattice parameter  $a$ . This model has been previously investigated only in the limit of NN interactions by applying Gutzwiller mean-field theory [29]. In our study we go beyond this common approximation and show that the phase diagram is far richer.

Many of the above model parameters are easily adjustable in experiments, some even over several orders of magnitude. The Rabi parameters can be directly controlled via the laser intensity (Rabi frequency  $\Omega$ , which also depends on the matrix elements of the chosen transition) and laser detuning  $\Delta$  [1], while the vdW interaction is determined by the Rydberg level considered. The remaining parameters are not as simple to control. The hopping of Rydberg-excited atoms is not yet an experimentally well controlled parameter since the OL,

trapping the ground-state (GS) atoms, is not the same for Rydberg states by default. Often, it is even of opposite sign [34–36]. Here we focus on the limiting case  $\eta = 0$ , motivated by the fact that the Rydberg part of the Hilbert space is dominated by the vdW interaction and the Rabi frequency, while the total kinetic energy contribution from  $|e\rangle$  will be small compared to  $|g\rangle$  due to low Rydberg fractions (similar to [6], see Appendix B). As the Rydberg states are perturbed by the Rabi process, their localization will be lifted anyway due to hybridization of  $|e\rangle$  with  $|g\rangle$ .

Local interactions are fixed by considering the quantum Zeno effect [37–39]. It describes the observation that loss channels with a bare loss rate  $\gamma_0 \gg U$  are strongly suppressed in the lattice, as this corresponds to a strong measurement of the lossy states, thus keeping them fixed at zero occupation. Experiments have shown the large cross section of molecular ion formation in Rydberg gases [9]. Due to the different electronic structures of such ions, they are not trapped by the confining potential, implying a large bare loss rate  $\gamma_0$ . The local quantum states susceptible to molecule formation or ionization correspond to Fock states of the form  $|n_g \geq 0, n_e > 0\rangle$ . We can model their loss-induced suppression by choosing “arbitrary” large values for both  $\lambda$  and  $\tilde{\lambda}$  (2).

### III. FROZEN-LIMIT MODEL

Due to the many possible spatial crystalline orderings, an efficient method to distinguish them is needed. Therefore we first analyze the frozen limit, where all spatial hopping terms are zero ( $J = 0$ ). This allows for a simple analytical investigation of the ground-state manifold with few approximations. Moreover, it makes for a useful exact starting point for considering finite hopping ( $J \neq 0$ ), which we simulate within RB-DMFT. Assuming a mean lattice filling  $\bar{n} < 1$ , where  $\bar{n} = \sum_i (\langle \hat{n}_i^g \rangle + \langle \hat{n}_i^e \rangle) / N$ , only empty or singly occupied sites are to be expected. We may also assume that such a system always has a spatially periodic ground state. For such crystalline order, we consequently need to consider only those sites  $i$  of the full Hamiltonian which are nonempty in order to calculate the energy:

$$\begin{aligned} H_i &= \frac{\Omega}{2} (\hat{b}_{g,i}^\dagger \hat{b}_{e,i} + \hat{b}_{e,i}^\dagger \hat{b}_{g,i}) - \Delta \hat{n}_i^e \\ &\quad - \mu (\hat{n}_i^g + \hat{n}_i^e) + \frac{V_{vdW}}{2} \sum_{j \neq i} \frac{\hat{n}_i^e \hat{n}_j^e}{|\mathbf{i} - \mathbf{j}|^6}. \end{aligned} \quad (8)$$

Any periodic superlattice structure can be constructed from a set of spanning vectors [one per spatial dimension, Fig. 1(a1)], which in our case are restricted to the discrete set of points given by the OL. Applying the Hartree approximation for a given set of spanning vectors  $(\mathbf{a}_1, \mathbf{a}_2)$  (given in units of lattice spacings  $a$ ), the Hamiltonian reduces to a set of self-consistent single-site problems with at most  $A_{\text{cluster}}^{(\mathbf{a}_1, \mathbf{a}_2)}$  different self-consistent values  $n_j^e = \langle \hat{n}_j^e \rangle$ , where  $A_{\text{cluster}}^{(\mathbf{a}_1, \mathbf{a}_2)}$  is the area (in units of lattice sites) spanned by the given vectors. Due to low filling  $\bar{n} < 1$  we consider only two values  $(n_A^e, n_B^e)$ , where each corresponds to one of the two sublattices defined by their sets of sites  $A$  and  $B$  [indicated by open and solid circles in Fig. 1(a2)] of a checkerboard version of the spanned superlattice.



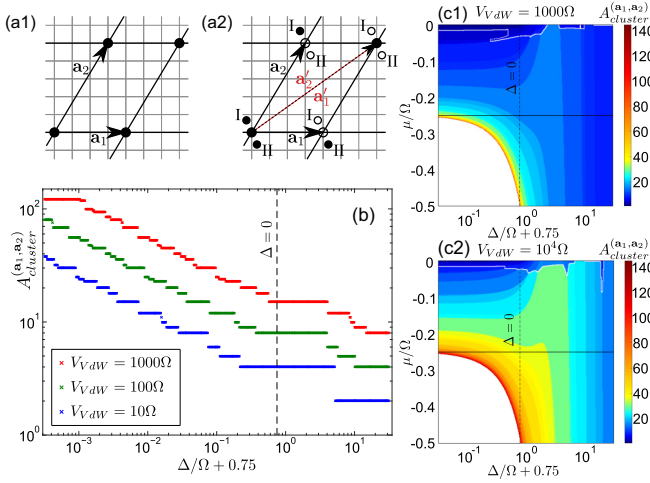


FIG. 1. (a1) Spanning vectors  $(\mathbf{a}_1, \mathbf{a}_2)$  define the Bravais cell of a superlattice for the underlying OL (gray). Black solid circles correspond to occupied sites, while the remaining sites are empty. (a2) Possible checkerboard generalizations of (a1), where spanning vectors connect two different sublattices (solid and open circles). Mapping to the striped versions (I and II) is explained in the text. In (b) and (c) different crystalline phases of the frozen-limit model can be distinguished by  $A_{\text{cluster}}^{(\mathbf{a}_1, \mathbf{a}_2)}$  (explained in the text). (b) shows devil's staircases (for values of the long-range interaction, increasing from bottom to top, as given in the legend) for the logarithmic approach to  $\Delta/\Omega = -3/4$  at  $\mu_0/\Omega = -1/4$  [solid lines in (c1) and (c2)]. Phases above white lines in (c1) and (c2) correspond to two-sublattice order with canted state orientation.

For given vectors  $(\mathbf{a}_1, \mathbf{a}_2)$  two further versions are indicated by I and II in Fig. 1(a2), where one of the two transformations  $\mathbf{a}_{1/2} \rightarrow \mathbf{a}'_{1/2} = \mathbf{a}_{1/2} + \mathbf{a}_{2/1}$  was applied. This allows for energy optimization via canted state orientation, which is equivalent to canted Ising antiferromagnetic (CIAF) order and becomes important for increased lattice fillings. Generally, frozen states (within the Hartree approximation) can be written as

$$|\Psi\rangle = \prod_C \prod_{i \in C} (\cos \phi_i |\downarrow\rangle_i + e^{i\theta_i} \sin \phi_i |\uparrow\rangle_i), \quad (9)$$

where the state of the full system is given by a product over a lattice of unit cells  $C$  containing  $N$  sites each, with an internal structure given by the set of  $\phi_i \in [0, \pi/2]$  and  $\theta_i \in [0, 2\pi]$  for  $i = 1, \dots, N$ . Setting at least one  $\phi_i \notin \{0, \pi/2\}$  yields CIAF order. In the case of the Mott-like frozen limit, the not yet specified quasispin states can, in principle, be any set of two bosonic Fock states, including the empty vacuum state  $|n_g = 0, n_e = 0\rangle$ . Note that the use of different particle numbers for the states at site  $i$ , for example, the combination of an empty site with any allowed Fock state on this site, implies  $\phi_i = 0, \pi/2$ . Also note that  $\theta_i = \pi$  combined with  $(\downarrow, \uparrow) = (g, e)$  corresponds to a dark state, as is used for an  $s$ -state to  $s$ -state transition (required for isotropically interacting  $^{87}\text{Rb}$  Rydberg states) to suppress decay via the intermediary  $p$  state. An example of CIAF order is schematically shown in Fig. 2, where the two sublattices correspond to the  $A$  and  $B$  sites.

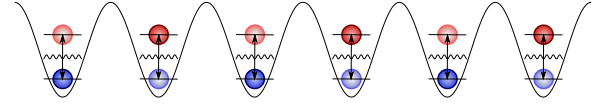


FIG. 2. Schematic representation of a one-dimensional CIAF state in an optical lattice. Colored circles correspond to the ground (blue, bottom row) and excited (red, top row) Fock states, and the opacity is related to the amplitudes in the local Fock combinations (9). A complete polarization of the state is suppressed by the Rabi process induced by the incident light field (small black waves and arrows).

For the interaction energy for each sublattice within the Hartree approximation we obtain ( $A \leftrightarrow B$ )

$$H_{vdW,A}^{\text{Hartree}} = V_{vdW} \hat{n}_A^e \left( \sum_{\mathbf{j} \in A \setminus 0} \frac{\langle n_A^e \rangle}{j^6} + \sum_{\mathbf{j} \in B} \frac{\langle n_B^e \rangle}{j^6} \right), \quad (10)$$

where  $\mathbf{j}$  points from a given site (0) of  $A$  to any site of both  $A$  and  $B$ . Thus the site-averaged grand-canonical potential  $f$  is simply given by  $f = \sum_i \langle H_i \rangle / A_{\text{cluster}}^{(\mathbf{a}_1, \mathbf{a}_2)} = \sum_{i=A,B} \frac{\langle H_i \rangle}{2} \bar{n}$  with the vdW interaction evaluated by (10).

Minimizing  $f$  with respect to a set  $\mathcal{V}_s$  of spanning vectors then yields the many-body ground-state phase diagram in the frozen limit for  $\bar{n} < 1$ , as shown in Figs. 1(b) and 1(c). For this variational minimization it is useful to represent the remaining sums over the sublattices  $A$  and  $B$  as functions of the spanning vectors,

$$V_{\mathbf{a}_1}^{\mathbf{a}_2} = \sum_{\mathbf{j} \in A \setminus 0} \frac{1}{j^6}, \quad W_{\mathbf{a}_1}^{\mathbf{a}_2} = \sum_{\mathbf{j} \in B} \frac{1}{j^6},$$

while it is furthermore helpful to introduce

$$R = R_{\mathbf{a}_1}^{\mathbf{a}_2} = \max(V_{\mathbf{a}_1}^{\mathbf{a}_2}, W_{\mathbf{a}_1}^{\mathbf{a}_2}) / \min(V_{\mathbf{a}_1}^{\mathbf{a}_2}, W_{\mathbf{a}_1}^{\mathbf{a}_2}) \quad (11)$$

as the crystal-structure-dependent ratio of the long-range interaction sums. The dependence of  $R_{\mathbf{a}_1}^{\mathbf{a}_2}$  on the spanning vectors is shown by the contour lines in Fig. 3. It should be noted that there is no dependence on the actual form of the interaction, as we use a scale-free long-range interaction in the present case. In order to perform the minimization procedure, we generate a set  $\mathcal{V}_s$  (as shown in Fig. 3), which needs to at least represent the whole range of superlattices, which can in principle be expected in the regime under consideration. In our frozen model (8) the on-site interaction  $U$  is neglected for  $\bar{n} < 1$ . With  $\Omega$  as the energy scale, only  $V_{vdW}$ ,  $\Delta$ , and  $\mu$  remain as tunable parameters, defining the region to be investigated.

Especially,  $V_{vdW}$  is important for the choice of  $\mathcal{V}_s$ , as it defines the blockade radius  $R_b = (C_6/\Omega)^{1/6}$  for Rydberg excitations, which corresponds to a radius of up to 5 OL sites for  $V_{vdW} \leq 10^4 \Omega$ . On a square lattice this would correspond to a volume of up to 25 lattice sites. In order to allow for even lower fillings, enabled by the chemical potential or the detuning, we will consider volumes of up to  $12 \times 12$  lattice sites. The complete set  $\mathcal{V}_s$  of spanning vectors used here is shown in Fig. 3, modulo similarity transformations for each pair.

If we then also define  $V = V_{vdW} \min(V_{\mathbf{a}_1}^{\mathbf{a}_2}, W_{\mathbf{a}_1}^{\mathbf{a}_2})$  and use the Rabi frequency  $\Omega$  as the energy scale, the self-consistency



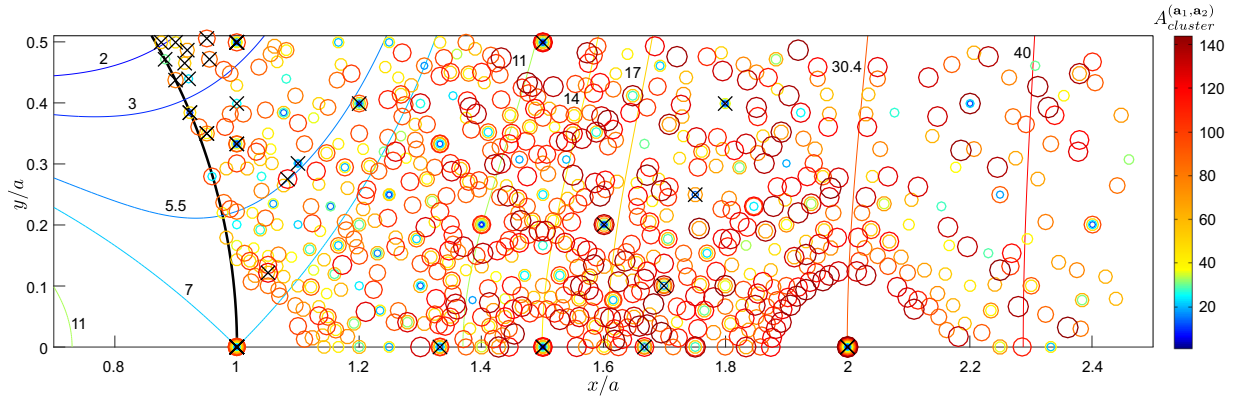


FIG. 3. Each colored (grayscale) marker represents a pair of tested spanning vectors (each in units of lattice spacing  $a$ ) from the set  $\mathcal{V}_s$ . Their coordinates are given by the larger vector, after a combined scaling and rotation of both vectors, so that the smaller vector is mapped onto  $(0,1)$ . They can thus appear only outside of the unit circle (thick black line). Their color and size correspond to the area of each crystal unit cell. In addition, also some contour lines for  $R_{(0,1)}^{(x,y)}$  are shown. Crossed markers correspond to crystal structures actually appearing as ground states of the atomic limit model in the blue-detuned regime for  $V_{dW} < 10^4 \Omega$ .

conditions for  $n_{A/B}^e = \langle \hat{n}_{A/B}^e \rangle$  in the many-body ground state are given by

$$n_{A/B}^e = 1 - n_{A/B}^e |V(n_{B/A}^e + Rn_{A/B}^e) - \Delta + \sqrt{1 + (V(n_{B/A}^e + Rn_{A/B}^e) - \Delta)^2}|. \quad (12)$$

The solutions of this effective model, where  $R$  is just the ratio of any inter- and intrasublattice interactions, are shown in Fig. 4 for some relevant values of  $R$  (compare Fig. 3).

As  $f = \sum_{i=A,B} \frac{\langle H_i \rangle}{2} \bar{n}$  within these limits and approximations, its minimization with respect to our set  $\mathcal{V}_s$  yields the many-body ground-state phase diagram in the atomic limit for

$\bar{n} < 1$ , as shown in Figs. 1(b) and 1(c). In the comparison of all lattice structures from the set  $\mathcal{V}_s$ , as shown in Fig. 3, the configurations of minimal energy anywhere in the analyzed parameter region [compare parameter ranges in Figs. 1(b) and 1(c)] are marked by crosses. Those points primarily accumulate where they correspond to either triangular order,  $\mathbf{a}_2 = (\sqrt{3}/2, 1/2)$ , or a square lattice,  $\mathbf{a}_2 = (1,0)$ . Points with increased  $R > 10$ , on the other hand, are more susceptible to the formation of CIAF order (as can be seen in Fig. 4). If one then considers only one of the two sublattices, for example, the one with the increased Rydberg fraction, it again resembles triangular order more closely, which is possible without the canted order while keeping the lattice filling constant. On the other hand, no spanning vectors with minimal energy are to be found beyond a radius of 2; in particular, the point  $(2,0)$  is the most distant (see Fig. 3), which rules out stripe-like order.

From (8) in the Hartree approximation it furthermore follows that the chemical potential  $\mu_0$ , determining the transition to the vacuum state, is given by

$$\mu_0 = -\frac{\Delta + \sqrt{\Omega^2 + \Delta^2}}{2}. \quad (13)$$

Approaching this limit by varying either  $\mu$ ,  $\Delta$ , or  $\Omega$  yields a devil's staircase of fractional lattice-commensurate fillings [see Fig. 1(b)], stabilized by the long-range interactions. Note that our ansatz allows only for fillings of the form  $\frac{1}{n}$  with  $n \in \mathbb{N}$  (see also [40,41]).

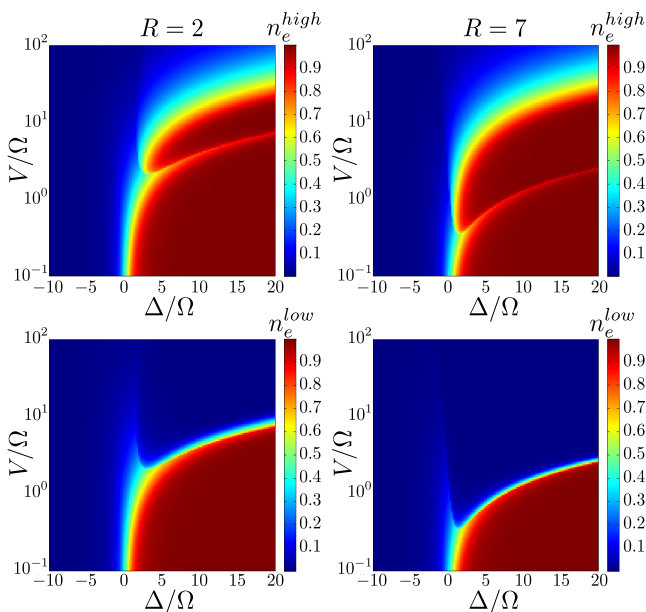


FIG. 4. Various solutions of the effective frozen model (12) for  $R = 2, 7$ . Shown are the Rydberg fractions  $n_e$  for each of the two sublattices, which are respectively indexed by whether the sublattice with high or low Rydberg fraction is considered. Canting appears if  $n_e^{\text{low}} \neq n_e^{\text{high}}$  and at least one of them is not equal to unity.

#### IV. ITINERANT CASE WITHIN RB-DMFT

We now use the frozen-limit results as an exact starting point for our RB-DMFT simulations since both models map to each other in the Hartree approximation for vanishing  $J$  and  $\bar{n} < 1$ . However, for nonzero  $J$  we cannot expect the crystal symmetry to always be given by the frozen-limit results. Therefore other crystalline structures corresponding to similar mean interatom distances are also simulated. Furthermore, RB-DMFT requires a truncation of the local Fock space. Since a hard cutoff, using only the first  $N_c$  Fock states, strongly restricts the

maximum observable local particle number in a condensate, we instead use a soft cutoff utilizing the *coherent-tail* state  $\propto \sum_{n=N_c}^{\infty} \frac{\alpha^n}{\sqrt{n!}} |n\rangle$  [42], where  $N_c = 4$ , leading to a negligible error in the calculated observables, which is maximal for values of  $J/\Omega > 0.1$ , where it is on the order of a few percent ( $< 3\%$ ). The ground state is then found by comparing the resulting lattice-averaged grand-canonical potentials  $f = \langle H \rangle / A_{\text{cluster}}$  for each of the considered crystal structures. In order to allow for checkerboard order on all cluster types (even those of odd-valued volume), we always simulate clusters generated by the spanning vectors  $(2 \cdot \mathbf{a}_1, 2 \cdot \mathbf{a}_2)$ .

Calculating  $f$  is not straightforward within RB-DMFT, as the kinetic energy  $E_{\text{kin}} = \langle H_{2BH, \text{kin}} \rangle$  is given in terms of *nonlocal* expectation values  $\langle \hat{b}_{\sigma,i}^\dagger \hat{b}_{\sigma,j} \rangle$ , which therefore cannot directly be calculated from the self-consistent local Anderson impurity models used by RB-DMFT. But it can be shown that within the RB-DMFT self-consistency conditions,  $E_{\text{kin}}$  can also be written in terms of connected local Green's functions  $\mathbf{G}_{\sigma,i}^C$  and Anderson impurity hybridization functions  $\Delta_{\sigma,i}$ , for which we will now give a short introduction regarding their role within DMFT.

### A. Kinetic energy and connected Green's functions

Starting from the connected normal real-space Green's function at equal times, with time ordering fixed by the infinitesimal time difference  $\epsilon < 0$ , we have

$$\begin{aligned} \lim_{\epsilon \rightarrow 0^-} G_{\sigma,ji}^{Cn}(\epsilon, 0) &= -(\langle \hat{b}_{\sigma,i}^\dagger \hat{b}_{\sigma,j} \rangle - \langle \hat{b}_{\sigma,i} \rangle \langle \hat{b}_{\sigma,j} \rangle) \\ &= \lim_{\epsilon \rightarrow 0^+} \sum_{n=-\infty}^{\infty} \frac{e^{i\omega_n \epsilon}}{\beta} G_{\sigma,ji}^{Cn}(i\omega_n) \end{aligned} \quad (14)$$

for the connected Green's functions  $G_{\sigma,ji}^{Cn}(i\omega_n)$  in bosonic Matsubara frequencies. The anomalous part is accordingly given by

$$\begin{aligned} \lim_{\epsilon \rightarrow 0^-} G_{\sigma,ji}^{Ca}(\epsilon, 0) &= -(\langle \hat{b}_{\sigma,i} \hat{b}_{\sigma,j} \rangle - \langle \hat{b}_{\sigma,i} \rangle \langle \hat{b}_{\sigma,j} \rangle) \\ &= \lim_{\epsilon \rightarrow 0^+} \sum_{n=-\infty}^{\infty} \frac{e^{i\omega_n \epsilon}}{\beta} G_{\sigma,ji}^{Ca}(i\omega_n). \end{aligned} \quad (15)$$

Thus expressing the total kinetic energy in terms of connected real-space Green's functions yields

$$\begin{aligned} E_{\text{kin}} &= - \sum_{ij\sigma} J_{ij}^\sigma \langle \hat{b}_{\sigma,i}^\dagger \hat{b}_{\sigma,j} \rangle \\ &= \sum_{ij\sigma} J_{ij}^\sigma \left( \lim_{\epsilon \rightarrow 0^+} \sum_{n=-\infty}^{\infty} \frac{e^{i\omega_n \epsilon}}{\beta} G_{\sigma,ji}^{Cn}(i\omega_n) - \phi_{\sigma,i}^* \phi_{\sigma,j} \right), \end{aligned}$$

where  $\phi_{\sigma,i} = \langle \hat{b}_{\sigma,i} \rangle$  is the local condensate order parameter of the atomic state  $\sigma$  at lattice site  $i$ , while  $J_{ij}^\sigma$  is the matrix of allowed hoppings in the system. This expression can be further simplified by employing both the local [(16) as in (36) from [43]] and lattice [(17) as in (37) from [43]] Dyson equations in Nambu notation, as regularly used within RB-DMFT. Here we suppress the state index  $\sigma$ , as this part of the derivation is independent of the atomic state. In Nambu notation for  $n \geq 0$  the real-space lattice Green's functions are represented as  $G_{ji}^{Cn}(+i\omega_n) = [\mathbf{G}_{ji}^C(i\omega_n)]_{11}$  and  $G_{ji}^{Cn}(-i\omega_n) = [\mathbf{G}_{ji}^C(i\omega_n)]_{22}$ ,

while the anomalous term is given by  $G_{ji}^{Ca}(+i\omega_n) = [\mathbf{G}_{ji}^C(i\omega_n)]_{12} = G_{ji}^{Ca}(-i\omega_n)$  and  $[\mathbf{G}_{ji}^C(i\omega_n)]_{21} = [\mathbf{G}_{ji}^C(i\omega_n)]_{21}^*$ . So

$$\mathbf{G}_i^C(i\omega_n)^{-1} = i\omega_n \sigma_z + \mu \mathbf{1}_2 + \Delta_i(i\omega_n) - \Sigma_i(i\omega_n), \quad (16)$$

$$[\mathbf{G}^C(i\omega_n)^{-1}]_{ij} = J_{ij} \mathbf{1}_2 + \delta_{ij} [i\omega_n \sigma_z + \mu \mathbf{1}_2 - \Sigma_i(i\omega_n)], \quad (17)$$

where the Pauli matrix  $\sigma_z$  is used due to Nambu notation. These equations are given in terms of local self-energies  $\Sigma_i(i\omega_n)$ , the Anderson impurity hybridization function  $\Delta_i(i\omega_n)$ , and the local impurity Green's function  $\mathbf{G}_i^C(i\omega_n) := [\mathbf{G}^C(i\omega_n)]_{ii}$  (DMFT self-consistency). Inserting  $\Sigma_i(i\omega_n)$  from (16) in (17), combined with a matrix multiplication by  $\mathbf{G}^C(i\omega_n)$  from the right, where we are interested in only the diagonal elements, yields

$$\begin{aligned} \sum_j [\mathbf{G}^C(i\omega_n)^{-1}]_{ij} [\mathbf{G}^C(i\omega_n)]_{ji} \\ = \sum_j \{ J_{ij} \mathbf{1}_2 - \delta_{ij} [\Delta_i(i\omega_n) - \mathbf{G}_i^C(i\omega_n)^{-1}] \} [\mathbf{G}^C(i\omega_n)]_{ji}. \end{aligned}$$

Further using the self-consistency property of the impurity Green's function leads to the identities

$$\sum_j J_{ij} [\mathbf{G}^C(i\omega_n)]_{ji} = \Delta_i(i\omega_n) \mathbf{G}_i^C(i\omega_n), \quad (18)$$

where only the diagonal parts are of interest to us. Considering the symmetries in Nambu notation, they allow us to simplify our expression for  $E_{\text{kin}}$ :

$$\begin{aligned} E_{\text{kin}} &= \frac{2}{\beta} \lim_{\epsilon \rightarrow 0^+} \sum_{i\sigma n \geq 0} \text{Re} \{ [\Delta_{\sigma,i}(i\omega_n) \mathbf{G}_{\sigma,i}^C(i\omega_n)]_{11} e^{i\omega_n \epsilon} \} \\ &\quad - \sum_{ij\sigma} J_{ij}^\sigma \phi_{\sigma,i}^* \phi_{\sigma,j} - \frac{\text{Tr}[\Delta_{\sigma,i}(0) \mathbf{G}_{\sigma,i}^C(0)]}{2\beta}. \end{aligned} \quad (19)$$

The remaining problem is due to the cutoff imposed on the Matsubara frequencies in the numerics, which implies that the limit of equal times is not simply given by setting  $\epsilon = 0$ . One can instead account for the cutoff by requiring that the particle number is given correctly:

$$-\frac{1}{\beta} \sum_n G_{R,\sigma,ii}^C(i\omega_n) e^{i\omega_n \epsilon} + \phi_{\sigma,i}^* \phi_{\sigma,i} \stackrel{!}{=} \langle \hat{n}_i^\sigma \rangle_{\text{AIM}}. \quad (20)$$

For every site and species this yields a value of  $\epsilon$ , which can be used to calculate the kinetic energy in the local representation (19), thereby allowing the complete calculation of the lattice-averaged grand-canonical potential  $f$  for each of the various crystal structures.

### B. Hybridization functions $\Delta_{\sigma,i}$ of the effective impurity model

The essence of RB-DMFT simulations is the mapping of a lattice model onto a set of self-consistent quantum impurity models. The primary aim of the mapping for each site is an optimal representation of the total action  $S$  in terms of an effective local impurity action  $S_{\text{eff}}$ . Suppressing the pseudospin

$\sigma$ , one has

$$S[b^*, b] = \int_0^\beta d\tau \left( \sum_i b_i^*(\tau) \frac{\partial b_i(\tau)}{\partial \tau} + H \right) = S_0 + C + \Delta S, \quad (21)$$

with  $H$  given by the model Hamiltonian (1) in terms of the boson fields  $b_i(\tau)$  as functions of imaginary time  $\tau$ . For a given site  $i \equiv 0$  we also introduce both

$$S_0 = \int_0^\beta d\tau \left( b_0^* \frac{\partial b_0}{\partial \tau} - \mu b_0^* b_0 + \frac{U}{2} |b_0|^4 \right),$$

$$\Delta S = \int_0^\beta d\tau \sum_{(0,i)} (-t_{0i} b_0^* b_i - t_{0i}^* b_i^* b_0).$$

In an approximative way, by integrating over the rest of the system, we derive the effective action  $S_{\text{eff}}$  for a given site  $i \equiv 0$  via

$$S_{\text{eff}} = S_0 + \int_0^\beta d\tau \sum_{(0,i)} (-t_{0i} b_0^* \langle b_i \rangle_C + t_{0i}^* b_0 \langle b_i^* \rangle_C) - \frac{1}{2} \int_0^\beta d\tau \int_0^\beta d\eta [b_0^*(\tau) b_0(\tau)] \mathbf{M}(\tau, \eta) [b_0(\eta) b_0^*(\eta)]^T,$$

where we introduce the cavity expectation value  $\langle \cdot \rangle_C$  for the system where the site of interest has been removed:

$$\langle x \rangle_C = \frac{\prod_{i \neq 0} \int \mathcal{D}b_i^* \mathcal{D}b_i x \exp(-C)}{\prod_{i \neq 0} \int \mathcal{D}b_i^* \mathcal{D}b_i \exp(-C)}. \quad (22)$$

Then one further obtains

$$M_{11}(\tau, \eta) = \sum_{i,j} t_{0i} t_{0j}^* [\langle b_i(\tau) b_j^*(\eta) \rangle_C - \langle b_i(\tau) \rangle_C \langle b_j^*(\eta) \rangle_C],$$

$$M_{22}(\tau, \eta) = \sum_{i,j} t_{0i}^* t_{0j} [\langle b_i^*(\tau) b_j(\eta) \rangle_C - \langle b_i^*(\tau) \rangle_C \langle b_j(\eta) \rangle_C],$$

$$M_{12}(\tau, \eta) = \sum_{i,j} t_{0i} t_{0j} [\langle b_i(\tau) b_j(\eta) \rangle_C - \langle b_i(\tau) \rangle_C \langle b_j(\eta) \rangle_C],$$

$$M_{21}(\tau, \eta) = \sum_{i,j} t_{0i}^* t_{0j}^* [\langle b_i^*(\tau) b_j^*(\eta) \rangle_C - \langle b_i^*(\tau) \rangle_C \langle b_j^*(\eta) \rangle_C].$$

On the other hand, we use exact diagonalization to solve the effective impurity model, representing the hybridization function in (16) for each site via a corresponding effective impurity bath. In this case for each site  $i \equiv 0$  an effective impurity model is defined as (with the internal degrees of freedom reinstated)

$$H_{\text{imp}}^{\text{eff}} = \sum_\sigma \left[ -\mu \hat{b}_{\sigma,0}^\dagger \hat{b}_{\sigma,0} + \frac{U_\sigma}{2} \hat{n}_0^\sigma (\hat{n}_0^\sigma - 1) - \hat{b}_{\sigma,0}^\dagger \left( \sum_j t_\sigma \langle \hat{b}_{\sigma,j} \rangle_C \right) - \hat{b}_{\sigma,0} \left( \sum_j t_\sigma \langle \hat{b}_{\sigma,j} \rangle_C \right)^\dagger \right] + \left( V_{vdW} \sum_{j \neq 0} \frac{\langle \hat{n}_j^e \rangle}{|j|^6} - \Delta \right) \hat{b}_{e,0}^\dagger \hat{b}_{e,0} + \frac{\Omega}{2} (\hat{b}_{g,0}^\dagger \hat{b}_{e,0} + \hat{b}_{e,0}^\dagger \hat{b}_{g,0}) + U \lambda \hat{n}_0^g \hat{n}_0^e + \underbrace{\sum_{l,\sigma} \left[ \epsilon_{l,\sigma} \hat{a}_{l,\sigma}^\dagger \hat{a}_{l,\sigma} + \left( V_{l,\sigma} \hat{a}_{l,\sigma}^\dagger \hat{b}_{\sigma,0} + V_{l,\sigma}^* \hat{a}_{l,\sigma} \hat{b}_{\sigma,0}^\dagger + W_{l,\sigma} \hat{a}_{l,\sigma} \hat{b}_{\sigma,0} + W_{l,\sigma}^* \hat{a}_{l,\sigma}^\dagger \hat{b}_{\sigma,0}^\dagger \right) \right]}_{H'_{\text{imp}}}, \quad (23)$$

where  $\sigma = g, e$ , so  $U_g = U$  and  $U_e = \tilde{\lambda}U$ . The hybridization function matrix  $\Delta_{\sigma,0}(i\omega_n)$  of this impurity model is given by all the bath terms  $H'_{\text{imp}}$ , which include any of the bath creation and annihilation operators  $\hat{a}_{l,\sigma}^\dagger$  and  $\hat{a}_{l,\sigma}$ . It has the form

$$\Delta_{\sigma,0}(i\omega_n) = \begin{pmatrix} \Delta_{\sigma}^{11}(i\omega_n) & \Delta_{\sigma}^{12}(i\omega_n) \\ \Delta_{\sigma}^{21}(i\omega_n) & \Delta_{\sigma}^{22}(i\omega_n) \end{pmatrix}, \quad (24)$$

where the different matrix elements are given by

$$\Delta_{\sigma}^{11}(i\omega_n) = \sum_l \left( \frac{V_{l,\sigma}^* V_{l,\sigma}}{\epsilon_{l,\sigma} - i\omega_n} + \frac{W_{l,\sigma}^* W_{l,\sigma}}{\epsilon_{l,\sigma} + i\omega_n} \right),$$

$$\Delta_{\sigma}^{22}(i\omega_n) = \sum_l \left( \frac{W_{l,\sigma}^* W_{l,\sigma}}{\epsilon_{l,\sigma} - i\omega_n} + \frac{V_{l,\sigma}^* V_{l,\sigma}}{\epsilon_{l,\sigma} + i\omega_n} \right),$$

$$\Delta_{\sigma}^{12}(i\omega_n) = \sum_l \left( \frac{V_{l,\sigma}^* W_{l,\sigma}^*}{\epsilon_{l,\sigma} - i\omega_n} + \frac{V_{l,\sigma}^* W_{l,\sigma}^*}{\epsilon_{l,\sigma} + i\omega_n} \right),$$

$$\Delta_{\sigma}^{21}(i\omega_n) = \sum_l \left( \frac{W_{l,\sigma} V_{l,\sigma}}{\epsilon_{l,\sigma} - i\omega_n} + \frac{W_{l,\sigma} V_{l,\sigma}}{\epsilon_{l,\sigma} + i\omega_n} \right).$$

All parameters  $V, W, \epsilon$  are fixed self-consistently, so that the effective impurity-bath hybridization is the best fit of the actual impurity-lattice hybridization as extracted from (16). When self-consistency has been achieved, the relation  $\Delta_{\sigma,0}(i\omega_n) \equiv \mathbf{M}_\sigma(i\omega_n)$  holds, where  $\mathbf{M}_\sigma(i\omega_n)$  is the representation of  $\mathbf{M}_\sigma(\tau, \eta) = \mathbf{M}_\sigma(\tau - \eta)$  in terms of Matsubara frequencies.

## V. RB-DMFT PHASE DIAGRAM

Minimizing  $f$ , as calculated in the described RB-DMFT scheme, with respect to the relevant crystal orders yields the ground-state phase diagram shown by the lines in Fig. 5(e). For selected points, we also show the spatial distribution of important local observables, such as the occupation numbers  $n_i^\sigma$ , squared condensate order parameters  $|\phi_i^\sigma|^2$ , and  $\langle \hat{b}_{g,i}^\dagger \hat{b}_{e,i} \rangle$ , with the latter related to in-plane magnetization of the pseudospin. The phase boundaries are obtained from kinks (second order) and jumps (first order) in the spatially averaged observable  $\bar{n}_e = \sum_i \langle \hat{n}_i^e \rangle / A_{\text{cluster}}^{(\mathbf{a}_1, \mathbf{a}_2)}$  [see Fig. 5(e)], which acts as an order parameter. Thus we find various ground-state phases,

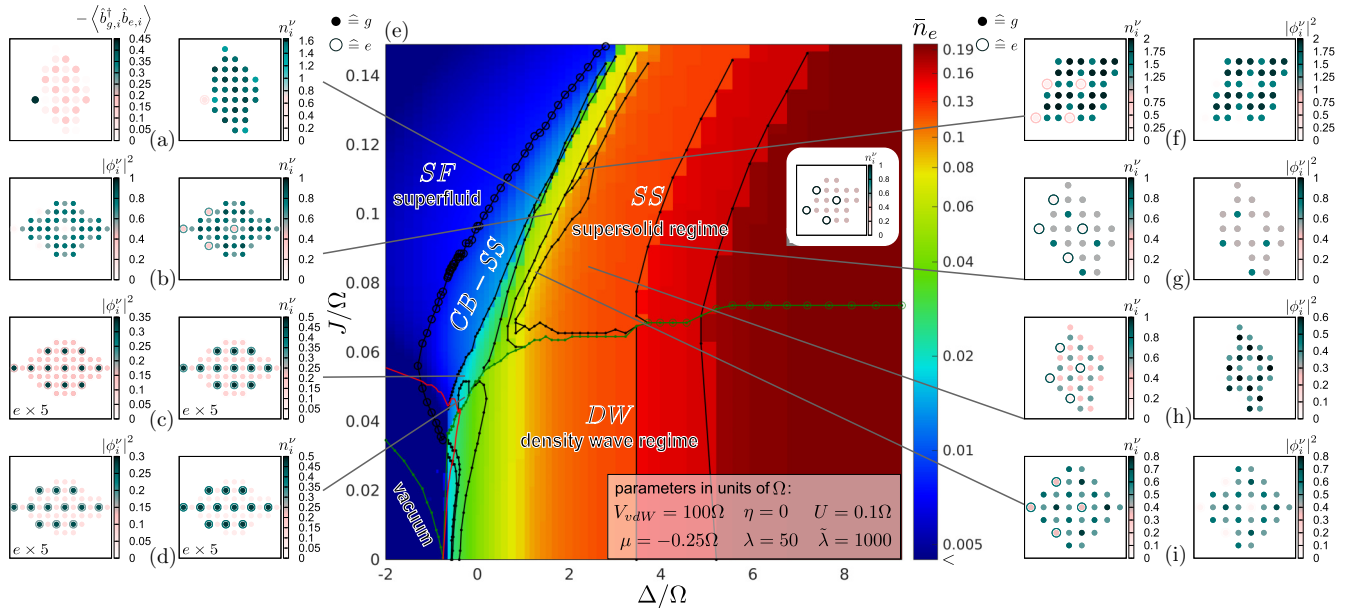


FIG. 5. Lines in (e) show the phase diagram of the two-species extended Bose-Hubbard model with vdW-interacting excited Rydberg species (1). Shown is the dependence of the average GS Rydberg fraction  $\bar{n}_e$  on detuning and hopping, while the fixed parameters of the model are given in the inset. The occurrence of a finite condensate order parameter at finite  $J$  is marked by the green (gray) line with dots. Transitions between different phases of supersolid (SS) order above this line, as well as between density wave (DW) ordered phases below, are separated by black lines (circles for second order, points for first order). As it has the simplest order beyond a homogeneous superfluid (SF), we specifically label the checkerboard supersolid (CB-SS) in the diagram. All DMFT results in the region between the red (gray) line without dots and vacuum have lattice-averaged grand-canonical potentials  $f > 0$ . (e) Lattice-averaged Rydberg fraction  $\bar{n}_e$  (with the smallest values for  $\Delta/\Omega < 0$ ), which is strongly related to the effective lifetime of Rydberg states [21]. (a)–(d), the inset in (e), and (f)–(i) show depictions of the spatial distribution of specified local observables. These plots correspond to different points indicated in the phase diagram in (e). If mentioned in a diagram, the values for excited states are rescaled by the indicated factor.

starting with the well-known homogeneous superfluid (SF) and the devil's staircase in the density wave (DW) regime at small hopping, separated by a peculiar series of supersolids. We can distinguish two distinct regimes of supersolids, dominated by either weak or strong Rydberg dressing, arising due to two competing effects. One is the melting, induced by a large hopping amplitude  $J$ , while the other is the crystallizing effect of the detuning  $\Delta$ . Since blue detuning facilitates Rydberg crystallization at higher densities, as well as a higher Rydberg fraction in general, the latter effect is easily understood.

Traversing the phase diagram in the supersolid regime, starting at high  $\Delta$  [Fig. 5(e), inset] and reducing its value continuously, one first finds a series of GS supersolids with growing wavelength, until there is a sudden drop in the wavelength, accompanied by a rising Rydberg condensate and a fast drop of the Rydberg fraction for the sites with the highest admixture of the Rydberg state [Figs. 5(a)–5(d)]. Contrary to the devil's staircase in the DW regime, the staircase in the SS regime does not end in an empty or homogeneous system, but instead with short-wavelength supersolids, most notably the checkerboard supersolid (CB-SS) [see also Fig. 5(c) and 5(d)], which is the only previously predicted SS phase [29]. The competition between crystallizing and melting effects becomes especially evident in the two cases where two supersolids meet, which both have the same number of sites in their unit cells, while their spanning vectors differ [Figs. 5(c) and 5(d) and 5(h) and 5(i)]. There the crystallizing effect dominates for small hopping, as the excitations minimize interaction energy

by maximizing their NN distances. For increased hopping the system then prefers the configuration with slightly reduced NN distances while restoring a spatial order commensurate with the OL. Additionally, the eight-site unit cells are almost degenerate, while the unit cell less favored by  $V_{vdW}$  has a transition into SF at lower  $J$ . Regarding the two distinct SS regimes with strong and weak dressings, the narrow phase dominated by a long-range order with a unit cell of 32 sites [Fig. 5(a)] implies crossover behavior. This phase marks the boundary between the two regimes, as it consists mostly of CB-SS (with the CB order strongly visible in  $\langle \hat{b}_{g,i}^\dagger \hat{b}_{e,i} \rangle$ ), interspersed by a low density of strongly dressed atom or impurities suppressing the short-range CB order.

Another noteworthy configuration appears in a band with a width  $\Delta/\Omega \approx 0.2$ , starting slightly above resonance [Fig. 5(b)]. There the ground-state condensate and the nearly Fock state Rydberg excited atoms are spatially separated from one another, as is the case for most of the interaction-dominated part of the SS regime. But in addition, the excitations are aligned in a triangular lattice, while the condensate is arranged on its dual honeycomb lattice, at least as much as possible on a square lattice.

Finally, since the effective total decay rate of excitations is directly proportional to the fraction  $n_e$  of their occupation [21], this quantity [Fig. 5(e)] implies that the region with low Rydberg occupation should be most suitable for experiment. Even at detunings  $\Delta > 0$ , Rydberg blockade causes a value of  $\bar{n}_e$  which is nearly two orders of magnitude less than the



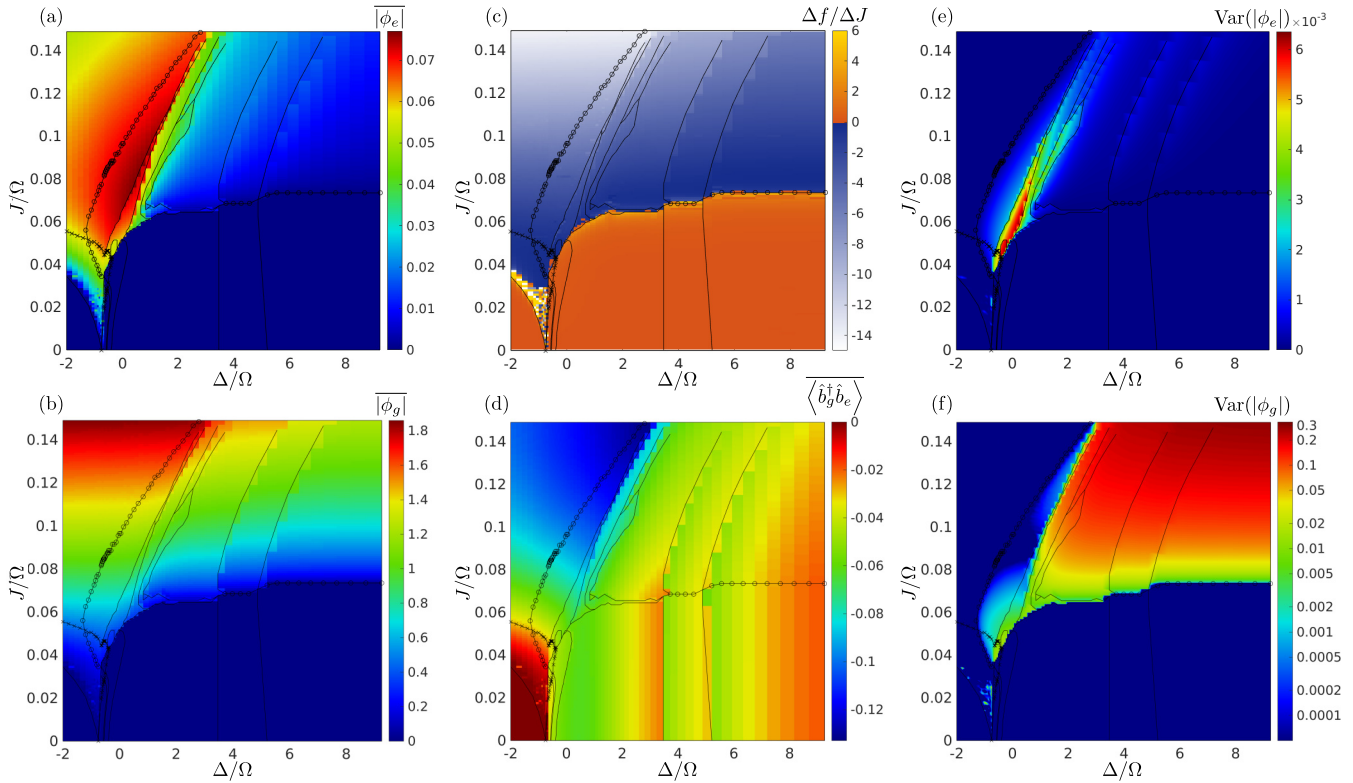


FIG. 6. Here we show the different averaged order parameters one may use to distinguish the different supersolid phases as explained in the text. (a) and (b) Spatially averaged condensate order parameters  $|\overline{\phi_\sigma}| = \sum_i |\phi_i^\sigma|/A$ . Averages are normalized by the size  $A$  of the system simulated within RB-DMFT. Both species have opposite but spatially constant phases, as one might expect from a dark state. (c) Difference quotient  $\Delta f/\Delta J$  of the mean grand-canonical potential  $f$  by the hopping amplitude  $J$ . (d) Spatial average of the local fluctuations  $\langle \hat{b}_{g,i}^\dagger \hat{b}_{e,i} \rangle$  induced by the Rabi term (6) of the Hamiltonian (1). A nonzero value is related to in-plane magnetization of the pseudospins  $\sigma = \{g, e\}$ , while its magnitude grows near resonance and with total particle number. (e) and (f) Spatial variance  $\text{Var}(|\phi_\sigma|) = \overline{|\phi_\sigma|^2} - |\overline{\phi_\sigma}|^2$  of the condensate order parameters. Note that for the excited state the maximum is close to  $\Delta/\Omega \approx 0$ , while in the ground state  $\Delta/\Omega > 1$  leads to the largest values. Lines correspond to those shown in Fig. 5(e), where circles represent second-order transitions, simple lines represent first-order transitions, and the line with crosses signifies the regime of  $f > 0$ , as explained in Fig. 5(e).

full resonant excitation of single atoms, thus increasing the feasibility of realizing the corresponding supersolids.

In conclusion, while dressed models break down close to resonant Rydberg dressing, the combined effort of an analytically solvable frozen-limit model and RB-DMFT simulations at finite hopping allows for the analysis of the rich phase diagram of (1). In particular we find two distinct regimes of supersolid order dominated by either weak or strong dressing reminiscent of the bistable behavior in nonitinerant dissipative systems [44–46]. Due to our limitation to periodic systems with finite unit cells, the behavior at the crossover remains an open question. It should also be noted that the Rabi frequency was taken to be in the range of a few megahertz, while so far realized values of hopping amplitudes reach only a fraction of this. But considering the phase diagram of the Bose-Hubbard model, the transition to supersolid phases can be expected at strongly reduced hopping for values of  $\mu$  close to zero where the assumption of low filling  $\bar{n} < 1$  breaks down, leaving this regime open for further research.

#### ACKNOWLEDGMENTS

We would like to thank M. Fleischhauer, T. Niederprüm, H. Ott, A. Pelster, M. Weidemüller, H. Weimer, S. Whitlock, and

J. Zeiher for insightful discussions. Support from the Deutsche Forschungsgemeinschaft (DFG) via DFG SPP 1929 GiRyd, DFG SFB/TR 49, DFG FOR 801, and the high-performance computing center LOEWE-CSC, as well as from the DAAD via PPP Serbia (Project No. 57215082), is gratefully acknowledged. I.V. acknowledges support from the Ministry of Education, Science, and Technological Development of the Republic of Serbia under Project No. ON 171017 and from the European Commission under H2020 project VI-SEEM, Grant No. 675121.

#### APPENDIX A: FURTHER OBSERVABLES

The phase boundaries for finite hopping  $J$ , shown in Fig. 5(e), were obtained via the spatially averaged values of the local observables, which act as order parameters of the system. As can be seen in Fig. 6, they exhibit either jumps or kinks at certain points in the phase diagram, allowing us to determine the phase boundaries as well as the order of the phase transitions. As the Rydberg fraction  $\bar{n}_e$  exhibits the most prominent changes [see Fig. 5(e)], it was used to obtain the phase boundaries between the various SS and DW phases.

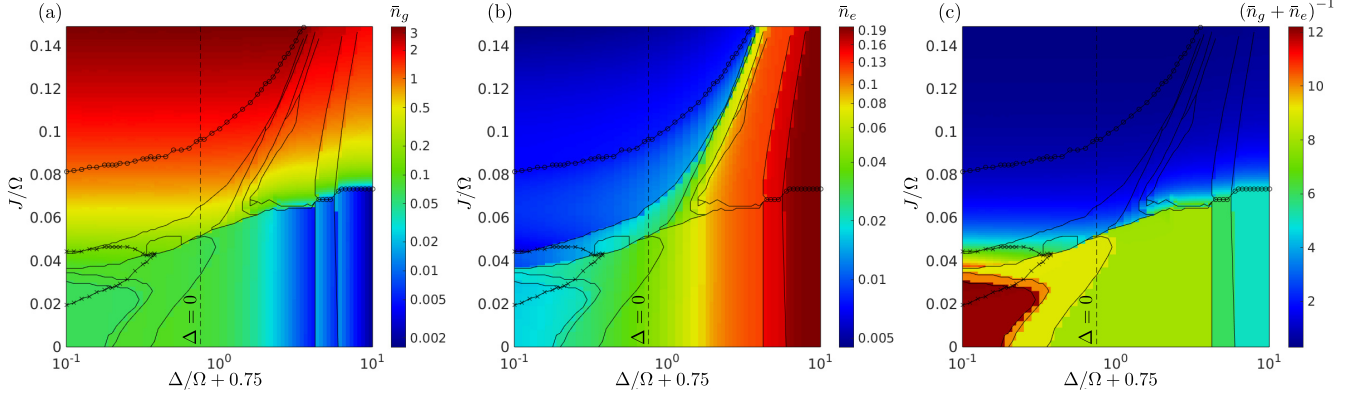


FIG. 7. (a) and (b) Averaged occupation numbers  $\bar{n}_\sigma = \sum_i n_i^\sigma / A$ , where  $A$  is the normalization due to the considered number of sites. Note that  $\Delta / \Omega > 0$  favors  $\bar{n}_e$  over  $\bar{n}_g$  in the DW phases. (c) The inverse of the average lattice filling becomes an integer in the DW regime. The values of these integers correspond to the area defined by the spanning vectors introduced earlier (e.g., equal to 12 in the lower left; compare also Fig. 1 in the main text). Lines correspond to those shown in Fig. 5(e), where circles represent second-order transitions, simple lines represent first-order transitions, and the line with crosses signifies the regime of  $f > 0$ , as explained in Fig. 5(e). The dashed lines represent the case of resonant detuning  $\Delta = 0$ .

Due to the complex nature of the model (1), additional observables allow for further characterization of its ground-state phases. While nonzero condensate order parameters  $\phi_i^\sigma = \langle \hat{b}_{\sigma,i} \rangle$  determine the occurrence of a superfluid (SF)ON [see Figs. 6(a) and 6(b)], the suppression of the spatial average  $|\overline{\phi_\sigma}|$  at large  $\Delta / \Omega$  is a result of the dominant interactions. The spatial variance  $\text{Var}(|\phi_\sigma|) = \overline{|\phi_\sigma|^2} - |\overline{\phi_\sigma}|^2$  of the condensate order parameters [see Figs. 6(e) and 6(f)] further extends and justifies the picture of two supersolid regimes due to the distinct behavior at small and large  $\Delta / \Omega$ . A vanishing value of these variances marks the loss of crystalline order and thus the transition from SS to a homogeneous SF. The large spatial variances in  $\phi_i^\sigma$ , on the other hand, are due to suppressed condensation on sites occupied by atoms strongly dressed with a Rydberg state. At the crossover between the two SS regimes, the observable related to the Rabi process (6),  $\langle \hat{b}_{g,i}^\dagger \hat{b}_{e,i} \rangle$ , also undergoes a significant change in behavior [see Fig. 6(d)]. Regarding the transitions between the various supersolid phases, we want to point out that divergences of  $\Delta f / \Delta J$  [see Fig. 6(c)] are almost absent in between SS phases and remarkably also at the SS-SF transition.

Note that in the region where the ground-state contribution  $\bar{n}_g$  vanishes [see Fig. 7(a)], the Rydberg states become almost pure number states [compare Figs. 7(b) and 7(c)]. As the corresponding property, namely, that  $\bar{n}_e$  nearly equals  $\frac{1}{q}$ , where  $q$  is the area of the unit cell corresponding to the inverse of the mean lattice filling at a vanishing condensate fraction, also extends into the region with a finite condensate, the Rydberg state can be understood to remain in a Fock state even for increased hopping amplitudes. Condensation then happens purely in the ground-state species, which implies that the condensate part spatially separates from the long-range interacting part of the system.

**APPENDIX B: INFLUENCE OF RYDBERG HOPPING**

To further probe our assumption that we can limit itinerant behavior to the  $|g\rangle$  component, namely, by setting  $\eta = 0$ , we

also compare our results to selected simulations with  $\eta = 1$ . As can be seen in the comparison of the average Rydberg fraction  $\bar{n}_e$ , shown in Fig. 8, hopping of Rydberg states has only a minor influence on the phases observed in the paper. It primarily leads to changes in parameter regions, where given phases are almost degenerate. This can be seen as one of the four-site unit cells vanishes for the chosen parameters, leading to one less step in Figs. 8(c) and 8(d). Otherwise, there are only small deformations of the boundaries.

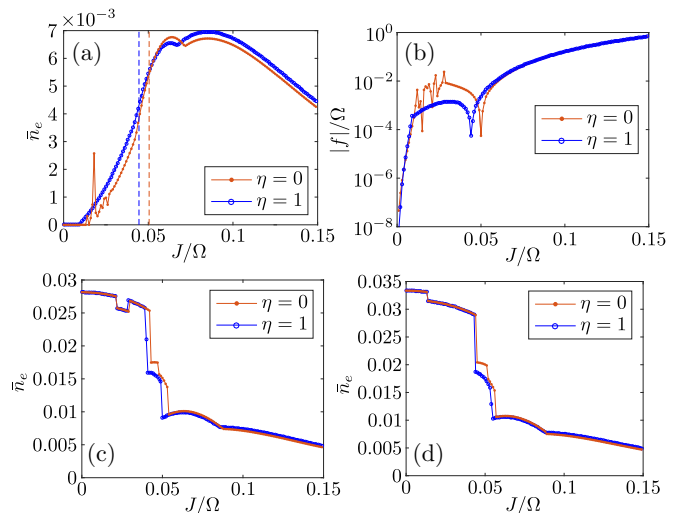


FIG. 8. (a), (c), and (d) Averaged Rydberg-state occupation numbers  $n_e = \bar{n}_e$  of (mostly) converged RB-DMFT simulations for parameters as given in the main text, except for  $\eta$ , which is given in the legend, with (a)  $\Delta / \Omega = -1$ , (c)  $-0.415$ , and (d)  $-0.303$ . The dashed lines in (a) mark  $J_c / \Omega$  where  $f$  changes sign, so results at low  $J / \Omega$  have a higher energy as the vacuum state  $|n_g = 0, n_e = 0\rangle$ . (b) The position of the sign change corresponds to a kink in the logarithmic plot  $|f|$ .

### APPENDIX C: COHERENT-TAIL-STATE TRUNCATION

In order to benchmark the choice of the Fock-space truncation, where we used a soft cutoff scheme, which replaces the highest Fock state  $N_c$  by the *coherent-tail* state  $\propto \sum_{n=N_c}^{\infty} \frac{\alpha^n}{\sqrt{n}}$  [42], we probed the influence of a changed truncation (i.e., changing  $N_c$ ) on the observables and especially on the lattice-averaged grand-canonical potential  $f$ . We did this in a parameter region where the largest deviations are expected. As the lattice filling increases above 3 atoms per site, thus close to the used cutoff  $N_c = 4$ , for small  $\Delta$  and large hopping [see Fig. 7(a)], we chose  $\Delta/\Omega = -0.8$  and  $J/\Omega > 0.05$  for the benchmark. Figures 9(a), 9(b) and 9(c) depict the observables  $\bar{\phi}_e$ ,  $\bar{n}_e$ , and  $\langle \hat{b}_g^\dagger \hat{b}_e \rangle$ , which have the largest deviations. As can be seen, changing  $N_c$  from 4 (used for all the main results) to 5 barely has any influence on these observables. The most pronounced changes appear for  $J/\Omega > 0.1$ , with only minor numerical changes in the values of the observables, while the SF  $\leftrightarrow$  CB-SS is shifted only very slightly. This can be seen from the kink in  $\bar{n}_e$ , as shown in Fig. 9(b) and its inset.  $f$  also experiences only minor deviations, which have a maximum around  $J/\Omega \approx 1.3$ , as shown in the inset of Fig. 9(d). We therefore conclude that our results can be considered converged with respect to the Fock-space cutoff.

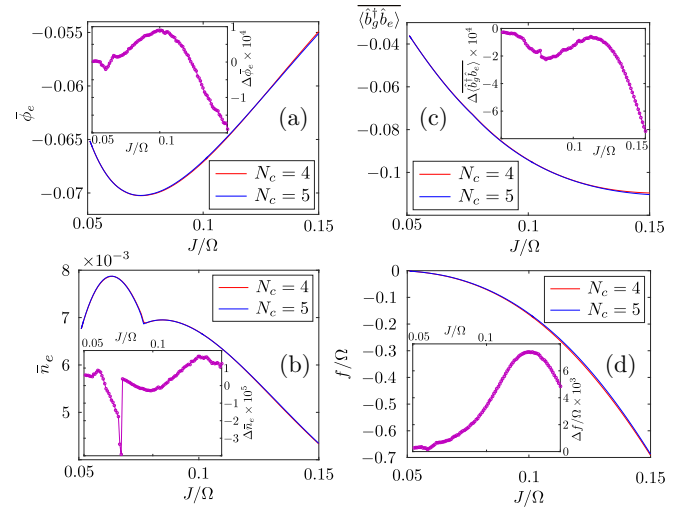


FIG. 9. The lattice-averaged observables (a)  $\bar{\phi}_e$ , (b)  $\bar{n}_e$ , and (c)  $\langle \hat{b}_g^\dagger \hat{b}_e \rangle$  as functions of  $J/\Omega$  for  $\Delta/\Omega = -0.8$ , with the remaining parameters as in Fig. 5 and with a truncation scheme as given in the legends. (d) The lattice-averaged grand-canonical potential  $f$ . All the insets depict each deviation for the two truncation schemes,  $N_c = 5$  and  $N_c = 4$  (the latter subtracted from the former).

- [1] I. Bloch and W. Zwerger, *Rev. Mod. Phys.* **80**, 885 (2008).
- [2] T. Lahaye, T. Koch, B. Fröhlich, M. Fattori, J. Metz, A. Griesmaier, S. Giovanazzi, and T. Pfau, *Nature (London)* **448**, 672 (2007).
- [3] M. A. Baranov, M. Dalmonte, G. Pupillo, and P. Zoller, *Chem. Rev.* **112**, 5012 (2012).
- [4] M. Saffman, T. G. Walker, and K. Mølmer, *Rev. Mod. Phys.* **82**, 2313 (2010).
- [5] H. Weimer, R. Löw, T. Pfau, and H. P. Büchler, *Phys. Rev. Lett.* **101**, 250601 (2008).
- [6] J. Honer, H. Weimer, T. Pfau, and H. P. Büchler, *Phys. Rev. Lett.* **105**, 160404 (2010).
- [7] N. Malossi, M. M. Valado, S. Scotto, P. Huillery, P. Pillet, D. Ciampini, E. Arimondo, and O. Morsch, *Phys. Rev. Lett.* **113**, 023006 (2014).
- [8] H. Schempp, G. Günter, M. Robert-de-Saint-Vincent, C. S. Hofmann, D. Breyel, A. Komnik, D. W. Schönleber, M. Gärttner, J. Evers, S. Whitlock, and M. Weidemüller, *Phys. Rev. Lett.* **112**, 013002 (2014).
- [9] T. Niederprüm, O. Thomas, T. Manthey, T. M. Weber, and H. Ott, *Phys. Rev. Lett.* **115**, 013003 (2015).
- [10] J. Zeiher, P. Schauß, S. Hild, T. Macrì, I. Bloch, and C. Gross, *Phys. Rev. X* **5**, 031015 (2015).
- [11] T. M. Weber, M. Hönig, T. Niederprüm, T. Manthey, O. Thomas, V. Guarrera, M. Fleischhauer, G. Barontini, and H. Ott, *Nat. Phys.* **11**, 157 (2015).
- [12] G. Günter, H. Schempp, M. Robert-de Saint-Vincent, V. Gavryusev, S. Helmrich, C. S. Hofmann, S. Whitlock, and M. Weidemüller, *Science* **342**, 954 (2013).
- [13] V. Bendkowsky, B. Butscher, J. Nipper, J. P. Shaffer, R. Löw, and T. Pfau, *Nature (London)* **458**, 1005 (2009).
- [14] P. Schauß, M. Cheneau, M. Endres, T. Fukuhara, S. Hild, A. Omran, T. Pohl, C. Gross, S. Kuhr, and I. Bloch, *Nature (London)* **491**, 87 (2012).
- [15] P. Schauss, J. Zeiher, T. Fukuhara, S. Hild, M. Cheneau, T. Macrì, T. Pohl, I. Bloch, and C. Gross, *Science* **347**, 1455 (2015).
- [16] B. Vermersch, M. Punk, A. W. Glaetzle, C. Gross, and P. Zoller, *New J. Phys.* **17**, 013008 (2015).
- [17] T. Pohl, E. Demler, and M. D. Lukin, *Phys. Rev. Lett.* **104**, 043002 (2010).
- [18] I. Lesanovsky and J. P. Garrahan, *Phys. Rev. A* **90**, 011603 (2014).
- [19] J. Schachenmayer, I. Lesanovsky, A. Micheli, and A. J. Daley, *New J. Phys.* **12**, 103044 (2010).
- [20] B. Capogrosso-Sansone, C. Trefzger, M. Lewenstein, P. Zoller, and G. Pupillo, *Phys. Rev. Lett.* **104**, 125301 (2010).
- [21] J. E. Johnson and S. L. Rolston, *Phys. Rev. A* **82**, 033412 (2010).
- [22] G. Pupillo, A. Micheli, M. Boninsegni, I. Lesanovsky, and P. Zoller, *Phys. Rev. Lett.* **104**, 223002 (2010).
- [23] F. Cinti, P. Jain, M. Boninsegni, A. Micheli, P. Zoller, and G. Pupillo, *Phys. Rev. Lett.* **105**, 135301 (2010).
- [24] S. Wüster, C. Ates, A. Eisfeld, and J. M. Rost, *New J. Phys.* **13**, 073044 (2011).
- [25] X. Li, W. V. Liu, and C. Lin, *Phys. Rev. A* **83**, 021602 (2011).
- [26] J. B. Balewski, A. T. Krupp, A. Gaj, S. Hofferberth, R. Löw, and T. Pfau, *New J. Phys.* **16**, 063012 (2014).
- [27] Y.-Y. Jau, A. M. Hankin, T. Keating, I. H. Deutsch, and G. W. Biedermann, *Nat. Phys.* **12**, 71 (2015).

- [28] J. Zeiher, R. v. Bijnen, P. Schauß, S. Hild, J.-y. Choi, T. Pohl, I. Bloch, and C. Gross, *Nat. Phys.* **12**, 1095 (2016).
- [29] K. Saha, S. Sinha, and K. Sengupta, *Phys. Rev. A* **89**, 023618 (2014).
- [30] E. Sela, M. Punk, and M. Garst, *Phys. Rev. B* **84**, 085434 (2011).
- [31] H. Weimer and H. P. Büchler, *Phys. Rev. Lett.* **105**, 230403 (2010).
- [32] C. Cohen-Tannoudji, J. Dupont-Roc, and G. Grynberg, *Atom-Photon Interactions: Basic Process and Applications* (Wiley-VCH, Weinheim, 2004).
- [33] F. Robicheaux and J. V. Hernández, *Phys. Rev. A* **72**, 063403 (2005).
- [34] S. K. Dutta, J. R. Guest, D. Feldbaum, A. Walz-Flannigan, and G. Raithel, *Phys. Rev. Lett.* **85**, 5551 (2000).
- [35] K. C. Younge, B. Knuffman, S. E. Anderson, and G. Raithel, *Phys. Rev. Lett.* **104**, 173001 (2010).
- [36] K. C. Younge, S. E. Anderson, and G. Raithel, *New J. Phys.* **12**, 023031 (2010).
- [37] B. Misra and E. C. G. Sudarshan, *J. Math. Phys.* **18**, 756 (1977).
- [38] J. J. García-Ripoll, S. Dürr, N. Syassen, D. M. Bauer, M. Lettner, G. Rempe, and J. I. Cirac, *New J. Phys.* **11**, 013053 (2009).
- [39] I. Vidanović, D. Cocks, and W. Hofstetter, *Phys. Rev. A* **89**, 053614 (2014).
- [40] A. Lauer, D. Muth, and M. Fleischhauer, *New J. Phys.* **14**, 095009 (2012).
- [41] L. Rademaker, Y. Pramudya, J. Zaanen, and V. Dobrosavljević, *Phys. Rev. E* **88**, 032121 (2013).
- [42] A. Geißler and W. Hofstetter, [arXiv:1611.10185](https://arxiv.org/abs/1611.10185).
- [43] I. Vasić, A. Petrescu, K. L. Hur, and W. Hofstetter, *Phys. Rev. B* **91**, 094502 (2015).
- [44] T. E. Lee, H. Häffner, and M. C. Cross, *Phys. Rev. Lett.* **108**, 023602 (2012).
- [45] C. Carr, R. Ritter, C. G. Wade, C. S. Adams, and K. J. Weatherill, *Phys. Rev. Lett.* **111**, 113901 (2013).
- [46] M. Marcuzzi, E. Levi, S. Diehl, J. P. Garrahan, and I. Lesanovsky, *Phys. Rev. Lett.* **113**, 210401 (2014).



# Phase transitions of the coherently coupled two-component Bose gas in a square optical lattice

Ulrike Bornheimer,<sup>1,2,3</sup> Ivana Vasić,<sup>4</sup> and Walter Hofstetter<sup>3</sup>

<sup>1</sup>Centre for Quantum Technologies, National University of Singapore, 3 Science Drive 2, 117543 Singapore

<sup>2</sup>MajuLab, CNRS-UNS-NUS-NTU International Joint Research Unit, UMI 3654, Singapore

<sup>3</sup>Institut für Theoretische Physik, Goethe-Universität Frankfurt am Main, Max-von-Laue-Straße 1, 60438 Frankfurt am Main, Germany

<sup>4</sup>Scientific Computing Laboratory, Center for the Study of Complex Systems, Institute of Physics Belgrade, University of Belgrade, Pregrevica 118, 11080 Belgrade, Serbia

(Received 16 May 2017; published 28 December 2017)

We investigate properties of an ultracold, two-component bosonic gas in a square optical lattice at unit filling. In addition to density-density interactions, the atoms are subject to coherent light-matter interactions that couple different internal states. We examine the influence of this coherent coupling on the system and its quantum phases by using Gutzwiller mean-field theory as well as bosonic dynamical mean-field theory. We find that the interplay of strong interspecies repulsion and coherent coupling affects the Mott insulator to superfluid transition and shifts the tip of the Mott lobe toward higher values of the tunneling amplitude. In the strongly interacting Mott regime, the resulting Bose-Hubbard model can be mapped onto an effective spin Hamiltonian that offers additional insights into the observed phenomena.

DOI: [10.1103/PhysRevA.96.063623](https://doi.org/10.1103/PhysRevA.96.063623)

## I. INTRODUCTION

Due to their highly controllable properties, systems of ultracold atoms are promising platforms for quantum simulations. One of the early successes in this direction was the observation of a superfluid-Mott insulator transition in a lattice Bose gas [1,2], as a prototype of a quantum phase transition. With recent advances in experimental techniques, present-day cold-atom experiments feature finite-range interactions, for example, in Rydberg dressed systems [3,4], as well as artificial gauge potentials that mimic magnetic fields [5,6]. All these achievements bring these setups closer to simulating complex condensed-matter systems.

Multicomponent systems, such as mixtures of different atoms or different hyperfine states of the same atomic species, introduce additional degrees of freedom that can be treated as pseudospin. In the weakly interacting limit, depending on the ratio of intracomponent and intercomponent interactions, two-component mixtures may exhibit phase separation [7]. The process of phase separation is substantially altered by introducing a coherent coupling term that enables a conversion of one internal atomic state into the other [8–19].

The binary bosonic mixtures in deep optical lattices [20–22] realize the two-component Bose-Hubbard model that hosts a rich phase diagram [23,24]. Despite intense experimental and theoretical efforts in the past two decades, there are many open questions related to the properties of bosonic mixtures in the strongly interacting regime. The demixing transition [25,26] and effects of the coherent coupling [27–29] have been addressed only recently in this regime of strong repulsive interactions in lattice models.

In this paper we investigate the phase diagram of a two-component Bose gas on a square lattice subject to coherent coupling between the two species. The interest in the properties of a two-dimensional coherently coupled system is both practical, as these systems are experimentally available, and conceptual with respect to the results for the related one-dimensional system [27,28]. It is well known that quantum fluctuations play a decisive role in low-dimensional models, such that continuous symmetries cannot be broken

for homogeneous one-dimensional systems and no long-range order can form. Furthermore, mean-field approaches are inapplicable in one dimension, and their accuracy increases with higher dimensions. Specifically, in the case that we study, a simple mean-field treatment might rule out one of the phases found in recent studies of one-dimensional lattice systems [27,28]. Thus, properties of a two-dimensional system require a separate study that we present in the following sections.

The remainder of the paper is organized as follows: In the next section we introduce the main model of our study and briefly outline the methods that we use throughout the paper. In Sec. III we address the case of finite bosonic coherences. In particular, we examine the neutral to polarized phase transition on top of the underlying condensate. The results for the case of stronger local interactions that lead to the superfluid-Mott transition with coherent coupling are presented in Sec. IV. The case of imbalanced hopping amplitudes is the subject of Sec. V. Finally, our main conclusions are summarized in Sec. VI.

## II. MODEL AND METHODS

We investigate the phase diagram of an extended Hubbard model describing a two-component Bose gas in a square optical lattice with an additional coherent coupling term. In second quantization the model explicitly reads

$$\begin{aligned} \hat{H}_{BH} = & - \sum_{(i,j)}^L (t_a \hat{a}_i^\dagger \hat{a}_j + t_b \hat{b}_i^\dagger \hat{b}_j + \text{H.c.}) \\ & + \frac{1}{2} \sum_i^L [U_a \hat{n}_{ia} (\hat{n}_{ia} - 1) + U_b \hat{n}_{ib} (\hat{n}_{ib} - 1)] \\ & + \sum_i^L (U_{ab} \hat{n}_{ia} \hat{n}_{ib} - \Omega \hat{a}_i^\dagger \hat{b}_i + \text{H.c.}), \end{aligned} \quad (1)$$

where  $\hat{a}_i^{(\dagger)}$  and  $\hat{b}_i^{(\dagger)}$  are the annihilation (creation) operators for bosonic species  $a$  and  $b$ , respectively, and  $\hat{n}_{ia}$  and  $\hat{n}_{ib}$  are their number operators. The tight-binding hopping amplitudes of

the respective species are denoted as  $t_a$  and  $t_b$ , and  $U_a$  and  $U_b$  are their on-site interaction. Interactions are generally assumed to be local and repulsive in this study. An on-site interaction between particles of different species is designated as  $U_{ab}$ , and the term proportional to  $\Omega$  allows for the conversion of one bosonic species into another on the same site. This last term is called the coherent coupling term. Local terms in the Hubbard Hamiltonian are summed over lattice sites  $1, \dots, L$ , and in the first term  $\langle i, j \rangle$  stands for the sum over all nearest-neighbor sites  $i$  and  $j$  of the square lattice. Throughout the paper we will consider the case of  $U_a = U_b = U$  and we set all scales by fixing  $U = 1$ . Our aim in this paper is to investigate possible ground states of the model (1).

Multicomponent bosonic systems are usually realized as mixtures of two hyperfine states of a single element. One of first experiments used sympathetically cooled  $|F = 1, m_f = -1\rangle$  and  $|F = 2, m_f = 2\rangle$  hyperfine states of  $^{87}\text{Rb}$  [30] for the realization of a spinor Bose-Einstein condensate. In a subsequent study [8], coherent coupling between two condensates of hyperfine states of  $^{87}\text{Rb}$  gas was implemented as a two-photon transition. The authors were able to transfer the complete population of the  $|F = 1, m_f = -1\rangle$  state of  $^{87}\text{Rb}$  to the  $|F = 2, m_f = 1\rangle$  state using a combination of radio frequency and a microwave field in an abrupt way, compared to the other time scales of the system. The choice of hyperfine states was motivated by the fact that the two states feel nearly identical confining potentials, can be conveniently coherently coupled and imaged selectively. In the more recent study [9], a very similar setup has been exploited to explore the Josephson effect through the measurement of the full time dynamics of spinor condensates. The mixing and demixing dynamics in the presence of coherent coupling of the two  $^{87}\text{Rb}$  states was experimentally addressed in Ref. [10].

In present-day experiments, coherent conversion is a very useful tool that expands a pool of phenomena that can be addressed in cold-atom experiments. For example, in order to introduce long-range interactions in cold-atom samples, a coherent coupling of a ground-state atom with a Rydberg excited state is used [3,31]. An application and detailed derivation of the coherent coupling term in the context of Rydberg dressing is given in a recent paper [32]. As another notable example we mention the recent realization of artificial gauge fields [5] in synthetic dimensions, which is directly based on a specially tailored coherent coupling of several internal atomic states [33,34].

It is well known that by reducing the ratio of the tunneling amplitude  $t_{a,b}$  over the repulsive interaction strength  $U$  at commensurate lattice filling, bosons exhibit a superfluid to Mott insulator transition [2,35]. On top of this, an effective magnetic ordering emerges on the Mott side in two-component bosonic mixtures [23,24]. These results are typically obtained for  $\Omega = 0$  in the regime of  $\gamma \leq 1$ , where we introduce the ratio between inter- and intraspecies interaction  $\gamma = U_{ab}/U$ . In the opposite case of  $\gamma \geq 1$ , it is energetically favorable for the two bosonic species to be spatially separated [7]. However, a finite  $\Omega$  will suppress this tendency by enabling a conversion between the two species. In this way, it allows us to address the regime  $\gamma > 1$ . Note that the model (1) conserves only the total number of particles and not the particle numbers of each species separately. In the limiting case  $\gamma \gg 1$ , only atoms of

one species are present as the system avoids the high energy cost of  $U_{ab}$ .

This reasoning already suggests that in addition to the well-understood superfluid to Mott phase transition, for the model (1) we are able to distinguish another phase transition characterized by the polarization order parameter,

$$\tilde{n}_i = \frac{\langle \hat{n}_{ia} \rangle - \langle \hat{n}_{ib} \rangle}{\langle \hat{n}_{ia} \rangle + \langle \hat{n}_{ib} \rangle}. \quad (2)$$

A strong interspecies interaction  $U_{ab}$  favors a polarized phase with finite  $\tilde{n}_i$ . In contrast, the  $\Omega$  term favors strong local coherence  $\langle a_i^\dagger b_i + b_i^\dagger a_i \rangle$  that corresponds to a neutral phase with  $\tilde{n}_i = 0$ . To establish boundaries between different phases as a function of the physical parameters of the Hamiltonian (1), we will use two approximate methods that we briefly outline here.

Features of the lattice Bose gas can be explored conveniently by means of the Gutzwiller mean-field theory [36,37], which amounts to decoupling nonlocal terms as

$$\hat{a}_i^\dagger \hat{a}_j \approx \phi_i^* \hat{a}_j + \phi_j \hat{a}_i^\dagger - \phi_i^* \phi_j, \quad (3)$$

where  $\phi_i^{(*)} = \langle \hat{a}_i^{(\dagger)} \rangle$  is a condensate order parameter that is obtained in a self-consistent way. The approximation becomes an exact description in several limits: in the limit of infinite lattice coordination number  $z$ , in the atomic limit ( $t = 0$ ); and in the weakly interacting limit, in the superfluid phase. However, for a vanishing condensate order parameter the lattice sites are completely decoupled within Gutzwiller mean-field theory and the description of the Mott domain is oversimplified. In order to go beyond this limitation, we will use bosonic dynamical mean field theory (BDMFT) [38–42].

Formally, BDMFT is derived as a second-order expansion of the full model (1) in terms of the inverse lattice coordination number. In comparison to Gutzwiller mean-field theory, we increase the order of the expansion by one [43]. The approximate effective problem obtained in this way is given by a bosonic Anderson impurity model. Parameters of the effective model are set by imposing a self-consistency in terms of the condensate order parameter and the local Green's function. The effective bosonic Anderson impurity model is solved using exact diagonalization. The main approximation of the method is the assumption of the locality of self-energies, which is consistent with the second-order expansion in the inverse of the coordination number [43,44]. The method captures local correlations exactly but treats nonlocal correlations at the mean-field level. In order to consider states that break translational symmetries, we use real-space BDMFT [41] in this paper. We address a lattice size of  $6 \times 6$  with periodic boundary conditions, with a special focus on a possible two-sublattice ordering. By performing additional calculations for larger lattices, we estimate finite-size effects on the transition points of our phase diagrams to be of the order 2% in relative units.

Both the Gutzwiller mean-field theory and BDMFT are implemented in the grand-canonical ensemble. To this end, we introduce a single chemical potential  $\mu$ ,  $\hat{H}_{BH} \rightarrow \hat{H}_{BH} - \mu \sum_i^L (\hat{a}_i^\dagger \hat{a}_i + \hat{b}_i^\dagger \hat{b}_i)$ , as the model (1) conserves only the total number of particles. In the next sections we present and discuss

results for the different ground states of model (1), obtained by using these approaches.

### III. THE SUPERFLUID REGIME

In this section we present the Gutzwiller analysis of the coherently coupled spinor Bose gas in the superfluid phase. In order to address states with a finite condensate fraction, we choose relatively high tunneling amplitudes  $t_a/U = t_b/U = 1/4$ . As the neutral to polarized phase transition is driven by the strong intercomponent interactions  $U_{ab}$ , we plot the polarization order parameter  $\tilde{n}_i$ , defined in Eq. (2), over the ratio  $\gamma = U_{ab}/U$  in Fig. 1(a).

Results for the model (1) without coherent coupling are plotted for reference (red solid line), and the transition from  $\tilde{n}_i = 0$  to  $|\tilde{n}_i| = 1$  is found at  $\gamma_c = 1$ . We understand from previous works that it is energetically favorable to have components of both species on each lattice site only in the case of weak interspecies repulsion. Strong interspecies repulsion leads to the polarized phase, where only particles of one species can be found on a single lattice site. For fixed atom densities the system will thus undergo phase separation. We notice that positive and negative values of  $\langle \hat{n}_{a,i} \rangle - \langle \hat{n}_{b,i} \rangle$  ( $\tilde{n}_i = \pm 1$ ) appear equally as results of numerical calculations with different initial conditions. This indicates two degenerate ground states in the polarized phase, as we will confirm in the following. In these calculations, initial parameters of the self-consistent loop or root search routines determine which of the ground states is selected, whereas in actual experiments the occurrence probabilities for both ground states are equal.

We now turn to the effects of a finite coherent coupling term and set  $\Omega/U = 0.1$ . While the polarization order parameter changes abruptly for vanishing coherent coupling [red solid line in Fig. 1(a)], it exhibits a continuous change for finite coherent coupling [blue dashed line in Fig. 1(a)]. Moreover, we notice that the coherent coupling shifts the transition point  $\gamma_c$  to higher values of the interspecies interaction. The same qualitative behavior was reported in Refs. [16,28] in the quasi-one-dimensional geometry for the regime of weak interactions, both with and without a lattice. Within Gross-Pitaevskii theory, it was found analytically that the polarized phase sets in at  $U_{ab}^c = U_{a,b} + 2\Omega/n$ . For the parameters given in Fig. 1, this relation yields a transition point at  $\gamma_c = 1.2$ . However, since the mentioned derivation is strictly valid only in the weakly interacting limit, where all bosons are condensed, the phase transition in Fig. 1 is expected to appear at a slightly different value of  $\gamma$ . In particular, we find that as the ratio  $t/U$  is lowered further, the transition point between the polarized and neutral phase is shifted in favor of the neutral phase. The region of the neutral phase extends toward higher values of  $\gamma$  and deviations with respect to the result obtained in the weakly interacting limit become more pronounced. This effect is further explored in the next section.

The observation of discontinuities in the polarization order parameter [Fig. 1(a)] draws our attention to the order of the observed phase transitions. We analyze this in Figs. 1(c) and 1(d), where the grand potential and its first derivative are plotted as functions of  $\gamma$ . As we use the grand-canonical description at zero temperature and explicitly include the chemical potential term, the grand potential is given by the

expectation value of our mean-field Hamiltonian. For  $\Omega = 0$ , we find that the first derivative of the grand potential is discontinuous at  $\gamma_c$ . This leads us to the conclusion that the neutral to polarized phase transition is of first order for  $\Omega = 0$ . In contrast, we observe a cusp in the same derivative for finite  $\Omega$ , implying that the phase transition is of second order.

To explore this in more detail, we plot the lowest energy eigenvalue of the mean-field Hamiltonian as a function of the condensate order parameters in Figs. 2 and 3 (left series). In both cases, for vanishing and for finite  $\Omega$ , we find a single energy minimum for the neutral phase at  $\gamma < \gamma_c$  [see Figs. 2(a1) and 3(a1)]. The condensate order parameters  $\phi_a$  and  $\phi_b$  corresponding to this minimum are equal. In the polarized regime for  $\gamma > \gamma_c$ , however, two degenerate energy minima are present [Figs. 2(a4) and 3(a4)]. The degeneracy stems from the fact that the ground state breaks the symmetry between the two species, while the Hamiltonian is symmetric with respect to the interchange of these two species. In the polarized phase with  $\Omega = 0$ , the condensate order parameter of one of the species is strictly zero, while the other one has a finite value. In contrast, both order parameters are finite but nonequal at finite values of  $\Omega$ , as also shown in Fig. 1(b).

Having established the properties of the neutral and polarized phase, we now discuss the transition between them.

For  $\Omega = 0$  and  $\gamma = \gamma_c$ , we find an infinitely degenerate energy minimum for constant  $\sqrt{\phi_a^2 + \phi_b^2}$ . In the vicinity of the transition point, a single minimum at  $\phi_a = \phi_b$  for  $\gamma < \gamma_c$  abruptly transforms into two minima found at “distant” positions in the  $\phi$  space for  $\gamma > \gamma_c$ . The lowest eigenvalue of the Gutzwiller mean-field Hamiltonian plotted along the unit density line over  $\alpha = \arctan(\phi_a/\phi_b)$  (right series of Fig. 2) provides the reason for that. The energy has a parabolic shape at around  $\alpha = 45^\circ$ . The coefficient of this parabola changes from being positive in the neutral phase, which results in a minimum at  $\alpha = 45^\circ$ , to being negative in the polarized phase, which results in two well-separated minima at  $\alpha = 0^\circ, 90^\circ$ .

At finite  $\Omega$ , we do not find an abrupt change in the minima at the transition point. The neutral minimum at  $\phi_a = \phi_b$  splits into two degenerate minima that evolve towards their final values with increasing  $\gamma$ . Accordingly, the energy plot along the unity density line (right series, Fig. 3) is not a parabola that simply flips the sign of its coefficient, but one that develops a bump at  $\alpha = 45^\circ$  and thus gradually shifts its minima away from that point.

### IV. SUPERFLUID-MOTT TRANSITION

Strong on-site interactions suppress density fluctuations and deplete the condensate. At commensurate densities, this mechanism drives a transition from a superfluid into a Mott insulator state. In this section we map out the phase diagram of the model defined in Eq. (1) as a function of the tunneling amplitude  $t/U$  and coherent coupling  $\Omega/t$  by using BDMFT at zero temperature.

In the limit of vanishing coherent coupling  $\Omega \rightarrow 0$ , for  $\gamma > 1$  (interspecies interaction stronger than intraspecies interaction) our BDMFT simulations, implemented in the grand-canonical ensemble, recover the well-known results for the Mott insulator to superfluid transition for a single bosonic

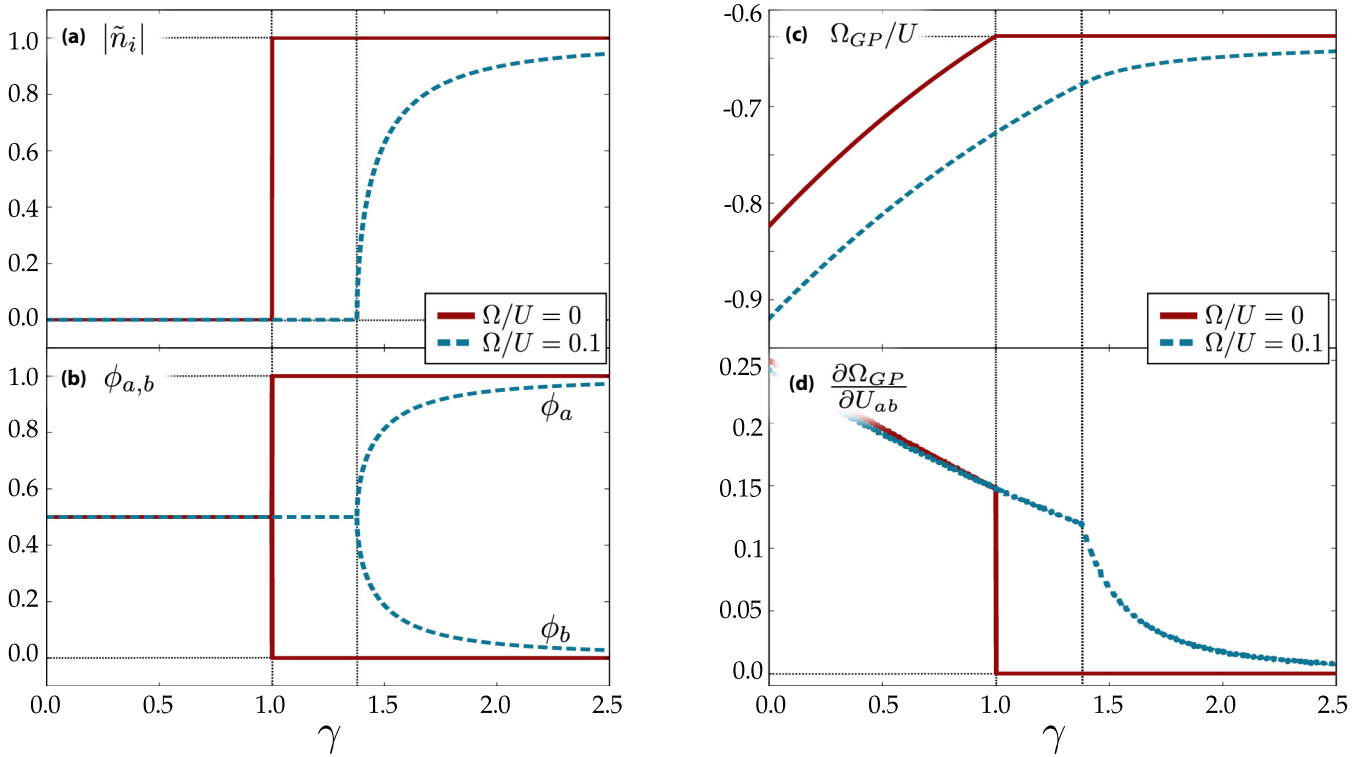


FIG. 1. (a) Absolute value of the polarization order parameter  $|\tilde{n}_i|$  defined in Eq. (2), (b) condensate order parameters  $\phi_a$  and  $\phi_b$ , (c) lowest eigenvalue of the mean-field Hamiltonian  $\Omega_{GP}$ , which corresponds to the grand-canonical potential at zero temperature, and (d) its first derivative. These are plotted as a function of the dimensionless interaction ratio  $\gamma = U_{ab}/U$  for unit filling  $n_a + n_b = 1$  and hopping amplitudes  $t_a/U = t_b/U = 1/4$ .

species on a square lattice [39,45]. At finite  $\Omega$  and  $t = 0$  (the atomic limit) and at a total filling  $\langle n_{ai} + n_{bi} \rangle = 1$ , the ground state has no polarization. This can easily be seen by considering a single-site Hamiltonian in the subspace spanned by  $|1,0\rangle = a_i^\dagger|0\rangle$  and  $|0,1\rangle = b_i^\dagger|0\rangle$ , which is given by

$$\begin{pmatrix} -\mu & -\Omega \\ -\Omega & -\mu \end{pmatrix}. \quad (4)$$

The ground state is  $|\text{GS}\rangle = (|0,1\rangle + |1,0\rangle)/\sqrt{2}$  and it is neutral, since  $\langle \text{GS}|n_{ai} - n_{bi}|\text{GS}\rangle = 0$ . In the following we investigate a range of tunneling amplitudes  $t_a/U = t_b/U = t/U \in [0.001, 0.1]$  and coherent couplings  $\Omega/t \in [0, 1]$ . We scan phase diagrams spanned by  $t/U$  and  $\mu/U$  at fixed  $\Omega/t$  to access points with total unit filling, as shown in Fig. 4 for  $\gamma = 8/5$ .

We begin our analysis with a small fixed ratio  $\Omega/t$ . In Fig. 4(a) we present the absolute value of the polarization order parameter  $|\tilde{n}|$  [Eq. (2)] for  $\Omega/t = 0.12$ . Increasing the tunneling  $t/U$  from a starting point near the atomic limit, we encounter a transition from the neutral into the polarized state, before reaching the tip of the first Mott lobe. With further increase of  $t/U$ , we find a second transition from the polarized Mott state into the polarized condensate state [see Fig. 4(a)]. At stronger  $\Omega/t \geq 0.28$ , we find that the whole Mott lobe is neutral and around the tip of the lobe, we have a transition from the neutral Mott directly into the polarized superfluid. An example of this behavior is shown in Fig. 4(b). Finally, for  $\Omega/t > 0.44$ , there is a transition from the neutral Mott insulator into the neutral superfluid,

followed by a second transition from a neutral into a polarized superfluid state [see Fig. 4(c)]. The change in the polarization on the superfluid side of the diagrams as a function of the chemical potential  $\mu$  [Figs. 4(a)–4(c), a vertical cut] can be understood as follows: by increasing the chemical potential  $\mu$ , the total density increases (not explicitly shown in figures) and the enhanced contribution of repulsive interactions can overcome the effect of the coupling  $\Omega$  that favors a neutral state.

A complete phase diagram as a function of  $\Omega/t$  and  $t/U$  at unit filling obtained from the previous type of calculation is presented in Fig. 5(a). The color plot gives the polarization  $|\tilde{n}|$ , the black squares form a transition line between the polarized and unpolarized states, and gray circles show the Mott insulator (left part) to superfluid (right part) transition line. The two transition lines marking the Mott insulator to superfluid transition and those marking the neutral to polarized transition coincide in the intermediate region. The Mott region extends up to  $t/U \approx 0.06$  for a fully polarized Mott to polarized superfluid transition (weak  $\Omega/t$ ), which is very close to the result for the Mott-lobe tip in a single-component case. At strong  $\Omega/t$  we have a neutral Mott to neutral superfluid transition that takes place at a higher value of  $t/U \approx 0.074$ , as strong  $U_{ab}$  plays a more pronounced role in this case. In the horizontal cut shown in Fig. 5(b) we explicitly show that at weak  $\Omega/t$  there are two second-order phase transitions. These transitions merge into a single transition point with a jump in polarization  $|\tilde{n}|$  at intermediate  $\Omega/t$ , as shown in Fig. 5(c). At even stronger  $\Omega/t$ , we find two separate transitions of the second order again.



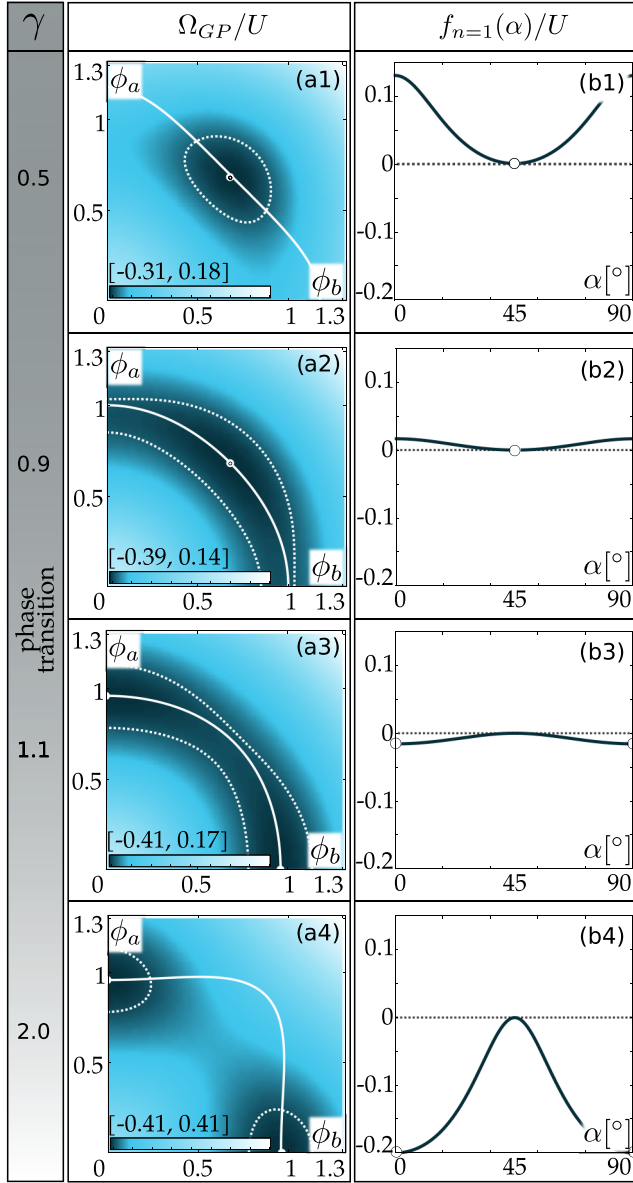


FIG. 2. Left series: Lowest energy eigenvalue  $\Omega_{GP}/U$  of the Gutzwiller mean-field Hamiltonian for  $\Omega/U = 0$  plotted versus the condensate order parameters  $\phi_a$  and  $\phi_b$ . White data points mark the position of the minimum, white solid lines mark unit density and white dashed lines the area of 0.02 around the minimum. Right series:  $\Omega_{GP}/U$  plotted along unit density lines (see white solid lines in left series) over the angle  $\alpha = \arctan(\phi_a/\phi_b)$ . Other Hamiltonian parameters are  $t_a/U = t_b/U = 1/4$  and  $\mu/U = 1$ .

In order to explain the neutral-polarized transition on the Mott side, we complement numerical BDMFT results with an insight obtained from an effective spin Hamiltonian, which is valid in the limit of strong interactions. The spin model is derived via second-order perturbation theory in the hopping amplitude and for unit filling. Starting from model (1), it is expressed in the pseudospin basis  $|\uparrow\rangle = |n_a = 1, n_b = 0\rangle$  and  $|\downarrow\rangle = |n_a = 0, n_b = 1\rangle$  [23,24,46]. Equivalently, one can also use the Schrieffer-Wolff transformation [47] to obtain the same

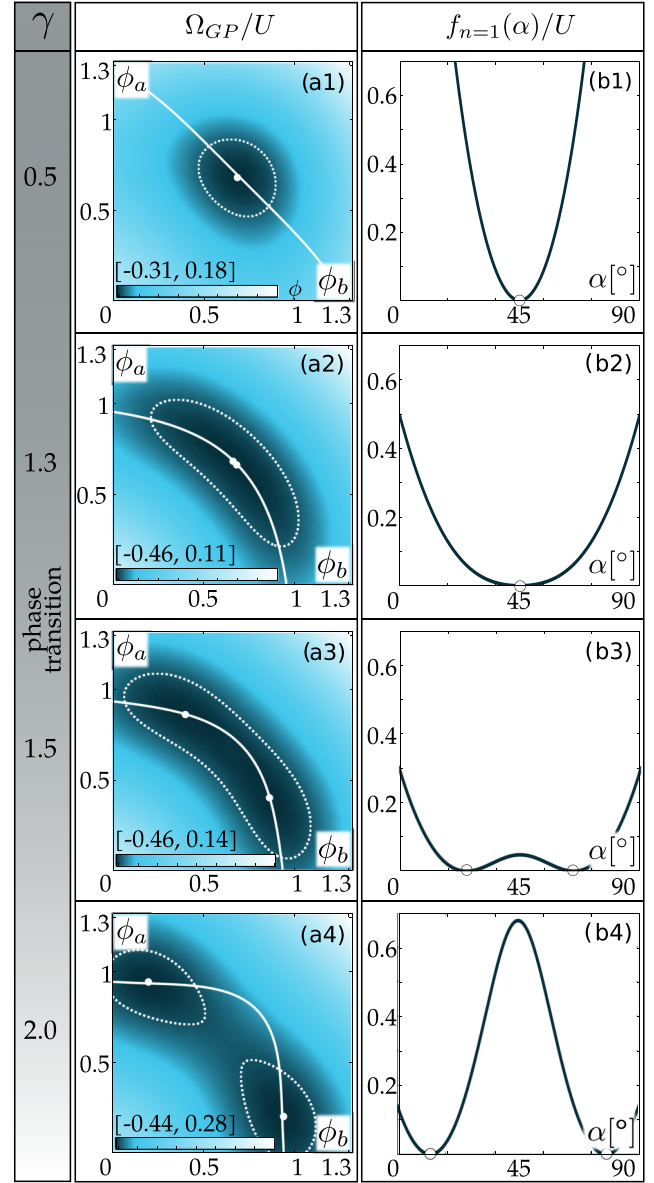


FIG. 3. Left series: Lowest energy eigenvalue  $\Omega_{GP}/U$  of the Gutzwiller mean-field Hamiltonian for  $\Omega/U = 0.1$  plotted versus the condensate order parameters  $\phi_a$  and  $\phi_b$ . White data points mark the position of the minimum, white solid lines mark unit density and white dashed lines the area of 0.02 around the minimum. Right series:  $\Omega_{GP}/U$  plotted along unit density lines (see white solid lines in left series) over the angle  $\alpha = \arctan(\phi_a/\phi_b)$ . Other Hamiltonian parameters are  $t_a/U = t_b/U = 1/4$  and  $\mu/U = 1$ .

effective Hamiltonian [27,28]:

$$\begin{aligned} \hat{H}_{\text{eff}} = & -J_{zz} \sum_{(i,j)} \hat{S}_i^z \hat{S}_j^z - J_{\perp} \sum_{(i,j)} (\hat{S}_i^x \hat{S}_j^x + \hat{S}_i^y \hat{S}_j^y) \\ & - J_z \sum_i \hat{S}_i^z - 2\Omega \sum_i \hat{S}_i^x, \end{aligned} \quad (5)$$

where we introduce  $\hat{S}_i^l = (1/2)(\hat{a}_i^\dagger, \hat{b}_i^\dagger)\sigma^l(\hat{a}_i, \hat{b}_i)$  using the Pauli matrices  $\sigma^l$  with  $l = x, y, z$ . For the parameters considered in this section ( $t_a/U = t_b/U = t/U$ ), the spin coupling constants simplify to  $J_{zz} = 4t^2(2\gamma - 1)/\gamma U$ ,  $J_{\perp} = 4t^2/\gamma U$ ,

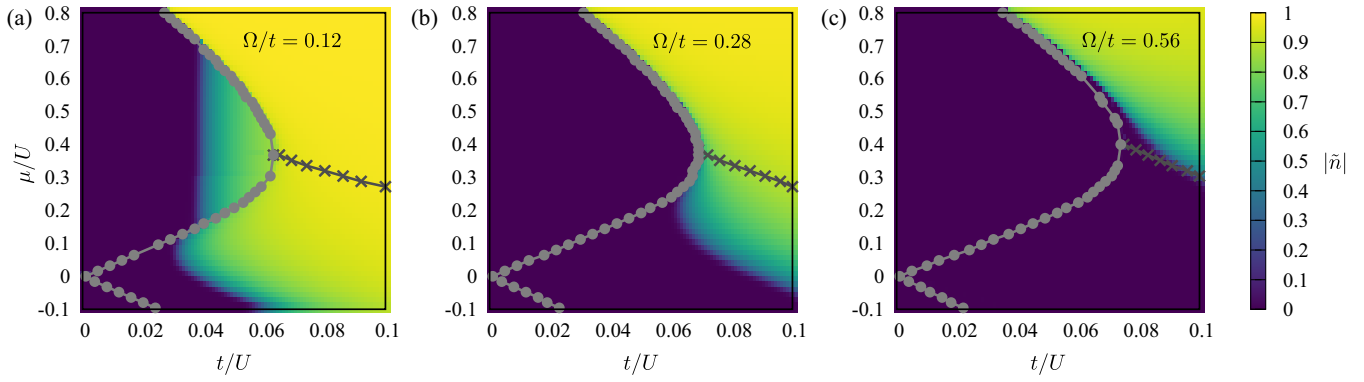


FIG. 4. Phase diagrams in the plane  $t/U$ - $\mu/U$  for  $\gamma = U_{ab}/U = 8/5$ . The color maps show the polarization  $|\bar{n}_i|$  defined in Eq. (2) for (a)  $\Omega/t = 0.12$ , (b)  $\Omega/t = 0.28$ , and (c)  $\Omega/t = 0.56$ . Dots show the Mott insulator to superfluid transition lines, and crosses mark lines of constant density  $\langle n_a + n_b \rangle = 1$  on the superfluid side.

and  $J_z = 0$ . Based on the model (5), in the strongly interacting limit of the Bose-Hubbard model with coherent coupling from Eq. (1), we expect to find different phases depending on the magnitude of the coefficients  $J_z$ ,  $J_{zz}$ ,  $J_\perp$ , and  $\Omega$ . In particular, the spin ordering along the  $z$  direction is equivalent to the finite polarization order parameter from Eq. (2), while spin alignment along the  $x$  direction corresponds to the neutral phase. At the transition line of the neutral and polarized phase we expect the spin couplings  $J_\perp$  and  $\Omega$ , that favor spin alignment in the  $x$  direction, to be comparable to the  $z$ -ordering term  $J_{zz}$ . This reasoning leads to an approximate condition for

the transition line

$$\frac{\Omega_c}{t} \propto \left(1 - \frac{1}{\gamma}\right) \frac{t}{U}. \quad (6)$$

We fit the numerical data according to this argumentation to  $\Omega_c/t \propto \alpha t/U$ , where  $\alpha$  is the fitting parameter [27]. For small  $t/U$ , we find  $\Omega_c/t \approx 3.2t/U$  for  $\gamma = 8/5$  (see Fig. 5) and  $\Omega_c/t \approx 2.15t/U$  for  $\gamma = 4/3$ . These fitting constants explicitly fulfill the  $(1 - 1/\gamma)$  dependence in Eq. (6).

## V. IMBALANCED HOPPING AMPLITUDES

Up to now we considered two fully equivalent bosonic components described by  $t_a = t_b$  and  $U_a = U_b = U$ . As a consequence, two degenerate solutions with  $\pm \bar{n}$  were found in the polarized regime. In this section we address a more general case of imbalanced hopping amplitudes  $t_a \neq t_b$ . This setting is experimentally available when two internal states of the same atomic species “perceive” different lattice depths, as in the so-called state-dependent optical lattices [22]. Moreover, the situation naturally occurs in Rydberg dressing [32] or in coherent coupling of atoms and molecules [48–50], where the two coupled states exhibit different properties.

We first investigate how the immobility of one bosonic component ( $t_b = 0$ ) affects the superfluid-Mott transition of the second coupled component. The BDMFT phase diagram in the  $t_a/U - \Omega/U$  plane at unit filling is presented in Fig. 6. We find that the imbalance in hopping amplitudes introduces a finite polarization  $\bar{n}$  and that the system is neutral only for  $t_a/U = 0$ . A finite polarization value on the Mott side of the diagram can be understood from the effective spin model defined in Eq. (5) that captures low-energy properties of the Hamiltonian (1) deep in the Mott domain. For the parameters considered in this section, the coefficients of the spin model (5) simplify to

$$J_{zz} = 2 \frac{t_a^2 + t_b^2}{U} \left(2 - \frac{1}{\gamma}\right), \quad (7)$$

$$J_z = 8 \frac{t_a^2 - t_b^2}{U}, \quad (8)$$

$$J_\perp = \frac{4t_a t_b}{\gamma U}, \quad (9)$$

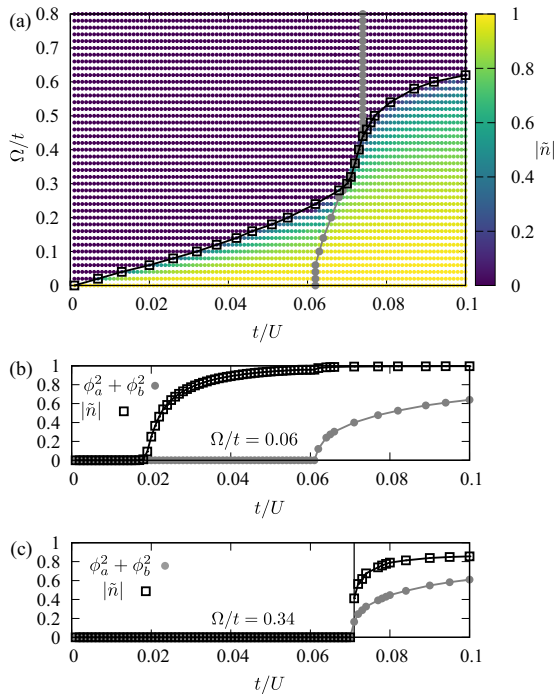


FIG. 5. (a) The phase diagram of the model at unit filling for  $\gamma = U_{ab}/U = 8/5$ . The color map shows the polarization  $|\bar{n}_i|$  defined in Eq. (2). Dots show the superfluid to Mott insulator transition line, and the squares give neutral to polarized transition line. Bottom plots: cuts through the phase diagram for (b)  $\Omega/t = 0.06$  and (c)  $\Omega/t = 0.34$ . Condensate order parameters and polarization  $|\bar{n}_i|$  are plotted as functions of  $t/U$  in (b) and (c).

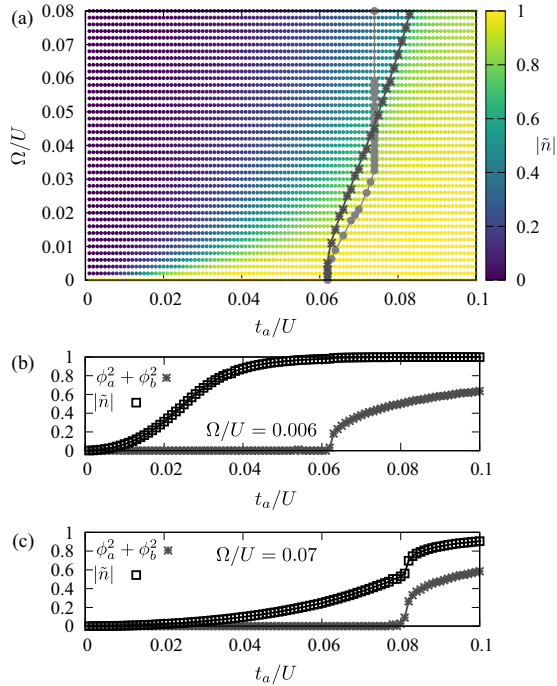


FIG. 6. (a) The phase diagram of the model at unit filling for  $\gamma = U_{ab}/U = 8/5$ ,  $t_b = 0$ . The color map shows the polarization  $|\tilde{n}|$  defined in Eq. (2). Stars show the superfluid to Mott insulator transition line for  $t_b = 0$ , and the dots give the same line for the balanced case  $t_a = t_b$ . Bottom plots: cuts through the phase diagram for (b)  $\Omega/U = 0.006$  and (c)  $\Omega/U = 0.07$ . Condensate order parameters and polarization  $|\tilde{n}|$  are plotted as functions of  $t_a/U$  in (b) and (c).

where we typically consider  $1 < \gamma < 2$ . According to Eq. (5), the coefficient  $J_z$  plays the role of an effective chemical potential that selects which of the two species is preferred in the polarized phase.

With an increase in the tunneling amplitude  $t_a/U$ , a transition from the polarized Mott state into the polarized superfluid state sets in, as shown in Figs. 6(b) and 6(c). As the coupling strength  $\Omega$  gets stronger, the transition points shown by star symbols in Fig. 6(a) are shifted toward higher values of  $t_a/U$ . In Fig. 6(a) we make a direct comparison of the transition lines obtained in the balanced ( $t_a = t_b$ ) and imbalanced ( $t_b = 0$ ) case. The two curves coincide at  $\Omega = 0$ , which corresponds to the fully polarized regime ( $\tilde{n} \approx 1$ ). As the tunneling imbalance favors polarization, for weak  $\Omega$  the superfluid transition occurs at smaller  $t_a/U$  in the imbalanced case in comparison to the balanced case. At stronger values of  $\Omega$ , as the contribution of immobile species gets stronger, we find the opposite effect: mixing with an immobile component reduces density fluctuations and as a result, we find that the Mott region extends well beyond the maximal value of  $t/U$  obtained in the balanced case. Additionally, we find that the coherent coupling introduces a finite condensate fraction of the immobile species in the region close to the transition boundary. However, for the parameter values that we have explored the effect is very weak.

We now investigate features of the Mott phase at unit filling for the case of imbalanced tunneling amplitudes in more detail. We consider both positive and negative tunneling matrix

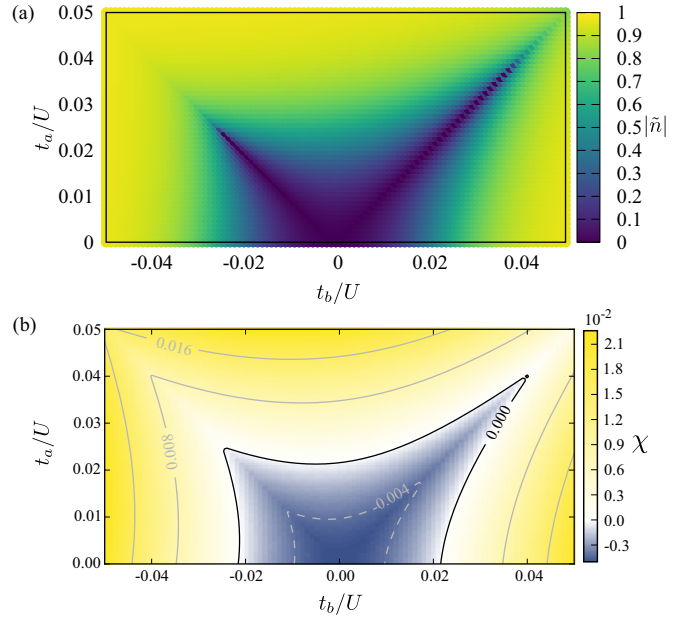


FIG. 7. (a) Absolute value of the polarization order parameter  $|\tilde{n}_i|$  in the  $t_a - t_b$  plane obtained by BDMFT. (b) Auxiliary function  $\chi$  defined in Eq. (10). Parameters:  $\gamma = U_{ab}/U = 8/5$ ,  $\mu = 0.2U_{ab}$ ,  $\Omega/U = 5 \times 10^{-3}$ .

elements. The tunneling matrix elements of the Bose-Hubbard model (1) can be controlled by periodic shaking [51,52]  $\hat{H}_{ps} = K \cos(\omega t) \sum_j j \hat{n}_j$ . Within Floquet theory, this type of shaking creates a Floquet spectrum with an effective hopping  $t_{\text{eff}} = t \mathcal{J}_0(K/\omega)$ , where  $\mathcal{J}_0$  is the Bessel function. Experimentally, this type of driving is realized by sinusoidally detuning the counterpropagating laser beams that constitute the optical lattice [53,54]. The effective hopping  $t_{\text{eff}}$  was measured by analyzing the expansion behavior of the condensate along this optical lattice, and it was found that up to  $K/\omega \approx 6$ , the data is in good agreement with the Bessel function renormalization of  $t_{\text{eff}}$  [53]. In the region between  $2.4 < K/\omega < 5.5$ , the Bessel function is negative  $\mathcal{J}_0(K/\omega) < 0$  and thus the effective hopping  $t_{\text{eff}}$  has an inverted sign. This corresponds to an inverted curvature of the respective energy band and the interference pattern from the time-of-flight analysis is shifted by half a Brillouin zone.

In Fig. 7(a) we present the absolute value of the polarization order parameter  $|\tilde{n}|$  as a function of tunneling rates  $t_a$  and  $t_b$ . Other parameters of the Hamiltonian (1) are set to  $\gamma = U_{ab}/U = 8/5$ ,  $\Omega/U = 5 \times 10^{-3}$ , and  $U_a = U_b = U$ . We limit ourselves to small absolute values of the ratios  $|t_a|/U$  and  $|t_b|/U$  and unit filling  $\langle n_a + n_b \rangle = 1$ , so that the system is in the Mott phase. Low values of the polarization are found for very weak tunneling amplitudes, in the region given by  $|t_{a,b}| < t_c$ , where we have  $t_c/U \approx 2.5 \times 10^{-3}$  for the data shown in Fig. 7. Along the diagonals  $t_a = \pm t_b$ , the neutral phase with  $\tilde{n} = 0$  extends up to the largest values of  $t_a$  and  $t_b$ . We notice a clear difference in the extension of the neutral phase for the case of  $t_a = t_b$  in comparison with the case of  $t_a = -t_b$ .

In order to explain the features observed in Fig. 7(a), we use the effective spin model defined in Eq. (5) that captures low-energy properties of the Hamiltonian (1) deep in the Mott

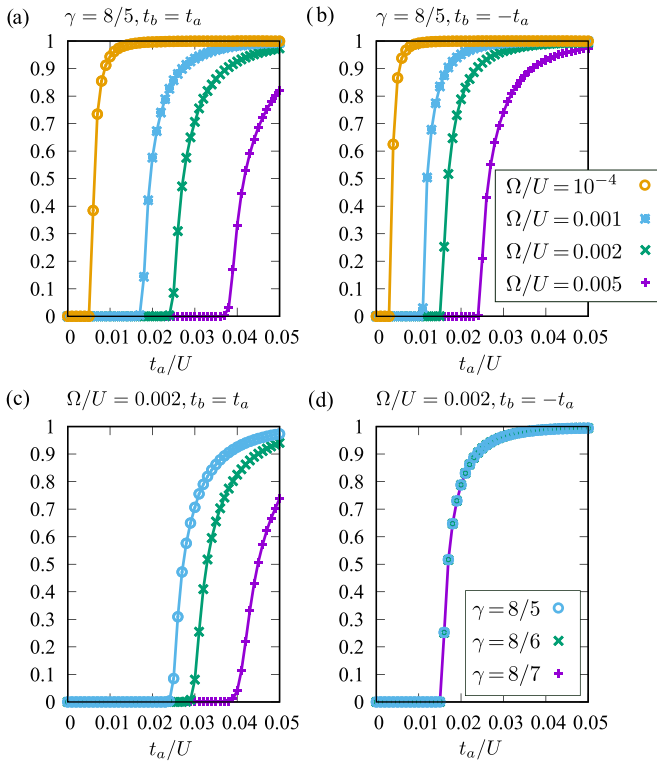


FIG. 8. Absolute value of the polarization order parameter  $|\tilde{n}_i|$  as a function of the hopping amplitude for  $t_b = t_a$  (left column) and  $t_b = -t_a$  (right column). Parameters:  $\mu = 0.2U_{ab}$ , (a), (b)  $\gamma = 8/5$ , (c), (d)  $\Omega/U = 0.002$ . In the two top plots (a) and (b), the value of the coherent coupling term is varied. In the two bottom plots, (c) and (d), we vary the value of  $\gamma$ . For  $t_a = -t_b$  we find that our results do not depend on the value of  $\gamma$ .

domain. We notice that  $J_{zz}$  increases quadratically both with  $t_a$  and  $t_b$ , which leads to the largest increment in this spin coupling term isotropically around  $t_a = t_b = 0$ . In contrast,  $J_z$  depends on the difference of the square of both hopping amplitudes and exhibits the strongest increase perpendicular to the diagonals  $t_a = \pm t_b$ . In our analysis, the value of  $\Omega$  is kept constant. Thus, it is the dominant quantity in the region around  $t_{a,b} \approx 0$  where all other spin couplings (7)–(9) are weak and where we find the neutral phase accordingly. The asymmetry between the negative and positive side of  $t_a$  in the plot shown in Fig. 7(a) arises due to the  $J_\perp$  coupling. For hopping amplitudes of the same sign, the  $J_\perp$  coupling is positive. As such, it lowers the energy of the neutral phase and thus shifts the phase transition to higher values of  $t_{a,b}$ . The opposite is true for hopping amplitudes of different sign.

To sum up the implications of the spin model and compare these to our numerical results, we examine the interplay of spin coupling amplitudes with the help of an auxiliary function  $\chi$ . All spin couplings that favor the polarized phase are marked with a positive sign, while the spin couplings favoring the neutral phase carry a negative sign:

$$\chi = J_{zz} + |J_z| - J_\perp - \Omega. \quad (10)$$

The roots of this function give an estimate for the neutral to polarized phase transition line, and the resulting plot in

Fig. 7(b) qualitatively recovers the structure of the numerical phase diagram.

We now investigate how the transitions from Fig. 7 are affected by the change in the interaction ratio  $\gamma$  and in the coherent coupling  $\Omega$ . It turns out that the corresponding  $t_a - t_b$  plots look qualitatively similar to the plot Fig. 7(a). In order to make a quantitative comparison, we plot the absolute value of the polarization  $|\tilde{n}|$  as a function of  $t_a$  for  $t_a = t_b$  (Fig. 8, left column) and for  $t_b = -t_a$  (Fig. 8, right column). In the plots shown in Figs. 8(a) and 8(b), we set  $\gamma = 8/5$  and vary  $\Omega$ . Our results show good agreement with the expectation  $t_c/U \approx \sqrt{\Omega/U}$  from Eq. (6) for the transition point  $t_c$ . For the two cases considered ( $t_a = t_b$  and  $t_a = -t_b$ ) only the proportionality constants are different.

In the plots presented in Figs. 8(c) and 8(d) we keep the value  $\Omega/U = 2 \times 10^{-3}$  fixed and change  $\gamma$ . For  $t_a = t_b$  our results are well approximated by  $t_c \approx (1 - 1/\gamma)^{-1/2}$ , in agreement with Eq. (6). In contrast, for  $t_a = -t_b$  we find that our results do not depend on the value of  $\gamma$ . This can be explained by looking at the spin coupling constants from Eqs. (7)–(10). As mentioned earlier, the  $J_\perp$  coupling opposes the impact of the  $\Omega$  term for hopping amplitudes of different sign. The relevant contribution to the auxiliary function  $\chi$  [defined in Eq. (10)] that leads to the aforementioned  $\gamma$  invariance, however, is given by the sum  $J_{zz} + |J_\perp|$ . The  $\gamma$  parts of both terms cancel, leaving  $\chi$  independent of  $\gamma$ .

## VI. SUMMARY AND DISCUSSION

In this work, we focused on a two-component mixture of coherently coupled bosons in a square optical lattice. We analyzed the phase transition between the polarized [finite  $\tilde{n}_i$ , Eq. (2)] and the neutral phase, driven by an interplay of the coherent coupling  $\Omega$  and the interspecies repulsion  $U_{ab}$  at unit filling  $\langle n_{ia} + n_{ib} \rangle = 1$  in the parameter region where interactions set the energy scale  $\Omega, t_a, t_b < U_a = U_b = U = 1 < U_{ab}$ .

By comparing Gutzwiller results with more demanding BDMFT calculations, we found that the former provide a reasonable description of the system in the superfluid regime. We investigated the energy landscape of the mean-field Hamiltonian as a function of the two condensate order parameters and established that the coherent coupling leads to a second-order phase transition between the polarized and the neutral phase. Furthermore, we found that the neutral phase is suppressed as the ratio of inter- and intraspecies interactions  $\gamma$  increases.

On the Mott side of the phase diagram, where BDMFT calculations provide a necessary extension of the simpler mean-field theory, for the balanced case  $t_a = t_b$  we found the polarized phase to be favored only at very low values of the coherent coupling [Fig. 5(a)]. From this, we concluded that the long-range order of the condensate seems to favor the polarized phase. To better understand our numerical results in the Mott phase, we used an effective spin model that provides a low-energy description of the full model. From the coupling constants of the effective model we inferred that the polarized to neutral transition line is approximately given by  $\frac{\Omega_c}{U} \propto (1 - 1/\gamma) \frac{t}{U}$ , in very good agreement with our numerical results (Fig. 5). The dominance of the neutral phase in the



deep Mott regime at unit filling agrees well with the other findings in this paper, as well as in the literature, especially with recent density matrix renormalization group calculations [27]. Furthermore, our BDMFT results indicate three possible transitions with increasing  $t/U$ , depending on the value of coherent coupling  $\Omega$  and interaction ratio  $\gamma = U_{ab}/U$ : polarized Mott states turn into a polarized superfluid, the polarized Mott phase turns directly into a neutral superfluid, and from the neutral Mott phase there is a transition to a neutral superfluid. The tip of the Mott lobe is positioned at the smallest value of  $t/U$  in the first case, while the lobe extends up to the largest value of the tunneling amplitude for the third case.

Finally, we explored the effects of imbalanced hopping amplitudes  $t_a \neq t_b$  for the two species. Our results show that the strong coherent coupling with an immobile state reduces density fluctuations and consequently extends the Mott region. For now, we considered the case of  $\gamma > 1$  and found that  $\Omega$  enforces a neutral phase for  $t_a = \pm t_b$  on the Mott side. An interesting asymmetry that shows up in the two latter cases was traced back to the sign change of one of the coupling constants in the effective spin model. In future work, we plan to consider the case of  $\gamma = 1/2$  and  $t_a = -t_b$ , where recent calculations

[29] suggested an occurrence of the  $xy$ -antiferromagnetic phase.

#### ACKNOWLEDGMENTS

Support by the Deutsche Forschungsgemeinschaft via DFG SFB/TR 49, DFG FOR 801, DFG SPP 1929 GiRyd and the high-performance computing center LOEWE-CSC is gratefully acknowledged. This work was supported in part by DAAD (German Academic and Exchange Service) under the BKM project. I.V. acknowledges support by the Ministry of Education, Science, and Technological Development of the Republic of Serbia under Project No. ON171017 and the BKM, and by the European Commission under H2020 project VI-SEEM, Grant No. 675121. Numerical simulations were partly run on the PARADOX supercomputing facility at the Scientific Computing Laboratory of the Institute of Physics Belgrade. U.B. acknowledges support by the Centre for Quantum Technologies (CQT) PhD program. The Centre for Quantum Technologies is a Research Centre of Excellence founded by the Ministry of Education, Singapore and the National Research Foundation, Prime Minister's Office, Singapore.

- 
- [1] M. Greiner, O. Mandel, T. Esslinger, T. W. Hänsch, and I. Bloch, *Nature (London)* **415**, 39 (2002).
- [2] I. Bloch, J. Dalibard, and W. Zwerger, *Rev. Mod. Phys.* **80**, 885 (2008).
- [3] R. Löw, H. Weimer, J. Nipper, J. B. Balewski, B. Butscher, H. P. Büchler, and T. Pfau, *J. Phys. B* **45**, 113001 (2012).
- [4] P. Schauß, J. Zeiher, T. Fukuhara, S. Hild, M. Cheneau, T. Macrì, T. Pohl, I. Bloch, and C. Gross, *Science* **347**, 1455 (2015).
- [5] J. Dalibard, F. Gerbier, G. Juzeliūnas, and P. Öhberg, *Rev. Mod. Phys.* **83**, 1523 (2011).
- [6] N. Goldman, G. Juzeliūnas, P. Öhberg, and I. B. Spielman, *Rep. Prog. Phys.* **77**, 126401 (2014).
- [7] C. J. Pethick and H. Smith, *Bose-Einstein Condensation in Dilute Gases* (Cambridge University Press, Cambridge, UK, 2002).
- [8] M. R. Matthews, D. S. Hall, D. S. Jin, J. R. Ensher, C. E. Wieman, E. A. Cornell, F. Dalfovo, C. Minniti, and S. Stringari, *Phys. Rev. Lett.* **81**, 243 (1998).
- [9] T. Zibold, E. Nicklas, C. Gross, and M. K. Oberthaler, *Phys. Rev. Lett.* **105**, 204101 (2010).
- [10] E. Nicklas, H. Strobel, T. Zibold, C. Gross, B. A. Malomed, P. G. Kevrekidis, and M. K. Oberthaler, *Phys. Rev. Lett.* **107**, 193001 (2011).
- [11] P. B. Blakie, R. J. Ballagh, and C. W. Gardiner, *J. Opt. B* **1**, 378 (1999).
- [12] C. P. Search and P. R. Berman, *Phys. Rev. A* **63**, 043612 (2001).
- [13] P. Tommasini, E. J. V. de Passos, A. F. R. de T. Piza, M. S. Hussein, and E. Timmermans, *Phys. Rev. A* **67**, 023606 (2003).
- [14] C. Lee, W. Hai, L. Shi, and K. Gao, *Phys. Rev. A* **69**, 033611 (2004).
- [15] I. M. Merhasin, B. A. Malomed, and R. Driben, *J. Phys. B* **38**, 877 (2005).
- [16] M. Abad and A. Recati, *Eur. Phys. J. D* **67**, 11 (2013).
- [17] S. Butera, P. Öhberg, and I. Carusotto, *Phys. Rev. A* **96**, 013611 (2017).
- [18] Z. Chen and B. A. Malomed, *Phys. Rev. E* **95**, 032217 (2017).
- [19] G. Shchedrin, D. Jaschke, and L. D. Carr, [arXiv:1610.09076](https://arxiv.org/abs/1610.09076).
- [20] J. Catani, L. De Sarlo, G. Barontini, F. Minardi, and M. Inguscio, *Phys. Rev. A* **77**, 011603 (2008).
- [21] D. M. Weld, P. Medley, H. Miyake, D. Hucul, D. E. Pritchard, and W. Ketterle, *Phys. Rev. Lett.* **103**, 245301 (2009).
- [22] B. Gadway, D. Pertot, R. Reimann, and D. Schneble, *Phys. Rev. Lett.* **105**, 045303 (2010).
- [23] E. Altman, W. Hofstetter, E. Demler, and M. D. Lukin, *New J. Phys.* **5**, 113 (2003).
- [24] A. B. Kuklov and B. V. Svistunov, *Phys. Rev. Lett.* **90**, 100401 (2003).
- [25] F. Lingua, M. Guglielmino, V. Penna, and B. C. Sansone, *Phys. Rev. A* **92**, 053610 (2015).
- [26] F. Lingua, B. Capogrosso-Sansone, F. Minardi, and V. Penna, *Sci. Rep.* **7**, 5105 (2017).
- [27] F. Zhan, J. Sabbatini, M. J. Davis, and I. P. McCulloch, *Phys. Rev. A* **90**, 023630 (2014).
- [28] L. Barbiero, M. Abad, and A. Recati, *Phys. Rev. A* **93**, 033645 (2016).
- [29] T. Groß, A. Celi, and M. Lewenstein, *Phys. Rev. A* **90**, 043628 (2014).
- [30] C. J. Myatt, E. A. Burt, R. W. Ghrist, E. A. Cornell, and C. E. Wieman, *Phys. Rev. Lett.* **78**, 586 (1997).
- [31] T. Pohl, E. Demler, and M. D. Lukin, *Phys. Rev. Lett.* **104**, 043002 (2010).
- [32] A. Geißler, I. Vasić, and W. Hofstetter, *Phys. Rev. A* **95**, 063608 (2017).
- [33] A. Celi, P. Massignan, J. Ruseckas, N. Goldman, I. B. Spielman, G. Juzeliūnas, and M. Lewenstein, *Phys. Rev. Lett.* **112**, 043001 (2014).
- [34] M. Mancini, G. Pagano, G. Cappellini, L. Livi, M. Rider, J. Catani, C. Sias, P. Zoller, M. Inguscio, M. Dalmonte, and L. Fallani, *Science* **349**, 1510 (2015).

- [35] M. P. A. Fisher, P. B. Weichman, G. Grinstein, and D. S. Fisher, *Phys. Rev. B* **40**, 546 (1989).
- [36] D. S. Rokhsar and B. G. Kotliar, *Phys. Rev. B* **44**, 10328 (1991).
- [37] W. Krauth, M. Caffarel, and J. P. Bouchaud, *Phys. Rev. B* **45**, 3137 (1992).
- [38] A. Hubener, M. Snoek, and W. Hofstetter, *Phys. Rev. B* **80**, 245109 (2009).
- [39] P. Anders, E. Gull, L. Pollet, M. Troyer, and P. Werner, *Phys. Rev. Lett.* **105**, 096402 (2010).
- [40] P. Anders, E. Gull, L. Pollet, M. Troyer, and P. Werner, *New J. Phys.* **13**, 075013 (2011).
- [41] Y. Li, M. R. Bakhtiari, L. He, and W. Hofstetter, *Phys. Rev. B* **84**, 144411 (2011).
- [42] M. Snoek and W. Hofstetter, Bosonic dynamical mean-field theory, in *Quantum Gases: Finite Temperature and Non-Equilibrium Dynamics*, edited by N. Proukakis, S. Gardiner, M. Davis, and M. Szymanska (Imperial College Press, London, 2013), pp. 1–10.
- [43] J. K. Freericks, H. R. Krishnamurthy, Y. Kato, N. Kawashima, and N. Trivedi, *Phys. Rev. A* **79**, 053631 (2009).
- [44] W. Metzner and D. Vollhardt, *Phys. Rev. Lett.* **62**, 324 (1989).
- [45] B. Capogrosso-Sansone, Ş. G. Söyler, N. Prokof'ev, and B. Svistunov, *Phys. Rev. A* **77**, 015602 (2008).
- [46] A. Petrescu and K. Le Hur, *Phys. Rev. Lett.* **111**, 150601 (2013).
- [47] J. R. Schrieffer and P. Wolff, *Phys. Rev.* **149**, 491 (1966).
- [48] N. Syassen, D. M. Bauer, M. Lettner, D. Dietze, T. Volz, S. Dürr, and G. Rempe, *Phys. Rev. Lett.* **99**, 033201 (2007).
- [49] M. L. Olsen, J. D. Perreault, T. D. Cumby, and D. S. Jin, *Phys. Rev. A* **80**, 030701 (2009).
- [50] L. de F. de Parny, V. G. Rousseau, and T. Roscilde, *Phys. Rev. Lett.* **114**, 195302 (2015).
- [51] D. H. Dunlap and V. M. Kenkre, *Phys. Rev. B* **34**, 3625 (1986).
- [52] A. Eckardt, C. Weiss, and M. Holthaus, *Phys. Rev. Lett.* **95**, 260404 (2005).
- [53] H. Lignier, C. Sias, D. Ciampini, Y. Singh, A. Zenesini, O. Morsch, and E. Arimondo, *Phys. Rev. Lett.* **99**, 220403 (2007).
- [54] A. Zenesini, H. Lignier, D. Ciampini, O. Morsch, and E. Arimondo, *Phys. Rev. Lett.* **102**, 100403 (2009).

**Dynamics of weakly interacting bosons in optical lattices with flux**Ana Hudomal,<sup>1</sup> Ivana Vasić,<sup>1</sup> Hrvoje Buljan,<sup>2</sup> Walter Hofstetter,<sup>3</sup> and Antun Balaz̃<sup>1</sup><sup>1</sup>*Scientific Computing Laboratory, Center for the Study of Complex Systems, Institute of Physics Belgrade, University of Belgrade, 11080 Belgrade, Serbia*<sup>2</sup>*Department of Physics, Faculty of Science, University of Zagreb, 10000 Zagreb, Croatia*<sup>3</sup>*Institut für Theoretische Physik, Johann Wolfgang Goethe-Universität, 60438 Frankfurt am Main, Germany*

(Received 19 September 2018; published 26 November 2018)

Realization of strong synthetic magnetic fields in driven optical lattices has enabled implementation of topological bands in cold-atom setups. A milestone has been reached by a recent measurement of a finite Chern number based on the dynamics of incoherent bosonic atoms. The measurements of the quantum Hall effect in semiconductors are related to the Chern-number measurement in a cold-atom setup; however, the design and complexity of the two types of measurements are quite different. Motivated by these recent developments, we investigate the dynamics of weakly interacting incoherent bosons in a two-dimensional driven optical lattice exposed to an external force, which provides a direct probe of the Chern number. We consider a realistic driving protocol in the regime of high driving frequency and focus on the role of weak repulsive interactions. We find that interactions lead to the redistribution of atoms over topological bands both through the conversion of interaction energy into kinetic energy during the expansion of the atomic cloud and due to an additional heating. Remarkably, we observe that the moderate atomic repulsion facilitates the measurement by flattening the distribution of atoms in the quasimomentum space. Our results also show that weak interactions can suppress the contribution of some higher-order nontopological terms in favor of the topological part of the effective model.

DOI: [10.1103/PhysRevA.98.053625](https://doi.org/10.1103/PhysRevA.98.053625)**I. INTRODUCTION**

Ultracold atoms in optical lattices provide a perfect platform for quantum simulations of various condensed-matter phenomena [1]. Yet, since charge-neutral atoms do not feel the Lorentz force, a big challenge in this field was realization of synthetic magnetic fields. After years of effort, artificial gauge potentials for neutral atoms were implemented by exploiting atomic coupling to a suitable configuration of external lasers [2,3]. These techniques were further extended to optical lattices, leading to the realization of strong, synthetic, magnetic fields. As a result, important condensed-matter models—the Harper-Hofstadter [4] and the Haldane model [5]—are nowadays available in cold-atom setups [6–9]. The key property of these models is their nontrivial topological content. In the seminal TKNN paper [10] it was shown that the quantization of the Hall conductivity observed in the integer Hall effect can be directly related to the topological index of the microscopic model—the Chern number.

Cold-atom realizations of topological models exploit periodic driving, either through laser-assisted tunneling [6,7] or by lattice shaking [8]. Using Floquet theory [11,12], a periodically driven system can be related to the time-independent effective Hamiltonian that corresponds to a relevant condensed-matter system. The mapping is known as Floquet engineering and its important features in the context of optical lattices are discussed in Refs. [13–20]. Because of important differences of cold-atom setups and their condensed-matter counterparts, new quench protocols for probing topological features were proposed [21–25]. Following up on these studies, the deflection of an atomic cloud as a response to external force was used to experimentally measure the Chern number in a nonelectronic system for the first time [26].

While Floquet engineering is a highly flexible and powerful technique, it poses several concerns. One of the main open questions is related to the interplay of driving and interactions which can heat up the system to a featureless, infinite-temperature regime according to general considerations [27,28]. In particular, it is shown that an initial Bose-Einstein condensate in a periodically driven optical lattice may become unstable due to two-body collisions [29] or through the mechanism of parametric resonance [28,30–36]. The preparation protocol, stability and a lifetime of strongly correlated phases, expected in the regime of strong interactions under driving is a highly debated topic at the moment [28,37,38].

In order to further explore the role of weak atomic interactions in probing topological features, here we consider the dynamics of weakly interacting incoherent bosons in a driven optical lattice exposed to an external force. The setup that we consider includes all basic ingredients for the Chern-number measurement [22,26]—the Chern number of the topological band can be extracted from the center-of-mass motion of atomic cloud in the direction transverse to the applied force. We assume an ideal initial state where the lowest topological band of the effective model is almost uniformly populated. The optimal loading sequence necessary to reach this state is considered in Refs. [39,40]. Following the recent experimental study [26], we assume that atoms are suddenly released from the trap and exposed to a uniform force. We perform numerical simulations for the full time-dependent Hamiltonian and take into account the effects of weak repulsive interactions between atoms within the mean-field approximation. We make a comparison between the dynamics governed by the effective and time-dependent Hamiltonian and delineate the

contribution of interactions to the center-of-mass response and to the overall cloud expansion dynamics. Our results show that interactions lead to the undesirable atomic transitions between topological bands [41], but we also find that a weak atomic repulsion can facilitate the Chern-number measurements in several ways.

The paper is organized as follows. In Sec. II we describe the model and introduce a method that we apply for the description of incoherent bosons. In Sec. III we address the dynamics of noninteracting incoherent bosons, and then in Sec. IV we address the regime of weak repulsive interactions. Finally, we summarize our results in Sec. V. Appendixes A to F provide further details.

## II. MODEL AND METHOD

In this section, we first present the driven model introduced in Ref. [26], and then derive the corresponding effective model and discuss its basic characteristics. At the end, we explain our choice of the initial state and outline the method that we use to treat the dynamics of weakly interacting incoherent bosons.

### A. Effective Floquet Hamiltonian

Interacting bosons in a two-dimensional optical lattice can be described by the Bose-Hubbard Hamiltonian

$$\begin{aligned} \hat{H}_{\text{BH}} = & -J_x \sum_{l,m} (\hat{a}_{l+1,m}^\dagger \hat{a}_{l,m} + \hat{a}_{l-1,m}^\dagger \hat{a}_{l,m}) \\ & -J_y \sum_{l,m} (\hat{a}_{l,m+1}^\dagger \hat{a}_{l,m} + \hat{a}_{l,m-1}^\dagger \hat{a}_{l,m}) \\ & + \frac{U}{2} \sum_{l,m} \hat{n}_{l,m} (\hat{n}_{l,m} - 1), \end{aligned} \quad (1)$$

where  $\hat{a}_{l,m}^\dagger$  and  $\hat{a}_{l,m}$  are creation and annihilation operators that create and annihilate a particle at the lattice site  $(l, m) = la\mathbf{e}_x + ma\mathbf{e}_y$  ( $a$  is the lattice constant),  $\hat{n}_{l,m} = \hat{a}_{l,m}^\dagger \hat{a}_{l,m}$  is the number operator,  $J_x$  and  $J_y$  are the hopping amplitudes along  $\mathbf{e}_x$  and  $\mathbf{e}_y$ , and  $U$  is the on-site interaction. In the derivation of the model (1) we use the single-band tight-binding approximation [1]. Although the experimental setup [26] is actually three dimensional, with an additional confinement in the third direction, our study is simplified to a two-dimensional lattice.

In order to engineer artificial gauge field in the experiment [26], hopping along  $\mathbf{e}_x$  was at first inhibited by an additional staggered potential

$$\hat{W} = \frac{\Delta}{2} \sum_{l,m} (-1)^l \hat{n}_{l,m}, \quad (2)$$

and then restored using resonant laser light. The experimental setup can be described by a time-dependent Hamiltonian

$$\tilde{H}(t) = \hat{H}_{\text{BH}} + \hat{V}(t) + \hat{W}, \quad (3)$$

where  $\hat{V}(t)$  is a time-dependent modulation

$$\begin{aligned} \hat{V}(t) = & \kappa \sum_{l,m} \hat{n}_{l,m} \left[ \cos\left(\frac{l\pi}{2} - \frac{\pi}{4}\right) \cos\left(\omega t - \frac{m\pi}{2} + \phi_0\right) \right. \\ & \left. + \cos\left(\frac{l\pi}{2} + \frac{\pi}{4}\right) \cos\left(-\omega t - \frac{m\pi}{2} + \frac{\pi}{2} + \phi_0\right) \right], \end{aligned} \quad (4)$$

$\kappa$  is the driving amplitude, and  $\omega = \Delta$  is the resonant driving frequency. We set the relative phase  $\phi_0$  between the optical-lattice potential and the running waves used for laser-assisted tunneling to  $\phi_0 = \pi/4$ .

Using Floquet theory, the time-evolution operator corresponding to the Hamiltonian (3) can be represented as

$$\hat{U}(t, t_0) = e^{-i\hat{W}t} e^{-i\hat{K}(t)} e^{-i(t-t_0)\hat{H}_{\text{eff}}} e^{i\hat{K}(t_0)} e^{i\hat{W}t_0}, \quad (5)$$

where  $\hat{H}_{\text{eff}}$  is the full time-independent effective Hamiltonian that describes slow motion and  $\hat{K}(t)$  is the time-periodic kick operator that describes micromotion [13,14].

For the moment, in this subsection we first consider the noninteracting model  $U = 0$ . We also assume that the driving frequency  $\omega$  is the highest energy scale, but that it is still low enough that the lowest-band approximation used in deriving Eq. (1) is still valid. In the leading order of the high-frequency expansion, the effective Hamiltonian  $\hat{H}_{\text{eff}}$  is given by

$$\begin{aligned} \hat{H}_{\text{eff},0} = & J'_x \sum_{l,m} [e^{i((m-l-1)\pi/2 - \pi/4)} \hat{a}_{l+1,m}^\dagger \hat{a}_{l,m} + \text{H.c.}] \\ & - J'_y \sum_{l,m} (\hat{a}_{l,m+1}^\dagger \hat{a}_{l,m} + \hat{a}_{l,m-1}^\dagger \hat{a}_{l,m}), \end{aligned} \quad (6)$$

where the renormalized hopping amplitudes are  $J'_x = \frac{J_x \kappa}{\sqrt{2\omega}} = J_y$  and  $J'_y = J_y (1 - \frac{\kappa^2}{2\omega^2})$ . A schematic representation of this model is presented in Fig. 1(a). The unit cell is shaded and the full lattice is spanned by the vectors  $\mathbf{R}_1 = (4, 0)$  and  $\mathbf{R}_2 = (1, 1)$ . Particle hopping around a plaquette in the counterclockwise direction acquires a complex phase  $-\frac{\pi}{2}$  and the model is equivalent to the Harper-Hofstadter Hamiltonian [4] for the case  $\alpha = 1/4$  [4]. The explicit form of the kick operator  $\hat{K}(t)$  from Eq. (3) is given in Appendix A.

Following Refs. [13,14], we find that additional corrections of the order  $J'_x/\omega$  contribute to the system's dynamics and we introduce another approximation for the effective Hamiltonian

$$\begin{aligned} \hat{H}_{\text{eff},1} = & \hat{H}_{\text{eff},0} + \frac{J_x^2}{\omega} \sum_{l,m} (-1)^l (2\hat{a}_{l,m}^\dagger \hat{a}_{l,m} \\ & + \hat{a}_{l+2,m}^\dagger \hat{a}_{l,m} + \hat{a}_{l-2,m}^\dagger \hat{a}_{l,m}). \end{aligned} \quad (7)$$

The derivation of Hamiltonian (7) is given in Appendix A and its schematic representation is given in Fig. 1(b). The  $J_x^2/\omega$  correction introduces next-nearest-neighbor hopping along  $x$  direction with opposite signs for lattice sites with either even or odd  $x$ -coordinate  $l$ . This term does not change the total complex phase per plaquette, but the unit cell is now doubled and thus the first Brillouin zone is halved. A similar term was engineered on purpose in order to implement the Haldane model [8].

In the next subsection we investigate properties of energy bands of both effective Hamiltonians,  $\hat{H}_{\text{eff},0}$  and  $\hat{H}_{\text{eff},1}$ . We use the units where  $\hbar = 1$  and  $a = 1$ . Unless otherwise stated, we set the parameters to the following values: lattice size  $100 \times 100$  sites, hopping amplitudes  $J'_x = J_y = 1 \equiv J$ , and the driving amplitude  $\kappa = 0.58\omega$ . This value of the driving amplitude was chosen to be the same as in the experiment [26]. In order to set the renormalized hopping amplitude along  $\mathbf{e}_x$  to  $J'_x = 1$ , the initial hopping amplitude has to be



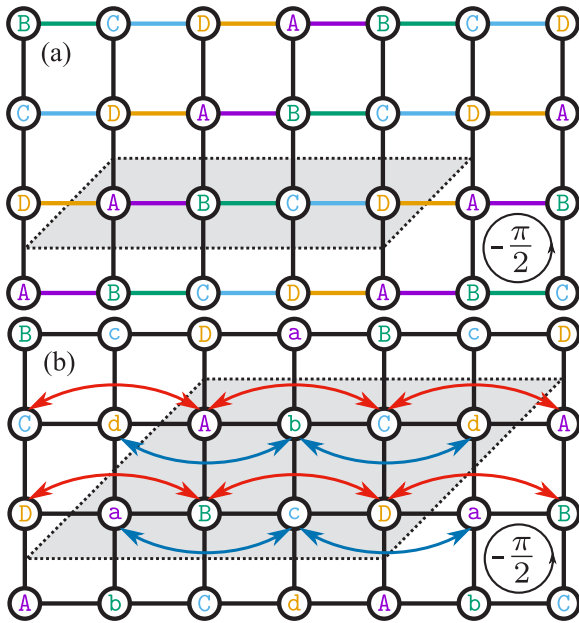


FIG. 1. Schematic representation of the model. The unit cells are shaded. (a) Effective Hamiltonian without correction,  $\hat{H}_{\text{eff},0}$  (6). Vertical links correspond to real hopping amplitudes (along  $\mathbf{e}_y$  direction), while the horizontal links to the right of lattice sites labeled A, B, C, and D correspond to complex hopping amplitudes with phases  $\frac{3\pi}{4}$ ,  $\frac{\pi}{4}$ ,  $-\frac{\pi}{4}$ , and  $-\frac{3\pi}{4}$ , respectively (when hopping from left to right). (b) Effective Hamiltonian with correction,  $\hat{H}_{\text{eff},1}$  (7). Red lines represent positive next-nearest-neighbor hopping amplitudes (connecting uppercase letters), while the blue lines represent negative next-nearest-neighbor hopping amplitudes (connecting lowercase letters). Nearest-neighbor hopping amplitudes are the same as in (a).

$J_x = \sqrt{2}\omega/\kappa = 2.44$ , and the correction term is therefore proportional to  $J_x^2/\omega = 5.95/\omega$ , so it cannot be safely neglected unless the driving frequency is very high.

### B. Band structure

Momentum-space representations of the effective Hamiltonians  $\hat{H}_{\text{eff},0}$  and  $\hat{H}_{\text{eff},1}$ , denoted by  $\hat{\mathcal{H}}_{\text{eff},0}(\mathbf{k})$  and  $\hat{\mathcal{H}}_{\text{eff},1}(\mathbf{k})$ , respectively, are derived in Appendix B. Band structures for the effective Hamiltonian  $\hat{\mathcal{H}}_{\text{eff},0}$  without the  $J_x^2/\omega$  correction, Eq. (B1), as well as for the effective Hamiltonian  $\hat{\mathcal{H}}_{\text{eff},1}$

including the correction term, Eq. (B2), are shown in Fig. 2 for the two values of driving frequencies  $\omega = 20$  and  $\omega = 10$ .

The Hamiltonian  $\hat{H}_{\text{eff},0}$  is the Harper-Hofstadter Hamiltonian for the flux  $\alpha = 1/4$ . It has four energy bands, where the middle two bands touch at  $E = 0$  and can therefore be regarded as a single band; see Fig. 2(a). The topological content of these bands is characterized by the topological index called the Chern number. The Chern number is the integral of the Berry curvature [42] over the first Brillouin zone divided by  $2\pi$ ,

$$c_n = \frac{1}{2\pi} \int_{\text{FBZ}} \boldsymbol{\Omega}_n(\mathbf{k}) \cdot d\mathbf{S}, \quad (8)$$

where  $n$  denotes the band number and the Berry curvature is  $\boldsymbol{\Omega}_n(\mathbf{k}) = i\nabla_{\mathbf{k}} \times \langle u_n(\mathbf{k}) | \nabla_{\mathbf{k}} | u_n(\mathbf{k}) \rangle$ , expressed in terms of eigenstates of the effective Hamiltonian  $|u_n(\mathbf{k})\rangle$ . The Chern numbers of the three well-separated bands are  $c_1 = 1$ ,  $c_2 = -2$ , and  $c_3 = 1$ .

Because the correction from Eq. (7) includes next-nearest-neighbor hopping terms, the elementary cell in real space is doubled [see Fig. 1(b)] and, as a consequence, the first Brillouin zone for the Hamiltonian  $\hat{\mathcal{H}}_{\text{eff},1}$  is reduced by a factor of 2 compared to  $\hat{\mathcal{H}}_{\text{eff},0}$ . There are now eight lattice sites in the unit cell and eight energy bands, but the number of gaps depends on the driving frequency. The new bands touch in pairs, in such a way that there are always maximally three well-separated bands. When the driving frequency is high enough, the correction is small and the gaps between the three bands remain open; see Fig. 2(b). The original band structure of  $\hat{\mathcal{H}}_{\text{eff},0}$  is recovered in the limit  $\omega \rightarrow \infty$ . The Berry curvature and the Chern number can be calculated using the efficient method presented in Ref. [43]. Our calculations confirm that the Chern numbers of  $\hat{\mathcal{H}}_{\text{eff},1}$  are equal to those of  $\hat{\mathcal{H}}_{\text{eff},0}$  ( $c_1 = 1$ ,  $c_2 = -2$ , and  $c_3 = 1$ ), as long as the gaps between the energy bands are open. The gaps close when the driving frequency is too low, see Fig. 2(c), and the Chern numbers of the subbands can no longer be properly defined.

### C. Dynamics of incoherent bosons

We need to take into account a contribution of weak, repulsive interactions. Full numerical simulations of an interacting many-body problem are computationally demanding, so we need a reasonable, numerically tractable approximation. To this end we will use the classical field method [44], which

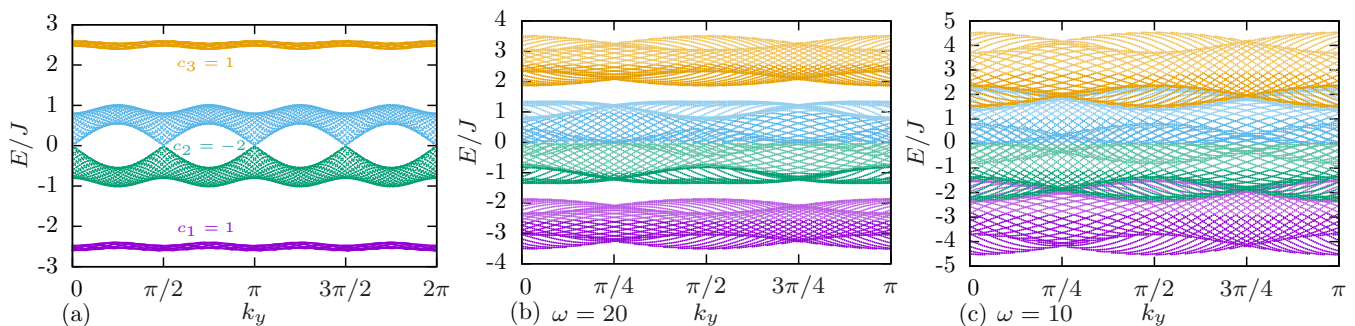


FIG. 2. Energy bands of the effective Hamiltonians. (a)  $\hat{\mathcal{H}}_{\text{eff},0}(\mathbf{k})$  Eq. (B1), which is without the  $J_x^2/\omega$  correction term. (b)  $\hat{\mathcal{H}}_{\text{eff},1}(\mathbf{k})$  Eq. (B2), which includes the correction term. Driving frequency  $\omega = 20$ ; gaps are open. (c) Same as (b), but with  $\omega = 10$ . Gaps are closed.

belongs to a broader class of truncated Wigner approaches [45]. This method is similar to the approach used to treat incoherent light in instantaneous media [46,47], known in optics as the modal theory.

The underlying idea of the method is to represent the initial state as an incoherent mixture of coherent states  $|\psi\rangle$ ,  $\hat{a}_{l,m}|\psi\rangle = \psi_{l,m}|\psi\rangle$  [44]. This is explained in more detail in Appendix C. In our study, we sample initial configurations of these coherent states with

$$|\psi(t=0)\rangle = \sum_{k=1}^{N_m} e^{i\phi_k} |k\rangle, \quad (9)$$

where  $\phi_k \in [0, 2\pi)$  are random phases and the states  $|k\rangle$  correspond closely to the lowest-band eigenstates of  $\hat{H}_{\text{eff}}$ . Each of  $N_{\text{samples}}$  initial states is time evolved and physical variables can be extracted by averaging over an ensemble of different initial conditions.

The time evolution of each of these coherent states is governed by

$$i \frac{d\psi_{l,m}(t)}{dt} = \sum_{ij} H_{lm,ij}(t) \psi_{i,j}(t) - F m \psi_{l,m}(t) + U |\psi_{l,m}(t)|^2 \psi_{l,m}(t), \quad (10)$$

where  $H_{lm,ij}(t) = \langle l, m | \hat{H}(t) | i, j \rangle$  are matrix elements of  $\hat{H}(t)$  from Eq. (3),  $F$  is the external force, and interactions  $U$  contribute with the last, nonlinear term. Formally, Eq. (10) takes the form of the Gross-Pitaevskii equation [48–50]. The performances and limitations of the method are discussed and reviewed in Ref. [51].

For comparison, we also consider the related time evolution governed by the effective Hamiltonian

$$i \frac{d\psi_{l,m}(t)}{dt} = \sum_{ij} h_{lm,ij}^{\text{eff}} \psi_{i,j}(t) - F m \psi_{l,m}(t) + U |\psi_{l,m}(t)|^2 \psi_{l,m}(t), \quad (11)$$

where  $h_{lm,ij}^{\text{eff}} = \langle l, m | \hat{h}^{\text{eff}} | i, j \rangle$ , with  $\hat{h}^{\text{eff}}$  being either  $\hat{H}_{\text{eff},0}$  from Eq. (6), or  $\hat{H}_{\text{eff},1}$  from Eq. (7). Equation (11) should be considered only as a tentative description of the system: the mapping between  $\hat{H}(t)$  and  $\hat{H}_{\text{eff}}$  is strictly valid only in the noninteracting regime and the interaction term may introduce complex, nonlocal, higher-order corrections [27]. However, we expect their contribution to be small in the limit  $U \rightarrow 0$ , and for time scales which are not too long [52–55].

In the following we use  $N_m = 300$  modes and accommodate  $N_p = 300$  particles per mode, so in total in the simulations we have  $N = N_m N_p = 90\,000$  bosons. Typical densities in real space are up to 100 particles per site and we choose the values of  $U$  in the range  $U \in [0, 0.05]$ . Other parameters:  $J'_x = J_y = 1$ ,  $\kappa/\omega = 0.58$ ,  $\omega = 10, 20$ , and  $F = 0.25J/a$ . The correction terms are non-negligible in this frequency range. In practice, we first numerically diagonalize the Hamiltonian (C2) from Appendix C and set our parameters in such a way that the lowest  $N_m$  modes have high overlap with the lowest band of the effective model. In the next step, we sample initial configurations (9). For each of  $N_{\text{samples}} = 1000$  sets of initial conditions we then time evolve Eq. (10) and extract quantities of interest by averaging over resulting

TABLE I. Four different cases: the same effective Hamiltonian is always used for the initial state and band definitions, either with or without the correction. The evolution is governed either by the time-dependent Hamiltonian or by the same effective Hamiltonian as the one that was used for the initial state and calculation of band populations.

Case	Initial state	Band populations	Evolution
1	$\hat{H}_{\text{eff},1}$	$\hat{H}_{\text{eff},1}$	$\hat{H}_{\text{eff},1}$
2	$\hat{H}_{\text{eff},1}$	$\hat{H}_{\text{eff},1}$	$\hat{H}(t)$
3	$\hat{H}_{\text{eff},0}$	$\hat{H}_{\text{eff},0}$	$\hat{H}_{\text{eff},0}$
4	$\hat{H}_{\text{eff},0}$	$\hat{H}_{\text{eff},0}$	$\hat{H}(t)$

trajectories. This value of  $N_{\text{samples}}$  is chosen to be high enough, so that the fluctuations are weak. We present and discuss results of our numerical simulations in the following sections.

### III. NONINTERACTING CASE

We start by addressing the dynamics of noninteracting bosons. In this case we set  $U = 0$  in Eq. (10) and numerically solve the single-particle Schrödinger equation without further approximations. Our aim is to numerically validate and compare the two approximations, Eqs. (6) and (7), for the effective Hamiltonian. To this purpose, we juxtapose results of the two approximative schemes with the numerically exact results obtained by considering the full time evolution governed by  $\hat{H}(t)$ . For clarity, the four different time evolutions that we consider in this section are summarized in Table I. We calculate the center-of-mass position  $x(t)$  and plot the results in Fig. 3. In this way we also find the regime of microscopic

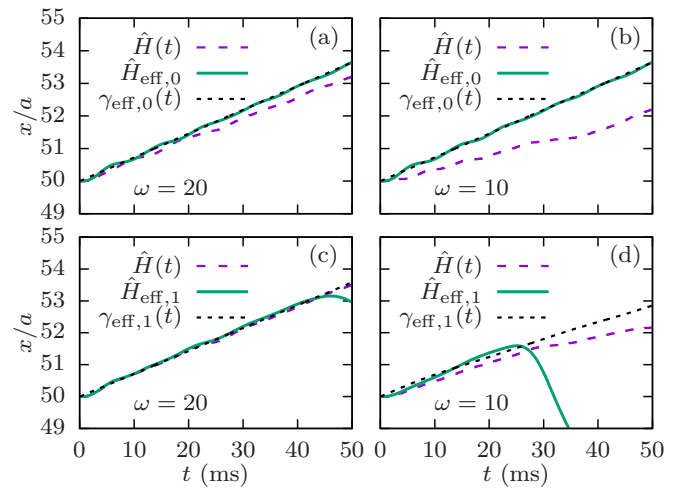


FIG. 3. Anomalous drift  $x(t)$ . Dashed purple lines: numerical simulations using the time-dependent Hamiltonian  $\hat{H}(t)$  (cases 2 and 4 from Table I). Solid green lines: effective Hamiltonians  $\hat{H}_{\text{eff},1}$  (c) and (d) and  $\hat{H}_{\text{eff},0}$  (a) and (b) (cases 1 and 3). Dotted black lines: theoretical prediction (14) from  $\gamma_{\text{eff},1}(t)$  or  $\gamma_{\text{eff},0}(t)$ . (a) Initial states and band populations obtained using the effective Hamiltonian  $\hat{H}_{\text{eff},0}$  without the correction (cases 3 and 4). Driving frequency  $\omega = 20$ . (b)  $\omega = 10$ . (c) Hamiltonian  $\hat{H}_{\text{eff},1}$  with the  $J_x^2/\omega$  correction (cases 1 and 2). Driving frequency  $\omega = 20$ . (d)  $\omega = 10$ .

parameters where the Chern-number measurement can be optimally performed.

First, we consider the basic Harper-Hofstadter Hamiltonian (6) and select the occupied modes  $|k\rangle$  of the initial state (C1) as eigenstates of the model from Eq. (9) for  $\hat{h}_{\text{eff}} = \hat{H}_{\text{eff},0}$ . As explained in the previous section, at the initial moment  $t_0 = 0$ , the confinement is turned off and the force  $\mathbf{F} = -F\mathbf{e}_y$  is turned on. As a consequence of the applied external force and the nonzero Chern number of the lowest band of the model (6), the particles exhibit an anomalous velocity in the direction perpendicular to the force [56]. In the ideal case, when the lowest band is fully populated, the theoretical prediction for the center-of-mass position in the  $\mathbf{e}_x$  direction is [26]

$$x(t) = x(t_0) + c_1 \frac{2Fa^2}{\pi\hbar} t, \quad (12)$$

where  $c_1 = 1$  is the Chern number (8) of the lowest band. However, even in the ideal case, due to the sudden quench of the linear potential, a fraction of particles is transferred to the higher bands. To take this effect into account, the authors of Ref. [26] introduced a filling factor  $\gamma(t)$

$$\gamma(t) = \eta_1(t) - \eta_2(t) + \eta_3(t), \quad (13)$$

where  $\eta_i(t)$  are populations of different bands of Hamiltonian (6) from Eq. (C4) in Appendix C and the plus and minus signs in Eq. (13) are defined according to the Chern numbers  $c_1 = 1$ ,  $c_2 = -2$ , and  $c_3 = 1$ . The final theoretical prediction is then [26]

$$x(t) = x(t_0) + c_1 \frac{2Fa^2}{\pi\hbar} \int_0^t \gamma(t') dt'. \quad (14)$$

In Fig. 3(a) we consider the anomalous drift for a high value of the driving frequency  $\omega = 20$ , where we expect the expansion in  $1/\omega$  to be reliable. We find an excellent agreement between the prediction (14) (dotted black line) and numerical calculation based on  $\hat{H}_{\text{eff},0}$  (solid green line). However, some deviations between the full numerical results (dashed purple line) and the results of the approximation scheme (solid green line) are clearly visible. These deviations are even more pronounced for  $\omega = 10$ , Fig. 3(b).

Now we turn to the effective model (7). In this case we select the modes of the initial state as eigenstates of Eq. (9) for  $\hat{h}_{\text{eff}} = \hat{H}_{\text{eff},1}$ . Moreover, we also consider band populations (C4) of the same model. In the case when  $\omega = 20$ , Fig. 3(c), the anomalous drift obtained using the effective Hamiltonian (7) (solid green line) closely follows the theoretical prediction (14). Moreover, from the same figure we can see that the effective Hamiltonian  $\hat{H}_{\text{eff},1}$  reproduces the behavior of the time-dependent Hamiltonian very well. All three curves almost overlap for intermediate times (5–40 ms); see Fig. 3(c). We attribute the long-time ( $>45$  ms) deviations to the finite-size effects introduced by the next-nearest-neighbor hopping terms, which cause the atomic cloud to reach the edge of the lattice faster. This effect is explained in more detail in Sec. IV B.

For a lower driving frequency  $\omega = 10$ , the effective and the time-dependent Hamiltonians do not agree so well anymore; see Fig. 3(d). The finite-size effects can be observed even earlier in this case (around 25 ms). This happens because the next-nearest-hopping terms are inversely proportional to the

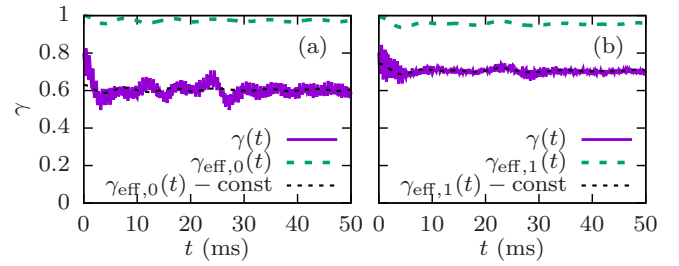


FIG. 4. Time evolution of the filling factor  $\gamma(t)$  for driving frequency  $\omega = 20$ . Solid purple lines: evolution governed by the time-dependent Hamiltonian  $\hat{H}(t)$  (cases 2 and 4 from Table I). Dashed green lines: evolution governed by the effective Hamiltonian  $\hat{H}_{\text{eff},1}$  or  $\hat{H}_{\text{eff},0}$  (cases 1 and 3). Dotted black lines: green lines shifted in order to compare them with purple lines. Shift is chosen so that the two lines approximately overlap. (a) Initial states and band populations obtained using the effective Hamiltonian  $\hat{H}_{\text{eff},0}$ , which is without the  $J_x^2/\omega$  correction term (cases 3 and 4). (b) Hamiltonian  $\hat{H}_{\text{eff},1}$  which is with the correction term (cases 1 and 2).

driving frequency. It is interesting to note that the prediction (14) is close to numerical data for short times even in this case when the gaps of the effective model are closed, see Fig. 2(c), and the Chern number of the lowest band is not well defined. In fact, it is surprising that the anomalous drift even exists in this case, as all subbands are now merged into a single band. We attribute this effect to our choice of the initial state. When the gaps are closed, it is hard to set the parameters in such a way that the lowest band is completely filled. The top of this band usually remains empty and the particles thus do not “see” that the gap is closed.

Time evolution of the filling factor  $\gamma(t)$  is plotted in Fig. 4 for four different cases from Table I—evolution using the effective Hamiltonian without correction  $\hat{H}_{\text{eff},0}$  [ $\gamma_{\text{eff},0}(t)$ , case 3, dashed green line in Fig. 4(a)], the effective Hamiltonian with correction  $\hat{H}_{\text{eff},1}$  [ $\gamma_{\text{eff},1}(t)$ , case 1, dashed green line in Fig. 4(b)], or the time-dependent Hamiltonian  $\hat{H}(t)$  [ $\gamma(t)$ , cases 2 and 4, solid purple lines]. At the initial moment  $\gamma(t_0 = 0) < 1$ , because the initial state was multiplied by the operator  $e^{-i\hat{k}(0)}$ . This introduces a shift between  $\gamma(t)$  and  $\gamma_{\text{eff},1}(t)$ . Apart from the shift, these two curves behave similarly, unlike the  $\gamma_{\text{eff},0}(t)$  curve that exhibits completely different behavior. Because of this, we use only  $\gamma_{\text{eff},1}(t)$  to estimate the value of the prediction (14).

We find that the values of  $\gamma_{\text{eff},1}(t)$  for  $\omega = 20$  are high:  $\geq 0.95$ ; see Fig. 4. For this reason, up to 50 ms the center-of-mass position  $x(t)$  exhibits roughly linear behavior with some additional oscillations. Interestingly, the anomalous drift  $x(t)$  exhibits quadratic behavior on short time scales in all cases from Fig. 3. In Appendix D, we explain this feature using the time-dependent perturbation theory and Fermi’s golden rule.

#### IV. INTERACTING CASE

We now investigate the effects of weak repulsive interactions. We work in the high-frequency regime and set  $\omega = 20$ . As shown in Sec. II B, for  $U = 0$  the effective Hamiltonian with correction,  $\hat{H}_{\text{eff},1}$ , is in this case equivalent to the Harper-Hofstadter Hamiltonian with flux  $\alpha = 1/4$ . Moreover, the



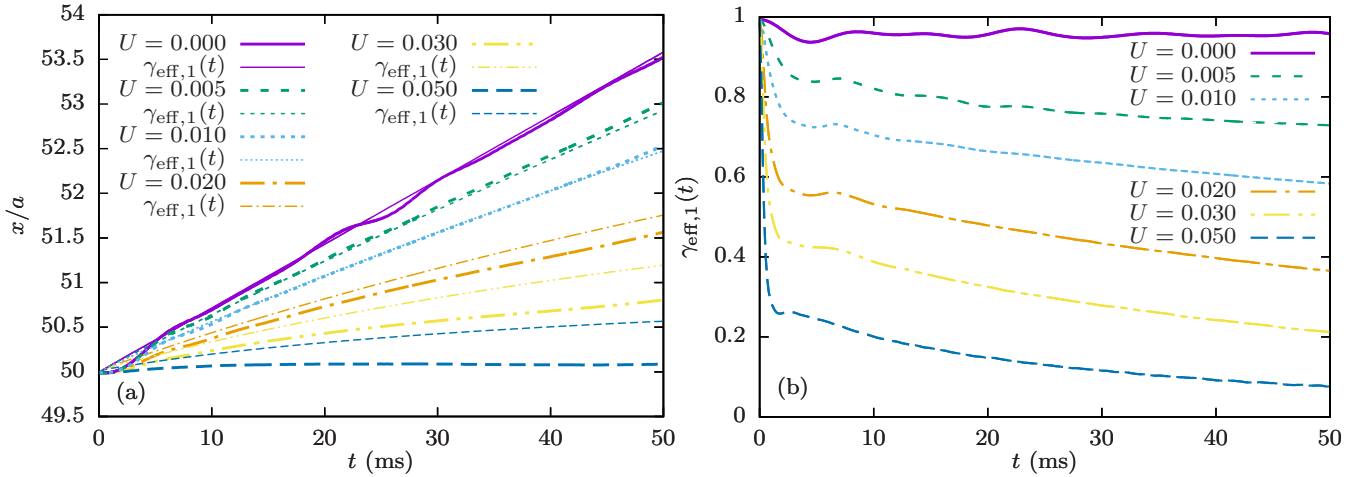


FIG. 5. Effects of interactions. (a) Anomalous drift  $x(t)$  for several different values of the interaction coefficient  $U$ .  $U$  is given in units where  $J = 1$ . Thick lines: numerical simulations using the time-dependent Hamiltonian  $\hat{H}(t)$ . Thin lines: theoretical prediction (14) from  $\gamma_{\text{eff},1}(t)$ . (b) Corresponding  $\gamma_{\text{eff},1}(t) = \eta_1(t) - \eta_2(t) + \eta_3(t)$ , obtained from simulations using the effective Hamiltonian  $\hat{H}_{\text{eff},1}$ .

same approximative form of the full effective model accurately reproduces the behavior of the time-dependent Hamiltonian up to 50 ms and thus provides a good starting point for the study of weakly interacting particles. We first consider the anomalous drift of the center of mass of the atomic cloud and then we inspect the expansion dynamics more closely in terms of atomic density distributions in real and momentum space.

### A. Anomalous drift and dynamics of band populations

To simulate the dynamics of many incoherent bosons, we use the classical field method presented in Sec. II C and propagate Eq. (10) in time. We assume that at  $t_0 = 0$  atoms are uniformly distributed over the lowest band of  $\hat{H}_{\text{eff},1}$ . For this reason, the initial state is the same as the one that we use in the noninteracting regime. In this way, the dynamics is initiated by an effective triple quench: at  $t_0 = 0$  the confining potential is turned off, atoms are exposed to the force  $\mathbf{F} = -F\mathbf{e}_y$ , and also the interactions between particles are introduced. The total number of particles is set to  $N = 90\,000$ , which amounts to approximately 100 particles per lattice site in the central region of the atomic cloud. We consider only weak repulsion  $U \leq 0.05$ .

The anomalous drift  $x(t)$  obtained using the full time-dependent Hamiltonian is shown in Fig. 5(a) for several different values of the interaction strength  $U$ . In comparison to the noninteracting regime, we find that the weak repulsive interactions inhibit the response of the center of mass to the external force. In particular, at  $t = 50$  ms the drift is reduced by about 15% for  $U = 0.005$  and it is further lowered by an increase in  $U$ . Finally, at  $U = 0.05$ , the anomalous drift is barely discernible. Interestingly, for weak  $U \in (0.001, 0.01)$  we find that the drift  $x(t)$  in the range of  $t \in (10, 50)$  ms looks “more linear” as a function of time in comparison to the noninteracting result.

We now analyze the anomalous drift in terms of the filling factor  $\gamma(t)$  and compare the results of Eq. (10) with the description based on Eq. (11). By solving Eq. (11) we obtain the filling factor  $\gamma_{\text{eff},1}(t)$  following Eq. (C4) and present

our results in Fig. 5(b). Whenever the results of Eq. (10) reasonably agree with the results obtained from Eq. (11), we are close to a steady-state regime with only small fluctuations in the total energy, as Eq. (11) preserves the total energy of the system. In this regime, during the expansion dynamics the interaction energy is converted into the kinetic energy and atoms are transferred to higher bands of the effective model. Consequently, the filling factor  $\gamma_{\text{eff},1}(t)$  is reduced. Typically, we find three different stages in the decrease of  $\gamma_{\text{eff},1}(t)$ .

In an early stage,  $t \leq t_1 = 5$  ms, a fast redistribution of particles over the bands of the effective model sets in due to the sudden quench of  $U$ . The factor  $\gamma_{\text{eff},1}(t)$  decays quadratically as a function of time down to  $\gamma_{\text{eff},1}(t_1) \approx 0.75$  for  $U = 0.01$ , and  $\gamma_{\text{eff},1}(t_1) \approx 0.25$  for  $U = 0.05$ . In this process the interaction energy of the system is quickly lowered as described in Appendix E. At later times  $t > 5$  ms, we observe a linear decay of the filling factor  $\gamma_{\text{eff},1}(t)$  as a function of time, that finally turns into an exponential decay at even later times ( $t > 10$  ms). Similar regimes are observed in other dynamical systems. For example, a decay rate of an initial state suddenly coupled to a bath of additional degrees of freedom exhibits these three stages [57]. The initial quadratic decay is often denoted as “the Zeno regime.” For longer propagation times, Fermi’s golden rule predicts the linear decay. At even longer time scales, when the repopulation of the initial state is taken into account, the time-dependent perturbation theory yields the exponential regime, known under the name of the Wigner-Weisskopf theory [57].

We now investigate this last regime in more detail. For the population of the lowest band  $\eta_1(t)$ , an exponential decay function  $f(t) = a + b e^{-ct}$  provides high quality fits for  $t \in (10, 50)$  ms; see Fig. 6(a) for an example. Similarly, the populations of two higher bands can also be fitted to exponential functions. The obtained exponential decay coefficients  $c$  for the lowest band population are plotted as a function of the interaction strength  $U$  in Fig. 6(b). The resulting dependence is approximately quadratic:  $c(U) = \alpha_0 + \alpha_1 U + \alpha_2 U^2$ . For small values of  $U$ , the exponents  $c(U)$  obtained for the dynamics governed by  $\hat{H}(t)$  and  $\hat{H}_{\text{eff},1}$  agree very well and



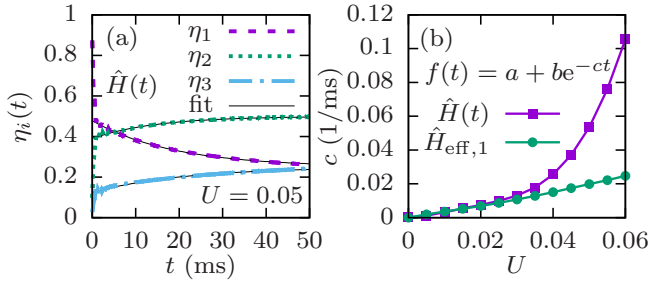


FIG. 6. (a) Evolution of the band populations  $\eta_i(t)$ . Dashed lines: numerical results obtained using the time-dependent Hamiltonian  $\hat{H}(t)$ . Solid black lines: exponential fit using  $f(t) = a + be^{-ct}$ . The coefficient  $a$  was fixed to  $a_1 = 0.25$ ,  $a_2 = 0.50$ , and  $a_3 = 0.25$  for the first, second, and third band, respectively. (b) Dependence of the exponential decay coefficients for the lowest band population  $\eta_1(t)$  on the interaction strength.  $U$  is given in units where  $J = 1$ .

exhibit linear behavior. At stronger interaction strengths  $U \geq 0.03$ , the approximation of Eq. (11) becomes less accurate as it omits the quadratic contribution in  $c(U)$  found in the full time evolution. In addition, the values of the exponents  $c$  are affected by the force strength  $F$  and driving frequency  $\omega$ .

As we now understand some basic features of  $\gamma_{\text{eff},1}(t)$ , we make an explicit comparison between the numerical results for the anomalous drift and the expectation (14). The dashed lines in Fig. 5(a) correspond to the theoretical prediction (14) calculated from  $\gamma_{\text{eff},1}(t)$ . For the intermediate interaction strengths  $U \leq 0.01$ , we find a very good agreement between the two. From this we conclude that the interaction-induced transitions of atoms to higher bands are the main cause of the reduced anomalous drift  $x(t)$  as a function of  $U$ . When the interactions become strong enough ( $U \sim 0.02$ ), the numerical results start to deviate from the theoretical prediction (14) with  $\gamma_{\text{eff},1}(t)$ . In this regime, Eq. (11) does not provide a reliable description of the dynamics, as higher-order corrections need to be taken into account.

### B. Real and momentum-space dynamics

So far we have considered the averaged response of the whole atomic cloud. We now inspect the expansion dynamics in a spatially resolved manner. The real-space probability densities at the initial moment and after 50 ms (75 driving periods) are shown in Figs. 7 and 8, and the corresponding momentum-space probability densities in Appendix F.

At the initial moment, the atomic cloud is localized in the center of the lattice. By setting  $r_0 = 20$  in the confining potential of Eq. (C2) and populating the lowest-lying states, we fix the cloud radius to  $r = 20$ , Fig. 7(a). The cloud density is of the order of 100 atoms per lattice site and a weak density modulation is visible along  $x$  direction. After the confining potential is turned off, and the external force in the  $-\mathbf{e}_y$  direction is turned on, the cloud starts to expand and move in the  $+\mathbf{e}_x$  direction. As shown in the previous subsection, the band populations and therefore the anomalous drift are significantly altered by the interaction strength, and this is also the case with the expansion dynamics; see Figs. 7 and 8.

In the noninteracting case, Fig. 7(b), the atomic cloud nearly separates into two parts moving in opposite directions

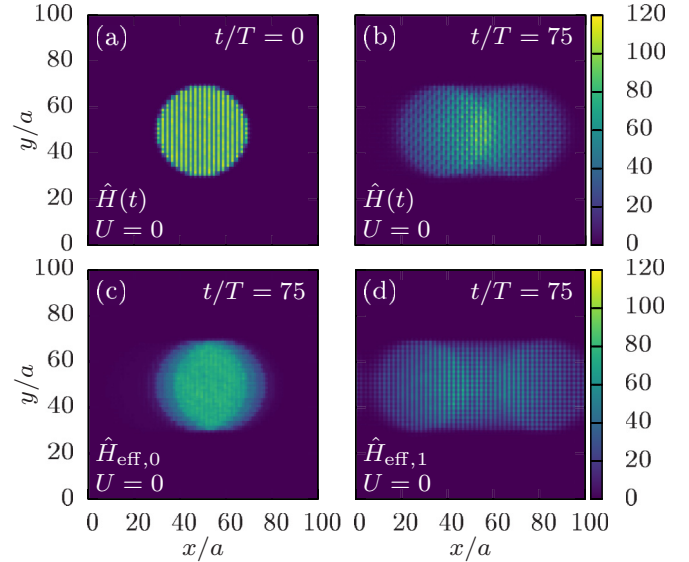


FIG. 7. Real-space density distribution, noninteracting case  $U = 0$ . (a) Initial state. (b) After 50 ms (75 driving periods), evolution using the time-dependent Hamiltonian  $\hat{H}(t)$ . (c) Evolution using effective Hamiltonian without correction  $\hat{H}_{\text{eff},0}$ . (d) Evolution using effective Hamiltonian with correction  $\hat{H}_{\text{eff},1}$ .

along  $x$  axes (while the center of mass still moves in the  $+\mathbf{e}_x$  direction). By comparing Fig. 7(c) and Fig. 7(d), we conclude that this effect stems from the next-nearest-neighbor hopping along  $x$  present in the effective Hamiltonian (7), as it does not happen in the effective model without the correction term (6). This type of separation was already observed in Ref. [22], where the next-nearest-neighbor hopping terms were also present. When the interactions between particles are included,

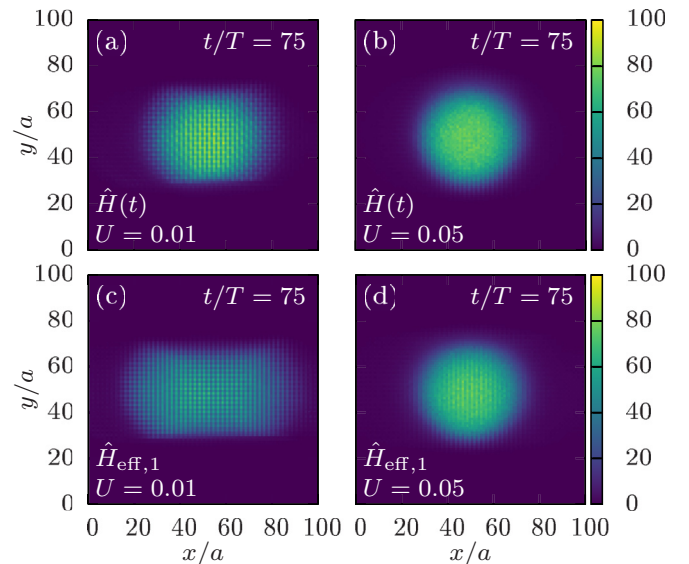


FIG. 8. Real-space density distribution after 50 ms (75 driving periods), interacting case.  $U$  is given in units where  $J = 1$ . (a) Evolution using the time-dependent Hamiltonian  $\hat{H}(t)$ ,  $U = 0.01$ . (b) Same with  $U = 0.05$ . (c) Evolution using the effective Hamiltonian  $\hat{H}_{\text{eff},1}$ ,  $U = 0.01$ . (d) Same with  $U = 0.05$ .

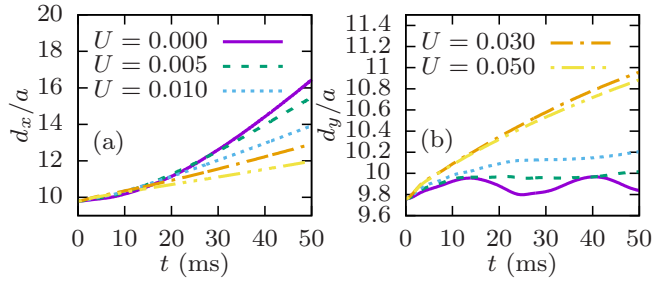


FIG. 9. Atomic cloud width for different interaction strengths, evolution using the time-dependent Hamiltonian  $\hat{H}(t)$ .  $U$  is given in units where  $J = 1$ . (a)  $d_x = \sqrt{\langle x^2 \rangle - \langle x \rangle^2}$ . (b)  $d_y = \sqrt{\langle y^2 \rangle - \langle y \rangle^2}$ .

this separation is not so prominent [Fig. 8(a),  $U = 0.01$ ], and it almost completely disappears when the interactions are strong enough [Fig. 8(b),  $U = 0.05$ ]. This is also the case when the evolution is governed by the effective Hamiltonian  $\hat{H}_{\text{eff},1}$ ; see Figs. 8(c) and 8(d). Atomic cloud widths  $d_x = \sqrt{\langle x^2 \rangle - \langle x \rangle^2}$  during the expansion are plotted in Fig. 9. We observe a slow expansion of the cloud in  $y$  direction, Fig. 9(b), and much faster expansion along  $x$  direction, Fig. 9(a), which comes about as a consequence of the cloud separation. On top of this, we observe that the interactions enhance expansion along  $y$ . Surprisingly, the opposite is true for the dynamics along  $x$ . This counterintuitive effect is often labeled as self-trapping and its basic realization is known for the double-well potential [58,59]. In brief, strong repulsive interactions can preserve the density imbalance between the two wells, as the system cannot release an excess of the interaction energy. In our case, the situation is slightly more involved as the cloud splitting is inherent (induced by the corrections of the ideal effective Hamiltonian). Apart from this, due to the driving the total energy is not conserved. However, our numerical results indicate that the interaction energy is slowly released in the second expansion stage, Fig. 14. Effectively, in this way the interactions cancel out the contribution of the next-nearest-neighbor hopping and favor the measurement of the properties of the model (6). In Fig. 10(a) we show that deviations between different approximations based on  $\hat{H}(t)$ ,

$\hat{H}_{\text{eff},1}$ , and  $\hat{H}_{\text{eff},0}$  in the anomalous drift  $x(t)$  nearly vanish at  $U = 0.01$ .

Another desirable effect might be that the interactions make the momentum-space probability density more homogeneous, see Appendix F, so that the real-space probability density becomes more localized. We can quantify momentum-space homogeneity using the inverse participation ratio  $R(t) = \frac{1}{\sum_i P_i^2(t)}$ , where  $P_i(t) = |\psi_i(t)|^2$  is the probability that the state  $\psi_i$  is occupied at time  $t$ . Minimal value of the inverse participation ratio (IPR) is 1 and it corresponds to a completely localized state, while the maximal value is equal to the total number of states (in our case 10 000) and corresponds to the completely delocalized state, where the particles have the same probability of being at any quasi-momentum  $\mathbf{k}$ . As stated before, the first Brillouin zone of the lowest band has to be as homogeneously populated as possible in order to properly measure the lowest band Chern number. From Fig. 10(b), we see that IPR increases in time when the interaction coefficient  $U$  is large enough, so we can conclude that the interactions are actually beneficial for measuring the Chern number, as they can “smooth out” the momentum-space probability density. In Fig. 10(c) we give estimates for the Chern number that can be extracted from our numerical data for different values of  $U$ . We find the best estimate  $c_1 \sim 0.99$  for the intermediate interaction strength  $U \sim 0.01$ .

### C. Staggered detuning

Here we briefly consider the effects of staggered detuning that was introduced in the experimental study [26] during the loading and band mapping sequences. This detuning can be described by an additional term

$$\frac{\delta}{2} \sum_{l,m} [(-1)^l + (-1)^m] \hat{n}_{l,m} \quad (15)$$

in the Hamiltonians  $\hat{H}(t)$  and  $\hat{H}_{\text{eff},1}$ . We will ignore the higher-order [at most  $O(\frac{1}{\omega^2})$ ] corrections that this term introduces to the effective Hamiltonian. Staggered detuning does not break the symmetry of the effective Hamiltonian  $\hat{H}_{\text{eff},1}$ , but if  $\delta$  is large enough, it can cause a topological phase

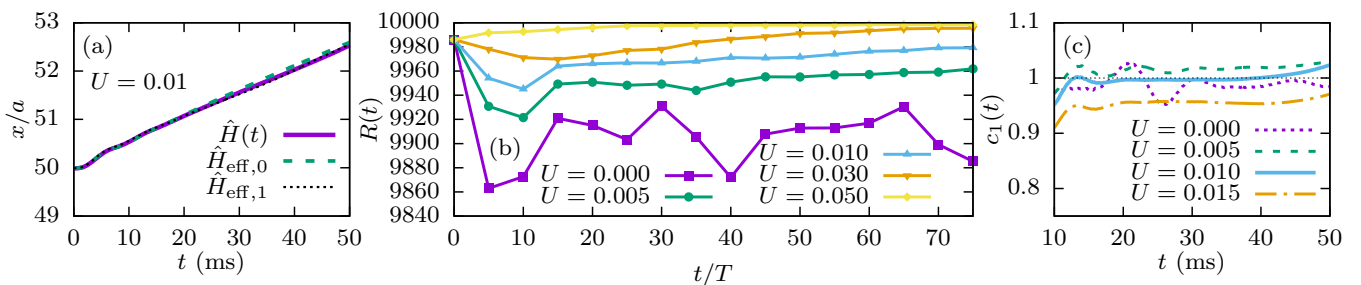


FIG. 10. (a) Comparison of anomalous drifts obtained from evolution using the time-dependent Hamiltonian  $\hat{H}(t)$  (solid purple line), effective Hamiltonian without correction  $\hat{H}_{\text{eff},0}$  (dashed green line) and effective Hamiltonian with correction  $\hat{H}_{\text{eff},1}$  (dotted black line). Intermediate interaction strength  $U = 0.01$ .  $U$  is given in units where  $J = 1$ . (b) Time evolution of the inverse participation ratio in momentum space for several different values of  $U$ . Evolution is performed using the time-dependent Hamiltonian  $\hat{H}(t)$ . When the interactions are strong enough, IPR approaches the maximal possible value (10 000 in this case), which is equal to the total number of states and corresponds to the completely delocalized state.  $U$  is given in units where  $J = 1$ . (c) Chern number of the lowest band obtained for different interaction strengths as the ratio of the theoretical prediction for the anomalous drift and numerical results:  $c_1(t) = (\frac{2fa^2}{\pi\hbar} \int_0^t \gamma_{\text{eff},1}(t') dt') / [x(t) - x(t_0)]$ .

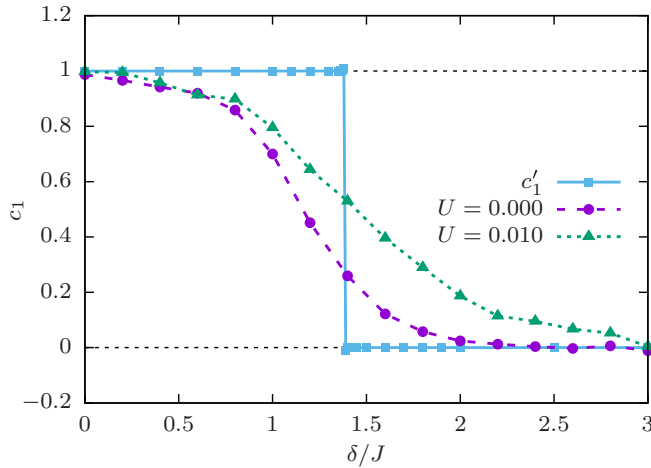


FIG. 11. Lowest band Chern numbers extracted from numerical data for several different values of detuning  $\delta$ . Purple circles: non-interacting case,  $U = 0$ . Green triangles:  $U = 0.01$ . Blue squares: theoretical values of the lowest band Chern number  $c'_1$ . A topological phase transition is visible at  $\delta_c \approx 1.38$ . The lines between points are only a guide to the eye.

transition and make all bands topologically trivial. By numerically calculating the Berry curvature and Chern numbers  $c'_i$ , we find that this transition occurs at  $\delta_c \approx 1.38 J$ ; see Fig. 11. This value is lower than the one for the ordinary Harper-Hofstadter Hamiltonian for  $\alpha = 1/4$ , which is  $\delta_c = 2 J$  [26], due to the different hopping amplitudes  $J'_x$  and  $J'_y$ , and due to the additional  $J_x^2/\omega$  correction that we consider.

We now investigate how this topological transition can be probed through the dynamical protocol used in the experiment. We again numerically calculate the anomalous drift and the evolution of the filling factor, but now with staggered detuning (15) included in the Hamiltonian  $\hat{H}_{\text{initial}}$  (C2) used to obtain the initial state, in the equations of motion (10) and (11), and in the definitions of the band populations  $\eta_i(t)$  (C4). Using these results, we repeat the procedure for the extraction of the lowest band Chern number from numerical data that was carried out in the previous section. The Chern number obtained by comparing the anomalous drift to the prediction calculated from the filling factor is then averaged over the time interval  $t \in (20, 40)$  ms. This interval was chosen in order to avoid the initial quadratic regime and the finite-size effects at later times. The resulting lowest band Chern numbers for several different values of detuning  $\delta$  in both the noninteracting case and the case of intermediate interaction strength  $U = 0.01$  are presented in Fig. 11.

We can see that the calculated value of the Chern number decreases from  $c_1 = 1$  to  $c_1 = 0$  with increasing detuning  $\delta$ . The obtained value of the Chern number is lower than 1 even before the phase transition occurs. This is due to our choice of the initial state, which is not perfectly homogeneous in momentum space. Close to the phase transition, both the energy bands and the Berry curvature have pronounced peaks at the same regions of the first Brillouin zone, and these regions are initially less populated. Because of this, the Berry curvature at these regions contributes less to the anomalous drift, which lowers the measured Chern number. This effect is

somewhat reduced by the interactions, as they smooth out the momentum-space probability density, and might also cancel out the detuning term. Similar interplay of interactions and staggering was observed in the fermionic Hofstadter-Hubbard model [60]. The obtained results are in line with experimental measurements [26].

## V. CONCLUSIONS

Motivated by the recent experimental results reporting the Chern numbers of topological bands in cold-atom setups, we studied numerically bosonic transport in a driven optical lattice. The considered driving scheme and the range of microscopic parameters were chosen to be close to those in a recent experimental study [26]. The driving frequency was set to be high enough in order to avoid strong energy absorption for the relevant time scales. Additionally, the system was restricted to a two-dimensional lattice, even though the actual experimental setup had continuous transverse degrees of freedom. This restriction stabilizes the system [29,31,41] and leads to lower heating rates than those in the experiment. It corresponds to the case of strongly confined third dimension.

We investigated bosonic dynamics for the full time-dependent Hamiltonian, the effective Floquet Hamiltonian, and included the effects of weak repulsive interactions between atoms using the mean-field approximation. In the non-interacting case, we found that the effective Hamiltonian and its band structure depend on the frequency of the drive  $\omega$  through an additional  $J_x^2/\omega$  correction term. The initial state was set as a mixture of incoherent bosons homogeneously populating the lowest band, but a possible direction of future research could be to simulate the full loading sequence of an initial Bose-Einstein condensate and to try to obtain the incoherent state through driving, as it was done in the experiment.

The main focus of this work is on the effects of weak interactions. For a weak atomic repulsion, atomic transitions to higher effective bands obtained in our simulations mainly occur due to a release of the initial interaction energy during the atomic-cloud expansion. Although the effect is undesirable, it can be properly taken into account in the extraction of the Chern number. At larger interaction strengths, the transitions are more pronounced as the system absorbs energy from the drive. In this regime the good agreement between the full and effective description is lost and the measurement should become more complicated. In addition to causing redistribution of atoms over bands, our results show that weak interactions can also be beneficial in measuring the Chern number. Their desirable effect comes about due to smoothing the atomic distribution over the topological band and due to canceling out the contribution of some less relevant terms to the bosonic dynamics.

## ACKNOWLEDGMENTS

This work was supported by the Ministry of Education, Science, and Technological Development of the Republic of Serbia under Projects ON171017, BKMh and TOP-FOP, the Croatian Science Foundation under Grant No. IP-2016-06-5885 SynthMagIA and the TOP-FOP project, and by DAAD (German Academic and Exchange Service) under the BKMh project. Numerical simulations were performed on the PARADOX supercomputing facility at the Scientific Computing

Laboratory of the Institute of Physics Belgrade. This research was funded by the Deutsche Forschungsgemeinschaft (DFG, German Research Foundation) via Research Unit FOR 2414 under project number 277974659. This work was also supported by the Deutsche Forschungsgemeinschaft (DFG) via the high-performance computing center LOEWE-CSC.

## APPENDIX A: EFFECTIVE MODEL

After a unitary transformation into the rotating frame  $\tilde{\psi} = e^{-i\hat{W}t}\psi$ , where  $\tilde{\psi}$  and  $\psi$  are the old and the new wave functions, and  $\hat{W}$  is the staggered potential, the new time-dependent Hamiltonian that describes the experimental setup is given by [26]

$$\hat{H}(t) = J_y \sum_{l,m} (\hat{a}_{l,m+1}^\dagger \hat{a}_{l,m} + \hat{a}_{l,m-1}^\dagger \hat{a}_{l,m}) + \hat{V}^{(+)} e^{i\omega t} + \hat{V}^{(-)} e^{-i\omega t} + \frac{U}{2} \sum_{l,m} \hat{n}_{l,m} (\hat{n}_{l,m} - 1), \quad (\text{A1})$$

where

$$\hat{V}^{(+)} = \kappa/2 \sum_{l,m} \hat{n}_{l,m} g(l, m) - J_x \sum_{l_{\text{odd}},m} (\hat{a}_{l+1,m}^\dagger \hat{a}_{l,m} + \hat{a}_{l-1,m}^\dagger \hat{a}_{l,m}), \quad (\text{A2})$$

$$\hat{V}^{(-)} = \kappa/2 \sum_{l,m} \hat{n}_{l,m} g^*(l, m) - J_x \sum_{l_{\text{even}},m} (\hat{a}_{l+1,m}^\dagger \hat{a}_{l,m} + \hat{a}_{l-1,m}^\dagger \hat{a}_{l,m}), \quad (\text{A3})$$

$$g(l, m) = \cos(l\pi/2 - \pi/4) e^{i(\phi_0 - m\pi/2)} + \cos(l\pi/2 + \pi/4) e^{i(m\pi/2 - \phi_0 - \pi/2)}. \quad (\text{A4})$$

The kick operator is given by

$$\hat{K}(t) = \frac{1}{i\omega} (\hat{V}^{(+)} e^{i\omega t} - \hat{V}^{(-)} e^{-i\omega t}) + O\left(\frac{1}{\omega^2}\right) \quad (\text{A5})$$

and the effective Hamiltonian by

$$\hat{H}_{\text{eff}} = \underbrace{\hat{H}_0}_{\hat{H}_{\text{eff}}^{(0)}} + \underbrace{\frac{1}{\omega} [\hat{V}^{(+)}, \hat{V}^{(-)}]}_{\hat{H}_{\text{eff}}^{(1)}} + \underbrace{\frac{1}{2\omega^2} ([[\hat{V}^{(+)}, \hat{H}_0], \hat{V}^{(-)}] + [[\hat{V}^{(-)}, \hat{H}_0], \hat{V}^{(+)}])}_{\hat{H}_{\text{eff}}^{(2)}} + O\left(\frac{1}{\omega^3}\right). \quad (\text{A6})$$

If we assume that the driving frequency is high and interactions are weak, the interaction term and almost all  $O(\frac{1}{\omega^2})$  terms can be neglected. After substituting Eqs. (A1), (A2), and (A3) into Eq. (A6) we obtain

$$\hat{H}_{\text{eff}}^{(0)} = -J_y \sum_{l,m} (\hat{a}_{l,m+1}^\dagger \hat{a}_{l,m} + \hat{a}_{l,m-1}^\dagger \hat{a}_{l,m}), \quad (\text{A7})$$

$$\hat{H}_{\text{eff}}^{(1)} = \frac{1}{\omega} \left[ \frac{\kappa}{2} \sum_{l,m} \hat{a}_{l,m}^\dagger \hat{a}_{l,m} g(l, m) - J_x \sum_{l_{\text{odd}},m} (\hat{a}_{l+1,m}^\dagger \hat{a}_{l,m} + \hat{a}_{l-1,m}^\dagger \hat{a}_{l,m}), \right. \quad (\text{A8})$$

$$\left. \frac{\kappa}{2} \sum_{l,m} \hat{a}_{l,m}^\dagger \hat{a}_{l,m} g^*(l, m) - J_x \sum_{l_{\text{even}},m} (\hat{a}_{l+1,m}^\dagger \hat{a}_{l,m} + \hat{a}_{l-1,m}^\dagger \hat{a}_{l,m}) \right] = \hat{H}_1 + \hat{H}_2 + \hat{H}_3 + \hat{H}_4.$$

We will now separately calculate each term:

$$\begin{aligned} \hat{H}_1 &= -\frac{J_x \kappa}{2\omega} \sum_{l_{\text{odd}},m,l',m'} g^*(l', m') [\hat{a}_{l+1,m}^\dagger \hat{a}_{l,m} + \hat{a}_{l-1,m}^\dagger \hat{a}_{l,m}, \hat{a}_{l',m'}^\dagger \hat{a}_{l',m'}] \\ &= -\frac{J_x \kappa}{2\omega} \sum_{l_{\text{odd}},m} [(g^*(l, m) - g^*(l+1, m)) \hat{a}_{l+1,m}^\dagger \hat{a}_{l,m} + (g^*(l, m) - g^*(l-1, m)) \hat{a}_{l-1,m}^\dagger \hat{a}_{l,m}], \end{aligned} \quad (\text{A9})$$

$$\begin{aligned} \hat{H}_2 &= -\frac{J_x \kappa}{2\omega} \sum_{l_{\text{even}},m,l',m'} g(l', m') [\hat{a}_{l',m'}^\dagger \hat{a}_{l',m'}, \hat{a}_{l+1,m}^\dagger \hat{a}_{l,m} + \hat{a}_{l-1,m}^\dagger \hat{a}_{l,m}] \\ &= \frac{J_x \kappa}{2\omega} \sum_{l_{\text{even}},m} [(g(l, m) - g(l+1, m)) \hat{a}_{l+1,m}^\dagger \hat{a}_{l,m} + (g(l, m) - g(l-1, m)) \hat{a}_{l-1,m}^\dagger \hat{a}_{l,m}], \end{aligned} \quad (\text{A10})$$

$$\begin{aligned} \hat{H}_3 &= \frac{J_x^2}{\omega} \sum_{l_{\text{odd}},m,l'_{\text{even}},m'} [\hat{a}_{l+1,m}^\dagger \hat{a}_{l,m} + \hat{a}_{l-1,m}^\dagger \hat{a}_{l,m}, \hat{a}_{l'+1,m'}^\dagger \hat{a}_{l',m'} + \hat{a}_{l'-1,m'}^\dagger \hat{a}_{l',m'}] \\ &= \frac{J_x^2}{\omega} \sum_{l_{\text{odd}},m} (2\hat{a}_{l+1,m}^\dagger \hat{a}_{l+1,m} + \hat{a}_{l+3,m}^\dagger \hat{a}_{l+1,m} + \hat{a}_{l-1,m}^\dagger \hat{a}_{l+1,m} - 2\hat{a}_{l,m}^\dagger \hat{a}_{l,m} - \hat{a}_{l+2,m}^\dagger \hat{a}_{l,m} - \hat{a}_{l-2,m}^\dagger \hat{a}_{l,m}) \\ &= \frac{J_x^2}{\omega} \sum_{l,m} (-1)^l (2\hat{a}_{l,m}^\dagger \hat{a}_{l,m} + \hat{a}_{l+2,m}^\dagger \hat{a}_{l,m} + \hat{a}_{l-2,m}^\dagger \hat{a}_{l,m}), \end{aligned} \quad (\text{A11})$$

$$\hat{H}_4 = \frac{\kappa^2}{4\omega} \sum_{l,m,l',m'} g(l,m)g^*(l',m')[\hat{a}_{l,m}^\dagger \hat{a}_{l,m}, \hat{a}_{l',m'}^\dagger \hat{a}_{l',m'}] = 0. \quad (\text{A12})$$

Using trigonometric identities and

$$g(l,m) - g(l \pm 1, m) = \pm \sqrt{2}(\sin[(2l \pm 1 - 1)\pi/4]e^{i(\pi/4 - m\pi/2)} + \sin[(2l \pm 1 + 1)\pi/4]e^{i(m\pi/2 - 3\pi/4)}), \quad (\text{A13})$$

we can rewrite the sum of terms (A9) and (A10) in a more convenient form:

$$\hat{H}_1 + \hat{H}_2 = \frac{J_x \kappa}{\sqrt{2}\omega} \sum_{l,m} (e^{i(m-l)\pi/2 - \pi/4} \hat{a}_{l,m}^\dagger \hat{a}_{l-1,m} + e^{-i(m-l-1)\pi/2 - \pi/4} \hat{a}_{l,m}^\dagger \hat{a}_{l+1,m}). \quad (\text{A14})$$

The only  $O(\frac{1}{\omega^2})$  ( $\hat{H}_{\text{eff}}^{(2)}$ ) term that cannot be neglected in the parameter range that we use is [26]

$$\frac{J_y}{2} \frac{\kappa^2}{\omega^2} \sum_{l,m} (\hat{a}_{l,m+1}^\dagger \hat{a}_{l,m} + \hat{a}_{l,m-1}^\dagger \hat{a}_{l,m}). \quad (\text{A15})$$

Finally, the effective Hamiltonian becomes

$$\hat{H}_{\text{eff},1} = \frac{J_x \kappa}{\sqrt{2}\omega} \sum_{l,m} (e^{i(m-l-1)\pi/2 - \pi/4} \hat{a}_{l+1,m}^\dagger \hat{a}_{l,m} + e^{-i(m-l)\pi/2 - \pi/4} \hat{a}_{l-1,m}^\dagger \hat{a}_{l,m}) - J_y \left(1 - \frac{1}{2} \frac{\kappa^2}{\omega^2}\right) \sum_{l,m} (\hat{a}_{l,m+1}^\dagger \hat{a}_{l,m} + \hat{a}_{l,m-1}^\dagger \hat{a}_{l,m}) \quad (\text{A16})$$

$$+ \frac{J_x^2}{\omega} \sum_{l,m} (-1)^l (2\hat{a}_{l,m}^\dagger \hat{a}_{l,m} + \hat{a}_{l+2,m}^\dagger \hat{a}_{l,m} + \hat{a}_{l-2,m}^\dagger \hat{a}_{l,m}), \quad (\text{A17})$$

with the renormalized nearest-neighbor hopping amplitudes  $J'_x = \frac{J_x \kappa}{\sqrt{2}\omega} = J_y$  and  $J'_y = J_y(1 - \frac{1}{2} \frac{\kappa^2}{\omega^2})$ , and a next-nearest-neighbor along  $\mathbf{e}_x$  hopping term proportional to  $\frac{J_x^2}{\omega}$  in (A17).

## APPENDIX B: EFFECTIVE HAMILTONIAN IN MOMENTUM SPACE

If we choose the unit cell as in Fig. 1(a) [lattice sites A = (1, 0), B = (2, 0), C = (3, 0), and D = (4, 0)], the momentum-space representation of the effective Hamiltonian without correction  $\hat{H}_{\text{eff},0}$  (6) is given by a  $4 \times 4$  matrix

$$\hat{\mathcal{H}}_{\text{eff},0}(\mathbf{k}) = \begin{pmatrix} 0 & J'_x e^{-i\frac{3\pi}{4}} - J'_y e^{-i\mathbf{k} \cdot \mathbf{R}_2} & 0 & J'_x e^{-i\frac{3\pi}{4} - i\mathbf{k} \cdot \mathbf{R}_1} - J'_y e^{i\mathbf{k} \cdot (\mathbf{R}_2 - \mathbf{R}_1)} \\ J'_x e^{i\frac{3\pi}{4}} - J'_y e^{i\mathbf{k} \cdot \mathbf{R}_2} & 0 & J'_x e^{-i\frac{\pi}{4}} - J'_y e^{-i\mathbf{k} \cdot \mathbf{R}_2} & 0 \\ 0 & J'_x e^{i\frac{\pi}{4}} - J'_y e^{i\mathbf{k} \cdot \mathbf{R}_2} & 0 & J'_x e^{i\frac{\pi}{4}} - J'_y e^{-i\mathbf{k} \cdot \mathbf{R}_2} \\ J'_x e^{i\frac{3\pi}{4} + i\mathbf{k} \cdot \mathbf{R}_1} - J'_y e^{i\mathbf{k} \cdot (\mathbf{R}_1 - \mathbf{R}_2)} & 0 & J'_x e^{-i\frac{\pi}{4}} - J'_y e^{i\mathbf{k} \cdot \mathbf{R}_2} & 0 \end{pmatrix}, \quad (\text{B1})$$

where  $\mathbf{R}_1$  and  $\mathbf{R}_2$  are the lattice vectors  $\mathbf{R}_1 = (4, 0)$  and  $\mathbf{R}_2 = (1, 1)$  and  $\mathbf{k}$  is in the first Brillouin zone, which is given by the reciprocal lattice vectors  $\mathbf{b}_1 = \frac{\pi}{2}(1, -1)$  and  $\mathbf{b}_2 = 2\pi(0, 1)$ .

When the  $\frac{J_x^2}{\omega}$  correction is included in the effective Hamiltonian,  $\hat{H}_{\text{eff},1}$  (7), the unit cell is doubled, see Fig. 1(b), and the first Brillouin zone is therefore halved. If we now choose the lattice sites a = (1, 0), B = (2, 0), c = (3, 0), D = (4, 0), A = (2, 1), b = (3, 1), C = (4, 1), and d = (5, 1) for the unit cell, the momentum-space representation of the effective Hamiltonian will be an  $8 \times 8$  matrix

$$\hat{\mathcal{H}}_{\text{eff},1}(\mathbf{k}) = \begin{pmatrix} -\frac{2J_x^2}{\omega} & J'_x e^{-i\frac{3\pi}{4}} & -\frac{J_x^2}{\omega}(1 + e^{i\mathbf{k} \cdot \mathbf{R}_1}) & J'_x e^{-i(\frac{3\pi}{4} - \mathbf{k} \cdot \mathbf{R}_1)} & 0 & -J'_y e^{i\mathbf{k} \cdot \mathbf{R}_2} & 0 & -J'_y e^{i\mathbf{k} \cdot \mathbf{R}_1} \\ J'_x e^{i\frac{3\pi}{4}} & \frac{2J_x^2}{\omega} & J'_x e^{-i\frac{\pi}{4}} & \frac{J_x^2}{\omega}(1 + e^{i\mathbf{k} \cdot \mathbf{R}_1}) & -J'_y & 0 & -J'_y e^{i\mathbf{k} \cdot \mathbf{R}_2} & 0 \\ -\frac{J_x^2}{\omega}(1 + e^{-i\mathbf{k} \cdot \mathbf{R}_1}) & J'_x e^{i\frac{\pi}{4}} & -\frac{2J_x^2}{\omega} & J'_x e^{i\frac{\pi}{4}} & 0 & -J'_y & 0 & -J'_y e^{i\mathbf{k} \cdot \mathbf{R}_2} \\ J'_x e^{i(\frac{3\pi}{4} - \mathbf{k} \cdot \mathbf{R}_1)} & \frac{J_x^2}{\omega}(1 + e^{-i\mathbf{k} \cdot \mathbf{R}_1}) & J'_x e^{-i\frac{\pi}{4}} & \frac{2J_x^2}{\omega} & -J'_y e^{-i\mathbf{k} \cdot (\mathbf{R}_1 - \mathbf{R}_2)} & 0 & -J'_y & 0 \\ 0 & 0 & 0 & -J'_y e^{i\mathbf{k} \cdot (\mathbf{R}_1 - \mathbf{R}_2)} & \frac{2J_x^2}{\omega} & J'_x e^{-i\frac{3\pi}{4}} & \frac{J_x^2}{\omega}(1 + e^{i\mathbf{k} \cdot \mathbf{R}_1}) & J'_x e^{-i(\frac{3\pi}{4} - \mathbf{k} \cdot \mathbf{R}_1)} \\ -J'_y e^{-i\mathbf{k} \cdot \mathbf{R}_2} & 0 & -J'_y & 0 & J'_x e^{i\frac{3\pi}{4}} & -\frac{2J_x^2}{\omega} & J'_x e^{-i\frac{\pi}{4}} & -\frac{J_x^2}{\omega}(1 + e^{i\mathbf{k} \cdot \mathbf{R}_1}) \\ 0 & -J'_y e^{-i\mathbf{k} \cdot \mathbf{R}_2} & 0 & -J'_y & \frac{J_x^2}{\omega}(1 + e^{-i\mathbf{k} \cdot \mathbf{R}_1}) & J'_x e^{i\frac{\pi}{4}} & \frac{2J_x^2}{\omega} & J'_x e^{i\frac{\pi}{4}} \\ -J'_y e^{-i\mathbf{k} \cdot \mathbf{R}_1} & 0 & -J'_y e^{-i\mathbf{k} \cdot \mathbf{R}_2} & 0 & J'_x e^{i(\frac{3\pi}{4} - \mathbf{k} \cdot \mathbf{R}_1)} & -\frac{J_x^2}{\omega}(1 + e^{-i\mathbf{k} \cdot \mathbf{R}_1}) & J'_x e^{-i\frac{\pi}{4}} & -\frac{2J_x^2}{\omega} \end{pmatrix}, \quad (\text{B2})$$



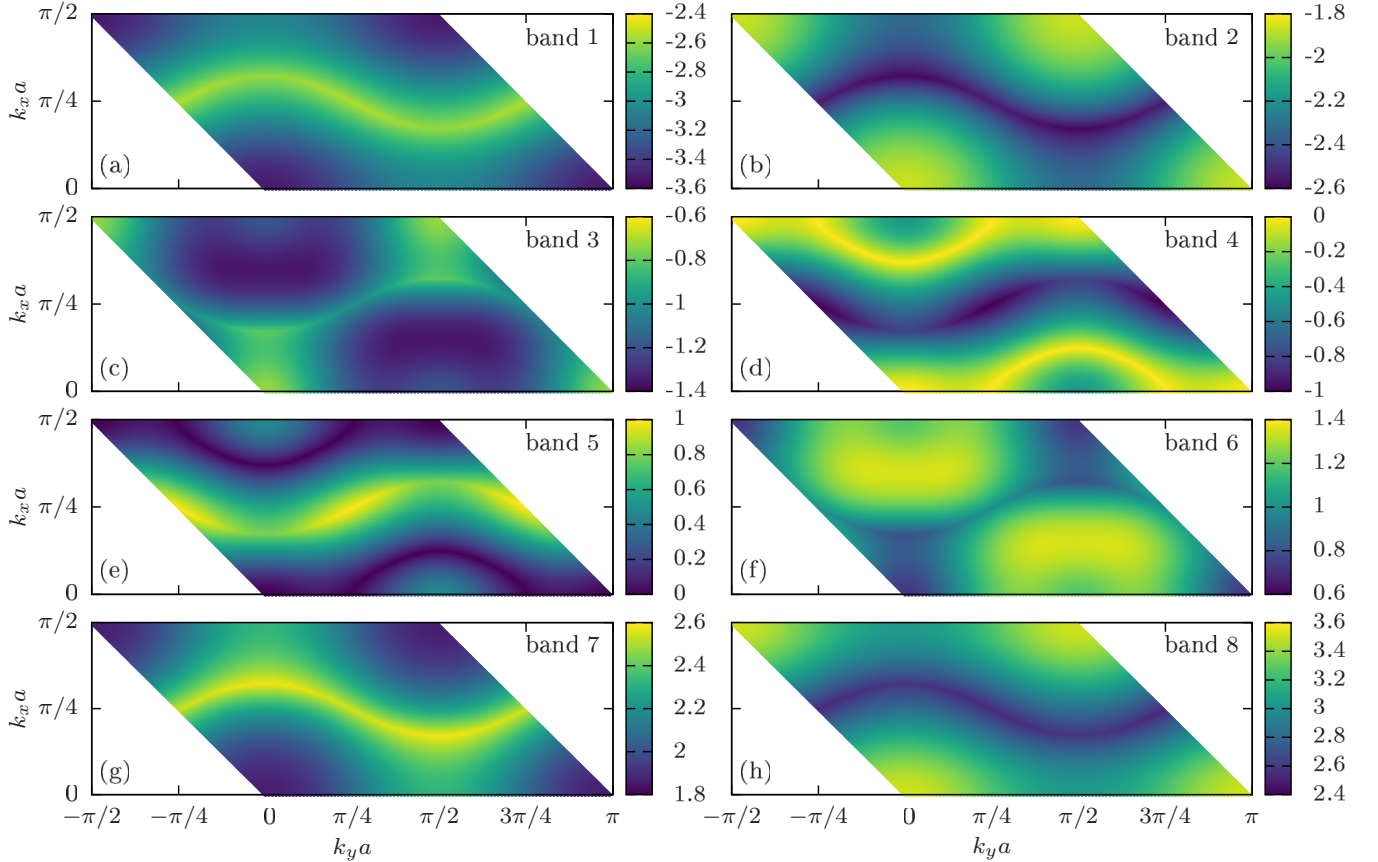


FIG. 12. Eight energy subbands of  $\hat{\mathcal{H}}_{\text{eff},1}(\mathbf{k})$  for the driving frequency  $\omega = 20$ . Subbands 1 and 2 form the lowest band with Chern number  $c_1 = 1$ , subbands 3, 4, 5, and 6 form the middle band with  $c_2 = -2$ , and subbands 7 and 8 form the highest band with  $c_3 = 1$ .

with the lattice vectors  $\mathbf{R}_1 = (4, 0)$  and  $\mathbf{R}_2 = (2, 2)$ . The reciprocal lattice vectors are then  $\mathbf{b}_1 = \frac{\pi}{2}(1, -1)$  and  $\mathbf{b}_2 = \pi(0, 1)$ .

The energy bands of  $\hat{\mathcal{H}}_{\text{eff},1}(\mathbf{k})$  are shown in Figs. 2 and 12.

### APPENDIX C: DESCRIPTION OF INCOHERENT BOSONS

In a typical condensed-matter system constituent particles are electrons. Due to their fermionic statistics, at low enough temperatures, and with Fermi energy above the lowest band, that band of the topological model is uniformly occupied, and consequently the transverse Hall conductivity can be expressed in terms of the Chern number (8) [10]. In contrast, weakly interacting bosons in equilibrium form a Bose-Einstein condensate in the band minima and only probe the local Berry curvature [21].

Yet in the experiment [26] the Chern number was successfully measured using bosonic atoms of  $^{87}\text{Rb}$ . This was possible because in the process of ramping up the drive (4), the initial Bose-Einstein condensate was transferred into an incoherent bosonic mixture. Conveniently, it turned out that the bosonic distribution over the states of the lowest band of the effective Floquet Hamiltonian was nearly uniform. Motivated by the experimental procedure, we model the initial

bosonic state by a statistical matrix

$$\rho(t=0) = \prod_{k=1}^{N_m} |k, N_p\rangle\langle k, N_p|, \quad (\text{C1})$$

where the states  $|k\rangle = a_k^\dagger|0\rangle$  approximately correspond to the lowest-band eigenstates of  $\hat{H}_{\text{eff}}$  and each of these  $N_m$  states is occupied by  $N_p$  atoms  $|k, N_p\rangle = \mathcal{N}(a_k^\dagger)^{N_p}|0\rangle$ .

A procedure for selecting the states  $|k\rangle$  is described in Refs. [22,26]. In order to probe the Chern number of the lowest band, the states  $|k\rangle$  should correspond closely to the lowest-band eigenstates of  $\hat{H}_{\text{eff}}$ . At the same time, in the experiment in the initial moment the atomic cloud is spatially localized. According to Refs. [22,26] the optimal approach is to consider a steep confining potential and to use the low-lying eigenstates of

$$\hat{H}_{\text{initial}} = \hat{h}^{\text{eff}} + \left(\frac{r}{r_0}\right)^\zeta, \quad (\text{C2})$$

where in our calculations  $\hat{h}^{\text{eff}}$  is either  $\hat{H}_{\text{eff},0}$  from Eq. (6) or  $\hat{H}_{\text{eff},1}$  from Eq. (7) and the parameters of the confining potential are set to  $r_0 = 20$ ,  $\zeta = 20$ .

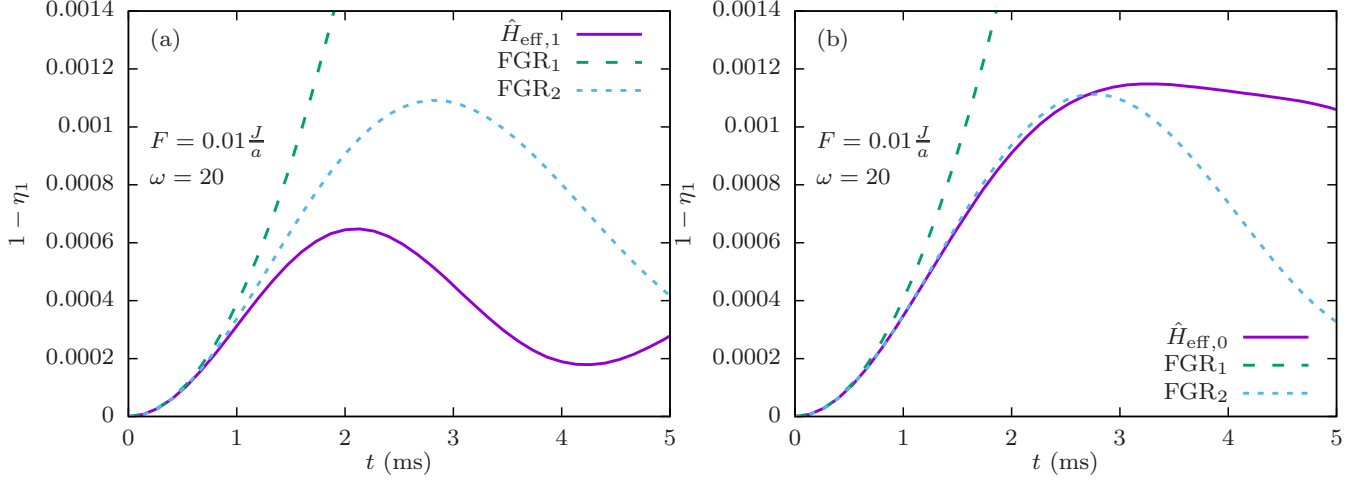


FIG. 13. Population in higher bands, comparison of numerical results (solid line) with the Fermi's golden rule in the first and second approximation (dashed lines). Band populations are calculated for an initial BEC in an eigenstate of the effective Hamiltonian and then averaged over (approximately) all states in the first band. (a) Initial state and evolution from the effective Hamiltonian with correction  $\hat{H}_{\text{eff},1}$ , Eq. (7). (b) Without the correction,  $\hat{H}_{\text{eff},0}$ , Eq. (6).

The dynamics of the initial state (C1) is induced by a double quench: at  $t_0 = 0$  the atomic cloud is released from the confining potential and exposed to a uniform force of intensity  $F$  along the  $y$  direction. During the whole procedure the driving providing the laser-assisted tunneling, defined in Eq. (4), is running.

The main observables of interest are the center-of-mass position along  $x$  direction

$$x(t) = \left\langle \sum_{l,m} l |\psi_{l,m}(t)|^2 \right\rangle \quad (\text{C3})$$

and the population of the  $i$ th band of the effective model

$$\eta_i(t) = \left\langle \sum_{|k\rangle \in i\text{th band}} \left| \sum_{l,m} \alpha_{lm}^{k*} \psi_{lm}(t) \right|^2 \right\rangle, \quad (\text{C4})$$

where the states  $|k\rangle = \sum_{l,m} \alpha_{lm}^k |l, m\rangle$  correspond to the eigenstates of the effective model. Here, angle brackets  $\langle \rangle$  denote averaging over  $N_{\text{samples}}$  sets of initial conditions.

In the case of noninteracting particles, these and other quantities can be numerically accessed by solving the single-particle time-dependent Schrödinger equation for  $N_m$  different initial states  $|k\rangle$ . This is equivalent to sampling the initial state according to Eq. (9).

In the end, we give two technical remarks. First, all our calculations are done in the rotating frame; see Eq. (A1) in Appendix A. The staggered potential (2) is removed in this way. Second, in the case when the evolution is governed by the time-dependent Hamiltonian (10), the initial state is multiplied by the operator  $e^{-i\hat{K}(0)}$  in order to properly compare these results to the ones obtained from the evolution governed by the effective Hamiltonian (11); see Eq. (5).

#### APPENDIX D: INITIAL QUADRATIC REGIME

For simplicity, we will consider only the case without the confining potential and with very weak force  $F = 0.01$ .

The initial state is a Bose-Einstein condensate in one of the eigenstates of the effective Hamiltonian. The results are later averaged over all first band eigenstates.

Fermi's golden rule predicts that the probability for transition from an initial state  $\psi_i$  to a final state  $\psi_f$ , induced by a perturbation  $\Delta\hat{H}$ , is proportional to the square of matrix elements  $|\langle\psi_i|\Delta\hat{H}|\psi_f\rangle|^2$ . In this case, the perturbation is  $\Delta\hat{H} = F\hat{y}$ . If we assume that the probability of a particle being in the initial state is always  $P_i(t) = |\psi_i(t)|^2 \approx 1$ , Fermi's golden rule predicts [61]

$$P_{i \rightarrow f}^{\text{FGR}_1}(t) = \frac{1}{\hbar^2} |\langle\psi_i|\Delta\hat{H}|\psi_f\rangle|^2 t^2. \quad (\text{D1})$$

If we now also consider transitions from the other states to the initial state, but keep the assumption that the populations in other states are small  $P_{j \neq i}(t) = |\psi_{j \neq i}(t)|^2 \ll 1$ , the time-dependent perturbation theory then predicts [61]

$$P_{i \rightarrow f}^{\text{FGR}_2}(t) = |\langle i|\Delta\hat{H}|f\rangle|^2 \frac{1 - 2e^{-\frac{\Gamma}{2\hbar}t} \cos\left(\frac{E_f - E_i}{\hbar}t\right) + e^{-\frac{\Gamma}{\hbar}t}}{(E_f - E_i)^2 + \frac{\Gamma^2}{4}}, \quad (\text{D2})$$

where  $\Gamma = \frac{2\pi}{\hbar} |\langle i|\Delta\hat{H}|f\rangle|^2$  and  $E_i$  ( $E_f$ ) is the energy of the initial (final) state.

We plot the numerical results and both theoretical predictions from Fermi's golden rule in Fig. 13. Here we can see that all three curves agree well for short times, the second approximation longer remains close to the numerical results, and that the initial quadratic regime is reproduced by theory. This is the so-called quantum Zeno regime [57].

#### APPENDIX E: ENERGY

Time evolution of kinetic and interaction energy per particle for different interaction strengths is plotted in Fig. 14. Here we define the kinetic energy per particle as the expectation value of the time-dependent Hamiltonian (A1) divided by the total number of particles  $E_{\text{kin}}(t) = \frac{1}{N} \langle \sum_{l,m,i,j} \psi_{l,m}^* \psi_{l,m} \rangle$

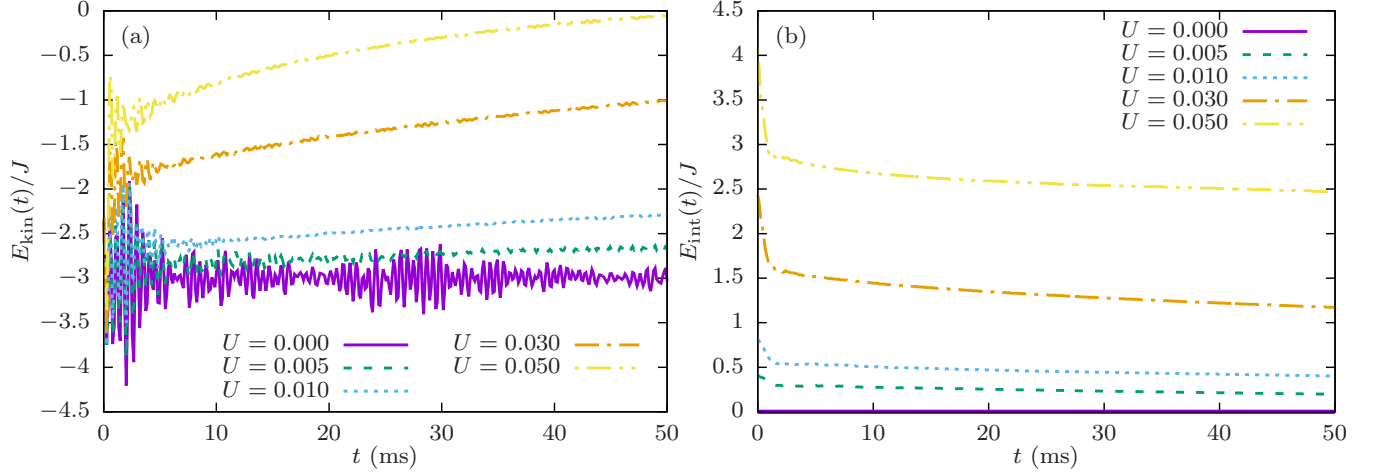


FIG. 14. (a) Kinetic energy per particle (expectation value of the time-dependent Hamiltonian  $E_{\text{kin}}(t) = \frac{1}{N} \langle \sum_{l,m,i,j} \psi_{l,m}^*(t) H_{l,m,ij}(t) \psi_{l,m}(t) \rangle$ ) divided by the total number of particles  $N$  for several different interaction strengths. (b) Interaction energy per particle  $E_{\text{int}}(t) = \frac{1}{N} \langle \sum_{l,m} |\psi_{l,m}(t)|^2 [|\psi_{l,m}(t)|^2 - 1] \rangle$ .  $U$  is given in units where  $J = 1$ .

$H_{l,m,ij}(t) \psi_{l,m}(t)$ , while the interaction energy per particle is  $E_{\text{int}}(t) = \frac{1}{N} \langle \sum_{l,m} |\psi_{l,m}(t)|^2 [|\psi_{l,m}(t)|^2 - 1] \rangle$ . Both energies grow with increasing interaction coefficient  $U$ .

When the interactions are strong enough and after long enough time, the atoms become equally distributed between the eigenstates of the Hamiltonian  $\hat{H}(t)$ . As the energy spectrum of  $\hat{H}(t)$  is symmetric around zero, the expectation value of  $\hat{H}(t)$  (kinetic energy) should be zero when all bands are equally populated. We can see this in Fig. 14(a), where the kinetic energy approaches zero at  $t \approx 50$  ms for the case  $U = 0.05$ .

The interaction energy at first rapidly decreases, as the cloud rapidly expands after turning off the confinement

potential  $\hat{V}_{\text{conf}}$ , and after that continues to slowly decrease as the cloud slowly expands; see Fig. 14(b).

These considerations also provide a possibility to discuss the applicability of the approximative method introduced in Sec. IV. As we work in the regime of high frequency  $\omega = 20$ , we find that for weak interaction, at short enough times of propagation, the energy is approximately conserved. At stronger values of  $U \geq 0.01$  we observe a slow increase in the total energy on the considered time scales. In both cases we do not find the onset of parametric instabilities [31]. If present, these instabilities are signaled by an order of magnitude increase in energy on a short time scale, that we do not find.

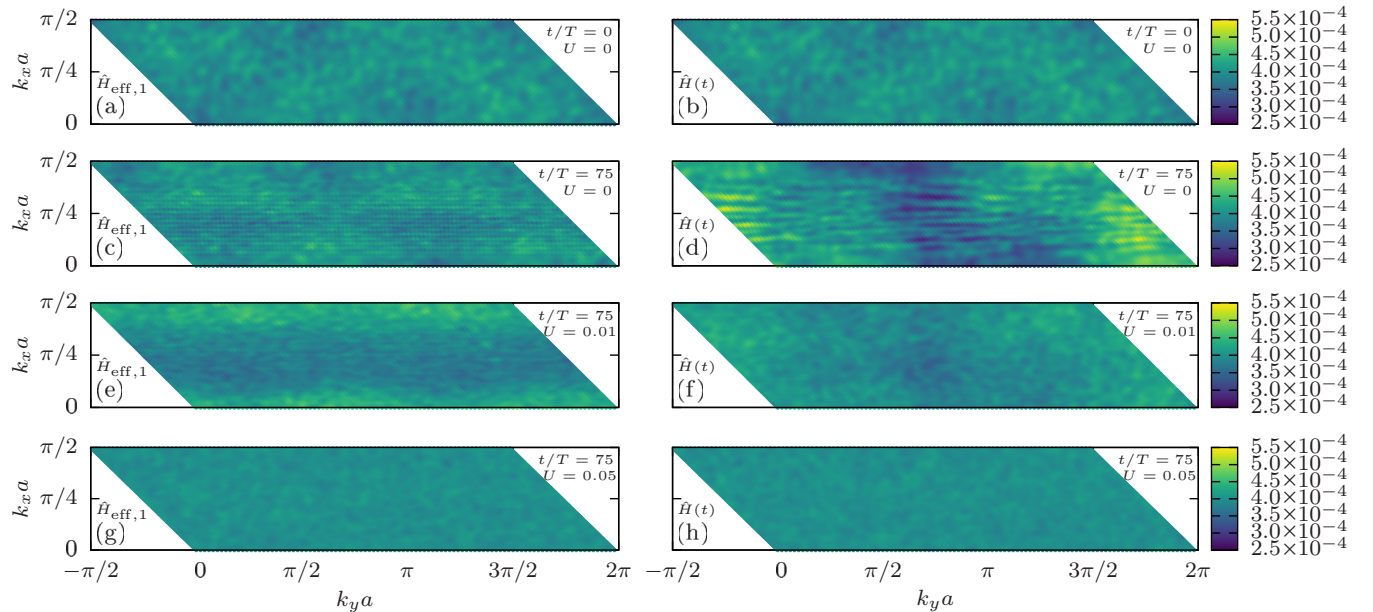


FIG. 15. Momentum-space density distribution in all bands,  $\eta_1(\mathbf{k}) + \eta_2(\mathbf{k}) + \eta_3(\mathbf{k})$ .  $U$  is given in units where  $J = 1$ . Left: evolution using the time-dependent Hamiltonian  $\hat{H}_{\text{eff},1}$ . Right: evolution using the time-dependent Hamiltonian  $\hat{H}(t)$ . (a), (b) Initial state. (c), (d) Final state after 50 ms (75 driving periods), noninteracting case  $U = 0$ . (e), (f)  $U = 0.01$ . (g), (h)  $U = 0.05$ .



In addition, the two-body interaction can deplete the occupancies of initial coherent modes [29,41] and limit the validity of our approach. In principle, these types of processes can be addressed by including quantum fluctuations along the lines of the full truncated Wigner approach [45]. Yet, we set our parameters in such a way that these additional contributions are small.

## APPENDIX F: MOMENTUM-SPACE DENSITY DISTRIBUTION

The momentum-space probability densities at the initial moment and after 75 driving periods (50 ms) are shown in Fig. 15. The interactions deplete the lowest band, but also smooth out the density distribution.

- 
- [1] I. Bloch, J. Dalibard, and W. Zwerger, *Rev. Mod. Phys.* **80**, 885 (2008).
- [2] Y.-J. Lin, R. L. Compton, K. Jiménez-García, J. V. Porto, and I. B. Spielman, *Nature (London)* **462**, 628 (2009).
- [3] J. Dalibard, F. Gerbier, G. Juzeliūnas, and P. Öhberg, *Rev. Mod. Phys.* **83**, 1523 (2011).
- [4] D. R. Hofstadter, *Phys. Rev. B* **14**, 2239 (1976).
- [5] F. D. M. Haldane, *Phys. Rev. Lett.* **61**, 2015 (1988).
- [6] M. Aidelsburger, M. Atala, M. Lohse, J. T. Barreiro, B. Paredes, and I. Bloch, *Phys. Rev. Lett.* **111**, 185301 (2013).
- [7] H. Miyake, G. A. Siviloglou, C. J. Kennedy, W. C. Burton, and W. Ketterle, *Phys. Rev. Lett.* **111**, 185302 (2013).
- [8] G. Jotzu, M. Messer, R. Desbuquois, M. Lebrat, T. Uehlinger, D. Greif, and T. Esslinger, *Nature (London)* **515**, 237 (2014).
- [9] M. E. Tai, A. Lukin, M. Rispoli, R. Schittko, T. Menke, D. Borgnia, P. M. Preiss, F. Grusdt, A. M. Kaufman, and M. Greiner, *Nature (London)* **546**, 519 (2017).
- [10] D. J. Thouless, M. Kohmoto, M. P. Nightingale, and M. den Nijs, *Phys. Rev. Lett.* **49**, 405 (1982).
- [11] G. Floquet, *Ann. Sci. Éc. Norm. Supér.* **12**, 47 (1883).
- [12] M. Grifoni and P. Hänggi, *Phys. Rep.* **304**, 229 (1998).
- [13] N. Goldman and J. Dalibard, *Phys. Rev. X* **4**, 031027 (2014).
- [14] N. Goldman, J. Dalibard, M. Aidelsburger, and N. R. Cooper, *Phys. Rev. A* **91**, 033632 (2015).
- [15] A. Eckardt and E. Anisimovas, *New J. Phys.* **17**, 093039 (2015).
- [16] M. Aidelsburger, S. Nascimbène, and N. Goldman, *C. R. Phys.* (2018), doi:10.1016/j.crhy.2018.03.002.
- [17] A. Eckardt, *Rev. Mod. Phys.* **89**, 011004 (2017).
- [18] N. R. Cooper, J. Dalibard, and I. B. Spielman, [arXiv:1803.00249](https://arxiv.org/abs/1803.00249) [Rev. Mod. Phys. (to be published)].
- [19] G. Sun and A. Eckardt, [arXiv:1805.02443](https://arxiv.org/abs/1805.02443).
- [20] K. M. Fujiwara, K. Singh, Z. A. Geiger, R. Senaratne, S. Rajagopal, M. Lipatov, and D. M. Weld, [arXiv:1806.07858](https://arxiv.org/abs/1806.07858).
- [21] H. M. Price and N. R. Cooper, *Phys. Rev. A* **85**, 033620 (2012).
- [22] A. Dauphin and N. Goldman, *Phys. Rev. Lett.* **111**, 135302 (2013).
- [23] M. Bukov and A. Polkovnikov, *Phys. Rev. A* **90**, 043613 (2014).
- [24] H. M. Price, O. Zilberberg, T. Ozawa, I. Carusotto, and N. Goldman, *Phys. Rev. B* **93**, 245113 (2016).
- [25] S. Muga, A. Dauphin, P. Massignan, L. Tarruell, M. Lewenstein, C. Lobo, and A. Celi, *SciPost Phys.* **3**, 012 (2017).
- [26] M. Aidelsburger, M. Lohse, C. Schweizer, M. Atala, J. T. Barreiro, S. Nascimbène, N. R. Cooper, I. Bloch, and N. Goldman, *Nat. Phys.* **11**, 162 (2015).
- [27] L. D'Alessio and M. Rigol, *Phys. Rev. X* **4**, 041048 (2014).
- [28] M. Bukov, S. Gopalakrishnan, M. Knap, and E. Demler, *Phys. Rev. Lett.* **115**, 205301 (2015).
- [29] S. Choudhury and E. J. Mueller, *Phys. Rev. A* **92**, 063639 (2015).
- [30] C. J. Kennedy, W. C. Burton, W. C. Chung, and W. Ketterle, *Nat. Phys.* **11**, 859 (2015).
- [31] S. Lellouch, M. Bukov, E. Demler, and N. Goldman, *Phys. Rev. X* **7**, 021015 (2017).
- [32] K. Plekhanov, G. Roux, and K. Le Hur, *Phys. Rev. B* **95**, 045102 (2017).
- [33] S. Lellouch and N. Goldman, *Quantum Sci. Technol.* **3**, 024011 (2018).
- [34] E. Michon, C. Cabrera-Gutiérrez, A. Fortun, M. Berger, M. Arnal, V. Brunaud, J. Billy, C. Petitjean, P. Schlagheck, and D. Guéry-Odelin, *New J. Phys.* **20**, 053035 (2018).
- [35] J. Näger, K. Wintersperger, M. Bukov, S. Lellouch, E. Demler, U. Schneider, I. Bloch, N. Goldman, and M. Aidelsburger, [arXiv:1808.07462](https://arxiv.org/abs/1808.07462).
- [36] T. Boulier, J. Maslek, M. Bukov, C. Bracamontes, E. Magnan, S. Lellouch, E. Demler, N. Goldman, and J. V. Porto, [arXiv:1808.07637](https://arxiv.org/abs/1808.07637).
- [37] K. Lelas, N. Drpić, T. Dubček, D. Jukić, R. Pezer, and H. Buljan, *New J. Phys.* **18**, 095002 (2016).
- [38] J. Motruk and F. Pollmann, *Phys. Rev. B* **96**, 165107 (2017).
- [39] W. W. Ho and D. A. Abanin, [arXiv:1611.05024](https://arxiv.org/abs/1611.05024).
- [40] A. Dauphin, D.-T. Tran, M. Lewenstein, and N. Goldman, *2D Mater.* **4**, 024010 (2017).
- [41] T. Bilitewski and N. R. Cooper, *Phys. Rev. A* **91**, 063611 (2015).
- [42] M. V. Berry, *Proc. R. Soc. London A* **392**, 45 (1984).
- [43] T. Fukui, Y. Hatsugai, and H. Suzuki, *J. Phys. Soc. Jpn.* **74**, 1674 (2005).
- [44] Y. Kagan and B. V. Svistunov, *Phys. Rev. Lett.* **79**, 3331 (1997).
- [45] A. Polkovnikov, *Ann. Phys. (N.Y.)* **325**, 1790 (2010).
- [46] H. Buljan, O. Cohen, J. W. Fleischer, T. Schwartz, M. Segev, Z. H. Musslimani, N. K. Efremidis, and D. N. Christodoulides, *Phys. Rev. Lett.* **92**, 223901 (2004).
- [47] O. Cohen, H. Buljan, T. Schwartz, J. W. Fleischer, and M. Segev, *Phys. Rev. E* **73**, 015601 (2006).
- [48] F. Dalfovo, S. Giorgini, L. P. Pitaevskii, and S. Stringari, *Rev. Mod. Phys.* **71**, 463 (1999).
- [49] L. Pitaevskii and S. Stringari, *Bose-Einstein Condensation* (Clarendon Press, Oxford, 2003).
- [50] C. J. Pethick and H. Smith, *Bose-Einstein Condensation in Dilute Gases* (Cambridge University Press, Cambridge, UK, 2008).
- [51] M. D. S. Gardiner, N. Proukakis, and M. Szymanska, *Finite Temperature and Non-Equilibrium Dynamics* (Imperial College Press, London, 2013).
- [52] T. Mori, T. Kuwahara, and K. Saito, *Phys. Rev. Lett.* **116**, 120401 (2016).
- [53] T. Kuwahara, T. Mori, and K. Saito, *Ann. Phys. (N.Y.)* **367**, 96 (2016).

- [54] D. A. Abanin, W. De Roeck, W. W. Ho, and F. Huveneers, *Phys. Rev. B* **95**, 014112 (2017).
- [55] D. Abanin, W. De Roeck, W. W. Ho, and F. Huveneers, *Commun. Math. Phys.* **354**, 809 (2017).
- [56] D. Xiao, M.-C. Chang, and Q. Niu, *Rev. Mod. Phys.* **82**, 1959 (2010).
- [57] V. Debierre, I. Goessens, E. Brainis, and T. Durt, *Phys. Rev. A* **92**, 023825 (2015).
- [58] G. J. Milburn, J. Corney, E. M. Wright, and D. F. Walls, *Phys. Rev. A* **55**, 4318 (1997).
- [59] S. Raghavan, A. Smerzi, S. Fantoni, and S. R. Shenoy, *Phys. Rev. A* **59**, 620 (1999).
- [60] D. Cocks, P. P. Orth, S. Rachel, M. Buchhold, K. Le Hur, and W. Hofstetter, *Phys. Rev. Lett.* **109**, 205303 (2012).
- [61] E. Merzbacher, *Quantum Mechanics*, 3rd ed. (Wiley, New York, 1998).

## Emergent Chiral Spin State in the Mott Phase of a Bosonic Kane-Mele-Hubbard Model

Kirill Plekhanov,<sup>1,2</sup> Ivana Vasić,<sup>3</sup> Alexandru Petrescu,<sup>4</sup> Rajbir Nirwan,<sup>5</sup> Guillaume Roux,<sup>1</sup>  
Walter Hofstetter,<sup>5</sup> and Karyn Le Hur<sup>2</sup>

<sup>1</sup>*LPTMS, CNRS, Univ. Paris-Sud, Université Paris-Saclay, 91405 Orsay, France*

<sup>2</sup>*Centre de Physique Théorique, Ecole Polytechnique, CNRS, Université Paris-Saclay, F-91128 Palaiseau, France*

<sup>3</sup>*Scientific Computing Laboratory, Center for the Study of Complex Systems, Institute of Physics Belgrade, University of Belgrade, 11080 Belgrade, Serbia*

<sup>4</sup>*Department of Electrical Engineering, Princeton University, Princeton, New Jersey 08544, USA*

<sup>5</sup>*Institut für Theoretische Physik, Goethe-Universität, 60438 Frankfurt/Main, Germany*

 (Received 28 July 2017; revised manuscript received 13 November 2017; published 10 April 2018)

Recently, the frustrated  $XY$  model for spins  $1/2$  on the honeycomb lattice has attracted a lot of attention in relation with the possibility to realize a chiral spin liquid state. This model is relevant to the physics of some quantum magnets. Using the flexibility of ultracold atom setups, we propose an alternative way to realize this model through the Mott regime of the bosonic Kane-Mele-Hubbard model. The phase diagram of this model is derived using bosonic dynamical mean-field theory. Focusing on the Mott phase, we investigate its magnetic properties as a function of frustration. We do find an emergent chiral spin state in the intermediate frustration regime. Using exact diagonalization we study more closely the physics of the effective frustrated  $XY$  model and the properties of the chiral spin state. This gapped phase displays a chiral order, breaking time-reversal and parity symmetry, but is not topologically ordered (the Chern number is zero).

DOI: [10.1103/PhysRevLett.120.157201](https://doi.org/10.1103/PhysRevLett.120.157201)

The last few decades have seen growing interest in the quest for exotic spin states [1]. Significant progress has been made both from the theoretical and experimental sides [2–4]. The best candidates are found in two-dimensional systems. Disordered phases are expected to occur in complex geometries, such as the kagome lattice [5–8], or in frustrated bipartite lattices, such as the square lattice with second-neighbor couplings [9,10]. Among basic lattices, the honeycomb hosts free Majorana fermions due to Kitaev anisotropic interactions [11], and raises questions when starting from the Hubbard model [12–14]. In such context and motivated by quantum magnets [15], frustrated Heisenberg models on the honeycomb lattice have been recently explored [16–29]. In parallel, some materials were found to realize the  $XXZ$  version of this model [30], and theoretical and numerical studies suggested that the  $XY$  version possibly hosted a chiral spin liquid state, with seemingly contradictory results [31–38]. As suggested in Ref. [39], in the intermediate frustration regime the ground-state physics could be mapped to a fermionic Haldane model [40] with topological Bloch bands at a mean-field level, as a result of Chern-Simons (ChS) gauge fields [41–45]. However, the topological nature of this spin state is still elusive.

Our objectives are twofold in this Letter. Motivated by cold atom experiments [46,47], we first study the phase diagram of the bosonic Kane-Mele-Hubbard (BKMH) model using bosonic dynamical mean-field theory

(B-DMFT) [48–54]. The Kane-Mele model [55] is the standard model with spin-orbit coupling that displays a  $\mathbb{Z}_2$  topological classification. Still, it has not yet been studied for interacting bosons, and for interacting fermions at the Mott transition it becomes magnetically ordered in the  $xy$  plane, with quantum fluctuations stabilizing the Neel ordering [56–58]. We explore the Mott regime of this model and show that it allows for a tunable realization of the frustrated  $XY$  model on the honeycomb lattice. Second, we use exact diagonalization (ED) and theoretical arguments to study the resulting  $XY$  model. We observe that an intermediate frustration regime hosts a chiral spin state with spontaneously broken time-reversal ( $\mathcal{T}$ ) and parity ( $\mathcal{P}$ ) symmetries, associated with antiferromagnetic ordering and the onset of local currents. Based on the calculation of the Chern number, we conclude that this state has no intrinsic topological order.

We start our analysis with the bosonic version of the Kane-Mele model [55] on the honeycomb lattice [Fig. 1(a)], which contains two species of bosons labeled by  $\sigma = \uparrow, \downarrow$ . In the presence of repulsive Bose-Hubbard interactions, the Hamiltonian reads

$$H = -t_1 \sum_{\sigma, \langle ij \rangle} [b_{\sigma, r_i}^\dagger b_{\sigma, r_j} + \text{H.c.}] + it_2 \sum_{\sigma, \langle\langle ik \rangle\rangle} \nu_{ik}^\sigma [b_{\sigma, r_i}^\dagger b_{\sigma, r_k} - \text{H.c.}] + \frac{U}{2} \sum_{\sigma, i} n_{\sigma, r_i} (n_{\sigma, r_i} - 1) + U_{\uparrow\downarrow} \sum_i n_{\uparrow, r_i} n_{\downarrow, r_i}. \quad (1)$$

Here,  $b_{\sigma,r_i}^\dagger$  ( $b_{\sigma,r_i}$ ) are creation (annihilation) operators at site  $i$ , and  $n_{\sigma,r_i} = b_{\sigma,r_i}^\dagger b_{\sigma,r_i}$  is the density operator.  $t_1$  ( $t_2$ ) is the amplitude of hopping to the first (second) neighbors, and  $\nu_{ik}^\uparrow = -\nu_{ik}^\downarrow = 1$  ( $-1$ ) for a left turn (right turn) on the honeycomb lattice. We assume a filling of one boson per site  $\langle n_{\uparrow,r_i} + n_{\downarrow,r_i} \rangle = 1$ . The Haldane model [40] for spinless fermions has been realized through Floquet engineering in cold atoms [59]. Similarly, spin-orbit models have been proposed in optical lattices setups [60–62] and experimentally achieved with photons [63–66]. All the ingredients required for a successful implementation of Eq. (1) are thus available.

*I. B-DMFT on BKMH model.*—The ground-state phase diagram of the BKMH model obtained from B-DMFT [48–53] is shown in Fig. 1(b). In order to address unusual states breaking translational symmetry, we use real-space B-DMFT [54,67–69]. Local effective problems represented by the Anderson impurity model are solved using exact diagonalization [54]. As found for the bosonic Haldane model at the same filling [70], three phases are competing: a uniform superfluid (SF), a chiral superfluid (CSF) and a Mott insulator (MI) (they are distinguished by the behaviors of the order parameter  $\langle b_{\sigma,r_i} \rangle$  and of the local currents  $J_{ij}^\sigma = \Im \mathbf{m} \langle b_{\sigma,r_i}^\dagger b_{\sigma,r_j} \rangle$  [54]).

We here focus on the MI phase. As shown in Fig. 1(b), the system enters the Mott phase when intraspecies ( $U$ ) and interspecies ( $U_{\uparrow\downarrow}$ ) interactions become strong enough. The internal structure of the MI phase is richer than in the bosonic Haldane model [70] and comprises different

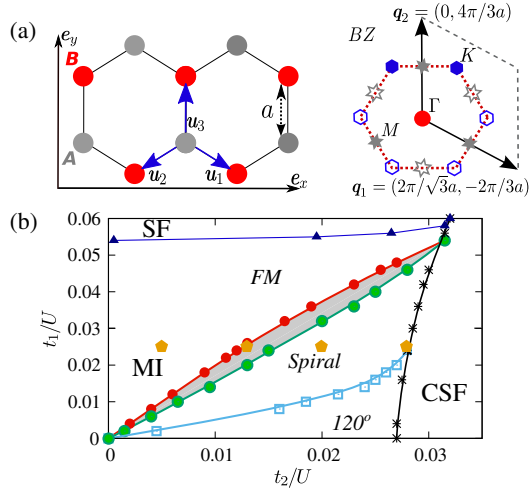


FIG. 1. (a) Honeycomb lattice and its first Brillouin zone. (b) Phase diagram of the BKMH model obtained using B-DMFT containing Mott insulator, uniform superfluid, and chiral superfluid phases with different regimes of the MI phase marked in italic. The central gray region corresponds to the states with no coplanar order. Parameters  $U_{\uparrow\downarrow}/U = 0.5$ ,  $\mu/U_{\uparrow\downarrow} = 0.5$ , lattice of 96 sites. “Pentagons” mark parameter values that we further explore in Figs. 2(a)–2(d).

regimes. Applying standard perturbation theory [71], one rewrites the Hamiltonian (1) in terms of pseudospin-1/2 operators  $S_{r_i}^+ = S_{r_i}^x + iS_{r_i}^y = b_{\uparrow,r_i}^\dagger b_{\downarrow,r_i}$ ,  $S_{r_i}^- = S_{r_i}^x - iS_{r_i}^y = b_{\downarrow,r_i}^\dagger b_{\uparrow,r_i}$  and  $S_{r_i}^z = (n_{\uparrow,r_i} - n_{\downarrow,r_i})/2$  as follows:

$$H = -\sum_{\langle ij \rangle} [J_1(S_{r_i}^+ S_{r_j}^- + \text{H.c.}) - K_1 S_{r_i}^z S_{r_j}^z] + \sum_{\langle\langle ik \rangle\rangle} [J_2(S_{r_i}^+ S_{r_k}^- + \text{H.c.}) + K_2 S_{r_i}^z S_{r_k}^z], \quad (2)$$

where  $J_i = t_i^2/U_{\uparrow\downarrow}$  and  $K_i = t_i^2(1/U_{\uparrow\downarrow} - 2/U)$ . We observe that the spin-1/2 frustrated XY model is realized when  $U = 2U_{\uparrow\downarrow}$  (for which  $K_i = 0$ ). Frustration is associated with the positive sign of the  $J_2$  term, which combines the sign of the bosonic exchange and the phase of  $\pi$  accumulated in the hoppings between second neighbors. The fermionic Kane-Mele model does not include such frustrating terms [56,72].

The properties of this effective XY model depend only on the ratio  $J_2/J_1 = (t_2/t_1)^2$ . In the classical limit, a coplanar ansatz [16,54,73] provides the following phase diagram: the ferromagnetic (FM) phase is stable for  $J_2/J_1 \leq 1/6$ , above which degenerate incommensurate spiral waves become energetically favored. Their wave vectors live on closed contours in the Brillouin zone. In the case of the Heisenberg model, quantum fluctuations were predicted to lift this degeneracy via an order-by-disorder mechanism [18].

B-DMFT on the BKMH model captures already deviations from this classical picture. In Figs. 2(a)–2(d), we study the coplanar spin ordering (arrows), in the presence of an external staggered magnetic field  $h_z$ , breaking the  $\mathcal{P}$  symmetry (bond-center reflection which interchanges sublattices A and B):

$$H_z = h_z \left( \sum_{i \in A} S_{r_i}^z - \sum_{j \in B} S_{r_j}^z \right). \quad (3)$$

It corresponds to a staggered chemical potential in the boson language [74] and we will understand its role hereafter. We directly infer some of the ordered phases: at low  $J_2/J_1$ , all spins are aligned in a FM order, while at large  $J_2/J_1$ , we recover a  $120^\circ$  order. For  $U_{\uparrow\downarrow}/U = 0.5$ ,  $t_1/U = 0.025$  in the range  $0.36 \lesssim J_2/J_1 \lesssim 1.23$  we observe a different configuration of spiral waves [Fig. 2(c)]. In addition, we find an exotic intermediate regime when  $0.25 \lesssim J_2/J_1 \lesssim 0.36$  (we notice that positions of phase boundaries are affected by  $h_z$ ), characterized by a chiral spin state (CSS) with no coplanar magnetic order [Fig. 2(b)]. This is reminiscent of the debated intermediate phase found in numerical studies on the XY model [31–38]. On the one hand, density matrix renormalization group [33,34] and coupled cluster method [35] results evidenced an antiferromagnetic Ising ordering, breaking  $\mathcal{P}$  while preserving translational invariance. On the other hand, this observation was not reported in ED [31,32] nor variational Monte Carlo

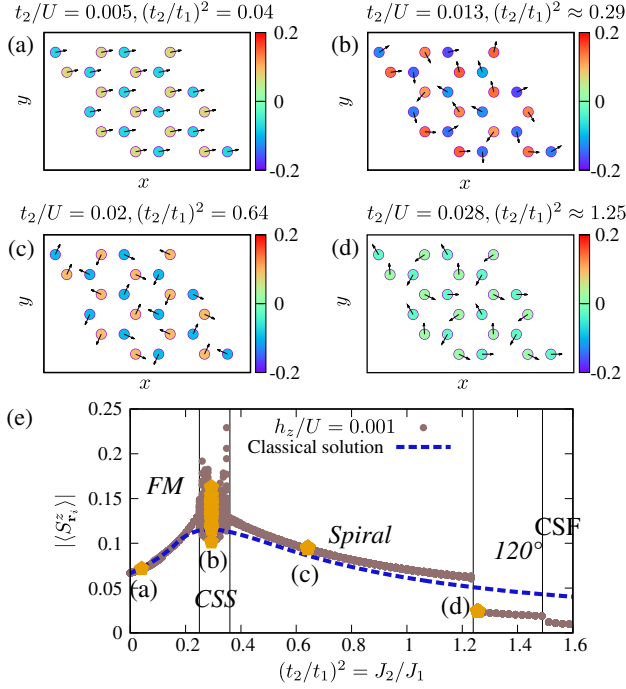


FIG. 2. Results of the B-DMFT for different values of  $(t_2/t_1)^2 = J_2/J_1$  for  $h_z/U = 10^{-3}$ ,  $U_{\uparrow\downarrow}/U = 0.5$ ,  $t_1/U = 0.025$  on a lattice of 24 sites. (a)–(d) Different spin configurations. The color palette gives  $\langle S_{r_i}^z \rangle$ , while arrows depict ordering in the  $xy$  plane. (a) Uniform state with ferromagnetic ordering; (b) chiral spin state with no coplanar order; (c) a configuration of spiral states, in which each pseudospin is aligned with only one of its three first neighbors and antialigned with two of its six second neighbors; (d) a  $120^\circ$  configuration. (e) Absolute value of  $|\langle S_{r_i}^z \rangle|$ . For each ratio  $(t_2/t_1)^2$  we plot the result for all 24 sites and compare it to the classical solution. Pentagons mark results presented in (a)–(d). Note that for finite values of  $h_z$  the border between the  $120^\circ$  Mott state and CSF is slightly shifted in favor of the Mott state.

[36–38] analyses, raising questions about the exact nature of this intermediate phase.

Mapping the model onto a fermionic one and performing a mean-field analysis [39,54], it was proposed that an intermediate frustration stabilizes a phase with spontaneously broken  $\mathcal{P}$  and  $\mathcal{T}$ . This phase is characterized by antiferromagnetic correlations and ChS fluxes staggered within the unit cell as in the celebrated Haldane model [40] and the authors suggested that it realizes the chiral spin liquid state of Kalmeyer-Laughlin [75,76]. In this context, we plot in Fig. 2(e), the response for the magnetization  $\langle S_{r_i}^z \rangle$  with respect to the field  $h_z$ . All phases except the CSS are characterized by a trivial response to the perturbation:  $\langle S_{r_i}^z \rangle \sim h_z$ , whereas  $\langle S_{r_i}^z \rangle$  is strongly fluctuating in the CSS (however we do not observe spontaneous symmetry breaking with B-DMFT). These results cannot be explained in the context of a simple coplanar ansatz, but could be related to a breaking of the degeneracy between two mean-field solutions in the ChS field theory description [54].

*II. ED on frustrated XY model.*—We complete the study of the effective frustrated XY model using ED and previously unaddressed probes such as the responses to  $\mathcal{P}$  and  $\mathcal{T}$  breaking perturbations and the topological description of the ground state. We consider lattices of 24–32 sites, with periodic boundary conditions, and fixed total magnetization  $S_{\text{tot}}^z = 0$  if not stated otherwise. First, phase boundaries are derived from the maxima of fidelity metric  $g$  [54], which probes the first derivative of the ground-state wave function [77–79]. The phase diagram of the XY model deduced from the ED calculations is given in Fig. 3(a). In agreement with the B-DMFT and previous numerical studies, we observe three phase transitions at  $J_2/J_1 \approx 0.21, 0.36$ , and  $1.32$ . Small deviations in these values from the B-DMFT results could be due to the finite size of ED clusters or nonperturbative interaction effects (the XY model does not describe correctly the physics of the Mott phase when  $t_i/U$  are too large). The nature of the phases detected with ED is verified by looking at the coplanar static structure factor

$$S_{\text{Spiral}}(\mathbf{q}) = 2 \sum_{i,j \in A} e^{i\mathbf{q} \cdot (\mathbf{r}_i - \mathbf{r}_j)} \langle S_{r_i}^x S_{r_j}^x \rangle. \quad (4)$$

Spiral waves display a maximum of  $S_{\text{Spiral}}$  at some wave vector(s)  $\mathbf{q}$  in the first Brillouin zone. We observe [54] that the phase in the region  $J_2/J_1 \lesssim 0.21$  corresponds to FM order since  $S_{\text{Spiral}}$  has a peak at  $\mathbf{q} = \Gamma$ . The phase at

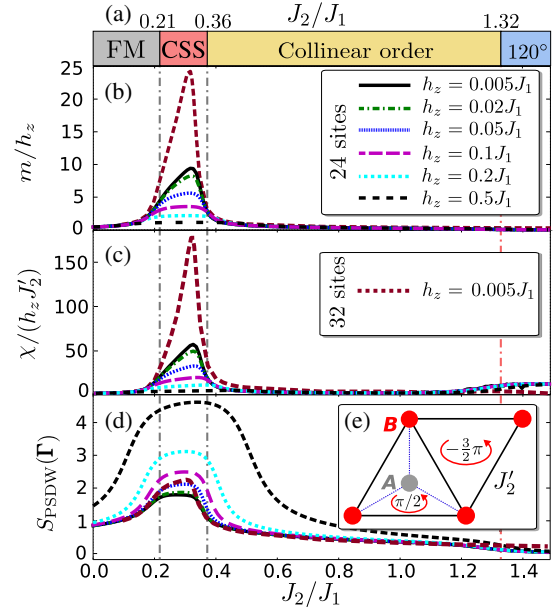


FIG. 3. Results of the ED. (a) Phase diagram of the frustrated XY model. (b)–(d) Variation of the observables with the dimensionless parameter  $J_2/J_1$  for different values of  $h_z$ , with  $J_2' = 0.01J_1$ , on a lattice of  $6 \times 2$  unit cells. (b) Difference of the average Ising magnetization on two sublattices  $m$ . (c) Scalar spin chirality  $\chi$ . (d) Pseudospin density wave structure factor  $S_{\text{PSDW}}(\Gamma)$ . (e) Schematic representation of the perturbation term  $H_{J_2'}$ .



$0.36 \lesssim J_2/J_1 \lesssim 1.32$  corresponds to a spiral wave with collinear order (structure factor has maxima at three  $\mathbf{M}$  points) as expected from the order by disorder mechanism. At  $1.32 \lesssim J_2/J_1$  the ground state is the  $120^\circ$  order spiral wave (structure factor has a peak at two Dirac points  $\mathbf{K}$ ). In the intermediate frustration regime ( $0.21 \lesssim J_2/J_1 \lesssim 0.36$ )  $S_{\text{spiral}}$  is flat in reciprocal space and we expect the ground state to be disordered in the  $xy$  plane. We notice that the exact positions of the phase transitions, especially collinear order  $\leftrightarrow 120^\circ$  order, are sensitive to the lattice choice [54]. The ground state in all phases is located in the same sector of the total momentum at point  $\Gamma$ . Based on the ChS field theory predictions, the order-by-disorder arguments and numerical observations, the CSS  $\leftrightarrow$  collinear order, and collinear order  $\leftrightarrow 120^\circ$  order phase transitions are expected to be first order, whereas the FM  $\leftrightarrow$  CSS phase transition to be second order.

We analyze the linear response to perturbations breaking  $\mathcal{P}$  and  $\mathcal{T}$ . We are interested in the relative magnetization between the two sublattices  $m = \langle m_{r_i} \rangle = \langle S_{r_i}^z - S_{r_i+u_3}^z \rangle$ , as well as the scalar spin chirality  $\chi = \langle \mathbf{S}_{r_i} \cdot (\mathbf{S}_{r_i+u_1} \times \mathbf{S}_{r_i+u_2}) \rangle$ . Here we suppose that  $i \in A$  and  $\mathbf{u}_i$  are vectors between first neighbor sites defined in Fig. 1(a). When calculating the chirality  $\chi$ , we add a perturbation corresponding to the second-neighbor hopping of the Haldane model, of amplitude  $J'_2$  and phase  $\pi/2$  [as shown in Fig. 3(e)]:

$$H_{J'_2} = J'_2 \sum_{\langle\langle ik \rangle\rangle} (e^{\pm i\pi/2} S_{r_i}^+ S_{r_k}^- + \text{H.c.}). \quad (5)$$

We are interested in the limit  $h_z, J'_2 \ll J_1$ . Results of the ED calculations are presented in Figs. 3(b)–3(c). The CSS reveals itself by sharp responses to such external fields. Moreover, the scaled quantities  $m/h_z$  and  $\chi/(h_z J'_2)$  tend to diverge when  $h_z, J'_2 \rightarrow 0$ , giving a strong indication for spontaneous symmetry breaking. This justifies our definition of the CSS, the properties of which can be observed experimentally by tracking on-site populations of bosons  $n_{\sigma,r_i}$  and currents  $J_{ij}^\sigma = \Im \mathbf{m} \langle b_{\sigma,r_i}^\dagger b_{\sigma,r_j} \rangle$  [80]. One can probe the antiferromagnetic ordering without breaking  $\mathcal{P}$  and  $\mathcal{T}$  by calculating the pseudospin density wave (PSDW) structure factor [31,32]:

$$S_{\text{PSDW}}(\mathbf{q}) = \sum_{i,j} e^{i\mathbf{q} \cdot (\mathbf{r}_i - \mathbf{r}_j)} \langle m_{r_i} m_{r_j} \rangle. \quad (6)$$

We observe in Fig. 3(d) that  $S_{\text{PSDW}}(\mathbf{q})$  has a peak at  $\mathbf{q} = \Gamma$  in the intermediate frustration regime. These features are hardly affected by moderate Ising interactions  $K_i/J_1 \sim 0.1$  in Eq. (2) [81].

The observed spin configuration of the CSS could describe the chiral spin liquid of Kalmeyer and Laughlin [75,76]. Yet, we know that chiral spin liquids are characterized by a topological degeneracy in the thermodynamic limit on a compact space [82–84]. In a two-dimensional

system with periodic boundaries one should have a fourfold degenerate ground state with two topological degeneracies per chirality sector. Still, because of finite size effects, one only expects an approximate degeneracy in simulations.

In Figs. 4(a)–4(b), we show the low-energy spectrum as a function of  $J_2/J_1$ , resolved in different sectors of total momentum  $\mathbf{Q}$ . As mentioned previously, the ground state always belongs to the sector  $\mathbf{Q} = \Gamma$ . In the intermediate frustration regime, we observe the onset of a gapped doubly degenerate ground-state manifold. The first excited state has the same momentum  $\mathbf{Q} = \Gamma$ , but lies in the opposite sector of  $\mathcal{P}$ . The first excited state also moves away in energy when the perturbations  $H_z$  and  $H_{J'_2}$  are switched on.

We probe the robustness of the low energy quasidegenerate state sector by performing Laughlin's gedanken experiment and pumping a quantum of magnetic flux through one of the nontrivial loops of the torus [85–87]. Numerically, this is achieved using twisted boundary conditions in a translational symmetry preserving manner. The results are given in Fig. 4(c). We observe that the same states in the sector  $\mathbf{Q} = \Gamma$  are nontrivially gapped for all twists. For the pumping of a single flux quantum we could not observe a spectral flow in the ground-state manifold, that, however, does not imply that the manifold is topologically trivial [88–90]. The topological nature of the ground-state manifold is unambiguously determined by calculating the Chern number [91–94]:

$$C = \frac{1}{2\pi} \int_0^{2\pi} \int_0^{2\pi} B(\theta_1, \theta_2) d\theta_1 d\theta_2. \quad (7)$$

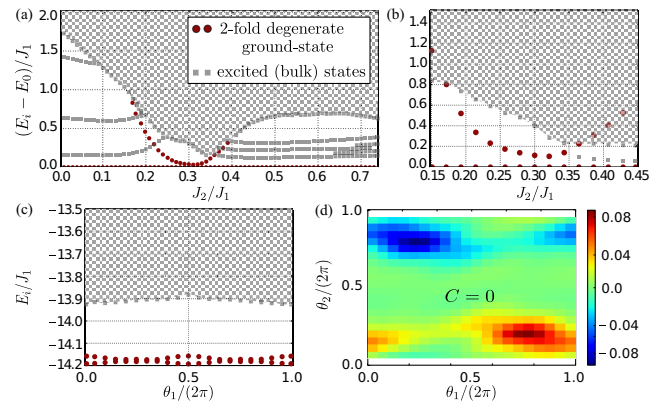


FIG. 4. ED calculations of the low energy spectra as a function of  $J_2/J_1$  showing (using red circles) the formation of a quasidegenerate twofold ground-state manifold (a) on a lattice of  $4 \times 3$  unit cells for various  $S_{\text{Tot}}^z$ ; (b) on a lattice of  $4 \times 4$  unit cells in the  $S_{\text{Tot}}^z = 0$  sector only. (c) Low energy spectrum as a function of the twist angle  $\theta_1$  for  $J_2/J_1 = 0.3$  and  $\theta_2 = 0$  on a lattice of  $4 \times 3$  unit cells. (d) Berry curvature calculated using the non-Abelian formalism resulting in a vanishing Chern number shown for  $J_2/J_1 = 0.3$ ,  $h_z/J_1 = J'_2/J_1 = 0.02$  on a lattice of  $4 \times 3$  unit cells.

Here  $\theta_1$  and  $\theta_2$  are two angles of twisted boundary conditions and  $B(\theta_1, \theta_2)$  is the Berry curvature [95]. We notice that two phases  $\theta_i$  ( $i = 1, 2$ ) introduced in the spin language would correspond to four phases  $\theta_i^\sigma$  in the language of bosons of the BKM model, for which the spin component  $\theta_i^\uparrow - \theta_i^\downarrow = \theta_i$  is fixed and the  $U(1)$  component  $\theta_i^\uparrow + \theta_i^\downarrow$  is free [96]. Since the two quasidegenerate ground states lie in the same symmetry sector and cannot be separated unless twists are trivial ( $\mathcal{P}$  cannot be used with twisted boundary conditions), we evaluate the Berry curvature using the gauge-invariant non-Abelian formulation [97–99]:  $B(\theta_1, \theta_2)\delta\theta_1\delta\theta_2 = \Im \ln \text{Det}[\mathcal{M}(\theta_1, \theta_2)]$ , where elements of the matrix  $\mathcal{M}$  are obtained as follows:

$$\begin{aligned} \mathcal{M}_{ij}(\theta_1, \theta_2) &= \langle \phi_i(\theta_1, \theta_2) | \phi_{\mu_1}(\theta_1 + \delta\theta_1, \theta_2) \rangle \\ &\times \langle \phi_{\mu_1}(\theta_1 + \delta\theta_1, \theta_2) | \phi_{\mu_2}(\theta_1 + \delta\theta_1, \theta_2 + \delta\theta_2) \rangle \\ &\times \langle \phi_{\mu_2}(\theta_1 + \delta\theta_1, \theta_2 + \delta\theta_2) | \phi_{\mu_3}(\theta_1, \theta_2 + \delta\theta_2) \rangle \\ &\times \langle \phi_{\mu_3}(\theta_1, \theta_2 + \delta\theta_2) | \phi_j(\theta_1, \theta_2) \rangle. \end{aligned} \quad (8)$$

Here,  $\delta\theta_1$  and  $\delta\theta_2$  refer to the numerical mesh along the  $\theta_1$  and  $\theta_2$ .  $i, j, \mu_i = 1, 2$  are indices of states  $|\phi_1\rangle$  and  $|\phi_2\rangle$  in the ground-state manifold and the summation over  $\mu_i$  is implicit. In Fig. 4(d), we show a typical shape of the Berry curvature. We find that the Chern number is zero in the intermediate frustration regime. This result suggests that the intermediate phase in the frustrated XY model is most likely to be a CSS with no topological order, as suggested in Refs. [33–35], and not the Kalmeyer-Laughlin state, with gauge fluctuations beyond the mean-field solution making the phase topologically trivial as in the fermionic Kane-Mele model [56–58].

To conclude, we studied the phase diagram of the bosonic Kane-Mele-Hubbard model on the honeycomb lattice. We have shown that an effective frustrated XY model appears in the Mott insulator phase. This model possesses an intermediate frustration regime with a non-trivial chiral spin state, which breaks both  $\mathcal{P}$  and  $\mathcal{T}$ . It displays a finite scalar spin chirality order and an anti-ferromagnetic Ising ordering, while remaining translationally invariant. Measuring the Chern number associated with this state reveals its nontopological nature.

We thank Loïc Herviou, Grégoire Misguich, Stephan Rachel, Cécile Repellin, and Tigran Sedrakyan for insightful discussions. This work has benefitted from discussions at CIFAR meetings in Canada and Société Française de Physique. Support by the Deutsche Forschungsgemeinschaft via DFG FOR 2414, DFG SPP 1929 GiRyd, and the high-performance computing center LOEWE-CSC is gratefully acknowledged. This work was supported in part by DAAD (German Academic and Exchange Service) under project BKM. I. V. acknowledges support by the Ministry of Education, Science, and Technological Development of the Republic of Serbia under projects ON171017 and BKM, and by the European Commission under H2020 project VI-SEEM, Grant

No. 675121. Numerical simulations were partly run on the PARADOX supercomputing facility at the Scientific Computing Laboratory of the Institute of Physics Belgrade. K. L. H. acknowledges support from PALM Labex, Paris-Saclay, Grant No. ANR-10-LABX-0039.

- 
- [1] C. Lhuillier and G. Misguich, in *High Magnetic Fields: Applications in Condensed Matter Physics and Spectroscopy*, edited by C. Berthier, L. P. Lévy, and G. Martinez (Springer, Berlin, Heidelberg, 2002), p. 161.
  - [2] L. Balents, *Nature (London)* **464**, 199 (2010).
  - [3] M. R. Norman, *Rev. Mod. Phys.* **88**, 041002 (2016).
  - [4] L. Savary and L. Balents, *Rep. Prog. Phys.* **80**, 016502 (2017).
  - [5] P. Lecheminant, B. Bernu, C. Lhuillier, L. Pierre, and P. Sindzingre, *Phys. Rev. B* **56**, 2521 (1997).
  - [6] S. Yan, D. A. Huse, and S. R. White, *Science* **332**, 1173 (2011).
  - [7] S. Depenbrock, I. P. McCulloch, and U. Schollwöck, *Phys. Rev. Lett.* **109**, 067201 (2012).
  - [8] B. Fåk, E. Kermarrec, L. Messio, B. Bernu, C. Lhuillier, F. Bert, P. Mendels, B. Koteswararao, F. Bouquet, J. Ollivier, A. D. Hillier, A. Amato, R. H. Colman, and A. S. Wills, *Phys. Rev. Lett.* **109**, 037208 (2012).
  - [9] H. J. Schulz and T. A. L. Ziman, *Europhys. Lett.* **18**, 355 (1992).
  - [10] H. J. Schulz, T. A. L. Ziman, and D. Poilblanc, *J. Phys. I (France)* **6**, 675 (1996).
  - [11] A. Kitaev, *Ann. Phys. (Amsterdam)* **321**, 2 (2006).
  - [12] Z. Y. Meng, T. C. Lang, S. Wessel, F. F. Assaad, and A. Muramatsu, *Nature (London)* **464**, 847 (2010).
  - [13] S. Sorella, Y. Otsuka, and S. Yunoki, *Sci. Rep.* **2**, 992 (2012).
  - [14] F. F. Assaad and I. F. Herbut, *Phys. Rev. X* **3**, 031010 (2013).
  - [15] R. Flint and P. A. Lee, *Phys. Rev. Lett.* **111**, 217201 (2013).
  - [16] J. Fouet, P. Sindzingre, and C. Lhuillier, *Eur. Phys. J. B* **20**, 241 (2001).
  - [17] F. Wang, *Phys. Rev. B* **82**, 024419 (2010).
  - [18] A. Mulder, R. Ganesh, L. Capriotti, and A. Paramekanti, *Phys. Rev. B* **81**, 214419 (2010).
  - [19] B. K. Clark, D. A. Abanin, and S. L. Sondhi, *Phys. Rev. Lett.* **107**, 087204 (2011).
  - [20] A. F. Albuquerque, D. Schwandt, B. Hetényi, S. Capponi, M. Mambrini, and A. M. Läuchli, *Phys. Rev. B* **84**, 024406 (2011).
  - [21] D. C. Cabra, C. A. Lamas, and H. D. Rosales, *Phys. Rev. B* **83**, 094506 (2011).
  - [22] J. Reuther, D. A. Abanin, and R. Thomale, *Phys. Rev. B* **84**, 014417 (2011).
  - [23] F. Mezzacapo and M. Boninsegni, *Phys. Rev. B* **85**, 060402 (2012).
  - [24] H. Zhang and C. A. Lamas, *Phys. Rev. B* **87**, 024415 (2013).
  - [25] R. Ganesh, J. van den Brink, and S. Nishimoto, *Phys. Rev. Lett.* **110**, 127203 (2013).
  - [26] S.-S. Gong, D. N. Sheng, O. I. Motrunich, and M. P. A. Fisher, *Phys. Rev. B* **88**, 165138 (2013).

- [27] Z. Zhu, D. A. Huse, and S. R. White, *Phys. Rev. Lett.* **110**, 127205 (2013).
- [28] S.-S. Gong, W. Zhu, L. Balents, and D. N. Sheng, *Phys. Rev. B* **91**, 075112 (2015).
- [29] F. Ferrari, S. Bieri, and F. Becca, *Phys. Rev. B* **96**, 104401 (2017).
- [30] H. S. Nair, J. M. Brown, E. Coldren, G. Hester, M. P. Gelfand, A. Podlesnyak, Q. Huang, and K. A. Ross, [arXiv:1712.06208](https://arxiv.org/abs/1712.06208).
- [31] C. N. Varney, K. Sun, V. Galitski, and M. Rigol, *Phys. Rev. Lett.* **107**, 077201 (2011).
- [32] C. N. Varney, K. Sun, V. Galitski, and M. Rigol, *New J. Phys.* **14**, 115028 (2012).
- [33] Z. Zhu, D. A. Huse, and S. R. White, *Phys. Rev. Lett.* **111**, 257201 (2013).
- [34] Z. Zhu and S. R. White, *Mod. Phys. Lett. B* **28**, 1430016 (2014).
- [35] R. F. Bishop, P. H. Y. Li, and C. E. Campbell, *Phys. Rev. B* **89**, 214413 (2014).
- [36] J. Carrasquilla, A. DiCiolo, F. Becca, V. Galitski, and M. Rigol, *Phys. Rev. B* **88**, 241109 (2013).
- [37] A. Di Ciolo, J. Carrasquilla, F. Becca, M. Rigol, and V. Galitski, *Phys. Rev. B* **89**, 094413 (2014).
- [38] T. Nakafuji and I. Ichinose, *Phys. Rev. A* **96**, 013628 (2017).
- [39] T. A. Sedrakyan, L. I. Glazman, and A. Kamenev, *Phys. Rev. Lett.* **114**, 037203 (2015).
- [40] F. D. M. Haldane, *Phys. Rev. Lett.* **61**, 2015 (1988).
- [41] E. Fradkin, *Phys. Rev. Lett.* **63**, 322 (1989).
- [42] J. Ambjørn and G. Semenoff, *Phys. Lett. B* **226**, 107 (1989).
- [43] A. Lopez, A. G. Rojo, and E. Fradkin, *Phys. Rev. B* **49**, 15139 (1994).
- [44] G. Misguich, T. Jolicoeur, and S. M. Girvin, *Phys. Rev. Lett.* **87**, 097203 (2001).
- [45] K. Sun, K. Kumar, and E. Fradkin, *Phys. Rev. B* **92**, 115148 (2015).
- [46] I. Bloch, J. Dalibard, and S. Nascimbene, *Nat. Phys.* **8**, 267 (2012).
- [47] N. Goldman, J. C. Budich, and P. Zoller, *Nat. Phys.* **12**, 639 (2016).
- [48] A. Georges, G. Kotliar, W. Krauth, and M. J. Rozenberg, *Rev. Mod. Phys.* **68**, 13 (1996).
- [49] K. Byczuk and D. Vollhardt, *Phys. Rev. B* **77**, 235106 (2008).
- [50] W.-J. Hu and N.-H. Tong, *Phys. Rev. B* **80**, 245110 (2009).
- [51] A. Hubener, M. Snoek, and W. Hofstetter, *Phys. Rev. B* **80**, 245109 (2009).
- [52] P. Anders, E. Gull, L. Pollet, M. Troyer, and P. Werner, *Phys. Rev. Lett.* **105**, 096402 (2010).
- [53] M. Snoek and W. Hofstetter, in *Quantum Gases: Finite Temperature and Non-Equilibrium Dynamics*, edited by N. Proukakis *et al.* (World Scientific, Singapore, 2013), p. 355.
- [54] See Supplemental Material at <http://link.aps.org/supplemental/10.1103/PhysRevLett.120.157201> for (i) details on the B-DMFT method; plots of the order parameters across the superfluid (SF and CSF)—Mott insulator phase transitions; (ii) classical solution of the spin model with and without applied external magnetic field; (iii) mean-field treatment of the spin model using Chern-Simons field theory; (iv) details on the ED measurement of the fidelity and the static structure factors; comparison of the lattices of  $6 \times 2$ ,  $4 \times 3$  and  $4 \times 4$  unit cells.
- [55] C. L. Kane and E. J. Mele, *Phys. Rev. Lett.* **95**, 226801 (2005).
- [56] S. Rachel and K. Le Hur, *Phys. Rev. B* **82**, 075106 (2010).
- [57] W. Wu, S. Rachel, W.-M. Liu, and K. Le Hur, *Phys. Rev. B* **85**, 205102 (2012).
- [58] M. Hohenadler, Z. Y. Meng, T. C. Lang, S. Wessel, A. Muramatsu, and F. F. Assaad, *Phys. Rev. B* **85**, 115132 (2012).
- [59] G. Jotzu, M. Messer, R. Desbuquois, M. Lebrat, T. Uehlinger, D. Greif, and T. Esslinger, *Nature (London)* **515**, 237 (2014).
- [60] C. J. Kennedy, G. A. Siviloglou, H. Miyake, W. C. Burton, and W. Ketterle, *Phys. Rev. Lett.* **111**, 225301 (2013).
- [61] J. Struck, J. Simonet, and K. Sengstock, *Phys. Rev. A* **90**, 031601 (2014).
- [62] Z. Yan, B. Li, X. Yang, and S. Wan, *Sci. Rep.* **5**, 16197 (2015).
- [63] M. Hafezi, E. A. Demler, M. D. Lukin, and J. M. Taylor, *Nat. Phys.* **7**, 907 (2011).
- [64] V. G. Sala, D. D. Solnyshkov, I. Carusotto, T. Jacqmin, A. Lemaître, H. Terças, A. Nalitov, M. Abbarchi, E. Galopin, I. Sagnes, J. Bloch, G. Malpuech, and A. Amo, *Phys. Rev. X* **5**, 011034 (2015).
- [65] L. Lu, J. D. Joannopoulos, and M. Soljacic, *Nat. Photonics* **8**, 821 (2014).
- [66] K. Le Hur, L. Henriët, A. Petrescu, K. Plekhanov, G. Roux, and M. Schiró, *C.R. Phys.* **17**, 808 (2016).
- [67] Y. Li, M. R. Bakhtiari, L. He, and W. Hofstetter, *Phys. Rev. B* **84**, 144411 (2011).
- [68] L. He, Y. Li, E. Altman, and W. Hofstetter, *Phys. Rev. A* **86**, 043620 (2012).
- [69] L. He, A. Ji, and W. Hofstetter, *Phys. Rev. A* **92**, 023630 (2015).
- [70] I. Vasić, A. Petrescu, K. Le Hur, and W. Hofstetter, *Phys. Rev. B* **91**, 094502 (2015).
- [71] A. B. Kuklov and B. V. Svistunov, *Phys. Rev. Lett.* **90**, 100401 (2003).
- [72] M. W. Young, S.-S. Lee, and C. Kallin, *Phys. Rev. B* **78**, 125316 (2008).
- [73] E. Rastelli, A. Tassi, and L. Reatto, *Physica (Amsterdam)* **97B+C**, 1 (1979).
- [74] G. W. Semenoff, *Phys. Rev. Lett.* **53**, 2449 (1984).
- [75] V. Kalmeyer and R. B. Laughlin, *Phys. Rev. Lett.* **59**, 2095 (1987).
- [76] V. Kalmeyer and R. B. Laughlin, *Phys. Rev. B* **39**, 11879 (1989).
- [77] P. Zanardi and N. Paunković, *Phys. Rev. E* **74**, 031123 (2006).
- [78] S.-J. Gu, *Int. J. Mod. Phys. B* **24**, 4371 (2010).
- [79] C. N. Varney, K. Sun, M. Rigol, and V. Galitski, *Phys. Rev. B* **82**, 115125 (2010).
- [80] M. Atala, M. Aidelsburger, M. Lohse, J. T. Barreiro, B. Paredes, and I. Bloch, *Nat. Phys.* **10**, 588 (2014).
- [81] P. H. Y. Li, R. F. Bishop, and C. E. Campbell, *Phys. Rev. B* **89**, 220408 (2014).
- [82] X. G. Wen, F. Wilczek, and A. Zee, *Phys. Rev. B* **39**, 11413 (1989).
- [83] X. G. Wen, *Phys. Rev. B* **40**, 7387 (1989).



- 
- [84] X.-G. Wen, *Adv. Phys.* **44**, 405 (1995).  
[85] R. B. Laughlin, *Phys. Rev. B* **23**, 5632 (1981).  
[86] R. B. Laughlin, *Phys. Rev. Lett.* **50**, 1395 (1983).  
[87] D. J. Thouless, *Phys. Rev. B* **40**, 12034 (1989).  
[88] Y.-F. Wang, Z.-C. Gu, C.-D. Gong, and D. N. Sheng, *Phys. Rev. Lett.* **107**, 146803 (2011).  
[89] C. Hickey, L. Cincio, and Z. Papić, and A. Paramekanti, *Phys. Rev. Lett.* **116**, 137202 (2016).  
[90] K. Kumar, H. J. Changlani, B. K. Clark, and E. Fradkin, *Phys. Rev. B* **94**, 134410 (2016).  
[91] Q. Niu, D. J. Thouless, and Y.-S. Wu, *Phys. Rev. B* **31**, 3372 (1985).  
[92] M. Kohmoto, *Ann. Phys. (N.Y.)* **160**, 343 (1985).  
[93] Y. Hatsugai, *J. Phys. Soc. Jpn.* **73**, 2604 (2004).  
[94] Y. Hatsugai, *J. Phys. Soc. Jpn.* **74**, 1374 (2005).  
[95] M. V. Berry, *Proc. R. Soc. A* **392**, 45 (1984).  
[96] L. Fu and C. L. Kane, *Phys. Rev. B* **74**, 195312 (2006).  
[97] R. Yu, X. L. Qi, A. Bernevig, Z. Fang, and X. Dai, *Phys. Rev. B* **84**, 075119 (2011).  
[98] H. Shapourian and B. K. Clark, *Phys. Rev. B* **93**, 035125 (2016).  
[99] K. Kumar, H. J. Changlani, B. K. Clark, and E. Fradkin, *Phys. Rev. B* **94**, 134410 (2016).

# Transport of Strongly Correlated Bosons in an Optical Lattice

Arya Dhar, Christian Baals, Bodhaditya Santra, Andreas Müllers, Ralf Labouvie, Thomas Mertz, Ivana Vasic, Agnieszka Cichy, Herwig Ott,\* and Walter Hofstetter

The transport of strongly correlated bosons in a three-dimensional optical lattice is studied within the Bose–Hubbard approximation. The transport is induced by a small displacement of the overall harmonic trapping potential. The subsequent relaxation dynamics is monitored by high precision density measurements with the help of scanning electron microscopy. Good agreement with a real space time-dependent Gutzwiller mean-field description is found.

## 1. Introduction

Transport properties are among the most characteristic features of materials. Understanding and engineering the transport of mass, charge, spin, or heat opens the door for the development of new devices with new functionality. For strongly correlated materials, transport properties are especially difficult to describe, yet, their understanding is mandatory to fully exploit their application potential. Model systems, such as ultracold quantum gases, are a class of tunable systems, which contain essential aspects of real materials but are still conceptually simple enough to be amenable to advanced theoretical modeling from first principles, thus enabling quantum simulations of strongly correlated condensed matter systems.<sup>[1]</sup> They are therefore ideal candidates to understand the connection between microscopic interaction mechanisms and global transport properties.

Ultracold quantum gases have often been studied in the context of being the ground state of a many-body Hamiltonian.<sup>[2]</sup> In recent years, however, increasing interest is focused on non-equilibrium dynamics, especially with respect to transport processes.<sup>[3,4]</sup> A paradigmatic class of quantum gases are lattice gases, where the particles are residing and moving in a periodic potential, created by interfering laser beams. Optical lattices allow for easy control of the tunneling and interaction parameters, thus tuning the correlations in the system. At the same time, the system can be mapped onto seminal model hamiltonians such as the Hubbard and the Bose-Hubbard model.<sup>[5]</sup> The superfluid to Mott-insulator transition of a bosonic gas<sup>[6]</sup> is a good example how microscopic interaction and hopping mechanisms determine the quantum phases in the lattice. Similarly, the interplay between onsite correlations and hopping, and the resulting metal to Mott-insulator transition has been realized and studied with interacting spin-1/2 fermions in an optical lattice.<sup>[7,8]</sup>

Transport processes in optical lattices have a long tradition in the research of ultracold quantum gases.<sup>[9]</sup> In order to directly measure transport in optical lattices, two experimental schemes have been developed: the motion of the particles under the influence of a constant force and the motion of a trapped atomic gas after a displacement. In the first case, the generic dynamics are Bloch oscillations,<sup>[10,11]</sup> whose contrast is strongly affected by the

Dr. A. Dhar, T. Mertz, Prof. W. Hofstetter  
Institut für Theoretische Physik, Max-von-Laue Str. 1  
Goethe Universität  
60438 Frankfurt am Main, Germany

Dr. A. Dhar  
Institut für Theoretische Physik  
Appelstr. 2  
Leibniz Universität  
30167 Hannover, Germany

C. Baals, Dr. B. Santra, Dr. A. Müllers, Dr. R. Labouvie  
Department of Physics and Research Center OPTIMAS  
Erwin-Schrödinger-Straße 46  
Technische Universität Kaiserslautern  
67663 Kaiserslautern, Germany  
E-mail: ott@physik.uni-kl.de

C. Baals, Prof. H. Ott  
Graduate School Materials Science in Mainz  
Staudinger Weg 9, 55128 Mainz, Germany

Dr. B. Santra  
Institut für Experimentalphysik und Zentrum für Quantenphysik  
Universität Innsbruck  
6020 Innsbruck, Austria

Prof. I. Vasic  
Scientific Computing Laboratory  
Center for the Study of Complex Systems  
Institute of Physics Belgrade  
University of Belgrade  
11080 Belgrade, Serbia

Dr. A. Cichy  
Faculty of Physics  
Adam Mickiewicz University  
ul. Umultowska 85, PL-61-614 Poznań, Poland

Dr. A. Cichy  
Institut für Physik  
Johannes Gutenberg-Universität Mainz  
Staudingerweg 9, D-55099 Mainz, Germany

DOI: 10.1002/pssb.201800752

presence of interactions with the same species or collisions with another species.<sup>[12]</sup> The dipolar oscillation in a displaced trap<sup>[9,13,14]</sup> is conceptually related to Bloch oscillation, as the physical displacement of a parabolic trap can be described by the application of a constant force. However, the inhomogeneity of the system effectively emulates a varying local force on the atoms.

Within the Bose-Hubbard model, the generic expected phenomenology is straightforward: below the quantum phase transition to the Mott-insulator, the system is superfluid, while for a Mott-insulator, transport should be essentially blocked. Thus, in a trap displacement experiment, one expects an oscillation of the whole cloud in the superfluid phase and the absence of motion in the insulating regime. This simple phenomenology is spoiled by several effects: the first is the inhomogeneity of the system. In local density approximation, this leads to a spatially varying chemical potential and the gas develops a shell structure.<sup>[15]</sup> Superfluid motion is therefore never fully suppressed. Moreover, the finite temperature, particle hole excitations and the finite system size allow for a finite mobility even in the Mott-insulating phase.<sup>[16]</sup> The overall motion of the gas in the Mott-insulating phase is therefore nontrivial and its theoretical description requires modeling and simulating the real-space density distribution.

This was addressed in an early theoretical study,<sup>[17]</sup> where interacting bosons in one- and two-dimensional optical lattices were subject to a instantaneous displacement of a harmonic confining trap, and the resulting dynamics of the many-body system was investigated by time-dependent Gutzwiller theory. While for weak interactions damped Bloch-type oscillations were found, strong repulsive onsite interactions in 1d lead to the formation of a Mott-insulator and complete blockade of the dynamics. In two spatial dimensions, on the other hand, at longer times a “melting” of the displaced Mott-insulator was observed and, depending on the lattice geometry, also thermalization toward an equilibrium state in the shifted trap.

The above considerations motivate a precision comparison between experiment and theory, which allows to benchmark theoretical models and simulation techniques, and to understand in more detail, for example, to which extent correlations between lattice sites have to be considered to describe the system dynamics. Earlier works have primarily focussed on the transport of weakly and strongly interacting atoms in one-dimensional systems,<sup>[9,13,14]</sup> where powerful numerical tools are available.<sup>[14]</sup> The experimental signature of the transport was deduced from time of flight imaging. However, to the best of our knowledge, the effects of interaction on the transport of bosonic atoms in a three-dimensional optical lattice has not been studied in detail with high precision both from an experimental and numerical perspective.

In this work, we combine powerful experimental and numerical in situ techniques to study the center of mass motion of a bosonic quantum gas in a three-dimensional optical lattice. Displacing the overall harmonic confinement by a small amount, we induce the dynamics. By a high precision density measurement, we monitor the density distribution with high spatial resolution. Varying the lattice depth, we map out the transport through the superfluid to Mott-insulator transition. Slicing the cloud into different parts, we can also compare the inner part of the cloud with the edges. The experimental results are compared to time dependent mean-field calculations within

the Gutzwiller ansatz. This method has been widely used to study time-dependent bosonic lattice problems, such as the creation of molecular Bose-Einstein condensate by dynamically melting a Mott-insulator,<sup>[18]</sup> many-body dynamics after a sudden shift of the harmonic trap,<sup>[17]</sup> creation of exotic condensates via quantum-phase-revival dynamics,<sup>[19]</sup> the Higgs-amplitude mode of strongly correlated lattice bosons,<sup>[20]</sup> collective modes of a harmonically trapped, strongly interacting Bose gas in an optical lattice,<sup>[21]</sup> quantum dynamics of interacting bosons in a three-dimensional disordered optical lattice,<sup>[22]</sup> and many more.<sup>[23–32]</sup> We also present results from a projection operator approach<sup>[33,34]</sup> with a finite energy cut-off, which we find to agree well with the Gutzwiller ansatz for our parameters.

## 2. Experimental Setup and Theoretical Model

The experimental sequence starts by preparing a Bose-Einstein condensate of <sup>87</sup>Rb atoms in an optical dipole trap, formed by a single beam CO<sub>2</sub> laser.<sup>[35]</sup> The atomic gas is cigar-shaped and the axial trap oscillation frequency is 10 Hz, while the two transverse oscillations frequencies are 145 Hz in the horizontal and 80 Hz in the vertical direction, respectively. The latter is reduced due to the gravitational sag. We then adiabatically switch on an anisotropic three-dimensional optical lattice, whose depths can be tuned individually in all three directions. After a short settling time, the dipole trap is shifted in the horizontal direction within 2 ms by about 1 μm with the help of a piezo actuated mirror, thus forcing the system out of equilibrium, (see **Figure 1**). The subsequent relaxation dynamics is imaged with the help of scanning electron microscopy (SEM)<sup>[36,37]</sup> for evolution times up to 150 ms. During the imaging procedure, the dynamics of the atomic cloud is frozen out in the optical lattice by increasing its strength to a value where tunneling is suppressed. From the SEM image of the atomic cloud, the size and the center-of-mass of the cloud are determined (**Figure 2**). Furthermore, the images are dissected into different slices for a detailed spatially resolved analysis of the mass transport. The optical lattice has a tetragonal symmetry with a lattice spacing of  $d_z = 547$  nm in the axial direction and  $d_x = d_y = 387$  nm in the two transverse directions. Due to geometrical constraints of the experimental setup, the orientation of the two transverse lattice axes is rotated by 45 degrees with respect to the vertical and horizontal direction.

The lattice depth is expressed in units of the recoil energy,  $E = \hbar^2 k^2 / (2m)$ , where  $k = \pi/d$  is the lattice vector and  $m$  is the mass of the atoms. As there are two different lattice constants in

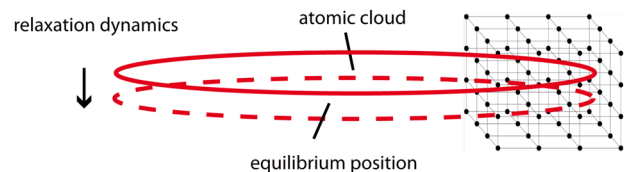


**Figure 1.** Setup. A cloud of ultracold bosons residing in a parabolic trap with superimposed three-dimensional optical lattice is shifted out of its equilibrium position. The subsequent relaxation dynamics is studied with high precision density measurements. The sketched optical lattice on the right side of the gas extends homogeneously over the whole cloud.

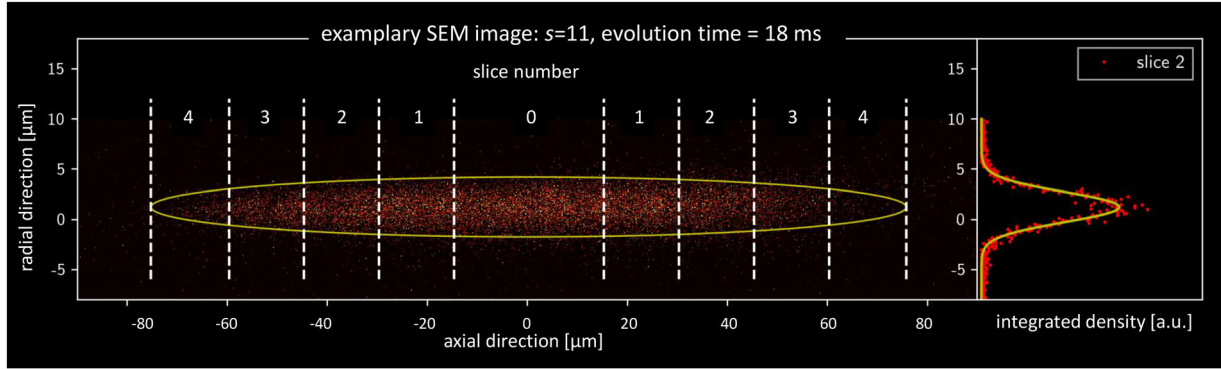


**Figure 2.** Scanning electron microscopy image of the BEC for  $s = 11$ . From Gaussian fits to the density distribution, we extract the center-of-mass of the cloud. For a more detailed analysis, we additionally slice the cloud into different segments and analyze the slices individually. Exemplary, on the right panel, we plot the radial atomic density for the second slice.

the present setup, we define individual dimensionless lattice depths,

$$s_a = \frac{V_a}{E_a} \quad (1)$$

where the index  $a = x, y, z$  denotes the corresponding lattice height  $V_a$  and recoil energy  $E_a$ . The values of  $s_a$  control the ratio of the interaction energy to the tunneling amplitude, giving rise to the different quantum phases of a Mott-insulator and a superfluid.

The experimental system can be suitably described by the Bose-Hubbard model in the lowest band approximation

$$H = - \sum_{\langle i,j \rangle} J_{ij} (\hat{b}_i^\dagger \hat{b}_j + h.c.) + \frac{U}{2} \sum_i \hat{n}_i (\hat{n}_i - 1) + \sum_i (\varepsilon_i - \mu) \hat{n}_i \quad (2)$$

where  $\hat{b}_i^\dagger$  ( $\hat{b}_i$ ) creates (annihilates) a bosonic particle at site  $i$ ,  $\hat{n}_i$  is the number operator at site  $i$ ,  $J_{ij}$  denotes the tunneling amplitude between nearest neighboring sites  $\langle i, j \rangle$  arising from the different lattice constants along the three directions forming the optical lattice,  $U$  is the onsite interaction energy,  $\varepsilon_i$  is the potential energy at site  $i$  and  $\mu$  is the chemical potential.

The tunneling couplings  $J_{ij}$  can take two different values, depending whether the particle moves along the transverse  $x$ - or  $y$ -direction ( $J_x = J_y$ ), or along the  $z$ -direction ( $J_z$ ). Within the tight binding approximation, the tunneling couplings  $J_a$  can be related to the lattice parameter with the following approximative expression,<sup>[38]</sup> valid for each lattice axis:

$$J_a \approx \frac{4}{\sqrt{\pi}} s_a^{3/4} E_a e^{-2\sqrt{s_a}}, \quad a = x, y, z. \quad (3)$$

The interaction energy for a tetragonal lattice reads<sup>[2]</sup>

$$U \approx \sqrt{\frac{8}{\pi}} s^{3/4} k_l a E_r \quad (4)$$

where  $s$ ,  $k_l$ , and  $E_r$  are the geometric means of the individual lattice directions. More precise values of the tunneling energy and the interaction energy can be retrieved by a band structure calculation, which we have used in this work. The values of  $U/J$  addressed in this work ranges from 0.60 to 8.21, where  $J = 2(J_x + J_y + J_z)$ .

To numerically study the relaxation dynamics after the shift of the dipole trap center, we use the time-dependent Gutzwiller mean-field approach, which is a well-established method, especially for higher dimensional systems.<sup>[39,40]</sup> We first calculate the ground state density distribution at  $T = 0$  for the given experimental parameters (see **Figure 3**). We then time evolve the system in the shifted trapping potential. To verify the results obtained from this approach at higher values of the interaction strengths, we retained first-order corrections due to correlations within the realm of the projection operator approach and compared the results obtained from both approaches.

To obtain the ground state, we use the time independent Gutzwiller variational ansatz

$$|\psi_{GW}\rangle = \prod_{\infty l} \sum_n c_n^{(l)} |n\rangle_l \quad (5)$$

where  $l$  denotes the site index and  $|n\rangle$  denotes the Fock occupation basis. The Gutzwiller state becomes exact in the limit of large and small interactions. In order to find the ground state, we minimize the energy functional of the full Hamiltonian with respect to this state.

$$E = \frac{\langle \psi_{GW} | \hat{H} | \psi_{GW} \rangle}{\langle \psi_{GW} | \psi_{GW} \rangle} \quad (6)$$

This effectively reduces to a minimization with respect to the coefficients,  $c_n^{(l)}$ .

After computing the ground state, we proceed to study the time dependence by considering the coefficients in the Gutzwiller state as time dependent, that is,  $c_n^{(l)}(t)$ .

By applying the time-dependent variational principle, we obtain the equations of motion for all of the coefficients,

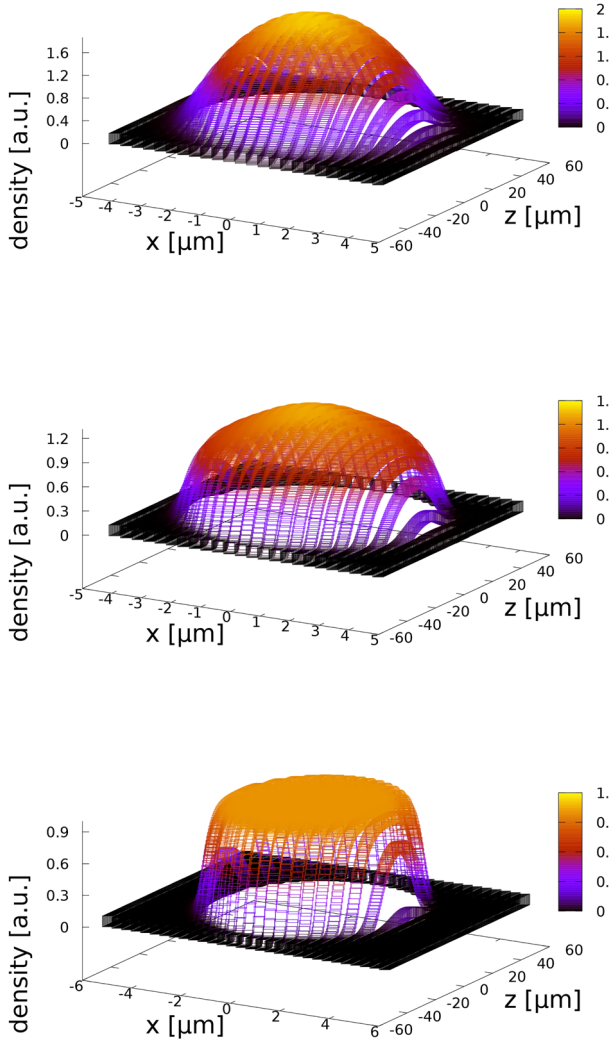


**Figure 3.** The ground state density distribution in the  $y = 0$  plane for three values of  $s = 7$  (top), 13 (middle), 16 (bottom) as simulated using Gutzwiller approximation. The density is given in atoms per lattice site.

$$i\partial_t c_n^{(l)} = -J_{l,l'} \sum_{l'} \left[ c_{n-1}^{(l)} \sqrt{n} \phi_{l'} + c_{n+1}^{(l)} \sqrt{n+1} \phi_{l'}^* \right] - \left[ \mu n - \frac{U}{2} n(n-1) - \varepsilon_i n \right] c_n^{(l)} \quad (7)$$

where the sum over  $l'$  goes over all the nearest neighboring sites to  $l$ , and  $\phi_l = \langle a_l \rangle$  is the condensate fraction at site  $l$ . The above equation corresponds to a set of  $N_c \times L$  first order coupled differential equations, where  $N_c$  is the size of the local Hilbert space and  $L$  is the total number of sites.

To analyze the dynamics of the Bose-Hubbard model beyond mean-field theory, we have also implemented the projection operator approach.<sup>[33,34,41]</sup> This method uses a canonical transformation such that it systematically eliminates hopping processes which connect states with a large energy difference. This energy cut-off is typically chosen as the onsite interaction energy  $U$ . This will generate an effective low-energy

Hamiltonian for the system in the strongly interacting limit. It should be noted that choosing this energy cut-off as infinity leads to the Gutzwiller mean-field approximation. The projection operator method gives improved phase boundaries for the superfluid to Mott-insulator transition, which are very close to the numerically exact Monte Carlo data in three spatial dimensions.<sup>[33]</sup>

To understand the projection operator approach, let us first divide our model Hamiltonian into two parts, one containing the interaction and one-body terms, and the other having the kinetic energy part:

$$H = H_0 + \sum_{\langle ij \rangle} T_{ij} \quad (8)$$

where  $H_0 = \frac{U}{2} \sum_i \hat{n}_i (\hat{n}_i - 1) - \mu \hat{n}_i + \varepsilon_i \hat{n}_i$ , and  $T_{ij} = -J_{ij} \hat{b}_i^\dagger \hat{b}_j$  is the anisotropic hopping rate. The kinetic energy can be written as  $T_{ij} = \sum_\beta T_{ij}^\beta$ , where

$$T_{ij}^\beta = -J_{ij} \sum_n g_\beta^n |n+1\rangle_i \langle n-\beta\rangle_j |n\rangle_j \langle n-\beta+1| \quad (9)$$

where  $g_\beta^n = \sqrt{(n+1)(n-\beta+1)}$ .  $T_{ij}^\beta$  connects local states differing in energy by  $\varepsilon_{ij}^\beta = \beta U + \varepsilon_i - \varepsilon_j$ , where  $\beta = 0, \pm 1, \pm 2, \dots$ . Let us now introduce an energy scale,  $\Delta E$  such that we consider a hopping process to be a low-energy process if  $|\varepsilon_{ij}^\beta| < \Delta E$ . For each bond  $\langle ij \rangle$ , we introduce a set  $\beta_{ij} : \beta \in \beta_{ij}$  if the above condition is satisfied for the low energy process.

We improve the variational ansatz to

$$|\psi(t)\rangle = e^{-i\mathcal{S}(t)} |\psi_{GW}\rangle \quad (10)$$

where  $|\psi_{GW}\rangle = \prod_l \sum_n c_n^{(l)}(t) |n\rangle_l$  is the Gutzwiller wave function, and the canonical transformation,  $\mathcal{S}$  introduces correlations between different lattice sites. The operator  $\mathcal{S}$  is defined in such a way that higher order hopping terms in  $H^*$ , as defined below, are systematically removed up to the order  $J(J//U)^{m-1}$ ,

$$H^* = \exp(i\mathcal{S}) H \exp(-i\mathcal{S}). \quad (11)$$

We limit ourselves to the leading approximation  $m = 1$ ,

$$\mathcal{S} \approx -i \sum_{\langle ij \rangle} \sum_{\beta \notin \beta_{ij}} \frac{T_{ij}^\beta}{\varepsilon_{ij}^\beta} \quad (12)$$

The energy cut-off is set as  $U$ . From the time dependent variational principle, we obtain improved equations of motion for the coefficients  $c_n^{(l)}(t)$ .<sup>[41]</sup>

### 3. Results

We first analyze the motion of the whole cloud during the relaxation process. The results are summarized in **Figure 4**, where the center-of-mass dynamics of the entire cloud after the sudden shift of the dipole trap center is plotted for different values of  $s = s_x = s_y = 1.25s_z$ . Figure 4 constitutes the main



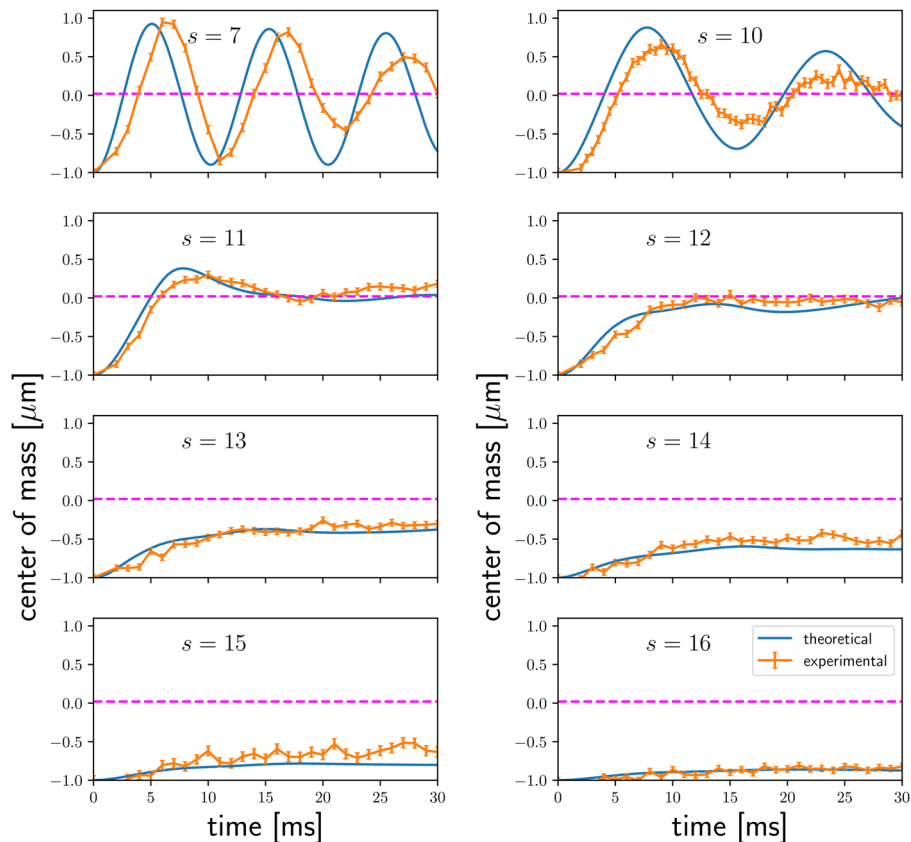


**Figure 4.** Time evolution of the center-of-mass after the harmonic trapping potential center is suddenly shifted. The experiment has been performed for different values of the lattice strength  $s$  as indicated in each of the subplots. Experimental data are shown in orange, the numerical simulation using time dependent Gutzwiller approximation is shown in blue. The magenta dashed line shows the position of the equilibrium position.

result of this work. An immediate look at the figure reveals the remarkable agreement obtained between the experimental and theoretical results for all the  $s$  values which have been considered.

We now discuss some important features of the time evolution as shown in Figure 4. For small values of  $s$ , there are large oscillations of the center-of-mass around the new trap center, shown by both theoretical and experimental results. These oscillations can be attributed to the dipolar oscillations set in by the sudden shift in the trap center.

The large amplitude of the oscillations can be traced back to the superfluid ground state covering the entire cloud. As the cloud is shifted by only two lattice sites, the whole cloud remains in the lowest band upon the displacement. The amplitude of the oscillations as obtained through the numerical simulations is found to be slightly more than that observed in the experiment. This can be due to the finite temperature effect in the experiments, which decreases the condensate fraction in the cloud, and introduces thermal fraction. On the contrary, the numerical simulations are carried out at zero temperature with the entire cloud being in the superfluid phase. The frequency difference of about 10 percent, which is visible for  $s = 7$  and  $s = 10$ , is most likely due to a long term drift of the dipole trapping potential between the initial calibration measurement and the actual experimental runs.

More interesting features in the dynamics appear for increasing lattice depth. The relaxation dynamics is not only slowed down by the decreasing tunneling coupling, the results change also qualitatively. Already for  $s = 11$ , there are practically no oscillations sustained for longer times. The center-of-mass overshoots the new trap center, but then slowly converges to the equilibrium value. We attribute the absence of oscillations to the interplay between the interaction and closed single particle orbits, which are due to the fact that the bandwidth is smaller than the chemical potential. Going from  $s = 12$  to  $s = 13$  shows a remarkable difference in the initial dynamics of the center-of-mass of the cloud. The system displays the initial fast movement for both the  $s$  values. For  $s = 12$ , it reaches the equilibrium value, whereas for  $s = 13$ , even for longer timescales, a small offset remains (see **Figure 5**, where we show the experimental data for a 5 times longer times scale).

Hereafter the system movement becomes significantly slower. For larger  $s$  values, the center-of-mass is not able to reach the new trap center in the timescales observed in the experiment. This is caused by the decrease of the condensate fraction and rise in the Mott-insulating region in the cloud, which prohibits the transport of the bosonic atoms. Higher values of  $s$  correspond to higher interaction strengths between the atoms, leading to localized wavefunctions describing them. For  $s = 16$ , the movement of the entire cloud is practically negligible compared

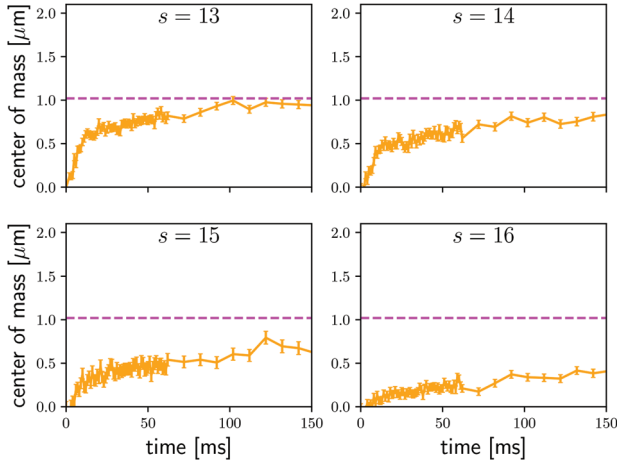


**Figure 5.** COM dynamics for longer times as observed in the experiment for higher values of  $s$ .

to the shift due to presence of the incompressible Mott-insulating region encompassing a vast region of the cloud.

To confirm our results, we looked at the ground state density distribution for the extreme values of  $s$  from the numerical simulations using Gutzwiller approximation and indeed, we find the superfluid and Mott-insulating phases in the cloud as shown in Figure 3. It shows the existence of superfluid phase in the entire cloud for  $s = 7$  whereas for  $s = 13$ , a thin MI shell arises in the intermediate region of the cloud, and a clear density plateau for  $s = 16$  implies the appearance of Mott-insulating region at the central part with superfluid wings. The simulations were carried out with typical system sizes of  $25 \times 25 \times 180$  sites along  $x, y, z$  directions, respectively. The larger number of sites along the  $z$  direction, which has the weakest trapping amplitude, were taken in accordance with the experiment. The choice of chemical potential was done such that the total number of particles were  $\approx 30000$ . Depending on the  $s$ -value, a convergence test was performed to select the appropriate occupation cut-off on a single site.

To have a deeper understanding of the movement of the atoms, we sliced the cloud in several sections as shown in Figure 2. The width of each of the slices is 100 pixels, which correspond to  $\approx 15 \mu\text{m}$ . The slices are paired because of the mirror symmetry. Each slice is integrated in the axial direction to get a 1D profile, which is fitted with a Gaussian function to determine its center. The error of this center is given by the standard deviation  $\sigma$  from the Gaussian fit divided by  $\sqrt{I}$ , where  $I$  is the summed intensity of the corresponding slice.

Since the movement of the atoms is related to the superfluid nature of the atomic cloud, it is instructive to first look at the condensate fraction of the different parts of the cloud, defined as

$$\Phi = \sum_{i \in \text{slice}} \frac{\phi_i^2}{n_i} \quad (13)$$

where  $\phi_i = \langle b_i \rangle$  at site  $i$ . This quantity cannot be measured in the current experimental setup and we resort to the numerical simulations, having already established the reliability on the data obtained from time-dependent Gutzwiller method. **Figure 6**

shows the condensate fraction of different slices corresponding to different values of  $s$ . For  $s = 7$ , we see that the entire cloud has condensate fraction close to 1. As the lattice depth increases, the condensate fraction in the inner slices decreases much faster than in the outer wings. This is a clear signature of the increasing Mott-insulating character in the inner sections of the cloud. Consequently, we expect for all lattice parameters a larger mobility of the atoms towards the edges of the cloud.

**Figure 7** shows the comparison between experiment and theory for the individual slices for  $s = 13$ . The experimental data for all slices look very similar. A closer look reveals that the outer slices show a slightly faster motion toward the equilibrium position as compared to the inner slices. For all slices, no oscillations are visible. The theoretical simulation shows a similar trend with respect to the motion: the inner slices have a slower initial motion towards the equilibrium position. This is compatible with the onset of a Mott-insulator shell in the trap center at  $s = 13$ . For the outer slices, however, the simulations predict clearly visible oscillations. This is in contrast to the experimental findings. From an analysis of the numerical data, we find that the outer shells indeed host a superfluid and can therefore undergo a damped oscillation. Two reasons can be responsible for the absence of oscillations in the experiment: In the experiment, we have a finite temperature of about  $T = 30 \text{ nK}$ . This is already sufficient to smear out the shell structure of the Mott-insulator plateaus significantly,<sup>[16]</sup> thus smearing out the dynamics of the slices. Another consequence of the finite temperature is the appearance of a normal (thermal) component at the edges of the cloud, which is not undergoing superfluid behavior. The appearance of a thermal component goes along with a depletion of the superfluid fraction. Note that the bandwidth of the optical lattice for  $s \geq 12$  is smaller than the thermal energy. This interpretation is compatible with the fact that the overall center-of-mass motion shows very good agreement, indicating the presence of an effective smearing out taking place in the experiment. A comparison of the individual slices for a lattice depth of  $s = 16$  shown in **Figure 8** shows qualitatively similar results. Again, the outer slices show

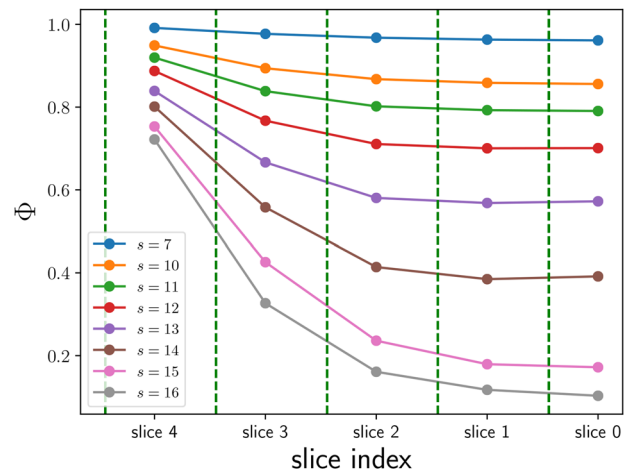


**Figure 6.** Ground state condensate fraction, explained in the text, for different slices marked by green dashed lines for various  $s$  values.



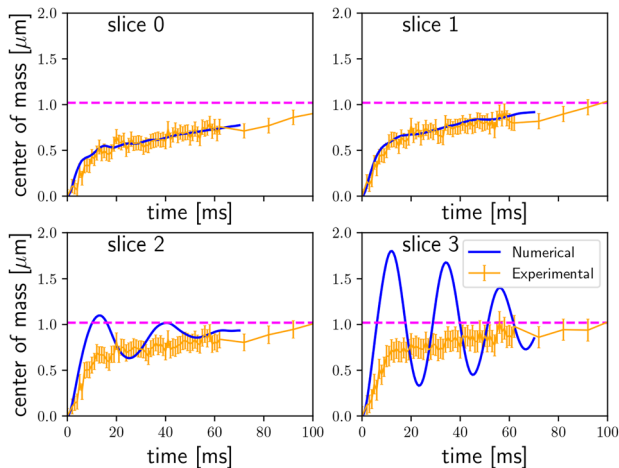


**Figure 7.** Comparison of the center-of-mass dynamics for different slices from the experiment (orange) and numerical simulations (blue) for  $s = 13$ . The slices are defined in Figure 2.

residual oscillations. Note that these oscillations persist, even though the cloud is well in the Mott-insulating regime. In addition to the above two reasons, one should also take into account the fact that the Gutzwiller approximation overestimates the condensate fraction, as discussed in ref. [33]. This can also contribute to the discrepancy between the theory and experimental results for the motion of the outer slices.

The results obtained from the time-dependent Gutzwiller method ignores quantum correlations between the different lattice sites. We implement an independent method based on the projection operator approach to include additional quantum correlations. The main motivation for this endeavour is to investigate the validity of the approximation in the Gutzwiller method. As discussed before, the projection operator approach with an infinite energy cut-off reduces to the Gutzwiller mean-field theory. Keeping a finite energy cut-off equal to the corresponding  $U$ , we can thus include hopping processes which

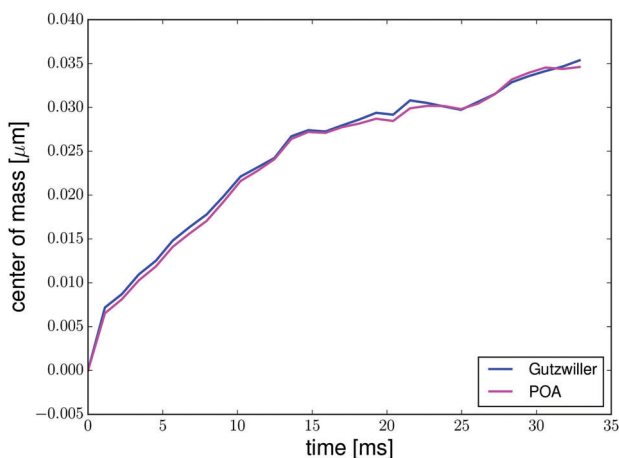


**Figure 8.** Comparison of the center-of-mass dynamics for different slices from the experiment (orange) and numerical simulations (blue) for  $s = 16$ . The slices are defined in Figure 2.

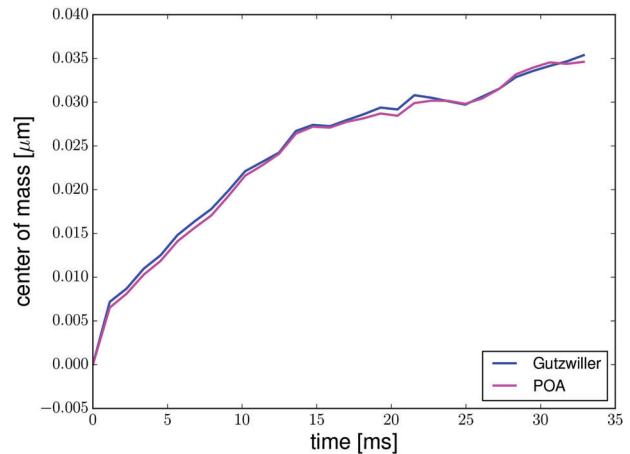


**Figure 9.** COM dynamics for a smaller system size obtained from time-dependent Gutzwiller (blue) and the projection operator approach method (magenta).

do not change the energy more than the energy cut-off, thus retaining quantum correlations with neighboring sites. However, for the projection operator approach, we are limited by smaller system sizes. **Figure 9** shows the COM dynamics for a smaller system size ( $12 \times 12 \times 14$  along  $x - y - z$ ) for  $s = 16$  obtained from time-dependent Gutzwiller projection operator approach method. Indeed they show remarkable agreement for timescales studied in this work. This result thus confirms the validity of the Gutzwiller approximation in this parameter regime.

## 4. Conclusions

We have studied transport of interacting bosons in an optical lattice, for a range of interaction strengths across the superfluid to Mott-insulator quantum phase transition, by using a high resolution scanning electron microscopy technique. We have clearly observed dipolar oscillations in the superfluid regime, whereas in the presence of a pronounced Mott-plateau the system showed a strongly suppressed mobility due to suppressed tunneling. We compared our experimental findings to simulations based on time-dependent Gutzwiller theory, and found very good agreement. For smaller system sizes, the time dependent Gutzwiller method was successfully benchmarked with the projection operator approach. Several open questions will be the subject of future research. These include the possible melting of the Mott-insulator at long time scales and the dependence of thermalization dynamics on the lattice geometry, as indicated by earlier studies.<sup>[17]</sup> Furthermore, it would be of interest to take into account by more advanced simulation techniques also the tunneling dynamics of the normal bosonic component at finite temperature.

## Acknowledgement

This work was funded by the Deutsche Forschungsgemeinschaft (DFG, German Research Foundation), project number 31867626 (SFB/TR 49, projects A3 and A9). We further acknowledge funding by the Deutsche

Forschungsgemeinschaft (DFG, German Research Foundation), project number 277625399 (SFB/TR 185) and project number 49741853 (Graduate School of excellence MAINZ). The research was also funded and by the state of Rhineland-Palatinate within the research center OPTIMAS and by the National Science Centre (NCN, Poland) under grant: UMO-2017/24/C/ST3/00357 (A.C.). I.V. acknowledges support by the Ministry of Education, Science, and Technological Development of the Republic of Serbia under Projects ON171017 and BKMh, and by DAAD (German Academic and Exchange Service) under the BKMh project.

## Conflict of Interest

The authors declare no conflict of interest.

## Keywords

bosonic Mott insulator, Gutzwiller approach, transport, ultracold quantum gases

Final Version: March 15, 2019

Received: December 21, 2018

Published online: April 15, 2019

- 
- [1] W. Hofstetter, T. Qin, *J. At. Mol. Phys.* **2018**, *51*, 082001.  
 [2] I. Bloch, J. Dalibard, W. Z. Weng, *Rev. Mod. Phys.* **2008**, *80*, 885.  
 [3] T. Kinoshita, T. Wenger, D. S. Weiss, *Science* **2004**, *305*, 1125.  
 [4] J. P. Brantut, J. Meineke, D. Stadler, S. Krinner, T. Esslinger, *Science* **2012**, *337*, 1069.  
 [5] I. Bloch, J. Dalibard, S. Nascimbène, *Nature Phys.* **2012**, *8*, 267.  
 [6] M. Greiner, O. Mandel, T. Esslinger, T. W. Hänsch, I. Bloch, *Nature* **2002**, *415*, 39.  
 [7] U. Schneider, L. Hackermüller, S. Will, T. Best, I. Bloch, T. Costi, R. Helmes, D. Rasch, A. Rosch, *Science* **2008**, *322*, 1520.  
 [8] R. Jördens, N. Strohmaier, K. Günter, H. Moritz, T. Esslinger, *Nature* **2008**, *455*, 204.  
 [9] F. S. Cataliotti, S. Burger, C. Fort, P. Maddaloni, F. Minardi, A. Trombettoni, A. Smerzi, M. Inguscio, *Science* **2001**, *293*, 843.  
 [10] M. Ben Dahan, E. Peik, J. Reichel, Y. Castin, C. Salomon, *Phys. Rev. Lett.* **1996**, *76*, 4508.  
 [11] G. Roati, E. de Mirandes, F. Ferlaino, H. Ott, G. Modugno, M. Inguscio, *Phys. Rev. Lett.* **2004**, *92*, 230402.  
 [12] H. Ott, E. de Mirandes, F. Ferlaino, G. Roati, G. Modugno, M. Inguscio, *Phys. Rev. Lett.* **2004**, *92*, 160601.  
 [13] C. D. Fertig, K. M. O'Hara, J. H. Huckans, S. L. Rolston, W. D. Phillips, J. V. Porto, *Phys. Rev. Lett.* **2005**, *94*, 120403.  
 [14] I. Danshita, C. W. Clark, *Phys. Rev. Lett.* **2009**, *102*, 030407.  
 [15] S. Fölling, A. Widera, T. Müller, F. Gerbier, I. Bloch, *Phys. Rev. Lett.* **2006**, *97*, 060403.  
 [16] F. Gerbier, *Phys. Rev. Lett.* **2007**, *99*, 120405.  
 [17] M. Snoek, W. Hofstetter, *Phys. Rev. A* **2007**, *76*, 051603.  
 [18] D. Jaksch, V. Venturi, J. I. Cirac, C. J. Williams, P. Zoller, *Phys. Rev. Lett.* **2002**, *89*, 040402.  
 [19] M. Buchhold, U. Bissbort, S. Will, W. Hofstetter, *Phys. Rev. A* **2011**, *84*, 023631.  
 [20] U. Bissbort, S. Götze, Y. Li, J. Heinze, J. S. Krauser, M. Weinberg, C. Becker, K. Sengstock, W. Hofstetter, *Phys. Rev. Lett.* **2011**, *106*, 205303.  
 [21] M. Snoek, *Phys. Rev. A* **2012**, *85*, 013635.  
 [22] P. Buonsante, L. Pezz'e, A. Smerzi, *Phys. Rev. A* **2015**, *91*, 031601.  
 [23] J. Wernsdorfer, M. Snoek, W. Hofstetter, *Phys. Rev. A* **2010**, *81*, 043620.  
 [24] M. Snoek, *EPL (Europhys. Lett.)* **2011**, *95*, 30006.  
 [25] M. Jreissaty, J. Carrasquilla, F. A. Wolf, M. Rigol, *Phys. Rev. A* **2011**, *84*, 043610.  
 [26] K. V. Krutitsky, P. Navez, *Phys. Rev. A* **2011**, *84*, 033602.  
 [27] J. S. Bernier, D. Poletti, P. Barmettler, G. Roux, C. Kollath, *Phys. Rev. A* **2012**, *85*, 033641.  
 [28] P. Buonsante, L. Orefice, A. Smerzi, *Phys. Rev. A* **2013**, *87*, 063620.  
 [29] D. S. Lühmann, *Phys. Rev. A* **2013**, *87*, 043619.  
 [30] A. Rapp, *Phys. Rev. A* **2013**, *87*, 043611.  
 [31] I. Vidanović, D. Cocks, W. Hofstetter, *Phys. Rev. A* **2014**, *89*, 053614.  
 [32] T. Mertz, I. Vasić, M. J. Hartmann, W. Hofstetter, *Phys. Rev. A* **2016**, *94*, 013809.  
 [33] C. Trefzger, K. Sengupta, *Phys. Rev. Lett.* **2011**, *106*, 095702.  
 [34] A. Dutta, C. Trefzger, K. Sengupta, *Phys. Rev. B* **2012**, *86*, 085140.  
 [35] T. Gericke, P. Würtz, D. Reitz, C. Ufeld, H. Ott, *Appl. Phys. B* **2007**, *89*, 447.  
 [36] T. Gericke, P. Würtz, D. Reitz, T. Langen, H. Ott, *Nat. Phys.* **2008**, *4*, 949.  
 [37] B. Santra, H. Ott, *J. Phys. B* **2015**, *48*, 122001.  
 [38] W. Zwerger, *J. Opt. B: Quantum Semiclassical Opt.* **2003**, *5*, S9.  
 [39] W. Metzner, D. Vollhardt, *Phys. Rev. Lett.* **1989**, *62*, 324.  
 [40] D. S. Rokhsar, B. G. Kotliar, *Phys. Rev. B* **1991**, *44*, 10328.  
 [41] C. H. Lin, R. Sensarma, K. Sengupta, S. Das Sarma, *Phys. Rev. B* **2012**, *86*, 214207.



# Winter School on Strongly Correlated Quantum Matter

## POSTER

### **Electronic Floquet Vortex States Induced by Light**

*Ahmadabadi, Iman*

We propose a scheme to create an electronic Floquet vortex state by irradiating the circularly-polarized laser light on the two-dimensional semiconductor. We study the properties of the Floquet vortex states analytically and numerically using methods analogous to the techniques used for the analysis of superconducting vortex states, while we exhibit that the Floquet vortex created in the current system has the wider tunability. To illustrate the impact of such tunability in quantum engineering, we demonstrate how this vortex state can be used for quantum information processing.

+

### **Study of 1D soft bosons via the MCTDH approach**

*Apostoli, Christian*

In this work we explore some of the capabilities of the multiconfiguration time-dependent Hartree approach (MCTDH), a general and powerful method to compute quantum dynamics simulations. Its strength lies in the particular ansatz it uses for the many-body wave function: a superposition, with time-dependent coefficients, of direct-product states which are built from a time-dependent one-particle basis. When one applies the time-dependent variational principle to this ansatz, a set of coupled equations is found for the coefficients and the one-particle basis functions. This ensures that, during a numerical solution of these equations, at every time the system is represented in a variationally optimal basis. We apply the MCTDH approach to a 1D system of soft bosons that undergoes a quantum phase transition from a standard Luttinger Liquid to a Cluster Luttinger Liquid (CLL). We simulate this system in real-time, and introduce a method for computing the energy of the low-lying excited states by observing the response of the system to a weak time-dependent periodic potential. In the Tonks-Girardeau condition, our results are in good accordance with the Bogolyubov spectrum.

+

### **Signatures of Many-Body Localization in the Dynamics of Two-Level Systems in Glasses (jointly presented with Federico Balducci)**

*Artiaco, Claudia*

Signatures of Many-Body Localization in the Dynamics of Two-Level Systems in

+

Glasses Abstract: We investigate the quantum dynamics of two-level systems (TLSs) in glasses at low temperatures (1 K and below). We study an ensemble of TLSs coupled to phonons. By integrating out the phonons within the framework of the GKSL master equation, we derive the explicit form of the interactions among TLSs and of the dissipative terms. We find that the dynamics of the system shows clear signatures of many-body localization physics (in particular a power-law decay of the concurrence, which measures pairwise entanglement also in non-isolated systems) even in the presence of dissipation, if the latter is not too large. This feature can be ascribed to the presence of strong, long-tailed disorder characterizing the distributions of the model parameters. Our findings show that assuming ergodicity when discussing TLS physics might not be justified for all kinds of experiments on low-temperature glasses.

### **Signatures of Many-Body Localization in the Dynamics of Two-Level Systems in Glasses (jointly presented with Claudia Artiago)**

*Balducci, Federico*

Signatures of Many-Body Localization in the Dynamics of Two-Level Systems in Glasses Abstract: We investigate the quantum dynamics of two-level systems (TLSs) in glasses at low temperatures (1 K and below). We study an ensemble of TLSs coupled to phonons. By integrating out the phonons within the framework of the GKSL master equation, we derive the explicit form of the interactions among TLSs and of the dissipative terms. We find that the dynamics of the system shows clear signatures of many-body localization physics (in particular a power-law decay of the concurrence, which measures pairwise entanglement also in non-isolated systems) even in the presence of dissipation, if the latter is not too large. This feature can be ascribed to the presence of strong, long-tailed disorder characterizing the distributions of the model parameters. Our findings show that assuming ergodicity when discussing TLS physics might not be justified for all kinds of experiments on low-temperature glasses.

+

### **Relaxation dynamics of the three-dimensional Coulomb Glass model**

*Bhandari, Preeti*

We consider the relaxation properties of electron glass, which is a system in which all the electron states are localized and the dynamics occurs through phonon-assisted hopping amongst these states. We model the system by a lattice of localized states which have random energies and interact through the Coulomb interaction. The presence of disorder and the long-range interaction makes the system glassy which results in slow dynamics towards reaching equilibrium, aging (system dynamics depending on the history), and memory effects. Further, a much-discussed question is whether there is an equilibrium transition to glassy phase or not as the temperature is lowered. The wide range of timescales involved in such systems makes it more difficult to solve numerically. We have modeled the kinetics of site-occupation numbers as Ising spins by Kawasaki Dynamics (spin-exchange) as in our system only half the sites are occupied and the number of particles is conserved. The master equation governing the dynamics is solved in mean-field approximation. We use the eigenvalue distribution of the dynamical matrix to characterize relaxation laws as a function of localization length at low temperatures. Our results demonstrate the dominant role played by the localization length on the relaxation laws. For very small localization lengths we find a crossover from exponential relaxation at long times to a logarithmic decay at intermediate times. No logarithmic

decay at the intermediate times is observed for large localization lengths.

## Quasiparticle dynamics of symmetry resolved entanglement after a quench: the examples of conformal field theories and free fermions

*Bonsignori, Riccarda*

The time evolution of the entanglement entropy is a key concept to understand the structure of a non-equilibrium quantum state. In a large class of models, such evolution can be understood in terms of a semiclassical picture of moving quasiparticles spreading the entanglement throughout the system. However, it is not yet known how the entanglement splits between the sectors of an internal local symmetry of a quantum many-body system. Here, guided by the examples of conformal field theories and free-fermion chains, we show that the quasiparticle picture can be adapted to this goal, leading to a general conjecture for the charged entropies whose Fourier transform gives the desired symmetry resolved entanglement  $S_n(q)$ . We point out two physically relevant effects that should be easily observed in atomic experiments: a delay time for the onset of  $S_n(q)$  which grows linearly with  $|\Delta q|$  (the difference from the charge  $q$  and its mean value), and an effective equipartition when  $|\Delta q|$  is much smaller than the subsystem size.

+

## Lieb-Robinson bounds and out-of-time order correlators in a long-range spin chain

*Colmenarez Gomez, Luis Andres*

Lieb-Robinson bounds quantify the maximal speed of information spreading in nonrelativistic quantum systems. We discuss the relation of Lieb-Robinson bounds to out-of-time order correlators, which correspond to different norms of commutators  $C(r, t) = [A(t), B]$  of local operators. Using an exact Krylov space-time evolution technique, we calculate these two different norms of such commutators for the spin-1/2 Heisenberg chain with interactions decaying as a power law  $1/r^\alpha$  with distance  $r$ . Our numerical analysis shows that both norms (operator norm and normalized Frobenius norm) exhibit the same asymptotic behavior, namely, a linear growth in time at short times and a power-law decay in space at long distance, leading asymptotically to power-law light cones for  $\alpha < 1$  and to linear light cones for  $\alpha > 1$ . The asymptotic form of the tails of  $C(r, t) t/r^\alpha$  is described by short-time perturbation theory, which is valid at short times and long distances.

+

## Extraction of many-body Chern number from a single wave function

*Dehghani, Hossein*

"The quantized Hall conductivity of integer and fractional quantum Hall (IQH and FQH) states is directly related to a topological invariant, the many-body Chern number. The conventional calculation of this invariant in interacting systems requires a family of many-body wave functions parameterized by twist angles in order to calculate the Berry curvature. In this work, we demonstrate how to extract the Chern number given a single many-body wave function, without knowledge of the Hamiltonian. We perform extensive numerical simulations involving IQH and FQH states to validate these methods. We also propose an ancilla-free experimental scheme for the measurement of this invariant. Specifically, we use the statistical correlations of randomized measurements to infer the MBCN of a wavefunction."

+

## Correspondence principle for quantum many-body scars

*Desaules, Jean-Yves*

Quantum many-body scars represent a weak form of ergodicity breaking that gives rise to robust periodic revivals in kinetically constrained quantum systems, such as the PXP model describing strongly-interacting Rydberg atoms. By analogy to quantum scars in single-particle quantum billiards, the many-body scarred eigenstates are distinguished by their anomalous overlap with the so-called quasimodes, i.e., the wave functions that concentrate along classical periodic orbits. While the classical orbits in the PXP model have previously been constructed using the Time-Dependent Variational Principle (TDVP), the corresponding quasimodes have only been found numerically. Here we introduce a new approach to constructing quasimodes in the PXP model based on the subspace symmetrised over permutations on each sublattice. We show that this method is amenable to analytic treatment and leads to an efficient construction of the quasimodes, allowing to study the dynamics of the PXP model in large systems on the order of hundreds of atoms. Finally, our approach provides a tractable way of introducing quantum fluctuations at all orders on top of the classical equations of motion defined by the TDVP.

+

## The effect of intrinsic quantum fluctuations on the phase diagram of anisotropic dipolar magnets

*Dollberg, Tomer*

LiHoF<sub>4</sub> is a quantum magnet known to be a good physical realization of the transverse field Ising model with dipolar interactions. Results from previous studies, using various Monte Carlo techniques and mean-field analyses, show a persistent discrepancy with experimental results for the  $B_x - T$  phase diagram. Namely, in the low  $B_x$  regime, the experimental phase boundary separating the ferromagnetic and paramagnetic phases has a much smaller dependence on magnetic field in comparison to the theoretical predictions. In this work we propose a mechanism which may account for the discrepancy. Offdiagonal terms of the dipolar interaction, more dominant in the disordered paramagnetic phase, reduce the energy of the paramagnetic phase, and consequently reduce the critical temperature. Using classical Monte Carlo simulations, in which we explicitly take the modification of the Ising states due to the offdiagonal terms into account, we show that the inclusion of these terms reduces  $T_c$  markedly at zero transverse field. We also show that the effect is diminished with increasing transverse field, leading to the above mentioned field dependence of the critical temperature.

+

## Vortices and Fractons

*Doshi, Darshil*

We discuss a simple and experimentally available realization of fracton physics. We note that superfluid vortices conserve total dipole moment and trace of the quadrupole moment of vorticity. This establishes a relation to a traceless scalar charge theory in two spatial dimensions. We also consider the limit where the number of vortices is large and show that emergent vortex hydrodynamics conserves these moments too. Finally, we compare the motion of vortices and of fractons on

+



curved surfaces; and find that they agree. This opens a route to experimental study of the interplay between fracton physics and curved space. Our conclusions also apply to charged particles in strong magnetic field. (Reference : D Doshi, A Gromov - arXiv preprint arXiv:2005.03015, 2020)

## **Anomalous Diffusion in Dipole- and Higher-Moment Conserving Systems**

*Feldmeier, Johannes*

The presence of global conserved quantities in interacting systems generically leads to diffusive transport at late times. Here, we show that systems conserving the dipole moment of an associated global charge, or even higher moment generalizations thereof, escape this scenario, displaying subdiffusive decay instead. Modelling the time evolution as cellular automata for specific cases of dipole- and quadrupole-conservation, we numerically find distinct anomalous exponents of the late time relaxation. We explain these findings by analytically constructing a general hydrodynamic model that results in a series of exponents depending on the number of conserved moments, yielding an accurate description of the scaling form of charge correlation functions. We analyze the spatial profile of the correlations and discuss potential experimentally relevant signatures of higher moment conservation.

+

## **Incommensurability-induced sub-ballistic narrow-band-states in twisted bilayer graphene**

*Gonçalves, Miguel*

We study the localization properties of electrons in incommensurate twisted bilayer graphene for small angles, encompassing the narrow-band regime, by numerically exact means. Sub-ballistic states are found within the narrow-band region around the magic angle. Such states are delocalized in momentum-space and follow non-Poissonian level statistics, in contrast with their ballistic counterparts found for close commensurate angles. Transport results corroborate this picture: for large enough systems, the conductance decreases with system size for incommensurate angles within the sub-ballistic regime. Our results show that incommensurability effects are of crucial importance in the narrow-band regime. The incommensurate nature of a general twist angle must therefore be taken into account for an accurate description of magic-angle twisted bilayer graphene.

+

## **Quantum scars of bosons with correlated hopping**

*Hudomal, Ana*

Recent experiments on Rydberg atom arrays have found evidence of anomalously slow thermalization and persistent density oscillations, which have been interpreted as a many-body analog of the phenomenon of quantum scars. Periodic dynamics and atypical scarred eigenstates originate from a "hard" kinetic constraint: the neighboring Rydberg atoms cannot be simultaneously excited. Here we propose a realization of quantum many-body scars in a 1D bosonic lattice model with a "soft" constraint in the form of density-assisted hopping. We discuss the relation of this model to the standard Bose-Hubbard model and possible experimental realizations using ultracold atoms. We find that this model exhibits similar phenomenology to the Rydberg atom chain, including weakly entangled eigenstates at high energy densities and the presence of a large number of exact zero energy states, with



distinct algebraic structure.

## **Model wavefunctions for interfaces between lattice quantum Hall states**

*Jaworowski, Błażej*

While the physics of the edges between topological orders and vacuum has been thoroughly investigated, less is known about the properties of interfaces between different topological orders. Such systems have recently attracted significant attention, partly due to their potential applications in quantum computing. However, they are difficult to study numerically in a bottom-up manner, because relatively large system sizes are needed to capture their properties correctly. In this work, we overcome this obstacle by employing the conformal field theory to create model wavefunctions for interfaces between two different Laughlin states on the lattice. These objects can be studied using Monte Carlo methods for systems much larger than available within the exact diagonalization approach. We study their properties such as the entanglement entropy scaling and the correlation functions. Similar wavefunctions are also created for systems with localized anyons, allowing to extract the charge, the density profile and the mutual statistics of these excitations. Within our approach, we can explicitly simulate the crossing of the interface by the anyons and show that some of them lose their fractional statistics in such a process, which is in accordance with earlier "top-down" results obtained from field theory, and is possibly related to the entanglement entropy scaling at the interface.

+

## **Floquet Gauge Pump**

*Kumar, Abhishek*

Gauge pumps are spatially-resolved probes that can reveal discrete symmetries due to nontrivial topology. We introduce the Floquet gauge pump whereby a dynamically engineered Floquet Hamiltonian is employed to reveal the inherent topology of the ground state in interacting systems. We demonstrate this concept in a 1D XY model with periodically driven couplings and a transverse field. In the high-frequency limit, we obtain a Floquet Hamiltonian consisting of the static XY and dynamically generated Dzyaloshinsky-Moriya interactions (DMI) terms. We show that anisotropy in the couplings facilitates a magnetization current across a dynamically imprinted junction. In fermionic language, this corresponds to an unconventional Josephson junction with both hopping and pairing tunneling terms. The magnetization current depends on the phases of complex coupling terms, with the XY interaction as the real and DMI as the imaginary part. It shows  $4\pi$  periodicity revealing the topological nature of the ground state manifold in the ordered phase, in contrast to the trivial topology in the disordered phase. We discuss the requirements to realize the Floquet gauge pump with interacting trapped ions.

+

## **Emergent Bloch oscillations in a kinetically constrained Rydberg spin lattice**

*Magoni, Matteo*

We explore the relaxation dynamics of elementary spin clusters of a kinetically constrained spin system. Inspired by experiments with Rydberg lattice gases, we focus on the situation in which an excited spin leads to a "facilitated" excitation of a neighboring spin. We show that even weak interactions that extend beyond nearest neighbors can have a dramatic impact on the relaxation behavior: they generate a +

linear potential, which under certain conditions leads to the onset of Bloch oscillations of spin clusters. These hinder the expansion of a cluster and more generally the relaxation of many-body states towards equilibrium. This shows that non-ergodic behavior in kinetically constrained systems may occur as a consequence of the interplay between reduced connectivity of many-body states and weak interparticle interactions. We furthermore show that the emergent Bloch oscillations identified here can be detected in experiment through measurements of the Rydberg atom density, and discuss how spin-orbit coupling between internal and external degrees of freedom of spin clusters can be used to control their relaxation behavior.

### **Quantifying the efficiency of state preparation via quantum variational eigensolvers**

*Matos, Gabriel*

Recently, there has been much interest in the efficient preparation of complex quantum states using low-depth quantum circuits, such as Quantum Approximate Optimization Algorithm (QAOA). While it has been numerically shown that such algorithms prepare certain correlated states of quantum spins with surprising accuracy, a systematic way of quantifying the efficiency of QAOA in general classes of models has been lacking. Here, we propose that the success of QAOA in preparing ordered states is related to the interaction distance of the target state, which measures how close that state is to the manifold of all Gaussian states in an arbitrary basis of single-particle modes. We numerically verify this for the ground state of the quantum Ising model with arbitrary transverse and longitudinal field strengths, a canonical example of a non-integrable model. Our results suggest that the structure of the entanglement spectrum, as witnessed by the interaction distance, correlates with the success of QAOA state preparation. We conclude that QAOA typically finds a solution that perturbs around the closest free-fermion state.

+

### **Improved qQuantum transport calculations for interacting nanostructures**

*Minarelli, Emma*

Nanoelectronics devices such as semiconductor quantum dots and single molecule transistors exhibit a rich range of physical behavior due to the interplay between orbital complexity, strong electronic correlations and device geometry. Understanding and simulating the quantum transport through such nanostructures is essential for rational design and technological applications. In this poster, I present theoretical reformulations electrical conductance formulae for interacting mesoscopic quantum transport calculations in linear response, and demonstrate the improvement over standard methods with several example applications using the numerical renormalization group technique. I will treat reformulations of the Meir-Wingreen formula in the context of non-proportionate coupling set-ups and by means of perturbative verification of the Ng ansatz; of the Oguri formula in non-Fermi Liquid states and of the Kubo formula for conductance.

+

### **Anyonic molecules in atomic fractional quantum Hall liquids: a quantitative probe of fractional charge and anyonic statistics**

*Muñoz de las Heras, Alberto*

+

We study the quantum dynamics of massive impurities embedded in a strongly interacting two-dimensional atomic gas driven into the fractional quantum Hall (FQH) regime under the effect of a synthetic magnetic field. For suitable values of the atom-impurity interaction strength, each impurity can capture one or more quasi-hole excitations of the FQH liquid, forming a bound molecular state with novel physical properties. An effective Hamiltonian for such anyonic molecules is derived within the Born-Oppenheimer approximation, which provides renormalized values for their effective mass, charge and statistics by combining the finite mass of the impurity with the fractional charge and statistics of the quasi-holes. The renormalized mass and charge of a single molecule can be extracted from the cyclotron orbit that it describes as a free particle in a magnetic field. The anyonic statistics introduces a statistical phase between the direct and exchange scattering channels of a pair of indistinguishable colliding molecules, and can be measured from the angular position of the interference fringes in the differential scattering cross section. Implementations of such schemes beyond cold atomic gases are highlighted, in particular in photonic systems.

## **Phases and Quantum Phase Transitions in an Anisotropic Ferromagnetic Kitaev-Heisenberg- $\Gamma$ Magnet**

*Nanda, Animesh*

We study the spin-1/2 ferromagnetic Heisenberg-Kitaev- $\Gamma$  model in the anisotropic (Toric code) limit to reveal the nature of the quantum phase transition between the gapped  $Z_2$  quantum spin liquid and a spin ordered phase (driven by Heisenberg interactions) as well as a trivial paramagnet (driven by pseudo-dipolar interactions,  $\Gamma$ ). The transitions are obtained by a simultaneous condensation of the Ising electric and magnetic charges-- the fractionalized excitations of the  $Z_2$  quantum spin liquid. Both these transitions can be continuous and are examples of deconfined quantum critical points. Crucial to our calculations are the symmetry implementations on the soft electric and magnetic modes that become critical. In particular, we find strong constraints on the structure of the critical theory arising from time reversal and lattice translation symmetries with the latter acting as an anyon permutation symmetry that endows the critical theory with a manifestly self-dual structure. We find that the transition between the quantum spin liquid and the spin-ordered phase belongs to a self-dual modified Abelian Higgs field theory while that between the spin liquid and the trivial paramagnet belongs to a self-dual  $Z_2$  gauge theory. We also study the effect of an external Zeeman field to show an interesting similarity between the polarised paramagnet obtained due to the Zeeman field and the trivial paramagnet driven the pseudo-dipolar interactions. Interestingly, both the spin liquid and the spin ordered phases have easily identifiable counterparts in the isotropic limit and the present calculations may shed insights into the corresponding transitions in the material relevant isotropic limit.

+

## **Restricted Boltzmann machine representation for the groundstate and excited states of Kitaev Honeycomb model**

*Noormandipour, Mohammadreza*

In this work, the capability of restricted Boltzmann machines (RBMs) to find solutions for the Kitaev honeycomb model is investigated. The measured groundstate (GS) energy of the system is compared and shown to reside within a few percent error of the analytically derived value of the energy per plaquette. Moreover, given a set of  $\uparrow$

single shot measurements of exact solutions of the model, an RBM is used to perform quantum state tomography and the obtained result has a 97% overlap with the exact analytic result. Furthermore, the possibility of realizing anyons in the RBM is discussed and an algorithm is given to build these anyonic excitations and braid them as a proof of concept for performing quantum gates and doing quantum computation.

## Exotic Phases in Rydberg Lattice Models

*Ohler, Simon*

Interacting systems of Rydberg atoms have attracted much attention recently, partly due to their strong interactions and high stability. Furthermore, experimental techniques have been proposed to include synthetic gauge fields and correlated hopping, where the excitation transport between two atoms depends on the quantum state of a third atom. In our work, we are considering a system of Rydberg atoms on a two-dimensional hexagonal lattice, including both synthetic gauge fields and correlated hopping. We numerically obtain a rich phase diagram, including two disordered regimes where we find evidence to support the existence of a chiral spin-liquid-state.

+

## Systematic large flavor fTWA approach to interaction quenches

*Osterkorn, Alexander*

Studying the out-of-equilibrium quantum dynamics in two-dimensional lattice models is challenging due to the lack of a general purpose simulation method. A new semiclassical approach to compute the quantum dynamics of fermions was recently developed by Davidson et. al [1], the fermionic truncated Wigner approximation (fTWA). Here, we adopt the method and combine it with the limit of high fermion degeneracy  $N$  as a well-defined semiclassical expansion parameter. On the poster we consider the well-known problem of an interaction quench in the two-dimensional Hubbard model to show that the method correctly describes prethermalization [2]. In addition we discuss whether the long-time thermalization dynamics is reproduced as well. As a second application we consider quenches in ordered phases of the large- $N$  Hubbard-Heisenberg model and show that the semiclassical time-evolution leads to dephasing and subsequent decay of the order parameter. [1] SM Davidson et. al., Annals of Physics 384, pages 128-141 (2017) [2] A Osterkorn and S Kehrein, arXiv:2007.05063

+

## Topological phonons in oxide perovskites controlled by light

*Peng, Bo*

Oxide perovskites have received widespread attention ever since their discovery due to the multiple physical properties they exhibit, including ferroelectricity, multiferroicity, and superconductivity. One prominent absence in this list of properties that oxide perovskites exhibit is electronic topological order. This is a consequence of the large band gaps of oxide perovskites, which make the band inversions necessary for topology impossible. We find that topological phonons – nodal rings, nodal lines, and Weyl points – are ubiquitous in oxide perovskites in terms of structures (tetragonal, orthorhombic, and rhombohedral), compounds ( $\text{BaTiO}_3$ ,  $\text{PbTiO}_3$ , and  $\text{SrTiO}_3$ ), and external conditions (photoexcitation, strain, and

+

temperature). In particular, in the tetragonal phase of these compounds all types of topological phonons can simultaneously emerge when stabilized by photoexcitation, whereas the tetragonal phase stabilized by thermal fluctuations only hosts a more limited set of topological phonon states. In addition, we find that the photoexcited carrier density can be used to control the emergent topological states, for example driving the creation/annihilation of Weyl points and switching between nodal lines and nodal rings. Overall, we propose oxide perovskites as a versatile platform in which to study topological phonons and their manipulation with light [1]. Reference: [1] Bo Peng, Yuchen Hu, Shuichi Murakami, Tiantian Zhang, Bartomeu Monserrat. Topological phonons in oxide perovskites controlled by light. *Science Advances* 6, eabd1618 (2020).

## Higher-order and fractional discrete time crystals in clean long-range interacting systems

*Pizzi, Andrea*

Discrete time crystals are periodically driven systems characterized by a response with periodicity  $nT$ , with  $T$  the period of the drive and  $n > 1$ . Typically,  $n$  is an integer and bounded from above by the dimension of the local (or single particle) Hilbert space, the most prominent example being spin-1/2 systems with  $n$  restricted to 2. Here we show that a clean spin-1/2 system in the presence of long-range interactions and transverse field can sustain a huge variety of different 'higher-order' discrete time crystals with integer and, surprisingly, even fractional  $n > 2$ . We characterize these (arguably prethermal) non-equilibrium phases of matter thoroughly using a combination of exact diagonalization, semiclassical methods, and spin-wave approximations, which enable us to establish their stability in the presence of competing long- and short-range interactions. Remarkably, these phases emerge in a model with continuous driving and time-independent interactions, convenient for experimental implementations with ultracold atoms or trapped ions.

+

## Anatomy of Z2 fluxes in anyon Fermi liquids and Bose condensates

*Pozo Ocaña, Óscar*

We study in detail the properties of pi-fluxes embedded in a state with a finite density of anyons that form either a Fermi liquid or a Bose-Einstein condensate. By employing a recently developed exact lattice bosonization in 2D, we demonstrate that such pi-flux remains a fully deconfined quasiparticle with a finite energy cost in a Fermi liquid of emergent fermions coupled to a Z2 gauge field. This pi-flux is accompanied by a screening cloud of fermions, which in the case of a Fermi gas with a parabolic dispersion binds exactly 1/8 of a fermionic hole. In addition there is a long-ranged power-law oscillatory disturbance of the liquid surrounding the pi-flux akin to Friedel oscillations. These results carry over directly to the pi-flux excitations in orthogonal metals. In sharp contrast, when the pi-flux is surrounded by a Bose-Einstein condensate of particles coupled to a Z2 gauge field, it binds a superfluid half-vortex, becoming a marginally confined excitation with a logarithmic energy cost divergence.

+

## Anomalous localization in spin chains coupled to non-local degree of freedom

*Rahmanian Koshkaki, Saeed*

+

It has recently been predicted that many-body localization survives the presence of coupling to a non-local degree of freedom, such as a cavity mode [PRL 122, 240402 (2019)]. This poster presents recent results on anomalous properties of localization in such a setup. First, we show that in a central qudit model, an inverted mobility edge occurs, meaning that infinite temperature states are localized while low energy states are delocalized. This model may be directly realized by extending recent work on artificial cavities using atom-like mirrors [Nature 569.7758: 692 (2019)]; similar results hold for central spin models or cavity QED with appropriate cavity non-linearity. Second, we suggest a platform for realizing time crystals in cavity QED and in the absence of drive.

## **Simulating hydrodynamics on NISQ devices with random circuits**

*Richter, Jonas*

An important milestone towards “quantum supremacy” has been recently achieved by using Google’s noisy intermediate-scale quantum (NISQ) device Sycamore to sample from the output distribution of (pseudo-)random circuits involving up to 53 qubits. We argue that such random circuits provide tailor-made building blocks for the simulation of quantum many-body systems on NISQ devices. Specifically, we propose a two-part algorithm consisting of a random circuit followed by a trotterized Hamiltonian time evolution, which we numerically exemplify by studying the buildup of spatiotemporal correlations in one- and two-dimensional quantum spin systems. Importantly, we find that the emerging hydrodynamic scaling of the correlations is highly robust with respect to the size of the Trotter step, opening the door to reach nontrivial time scales with a small number of elementary gates. While errors within the random circuit are shown to be irrelevant for our approach, we furthermore unveil that meaningful results can be obtained for noisy time evolutions with error rates achievable on near-term hardware.

+

## **Generative Model Learning For Molecular Electronics**

*Rigo, Jonas*

The use of single-molecule transistors in nanoelectronics devices requires a deep understanding of the generalized ‘quantum impurity’ models describing them. Microscopic models comprise molecular orbital complexity and strong electron interactions while also treating explicitly conduction electrons in the external circuit. No single theoretical method can treat the low-temperature physics of such systems exactly. To overcome this problem, we use a generative machine learning approach to formulate effective models that are simple enough to be treated exactly by methods such as the numerical renormalization group, but still capture all observables of interest of the physical system.

+

## **Scattering Processes via Tensor Network Simulations**

*Rigobello, Marco*

Scattering processes are a crucial ingredient for the investigation of the fundamental interactions. Working in the framework of Hamiltonian lattice quantum field theory, we attack this problem via numerical tensor network simulations. We focus on the theory of quantum electrodynamics in  $1 + 1$  spacetime dimensions but develop a +



set of tools which are relevant for a broader class of  $1 + 1$  dimensional quantum field theories. Specifically, we identify a matrix product state representation of the initial momentum wave packet and compute its real-time dynamics. The outcome of some scattering simulations is presented.

### **Long-range Ising chains: eigenstate thermalization and symmetry breaking of excited states**

*Russomanno, Angelo*

We use large-scale exact diagonalization to study the quantum Ising chain in a transverse field with long-range power-law interactions decaying with exponent  $\alpha$ . Analyzing various eigenstate and eigenvalue properties, we find numerical evidence for ergodic behavior in the thermodynamic limit for  $\alpha > 0$ , i.e. for the slightest breaking of the permutation symmetry at  $\alpha = 0$ . Considering an excited-states fidelity susceptibility, an energy-resolved average level-spacing ratio and the eigenstate expectations of observables, we observe that a behavior consistent with eigenstate thermalization first emerges at high energy densities for finite system sizes, as soon as  $\alpha > 0$ . We argue that ergodicity moves towards lower energy densities for increasing system sizes. While we argue the system to be ergodic for any  $\alpha > 0$ , we also find a peculiar behaviour near  $\alpha = 2$  suggesting the proximity to a yet unknown integrable point. We further study the symmetry-breaking properties of the eigenstates. We argue that for weak transverse fields the eigenstates break the  $\mathbb{Z}_2$  symmetry, and show long-range order, at finite excitation energy densities for all the values of  $\alpha$  we can technically address ( $\alpha \leq 1.5$ ). Our contribution settles central theoretical questions on long-range quantum Ising chains and are also interesting for the nonequilibrium dynamics of trapped ions.

+

### **Pyrochlore $S = \frac{1}{2}$ Heisenberg antiferromagnet at finite temperature**

*Schäfer, Robin*

We use a combination of three computational methods to investigate the notoriously difficult frustrated three-dimensional pyrochlore  $S=1/2$  quantum antiferromagnet, at finite temperature  $T$ : canonical typicality for a finite cluster of  $2 \times 2 \times 2$  unit cells (i.e., 32 sites), a finite- $T$  matrix product state method on a larger cluster with 48 sites, and the numerical linked cluster expansion (NLCE) using clusters up to 25 lattice sites, including nontrivial hexagonal and octagonal loops. We calculate thermodynamic properties (energy, specific heat capacity, entropy, susceptibility, magnetization) and the static structure factor. We find a pronounced maximum in the specific heat at  $T = 0.57J$ , which is stable across finite size clusters and converged in the series expansion. At  $T \approx 0.25J$  (the limit of convergence of our method), the residual entropy per spin is  $0.47k_B \log(2)$ , which is relatively large compared to other frustrated models at this temperature. We also observe a nonmonotonic dependence on  $T$  of the magnetization at low magnetic fields, reflecting the dominantly nonmagnetic character of the low-energy states. A detailed comparison of our results to measurements for the  $S = 1$  material  $\text{NaCaNi}_2\text{F}_7$  yields a rough agreement of the functional form of the specific heat maximum, which in turn differs from the sharper maximum of the heat capacity of the spin ice material  $\text{Dy}_2\text{Ti}_2\text{O}_7$ .

+

### **Scattering of mesons in quantum simulators**

+



Simulating real-time evolution in theories of fundamental interactions represents one of the central challenges in contemporary theoretical physics. Cold-atom platforms represent promising candidates to realize quantum simulations of non-perturbative phenomena in gauge theories, such as vacuum decay and hadron collisions, in extreme conditions prohibitive for direct experiments. In this work, we demonstrate that present-day quantum simulators can give access to S-matrix measurements of elastic and inelastic meson collisions in Abelian gauge theories, mimicking experiments with linear particle accelerators. Considering for definiteness a  $(1 + 1)$ -dimensional  $\mathbb{Z}_2$ -lattice gauge theory realizable with Rydberg-atom arrays, we solve the meson scattering problem exactly in the limit of large fermion mass and for arbitrary coupling strength.

## Neural network wave functions and the sign problem

*Szabó, Attila*

Neural quantum states are a promising approach to study many-body quantum physics. However, they face a major challenge when applied to lattice models: Neural networks struggle to converge to ground states with a nontrivial sign structure. In this talk, I present a neural network architecture with a simple, explicit, and interpretable phase ansatz, which can robustly represent such states and achieve state-of-the-art variational energies for both conventional and frustrated antiferromagnets. In the first case, the neural network correctly recovers the Marshall sign rule without any prior knowledge. For frustrated magnets, our approach uncovers low-energy states that exhibit the Marshall sign rule but does not reach the true ground state, which is expected to have a different sign structure. I discuss the possible origins of this "residual sign problem" as well as strategies for overcoming it, which may allow using neural quantum states for challenging spin liquid problems.

+

## Separation-dependent emission pathways of quantum emitters

*Talukdar, Jugal*

System-environment interactions have been studied extensively for many decades and recent developments in quantum optics and circuit QED provide intriguing possibilities for realizing non-linear environments. The Bose-Hubbard lattice for photons, e.g., has been realized experimentally using superconducting circuits, thereby providing an exciting platform to study effective interactions between quantum emitters mediated by the engineered photonic environment. We consider a collection of macroscopically separated two-level emitters coupled to a non-linear environment and study the dissipative dynamics. Specifically, we report our theoretical progress on understanding the criteria for the existence of specific emission pathways as a function of the positions of the emitters.

+

## Continuous matrix product operator approach to finite temperature quantum states

*Tang, Wei*

+

We present an algorithm for studying quantum systems at finite temperature using continuous matrix product operator representation. The approach handles both short-range and long-range interactions in the thermodynamic limit without incurring any time discretization error. Moreover, the approach provides direct access to physical observables including the specific heat, local susceptibility, and local spectral functions. After verifying the method using the prototypical quantum XXZ chains, we apply it to quantum Ising models with power-law decaying interactions and on the infinite cylinder, respectively. The approach offers predictions that are relevant to experiments in quantum simulators and the nuclear magnetic resonance spin-lattice relaxation rate.

### **Semiclassical theory of finite temperature dynamics of the sine-Gordon model**

*Vörös, Dániel*

We investigate the finite temperature dynamics of the sine-Gordon model by studying its dynamical correlation functions at low temperatures in the semiclassical approach. Going beyond previous analyses based on perfectly reflective or transmissive collision dynamics of the gapped solitonic excitations, we focus on the generic case when both transmissive and reflective scatterings are present. We argue that the behaviour of the correlation functions is qualitatively different from both special cases, in particular, the autocorrelation function decays in time neither exponentially nor as a power-law, but assumes a squeezed exponential form. Supporting our claim, we perform numerical simulations utilizing the exact S-matrix of the model.

+

### **Vortex-Phase in Non-Centrosymmetric Antiferromagnets**

*Wolba, Benjamin*

In this work we consider two-dimensional, non-centrosymmetric antiferromagnets, for which the competition between exchange and Dzyaloshinskii-Moriya interaction leads to the formation of spatially modulated phases of the staggered order parameter. Within the framework of Ginzburg-Landau theory we show that by applying a magnetic field parallel to the c-axis, which thus induces easy-plane anisotropy, one can stabilize a square lattice of vortices close to Neel temperature. Upon decreasing temperature, this vortex phase undergoes spontaneous symmetry breaking into a rectangular phase, which was not anticipated before. We discuss the relevance of our results for the chiral antiferromagnet Ba<sub>2</sub>CuGe<sub>2</sub>O<sub>7</sub>.

+

### **The Mott Transition as a Topological Phase Transition**

*Wong, Patrick*

We show that the Mott metal-insulator transition in the standard one-band Hubbard model can be understood as a topological phase transition. Our approach is inspired by the observation that the mid-gap pole in the self-energy of a Mott insulator resembles the spectral pole of the localized surface state in a topological insulator. We use numerical renormalization group--dynamical mean-field theory to solve the infinite-dimensional Hubbard model and represent the resulting local self-energy in terms of the boundary Green's function of an auxiliary tight-binding chain without interactions. The auxiliary system is of generalized Su-Schrieffer-Heeger

+

model type; the Mott transition corresponds to a dissociation of domain walls.

## Dipolar dimer liquid

Zhang, Junyi

Motivated by water, we proposed a lattice liquid model of dipolar dimers. We show that on bipartite lattice it can be exactly mapped to annealed Ising models on random graphs. With exactly solved Ising models, we cannot only prove the existence of the liquid-liquid phase transition, but also bound the critical temperature tightly around  $k_B T_c = 3.5J$ , which is also confirmed by Monte Carlo simulation.

+

## Random multipolar driving: tunably slow heating through spectral engineering

Zhao, Hongzheng

We study heating in interacting quantum many-body systems driven by random sequences with  $n$ -multipolar correlations, corresponding to a polynomially suppressed low frequency spectrum. For  $n \geq 1$ , we find a prethermal regime, the lifetime of which grows algebraically with the driving rate, with exponent  $2n + 1$ . A simple theory based on Fermi's golden rule accounts for this behaviour. The quasiperiodic Thue-Morse sequence corresponds to the  $n \rightarrow \infty$  limit, and accordingly exhibits an exponentially long-lived prethermal regime. Despite the absence of periodicity in the drive, and in spite of its eventual heat death, the prethermal regime can host versatile non-equilibrium phases, which we illustrate with a random multipolar discrete time crystal.

+

## Subdiffusive dynamics and critical quantum correlations in a disorder-free localized Kitaev honeycomb model

Zhu, Guo-Yi

Disorder-free localization has recently emerged as a mechanism for ergodicity breaking in homogeneous lattice gauge theories. In this work we show that this mechanism can lead to unconventional states of quantum matter as the absence of thermalization lifts constraints imposed by equilibrium statistical physics. We study a Kitaev honeycomb model in a skew magnetic field subject to a quantum quench from a fully polarized initial product state and observe nonergodic dynamics as a consequence of disorder-free localization. We find that the system exhibits a subballistic entanglement growth and quantum correlation spreading, which is otherwise typically associated with thermalizing systems. In the asymptotic steady state the Kitaev model develops volume-law entanglement and power-law decaying dimer quantum correlations at an energy density where the equilibrium model only displays paramagnetic and noncritical properties. Our work sheds light onto the potential for disorder-free localized lattice gauge theories to realize quantum states in two dimensions with properties beyond what is possible in an equilibrium context.

+

## Bulletin of the American Physical Society

### APS March Meeting 2021

Volume 66, Number 1

Monday–Friday, March 15–19, 2021; Virtual; Time Zone: Central Daylight Time, USA

#### Session Y44: Thermalization and Chaos

11:30 AM–2:18 PM, Friday, March 19, 2021

Sponsoring Unit: DCMP

Chair: Marko Znidaric, Univ of Ljubljana

#### **Abstract: Y44.00008 : Quantum scars of bosons with correlated hopping\***

12:54 PM–1:06 PM Live

← Abstract →

#### **Presenter:**

Ana Hudomal

(School of Physics and Astronomy, University of Leeds)

#### **Authors:**

Ana Hudomal

(School of Physics and Astronomy, University of Leeds)

Ivana Vasic

(Scientific Computing Laboratory, Institute of Physics Belgrade)

Nicolas Regnault

(Department of Physics, Princeton University)

Zlatko Papic

(School of Physics and Astronomy, University of Leeds)

Recent experiments on Rydberg atom arrays have found evidence of anomalously slow thermalization and persistent density oscillations, which have been interpreted as a many-body analog of the phenomenon of quantum scars. Periodic dynamics and atypical scarred eigenstates originate from a "hard" kinetic constraint: the neighboring Rydberg atoms cannot be simultaneously excited. Here we propose a realization of quantum many-body scars in a 1D bosonic lattice model with a "soft" constraint in the form of density-assisted hopping. We discuss the relation of this model to the standard Bose-Hubbard model and possible experimental realizations using ultracold atoms. We find that this model exhibits similar phenomenology to the Rydberg atom chain, including weakly entangled eigenstates at high energy densities and the presence of a large number of exact zero energy states, with distinct algebraic structure.

\*A.H. acknowledges support by the Leverhulme Trust Research Leadership Award RL-2019-015 and funding provided by the Institute of Physics Belgrade, through the grant by the Serbian Ministry of Education, Science, and Technological Development.

# Boulder School for Condensed Matter and Materials Physics

## Student Poster Abstracts

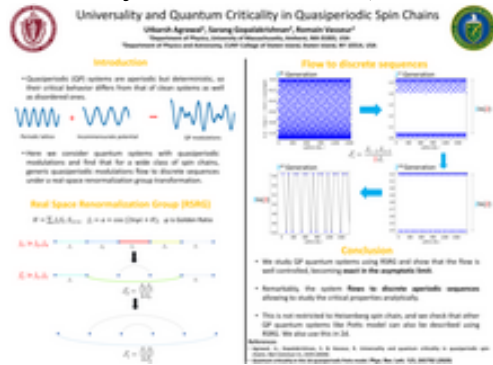


**Utkarsh Agrawal**

[uagrawal@umass.edu](mailto:uagrawal@umass.edu)

<mailto:uagrawal@umass.edu>

University of Massachusetts, Amherst



### Universality and Quantum Criticality in Quasiperiodic Spin Chains

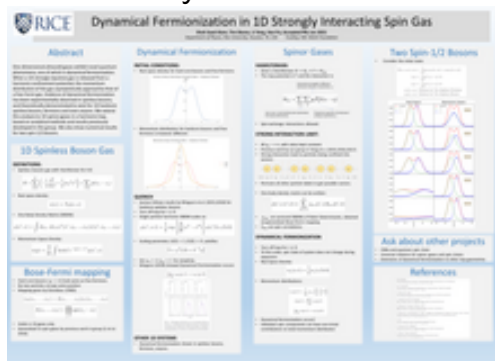
Quasiperiodic systems are aperiodic but deterministic, so their critical behaviour differs from that of clean systems as well as disordered ones. Quasiperiodic criticality was previously understood only in the special limit where the couplings follow discrete quasiperiodic sequences. Here we consider generic quasiperiodic modulations; we find, remarkably, that for a wide class of spin chains, generic quasiperiodic modulations flow to discrete sequences under a real-space renormalization group transformation. These discrete sequences are therefore fixed points of a **functional** renormalization group. This observation allows for an asymptotically exact treatment of the critical points. We use this approach to analyze the quasiperiodic Heisenberg, Ising, and Potts spin chains, as well as a phenomenological model for the quasiperiodic many-body localization transition.



**Shah Saad Alam**

[sa59@rice.edu](mailto:sa59@rice.edu) (<mailto:sa59@rice.edu>)

Rice University



## Dynamical Fermionization in One-Dimensional Spinor Gases

One dimensional ultracold gases exhibit novel quantum phenomena, one of which is dynamical fermionization. When a 1D strongly repulsive gas is released from a harmonic confinement potential, the momentum distribution of the gas asymptotically approaches that of a free Fermi gas. Evidence of dynamical fermionization has been experimentally observed in spinless bosons, and theoretically demonstrated to exist for 1D hardcore spinless bosons, fermions and even anyons. We extend this analysis to 1D spinor gases in a harmonic trap, based on analytical methods and results previously developed in the group. We also show numerical results for two spin-1/2 bosons.\*

(Accepted PRL Jun 2021)

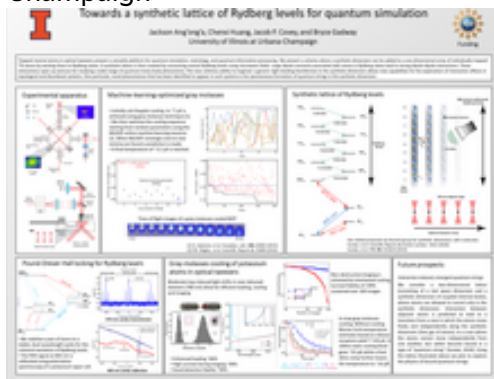


**Jackson Ang'ong'a**

[angonga2@illinois.edu](mailto:angonga2@illinois.edu)

<mailto:angonga2@illinois.edu>

University of Illinois, Urbana-Champaign



## Towards a synthetic lattice of Rydberg levels for quantum simulation

Rydberg atoms in optical tweezer arrays present a versatile platform for quantum simulation, metrology and quantum information processing. We present a scheme that extends the capabilities of this platform by adding a synthetic dimension where several Rydberg levels are coupled by microwave fields to create a lattice. The near arbitrary ability to engineer a generic tight-binding Hamiltonian in the synthetic dimension, in addition to strong dipole-dipole interactions present in Rydberg atomic gases, allows new capabilities for the exploration of interaction effects in topological and disordered systems.



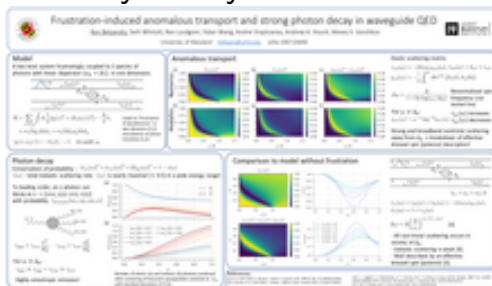


**Ron Belyansky**

[ron.belyansky@gmail.com](mailto:ron.belyansky@gmail.com)

<mailto:ron.belyansky@gmail.com>

University of Maryland



## Frustration-induced anomalous transport and strong photon decay in waveguide QED

We study the propagation of photons in a one-dimensional environment consisting of two non-interacting species of photons frustratingly coupled to a single spin-1/2. The ultrastrong frustrated coupling leads to an extreme mixing of the light and matter degrees of freedom, resulting in the disintegration of the spin and a breakdown of the “dressed-spin”, or polaron, description. Using a combination of numerical and analytical methods, we show that the elastic response becomes increasingly weak at the effective spin frequency, showing instead an increasingly strong and broadband response at higher energies. We also show that the photons can decay into multiple photons of smaller energies. The total probability of these inelastic processes can be as large as the total elastic scattering rate, or half of the total scattering rate, which is as large as it can be. The frustrated spin induces strong anisotropic photon-photon interactions that are dominated by inter-species interactions. Our results are relevant to state-of-the-art circuit and cavity quantum electrodynamics experiments.

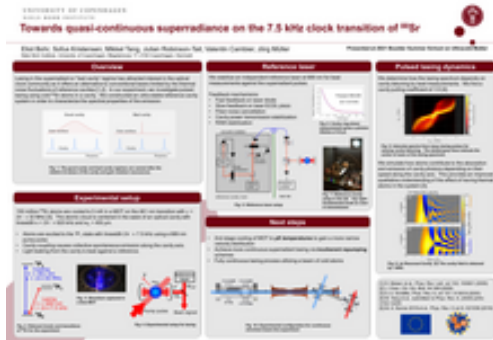


**Eliot Bohr**

[eliot.bohr@nbi.ku.dk](mailto:eliot.bohr@nbi.ku.dk)

[\(mailto:eliot.bohr@nbi.ku.dk\)](mailto:eliot.bohr@nbi.ku.dk)

University of Copenhagen Niels Bohr  
Institute



**Kieran Bull**

[pykb@leeds.ac.uk](mailto:pykb@leeds.ac.uk)

[\(mailto:pykb@leeds.ac.uk\)](mailto:pykb@leeds.ac.uk)

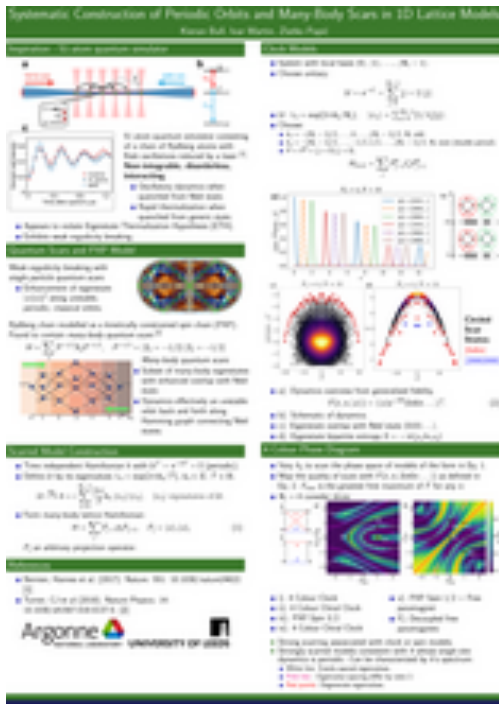
University of Leeds

## Towards quasi-continuous superradiance on the 7.5 kHz clock transition of 88-Sr

Lasing in the superradiant or “bad cavity” regime has attracted interest in the optical clock community as it offers an alternative to conventional lasers limited by the thermal noise fluctuations of reference cavities. In our experiment, we investigate pulsed lasing using cold 88-Sr atoms in a cavity. We constructed an ultra-stable reference cavity system in order to characterize the spectral properties of the emission. We present results on dynamics of pulsed lasing at mK temperatures and discuss updates to the experiment which we are currently developing to increase the duration of these pulses.

## Systematic construction of scarred many-body dynamics in 1D lattice models

We introduce a family of non-integrable 1D lattice models that feature robust periodic revivals under a global quench from certain initial product states, thus generalizing the phenomenon of many-body scarring recently observed in Rydberg atom quantum simulators. Our construction is based on a systematic embedding of the single-site unitary dynamics into a kinetically-constrained many-body system. We numerically demonstrate that this construction yields new families of models with robust wave-function revivals, and it includes kinetically-constrained quantum clock models as a special case. We show that scarring dynamics in these models can be decomposed into a period of nearly free clock precession and an interacting bottleneck, shedding light on their anomalously slow thermalization when quenched from special initial states.



**Eli Chertkov**  
[eli.chertkov@gmail.com](mailto:eli.chertkov@gmail.com)  
<mailto:eli.chertkov@gmail.com>  
 University of Illinois, Urbana-Champaign

## Numerical evidence for many-body localization in two and three-dimensions

Disordered quantum systems that exhibit many-body localization (MBL), the interacting generalization of Anderson localization, break the usual paradigm of quantum statistical mechanics and do not reach thermal equilibrium at long times. These systems exhibit a myriad of interesting properties, such as unusual entanglement and dynamics, and have been a subject of intense theoretical, numerical, and experimental study. Many properties of MBL are due to the existence of quasilocal integrals of motion known as localized bits, or “l-bits.” In this work, we present a new, general algorithm for constructing l-bits. While past numerical investigations of MBL have been primarily limited to one-dimensional chains, we show that our method can be used in arbitrary dimension. Our numerical results reveal some signatures of MBL in two and three-dimensional disordered Hamiltonians.



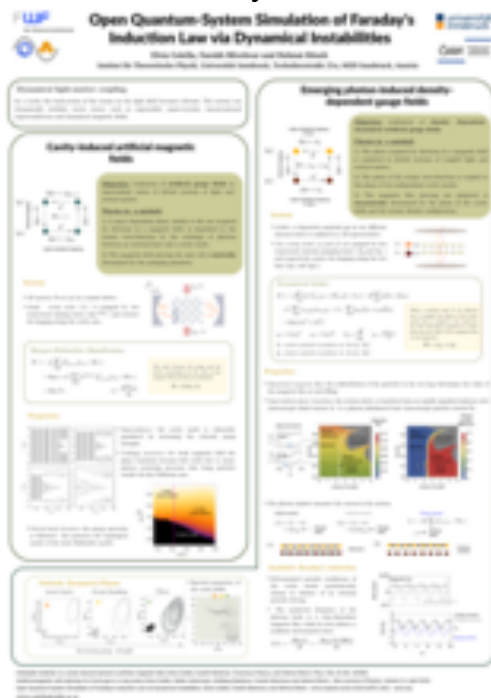


**Elvia Colella**

[elvia.colella@uibk.ac.at](mailto:elvia.colella@uibk.ac.at)

<mailto:elvia.colella@uibk.ac.at>

Innsbruck University



**Ceren Dag**

[cbdag@umich.edu](mailto:cbdag@umich.edu)

<mailto:cbdag@umich.edu>

University of Michigan

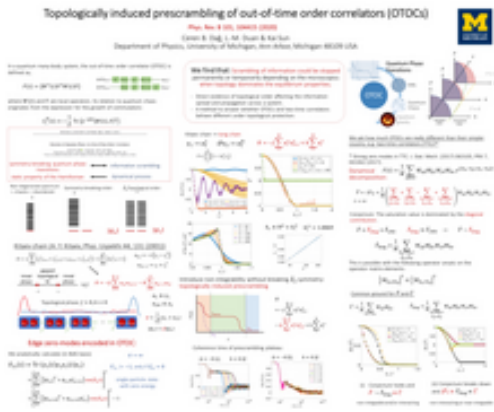
## Open Quantum-System Simulation of Faraday's Induction Law via Dynamical Instabilities

We propose a novel type of cavity-QED set up to study the physics of dynamical gauge potentials. Atomic tunneling along opposite directions in the two legs of the ladder is mediated by photon scattering from transverse pump lasers to two distinct cavity modes. The steady-state atomic motion along the legs of the ladder leads either to a pure chiral current, screening the induced dynamical magnetic field as in the Meissner effect, or generates simultaneously chiral and particle currents. For sufficiently strong pump the system enters into a dynamically unstable regime exhibiting limit-cycle and period-doubled oscillations. An electromotive force is induced in this dynamical regime as expected from an interpretation based on Faraday's law of induction for the time-dependent synthetic magnetic flux.

## Topologically induced prescrambling and dynamical detection of topological phase transitions at infinite temperature

We report a numerical observation where the infinite-temperature out-of-time-order correlators (OTOCs) directly probe quantum phase transitions at zero temperature, in contrast to common intuition where low energy quantum effects are washed away by strong thermal fluctuations at high temperature. By comparing numerical simulations with exact analytic results, we determine that this phenomenon has a topological origin and is highly generic, as long as the underlying system can be mapped to a 1D Majorana chain. Using the Majorana basis, we show that the infinite-temperature OTOCs probe zero-temperature quantum phases via detecting the presence of





Majorana zero modes at the ends of the chain that is associated with 1D  $Z_2$  topological order. Hence, we show that strong zero modes also affect OTOCs and scrambling dynamics. Our results demonstrate an intriguing interplay between information scrambling and topological order, which leads to a new phenomenon in the scrambling of generic non-integrable models: topological order induced prescrambling, paralleling the notion of prethermalization of two-time correlators, that defines a time-scale for the restricted scrambling of topologically-protected quantum information.



**Anna Dawid-Lekowska**  
[Anna.Dawid@fuw.edu.pl](mailto:Anna.Dawid@fuw.edu.pl)  
<mailto:Anna.Dawid@fuw.edu.pl>  
 University of Warsaw

## Phase Detection with Neural Networks: Interpreting the Black Box

Neural networks (NNs) usually hinder any insight into the reasoning behind their predictions. We demonstrate how influence functions can unravel the black box of NN when trained to predict the phases of the one-dimensional extended spinless Fermi-Hubbard model at half-filling. Results provide strong evidence that the NN correctly learns an order parameter describing the quantum transition in this model. We demonstrate that influence functions allow to check that the network, trained to recognize known quantum phases, can predict new unknown ones within the data set. Moreover, we show they can guide physicists in understanding patterns responsible for the phase transition. This method requires no a priori knowledge on the order parameter, has no dependence on the NN's architecture or the underlying physical model, and is therefore applicable to a broad class of physical models or experimental data.



[1] A. Dawid et al. 2020. New J. Phys. 22 115001

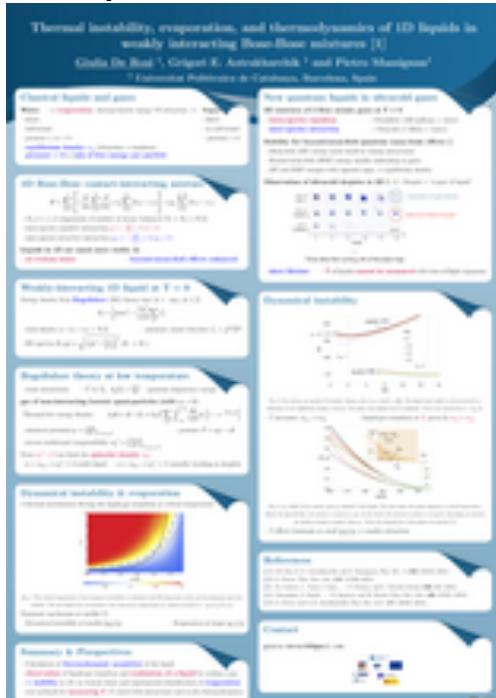


**Giulia De Rosi**

[giulia.derosi88@gmail.com](mailto:giulia.derosi88@gmail.com)

<mailto:giulia.derosi88@gmail.com>

UPC - Universitat Politècnica de Catalunya



## Thermal instability, evaporation, and thermodynamics of 1D liquids in weakly interacting Bose-Bose mixtures

Giulia De Rosi, Grigori E. Astrakharchik, and Pietro Massignan

UPC - Universitat Politècnica de Catalunya  
(Barcelona)

We study the low-temperature thermodynamics of weakly interacting uniform liquids in one-dimensional attractive Bose-Bose mixtures. The Bogoliubov approach is used to simultaneously describe quantum and thermal fluctuations. First, we investigate in detail two different thermal mechanisms driving the liquid-to-gas transition, the dynamical instability, and the evaporation, and we draw the phase diagram. Then, we compute the main thermodynamic quantities of the liquid, such as the chemical potential, the Tan's contact, the adiabatic sound velocity, and the specific heat at constant volume. The strong dependence of the thermodynamic quantities on the temperature may be used as a precise temperature probe for experiments on quantum liquids.

G. De Rosi, G. E. Astrakharchik, and P. Massignan, Phys. Rev. A 103, 043316 (2021)



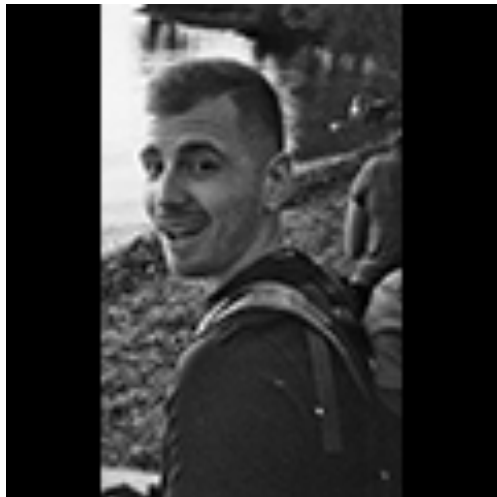
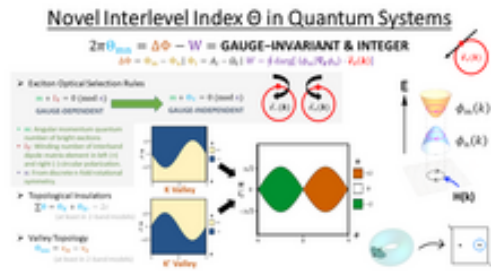
**Tharindu W. Fernando**

[tharindu@uw.edu](mailto:tharindu@uw.edu)

<mailto:tharindu@uw.edu>

## Novel Interband Topological Invariant in Condensed Matter

The physical significance of a recently-proposed gauge-invariant interband index is not immediately clear in condensed matter systems. In this poster presentation, I summarize some results from 3+ years of my work on the index. These include potentially new applications in topological insulators, exciton selection rules, and the topological characterizations of 'valleys'.

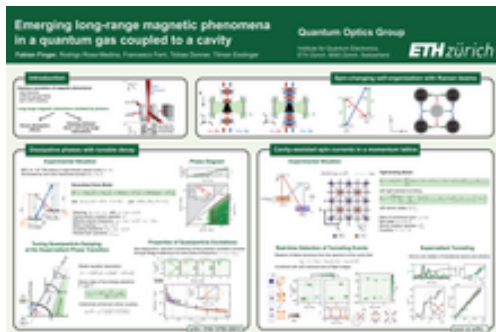


**Fabian Finger**

[ffinger@phys.ethz.ch](mailto:ffinger@phys.ethz.ch)

<mailto:ffinger@phys.ethz.ch>

Institute for Quantum Electronics, ETH Zurich



## Emerging long-range magnetic phenomena in a quantum gas coupled to a cavity

Dissipative and coherent processes are at the core of the evolution of many-body systems. Their competition and interplay can lead to new phases of matter, instabilities, and complex non-equilibrium dynamics. However, probing these phenomena at a microscopic level in a setting of well-defined, controllable coherent and dissipative couplings often proves challenging. In our setup, we realize such a quantum many-body system using a  $^{87}\text{Rb}$  spinor Bose-Einstein condensate (BEC) strongly coupled to a single optical mode of a lossy cavity. Two transverse laser fields incident on the BEC allow for cavity-assisted Raman transitions between different motional states of two neighboring spin levels.

In a first set of experiments, adjusting the imbalance between the drives enables us to tune the competition between coherent dynamics and dissipation, with the appearance of a dissipation-stabilized phase and bistability. We relate the observed phases to microscopic elementary processes in the open system by characterizing the properties of the underlying polariton modes. Moreover, we report on recent results showing collective spin dynamics in a cavity via superradiant Raman scattering. We identify the collective nature of the transitions and leverage the leaking photon field to gain real-time, non-destructive readout of the system's dynamics.

Together, our results open new avenues for investigating non-Hermitian systems, spin-orbit coupling in dissipative settings, and transport phenomena in light-matter systems.





**Sayed Ali Akbar Ghorashi**

[sghorashi@wm.edu](mailto:sghorashi@wm.edu)

<mailto:sghorashi@wm.edu>

William & Mary



## Higher-Order Weyl Semimetals

We investigate higher-order Weyl semimetals (HOWSMs) having bulk Weyl nodes attached to both surface and hinge Fermi arcs. We identify a new type of Weyl node, which we dub a 2nd-order Weyl node, that can be identified as a transition in momentum space in which both the Chern number and a higher order topological invariant change. As a proof of concept we use a model of stacked higher order quadrupole insulators (QI) to identify three types of WSM phases: 1st order, 2nd order, and hybrid order. The model can also realize type-II and hybrid-tilt WSMs with various surface and hinge arcs. After a comprehensive analysis of the topological properties of various HOWSMs, we turn to their physical implications that show the very distinct behavior of 2nd-order Weyl nodes when they are gapped out. We obtain three remarkable results: (i) the coupling of a 2nd-order Weyl phase with a conventional 1st-order one can lead to a hybrid-order topological insulator having coexisting surface cones and flat hinge arcs that are independent and not attached to each other. (ii) A nested 2nd-order inversion-symmetric WSM by a charge-density wave (CDW) order generates an insulating phase having coexisting flatband surface and hinge states all over the Brillouin zone. (iii) A CDW order in a time-reversal symmetric higher-order WSM gaps out a 2nd-order node with a 1st-order node and generates an insulating phase having coexisting surface Dirac cone and hinge arcs. Moreover, we show that a measurement of charge density in the presence of magnetic flux can help to identify some classes of 2nd-order WSMs. Finally, we show that periodic driving can be utilized as a way for generating HOWSMs. Our results are relevant to metamaterials as well as various phases of  $\text{Cd}_3\text{As}_2$ ,  $\text{KMgBi}$ , and rutile-structure  $\text{PtO}_2$  that have been predicted to realize higher order Dirac semimetals.



**Tomohiro Hashizume**

[tomohiro.hashizume@strath.ac.uk](mailto:tomohiro.hashizume@strath.ac.uk)

<mailto:tomohiro.hashizume@strath.ac.uk>

## Deterministic fast scrambling with neutral atom arrays

Fast scramblers are the systems which can propagate the information across the system in a timescale which only scales logarithmically with the system size. We propose a deterministic fast-scrambling circuit, which can be implemented in the near-future experiments using neutral atoms. The protocol utilizes the highly non-local geometry created by the shuffling of atoms using optical tweezers. We show that Page-scrambled state, a pure state in which every random subsystem are maximally entangled, can be generated with our protocol in the number of operations which only increases logarithmically with the system size. We also show that the proposed circuit has high resistance against

University of Strathclyde



**Michael Highman**  
[highman2@illinois.edu](mailto:highman2@illinois.edu)  
<mailto:highman2@illinois.edu>  
 University of Illinois at Urbana-Champaign

the depolarization noise. This makes the circuit an ideal circuit to be used for the quantum teleportation protocols.

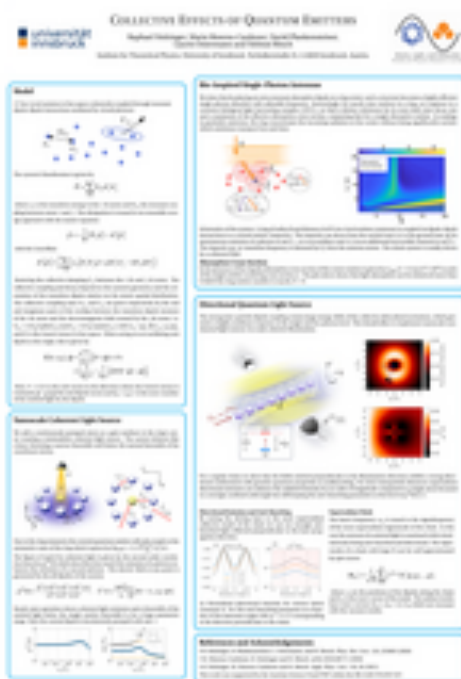
## Quantum Cluster-states of Ultracold Polar Molecules

Ultracold molecules have seen recent success as a tool in ultracold chemistry, probing fundamental physics, and quantum simulation. The plentiful array of internal states in molecules enables their use in a wide range of studies. As such, certain states of ultracold polar molecules demonstrate the ability to interact coherently over long times through coupling of their electric dipole moments, a quality of interest towards efforts in producing stable and noise-resistant qubits. This dipolar exchange interaction can entangle qubits through microwave coupling of anisotropic rotational states in  $^{23}\text{Na}^{87}\text{Rb}$  and synthesize a cluster-state, opening the door for cluster-state computing. To resolve and process information after measurement, cluster-state computing relies on the ability to monitor constituent qubits of the state non-destructively and selectively. Presented here is a non-demolition imaging scheme that takes advantage of anisotropic rotational states of polar molecules. Additionally, described here are methods of fabrication and manipulation of  $^{23}\text{Na}^{87}\text{Rb}$  qubits for future work towards cluster-state computing.

With Garrett Williams



**Raphael Holzinger**  
[raphael.holzinger@uibk.ac.at](mailto:raphael.holzinger@uibk.ac.at)  
(<mailto:raphael.holzinger@uibk.ac.at>)  
Institute for Theoretical Physics,  
Innsbruck, Austria



## Collective Effects of Quantum Emitters

Recent studies have shown that sub-wavelength sized rings of quantum emitters possess subradiant eigenmodes which mimic high-Q optical resonators. We add a continuously pumped atom as a gain medium in the ring's center creating a minimalistic coherent light source. The system behaves like a thresholdless laser, featuring a narrow linewidth well below the natural linewidth of the constituent atoms. We also show that by placing an extra resonant absorptive dipole at the ring center, such a structure becomes a highly efficient single-photon absorber with tailorable frequency. Interestingly, for exactly nine emitters in a nonagon, as it appears in a common biological light-harvesting complex (LHC2), we find a distinct minimum for its most dark state decay rate and a maximum of the effective absorption cross-section, surpassing that for a single absorptive emitter. Furthermore we show the implementation of nanoscale non-classical light sources via weak coherent illumination. At the generic tailored examples of regular chains we show that the fields emitted perpendicular to the illumination direction exhibit a strong directional confinement with genuine quantum properties as antibunching.



**Ana Hudomal**  
[a.hudomal@leeds.ac.uk](mailto:a.hudomal@leeds.ac.uk)  
(<mailto:a.hudomal@leeds.ac.uk>)

## Quantum scars of bosons with correlated hopping

Recent experiments have shown that preparing an array of Rydberg atoms in a certain initial state can lead to anomalously slow thermalization and persistent density oscillations [1]. This type of non-ergodic behavior has been attributed to the existence of “quantum many-body scars”, i.e., atypical eigenstates that have high overlaps with a small subset of vectors in the Hilbert space. Periodic dynamics and many-body scars are believed to originate from a “hard” kinetic constraint: due to strong interactions, two neighboring Rydberg atoms cannot be simultaneously excited. Here we propose a realization of quantum many-body scars in a 1D bosonic lattice model with a “soft” constraint in the



University of Leeds



form of density-assisted hopping [2]. We find that this model exhibits similar phenomenology to the Rydberg atom chain, including weakly entangled eigenstates at high energy densities and the presence of a large number of exact zero energy states, with distinct algebraic structure. We discuss the relation of this model to the standard Bose-Hubbard model and possible experimental realizations using ultracold atoms.

References:

- [1] H. Bernien et al., Nature 551, 579 (2017).
- [2] A. Hudomal, I. Vasic, N. Regnault, and Z. Papis, Commun. Phys. 3, 99 (2020).

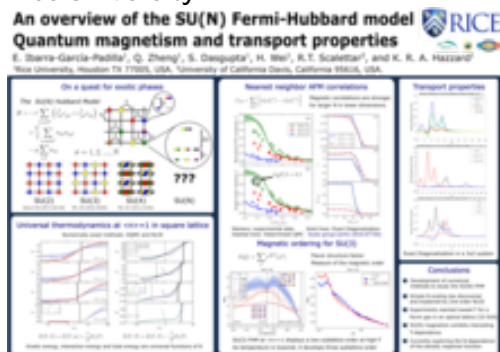


**Eduardo Ibarra Garcia Padilla**

[eibarragp@rice.edu](mailto:eibarragp@rice.edu)

<mailto:eibarragp@rice.edu>

Rice University



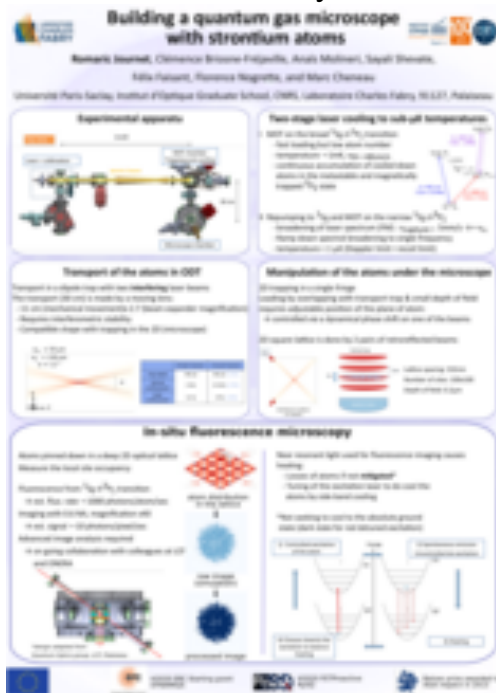
## An overview of the SU(N) Fermi Hubbard model: Quantum magnetism and transport properties

The SU(2) symmetric Fermi Hubbard model (FHM) plays an essential role in the understanding of strongly correlated fermionic many-body systems. When the system is in the one particle per site and strongly interacting limit  $U \gg t$ , it is effectively described by the Heisenberg Hamiltonian. In this limit, extending the typical SU(2) symmetry to SU(N) has been predicted to give exotic phases of matter in the ground state, with complicated dependence of the ground state on N. In this overview we discuss the N-dependence of thermodynamic properties, magnetic correlations and transport properties of the SU(N) Fermi Hubbard model at finite temperature and away from the Heisenberg limit. In particular we address the question of what signatures of the exotic ground states survive at finite-temperature, especially in the currently experimentally relevant regime near or above the superexchange energy. Our results are obtained with Exact Diagonalization, Numerical Linked Cluster Expansions and Determinant Quantum Monte Carlo and span a wide range of interaction strengths, temperatures, fillings and values of N.



**Romaric Journet**

[romaric.journet@institutoptique.fr](mailto:romaric.journet@institutoptique.fr)  
(<mailto:romaric.journet@institutoptique.fr>)  
Laboratoire Charles Fabry



## Shelving spectroscopy of strontium intercombination line in a vapor cell

The relaxation dynamics of quantum many-body systems after a quench is so far a mostly unsolved problem. We plan on using a quantum gas microscope to study the relaxation dynamics of a 2D strontium gas in an optical lattice. The quantum gas microscope approach will allow us to probe the spatial distribution of atoms with single atom and single lattice site resolution.

In this poster, I present the experimental apparatus that was designed for our experiment. I discuss the challenges that were addressed and how we chose to circumvent them. More precisely, I tackle the topics of collimation and cooling of a strontium gas from several hundreds of degrees to a few  $\mu\text{K}$ . I also present the design of the optical dipole traps for the lattices and a transport of a cold atomic cloud. Finally, a section of the poster summarizes the constraints on achieving detection of single atoms in a 2D lattice with an *in situ* imaging.

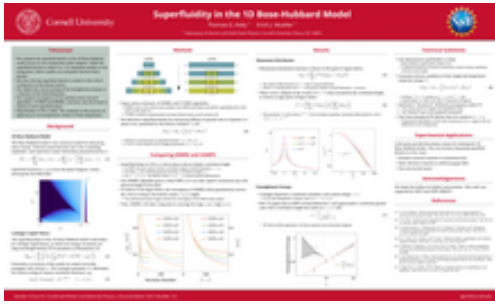


**Thomas Kiely**

[tgk37@cornell.edu](mailto:tgk37@cornell.edu)  
(<mailto:tgk37@cornell.edu>)  
Cornell University

## Superfluidity in the 1D Bose-Hubbard Model

We study superfluidity in the 1D Bose-Hubbard model using an infinite variational matrix product state technique. We determine the superfluid density as a function of the Hubbard parameters by calculating the energy cost of phase twists in the thermodynamic limit. As the system is critical, correlation functions decay as power laws and the entanglement entropy grows with the bond dimension of our variational state. We relate the resulting scaling laws to the superfluid density. We compare two different algorithms for optimizing the infinite matrix product state and develop a physical explanation why one of them (VUMPS) is more efficient than the other (iDMRG). Finally, we comment on finite-temperature superfluidity in one dimension and how our results



can be realized in cold atom experiments.



**Francisco Machado**

[fmachado@berkeley.edu](mailto:fmachado@berkeley.edu)

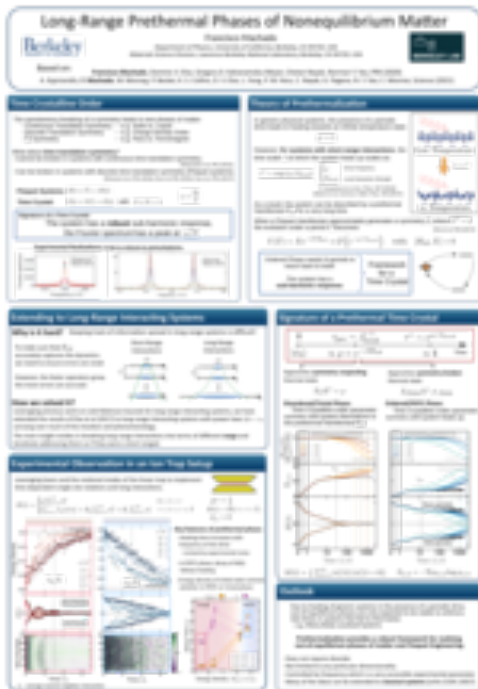
<mailto:fmachado@berkeley.edu>

University of California, Berkeley

## Long-Range Prethermal Phases of Nonequilibrium Matter

Recent developments in atomic, molecular and optical systems have enabled unprecedented access to novel out-of-equilibrium behavior—even in strongly interacting many-body systems. Such techniques have led to an explosion of excitement in this field, with particular attention being given to periodically driven system. In such systems the discrete time translation symmetry of the evolution can lead to entirely new phases of matter, but also to one major hurdle: the heating problem. More specifically, a generic strongly interacting driven system will continuously absorb energy from the drive until it approaches the infinite temperature state at late times, destroying any interesting out-of-equilibrium behavior.

Here, I will discuss how Floquet prethermalization enables us to overcome this problem and realize novel out-of-equilibrium phases. By focusing on high-frequency driven systems, the heating absorption rate from the drive becomes exponentially small, enabling a parametrically large time scale for observing out-of-equilibrium phenomena. I will discuss our work extending this approach to long-range interacting systems and how an emergent symmetry can arise (protected by the time translation symmetry of the drive). Leveraging this emergent symmetry, I will present an example how a novel time crystalline phase can be stabilized — the one dimensional prethermal time crystal— and discuss a recent experimental observation of this phenomena.





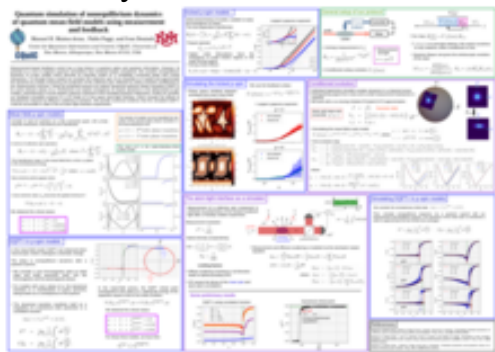


**Manuel Munoz-Arias**

[mhmunoz@unm.edu](mailto:mhmunoz@unm.edu)

<mailto:mhmunoz@unm.edu>

University of New Mexico



## Quantum simulation of nonequilibrium dynamics of quantum mean-field models using measurement and feedback

Measurement-based feedback control has a long history in quantum optics and quantum information. However, its potential as a tool to engineer quantum simulations has remained largely unexplored. We consider nonequilibrium dynamics of p-spin models which describe an Ising-like model on a completely connected graph with p-body interactions. To simulate these models, we consider the collective spin of an ensemble on N qubits and approximate the dynamics by weakly measuring one projection of the collective spin, followed by unitary evolution conditioned on the measurement outcome. Using the proposed protocol we explore dynamical quantum phase transitions (DQPT-I) for some relevant values of p. Furthermore, we explore emergence of chaotic dynamics in the delta-kicked p-spin models, characterizing it via the largest Lyapunov exponent of the simulated quantum trajectories. Finally, we consider our feedback simulation protocol in a 1D model of a free space atom-light interface, which includes the effects of decoherence induced by diffusive scattering of photons. We provide numerical evidence that the simulated DQPT-I could be accessible in state of the art atom-light interface experiments.



**Eulàlia Nicolau**

[eulalia.nicolau@uab.cat](mailto:eulalia.nicolau@uab.cat)

<mailto:eulalia.nicolau@uab.cat>

Universitat Autònoma de Barcelona

## Aharonov-Bohm caging of N bosons in a lattice of rings

We study a system of a few ultracold bosons loaded into the states with orbital angular momentum  $l=1$  of a one-dimensional staggered lattice of rings. By analyzing the strong-interaction limit, we demonstrate how the geometry of the system can be engineered to produce complex tunnelings that yield a  $\pi$  flux through the plaquettes. We find nontrivial topological band structures and we demonstrate how the system is able to exhibit Aharonov-Bohm caging in N-particle subspaces even in the presence of a dispersive single-particle spectrum. All the analytical results are benchmarked through exact diagonalization simulations.





**Daniel Paz**  
[dap12d@gmail.com](mailto:dap12d@gmail.com)  
<mailto:dap12d@gmail.com>  
 Michigan State University



## Modified fluctuation-dissipation relation in driven-dissipative systems

Fluctuation-dissipation relations (FDRs) and time-reversal symmetry (TRS), two pillars of statistical mechanics, are both broken in generic driven-dissipative systems. These systems rather lead to non-equilibrium steady states far from thermal equilibrium. Driven-dissipative Ising-type models, however, are widely believed to exhibit effective thermal critical behavior near their phase transitions. Contrary to this picture, we show that both the FDR and TRS are broken even macroscopically at, or near, criticality. This is shown by inspecting different observables, both even and odd operators under time-reversal transformation, that overlap with the order parameter. Remarkably, however, a modified form of the FDR as well as TRS still holds, but with drastic consequences for the correlation and response functions as well as the Onsager reciprocity relations.

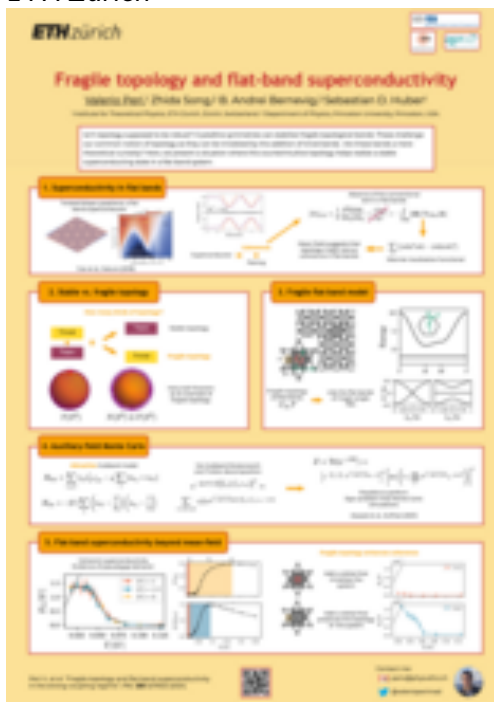


**Valerio Peri**

[periv@phys.ethz.ch](mailto:periv@phys.ethz.ch)

[\(mailto:periv@phys.ethz.ch\)](mailto:periv@phys.ethz.ch)

ETH Zurich



**Lukas Rammelmüller**

[lukas.rammelmuller@physik.uni-muenchen.de](mailto:lukas.rammelmuller@physik.uni-muenchen.de)

[\(mailto:lukas.rammelmuller@physik.uni-muenchen.de\)](mailto:lukas.rammelmuller@physik.uni-muenchen.de)

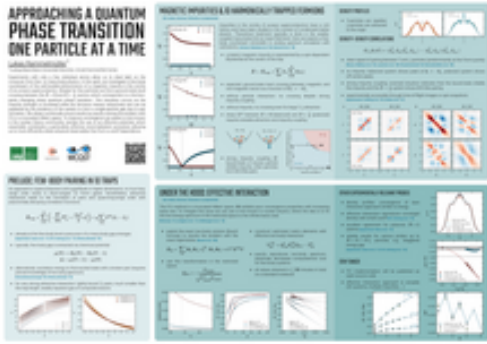
## Fragile topology and flat-band superconductivity

Recent theoretical works unveiled that crystalline symmetries can stabilize topologically fragile Bloch bands that challenge our very notion of topology: one can trivialize these bands through the addition of trivial Bloch bands. Here, we show via auxiliary-field Monte Carlo simulations how fragile topology enhances the superfluid weight and hence the superconducting critical temperature. This feature is particularly relevant in flat-band systems where the conventional contribution to the superfluid weight vanishes and might explain the high transition temperature observed in magic-angle twisted bilayer graphene.

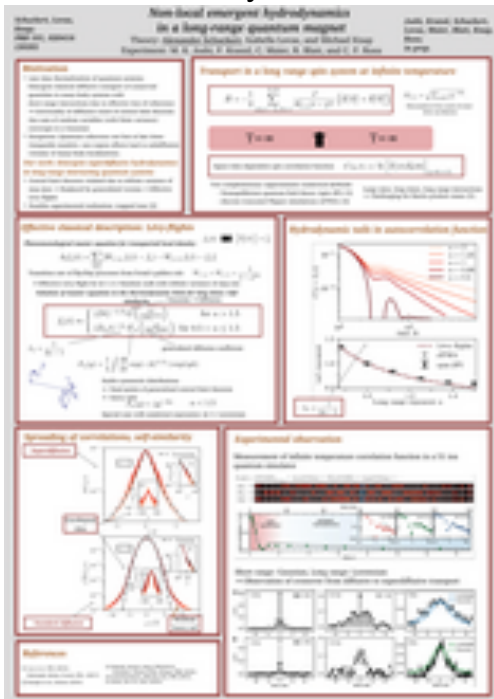
## Approaching a Quantum Phase Transition one Atom at a Time

Experiments with only a few individual atoms allow us to shed light on the crossover from few- to many-body physics. In this spirit, we investigate a few-body counterpart of the well-studied phenomenon of a magnetic impurity in the vicinity of an s-wave superconductor. Already for few particles we find a ground-state level crossing between a non-magnetic and a magnetic sector, which corresponds to a fermion-parity changing sharp quantum phase transition. This transition occurs as the impurity strength is increased while the fermions interact attractively and can be explained by the tendency of the system to form a single-particle gap due to pair formation. We obtain numerically sound results by exactly solving the problem with FCI in a truncated

[muenchen.de](http://muenchen.de)  
LMU Munich



**Alexander Schuckert**  
[alexander.schuckert@tum.de](mailto:alexander.schuckert@tum.de)  
(<mailto:alexander.schuckert@tum.de>)  
Technical University of Munich



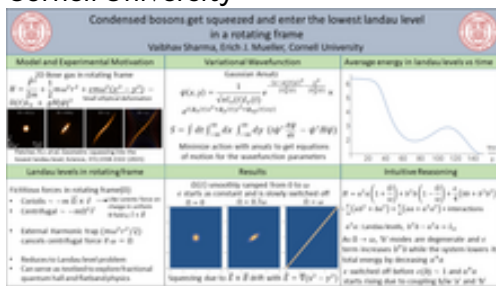
Hilbert space. To improve convergence we exploit a trick known in the nuclear theory community, namely the use of an effective potential, which essentially constitutes a particularly effective renormalization procedure allowing us to more efficiently obtain physical observables free from a cutoff dependence.

## Superdiffusive emergent hydrodynamics in trapped ion quantum simulators

Generic short-range interacting quantum systems with a conserved quantity exhibit universal diffusive transport at late times. We employ non-equilibrium quantum field theory and semi-classical phase-space simulations to show how this universality is replaced by a more general transport process in a long-range XY spin chain at infinite temperature with couplings decaying algebraically with distance as  $r^{-\alpha}$ . While diffusion is recovered for  $\alpha > 1.5$ , longer-ranged couplings with  $0.5 < \alpha \leq 1.5$  give rise to effective classical Lévy flights; a random walk with step sizes drawn from a distribution with algebraic tails. We find that the space-time dependent spin density profiles are self-similar, with scaling functions given by the stable symmetric distributions. As a consequence, for  $0.5 < \alpha \leq 1.5$  autocorrelations show hydrodynamic tails decaying in time as  $t^{-1/(2\alpha-1)}$  and linear-response theory breaks down. We also discuss the recent observation of these unconventional hydrodynamics in a trapped ion quantum simulator.



**Vaibhav Sharma**  
[vs492@cornell.edu](mailto:vs492@cornell.edu)  
[\(mailto:vs492@cornell.edu\)](mailto:vs492@cornell.edu)  
 Cornell University

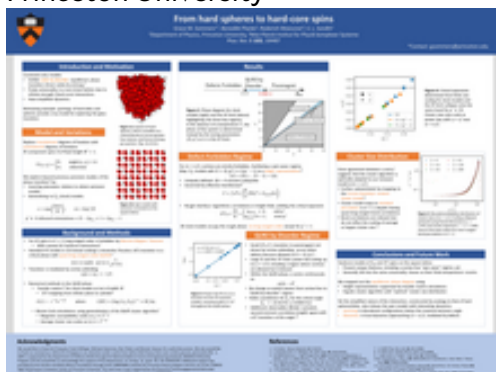


## Condensed bosons get squeezed and enter the lowest Landau level in a rotating frame

Motivated by a recent experiment, we model interacting bosons in a harmonic trap with a rotating elliptical deformation. The system Hamiltonian in the rotating frame is equivalent to the Hamiltonian for a charged particle in a uniform magnetic field. Bosons condensed in the lowest Landau level can serve as a route to study fractional quantum Hall physics and strong interaction effects in a flat band with neutral cold atoms. We show how bosons in this situation can dynamically enter the lowest Landau level. We use a time-dependent variational wavefunction approach to efficiently model the dynamics. We find that our approach reliably captures a dynamical squeezing of the Bose gas observed in the experiment. We also find that the bosons macroscopically occupy the lowest Landau level only if the elliptical deformation is switched off slowly over a particular timescale. We estimate this timescale and provide an intuitive understanding of the phenomena.



**Grace Sommers**  
[gsommers@princeton.edu](mailto:gsommers@princeton.edu)  
[\(mailto:gsommers@princeton.edu\)](mailto:gsommers@princeton.edu)  
 Princeton University



## From hard spheres to hard-core spins

A system of hard spheres exhibits physics that is controlled only by their density. This comes about because the interaction energy is either infinite or zero, so all allowed configurations have exactly the same energy. The low-density phase is liquid, while the high-density phase is crystalline, an example of “order by disorder” as it is driven purely by entropic considerations. Here we study a family of hard spin models, which we call hard-core spin models, where we replace the translational degrees of freedom of hard spheres with the orientational degrees of freedom of lattice spins. Their hard-core interaction serves analogously to divide configurations of the many spin system into allowed and disallowed sectors. We present detailed results on the square lattice in  $d=2$  for a set of models with  $Z_N$  symmetry, which generalize Potts models, and their  $U(1)$  limits, for ferromagnetic and antiferromagnetic senses of the interaction, which we refer to as exclusion and inclusion models. As the exclusion and inclusion angles are varied, we find a Kosterlitz-Thouless phase transition between a disordered phase and a phase with quasi-long-ranged order, which is the form order by disorder takes in these systems. These results follow from a set of height representations, an ergodic cluster algorithm, and transfer matrix calculations.

Reference: Grace M. Sommers, Benedikt Placke,



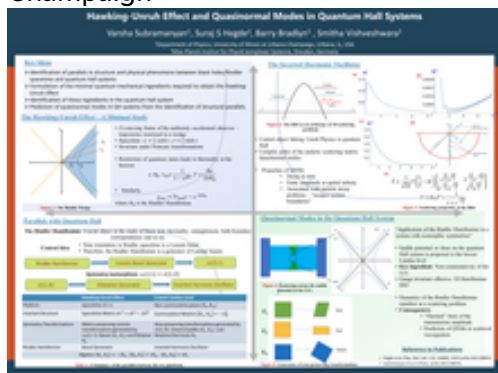


**Varsha Subramanyan**

[varshas2@illinois.edu](mailto:varshas2@illinois.edu)

[\(mailto:varshas2@illinois.edu\)](mailto:varshas2@illinois.edu)

University of Illinois, Urbana-Champaign



**Federica Maria Surace**

[federicamsurace@gmail.com](mailto:federicamsurace@gmail.com)

[\(mailto:federicamsurace@gmail.com\)](mailto:federicamsurace@gmail.com)

SISSA

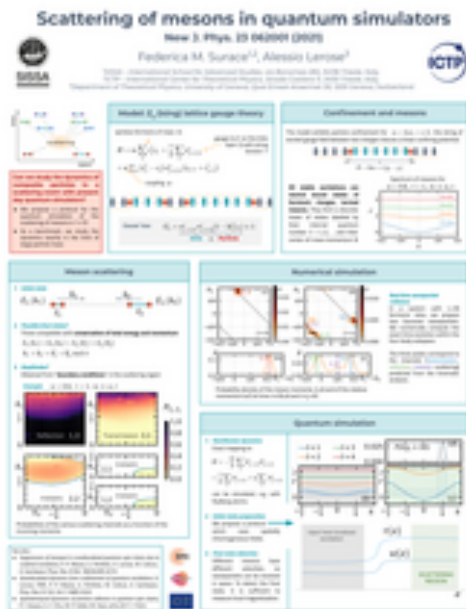
Roderich Moessner, and S. L. Sondhi, Phys. Rev. B 103, 104407 (2021).

## Quasinormal Modes and Hawking-Unruh Effect in Quantum Hall Systems

In this work, we take a closer look at wavepacket scattering through a quantum point contact (QPC) in an integer quantum Hall system. We model the QPC as a hyperbolic potential which takes the form of an inverted harmonic oscillator (IHO) in the lowest Landau level. The symmetry isomorphisms that this system shares with 1D quantum phase space as well as as (2+1)D Rindler spacetime leads to parallels of relativistic phenomena in this non-relativistic scattering setup. We exploit this connection to study quantum Hall parallels to quasinormal modes, the Hawking-Unruh effect, quantum optics etc.

## Scattering of mesons in quantum simulators

Simulating real-time evolution in theories of fundamental interactions represents one of the central challenges in contemporary theoretical physics. Cold-atom platforms stand as promising candidates to realize quantum simulations of non-perturbative phenomena in gauge theories, such as vacuum decay and hadron collisions, in prohibitive conditions for direct experiments. In this work, we demonstrate that present-day quantum simulators can imitate linear particle accelerators, giving access to S-matrix measurements of elastic and inelastic meson collisions in low-dimensional abelian gauge theories. Considering for definiteness a (1 + 1)-dimensional Z<sub>2</sub>-lattice gauge theory realizable with Rydberg-atom arrays, we present protocols to observe and measure selected meson-meson scattering processes. We provide a benchmark theoretical study of scattering amplitudes in the regime of large fermion mass, including an exact solution valid for arbitrary coupling strength. This



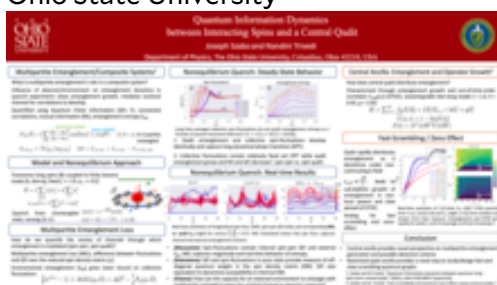
allows us to discuss the occurrence of inelastic scattering channels, featuring the production of new mesons with different internal structures. We present numerical simulations of realistic wavepacket collisions, which reproduce the predicted cross section peaks. This work highlights the potential of quantum simulations to give unprecedented access to real-time scattering dynamics.



**Joseph Szabo**  
[szabo.48@osu.edu](mailto:szabo.48@osu.edu)  
<mailto:szabo.48@osu.edu>  
 Ohio State University

## Detecting quantum phases by probing ancillary qubits

Understanding the role of entanglement and its dynamics in composite quantum systems lies at the forefront of quantum matter studies. Here we investigate competing entanglement dynamics in an open Ising-spin chain that allows for exchange with an external central qudit probe. We propose a new metric dubbed the multipartite entanglement loss (MEL) that provides an upper bound on information entropy shared between the spins and qudit probe, serving to unify physical spin-fluctuations, Quantum Fisher Information (QFI), and bipartite entanglement entropy. We find interestingly that collective spin-fluctuations which serve as a witness for multipartite spin-spin entanglement, can also be used to quantify the composite entanglement shared between spins and qudit environment. In addition to studying the entanglement dynamics of the qudit in a weak probe capacity, we also study how just a single, non-local ancillary qubit is able to distribute entanglement and operator content. Using entanglement entropy and out-of-time-order correlations, we find that in the weak coupling regime, the non-local nature of central qubit allows for rapid entanglement distribution and in the strong coupling limit, the star-local system develops sub-ballistic growth of entanglement and slow operator growth.



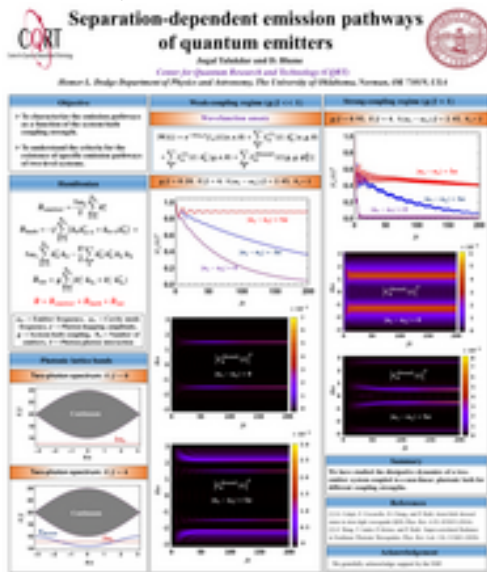


**Jugal Talukdar**

[jugal.talukdar@ou.edu](mailto:jugal.talukdar@ou.edu)

(<mailto:jugal.talukdar@ou.edu>)

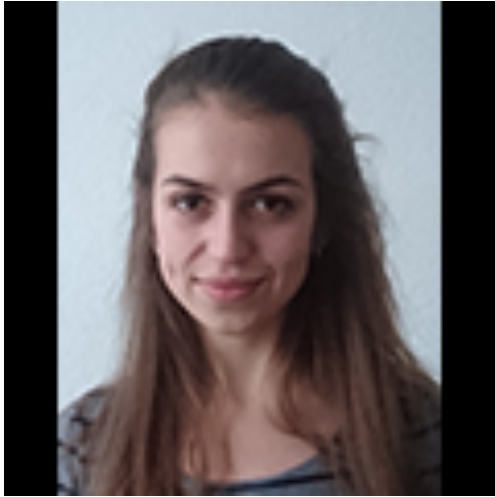
University of Oklahoma, Norman



## Separation-dependent emission pathways of quantum emitters

System-environment interactions have been studied extensively for many decades and recent developments in quantum optics and circuit QED provide intriguing possibilities for realizing non-linear environments. The Bose-Hubbard lattice for photons, e.g., has been realized experimentally using superconducting circuits, thereby providing an exciting platform to study effective interactions between quantum emitters mediated by the engineered photonic environment. We consider a collection of macroscopically separated two-level emitters coupled to a non-linear environment and study the dissipative dynamics. Specifically, we report our theoretical progress on understanding the criteria for the existence of specific emission pathways as a function of the positions of the emitters.



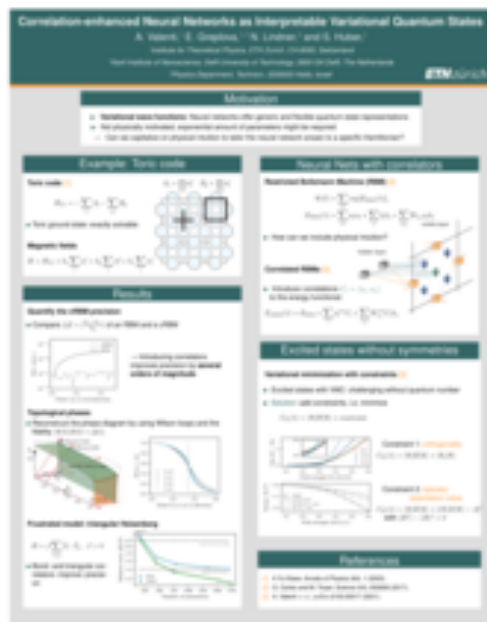


**Agnes Valenti**

[avalenti@phys.ethz.ch](mailto:avalenti@phys.ethz.ch)

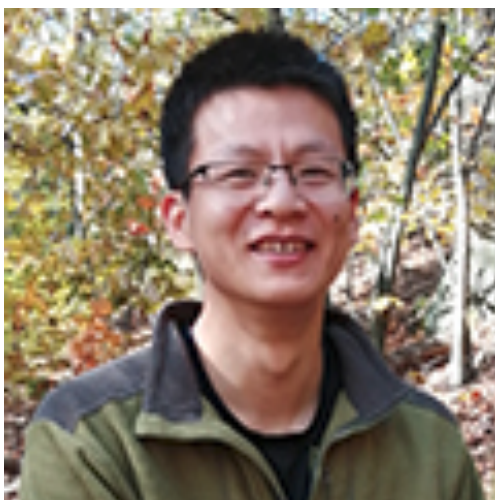
[\(mailto:avalenti@phys.ethz.ch\)](mailto:avalenti@phys.ethz.ch)

ETH Zurich



## Correlation-Enhanced Neural Networks as Interpretable Variational Quantum States

Variational methods have proven to be excellent tools to approximate ground states of complex many body Hamiltonians. Generic tools like neural networks are extremely powerful, but their parameters are not necessarily physically motivated. Thus, an efficient parametrization of the wave-function can become challenging. In this letter we introduce a neural-network based variational ansatz that retains the flexibility of these generic methods while allowing for a tunability with respect to the relevant correlations governing the physics of the system. We illustrate the success of this approach on topological, long-range correlated and frustrated models. Additionally, we introduce compatible variational optimization methods for exploration of low-lying excited states without symmetries that preserve the interpretability of the ansatz.



**Botao Wang**

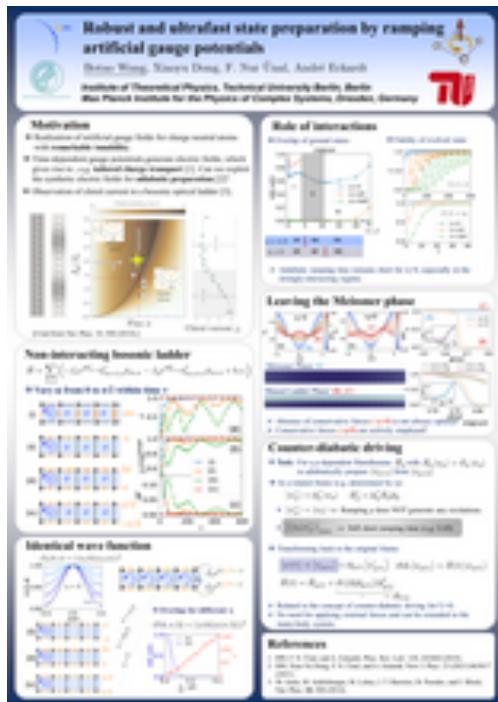
[botao@pks.mpg.de](mailto:botao@pks.mpg.de)

[\(mailto:botao@pks.mpg.de\)](mailto:botao@pks.mpg.de)

Max Planck Institute for the Physics of Complex Systems

## Engineering artificial gauge potentials for rapid adiabatic state preparation

The implementation of static artificial magnetic fields in ultracold atomic systems has been established as a powerful tool, e.g. for simulating quantum-Hall physics with charge-neutral atoms. Taking an interacting bosonic flux ladder as a minimal model, we investigate protocols for adiabatic state preparation based on ramping up the vector potential (in the form of Peierls phases), which is engineered to give rise to the desired magnetic flux. We find that the time required for adiabatic state preparation dramatically depends on the spatial pattern of Peierls phases used to create the flux. This is explained by the fact that, while different patterns (i.e. vector potentials) just correspond to different gauges for static fluxes, they induce different electric fields during the ramp. Remarkably, we find that for an optimal choice, it



allows for preparing the ground state almost instantaneously. This can be related to counter-diabatic driving and may open up new possibilities for robust state preparation.

Authors: Botao Wang, Xiaoyu Dong, F. Nur ünal, and André Eckardt



**Dariusz Wiater**

[dariusz.wiater@fuw.edu.pl](mailto:dariusz.wiater@fuw.edu.pl)

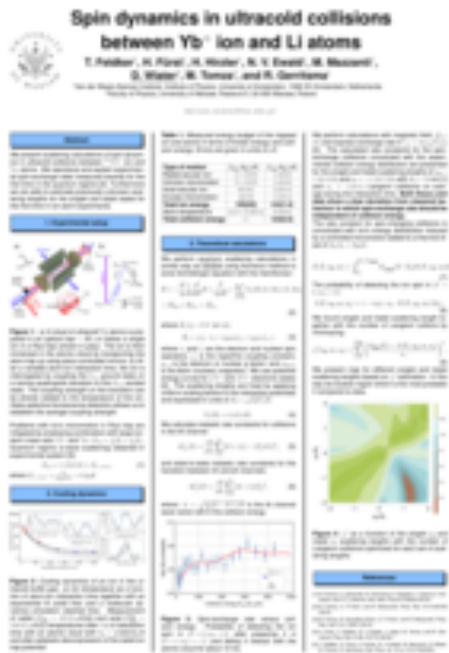
<mailto:dariusz.wiater@fuw.edu.pl>

University of Warsaw

## Spin dynamics in ultracold collisions between Yb<sup>+</sup> ion and Li atoms in the quantum regime

Significant advances in precision measurements in the quantum regime have been achieved with trapped ions and atomic gases at the lowest possible temperatures. These successes have inspired ideas to merge the two systems [1]. Remarkably, in spite of its importance, experiments with ion-atom mixtures remained firmly confined to the classical collision regime, but recently buffer gas cooling of a single ion in a Paul trap to the quantum regime of ion-atom collisions has been realized [2]. The collision energy as small as 1.15(0.23) times the s-wave energy (or 9.9(2.0)  $\mu\text{K}$ ) has been achieved for a trapped ytterbium ion in an ultracold lithium gas. We have observed a deviation from classical Langevin theory by studying the spin-exchange dynamics, indicating quantum effects in the collisions. Here, we present a theoretical description of the quantum ion-atom scattering used to guide and interpret the recent experiment [2]. By developing a theoretical model of measured energy-dependent spin-exchange rate constants, we have obtained singlet and triplet ion-atom scattering lengths. Next, we identify experimentally accessible Feshbach resonances in the mentioned systems and predict their properties. Control of both elastic scattering and related cooling rates, as well as inelastic spin-changing collisions, with the magnetic field is proposed and investigated to guide ongoing experimental efforts. Ion-atom Feshbach resonances in analogy to well-established techniques for neutral systems will be an important tool to manipulated ultracold ion-atom mixtures.

[1] Tomza et al, Rev. Mod. Phys. 91, 035001 (2019).



[2] Feldker et al, Nature Physics volume 16, pages 413–416(2020)



**Garrett Williams**

[grw5@illinois.edu](mailto:grw5@illinois.edu)

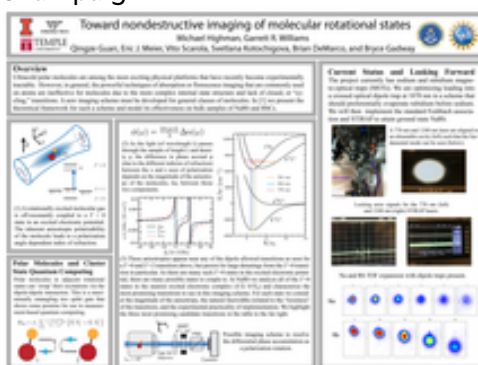
<mailto:grw5@illinois.edu>

University of Illinois, Urbana-Champaign

## Quantum Cluster-states of Ultracold Polar Molecules

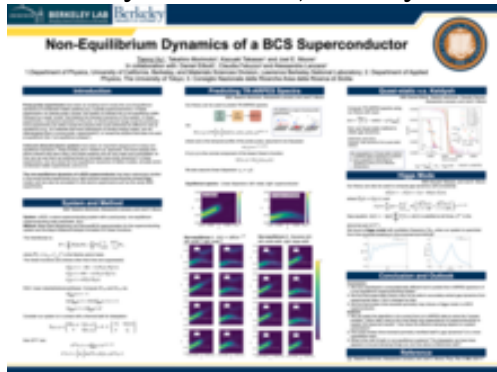
Ultracold molecules have seen recent success as a tool in ultracold chemistry, probing fundamental physics, and quantum simulation. The plentiful array of internal states in molecules enables their use in a wide range of studies. As such, certain states of ultracold polar molecules demonstrate the ability to interact coherently over long times through coupling of their electric dipole moments, a quality of interest towards efforts in producing stable and noise-resistant qubits. This dipolar exchange interaction can entangle qubits through microwave coupling of anisotropic rotational states in  $^{23}\text{Na}^{87}\text{Rb}$  and synthesize a cluster-state, opening the door for cluster-state computing. To resolve and process information after measurement, cluster-state computing relies on the ability to monitor constituent qubits of the state non-destructively and selectively. Presented here is a non-demolition imaging scheme that takes advantage of anisotropic rotational states of polar molecules. Additionally, described here are methods of fabrication and manipulation of  $^{23}\text{Na}^{87}\text{Rb}$  qubits for future work towards cluster-state computing.

With Michael Highman





**Tianrui Xu**  
[tianrui\\_xu@berkeley.edu](mailto:tianrui_xu@berkeley.edu)  
([mailto:tianrui\\_xu@berkeley.edu](mailto:tianrui_xu@berkeley.edu))  
University of California, Berkeley



## Non-Equilibrium Dynamics of a BCS Superconductor

Recently developed experimental tools that control and probe many-body quantum systems have provided access to new time and length scales of various quantum systems. Techniques such as pump-probe experiments and cavity quantum electrodynamics have enabled us to explore and understand the phases and orders of previously difficult-to-study many-body systems such as the Cuprate superconductors.

Here, I will present our theoretical investigations of a non-equilibrium BCS system with a time-varying order parameter. We focus on the transient dynamics of such systems, and developed a theory using the Baym-Kadanoff-Keldysh formalism that enables us to study the dynamics of the system in contact with a thermal bath for dissipation. We then use our theory to look at two different types of gap dynamics. First, we try to understand some measurements of a type of pump-probe experiment: the time- and angle-resolved photoemission spectroscopy (tr-ARPES), and discuss the limit of the quasi-static method currently used to understand these measurements. Second, we study the gap dynamics of a BCS system initially prepared in some time-reversal-breaking states, and found a possible Higgs mode in such systems.



**Hong Yang**  
[yanghongphy@gmail.com](mailto:yanghongphy@gmail.com)  
(<mailto:yanghongphy@gmail.com>)  
The University of Tokyo

## Symmetry-protected Topological Phases in Spinful Bosons with a Flat Band

We theoretically demonstrate that interacting symmetry-protected topological (SPT) phases can be realized with ultracold spinful bosonic atoms loaded on the lattices which have a flat band at the bottom of the band structure. Ground states of such systems are not conventional Mott insulators in the sense that the ground states possess not only spin fluctuations but also non-negligible charge fluctuations. The SPT phases in such systems are determined by both spin and charge fluctuations at zero temperature. We find that the many-body ground states of such systems can be exactly obtained in some special cases, and these exact ground states turn out to serve as representative states of the SPT phases. As a concrete example, we demonstrate that spin-1 bosons on a sawtooth chain can be in an SPT phase protected by  $Z_2 \times Z_2$  spin rotation symmetry or time-reversal symmetry, and this SPT phase is a result of spin fluctuations. We also show that spin-3 bosons on a kagome lattice can be in an SPT phase protected by  $D_2$  point group symmetry, but this SPT phase is, however, a result of charge fluctuations.





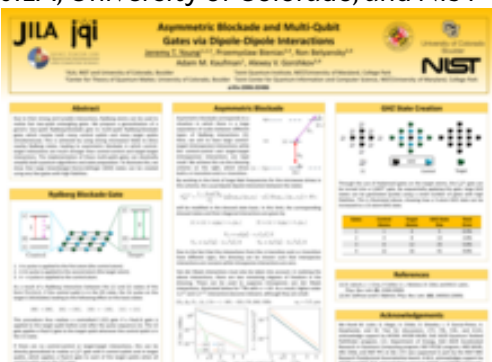
[1] Hong Yang, Hayate Nakano, and Hosho Katsura, Phys. Rev. Research 3, 023210 (2021)



**Jeremy Young**  
[jeremy.young@jila.colorado.edu](mailto:jeremy.young@jila.colorado.edu)  
<mailto:jeremy.young@jila.colorado.edu>  
 JILA, University of Colorado, and NIST

## Asymmetric blockade and multi-qubit gates via dipole-dipole interactions

Due to their strong and tunable interactions, Rydberg atoms can be used to realize fast two-qubit entangling gates. We propose a generalization of a generic two-qubit Rydberg-blockade gate to multi-qubit Rydberg-blockade gates which involve both many control qubits and many target qubits simultaneously. This is achieved by using strong microwave fields to dress nearby Rydberg states, leading to asymmetric blockade in which control-target interactions are much stronger than control-control and target-target interactions. The implementation of these multi-qubit gates can drastically simplify both quantum algorithms and state preparation. To illustrate this, we show that large Greenberger-Horne-Zeilinger (GHZ) states can be created using very few gates with high fidelities.





**Yaakov Yudkin**

[yaakov.yudkin@gmail.com](mailto:yaakov.yudkin@gmail.com)

[\(mailto:yaakov.yudkin@gmail.com\)](mailto:yaakov.yudkin@gmail.com)

Bar-Ilan University



## Efimov Energy Level Rebounding from the Atom-Dimer Continuum

Efimov physics with its ladder of weakly bound three-atomic molecules (trimers) is a fundamental building block of universal few-body physics. The van der Waals interaction, which governs the collisions between ultracold atoms, was found to provide a new twist to the concept of universality in the regime where no weakly bound two-body bound states (dimers) exist. The opposite regime (where the dimer exists) does not follow the same rule and behaves increasingly non-universal, especially for the two lowest Efimov energy levels. To probe this challenging regime we create a coherent superposition of dimers and trimers and extract the energy difference from a measurement of their time evolution. As a result we reveal yet another twist, this time within the non-universality of the first excited Efimov energy level. Instead of merging with the atom-dimer continuum it rebounds from it and becomes a deeper bound state again. Instead of a tangential approach between the two levels we observe a rather narrow resonance, providing a new challenge and a possible guide for realistic few-body theories.

---

Yale

Copyright © 2024 Yale University · All rights reserved

# Transport in optical lattices with flux

**A. Hudomal<sup>1</sup>, I. Vasić<sup>1</sup>, H. Buljan<sup>2</sup>, W. Hofstetter<sup>3</sup>, and A. Balaz̄<sup>1</sup>**

<sup>1</sup> *Scientific Computing Laboratory, Center for the Study of Complex Systems,  
Institute of Physics Belgrade, University of Belgrade, Serbia*

<sup>2</sup> *Department of Physics, University of Zagreb, Croatia*

<sup>3</sup> *Institut für Theoretische Physik, Johann Wolfgang Goethe-Universität, Frankfurt am Main, Germany*

e-mail: [hudomal@ipb.ac.rs](mailto:hudomal@ipb.ac.rs)

Different condensed matter systems, such as electrons in a crystal lattice, can be simulated using ultracold atoms in optical lattices. Unlike electrons, atoms are electrically neutral and therefore do not feel the effects of magnetic field. Artificial gauge potentials have been recently realized in cold-atom experiments with periodically driven optical lattices [1, 2]. In such systems, atoms subjected to a constant external force gain an anomalous velocity in the direction transverse to the direction of the applied force.

Taking into consideration realistic experimental conditions, we perform numerical simulations in order to investigate the dynamics of atomic clouds and relate it to the Chern number of the effective model. We consider incoherent bosons and the full time-dependent Hamiltonian. The effects of weak repulsive interactions between atoms are taken into account using the mean-field approximation.

Our results show that driving, external force and interactions all cause heating and transitions to higher bands, which have significant effects on the dynamics. It turns out that weak interactions can be beneficial, because they make the momentum-space probability density more homogeneous. In the future, we also plan to study the details of the atomic-cloud expansion dynamics, and to simulate the full loading sequence of an initial Bose-Einstein condensate, as it was done in the experiment [2].

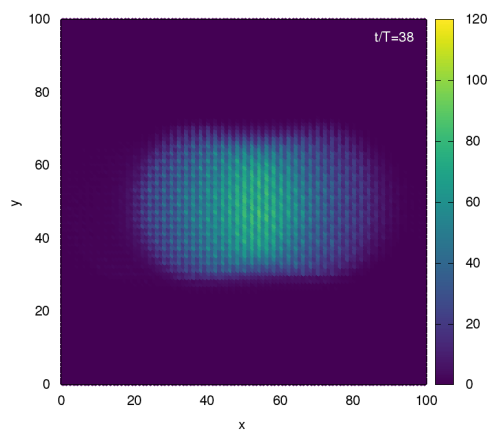


Figure 1: Density profile of an atomic cloud during expansion dynamics after release from a trap in the presence of an artificial gauge field and external force.

- [1] G. Jotzu, M. Messer, R. Desbuquois, M. Lebrat, T. Uehlinger, D. Greif, and T. Esslinger, *Nature* **515**, 237 (2014).
- [2] M. Aidelsburger, M. Lohse, C. Schweizer, M. Atala, J. T. Barreiro, S. Nascimbène, N. R. Cooper, I. Bloch, and N. Goldman, *Nat. Phys.* **11**, 162 (2015).



GÖRG<sup>1</sup>, NATHAN GOLDMAN<sup>2</sup>, GREGOR JOTZU<sup>1</sup>, MICHAEL MESSER<sup>1</sup>, KILIAN SANDHOLZER<sup>1</sup>, RÉMI DESBUQUOIS<sup>1</sup>, and TILMAN ESSLINGER<sup>1</sup> — <sup>1</sup>Institute for Quantum Electronics, ETH Zurich, Zurich, Switzerland — <sup>2</sup>CENOLI, Université Libre de Bruxelles, Brussels, Belgium

The appearance of topological properties in lattice systems caused by a non-trivial topological band structure in the bulk is closely related to the existence of chiral edge modes via the bulk-edge correspondence. These edge states appear at the interface of two spatial regions with a distinct topology, which for example naturally arise at the boundaries of a sample surrounded by vacuum. In cold atom systems, these edge modes are difficult to detect, since the underlying harmonic trapping potential does not feature sharp boundaries. Therefore, we propose a different method to design topological interfaces within the bulk of the system. We illustrate this scheme by an optical lattice realization of the Haldane model, where a spatially varying lattice beam leads to the appearance of distinct topological phases in separated regions of space. The versatility of the method allows to tune the position, the localization length and the chirality of the edge modes. We numerically study the propagation of wave packets in such a system and demonstrate the feasibility to experimentally detect chiral edge states. Finally, we show that the edge modes, unlike the bulk states, are topologically protected against the effects of disorder, which makes a random potential a powerful tool to detect edge states in cold atom setups.

Q 53.16 Thu 17:00 P OGs

**Transport dynamics in optical lattices with flux** — ●ANA HUDOMAL<sup>1</sup>, IVANA VASIĆ<sup>1</sup>, WALTER HOFSTETTER<sup>2</sup>, and ANTUN BALAZ<sup>1</sup> — <sup>1</sup>Scientific Computing Laboratory, Center for the Study of Complex Systems, Institute of Physics Belgrade, University of Belgrade, Serbia — <sup>2</sup>Institut für Theoretische Physik, Johann Wolfgang Goethe-Universität, Frankfurt am Main, Germany

Recent cold atom experiments have realized artificial gauge fields in periodically modulated optical lattices [1,2]. We study the dynamics of atomic clouds in these systems by performing numerical simulations using the full time-dependent Hamiltonian and comparing these results to the semiclassical approximation. Under constant external force, atoms in optical lattices with flux exhibit an anomalous velocity in the transverse direction. We investigate in detail how this transverse drift is related to the Berry curvature and Chern number, taking into account realistic experimental conditions.

[1] G. Jotzu et al., *Nature* **515**, 237 (2014).

[2] M. Aidelsburger et al., *Nature Phys.* **11**, 162 (2015).

Q 53.17 Thu 17:00 P OGs

**Towards the investigation of collective scattering in nanofiber-trapped atomic ensembles** — ●ADARSH S. PRASAD, JAKOB HINNEY, SAMUEL RIND, PHILIPP SCHNEEWEISS, JÜRGEN VOLZ, CHRISTOPH CLAUSEN, and ARNO RAUSCHENBEUTEL — TU Wien - Atominstitut, Stadionallee 2, 1020 Wien, Austria

We realize an efficient optical interface between guided light and laser-cooled atoms which are arranged in two linear arrays in a two-color evanescent-field dipole trap created around an optical nanofiber [1]. In this configuration, the probability of a nanofiber-guided photon being absorbed and then re-emitted into free space by a trapped atom is as high as 10%. For a periodic array of atoms, interference of the fields scattered by different atoms result in a collective emission into a cone with a well-defined angle with respect to the fiber axis. We plan to study this collective emission and its dependence on various experimental parameters. The next step will be to adjust the periodicity of the atomic array to fulfill the Bragg condition such that fiber-guided light is strongly back-reflected [2]. Here, the interaction between the atomic array and the fiber-guided light depends strongly on the polarization of the light field. In particular, light that is polarized in (orthogonal to) the plane of atoms will be weakly (strongly) reflected. We want to implement such highly reflecting atomic arrays, which could then be used to implement cavity quantum electrodynamics experiments in which the resonator itself is made of quantum emitters.

[1] E. Vetsch et al., *Phys. Rev. Lett.* **104**, 203603 (2010).

[2] Fam Le Kien et. al., *Phys. Rev. A* **90**, 063816 (2014).

Q 53.18 Thu 17:00 P OGs

**Setup of a new micro-structured linear Paul trap with integrated solenoids and reduced axial micromotion** — ●H. SIEBENEICH, D. KAUFMANN, T. GLOGER, P. KAUFMANN, M. JOHANNING, and CH. WUNDERLICH — Department Physik, Universität Siegen, 57068 Siegen, Germany

We present the status of a new 3d segmented ion trap setup with integrated solenoids, in which an improved design allows for a substantial reduction of axial micromotion and for an increased magnetic gradients. Our trap consists of three layers of gold plated alumina, where the segmented outer layers provide the trapping potentials [1], and the middle layer contains solenoids that are used to create a magnetic field gradient [2]. The gradient gives rise to coupling between the ions' internal and motional states. The trap is mounted on a ceramic chip carrier that, at the same time, acts as an ultra-high vacuum interface, featuring about 100 thick-film printed current and voltage feedthroughs. The thick film interface has been improved by replacing previously used Ag-Pd layers by Au layers which reduced their resistivity by a factor of eight. The previously high resistivity used to be a bottleneck for achieving high solenoid currents and thus a magnetic gradient. The shape of the solenoids was redesigned, leading to an expected reduction of axial micromotion by four orders of magnitudes. [1] S.A. Schulz et al.: Sideband cooling and coherent dynamics in a microchip multi-segmented ion trap, *New Journal of Physics*, Volume 10, April 2008 [2] D. Kaufmann et al.: Thick-film technology for ultra high vacuum interfaces of micro-structured traps, *Appl Phys B* (2012) 107:935-943

Q 53.19 Thu 17:00 P OGs

**Design and construction of a Perpetual Atom Laser Machine** — ●CHUN-CHIA CHEN, SHAYNE BENNETTS, BENJAMIN PASQUIOU, and FLORIAN SCHRECK — Institute of Physics, University of Amsterdam, Amsterdam, The Netherlands

We have developed a machine aimed at producing a perpetual atom laser, a long standing goal within atomic physics. Continuous production of Bose-Einstein condensate (BEC) or an atom laser requires two incompatible cooling processes, laser cooling a gas sample, then cooling evaporatively until degeneracy is reached. In order to produce a perpetual output these stages take place simultaneously in different parts of our machine. To protect the condensate from scattered photon heating we use a combination of physical separation, baffles and a "transparency" beam. Our machine has now demonstrated a perpetual MOT of  $2 \times 10^9$  <sup>88</sup>Sr atoms with temperatures as low as 20 μK on a 7.4-kHz wide laser cooling transition with a continuous loading rate of  $7 \times 10^8$  atoms/s. Using a different set of parameters and location we have also demonstrated a perpetual MOT of  $2 \times 10^8$  <sup>88</sup>Sr at 2 μK with a loading rate of  $9 \times 10^7$  atoms/s which we have successfully loaded into a dipole trap. By switching to the 0.5% abundance <sup>84</sup>Sr isotope we are able to evaporate to BECs of  $3 \times 10^5$  <sup>84</sup>Sr atoms. Critically, for the second location we have validated the effectiveness of our architecture in protecting a BEC from scattered broad-linewidth laser cooling light, which is used in the first cooling stages. We will describe our design and the performance demonstrated so far.

Q 53.20 Thu 17:00 P OGs

**Optical trapping of neutral mercury** — ●HOLGER JOHN and THOMAS WALTHER — Technische Universität Darmstadt, Institut für Angewandte Physik, Schlossgartenstraße 7, 64289 Darmstadt

Laser-cooled mercury constitutes an interesting starting point for various experiments, in particular in light of the existence of bosonic and fermionic isotopes. On the one hand the fermionic isotopes could be used to develop a new time standard based on an optical lattice clock employing the <sup>1</sup>S<sub>0</sub> - <sup>3</sup>P<sub>0</sub> transition. Another interesting venue is the formation of ultra cold Hg-dimers employing photo-association and achieving vibrational cooling by employing a special scheme.

The laser system is based on an interference-filter stabilized external cavity diode laser with excellent spectral properties combined with a home built non-cryogenic fiber amplifier for the 1015nm fundamental wavelength with a slope-efficiency of more than 35 % delivering up to 4W of pump limited output power. The fundamental wavelength is frequency doubled twice to reach the cooling transition at 253.7 nm. The challenging requirements meeting the natural linewidth of 1.27 MHz are mastered by use of a ULE reference resonator.

After integrating a 2D-MOT as an atom source to the vacuum system the first measurements of ultra-cold atoms with the new laser system will be reported.

Q 53.21 Thu 17:00 P OGs

**Diffusion of Single Atoms in Bath** — ●DANIEL ADAM, FARINA KINDERMANN, TOBIAS LAUSCH, DANIEL MAYER, FELIX SCHMIDT, STEVE HAUPT, MICHAEL HOHMANN, NICOLAS SPETHMANN, and ARTUR WIDERA — TU Kaiserslautern, Department of Physics, Kaiserslautern, Germany

## Q 35: Quantum Gases (Fermions) II

Time: Tuesday 14:00–16:15

Location: K 1.022

Q 35.1 Tue 14:00 K 1.022

**Artificial gauge potentials in periodically driven optical lattices: numerical simulations of atomic transport**— ●ANA HUDOMAL<sup>1</sup>, IVANA VASIĆ<sup>1</sup>, HRVOJE BULJAN<sup>2</sup>, WALTER HOFSTETTER<sup>3</sup>, and ANTUN BALAZ<sup>1</sup> — <sup>1</sup>Scientific Computing Laboratory, Center for the Study of Complex Systems, Institute of Physics Belgrade, University of Belgrade, Serbia — <sup>2</sup>Department of Physics, University of Zagreb, Croatia — <sup>3</sup>Institut für Theoretische Physik, Johann Wolfgang Goethe-Universität, Frankfurt am Main, Germany

Artificial gauge potentials have been recently realized in cold-atom experiments with periodically driven optical lattices [1,2]. In such systems, atoms subjected to a constant external force gain an anomalous velocity in the direction transverse to the direction of the applied force. Taking into consideration realistic experimental conditions, we perform numerical simulations in order to investigate the dynamics of atomic clouds and relate it to the Chern number of the effective model. We use the full time-dependent Hamiltonian and take into account the effects of weak repulsive interactions between atoms. The results are compared to the semiclassical approximation.

[1] G. Jotzu et al., *Nature* **515**, 237 (2014).[2] M. Aidelsburger et al., *Nature Phys.* **11**, 162 (2015).

Q 35.2 Tue 14:15 K 1.022

**Experimental characterization and control of Floquet states in a periodically driven two-body quantum system**

— ●KILIAN SANDHOLZER, RÉMI DESBUQUOIS, MICHAEL MESSER, FREDERIK GÖRG, JOAQUÍN MINGUZZI, GREGOR JOTZU, and TILMAN ESSLINGER — Institute for Quantum Electronics, ETH Zürich, Zürich, Switzerland

Floquet engineering is a powerful tool to modify properties of a static system such as opening topological gaps or controlling magnetic order. The versatility of cold atom experiments offers the possibility to implement many of these schemes. Nonetheless, preparing a certain Floquet state that has the desired properties in this out-of-equilibrium situation is a more difficult task, especially when the driving frequency is close to a characteristic energy scale of the system. In this work, we prepare fermionic atoms in a driven optical lattice such that the system can be described by two interacting particles on a double well potential with a periodically modulated tilt. In the case of near-resonant driving we achieve to enter adiabatically individual Floquet states by using a two-step ramping protocol. In addition, the fast coherent dynamics inherently connected to the drive are studied in detail. Finally, an analytical derivation of the effective time-independent Hamiltonian of the realized system is presented and then compared to numerical studies and experimental data.

Q 35.3 Tue 14:30 K 1.022

**Dynamics of driven interacting many-body systems**

— ●MICHAEL MESSER, FREDERIK GÖRG, KILIAN SANDHOLZER, JOAQUÍN MINGUZZI, RÉMI DESBUQUOIS, and TILMAN ESSLINGER — Institute for Quantum Electronics, ETH Zurich, 8093 Zurich, Switzerland

Periodic driving can be used to coherently control the properties of a many-body state and to engineer new phases which are not accessible in static systems. The successful implementation of a periodically driven Fermi-Hubbard model on a 3D hexagonal lattice offers the possibility to explore the intriguing dynamics of Floquet many-body systems. A theoretical analysis of driven many-body Hamiltonians is inherently challenging, however, in combination with our experiments a deeper understanding seems feasible.

By controlling the detuning between shaking frequency and interactions, and setting a variable strength of the periodic drive, we achieve independent control over the single particle tunneling and the magnetic exchange energy. This control allows us to investigate the dynamics and build-up of nearest-neighbor spin-spin correlations. Furthermore, we explore possible mechanisms behind the formation of correlations in interacting Floquet systems. In addition, we can analyze the creation of double occupancies, as one mechanism to form excitations.

Q 35.4 Tue 14:45 K 1.022

**Enhancement and sign change of magnetic correlations in a driven quantum many-body system**— ●FREDERIK GÖRG<sup>1</sup>, MICHAEL MESSER<sup>1</sup>, KILIAN SANDHOLZER<sup>1</sup>, JOAQUÍN MINGUZZI<sup>1</sup>,GREGOR JOTZU<sup>1,2</sup>, RÉMI DESBUQUOIS<sup>1</sup>, and TILMAN ESSLINGER<sup>1</sup> — <sup>1</sup>Institute for Quantum Electronics, ETH Zurich, 8093 Zurich, Switzerland — <sup>2</sup>Max Planck Institute for the Structure and Dynamics of Matter, 22761 Hamburg, Germany

Strong periodic driving can be used to control the properties of interacting quantum systems. In solid state experiments, ultrashort laser pulses are employed to tune the charge order as well as magnetic and superconducting properties of materials. At the same time, continuous driving has been used in cold atom experiments to engineer novel effective Floquet-Hamiltonians which feature for example a topological bandstructure. We realize a strongly interacting Fermi gas in a periodically driven hexagonal optical lattice and investigate its charge and magnetic properties. We first demonstrate that in the high-frequency regime, the effective description of the many-body system by a renormalized tunnelling amplitude remains valid by comparing our results to an equivalent static system. When driving at a frequency close to the interaction energy, we show that anti-ferromagnetic correlations can be enhanced or even switched to ferromagnetic ordering. Our observations can be explained by a microscopic model, in which the particle tunnelling and magnetic exchange energies can be controlled independently. Therefore, Floquet engineering constitutes an alternative route to experimentally investigate unconventional pairing.

Q 35.5 Tue 15:00 K 1.022

**Manipulating and probing excitations of a Chern insulator by Floquet engineering an optical solenoid**

— ●BOTAO WANG, NUR ÜNAL, and ANDRÉ ECKARDT — Max Planck Institute for the Physics of Complex Systems, Dresden, Germany

The realization of artificial gauge fields in optical lattice systems has paved a way to the experimental investigation of various topological quantum effects. Here we propose a realistic scheme for realizing tunable local (solenoid type) artificial magnetic fields by means of Floquet engineering. We show that such an optical solenoid field can be used to coherently manipulate and probe Chern insulator states of the Hofstadter Hamiltonian. In particular, we investigate the possibility to create local quasiparticle and quasihole excitations, to coherently populate edge modes, and to achieve quantized charge pumping. All these effects are manifested on the spatial density distributions, which can be measured directly in quantum-gas microscopes.

Q 35.6 Tue 15:15 K 1.022

**Characterizing topology by dynamics: Chern number from linking number**— ●MATTHIAS TARNOWSKI<sup>1,2</sup>, NUR ÜNAL<sup>3</sup>, NICK FLÄSCHNER<sup>1,2</sup>, BENNO REM<sup>1,2</sup>, ANDRÉ ECKARDT<sup>3</sup>, KLAUS SENGSTOCK<sup>1,2,4</sup>, and CHRISTOF WEITENBERG<sup>1,2</sup> — <sup>1</sup>Institut für Laserphysik, Universität Hamburg, 22761 Hamburg, Germany — <sup>2</sup>The Hamburg Centre for Ultrafast Imaging, 22761 Hamburg, Germany — <sup>3</sup>Max-Planck-Institut für Physik komplexer Systeme, Nöthnitzer Straße 38, 01187 Dresden, Germany — <sup>4</sup>Zentrum für Optische Quantentechnologien, Universität Hamburg, 22761 Hamburg, Germany

Topology plays an important role in modern solid state physics describing intriguing quantum states such as topological insulators. It is an intrinsically non-local property and therefore challenging to access, often studied only via the resulting edge states. Here, we report on a new approach by connecting the Chern number with the dynamical evolution of highly excited states of the system and demonstrate it experimentally with cold atoms in hexagonal optical lattices. We study the contour of dynamically created vortex pairs in momentum space following a sudden quench into the system of interest and infer the Chern number of the post-quench Hamiltonian from the topology of the contour, quantified by the linking number with the static vortices. Our work exploits a direct mapping between two topological indices and allows detecting topology by the naked eye.

Q 35.7 Tue 15:30 K 1.022

**1D fermionic Floquet topological insulators with Hubbard interaction**— ●HAIXIN QIU<sup>1</sup> and JOHANN KROHA<sup>1,2</sup> — <sup>1</sup>Physikalisches Institut und Bethe Center for Theoretical Physics, Universität Bonn, Nussallee 12, 53115 Bonn, Germany — <sup>2</sup>Center for Correlated Matter, Zhejiang University, Hangzhou, Zhejiang 310058, China

The fermionic Rice-Mele model is a standard model for quantum ratchet transport in periodically driven, one-dimensional, bipartite

## Q 25: Poster: Quantum Optics and Photonics I

Time: Tuesday 16:30–18:30

Location: S Atrium Informatik

Q 25.1 Tue 16:30 S Atrium Informatik

**Unequal-time correlations in Bose-Einstein condensates** — ●LINDA SHEN<sup>1,2</sup> and MARTIN GÄRTNER<sup>2</sup> — <sup>1</sup>Institut für Theoretische Physik, Philosophenweg 16, 69120 Heidelberg, Germany — <sup>2</sup>Kirchhoff-Institut für Physik, Im Neuenheimer Feld 227, 69120 Heidelberg, Germany

We develop measurement schemes for unequal-time correlation functions in a Bose-Einstein condensate (BEC). Both the spectral and statistical components of the two-point correlation function are investigated out of equilibrium. Thereby, the time-evolution of a BEC is computed numerically using classical-statistical simulation methods based on the Gross-Pitaevskii equation.

The spectral correlation function is approached by linear response methods, which are in principle applicable to both numerical computations as well as experimental measurements. The statistical correlation function can be computed directly in the classical-statistical approximation. Extracting the unequal-time statistical function experimentally, however, requires involved techniques in order to avoid quantum back action effects. We propose to use a non-invasive measurement protocol where the system is weakly coupled to an ancillary system.

In thermal equilibrium, the spectral and statistical components are related by the fluctuation-dissipation theorem. Measuring both will allow a better understanding of how the fluctuation-dissipation theorem builds up as the system approaches equilibrium.

Q 25.2 Tue 16:30 S Atrium Informatik

**Quantum Droplets with Tilted Dipoles** — ●MANUEL SCHMITT<sup>1</sup>, VLADIMIR VELJIĆ<sup>2</sup>, ANTUN BALAZ<sup>2</sup>, and AXEL PELSTER<sup>1</sup> — <sup>1</sup>Research Center OPTIMAS and Department of Physics, Technische Universität Kaiserslautern, Germany — <sup>2</sup>Scientific Computing Laboratory, Center for the Study of Complex Systems, Institute of Physics Belgrade, University of Belgrade, Serbia

Since 2005 there have been many striking advancements in Bose-Einstein condensates (BECs) with dipolar interactions, the most recent one being the discovery of quantum droplets, which are stabilized due to quantum fluctuations [1, 2]. With a variational approach we investigate the influence of a tilted dipole axis on quantum droplets in a wave guide-like setup [3]. At first we generalize for one quantum droplet the energy functional for the extended Gross-Pitaevskii theory to tilted dipoles and determine the resulting deformation of the cloud as well as its stability as a function of the tilting angle. Furthermore, we consider two quantum droplets in a trap and calculate how their equilibrium distance depends on the tilting of the dipole axis. With this we gain new insight into the emergence of filaments of dipolar BECs.

[1] M. Schmitt et al., *Nature* **539**, 259 (2016)[2] L. Chomaz et al., *Phys. Rev. X* **6**, 041039 (2016)[3] I. Ferrier-Barbut et al., *Phys. Rev. Lett.* **116**, 215301 (2016)

Q 25.3 Tue 16:30 S Atrium Informatik

**Many-body Multifractality in Fock space for Interacting Bosons** — JAKOB LINDINGER, ANDREAS BUCHLEITNER, and ●ALBERTO RODRÍGUEZ — Physikalisches Institut, Albert-Ludwigs-Universität Freiburg, Hermann-Herder-Straße 3, D-79104 Freiburg, Germany

We analyse the many-body multifractality of the Bose-Hubbard Hamiltonian's eigenstates in Fock space, for arbitrary values of the interparticle interaction. For the ground state, generalized fractal dimensions unambiguously signal, even for small system sizes, the emergence of a Mott insulator. We show that the scaling of the derivative of any generalised fractal dimension with respect to the interaction strength encodes the critical point of the superfluid to Mott insulator transition, and we establish that the transition can be quantitatively characterized by one single wavefunction amplitude from the exponentially large Fock space [1]. Furthermore, multifractality of the excited eigenstates is investigated and the possible existence of localization in Fock space is thoroughly studied.

[1] J. Lindinger, A. Buchleitner, A. Rodríguez, arXiv:1810.06369

Q 25.4 Tue 16:30 S Atrium Informatik

**Dynamics in multi-species bosonic systems** — TOBIAS BRÜNNER, ●GABRIEL DUFOUR, ALBERTO RODRÍGUEZ, and ANDREAS

BUCHLEITNER — Physikalisches Institut, Albert-Ludwigs-Universität Freiburg, Hermann-Herder-Straße 3, D-79104 Freiburg, Germany

The dynamics of bosons in multimode systems is determined by an involved interplay between interactions and indistinguishability-induced many-particle interference. We construct a formalism to investigate systematically the dynamics of multiple bosonic species, distinguishable by an internal degree of freedom which is insensitive to the time evolution. We unveil how interparticle interactions lead to a hierarchy of interaction-induced interference processes, such that even the dynamics of single-particle observables is influenced by the degree of indistinguishability (DOI). Time-averaged expectation values of observables dominated by two-particle interference are shown to correlate with a measure of the DOI for initial Fock states [1]. Time-resolved features of the dynamics, such as the frequency content of the signals, are also influenced by the DOI and reveal the interacting or non-interacting nature of the system. We show that this can be understood from the symmetry properties of the Hamiltonian based on group-theoretical arguments [2].

[1] T. Brünner, G. Dufour, A. Rodríguez, A. Buchleitner, *Phys. Rev. Lett.* **120**, 210401 (2018)[2] T. Brünner, PhD Thesis, Albert-Ludwigs-Universität Freiburg (2018). <https://doi.org/10.6094/UNIFR/16683>

Q 25.5 Tue 16:30 S Atrium Informatik

**Rotational cooling of molecules in a BEC** — ●MARTIN WILL, TOBIAS LAUSCH, and MICHAEL FLEISCHHAUER — University of Kaiserslautern, 67663 Kaiserslautern, Germany

We discuss the rotational cooling of homonuclear diatomic molecules in a Bose-Einstein-condensate (BEC). For typical molecules there is no frictionless rotation since the dominant cooling occurs via emission of particle-like phonons. Only for macro-dimers, whose size becomes larger than the condensate healing length, a Landau-like, critical angular momentum exists below which phonon emission is suppressed. We find that the phonon-induced angular momentum relaxation is much faster than the cooling of linear motion of impurities in a BEC. This also leads to a finite lifetime of angulons, quasi-particles of rotating molecules coupled to orbital angular-momentum phonons. The lifetimes are however still smaller than typical angulon binding energies. We analyze the dynamics of rotational cooling for homo-nuclear diatomic molecules based on a quantum Boltzmann equation including single- and two-phonon scattering and discuss the effect of thermal phonons. For typical molecules two-phonon scattering becomes relevant at finite temperature.

Q 25.6 Tue 16:30 S Atrium Informatik

**Coexistence of phase transitions and hysteresis near the onset of Bose-Einstein condensation** — MICHAEL MAENNEL<sup>3</sup> and ●KLAUS MORAWETZ<sup>1,2</sup> — <sup>1</sup>Münster University of Applied Sciences, Stegerwaldstrasse 39, 48565 Steinfurt, Germany — <sup>2</sup>International Institute of Physics- UFRN, Campus Universitário Lagoa nova, 59078-970 Natal, Brazil — <sup>3</sup>Informatik DV, Petersstr. 14, 04109 Leipzig, Germany

Multiple phases occurring in a Bose gas with finite-range interaction are investigated [2]. In the vicinity of the onset of Bose-Einstein condensation (BEC), the chemical potential and the pressure show a van der Waals-like behavior indicating a first-order phase transition for weak interactions like Hartree-Fock or Popov approximation. However, for strong interactions there remains a multivalued region for the T-matrix approximation even after the Maxwell construction, which is interpreted as a density hysteresis [1]. This unified treatment of normal and condensed phases becomes possible due to the recently found scheme to eliminate self-interactions in the T-matrix approximation, which allows one to calculate properties below and above the critical temperature [3,4]. [1] *Phys. Rev. A* **87** (2013) 053617, [2] *New J. Phys.* **12** (2010) 033013, [3] *J. Stat. Phys.* **143** (2011) 482, [4] *Phys. Rev. B* **84** (2011) 094529

Q 25.7 Tue 16:30 S Atrium Informatik

**Dynamics of weakly interacting bosons in optical lattices with flux** — ●ANA HUDOMAL<sup>1</sup>, IVANA VASIĆ<sup>1</sup>, HRVOJE BULJAN<sup>2</sup>, WALTER HOFSTETTER<sup>3</sup>, and ANTUN BALAZ<sup>1</sup> — <sup>1</sup>Scientific Computing Laboratory, Center for the Study of Complex Systems, Institute of Physics

Belgrade, University of Belgrade, Serbia — <sup>2</sup>Department of Physics, Faculty of Science, University of Zagreb, Croatia — <sup>3</sup>Institut für Theoretische Physik, Johann Wolfgang Goethe-Universität, Frankfurt am Main, Germany

Realization of strong synthetic magnetic fields in driven optical lattices has enabled implementation of topological bands in cold-atom setups [1,2]. A milestone has been reached by a recent measurement of a finite Chern number based on the dynamics of incoherent bosonic atoms [2]. Motivated by these recent developments, we investigate the dynamics of weakly interacting incoherent bosons in a two-dimensional driven optical lattice exposed to an external force, which provides a direct probe of the Chern number [3]. We find that interactions lead to the redistribution of atoms over topological bands both through the conversion of interaction energy into kinetic energy during the expansion of the atomic cloud and due to an additional heating. Remarkably, we observe that the moderate atomic repulsion facilitates the measurement by flattening the distribution of atoms in the quasimomentum space.

- [1] G. Jotzu et al., *Nature* **515**, 237 (2014).  
 [2] M. Aidelsburger et al., *Nature Phys.* **11**, 162 (2015).  
 [3] A. Hudomal et al., *Phys. Rev. A* **98**, 053625 (2018).

Q 25.8 Tue 16:30 S Atrium Informatik

**Quench dynamics and boundary condition dependence of the one-dimensional extended Bose Hubbard model** — ●SEBASTIAN STUMPER, JUNICHI OKAMOTO, and MICHAEL THOSS — Institute of Physics, University of Freiburg, Freiburg, Germany

The one-dimensional extended Bose Hubbard model exhibits a variety of quantum phases due to its competing interactions. For large on-site interactions, a Mott insulating (MI) phase exists, while a charge density wave (CDW) phase becomes dominant for large nearest-neighbour interactions. In between these phases, there exists a topologically non-trivial phase of a Haldane insulator (HI), which is characterized by a non-local string order (*Phys. Rev. Lett.* **97**, 260401 (2006)). Ground state properties and low energy spectra are, however, very sensitive to the treatment of boundary conditions (arXiv:1403.2315 (2014)). We study an open chain of the extended Bose Hubbard model for various configurations of chemical potentials applied at the edges using the density matrix renormalization group method (*Comput. Phys. Commun.* **225**, 59 (2018)). Without edge potentials, the CDW and HI phases show a non-degenerate ground state, and the order parameters change signs in the middle of the chain. This feature is robust against finite size scaling and is explained by a simple effective picture for the low energy states. On the other hand, with large edge potentials, the sign change of the order parameters disappears, and we recover uniform bulk ground states. Furthermore, we simulate quenched dynamics with initial states from MI, HI and CDW phases and discuss the results in terms of our findings on the equilibrium cases.

Q 25.9 Tue 16:30 S Atrium Informatik

**Staggered-immersion cooling of a quantum gas in optical lattices** — ●BING YANG<sup>1,2,3</sup>, HUI SUN<sup>1,2,3</sup>, CHUN-JIONG HUANG<sup>2,3</sup>, HAN-YI WANG<sup>1,2,3</sup>, YOU-JIN DENG<sup>2,3</sup>, HAN-NING DAI<sup>1,2,3</sup>, ZHEN-SHENG YUAN<sup>1,2,3</sup>, and JIAN-WEI PAN<sup>1,2,3</sup> — <sup>1</sup>Physikalisches Institut, Ruprecht-Karls-Universität Heidelberg, Im Neuenheimer Feld 226, 69120 Heidelberg, Germany — <sup>2</sup>Hefei National Laboratory for Physical Sciences at Microscale and Department of Modern Physics, University of Science and Technology of China, Hefei, Anhui 230026, China — <sup>3</sup>CAS Centre for Excellence and Synergetic Innovation Centre in Quantum Information and Quantum Physics, University of Science and Technology of China, Hefei, Anhui 230026, China

Here we realize efficient cooling of ten thousand ultracold bosons in staggered optical lattices. By immersing Mott-insulator samples into removable superfluid reservoirs, thermal entropy is extracted from the system. Losing less than half of the atoms, we lower the entropy of a Mott insulator by 65-fold, achieving a record-low entropy per particle of  $0.0019 k_B$  ( $k_B$  is the Boltzmann constant). We further engineer the sample to a defect-free array of isolated single atoms and successfully transfer it into a coherent many-body state. The present staggered-immersion cooling opens up an avenue for exploring novel quantum matters and promises practical applications in quantum information science.

Q 25.10 Tue 16:30 S Atrium Informatik

**Simulation of the Quantum Rabi Model with Ultracold Rubidium Atoms in the Deep Strong Coupling Regime** — ●GERAM HUNANYAN<sup>1</sup>, JOHANNES KOCH<sup>1</sup>, MARTIN LEDER<sup>1</sup>, ENRIQUE

RICO<sup>2,3</sup>, CARLOS SABIN<sup>4</sup>, ENRIQUE SOLANO<sup>2,3</sup>, and MARTIN WEITZ<sup>1</sup> — <sup>1</sup>Institut für Angewandte Physik Bonn, Wegelerstr. 8, D-53115 Bonn, Germany — <sup>2</sup>Department of Physical Chemistry, University of the Basque Country UPV/EHU, Apartado 644, E-48080 Bilbao, Spain — <sup>3</sup>IKERBASQUE, Basque Foundation for Science, Maria Diaz de Haro 3, E-48013 Bilbao, Spain — <sup>4</sup>Instituto de Fisica Fundamental, CSIC, Serrano 113-bis, E-28006 Madrid, Spain

The Quantum Rabi Model (QRM) has been applied to describe the dynamics of a two-level quantum system interacting with a single bosonic mode. Although a fair quantity of experiments explore the strong coupling regime of the QRM, where due to the still limited coupling strength the system can be transformed to the widely known Jaynes-Cummings Model, researchers are just beginning to exploit the regime where the full QRM must be considered. Our experimental implementation to simulate the QRM uses ultracold rubidium atoms in an optical lattice potential, with the effective two-level quantum system being simulated by different Bloch bands in the first Brillouin zone. The bosonic mode is represented by the oscillations of the atoms in an optical dipole trapping potential. We experimentally observe the atomic dynamics in the deep strong coupling regime. The present status of results will be presented.

Q 25.11 Tue 16:30 S Atrium Informatik

**Probing the mott-insulator state in optical lattices with photoassociation collisions** — ●HUI SUN, BING YANG, ZHEN-SHENG YUAN, and JIAN-WEI PAN — Physikalisches Institut, Ruprecht-Karls-Universität Heidelberg, Im Neuenheimer Feld 226, 69120 Heidelberg, Germany

The photoassociation collision is a process two colliding atoms form an excited molecular state after absorbing a photon, which can be used to remove doublons in optical lattices. In this work, we present the detection of a bosonic Mott-insulator state in optical lattices via photoassociation collisions. The photoassociation frequency and collision strength in the  $0_{g^-}$  molecular channel are calibrated in ultracold quantum gases of Rb<sup>87</sup>. Then we measure the density distributions of two-dimensional Mott-insulator states in optical lattices after illuminated by a photoassociation light, which is  $13.6 \text{ cm}^{-1}$  red detuned to the D2 line. From the density profiles, we extract the temperatures of the Mott-insulators and demonstrate an improvement of the measurement precision. This new method extends our ability to probe this ultracold strongly correlated systems.

Q 25.12 Tue 16:30 S Atrium Informatik

**Probing Equilibration of Isolated Quantum Systems in a Spinor Bose-Einstein Condensate** — ●STEFAN LANNIG, RODRIGO ROSA-MEDINA PIMENTEL, MAXIMILIAN PRÜFER, PHILIPP KUNKEL, ALEXIS BONNIN, HELMUT STROBEL, and MARKUS K. OBERTHALER — Kirchhoff-Institut für Physik, Im Neuenheimer Feld 227, 69120 Heidelberg

If and how isolated quantum systems eventually reach thermal equilibrium is still an open question. To address this we experimentally investigate the spin dynamics of a Bose-Einstein condensate of <sup>87</sup>Rb. In particular, we focus on the long-time dynamics in the  $F = 1$  hyperfine manifold, which realises a spin-1 system. We prepare the system in different out-of-equilibrium states and probe its subsequent evolution by applying a new readout technique which allows to simultaneously extract multiple spin projections. We observe that the kinetic temperature, leading to a finite non-condensed fraction, impacts the coherent evolution and relaxation of the spin observables.

Using local control of the spin orientation and atomic density we aim at further exploring and understanding the relaxation processes involved in the temporal evolution of a 1-d spinor system. We investigate the response of the system to controlled local perturbations which can be connected to spatial and temporal correlations offering new observables for characterisation of general many-particle quantum dynamics.

Q 25.13 Tue 16:30 S Atrium Informatik

**Non-equilibrium dynamics of interacting Bosons in an optical lattice** — ●JENS BENARY<sup>1</sup>, CHRISTIAN BAALS<sup>1,2</sup>, JIAN JIANG<sup>1</sup>, and HERWIG OTT<sup>1</sup> — <sup>1</sup>Department of Physics and OPTIMAS research center, Technische Universität Kaiserslautern, 67663 Kaiserslautern, Germany — <sup>2</sup>Graduate School Materials Science in Mainz, 55128 Mainz, Germany

We study the non-equilibrium dynamics of ultracold Bose gases using a scanning electron microscope. In our latest setup an optical system

## DY 7: Focus Session: Facets of Many-Body Quantum Chaos (organised by Markus Heyl and Klaus Richter) (joint session DY/TT)

This session covers the same topics as the TT-DY-MA symposium with the same name and five invited speakers on Tuesday, September 28th.

Time: Wednesday 10:00–13:00

Location: H6

DY 7.1 Wed 10:00 H6

**Probing many-body quantum chaos with quantum simulators using randomized measurements** — LATA K JOSHI<sup>1,2</sup>, ●ANDREAS ELBEN<sup>1,2,3</sup>, AMIT VIKRAM<sup>4,5</sup>, BENOIT VERMERSCH<sup>1,2,6</sup>, VICTOR GALITSKI<sup>4</sup>, and PETER ZOLLER<sup>1,2</sup> — <sup>1</sup>Center for Quantum Physics, University of Innsbruck, Innsbruck A-6020, Austria — <sup>2</sup>Institute for Quantum Optics and Quantum Information of the Austrian Academy of Sciences, Innsbruck A-6020, Austria — <sup>3</sup>Institute for Quantum Information and Matter and Walter Burke Institute for Theoretical Physics, California Institute of Technology, Pasadena, CA 91125, USA — <sup>4</sup>Joint Quantum Institute, University of Maryland, College Park, MD 20742, USA — <sup>5</sup>Condensed Matter Theory Center, Department of Physics, University of Maryland, College Park, MD 20742, USA — <sup>6</sup>Univ. Grenoble Alpes, CNRS, LPMCM, 38000 Grenoble, France

Randomized measurements provide a novel toolbox to probe many-body quantum chaos in quantum simulators, utilizing observables such as out-of-time ordered correlators and spectral form factors (SFFs). Here, I will focus on a protocol to access the SFF, characterizing the energy eigenvalue statistics, in quantum spin models. In addition, I will introduce partial spectral form factors (pSFFs) which refer to subsystems of the many-body system and reveal unique insights into energy eigenstate statistics. I will show that our randomized measurement protocol allows to access both, SFF and pSFFs. It provides thus a unified testbed to probe many-body quantum chaotic behavior, thermalization and many-body localization in closed quantum systems.

DY 7.2 Wed 10:15 H6

**Exploring the bound on chaos due to quantum criticality** — ●MATHIAS STEINHUBER, JUAN-DIEGO URBINA, and KLAUS RICHTER — University of Regensburg, Regensburg, Germany

The ‘bound on chaos’ proposed by Maldacena, Shenker and Stanford [1] predicts a temperature-dependent upper bound on the initial exponential growth rate  $\lambda_{\text{OTOC}} \leq 2\pi T$  for out-of-time-order correlators (OTOCs) in quantum systems with chaotic classical limit. We explore the temperature dependence of the quantum Lyapunov exponent  $\lambda_{\text{OTOC}}$  in Bose-Hubbard systems near criticality of the ground state [2]. We find the conditions for a non-trivial temperature dependence satisfying the bound, indicating the requirement that the system shows signatures of classical instability at the ground state while reaching the semiclassical regime at the same time. This is guaranteed by many-body systems with a well defined mean-field limit close to a bifurcation [3].

[1] Maldacena J., Shenker S. H. & Stanford D. A bound on chaos. *Journal of High Energy Physics* 2016, 106 (2016).

[2] Hummel, Q., Geiger, B., Urbina, J. D. & Richter, K. Reversible Quantum Information Spreading in Many-Body Systems near Criticality. *Phys. Rev. Lett.* 123, 160401 (2019).

[3] Eilbeck, J., Lomdahl, P. & Scott, A. The discrete self-trapping equation. *Physica D: Nonlinear Phenomena* 16, 318-338 (1985).

DY 7.3 Wed 10:30 H6

**Critically slow operator dynamics in constrained many-body systems** — ●JOHANNES FELDMER<sup>1,2</sup> and MICHAEL KNAP<sup>1,2</sup> — <sup>1</sup>Technical University of Munich — <sup>2</sup>Munich Center for Quantum Science and Technology (MCQST)

The far-from-equilibrium dynamics of generic interacting quantum systems is characterized by a handful of universal guiding principles, among them the ballistic spreading of initially local operators. Here, we show that in certain constrained many-body systems the structure of conservation laws can cause a drastic modification of this universal behavior. As an example, we study operator growth characterized by out-of-time-order correlations (OTOCs) in a dipole-conserving fracton chain. We identify a critical point with sub-ballistically moving OTOC front, that separates a ballistic from a dynamically frozen phase. This

critical point is tied to an underlying localization transition and we use its associated scaling properties to derive an effective description of the moving operator front via a biased random walk with long waiting times. We support our arguments numerically using classically simulable automaton circuits.

DY 7.4 Wed 10:45 H6

**Universal equilibration dynamics of the Sachdev-Ye-Kitaev model** — ●SOUMIK BANDYOPADHYAY, PHILIPP UHRICH, ALESSIO PAVIGLIANITI, and PHILIPP HAUKE — INO-CNR BEC Center and Department of Physics, University of Trento, Via Sommarive 14, I-38123 Trento, Italy

The Sachdev-Ye-Kitaev (SYK) model was introduced in the context of explaining the properties of “strange metals,” and has been found to manifest the characteristics of a quantum theory which is holographically dual to extremal charged black holes with two-dimensional anti-de Sitter horizons. Being maximally chaotic, black holes are the best known scramblers of quantum information in nature. Same features are shared by the SYK model, which has triggered a massive interest in its chaotic dynamics. Yet, many questions about the dynamics of the SYK model remain open. In this presentation, we shall be discussing the equilibration process of a fermionic system under the SYK Hamiltonian evolution. Our study, based on a state-of-the-art exact diagonalization method, reveals that the system exhibits an universal equilibration process. By devising a master equation for disordered systems, we successfully explain some of the key features of this dynamics. We infer the universality from the spectral analysis of the corresponding Liouvillian. We expect our findings shed light on challenging questions for systems far from equilibrium, such as, thermalization of closed and disordered quantum many-body systems.

DY 7.5 Wed 11:00 H6

**Periodic orbit sums and their relation to JT gravity correlators** — ●FABIAN HANEDER, TORSTEN WEBER, CAMILO MORENO, JUAN DIEGO URBINA, and KLAUS RICHTER — University of Regensburg, Germany

Jackiw-Teitelboim (JT) gravity is a two-dimensional dilaton gravity theory originally used to describe the near-horizon physics of charged, static black holes, but has recently garnered much attention due to its exact duality to a particular double-scaled Hermitian matrix model [1]. Applications are believed to be as a toy model for the black hole information paradox, the AdS/CFT correspondence, and holography and quantum gravity more generally.

The duality with a matrix model suggests the existence of a classical chaotic system which, after semiclassical (periodic orbit) quantisation [2], leads to the same spectral correlations. Finding such a system would solve the long-standing problem of identifying a single dual, rather than an ensemble of theories, as expected from orthodox AdS/CFT.

In this contribution, we will give a very brief overview of the JT/matrix model duality and show the structural similarity of JT correlators and stochastically projected periodic orbit sums, at the level of the one-point function, as well as propose a candidate dual system.

[1] P. Saad, S. Shenker, D. Stanford, arXiv:1903.11115

[2] See e.g. M. Gutzwiller, *Chaos in classical and quantum mechanics*, Springer 2019

DY 7.6 Wed 11:15 H6

**Entanglement entropy of fractal states** — GIUSEPPE DE TOMASI<sup>1</sup> and ●IVAN KHAYMOVICH<sup>2</sup> — <sup>1</sup>T.C.M. Group, Cavendish Laboratory, JJ Thomson Avenue, Cambridge CB3 0HE, United Kingdom — <sup>2</sup>Max Planck Institute for the Physics of Complex Systems

In this talk we will discuss the relations between entanglement (and Renyi) entropies and fractal dimensions  $D_q$  of many-body wavefunctions.

As a simple example we introduce a new class of *sparse* random pure states being fractal in the corresponding computational basis and show that their entropies reach the upper bound of Page value for fractal di-

mension larger than the subsystem size ( $D_q > 0.5$  for equipartitioning) and grow linearly with  $D_q$  otherwise.

Moreover this dependence poses the upper bound for entanglement and Renyi entropies for any multifractal states and uncovers the relation between multifractality and entanglement properties of many-body wavefunctions.

**15 min. break.**

DY 7.7 Wed 11:45 H6

**Chaos for Interacting Bosons and Random Two-Body Hamiltonians** — LUKAS PAUSCH<sup>1</sup>, EDOARDO CARNIO<sup>1,2</sup>, ANDREAS BUCHLEITNER<sup>1,2</sup>, and ALBERTO RODRÍGUEZ<sup>3</sup> — <sup>1</sup>Physikalisches Institut, Albert-Ludwigs-Universität-Freiburg, Hermann-Herder-Straße 3, D-79104, Freiburg, Germany — <sup>2</sup>EUCOR Centre for Quantum Science and Quantum Computing, Albert-Ludwigs-Universität Freiburg, Hermann-Herder-Straße 3, D-79104, Freiburg, Germany — <sup>3</sup>Departamento de Física Fundamental, Universidad de Salamanca, E-37008 Salamanca, Spain

We investigate the chaotic phase of the Bose-Hubbard model [1] in relation to the bosonic embedded random-matrix ensemble, which mirrors the dominant few-body nature of many-particle interactions, and hence the Fock space sparsity of quantum many-body systems. Within the chaotic regime, mean and fluctuations of the fractal dimensions of Bose-Hubbard eigenstates show clear fingerprints of ergodicity and are well described by the embedded ensemble, which is furthermore able to capture the energy dependence of the chaotic phase. Despite such agreement, the distributions of the fractal dimensions for these two models depart from each other and from the Gaussian orthogonal ensemble as Hilbert space grows.

[1] L. Pausch et al, Phys. Rev. Lett. **126**, 150601 (2021).

DY 7.8 Wed 12:00 H6

**Orthogonal quantum many-body scars** — HONGZHENG ZHAO<sup>1</sup>, ADAM SMITH SMITH<sup>2</sup>, FLORIAN MINTERT<sup>1</sup>, and JOHANNES KNOLLE<sup>1,3,4</sup> — <sup>1</sup>Blackett Laboratory, Imperial College London, London, United Kingdom — <sup>2</sup>School of Physics and Astronomy, University of Nottingham, University Park, Nottingham, United Kingdom — <sup>3</sup>Department of Physics TQM, Technical University of Munich, Munich, Germany — <sup>4</sup>Munich Center for Quantum Science and Technology, Munich, Germany

Quantum many-body scars have been put forward as counterexamples to the Eigenstate Thermalization Hypothesis. These atypical states are observed in a range of correlated models as long-lived oscillations of local observables in quench experiments starting from selected initial states. The long-time memory is a manifestation of quantum non-ergodicity generally linked to a sub-extensive generation of entanglement entropy, the latter of which is widely used as a diagnostic for identifying quantum many-body scars numerically as low entanglement outliers. Here we show that, by adding kinetic constraints to a fractionalized orthogonal metal, we can construct a minimal model with orthogonal quantum many-body scars leading to persistent oscillations with infinite lifetime coexisting with rapid volume-law entanglement generation. Our example provides new insights into the link between quantum ergodicity and many-body entanglement while opening new avenues for exotic non-equilibrium dynamics in strongly correlated multi-component quantum systems. Reference: <https://arxiv.org/abs/2102.07672>

DY 7.9 Wed 12:15 H6

**Genuine many-body quantum scarring in a periodic Bose-Hubbard ring** — QUIRIN HUMMEL and PETER SCHLAGHECK — Université de Liège (Belgium)

Quantum scars have been known for decades to exist in quantum systems of low dimensionality (e.g. “quantum billiards”): While most

eigenstates of a classically chaotic system are typically spread across the accessible phase space, individual states exist that are concentrated along unstable classical periodic orbits. On the other hand, recent studies in many-body quantum systems that admit no known meaningful classical limits have revealed eigenstates - now termed “quantum many-body scars” - that feature quantum mechanical properties reminiscent of scenarios of quantum scarring. An unambiguous classification as scars in the original sense, however, remains controversial, if not fundamentally impossible due to the lack of a classical limit. In order to bridge this gap, we investigate the phenomenon of quantum scarring in the prototypical Bose-Hubbard model, a many-body quantum system that combines both, a well-defined formally classical description and the typical high-dimensionality of many-body systems identified with the number of sites that constitute the one-body state space.

DY 7.10 Wed 12:30 H6

**Quantum scars of bosons with correlated hopping** — ANA HUDOMAL<sup>1,2</sup>, IVANA VASIĆ<sup>2</sup>, NICOLAS REGNAULT<sup>3,4</sup>, and ZLATKO PAPIĆ<sup>1</sup> — <sup>1</sup>School of Physics and Astronomy, University of Leeds, United Kingdom — <sup>2</sup>Institute of Physics Belgrade, University of Belgrade, Serbia — <sup>3</sup>Joseph Henry Laboratories and Department of Physics, Princeton University, USA — <sup>4</sup>Laboratoire de Physique de l’École Normale Supérieure, ENS, CNRS, Paris, France

Recent experiments have shown that preparing an array of Rydberg atoms in a certain initial state can lead to unusually slow thermalization and persistent density oscillations [1]. This type of non-ergodic behavior has been attributed to the existence of “quantum many-body scars”, i.e., atypical eigenstates that have high overlaps with a small subset of vectors in the Hilbert space. Periodic dynamics and many-body scars are believed to originate from a “hard” kinetic constraint: due to strong interactions, no two neighbouring Rydberg atoms are both allowed to be excited. Here we propose a realization of quantum many-body scars in a 1D bosonic lattice model with a “soft” constraint: there are no restrictions on the allowed boson states, but the amplitude of a hop depends on the occupancy of the hopping site. We find that this model exhibits similar phenomenology to the Rydberg atom chain, including weakly entangled eigenstates at high energy densities and the presence of a large number of exact zero energy states [2].

[1] H. Bernien et al., Nature **551**, 579 (2017).

[2] A. Hudomal et al., Commun. Phys. **3**, 99 (2020).

DY 7.11 Wed 12:45 H6

**Quantum local random networks and the statistical robustness of quantum scars** — FEDERICA MARIA SURACE<sup>1,2</sup>, MARCELLO DALMONTE<sup>1,2</sup>, and ALESSANDRO SILVA<sup>1</sup> — <sup>1</sup>International School for Advanced Studies (SISSA), via Bonomea 265, 34136 Trieste, Italy — <sup>2</sup>The Abdus Salam International Centre for Theoretical Physics (ICTP), Strada Costiera 11, 34151 Trieste, Italy

We investigate the emergence of quantum scars in a general ensemble of random Hamiltonians (of which the PXP is a particular realization), that we refer to as quantum local random networks. We find two types of scars, that we call stochastic and statistical. We identify specific signatures of the localized nature of these eigenstates by analyzing a combination of indicators of quantum ergodicity and properties related to the network structure of the model. Within this parallelism, we associate the emergence of statistical scars to the presence of motifs in the network, that reflects how these are associated to links with anomalously small connectivity (as measured, e.g., by their betweenness). Most remarkably, statistical scars appear at well-defined values of energy, predicted solely on the basis of network theory. We study the scaling of the number of statistical scars with system size: below a threshold connectivity, we find that the number of statistical scars increases with system size. This allows to define the concept of statistical stability of quantum scars.



## Transport dynamics in optical lattices with flux

A. Hudomal<sup>1</sup>, I. Vasić<sup>1</sup>, H. Buljan<sup>2</sup>, W. Hofstetter<sup>3</sup>, and A. Balaž<sup>1</sup>

<sup>1</sup>*Scientific Computing Laboratory, Center for the Study of Complex Systems,  
Institute of Physics Belgrade, University of Belgrade, Serbia*

<sup>2</sup>*Department of Physics, University of Zagreb, Croatia*

<sup>3</sup>*Institut für Theoretische Physik, Johann Wolfgang Goethe-Universität,  
Frankfurt am Main, Germany*

e-mail:ana.hudomal@ipb.ac.rs

Recent cold atom experiments have realized artificial gauge fields in periodically modulated optical lattices [1,2]. We study the dynamics of atomic clouds in such systems by performing numerical simulations using the full time-dependent Hamiltonian and compare results with the semiclassical approximation. Under constant external force, atoms in optical lattices with flux exhibit an anomalous velocity in the transverse direction. We investigate in detail how this transverse drift is related to the Berry curvature and Chern number, taking into account realistic experimental conditions.

### REFERENCES

- [1] G. Jotzu, M. Messer, R. Desbuquois, M. Lebrat, T. Uehlinger, D. Greif, T. Esslinger, *Nature* **515**, 237 (2014).
- [2] M. Aidelsburger, M. Lohse, C. Schweizer, M. Atala, J. T. Barreiro, S. Nascimbène, N. R. Cooper, I. Bloch, N. Goldman, *Nat. Phys.* **11**, 162 (2015).

## Excitation spectra of a Bose-Einstein condensate with an angular spin-orbit coupling

I. Vasić and A. Balaž

*Scientific Computing Laboratory, Center for the Study of Complex Systems,  
Institute of Physics Belgrade, University of Belgrade, Pregrevica 118, 11080 Belgrade, Serbia  
e-mail:ivana.vasic@ipb.ac.rs*

A theoretical model of a Bose-Einstein condensate with an angular spin-orbit coupling has recently been proposed [1,2] and it has been established that a half-skyrmion represents the ground state in a certain regime of spin-orbit coupling and interaction. We investigate low-lying excitations of this phase by using the Bogoliubov method and numerical simulations of the time-dependent Gross-Pitaevskii equation [3]. We find that a sudden shift of the trap bottom results in a complex two-dimensional motion of the system's center of mass. This response is markedly different from the response of a competing phase, and comprises two dominant frequencies. Moreover, the breathing mode frequency of the half-skyrmion is set by both the spin-orbit coupling and the interaction strength, while in the competing state it takes a universal value. Effects of interactions are especially pronounced at the transition between the two phases.

### REFERENCES

- [1] M. DeMarco and H. Pu, Phys. Rev. A 91, 033630 (2015).
- [2] Y.-X. Hu, C. Miniatura, and B. Grémaud, Phys. Rev. A 92, 033615 (2015).
- [3] I. Vasić and A. Balaž, Phys. Rev. A 94, 033627 (2016).

## Searching for quantum scars in constrained bosonic models

A. Hudomal<sup>1</sup>, I. Vasić<sup>1</sup>, N. Regnault<sup>2</sup> and Z. Papić<sup>3</sup>

<sup>1</sup>*Scientific Computing Laboratory, Center for the Study of Complex Systems,  
Institute of Physics Belgrade, University of Belgrade, Serbia*

<sup>2</sup>*Laboratoire de Physique de l'Ecole Normale Supérieure, ENS, Université PSL,  
CNRS, Sorbonne Université, Université Paris-Diderot,  
Sorbonne Paris Cité, Paris, France*

<sup>3</sup>*School of Physics and Astronomy, University of Leeds, United Kingdom  
e-mail: hudomal@ipb.ac.rs*

Recent experiments on arrays of Rydberg atoms have shown that preparing a system in a certain initial state can lead to unusually slow thermalization and persistent density oscillations [1]. This type of non-ergodic behavior has been attributed to the existence of “quantum many-body scars”, i.e., atypical, weakly-entangled eigenstates of the system that have high overlaps with a small subset of vectors in the Hilbert space. Periodic dynamics and many-body scars are believed to originate from a “hard” kinetic constraint: due to strong interactions, no two neighbouring atoms are both allowed to be in an excited Rydberg state. Here we investigate quantum many-body scars in a 1D bosonic lattice model with a “soft” constraint: there are no restrictions on the allowed boson states and the particles can hop freely, but the amplitude of a hop depends on the occupancy of the hopping site. We find that this model exhibits similar phenomenology to the Rydberg atom chain, including weakly entangled eigenstates at high energy densities and the presence of a large number of exact zero energy states, with distinct algebraic structure. We discuss the relation of this model to the standard Bose-Hubbard model and possible experimental realizations using ultracold atoms.

### REFERENCES

[1] H. Bernien et al., *Nature* 551, 579 (2017).

## Probing fractional Hall states in driven optical lattices

I. Vasić<sup>1</sup>, A. Hudomal<sup>1</sup> and N. Regnault<sup>2</sup>

<sup>1</sup>*Scientific Computing Laboratory, Center for the Study of Complex Systems,  
Institute of Physics Belgrade, University of Belgrade, Serbia*

<sup>2</sup>*Laboratoire de Physique de l'Ecole Normale Supérieure, ENS, Université PSL,  
CNRS, Sorbonne Université, Université Paris-Diderot,  
Sorbonne Paris Cité, Paris, France  
e-mail: ivana.vasic@ipb.ac.rs*

Driven optical lattices enrich the set of quantum models that can be simulated in cold-atom experiments [1, 2]. General arguments suggest that the interplay of strong interactions and driving in a thermodynamically large system introduces heating, leading to a featureless infinite-temperature state in the long-time limit [3, 4]. Recently, several papers have focused on a possibility of prethermalization, arguing that some strongly correlated states can be probed on experimentally relevant timescales, before reaching the infinite-temperature limit [5, 6]. We investigate ways to prepare and probe fractional Hall states in a few-particle bosonic sample in a driven optical lattice.

### REFERENCES

- [1] G. Jotzu et al., *Nature (London)* 515, 237 (2014).
- [2] M. Aidelsburger et al., *Nat. Phys.* 11, 162 (2015).
- [3] L. D'Alessio, M. Rigol, *Phys. Rev. X* 4, 041048 (2014).
- [4] A. Lazarides, A. Das, R. Moessner, *Phys. Rev. E* 90, 012110 (2014).
- [5] T. Mori, T. Kuwahara, K. Saito, *Phys. Rev. Lett.* 116, 120401 (2016).
- [6] D. A. Abanin et al., *Phys. Rev. B* 95, 014112 (2017).

## Ground state and collective modes of dipolar BECs

D. Vudragović<sup>1</sup>, V. Veljić<sup>1</sup>, I. Vasić<sup>1</sup> and A. Balaž<sup>1</sup>

<sup>1</sup> *Scientific Computing Laboratory, Center for the Study of Complex Systems,  
Institute of Physics Belgrade, University of Belgrade, Serbia*  
e-mail: dusan.vudragovic@ipb.ac.rs

We study the effects of the dipole-dipole interaction on the ground state and collective modes of quasi-one-dimensional dipolar Bose-Einstein condensates of atomic gases of chromium  $^{52}\text{Cr}$ , erbium  $^{168}\text{Er}$ , and dysprosium  $^{164}\text{Dy}$ . Through extensive numerical simulations and detailed variational treatment, we analyze the dependence of condensate widths on the dipole-dipole interaction strength, as well as the interaction-induced frequency shifts of collective oscillation modes. Furthermore, we show that the Gaussian variational approach gives a good qualitative description of the system's ground state, and an excellent quantitative description of the condensates' low-lying excitation modes.

## Transport of cold bosonic atoms in optical lattices

I. Vasić and J. Vučićević

*Institute of Physics Belgrade, University of Belgrade, Serbia*

e-mail: [ivana.vasic@ipb.ac.rs](mailto:ivana.vasic@ipb.ac.rs)

Cold atoms in optical lattices provide a clean realization of the Hubbard model. While the focus of early experiments was on understanding quantum phase transitions driven by the interplay of hopping and local interactions [1], more recent experiments aim at studying quantum transport in these setups. The onset of bad-metal behavior, characterized by the resistivity linear in temperature, has been investigated recently [2,3]. While the conductivity of the fermionic version of the model has been addressed in much detail both from the theoretical and experimental perspective, far less is known about transport in the bosonic version [4]. We investigate conductivity in the strongly-interacting regime of the Bose-Hubbard model. We address the high-temperature regime and use numerically exact calculations for small lattice sizes. At weak tunneling, we find multiple peaks in the optical conductivity that stem from the Hubbard bands present in the many-body spectrum. This feature is slowly reduced as the tunneling rate gets stronger. Further, we find the regime of linear resistivity. When the interactions are very strong, the leading inverse-temperature coefficient in conductivity is proportional to the tunneling amplitude. As the tunneling becomes stronger, this dependence takes quadratic form.

### REFERENCES

- [1] I. Bloch *et al.*, Rev. Mod. Phys. 80, 885 (2008).
- [2] P.T. Brown *et al.*, Science 363, 379 (2019).
- [3] J. Vučićević *et al.*, Phys. Rev. Lett. 123, 036601 (2019).
- [4] N.H. Lindner, A. Auerbach, Phys. Rev. B 81, 054512 (2010).



# Searching For Quantum Scars In Constrained Bosonic Models

Ana Hudomal<sup>a</sup>, Ivana Vasić<sup>a</sup>, Nicolas Regnault<sup>b</sup> and Zlatko Papić<sup>c</sup>

<sup>a</sup>*Scientific Computing Laboratory, Center for the Study of Complex Systems, Institute of Physics  
Belgrade, University of Belgrade, Serbia*

<sup>b</sup>*Laboratoire de Physique de l'Ecole Normale Supérieure, ENS, Université PSL, CNRS, Sorbonne  
Université, Université Paris-Diderot, Sorbonne Paris Cité, Paris, France*

<sup>c</sup>*School of Physics and Astronomy, University of Leeds, United Kingdom*

**Abstract.** Recent experiments on arrays of Rydberg atoms have shown that preparing a system in a certain initial state can lead to unusually slow thermalization and persistent density oscillations [1]. This type of non-ergodic behavior has been attributed to the existence of “quantum many-body scars”, i.e., atypical, weakly-entangled eigenstates of the system that have high overlaps with a small subset of vectors in the Hilbert space. Periodic dynamics and many-body scars are believed to originate from a “hard” kinetic constraint: due to strong interactions, no two neighbouring atoms are both allowed to be in an excited Rydberg state. Here we investigate quantum many-body scars in a 1D bosonic lattice model with a “soft” constraint: there are no restrictions on the allowed boson states and the particles can hop freely, but the amplitude of a hop depends on the occupancy of the hopping site. We find that this model exhibits similar phenomenology to the Rydberg atom chain, including weakly entangled eigenstates at high energy densities and the presence of a large number of exact zero energy states, with distinct algebraic structure. We discuss the relation of this model to the standard Bose-Hubbard model and possible experimental realizations using ultracold atoms.

## REFERENCES

1. H. Bernien, S. Schwartz, A. Keesling, H. Levine, A. Omran, H. Pichler, S. Choi, A. S. Zibrov, M. Endres, M. Greiner, V. Vuletić, and M. D. Lukin, *Nature* **551**, 579-584 (2017).

# Conductivity of Cold Bosonic Atoms in Optical Lattices

Ivana Vasić and Jakša Vučićević

*Institute of Physics Belgrade, University of Belgrade, Pregrevica 118, 11080 Belgrade, Serbia*

**Abstract.** Cold atoms in optical lattices provide a clean realization of the Hubbard model. While the focus of early experiments was on understanding quantum phase transitions driven by the interplay of hopping and local interactions [1], more recent experiments aim at studying quantum transport in these setups. The onset of bad-metal behavior, characterized by the resistivity linear in temperature, has been investigated recently [2, 3]. While the conductivity of the fermionic version of the model has been addressed in much detail both from the theoretical and experimental perspective, far less is known about transport in the bosonic version [4]. We investigate conductivity in the strongly-interacting regime of the Bose-Hubbard model. We address the high-temperature regime and use numerically exact calculations for small lattice sizes. At weak tunneling, we find multiple peaks in the optical conductivity that stem from the Hubbard bands present in the many-body spectrum. This feature is slowly reduced as the tunneling rate gets stronger. Further, we find the regime of linear resistivity. When the interactions are very strong, the leading inverse-temperature coefficient in conductivity is proportional to the tunneling amplitude. As the tunneling becomes stronger, this dependence takes quadratic form.

## REFERENCES

1. Bloch I., Dalibard J., and Zwirger W., *Rev. Mod. Phys.* **80**, 885-964 (2008).
2. Brown, P. T., et al., *Science* **363**, 379-382 (2019).
3. Vučićević J., Kokalj, J., Žitko R., Wentzell N., Tanasković D., and Mravlje J., *Phys. Rev. Lett.* **123**, 036601 (2019).
4. Lindner N. H. and Auerbach A., *Phys. Rev. B* **81**, 054512 (2010).